

UC Berkeley

UC Berkeley Electronic Theses and Dissertations

Title

Time-Domain Studies as a Probe of Stellar Evolution

Permalink

<https://escholarship.org/uc/item/2mm8338z>

Author

Miller, Adam Andrew

Publication Date

2013

Peer reviewed|Thesis/dissertation

Time-Domain Studies as a Probe of Stellar Evolution

By

Adam Andrew Miller

A dissertation submitted in partial satisfaction of the

requirements for the degree of

Doctor of Philosophy

in

Astrophysics

in the

Graduate Division

of the

University of California, Berkeley

Committee in charge:

Professor Joshua S. Bloom, Chair

Professor Eliot Quataert

Professor Gibor Basri

Professor William Holzapfel

Fall 2013

Time-Domain Studies as a Probe of Stellar Evolution

Copyright 2013
by
Adam Andrew Miller

Abstract

Time-Domain Studies as a Probe of Stellar Evolution

by

Adam Andrew Miller

Doctor of Philosophy in Astrophysics

University of California, Berkeley

Professor Joshua S. Bloom, Chair

Stellar evolution proceeds on timescales of millions to billions of years, however, most stars in both the birthing and dying processes will punctuate their lives with short-lived (few days to a year) eruptions or explosions that lead to dramatic changes in the brightness of the star. Observational studies of these events are the foundation upon which time-domain astronomy is built. While these events are short lived, they often provide some of our most significant insights into stellar evolution.

This dissertation focuses on the use of time-domain techniques to discover and characterize these rare astrophysical gems, while also addressing some gaps in our understanding of the earliest and latest stages of stellar evolution. The observational studies presented herein can be grouped into three parts: (i) the study of stellar death (supernovae); (ii) the study of stellar birth; and (iii) the use of modern machine-learning algorithms to discover and classify variable sources.

I present observations of supernova (SN) 2006gy, the most luminous SN ever at the time of discovery, and the even-more luminous SN 2008es. Together, these two supernovae (SNe) demonstrate that core-collapse SNe can be significantly more luminous than thermonuclear type Ia SNe, and that there are multiple channels for producing these brilliant core-collapse explosions. For SN 2006gy I show that the progenitor star experienced violent, eruptive mass loss on multiple occasions during the centuries prior to explosion, a scenario that was completely unexpected within the cannon of massive-star evolution theory. I also present observations of SN 2008iy, one of the most unusual SNe ever discovered. Typical SNe take $\lesssim 3$ weeks to reach peak luminosity; SN 2008iy exhibited a slow and steady rise for ~ 400 days before reaching maximum brightness. The best explanation for such behavior is that the progenitor of SN 2008iy experienced an episodic phase of mass loss ~ 100 yr prior to explosion. The three SNe detailed in this dissertation have altered our understanding of massive-star mass loss, namely, these SNe provide distinct evidence that post-main sequence mass loss, for at least some massive stars, occurs in sporadic fits, rather than being steady. They also demonstrate that core collapse is not restricted to the red supergiant and Wolf-Rayet stages of

stellar evolution as theory predicted. Instead, some massive stars explode while in a luminous blue variable-like state.

I also present observations of the newly discovered FU Orionis variable, PTF 10qpf. FU Orionis stars are young stellar objects (YSOs) that exhibit long-lasting ($\gtrsim 10$ yr), large-amplitude ($\gtrsim 5$ mag) eruptions due to accretion instabilities in the star+disk system. These eruptions, for which there are precious few examples, play an important role in (i) determining the final mass and angular momentum of the newly born star, (ii) clearing the circumstellar envelope from which the star forms, and (iii) the formation of planets, and ultimately life, in the circumstellar disk. PTF 10qpf is only the fourth FU Orionis variable with detailed observations taken during the course of eruption. Furthermore, it is the best observed FU Orionis star prior to eruption, with both optical spectra and infrared photometry demonstrating that the star was a normal classical T Tauri star before its outburst. This discovery shows that the FU Orionis phenomenon is not reserved for only the most-massive YSOs, as had previously been suggested.

As robotic observing and automated data processing procedures render the standard transient discovery process mundane, we are quickly approaching an era where we will be overwhelmed with discoveries. The Large Synoptic Survey Telescope (LSST), with a planned start in 2020, is expected to discover ~ 50 million variable stars, an orders-of-magnitude leap over the currently known number of variables. As data volumes grow to these enormous sizes, it is clear that classical discovery and characterization techniques relying on the visual inspection of data are no longer tractable. In the final chapters of this dissertation, I present a scaleable machine-learning framework capable of identifying rare sources in a time-domain dataset, while also providing classifications for the most prevalent source types in the survey. Following a search of the variables identified in the All Sky Automated Survey, I discover four bright R Coronae Borealis stars, carbon-rich supergiants in a short-lived phase of late stellar evolution. The discovery of these stars, which were identified via a fully automated procedure, represent an important proof-of-concept demonstrating that advanced algorithmic procedures can unearth the rare astronomical sources that lead to leaps in our understanding of stellar evolution. I close with the presentation of a new machine-learning methodology for inferring the fundamental atmospheric properties of stars, T_{eff} , $\log g$, and [Fe/H], without obtaining spectra. While the development of these tools, which predict the atmospheric parameters from photometric light curves, are still in their infancy, I argue that their continued development will enable the conversion of large photometric time-domain surveys, such as LSST, into pseudo-spectrographs.

• • •

Astrophysical science should no longer be viewed as a static tableau but instead as the unraveling of violent beginnings in a dynamic cosmos. The use of machine learning to extract novel results from large astronomical datasets occupies an instrumental portion of a burgeoning 21st century revolution in the way we conduct ourselves as scientists – the poetic connection of this modern approach applied to the millennia-old practice of monitoring the heavens will uncover a universe of new mysteries.

For my mother and father,
who always encouraged me to pursue what I love,
consequences be damned.

Contents

List of Figures	vi
List of Tables	viii
Acknowledgments	xi
Preface	xiii
1 Introduction	1
1.1 History of Time-Domain Astronomy	2
1.1.1 Early Discoveries of Variable Sources: \sim 1600–1900	2
1.1.2 The Golden Era: \sim 1900–1930	4
1.1.3 The Pan-Chromatic Era: \sim 1960–1990s	6
1.1.4 The Modern Era: Second Coming of the Golden Age	7
1.2 What’s Inside? An Outline of this Dissertation	9
1.2.1 Death	9
1.2.2 Birth	13
1.2.3 Rise of the Machines	14
2 The Exceptionally Luminous Type II-L SN 2008es	17
2.1 Introduction	17
2.2 Observations	18
2.3 Photometric Results	26
2.4 Spectroscopy	30
2.5 Discussion	31
2.5.1 The Physical Nature of SN 2008es	31
2.5.2 The Host of SN 2008es	33
2.5.3 Rates of Extremely Luminous SN 2008es-like Events	35
2.6 Conclusions	35
3 New Observations of the Very Luminous Supernova 2006gy: Evidence for Echoes	37
3.1 Introduction	37

3.2	Observations	40
3.3	Discussion	45
3.3.1	Early-Time NIR Observations	45
3.3.2	Late-Time NIR Observations	47
3.3.3	Observed Color Evolution from HST Observations	56
3.3.4	Location of the Scattering Dust	58
3.4	Conclusions and Future Work	61
4	SN 2008iy: An Unusual Type IIn Supernova with an Enduring 400 Day Rise Time	65
4.1	Introduction	66
4.2	Observations	66
4.2.1	Photometry	66
4.2.2	Spectroscopy	71
4.2.3	Host Galaxy	71
4.3	Results	73
4.3.1	Photometric Analysis	73
4.3.2	Spectroscopic Analysis	74
4.3.3	X-ray Analysis	79
4.4	Discussion	79
4.4.1	Mass Loss in the SN 2008iy Progenitor	79
4.4.2	Late-Time Emission and the Similarity to SN 1988Z	82
4.4.3	Origin of the 400 Day Rise Time and Implications for the Progenitor	83
4.4.4	Similarities to Very Luminous SNe IIn	86
4.4.5	The Host of SN 2008iy	87
4.5	Conclusions	88
5	Evidence for an FU Orionis-like Outburst from a Classical T Tauri Star	90
5.1	Introduction	91
5.2	Pre-Outburst Observations of LkH α 188-G4	92
5.3	2009 and 2010 Observations	95
5.3.1	Optical Photometry and an Independent Discovery	95
5.3.2	Near-Infrared Photometry	98
5.3.3	Optical Spectroscopy	100
5.4	Analysis	102
5.4.1	Image Morphology and Photometric Analysis	102
5.4.2	Spectroscopic Analysis	105
5.5	Discussion and Conclusions	114
6	Discovery of Bright Galactic R Coronae Borealis and DY Persei Variables: Rare Gems Mined from ACVS	116
6.1	Introduction	117

6.2	Candidate Selection	119
6.2.1	Advantages of Machine-Learning Classification	119
6.2.2	The Training Set	120
6.2.3	The Candidates	122
6.2.4	Feature Importance	123
6.3	Archival Data and New Observations	125
6.3.1	ASAS Photometry	125
6.3.2	Spectroscopy	127
6.4	Analysis	127
6.4.1	Spectroscopic Confirmation	127
6.4.2	Photometric Behavior	132
6.4.3	Pulsations	134
6.4.4	Spectral Energy Distributions	135
6.4.5	Near-Infrared Variability	138
6.5	Individual Stars	139
6.5.1	ASAS 170541–2650.1 (GV Oph)	139
6.5.2	ASAS 162229–4835.7 (IO Nor)	139
6.5.3	ASAS 165444–4925.9 (C* 2377)	140
6.5.4	ASAS 203005–6208.0 (NSV 13098)	140
6.5.5	ASAS 191909–1554.4 (V1942 Sgr)	140
6.5.6	ASAS 162232–5349.2 (C* 2322)	141
6.5.7	ASAS 065113+0222.1 (C* 596)	141
6.5.8	ASAS 182658+0109.0 (C* 2586)	141
6.6	Discussion	141
6.6.1	New Candidates From An Expanded Training Set	141
6.6.2	Future Improvements to the Classifier	143
6.7	Conclusions	145
7	A Systematic, Spectroscopic Survey of Optical Variability	147
7.1	Introduction	148
7.2	Survey Design	149
7.2.1	Sloan Digital Sky Survey – Stripe 82	149
7.2.2	Hectospec	150
7.2.3	Target Selection	152
7.3	Observations and Reductions	156
7.3.1	Hectospec Observations	156
7.3.2	Reductions	159
7.3.3	Stellar Atmospheric Parameters Estimation	160
7.4	Analysis of Variable Sources	161
7.4.1	Photometric Characteristics	161
7.4.2	Spectroscopic Characteristics	165
7.5	Estimating T_{eff} , $\log g$, and [Fe/H] From Light Curves	167

7.5.1	Random Forest Regression	167
7.5.2	Colors vs. Light Curves	170
7.5.3	RFR Model Optimization	171
7.6	Discussion	180
7.6.1	Conclusions	180
7.6.2	Future Improvements to the Regression Models	181
7.6.3	The Future of Time-Domain Surveys	182
A	Publications	248
Bibliography		252

List of Figures

1.1	HR diagram highlighting the variables presented in this dissertation	3
1.2	Light curves of variable sources showing extreme variability	12
2.1	Light curve of SN 2008es	22
2.2	Spectral evolution of SN 2008es.	25
2.3	Spectral comparisons of SN 2008es to two SNe II-L	27
2.4	Photospheric and bolometric luminosity evolution of SN 2008es	28
2.5	SEDs of SN 2008es corrected for Galactic extinction.	29
2.6	Velocity evolution of He I and H β	32
2.7	Rest-frame brightness evolution of the five most luminous known SNe	34
3.1	Example subtraction of PAIRITEL NIR images of SN 2006gy	41
3.2	Light curve of SN 2006gy	42
3.3	Late-time optical and NIR images of SN 2006gy	46
3.4	SED evolution of SN 2006gy	48
3.5	Bolometric luminosity of SN 2006gy	51
3.6	Schematic diagram of an IR echo	54
3.7	Late-time SED of SN 2006gy	57
3.8	Evidence for a scattered-light echo from the blue optical emission from SN 2006gy	59
3.9	Position of the scattering dust, D , as a function of g and ω	62
4.1	The rise and decline of SN 2008iy	68
4.2	Filtered photometry of SN 2008iy	70
4.3	Spectral sequence of SN 2008iy	72
4.4	Detailed view of the H α profile of SN 2008iy	76
4.5	Evolution of the H α profile of SN 2008iy	78
5.1	SED of LkH α 188-G4 before and after eruption	94
5.2	P48 light curve showing the outburst of LkH α 188-G4/PTF 10qpf	96
5.3	False-color <i>riz</i> image of PTF 10qpf	99
5.4	Optical reflection nebula surrounding PTF 10qpf	103
5.5	False-color <i>JHK_s</i> image of PTF 10qpf	104
5.6	Low-resolution spectra of PTF 10qpf	105

5.7	Spectral comparison of PTF 10qpf	107
5.8	Keck HIRES spectra of PTF 10qpf	108
5.9	Keck HIRES high-resolution spectra of the Li I λ 6706 and Ca I λ 6717 region of PTF 10qpf	110
5.10	Fe I profiles displayed by PTF 10qpf	111
5.11	TripleSpec NIR spectrum of PTF 10qpf	112
6.1	Optical finding charts of the newly discovered RCB stars and DYPers	124
6.2	Dangers of selecting candidate sources via hard cuts in a many dimensional space	126
6.3	ASAS V-band light curves of newly discovery RCB stars and DYPers	128
6.4	Blue optical spectra of the new candidate RCB stars	130
6.5	Blue optical spectra of the four new DYPer candidates	131
6.6	Evidence for periodic variability in RCB stars	136
6.7	SEDs for newly discovered RCB stars and DYPers	137
6.8	Light curves of candidate new RCB stars	144
7.1	Color-color diagrams for variables in Stripe 82	151
7.2	Color-color diagrams showing Hectospec targets	157
7.3	Skewness distribution for stellar variables in Stripe 82	163
7.4	MAD in the g band versus MAD in the i for stellar variables	164
7.5	T_{eff} against $\log g$ for stellar UW VSC sources	166
7.6	Light-curve features against atmospheric parameters (1)	168
7.7	Light-curve features against atmospheric parameters (2)	169
7.8	Random forest regression using photometric colors and light-curve features	172
7.9	Forward feature selection for T_{eff}	175
7.10	Forward feature selection for $\log g$	176
7.11	Forward feature selection for [Fe/H]	177
7.12	Optimal random forest model selection	178
7.13	Final random forest regression models for T_{eff} , $\log g$, and [Fe/H]	179

List of Tables

2.1	PAIRITEL Observations of SN 2008es	19
2.2	KAIT Observations of SN 2008es	20
2.3	Nickel Observations of SN 2008es	21
2.4	PFCam Observations of SN 2008es	21
2.5	UVOT Observations of SN 2008es	23
2.5	UVOT Observations of SN 2008es	24
2.6	Log of Spectroscopic Observations	26
3.1	PAIRITEL Observations of SN 2006gy	43
3.1	PAIRITEL Observations of SN 2006gy	44
3.2	Keck AO Observations of SN 2006gy	45
3.3	HST day 810 Observations of SN 2006gy	45
4.1	Deep Sky Observations of SN 2008iy	67
4.2	PAIRITEL Observations of SN 2008iy	69
4.3	Nickel Observations of SN 2008iy	70
4.4	UVOT Observations of SN 2008iy	71
4.5	Log of spectroscopic observations	72
4.6	$\text{H}\alpha$ line widths, luminosity, equivalent width, and ratio to $\text{H}\beta$	78
5.1	IPHAS Observations of Lk $\text{H}\alpha$ 188-G4	93
5.2	P48 <i>R</i> -Band Photometry of Lk $\text{H}\alpha$ 188-G4	97
5.2	P48 <i>R</i> -Band Photometry of Lk $\text{H}\alpha$ 188-G4	98
5.3	P60 Observations of Lk $\text{H}\alpha$ 188-G4	99
5.4	PAIRITEL Observations of Lk $\text{H}\alpha$ 188-G4	100
5.5	Log of spectroscopic observations	101
6.1	Known RCB stars in ACVS	121
6.2	RCB candidates with $P(\text{RCB}) > 0.1$ from the MACC	123
6.3	Log of spectroscopic observations	129
6.4	Observational properties of new RCB stars and DYPers	133
6.5	Rejected RCB candidates	133
6.6	2MASS and DENIS NIR measurements	139

6.7	New RCB/DYPer candidates using an augmented training set	142
7.1	Summary of Variable Sources in Stripe 82	153
7.2	Summary of Hectospec Target Priorities	155
7.3	Summary of Hectospec Observations	158
7.4	Results from the Optimal RFR Models	180
7.5	SSPP Stellar Parameters for Hectospec Targets	183
7.5	SSPP Stellar Parameters for Hectospec Targets	184
7.5	SSPP Stellar Parameters for Hectospec Targets	185
7.5	SSPP Stellar Parameters for Hectospec Targets	186
7.5	SSPP Stellar Parameters for Hectospec Targets	187
7.5	SSPP Stellar Parameters for Hectospec Targets	188
7.5	SSPP Stellar Parameters for Hectospec Targets	189
7.5	SSPP Stellar Parameters for Hectospec Targets	190
7.5	SSPP Stellar Parameters for Hectospec Targets	191
7.5	SSPP Stellar Parameters for Hectospec Targets	192
7.5	SSPP Stellar Parameters for Hectospec Targets	193
7.5	SSPP Stellar Parameters for Hectospec Targets	194
7.5	SSPP Stellar Parameters for Hectospec Targets	195
7.5	SSPP Stellar Parameters for Hectospec Targets	196
7.5	SSPP Stellar Parameters for Hectospec Targets	197
7.5	SSPP Stellar Parameters for Hectospec Targets	198
7.5	SSPP Stellar Parameters for Hectospec Targets	199
7.5	SSPP Stellar Parameters for Hectospec Targets	200
7.5	SSPP Stellar Parameters for Hectospec Targets	201
7.5	SSPP Stellar Parameters for Hectospec Targets	202
7.5	SSPP Stellar Parameters for Hectospec Targets	203
7.5	SSPP Stellar Parameters for Hectospec Targets	204
7.5	SSPP Stellar Parameters for Hectospec Targets	205
7.5	SSPP Stellar Parameters for Hectospec Targets	206
7.5	SSPP Stellar Parameters for Hectospec Targets	207
7.5	SSPP Stellar Parameters for Hectospec Targets	208
7.5	SSPP Stellar Parameters for Hectospec Targets	209
7.5	SSPP Stellar Parameters for Hectospec Targets	210
7.5	SSPP Stellar Parameters for Hectospec Targets	211
7.5	SSPP Stellar Parameters for Hectospec Targets	212
7.5	SSPP Stellar Parameters for Hectospec Targets	213
7.5	SSPP Stellar Parameters for Hectospec Targets	214
7.5	SSPP Stellar Parameters for Hectospec Targets	215
7.5	SSPP Stellar Parameters for Hectospec Targets	216
7.5	SSPP Stellar Parameters for Hectospec Targets	217
7.5	SSPP Stellar Parameters for Hectospec Targets	218

7.5	SSPP Stellar Parameters for Hectospec Targets	219
7.5	SSPP Stellar Parameters for Hectospec Targets	220
7.5	SSPP Stellar Parameters for Hectospec Targets	221
7.5	SSPP Stellar Parameters for Hectospec Targets	222
7.5	SSPP Stellar Parameters for Hectospec Targets	223
7.5	SSPP Stellar Parameters for Hectospec Targets	224
7.5	SSPP Stellar Parameters for Hectospec Targets	225
7.5	SSPP Stellar Parameters for Hectospec Targets	226
7.5	SSPP Stellar Parameters for Hectospec Targets	227
7.5	SSPP Stellar Parameters for Hectospec Targets	228
7.5	SSPP Stellar Parameters for Hectospec Targets	229
7.5	SSPP Stellar Parameters for Hectospec Targets	230
7.5	SSPP Stellar Parameters for Hectospec Targets	231
7.5	SSPP Stellar Parameters for Hectospec Targets	232
7.5	SSPP Stellar Parameters for Hectospec Targets	233
7.5	SSPP Stellar Parameters for Hectospec Targets	234
7.5	SSPP Stellar Parameters for Hectospec Targets	235
7.5	SSPP Stellar Parameters for Hectospec Targets	236
7.5	SSPP Stellar Parameters for Hectospec Targets	237
7.5	SSPP Stellar Parameters for Hectospec Targets	238
7.5	SSPP Stellar Parameters for Hectospec Targets	239
7.5	SSPP Stellar Parameters for Hectospec Targets	240
7.5	SSPP Stellar Parameters for Hectospec Targets	241
7.5	SSPP Stellar Parameters for Hectospec Targets	242
7.5	SSPP Stellar Parameters for Hectospec Targets	243
7.5	SSPP Stellar Parameters for Hectospec Targets	244
7.5	SSPP Stellar Parameters for Hectospec Targets	245
7.5	SSPP Stellar Parameters for Hectospec Targets	246
7.5	SSPP Stellar Parameters for Hectospec Targets	247

Acknowledgments

More than any other portion of this dissertation, I dread writing these acknowledgments. During the course of conducting the research described herein, I received help and support from an almost endless list of people; I want to thank all of you, but, much to my dismay, I fear that I will forget someone.

I must begin by recognizing my advisor Josh Bloom, without whom I never would have learned to step back from the process and identify the true importance of the work we did during that past \sim 6 years. Josh always encouraged me after failures, even when they were of the spectacular variety, and he would always push me the hardest following success. Josh: your council (and shared interest in the use of ethanol) made this dissertation possible; the achievements presented herein are a reflection of your dedication as an advisor.

I have also been fortunate to work closely with Professors Alex Filippenko and Lynne Hillenbrand during my graduate career. At times, both Alex and Lynne served as advisors, and without their help my work on supernovae and outbursting young stellar objects would have been, at best, less informed, and, at worst, patently false. I am also grateful to Professors Eliot Quataert, Gibor Basri, and Bill Holzapfel, who, along with Josh, served as my dissertation committee and provided useful feedback during both the planning and writing stages of this dissertation.

I am, and may forever remain, in debt to a large cadre of friends who happen to also be colleagues. First and foremost, I would like to thank Ryan Chornock, who taught me what it meant to work hard as a researcher and to pursue the deepest truths from the available data. Ryan: I will never forget your willingness to stay up late discussing supernova spectroscopy or the latest sporting results; I was so depressed when you left Berkeley that my research was rudderless for several consecutive months. Dan Perley essentially taught me everything I know about photometry and never tired of my endless stream of questions during my first year at Berkeley. Dan: I will never forget your ability to shun food in favor of a computer screen while pursing the latest and greatest transient. I had countless interesting and productive conversations with Dovi Poznanski. Dovi: I have often considered taking up smoking so that we could take more cigarette breaks together. Ryan, Jeff, Mo, and Thea: you all left before me so I have never had the chance to call a SNAGMRF meeting to order. Maybe one day at an upcoming reunion. Nathan Smith got me hooked on interacting supernovae, an addiction that yielded \sim 50% of this dissertation. Peter Nugent always made time to help me develop software pipelines, even if he never made time to play me in basketball. My research on young

stellar objects would not have been possible without the help of Kevin Covey, who I hope will one day learn that nothing bad will happen if he shares a taste of his beer. Weidong Li was always busy, and always happy to immediately drop whatever he was working on to help me with whatever I was working on. Weidong: I still eat vegetables every day and will never stop refining my ping pong technique, though I doubt I will ever reach your level. Nat Butler got me started on thinking about advanced statistical techniques as applied to astronomy, and introduced me to the wonders of balance bikes. Brad Cenko drove me to countless rounds of golf, during which we would always talk at least a little bit about astronomy. I bothered Dan Starr a countless number of times looking for solutions to computing problems, and he never tired of helping me. I would know almost nothing about machine learning were it not for Joey Richards, who introduced me to the In-N-Out challenge, which may not have been a good thing. Finally, I wish to thank Chris Klein, who took his lumps right along with me on the many projects that we have collaborated on over the years. If ever they make a bad buddy cop movie about two astronomers I am positive that film will star Chris and myself.

Additionally, I want to thank all the folks that have helped me obtain data or flesh out ideas over the years. Without K. Stassun, A. Gal-Yam, M. Kasliwal, I. Kleiser, S. Kulkarni, N. Law, P. Muirhead, E. Ofek, R. Quimby, J. Eisner, B. Rojas-Ayala, R. Dekany, G. Rahmer, D. Hale, R. Smith, J. Jacobsen, J. Zolkower, V. Velur, R. Walters, J. Henning, K. Bui, D. McKenna, L. Rebull, J. Johnson, J. S. Pineda, M. Bottom, P. Thrasher, M. Kislayk, J. Rex, J. Choi, J. Kong, K. Clubb, A. Morgan, D. Cohen and I. Shivvers, R. Hernandez, A. Miranda, M. Hernandez, C. V. Griffith, N. Joubert, B. Macomber, M. Kandrashoff, and A. Morton significant portions of this dissertation would not have been possible. The front office staff of the Berkeley astronomy department, especially Dexter and Nina, have always been helpful while doing whatever they can to help me avoid getting stuck within the existing bureaucratic muck so that I could focus on my research.

I also wish to thank Simon Hodgkin, Suzanne Aigrain, and Jonathan Irwin for getting me hooked on time-domain astronomy. I may have never walked the path of this dissertation were it not for you guys.

I am deeply thankful to have received two fellowships that supported me during my time as a graduate student. Without the UC Berkeley Chancellor's Fellowship and the National Science Foundation Graduate Research Fellowship, I would not have had the same freedom to pursue my research interests.

On multiple occasions during the past six years I would have lost my mind were it not for the distraction of cooking a warm, tasty meal to be consumed with a nice bottle of wine. Jon, Beem, Omer, Svetlana, Angela, and Brittany – thanks for keeping me sane (and for filling my belly).

Finally, I wish to thank my family. Hopefully I have made you proud: everyday I work hard to try and reach the same lofty heights as the rest of you.

This dissertation was typeset using the [ucastrothes](#) L^AT_EX template.

Preface

Time-domain astronomy is the study of celestial objects that “go bump in the night,” specifically, those sources whose brightness or spectral characteristics change on a timescale of, at most, a few years, but more typically only a few days. My entire career as a graduate student has focused on problems within the realm of time-domain astronomy. This started with my search for planets outside our solar-system while completing a Master’s degree at the University of Cambridge ([Miller et al. 2008a](#)), and continued with my work on supernovae (SNe), exploding stars, and variable stars with the research groups of Professors Alex Filippenko and Josh Bloom as a PhD student at the University of California – Berkeley. This latter work comprises the main body of this dissertation, which touches on the death of stars (Chapters [2–4](#)), the birth of stars (Chapter [5](#)), and a lot of the stuff in between (Chapters [6–7](#)).

It has not always been clear that repeated observations of the sky would reveal changes in the heavens. Aristotle believed that everything beyond the Sun and the Moon was made of a single permanent and incorruptible element, quintessence. This idea dominated western thought for nearly two millennia before Tycho Brahe and Johannes Kepler each observed the appearance of a previously unobserved star in 1572 and 1604, respectively.^{[1](#)} These discoveries stood in stark contrast to the idea of an incorruptible quintessence.

While we now know Aristotle’s theory to be incorrect, his basic supposition that the stars do not change is not far from the truth: the vast, vast majority of stars do not undergo any significant or observable changes. For the most part, stellar evolution proceeds at a pace that makes snails look like speed demons. Beginning with an agitated and tantrum-filled birth, followed by a more relaxed but still fitful adolescence, the stars eventually settle into a long period of relative stability. For the Sun, this period lasts about 10 billion years – I am far too impatient to wait that long!^{[2](#)} After this middle-aged phase most stars undergo a series of dramatic transformations, changing in size and temperature by factors of more than 100, before ultimately settling into a quiet death. A small, but nevertheless remarkable, subset refuse to go silently and instead punctuate their lives with a brilliant supernova. In some cases, the brightness of the exploding star rivals that of all the other stars in its host galaxy combined. These spectacular events, and others at different stages in the stellar

¹Each of these events was referred to as a nova, latin for “new star.” Novae were the most common type of variable discovered until ~1900 ([Hoffleit 1986](#)). We now know that these two particular events were supernovae, magnificent explosions that are more than 100 times brighter than a normal nova.

²I am also sure that UC Berkeley would kick me out well before we ever reached that point.

evolution cycle, have always fascinated me – they form the main focus of my dissertation. The remainder of this preface contains a brief, and non-exhaustive, overview of stellar evolution to set the stage for the following chapters. The remainder of the preface is aimed at a non-professional general audience, who, I imagine, will also enjoy the discussion on the history of time-domain astronomy in Chapter 1.

Stellar Evolution

For nearly half a century we have had evidence that the Universe is not infinitely old, a consequence of which is that all stars must have at some point been born. While a number of factors contribute to the diverse ways in which a star can die, all stars are born from molecular clouds. Molecular clouds are self-gravitating objects that contain large amounts of gas and dust, up to 10 million times the mass of the sun (M_{\odot}), with low temperatures (~ 10 K)³ and high densities such that molecular gas can form. If the cloud is significantly perturbed it can fragment, with the individual remnants leading to the birth of new stars. Following fragmentation, gravity within each segment causes the gas and dust to collapse in on itself. Conservation of angular momentum prevents the gas and dust from all falling directly toward the center of the fragment, and as a result a central object is formed, which is orbited by a disk composed of gas and dust. The central object, or protostar, continues to contract due to gravity while the disk slowly deposits its material onto the protostar. Occasionally this process becomes unstable leading to an eruption from the star+disk system during which its brightness increases by a factor of ~ 100 (these outbursts, known as FU Orionis eruptions are detailed more in Chapter 5). It is within this disk of material that planets eventually form.

The contraction of the protostar leads to the compression and heating of the gas until the core temperature in the protostar reaches ~ 10 million K. At these temperatures hydrogen (H) fusion begins, whereby four H atoms are converted into helium (He). This fusion releases energy in the form of light particles, known as photons, which heat the gas to produce sufficient gas pressure to counteract the force of gravity and halt the collapse of the star. Upon reaching this balanced state of hydrostatic equilibrium, where the pressure perfectly counteracts gravity, the star continues to burn H into He in its core. This stage of a star’s life is known as the main sequence and it is the longest-lived state within the stellar lifecycle. The continued evolution and lifetime of a star following birth are almost entirely determined by the initial mass of the star, though the metallicity, fraction of the star composed of atoms heavier than He, and binarity, whether or not the star was born with a companion star, also play a role.

As the mass of a star, M_* , increases so too must the rate of fusion, since a larger pressure is needed to counteract the force of gravity. Although high-mass stars have more H fuel than

³Scientists typically measure temperatures on the “natural scale” of Kelvin (K), whereby 0 K corresponds to absolute zero. It is physically impossible for anything to be colder than 0 K. Needless to say, 10 K = $-263.15^{\circ}\text{C} = -441.67^{\circ}\text{F}$ is about as cold as it gets in the Universe.

a star similar to the Sun, they live significantly shorter lives because they consume their fuel very rapidly. A typical high-mass star, those that are born with a mass at least ~ 10 times greater than the sun, will live on the main sequence for less than 10 million years. These stars are extremely rare: as a molecular cloud fragments it is far more likely to form low mass stars, which combined with their relatively short lives means they are difficult to come by. While on the main sequence, high-mass stars are intrinsically brighter and have hotter surfaces than their lower mass counterparts. The high energy photons exert enormous pressure on the metals⁴ in the stellar atmosphere, resulting in significant winds being blown from the surfaces of these stars. As the metallicity of a high-mass star increases so does the strength of the wind, and in the most extreme cases these winds can remove \sim half of the initial stellar mass while on the main sequence.

Eventually all of the H in the core of the star is consumed and only He remains. At this point, as core H fusion halts, the pressure necessary to maintain hydrostatic equilibrium is no longer provided. The internal gravity within the core causes it to contract until it reaches a temperature of ~ 100 million K at which point He is fused into carbon (C). Meanwhile, H just outside the core is compressed as the core contracts and H fusion occurs in a shell around the core. Energy released from this shell burning causes the outer layers of the star to expand, which increases the size of the star while also causing its surface to cool. This is known as the red supergiant (RSG) phase; if strong winds have stripped the star of its outer layers while on the main sequence then there is no H envelope capable of expanding into a RSG and the star becomes a hot, compact Wolf-Rayet (WR) star. The most massive stars, those with $M_* \gtrsim 50M_\odot$, remain hot as they evolve off the main sequence and become luminous blue variable (LBV) stars. LBVs occasionally undergo large scale eruptions in their outer layers that drive significant mass loss. These eruptions can deposit substantial amounts of material in a shell or cocoon around the star. For each of these type of star, once the He fuel is consumed the core once again contracts until it is hot enough to fuse C, while outside the core there is a shell of He fusion surrounded by a shell of H fusion. The process of fuel exhaustion and core contraction continues, each time adding a new shell burning the atoms that previously were fused in the core, with successively heavier elements made until the core is composed of iron (Fe) ash. Fusing Fe to heavier elements does not release energy. Thus, once the entire core is converted to Fe there is no longer any pressure to counteract gravity and the core of the star collapses in a free fall until the neutrons within the gas reach their compressible limit. The neutrons now exert a quantum mechanical degeneracy pressure that counteracts the force of gravity, and a neutron star is born. As the outer layers of the star fall onto the neutron star they bounce and are ejected into outer space at enormous speeds $\sim 10\text{--}15,000$ km s $^{-1}$ in a spectacular explosion known as a supernova (SN).⁵ SNe are classified via their spectra: type II SNe show evidence for H in their spectra while type I do not. The observed type of core-collapse supernova (CCSN) depends on the state of the star at the time of explosion, which, in turn, determines what powers the observed luminosity:

⁴Unlike chemists, biologists, or even your everyday run-of-the-mill physicist, astronomers have an unusual convention whereby they refer to all atoms heavier than He as being “metals.”

⁵At these speeds SN ejecta could circle the Earth in about 2 seconds.

- RSGs give rise to type IIP supernovae (SNe). The energy from the explosion ionizes the H in the outer envelope. As the ionized ejecta expand and cool the free protons and electrons recombine to once again form H atoms, and in the process emit the radiation that we ultimately detect from these explosions.
- WR stars give rise to type Ib/c SNe. The radiation from these SNe is initially powered by the internal energy from the explosion, however, after only a few days time, photons emitted from radioactive material created in the explosion dominate the luminosity of the SN.
- LBVs are surrounded by massive amounts of material, and the collision of the SN ejecta with this material rapidly converts the kinetic energy of the ejecta into photons. These collision powered explosions are known as type IIn SNe.

Many of these details only became clear over roughly the past seven years, as before this time it was believed that LBVs could not explode as SNe (see Chapters 2, 3, and 4 for further details).

Following the ejection of the outer layers of the star all that remains is a neutron star; in theory some massive stars can collapse directly into a black hole (BH) at the end of their lives, however, this scenario has never been observed. Finally, it should be noted that the SNe ejecta, which include the metals formed in the core of the star, are responsible for the chemical enrichment of the universe.

Lower mass stars, similar to the Sun, spend the majority of their lives fusing H into He while on the main sequence. Within this mass range the higher mass stars have the shortest lives, while a star like the sun remains on the main sequence for \sim 10 billion years. Like the high-mass stars, these stars will eventually consume all of the H in their cores at which point the He core begins contracting. This leads to the onset of H shell burning, which dumps additional He onto the core while also expanding the radial extent of envelope of the star such that it becomes \sim 100-1000 times larger than it was on the main sequence. This is known as the red giant phase of stellar evolution. Eventually, the temperature in the core is sufficient to fuse He leading to an expansion of the core, which puts a halt to the H shell burning. The envelope contracts, though not to the main sequence size of the star, and the star stably fuses He during the horizontal branch phase of its evolution. Unlike the high-mass stars fusion will not proceed beyond C in the core. After the He is exhausted, the core contracts and He shell burning begins causing the star to expand and become an asymptotic giant branch star. During this phase strong winds on the stellar surface strip away the outer laters of the star leaving only the core, composed primarily of C and oxygen (O) which continues to contract until the electrons in the gas reach their compressible limit. This quantum mechanical degeneracy pressure restores the core to hydrostatic equilibrium once it has shrunk to roughly the size of the Earth. The leftover core, known as a white dwarf (WD) star, is hot shortly after it is born, but has no renewable energy source. As the WD radiates, it loses internal heat and continually cools and fades for all eternity. Unless the star was born with a binary companion, a fading WD is the fate of all Sun-like stars.

If the star was born with a companion, then the evolutionary path can be significantly

altered, typically after the star evolves off the main sequence. As the envelope of the primary star⁶ expands the outer layers can extend to great distances from the core such that the gravitational attraction of the secondary star is stronger than that of the primary. When this happens mass is transferred from the primary to the secondary, increasing the mass of the secondary and accelerating its evolution, while the evolution of the primary decelerates. Eventually the secondary star will become a red giant at which point it may transfer mass from its envelope onto the primary star. In this way mass transfer can occur back and forth between the stars on multiple occasions. This process is far more interesting once one of the stars has evolved to become a compact object, such as a WD, neutron star, or black hole. As material falls onto the compact object it is heated to several million K and emits X-rays. Following mass transfer, runaway He burning can occur on the surface of a neutron star leading to a short and intense outburst of X-rays. As H is added to the surface of a WD it will eventually be compressed and heated to the point of ignition whereby runaway fusion occurs on the surface of the star leading to a astoundingly bright explosion. This is the origin of novae. Novae can occur multiple times on the same WD if the donor star continues to transfer mass after an explosion. As material is added to the WD and it approaches a mass of $1.4M_{\odot}$ electron degeneracy pressure can no longer support the WD: unstable burning begins and the WD explodes as a type Ia SN. Type Ia SNe are final: the entire WD is destroyed in the explosion and there is no remnant, unlike a CCSN.

While our knowledge of the stars has progressed a great deal during the last century, there are still many gaps in our understanding of astrophysical phenomena. For instance, while we have observational evidence that massive stars undergo extreme mass loss over the course of their lives and that binary stars can transfer mass from one star to another, we still do not fully understand the physics driving these processes. To better understand these and other issues, I am, along with several other astronomers in the community, designing new observational experiments to solve some of these puzzles. This dissertation contains a variety of time-domain observations designed to improve our understanding of (i) massive stars and the connection between mass loss and supernovae, (ii) the outbursts from sun-like stars during the early stages of formation, as well as (iii) the rare, enigmatic R Coronae Borealis stars, which can suddenly and dramatically fade to the point where they are temporarily undetectable. While the relatively short duration of these different events marks them as temporary, they nevertheless have a major impact on both the stars in which they occur and their surrounding environments.

⁶The more massive star while both are on the main sequence is referred to the primary star, while the less massive star is referred to as the secondary.

Chapter 1

Introduction

The study of the time-domain has led to some of the most fundamental and surprising discoveries in the history of astronomy. Beginning with the realization that the heavens were not constant and continuing through to the recent and completely unexpected discovery that a mysterious dark energy is driving the accelerated expansion of the Universe (Riess et al. 1998; Perlmutter et al. 1999), observations of variable phenomena have routinely played an important role in our understanding of the Universe. This dissertation features multiple investigations of the time-domain probing a variety of stellar astrophysics. The phenomena discussed herein are extreme, rare, and typically characterized by large-amplitude variability.¹

The extreme phenomena characterized in this dissertation can be considered rare because they only occur during the earliest or latest stages of stellar evolution. With the exception of the final chapter, which contains a systematic survey of all types of variability, I fully ignore main-sequence stars.² An illustrated summary of the stellar variables discussed in Chapters 2–6 is shown in the Hertzsprung-Russell (HR) diagram in Figure 1.1. Eight different stellar models, derived using the **Modules for Experiments in Stellar Astrophysics** (MESA; Paxton et al. 2011) software package, show the pre-main sequence to post-main sequence evolution of stars with initial masses between $0.3\text{--}30 M_{\odot}$. The zero-age main sequence (ZAMS) is highlighted, along with the rough boundaries of the Cepheid instability strip. As a star evolves into the instability strip the κ mechanism causes the star to undergo radial pulsations. These pulsations are the cause of the observed variability in the well-known δ Scuti, RR Lyrae, and Cepheid classes of variability. Highlighted in Figure 1.1 are the approximate locations of type IIn SNe, FU Orionis stars, and R Coronae Borealis stars, all of which are featured in this dissertation. Type IIn SNe are hydrogen-rich core-collapse SNe that show evidence for interaction between the SN ejecta and a dense circumstellar medium. The origins of these explosions is debated, but recent evidence points to these SNe

¹One might facetiously suggest that I am only interested in stars whose brightness changes by at least a factor of 100. While this is not the case, investigating said sources certainly helps to combat the drudgery of Monday mornings.

²Before you scoff, I must ask: what would you find more interesting on a Monday at 9 am? A star that just exploded or a star that essentially will not change for the next 10 billion years?

coming from luminous blue variable stars (see §1.2.1, and Chapters 2, 3, and 4). FU Orionis outbursts occur when the accretion rate onto the disk of a young stellar object increases by several orders of magnitude. These eruptions are isolated to relatively low-mass stars ($\lesssim 3\text{--}4 M_{\odot}$), and occur during the pre-main sequence phase of evolution (see §1.2.2 and Chapter 5). The origin of R Coronae Borealis stars is still highly uncertain (see §1.2.3), though it is known that these stars are in a late stage of stellar evolution because there is no H in their atmospheres. They are believed to be the result of white dwarf-white dwarf mergers or the final He flash in asymptotic giant branch stars, which is why they are shown in two different locations in Figure 1.1. Chapter 6 describes the search for new Galactic R Coronae Borealis stars. Prior to outlining the major results of this dissertation, I provide a brief review of the history of time-domain astronomy below.

1.1 History of Time-Domain Astronomy

Observers of the heavens have always held a keen interest in variable phenomena. The first nova was recorded by Chinese astronomers in 2296 BCE (Hoffleit 1986), and yet, despite millennia of study and numerous observations very little was understood about the variable sky until the past \sim century. Nevertheless, the study of the time domain has led to several of the most important astronomical discoveries and continues to surprise and excite astronomers to this day.

1.1.1 Early Discoveries of Variable Sources: \sim 1600–1900

Early discoveries of variable sources were often made by pure chance as observers familiar with a constellation would recognize a star that was previously absent. Thus, all of the early discoveries were either novae or SNe. By 1596, when Fabricius discovered the variability of Mira, \sim 121 novae had been discovered (Hoffleit 1986), virtually all of them by Chinese astronomers. Efforts over the following few centuries to uncover additional variable stars were hindered by a variety of factors, including: disparate systems used to measure changes in a star’s brightness, difficulty communicating the positions of suspected variables to other astronomers, and the lack of a centralized organization to record and publish light curves, measurements of stellar brightness as a function of time.

The earliest catalog of variable stars was compiled by E. Pigott in 1786, and it contained only 12 confirmed and 38 suspected variables (Hogg 1984). Discoveries of new variables remained limited through the mid-nineteenth century. In 1844, with only 18 confirmed variables known, F.W.A. Argelander wrote *An appeal to the friends of astronomy*, which called for a cooperative effort of astronomers across the globe to compile and publish their observations of variable stars so as to achieve the most accurate records possible (Hogg 1984). Argelander considered the study of variable stars an ideal pursuit for the amateur astronomer, which had a direct influence on the founding of the American Association of Variable Star Observers (AAVSO) in 1911. Encouraged by the appeal, several observers across the globe

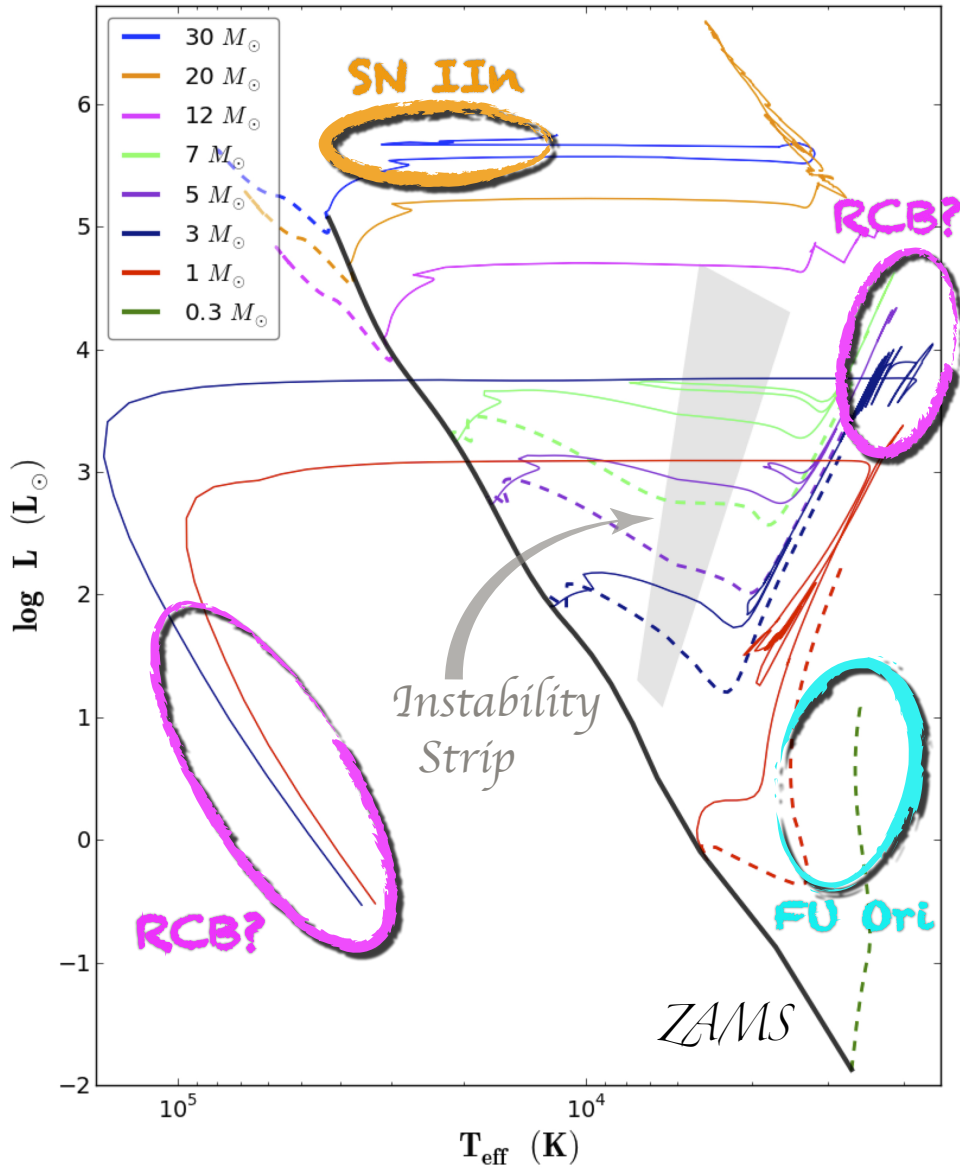


Figure 1.1: HR diagram showing the evolution of several stars as a function of stellar mass. Evolution models were derived using the MESA software package. Pre-main sequence evolution is shown as dashed lines, while post-main sequence evolution is shown as solid lines. Massive stars ($> 10 M_\odot$) are evolved through the point of core collapse, intermediate mass stars ($5-7 M_\odot$) are evolved through the asymptotic-giant-branch phase, while low mass stars ($< 3 M_\odot$) are evolved for \sim a Hubble time. Thus, only the 1 and $3 M_\odot$ stars are shown on the white-dwarf cooling track. The zero-age main sequence (ZAMS) is shown as a solid black line, while the Cepheid instability strip is highlighted by a shaded grey region. The approximate locations of type IIn SNe, R Coronae Borealis stars, and FU Orionis stars are outlined in orange, magenta, and cyan, respectively (see text for further details).

began searching for variable stars. Technological advances around 1880 significantly improved their efforts, in particular: telescope drives became accurate enough to track stars as they moved across the sky, while at the same time photographic emulsions became sensitive enough to detect stars fainter than the eye could see through a telescope (Percy 2007).

The importance of these technological advances for the study of variable stars cannot be overstated. Photographic plates, capable of imaging wide areas of the sky, could be exposed for several hours at a time allowing hundreds of variables to be studied simultaneously. Furthermore, the plates provided a physical record of the brightness and position of the stars on a given date. Measurements could be repeated and confirmed years after the initial observations took place, and systematic time-domain surveys, whereby the same regions of the sky could be repeatedly imaged, were now possible.

Around the same time the development of spectrographs became a powerful tool for studying variables as well.³ Spectroscopy allowed the variable stars to be directly compared to normal stars, while also showing clear distinctions between the different types of variables.

E.C. Pickering, the director of the Harvard College Observatory (HCO) from 1877 until his death in 1919, was particularly enthusiastic about studying and discovering variables. The HCO had observatories all over the world, and quickly established a collection of tens of thousands of plates (Hogg 1984).⁴ Building upon Argelander's earlier appeal, Pickering would write *A plan for securing observations of variable stars* in 1882, noting that he believed the study would particularly appeal to women (Hogg 1984). Indeed, the turn of the twentieth century was an extremely productive period for female astronomers as Pickering encouraged and hired dozens of female astronomers, albeit at lower wages than he paid men (Percy 2007). As Annie J. Cannon noted at the founding of the AAVSO, in 1844 at the time of Argelander's appeal only 18 variables were known, by 1911 there were 4000, most of them discovered by women (Hogg 1984).

1.1.2 The Golden Era: ~1900–1930

The earliest attempt to classify the variable stars was made by Pigott in the late 18th century. Pickering developed a more complex scheme in 1880, which he later updated in 1911 (Hogg 1984). These early efforts were important as classification and physical understanding go hand in hand, yet these initial schemes were limited to descriptions of the shape, amplitude, and time scale of the light curve (Percy 1986). Within Pickering's scheme, a correct physical understanding was available only for the Type V class, known as variables of the Algol type.

³Photographic plates, and modern electronic imagers, measure the total brightness of a star in a single bandpass, e.g., the total amount of red or blue visible light being emitted by the star. Spectrographs disperse the light from the star such that the relative brightness at all wavelengths can be measured. Thus, spectroscopy can be used to study the chemical composition of a stellar atmosphere as well as the motion of a star towards or away from the Earth.

⁴The permanence of these records is astounding. Virtually all of the plates taken by the HCO are still owned by the Smithsonian Institution, and there is a current effort to scan and digitize these plates (Grindlay et al. 2009). Once the project is complete, astronomers will have access to an unprecedented set of light curves with time baselines more than 100 yr long.

In 1783 J. Goodricke,⁵ in consultation with Pigott, surmised that the periodic decrease in brightness of the star Algol was the result of an orbiting companion passing in front of the star and eclipsing some of its light (Hoffleit 1986). Spectroscopic observations taken by H.C. Vogel in 1889 allowed him to determine the orbital parameters of Algol, thus clearly confirming Goodricke’s eclipse theory. A few decades later Russell (1912a,b) would develop the formulae necessary to measure the masses and radii of eclipsing binary stars, providing, for the first time, the tools necessary to derive the fundamental properties of the stars. To this day eclipsing binaries provide the best and most accurate measurements of stellar masses and radii (e.g., Torres et al. 2010).

A physical understanding of the other classes in Pickering’s scheme remained obscure at the turn of the twentieth century. It was often speculated that the observed variability was caused by spots on the surface of a rotating star, in analogy to the observed sunspots, however, these arguments were seldom satisfactory (Hoffleit 1986).⁶ Developing a theory for novae, Pickering’s Type Ia variables, remained particularly challenging. Brahe speculated that they were the result of cosmic vapors coalescing to create new stars. Many believed they were acts of God. Isaac Newton attributed them to the close passage of two comets, while several other theories considering collisions with comets, meteor streams, asteroids, swarms of asteroids, and planets were put forth (Hoffleit 1986). A substantially correct theory was not developed until detailed spectroscopic observations of Nova Aquilae 1918 led W.S. Adams and J. Evershed to conclude that a nova was the result of a shell of gas being thrown off a star at high velocities (Hogg 1984). Arguments invoking either spots or eclipses were typically adopted to explain the Type IIa class – long period variables, the Type IVa class – ordinary variables of short period, and the “cluster type” variables discovered by S.I. Bailey.⁷ As early as 1873 A. Ritter had proposed that pulsation, the radial expansion and contraction of a star, may be responsible for the variability of these types. It was the theoretical formalism presented in Eddington (1918, 1919), which built upon observations from Shapley (1914), that firmly established the pulsational nature of Cepheids, Miras, and RR Lyrae stars. These leaps in our understanding of pulsation came alongside a drastically improved understanding of stellar structure and evolution: A. Eddington had to develop models of the stars to explain pulsation and vice versa. All of this work culminated in his seminal book *The Internal Constitution of the Stars* (1926), which is still regarded as one of the greatest astronomical texts ever written.

It was also recognized during this time that the usefulness of variable stars is not limited

⁵It fascinates me that every resource that mentions Goodricke finds it necessary to mention that he was a deaf mute (and in a footnote to the footnote, I, too, am now guilty of such proclamations). Perhaps I am being terse, but I fail to see how being a deaf mute would prevent one from measuring brightness variations of a star, and then interpreting those variations. Now, were Goodricke blind, I would find his discovery and interpretation of the variable stars far more astounding.

⁶A century later it is interesting to note that the vast majority of the observed variable stars are indeed rotating, spotted stars (see e.g., Chapter 7, Basri et al. 2010). These variations are slight, however, rendering them undetectable with the technology available before the twentieth century.

⁷Pickering’s long period variables, ordinary variables of short period, and “cluster type variables,” are presently referred to as Mira-like, Cepheid, and RR Lyrae variables, respectively.

to providing insights into stellar structure and evolution: they were utilized to uncover some of the most important astronomical discoveries of the twentieth century. While employed by Pickering, Henrietta S. Leavitt discovered 1777 variables in the Magellanic Clouds ([Leavitt 1908](#)), and noted that Cepheid variables with long periods were brighter than those with short periods. Given that each of these variables were located within the Clouds and at roughly the same distance this landmark discovery meant that the longer-period Cepheids were more luminous. Leavitt published the Cepheid period-luminosity relation in 1912 ([Leavitt & Pickering 1912](#)). The following year E. Hertzsprung measured the distance to several Cepheid variables in the Milky Way, which enabled an absolute calibration for Leavitt's period-luminosity relation ([Hertzsprung 1913](#)). These discoveries established Cepheids as the most important distance indicator of the time.⁸ In 1924 E.P. Hubble discovered Cepheids in the Andromeda nebula and used them to measure a distance of \sim 855,000 lightyears ([Hubble 1925](#)). At the time it was unclear whether or not Andromeda and other spiral nebulae were part of the Milky Way; Hubble's measurements ended the controversy by demonstrating the nebulae to be "island universes," similar to, and not part of, the Milky Way ([Hogg 1984](#)). In the years after this discovery Hubble continued determining the distances to nebulae for which V. Slipher had taken spectra to measure their velocities. In 1929 he published the surprising discovery that not only were all extragalactic nebulae, or galaxies, moving away from the Milky Way, but the more distant galaxies were receding at greater velocities than the nearby galaxies ([Hubble 1929](#)). Conventional wisdom at the time held that the Universe was static, Hubble's observations showed that it was, in fact, expanding. Decades later it would be shown that the luminosity of type Ia SNe is related to the time it takes the SN to decline from peak brightness ([Phillips 1993](#)). Thus, like Cepheids, the distances to type Ia SNe, which are far more luminous than Cepheids and can therefore be observed in more distant galaxies, can be measured quite accurately. In 1998, observations of very distant type Ia SNe, including some obtained by the *Hubble Space Telescope*, showed that the Universe is not only expanding, but that the expansion is *accelerating* ([Riess et al. 1998](#); [Perlmutter et al. 1999](#)).⁹ Thus, variable stars have taught us that the universe is not static, while also revealing the presence of a mysterious new energy which works in opposition to gravity.

1.1.3 The Pan-Chromatic Era: \sim 1960–1990s

As the twentieth century unfolded technological advances enabled time-domain studies at wavelengths outside the traditionally studied visible range. In addition to opening a new window into the interaction of novae, SNe, and Miras with their local environments, radio observations also led to the discovery of pulsars ([Hewish et al. 1968](#)). Pulsars are magnetized

⁸It is straightforward to measure the apparent brightness of a Cepheid, while a determination of its period provides its luminosity, or intrinsic brightness. The ratio of the apparent brightness to the intrinsic brightness is related to one over the distance squared, and thus a measurement of the apparent brightness and period of a Cepheid yields its distance.

⁹The cause of this acceleration is still unknown. Without reservation it can be said that, currently, this is the biggest mystery in all of physics or astronomy.

neutron stars with beams of light that periodically sweep past the earth. They are the remnants of CCSNe. Ultraviolet (UV) observations are only possible above the atmosphere, meaning this field did not take off until the 1960s with the launching of the first UV telescopes. Spectra taken by these telescopes provided new insight into hot stars such as luminous blue variables and Wolf-Rayet stars (Percy 2007). X-rays and gamma-rays must also be observed from outer space. X-ray satellites have been launched since the 1970s, and their ability to detect emission from very hot gas has been essential to the study of compact object binaries (e.g., Blumenthal & Tucker 1974). In the 1960s the military launched several secret VELA satellites designed to detect gamma-ray emission from covert, Soviet nuclear weapon tests. Serendipitously, these satellites detected gamma-ray bursts (GRBs; Klebesadel et al. 1973), which are the most optically luminous explosions created in nature (Bloom et al. 2009; Perley et al. 2011). GRBs have two types and originate from either a special subset of CCSNe or the merger of two neutron stars.

1.1.4 The Modern Era: Second Coming of the Golden Age

Much as a few technological improvements ushered in the wide-spread use of photographic plates and the unprecedented ability to simultaneously study and discover hundreds of variable stars, the falling cost of modern detectors along with the ever-increasing capability of computers has ushered in a second golden era for time-domain astronomy. Where it once took photographic plates several hours to detect faint stars over a field of view (FOV) of several square degrees (e.g., Grindlay et al. 2009), modern instruments can detect stars that are \sim 100 times fainter in \sim 60 s (e.g., Law et al. 2009). The use of parallel processing computers enables these images to be fully reduced and analyzed just a few minutes after they have been obtained.

As a brief aside, the importance of computers in the recent advance of time-domain surveys cannot be emphasized enough. Around the turn of the 20th century variable sources were discovered by visually comparing two plates taken at separate times to see if any stars changed in brightness. While several methods and machines were developed to ease the comparisons (Hoffleit 1986), the work proved to be challenging and laborious. Currently, individual surveys routinely produce more than 100,000 images per year, as a result the visual comparison of images would prove tedious. Image subtraction (e.g., Alard & Lupton 1998) enables the direct comparison of two images taken at different times in minutes or less, while identifying variable sources that would otherwise remain undetected to the naked eye. Not only do computers rapidly reduce and analyze new observations, they also enable detailed simulations of complex phenomena, such as pulsation or mass transfer in short period binaries.

There are now dozens of recent or on-going time-domain surveys, each optimized in a different manner to study a variety of physical phenomena. Some prominent examples include the following:

1. The MACHO project (Alcock et al. 1996) observed more than 40 million stars in the

- Large Magellanic Cloud (LMC), the Small Magellanic Cloud (SMC) and the Galactic Bulge to search for massive compact halo objects via the microlensing technique.
2. The Optical Gravitational Lensing Experiment (OGLE; [Udalski et al. 1992](#)) has observed the LMC, SMC, and Galactic Bulge for more than twenty years. In addition to searching for massive compact halo objects, they have produced numerous studies discovering and classifying variable stars, with more than 400,000 classified sources identified to date (see [Soszyński et al. 2013](#) and references therein).
 3. The Lick Observatory Supernova Search ([Leaman et al. 2011](#)) monitors more than 10,000 nearby galaxies annually in order to better understand the physical processes behind stellar explosions, while also placing constraints on the relative rates of the different types of SNe ([Li et al. 2011b,a](#)).
 4. The Supernova Legacy Survey ([Astier et al. 2006](#)) searched for very distant type Ia SNe in order to precisely measure the nature of the acceleration of the universe.
 5. The Deep Lens Survey ([Becker et al. 2004](#)) searched for transient emission on short timescales from faint objects.
 6. The Faint Sky Variability Survey ([Groot et al. 2003](#)) searched for and discovered the faintest known variable stars.
 7. The All Sky Variability Survey (ASAS; [Pojmański 2001](#)) observes the entire visible sky every few nights to a faintness level similar to the old Harvard plate surveys.
 8. The *Swift* gamma-ray burst mission ([Gehrels et al. 2004](#)) continuously monitors most of the sky at X-ray wavelengths in order to detect new GRBs.
 9. The Palomar Transient Factory (PTF; [Rau et al. 2009](#)) is a systematic survey of the transient sky with a particular focus on finding explosive phenomena that are brighter than novae and fainter than SNe.
 10. The *Kepler* planet-detection mission ([Borucki et al. 2010](#)) is a space satellite that continually observed \sim 150,000 stars while searching for planets that are similar in size to that of the Earth.

The study of the time-domain has delivered tremendous progress in advancing our understanding of the Universe. In 1911 there were only 4000 known variable stars ([Hogg 1984](#)), now there are individual surveys that have discovered and classified more than 400,000 (e.g., OGLE). Some highlights over the past \sim century include: Cepheid variables in nebulae showing that the Universe extends far beyond the Milky Way, eclipsing variables providing the best and most accurate means of measuring stellar masses and radii, the discovery that the universe is expanding and later that the expansion is accelerating. Time-domain surveys continue to provide surprising results. For example, while the existence of planets outside our solar system had long been suspected, within the past 20 years it has been discovered that not only are planetary systems common around other stars, but they have a wide diversity of configurations that stand in stark contrast to our own solar system (e.g., [Mayor & Queloz 1995](#); [Marcy et al. 1997](#); [Batalha et al. 2013](#)). As the methods and instrumentation continue to advance, we can be sure that more exciting discoveries await in the years to come.

1.2 What's Inside? An Outline of this Dissertation

This dissertation contains original research that explores different stages of stellar evolution via various time-domain techniques. Broadly speaking it can be divided into three parts: (i) the study of unusual and extremely luminous SNe (Chapters 2, 3, and 4); (ii) eruptions during the birth of a sun-like star (Chapter 5), and (iii) the use of machine learning applied to modern time-domain surveys as a means toward classification and discovery of rare sources (Chapters 6 and 7).

1.2.1 Death

In 2006, around the time I started my graduate studies, the diversity of core-collapse supernovae (CCSNe) was believed to be fairly well characterized. The most massive stars ($M_* \gtrsim 40M_\odot$) would evolve off the main sequence to become luminous blue variables (LBVs), eventually shedding their entire H envelopes to become Wolf-Rayet (WR) stars, without ever passing through a red supergiant (RSG) phase (Humphreys & Davidson 1979). These stars would eventually explode giving rise to type Ib/c SNe. Less massive stars ($M_* \sim 10 - 25M_\odot$) would evolve to become RSGs before exploding as H-rich type II SNe (Heger et al. 2003). More exotic scenarios, such as a pair-instability supernova (PISN; Barkat et al. 1967; Rakavy & Shaviv 1967; Bond et al. 1984),¹⁰ were believed to be possible for extremely high-mass ($M_* \sim 100M_\odot$), low-metallicity stars, but such events were not expected to be detected in the local universe.

Following explosion, the luminosity of CCSNe could be powered via a combination of three primary mechanisms, all of which were directly observed in the famous SN 1987A, which occurred in the Large Magellanic Cloud (Arnett et al. 1989; McCray 1993):

1. The thermalization of photons produced during the radioactive decay of ^{56}Ni and ^{56}Co . Radioactivity contributes to the luminosity of all CCSNe, and it is the dominant energy source of type Ib/c SNe, which lack H in their spectra.
2. The recombination of H in the SN ejecta that was ionized as the SN shockwave passed through the outer envelope of the star. The luminosity of type IIP SNe, so named because their light curves exhibit a long plateau phase where the luminosity remains constant as a recombination wave recedes through the ejecta, are initially illuminated due to recombination for ~ 100 days before radioactivity becomes the dominant source of luminosity (Poznanski et al. 2009; Arcavi et al. 2012).
3. The collision of SN ejecta with dense material in the circumstellar medium (CSM) of the progenitor star. The luminosity of type IIn SNe is dominated via the shockwaves driven by these collisions.

¹⁰A pair-instability SN differs from a traditional CCSNe in that the core never reaches the point of Si to Fe fusion. Instead, following C fusion, electron positron pair production occurs following either gamma-ray-gamma-ray or gamma-ray-nuclei collisions, which robs the core of thermal pressure support. The star contracts leading to unstable O burning, and the resulting explosion can produce huge amounts of ^{56}Ni and a luminosity orders of magnitude larger than typical CCSNe (Scannapieco et al. 2005).

All CCSNe were known to be less luminous than the thermonuclear type Ia explosions from white dwarfs, with the exception of a few type Ic SNe associated with gamma-ray bursts (Woosley & Bloom 2006).

While the mechanism powering the luminosity of the differing types of CCSNe were well known, there were a number of outstanding questions that remained unanswered concerning the evolution of massive stars. In particular, it was unclear how the massive progenitor stars that become CCSNe map to their final SN type (Gal-Yam et al. 2007). A major factor contributing to the uncertainty in this mapping was the incomplete understanding of mass loss during post-main sequence evolution. Models and numerical simulations assumed mass loss to be steady with rates that were semi-empirical and scalable by metallicity (e.g., Maeder & Meynet 1994; Meynet et al. 1994; Langer et al. 1994; Langer 1998; Heger et al. 2003). In order for these models to match certain observations, such as WR star masses and luminosities, and the relative number of WR and OB stars, the adopted steady-state mass-loss rates had to be increased by a factor of ~ 2 relative to the empirical values (Maeder & Meynet 1994; Meynet et al. 1994). These enhanced mass-loss rates were in conflict with multiple lines of observation (e.g., Smith & Owocki 2006). For instance, even in the most extreme cases, steady, line-driven mass loss could not explain the massive envelopes observed around LBVs (Smith & Owocki 2006). The expectation of these models was also that the most massive stars ($\gtrsim 40 M_{\odot}$) would only explode after reaching the WR stage, while lower mass stars would explode as RSGs. This expectation stood in stark contrast to SN 1987A, which was observed to be a blue supergiant at the time of explosion (Arnett et al. 1989).

A reliance on models could be circumvented, however, if, like SN 1987A, the progenitor star was observed prior to the time of core collapse. Using observations taken with the *Hubble Space Telescope*, several progenitors had been identified by 2006 (see Li et al. 2007 and references therein). These identifications were strictly limited to type IIP SNe, which were all shown to be RSGs no more than a few years prior to explosion (Smartt 2009). The single notable exception was SN 2005gl, observed to be a LBV at the time of explosion (Gal-Yam & Leonard 2009), which could not happen according to the standard picture of massive star evolution (Heger et al. 2003). In the following years, the research presented here (see Chapters 2, 3, 4), in conjunction with other studies, would show that many aspects of the standard picture were wrong.

A major challenge to the conventional theory of massive stars and CCSNe occurred in Sep. 2006 when an unusual transient was discovered in the center of the galaxy NGC 1260. With an optical position consistent with the galaxy nucleus, and a luminosity much larger than a typical SN, the event was thought to be an Active Galactic Nucleus (AGN) outburst. However, the amplitude of the outburst ($\Delta m > 5$ mag) and the relatively short rise time (~ 2 months) were inconsistent with known AGN. High-resolution imaging later confirmed the transient to be offset from the nucleus by $\sim 1''$ (a projected separation of ~ 380 pc at the distance of NGC 1260), and the source, which peaked at $M_R \approx -21.7$ mag ($L \approx 2 \times 10^{44} \text{ erg s}^{-1}$), was confirmed as a SN and named SN 2006gy (Smith et al. 2007; Ofek et al. 2007). Following confirmation as a genuine SN, the nature of SN 2006gy remained mysterious: possible explanations for the extreme luminosity included (i) the production of

several M_{\odot} of radioactive ^{56}Ni in a PISN (Smith et al. 2007; Ofek et al. 2007), or (ii) the collision of the SN ejecta with a dense, highly-opaque shell in the progenitor's CSM (Smith & McCray 2007). The former would have been particularly intriguing since PISN were not expected to occur in the local universe. In Chapter 3, I present evidence for long lived light echoes from SN 2006gy, the presence of which ruled out the PISN hypothesis while confirming a massive progenitor CSM. This CSM could not have been created via steady winds, and instead must have been the result of an episodic eruption. Such eruptions are only observed from LBVs, meaning that SN 2006gy, like SN 2005gl, exploded during an evolutionary state that was wholly unexpected according to theoretical models. Far more compelling evidence for the first known PISN would come with our discovery of SN 2007bi, which produced $\gtrsim 3M_{\odot}$ of ^{56}Ni (Gal-Yam et al. 2009).

SN 2006gy was the first of ~ 20 new SNe that are >10 times brighter than the typical type Ia SN and >100 times brighter than the typical CCSN (see Chapter 2). The luminosity of a subset of these explosions cannot be explained by the three mechanisms outlined above (Quimby et al. 2011), and as a result it is believed that they may constitute a new class of SNe (Gal-Yam 2012). In Chapter 2 I present a study of SN 2008es, which, at the time of discovery, was the second most luminous SN ever observed. At the time, it was puzzling as to why a few new experiments were detecting several examples of these super-luminous supernovae (SLSNe), while decade-old experiments (e.g., KAIT; Filippenko et al. 2001; Leaman et al. 2011) had discovered none. In Chapter 2, I calculate the rates of SLSNe and show that relative to typical CCSNe these events are intrinsically rare. The newer surveys included significantly more low-luminosity galaxies, which led to their discovery of SLSNe. I also provide preliminary evidence that SLSNe preferentially occur in low-luminosity host galaxies, a prediction that has largely been borne out by the ensuing discoveries of SLSNe (Gal-Yam 2012).

Further evidence for episodic mass loss, and the connection between LBVs and some CCSNe is shown in Chapter 4 on SN 2008iy. SN 2008iy is remarkable in that it took ~ 400 d to reach peak brightness, a record for SNe, which typically have rise times $\lesssim 3$ weeks (see Figure 1.2). Using both optical and X-ray observations I show that the progenitor mass-loss rate was $\dot{M} \sim 10^{-2} M_{\odot} \text{ yr}^{-1}$ (Miller et al. 2010b), which is \sim two orders of magnitude higher than the steady mass-loss rates for any known Galactic supergiants (e.g., Smith et al. 2009a). I show that the long rise-time suggests that the mass loss peaked a \sim century prior to the explosion, which along with the large mass-loss rates points to an LBV-like eruption shortly preceding core collapse. Perhaps the best evidence connecting episodic mass loss and CCSNe came from SN 2009ip which in 2009 was erroneously identified as a SN. Following the announcement of SN 2009ip, I found evidence for a previous outburst from the same source in 2005 as well as a luminous star ($M_V \approx -10.1$; $M_* \approx 60M_{\odot}$) at the position of the transient in previous *Hubble Space Telescope* imaging (Miller et al. 2009a). We later showed that these outbursts were consistent with Galactic LBVs (Smith et al. 2010b). Additional outbursts have been observed from SN 2009ip since 2009, and during Sep. 2012 the star actually exploded giving rise to a genuine type IIn SN within the recently created dense CSM (e.g., Mauerhan et al. 2013).

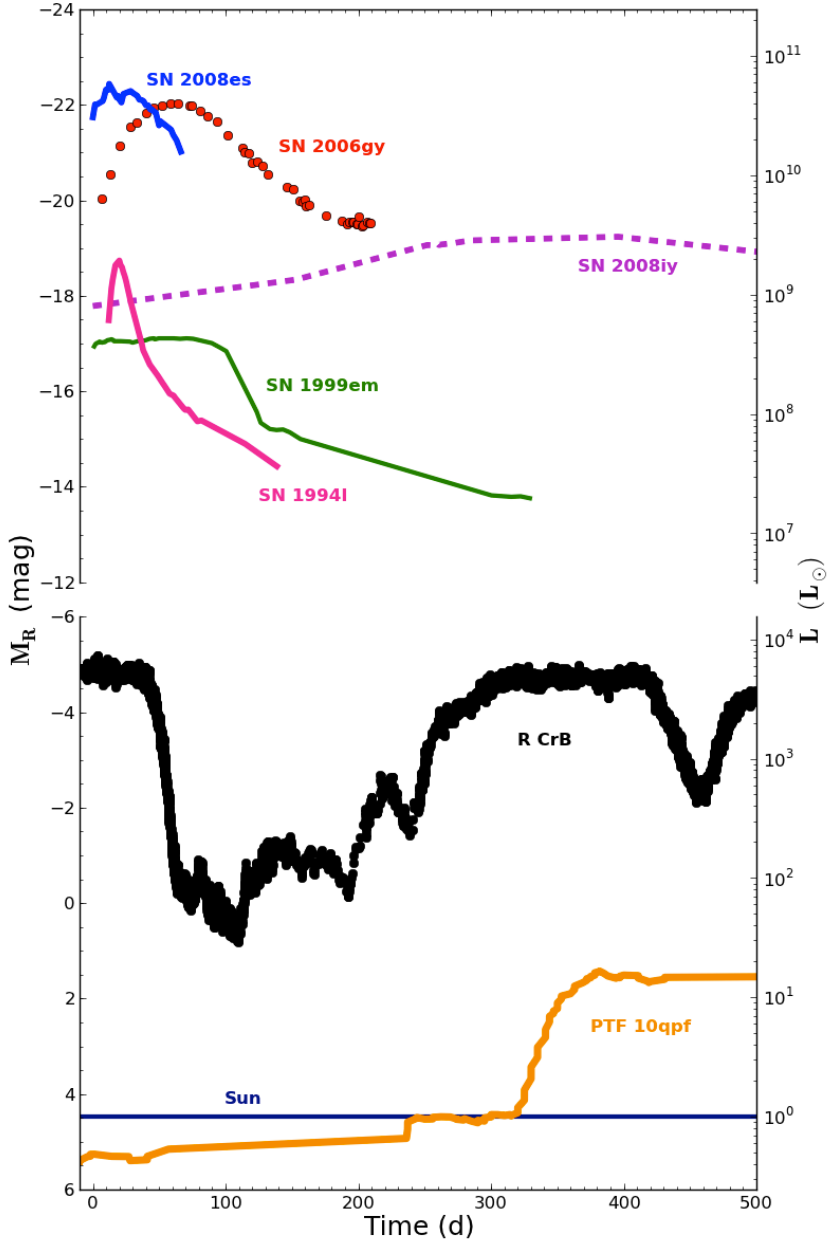


Figure 1.2: Light curves of the extreme variables presented in this dissertation. Note that there is a break in the ordinate, and that the luminosity scale on the right assumes no bolometric correction relative to the R band luminosity. For reference, the canonical type IIP SN 1999em (Leonard et al. 2002) and type Ic SN 1994I (Clocchiatti et al. 2008) are shown, as is the light curve of the sun. The SLSNe 2008es (Chapter 2) and 2006gy (Chapter 3) are more than two orders of magnitude more luminous than type IIp SNe, the most common type of CCSN (Li et al. 2011b). SN 2008iy (Chapter 4) did not prove to be exceptionally luminous, but the ~ 400 d rise time is a record for SNe. PTF 10qpf (Chapter 5) is an actively accreting young star in the process of eruption due to an instability in its accretion disk. Finally, R CrB shows an example light curve of the enigmatic R Coronae Borealis variables which are discussed in Chapter 6.

In sum, this work, including the results presented in Chapters 2, 3, and 4, showed that significant revisions are required for massive star evolution models. In particular, (i) mass loss is not steady and, during the last stages just prior to core-collapse, can be dominated by episodic eruptions during which the mass-loss rates can reach up to $\sim 1 M_{\odot} \text{ yr}^{-1}$, (ii) massive stars can explode while in the LBV state, and (iii) under certain conditions CCSNe can produce luminosities ~ 10 times greater than those of type Ia SNe.

1.2.2 Birth

A defining characteristic of young stars is their variability (e.g., Joy 1945). Brightness variations can be observed on virtually all timescales (minutes to decades), with amplitudes of a few percent to a few magnitudes (Grankin et al. 2007). These variations are typically associated with different effects occurring on the surface of the star, within the disk, or via the interaction of the two, such as the rotational modulation of starspots, accretion, or occultations (see e.g., Herbst et al. 1994). In many cases it is difficult to disentangle the role of each of these effects while observing individual sources (Findeisen et al. 2013).

In addition to this lower amplitude variability, it is generally accepted that most, if not all, young stars undergo large amplitude outbursts at some point during their early formation stages (Herbig 1977). These outbursts, during which the bolometric luminosity of the system can increase by factors of more than 100, can last anywhere from a few days to several centuries in duration. Models in which the radiation is produced following a rapid increase in the disk accretion rate can successfully explain most of the observations (Hartmann & Kenyon 1996), though alternate theories invoking a rapidly rotating, extended-envelope star resolve some of the issues not addressed by the accretion models (e.g., Herbig 1989; Herbig et al. 2003). For the disk instability scenario it is unclear what triggers the outburst; thermal instabilities seem the likely explanation (Hartmann & Kenyon 1996), but interactions with companion stars on highly eccentric orbits (Bonnell & Bastien 1992) or planets embedded within the disk (Lodato & Clarke 2004) better explain the observed rise times of such events. It is clear that additional theoretical work is needed, however, there are insufficient observations to constrain or discriminate between all the possible scenarios.

Traditionally, young stellar objects (YSOs) with extreme variability are identified as belonging to either the large-amplitude ($\gtrsim 5$ mag), long-duration (> 10 yr) FU Orionis class, or the smaller amplitude ($\lesssim 3$ mag), shorter duration (\sim months) EX Lupi, or EXor, class (see Herbig 1977, 1989; Hartmann & Kenyon 1996). These YSO outbursts are of great interest due to their potential importance in the star and planet formation process. FU Orionis outbursts are believed to be repetitive, and it is possible that low-mass stars accrete more than half their final mass during FU Orionis eruptions (Hartmann & Kenyon 1996). The strong winds and outflows produced during eruption likely play a role in the disruption of the circumstellar envelope from which the star forms while also impacting the surrounding interstellar medium (Croswell et al. 1987). Additionally, the enhanced UV and X-ray emission likely effects the planet formation process and the corresponding development of life (Herbig 1977).

Despite their importance, few systematic efforts have been made to catch FU Orionis stars

in the act of eruption. To date there are \sim 20 identified FU Orionis candidates (Reipurth & Aspin 2010), but only FU Ori, V1057 Cyg, and V1515 Cyg have detailed observations during the rising phase of the outburst. In 2010, \sim daily monitoring of the North America Nebula by the Palomar Transient Factory unearthed a new FU Orionis variable. In Chapter 5 I present detailed observations of PTF 10qpf, only the fourth well-sampled outburst from an FU Orionis-like object. Fortunately, PTF 10qpf was observed extensively prior to its outburst, including a low-resolution spectrum obtained by Cohen & Kuhi (1979) as well as mid-infrared observations from multiple space missions including *IRAS*, *Spitzer*, and *Akari*. These observations unambiguously show that PTF 10qpf was a normal classical T Tauri star prior to eruption, while our collection of optical and infrared observations identify the star as a definitive member of the FU Orionis class. I show that PTF 10qpf is on the low end of the mass and luminosity distribution for FU Orionis variables, which proves that these events are not confined to only the highest mass classical T Tauri stars, as had previously been suggested (Herbig 1989).

1.2.3 Rise of the Machines

Time-domain surveys are poised to usher in a new golden era of astronomical research that captures the dynamic nature of the universe. This promise does not come without challenges: astronomical toolkits were developed in an environment where humans could inspect every image and spectrum after they were obtained, but the rapid expanse of data collected by modern experiments has outpaced traditional analysis procedures. For instance, the Large Survey Synoptic Telescope (LSST; Ivezić et al. 2008a) will image the entire southern sky to a depth of $m_r \approx 24.5$ mag every 3 nights. One of the pre-eminent challenges facing future astronomical surveys, as current surveys are already running into these issues, is the extraction of novel results from complex data streams. The full exploitation of the information obtained by these experiments, especially LSST, requires a major shift in our methods and relationship to data: humans must be removed from the discovery process in favor of machines. This constitutes a paradigm shift in our approach to astrophysics: for several millennia we have literally looked at stars and galaxies to understand the universe – the abstraction of this process is profound.

Hoping to address some of these issues, we have developed an array of supervised machine-learning algorithms designed to provide classifications of variable sources found in time-domain surveys. Our framework uses empirical observations of known sources, called a training set, to assign probabilistic classifications for newly discovered, unknown objects (Richards et al. 2012b). This work has led to the classification of all the variable sources in the All Sky Automated Survey (ASAS; see Richards et al. 2012a), which will serve as a stepping stone toward similar efforts with PTF and LSST. The Machine Learned ASAS Classification Catalog (MACC), is the first of its kind, and in it we solved several of the challenges faced by current and future surveys, including: effective reduction of the dimensionality of the data, a solution to sample selection bias,¹¹ and the removal of human beings from the classification

¹¹ Astronomical classification often depends on the construction of training sets from historical surveys of

loop.

In Chapter 6, I demonstrate that a probabilistic catalog can be used to efficiently discover the enigmatic R Coronae Borealis stars (RCBs). RCB are rare, carbon-rich, hydrogen-deficient, supergiants that exhibit spectacular, aperiodic declines in brightness (Δm_V up to 8 mag). No consensus about the true physical nature of these stars has been reached to date, but two leading theories have emerged: RCB are thought to be either the product of a CO and He white dwarf merger or the final He shell flash from a planetary nebula central star (Clayton 1996). The former is particularly intriguing, because these systems may then provide insight into the higher mass white dwarf mergers that give rise to Type Ia SNe.

Only \sim 60 Galactic RCBs were known prior to the four new examples presented in Chapter 6. These new discoveries are all bright ($m_V \lesssim 13$ mag), meaning they are particularly useful for follow-up observations. The MACC-enabled search also led to the discovery of four Dy Perseus-like stars (DYPers), which tripled the number of known DYPers in the Galaxy. DYPers have cooler photospheres than RCB, but otherwise possess several of the same physical characteristics. It is currently an outstanding question as to whether DYPers are the low temperature analogs to RCB, or some other type of star formed via a different process. With an expected \sim 6000 RCB in the Milky Way (Clayton 2012), the paucity of known Galactic sources is puzzling, especially because RCBs are luminous and exhibit a unique variability signature. The gap between the expected and known numbers of RCB stars in the galaxy can be attributed, at least in part, to an observational bias in the methods used to search for these systems. I demonstrate in Chapter 6 that half of the newly identified RCB and DYPers in our machine-learning catalog would have been missed using traditional search methods. I also demonstrate that newly discovered RCBs improve the classifier and discover new candidates that were missed via the initial search. Such refinements are illustrative of the power of machine learning, as new candidates from the classifier are confirmed, the confirmations provide feedback for the machine to refine and improve its model.

In Chapter 7, I present the results of the first ever unbiased, spectroscopic survey of variability. Using spectra obtained from both the Sloan Digital Sky Survey and Hectospec on the 6.5-m Multi-Mirror Telescope, I show that for a magnitude limited survey, the majority of variable sources are G and K dwarfs, even at high galactic latitudes. I also demonstrate that photometric light curves can be used to infer the physical properties (T_{eff} , $\log g$, and [Fe/H]) of variable sources. These results suggest that the fastest and most efficient way to probe Galactic structure is via photometric time-domain surveys. They also tantalizingly hint that it may be possible to use machine learning to turn photometric-only surveys, such as LSST, into quasi-spectrographs (see Chapter 7).

As new surveys continue to be developed I look forward to the challenges associated with these massive datasets, and I hope to uncover new and exciting phenomena.

brighter, closer sources than those detected in newer, and typically deeper, surveys. This is known as sample selection bias and it leads to unreliable classifications for most sources located in a previously unexplored portion of parameter space.

Acknowledgments

I am greatly indebted to J. Schwab and J. Shiode who provided the MESA output for the stellar evolution models shown in Figure 1.1. I wish to thank E. Griffin for a useful discussion on the history of time-domain astronomy.

Chapter 2

The Exceptionally Luminous Type II-L SN 2008es

We report on our early photometric and spectroscopic observations of the extremely luminous Type II supernova (SN) 2008es. With an observed peak optical magnitude of $m_V = 17.6$ mag and at a redshift $z = 0.213$, SN 2008es had a peak absolute magnitude of $M_V = -22.5$ mag, making it the second most luminous SN ever observed. The photometric evolution of SN 2008es exhibits a fast decline rate (~ 0.042 mag day $^{-1}$), similar to the extremely luminous Type II-L SN 2005ap. We show that SN 2008es spectroscopically resembles the luminous Type II-L SN 1979C. Although the spectra of SN 2008es lack the narrow and intermediate-width line emission typically associated with the interaction of a SN with the circumstellar medium (CSM) of its progenitor star, we argue that the extreme luminosity of SN 2008es is powered via strong interaction with a dense, optically-thick CSM. The integrated bolometric luminosity of SN 2008es yields a total radiated energy at ultraviolet (UV) and optical wavelengths of $\gtrsim 10^{51}$ ergs. Finally, we examine the apparently anomalous rate at which the Texas Supernova Search has discovered rare kinds of supernovae (SNe), including the four most luminous SNe observed to date, and find that their results are consistent with those of other modern SN searches.

2.1 Introduction

Wide-field synoptic optical imaging surveys are continuing to probe the parameter space of time-variable phenomena with increasing depth and temporal coverage (e.g., [Becker et al. 2004](#); [Morales-Rueda et al. 2006](#); [Bramich et al. 2008](#)), unveiling a variety of transients ranging from the common ([Rau et al. 2008](#)) to the unexplained (e.g., [Barbary et al. 2009](#)). Untargeted (“blind”) synoptic wide-field imaging surveys, such as the Texas Supernova Search (TSS; [Quimby 2006](#)) conducted with the ROTSE-III 0.45-m telescope ([Akerlof et al. 2003](#)), have uncovered an unusually large number of rare transients, including the three most luminous supernovae observed to date: SN 2005ap ([Quimby et al. 2007a](#)), SN 2006gy ([Ofek](#)

et al. 2007; Smith et al. 2007), and SN 2006tf (Smith et al. 2008a). Observations of these very luminous events are starting to allow the detailed physical study of the extrema in core-collapse SNe. They appear to be powered in part by their interaction with a highly dense CSM (see Smith et al. 2008a, and references therein), though other possibilities have been advanced. Clearly the discovery of more such events would allow an exploration of the variety of the phenomenology as related to the diversity of progenitors and CSM.

Recently the TSS discovered yet another luminous transient on 2008 Apr 26.23 (UT dates are used throughout this Chapter), which they suggested was a variable active galactic nucleus at a redshift $z = 1.02$ (Yuan et al. 2008). Gezari & Halpern (2008) then hypothesized that the transient was a flare from the tidal disruption of a star by a supermassive black hole. Miller et al. (2008b) first identified SN 2008es as potentially an extremely luminous Type II SN (see also Gezari et al. 2008), and we later definitively confirmed this with further spectroscopic observations (Chornock et al. 2008a); the event was assigned the name SN 2008es by the IAU (Chornock et al. 2008b).

Here we present our analysis of SN 2008es which is classified as a Type II-L SN based on the observed linear decline in the photometric light curve (Barbon et al. 1979; Doggett & Branch 1985). Located at $\alpha = 11^{\text{h}}56^{\text{m}}49.06^{\text{s}}$, $\delta = +54^{\circ}27'24.77''$ (J2000.0) with $z = 0.213$, SN 2008es has a peak optical magnitude of $M_V = -22.5$ mag, among SNe second only to SN 2005ap. Aside from the extreme luminosity, SN 2008es is of great interest since detailed UV-through-infrared observations provide a unique opportunity to study the mass-loss properties of an evolved post-main sequence massive star via its interaction with the surrounding dense CSM.

The outline of this Chapter is as follows: we present our observations in §2.2, the photometric and spectroscopic analyses of this and public (NASA) data in §2.3 and §2.4, respectively. A discussion and finally conclusions are given in §2.5 and §2.6. Throughout this Chapter we adopt a concordance cosmology of $H_0 = 70 \text{ km s}^{-1} \text{ Mpc}^{-1}$, $\Omega_M = 0.3$, and $\Omega_\Lambda = 0.7$.

2.2 Observations

Here we present our ground-based optical and near-infrared (NIR) photometry and optical spectroscopy, along with space-based *Swift* UV, optical, and X-ray observations. NIR photometry of SN 2008es was obtained simultaneously in J , H , and K_s with the Peters Automated Infrared Imaging Telescope (PAIRITEL; Bloom et al. 2006) beginning 2008 May 16. To improve the photometric signal-to-noise ratio (S/N), we stacked images over multiple nights. For the K_s images the S/N of the SN remained low, despite the stacks made over multiple epochs, and therefore we do not include these data in our subsequent analysis. Aperture photometry, using a custom pipeline, was used to measure the J and H photometry of the isolated SN calibrated to the 2MASS catalog (see Bloom et al. 2009). The resulting light curves are presented in Figure 2.1. The final PAIRITEL photometry is reported in Table 2.1.

Table 2.1: PAIRITEL Observations of SN 2008es

$t_{\text{mid}}^{\text{a}}$ (day)	Obs. window ^b (day)	Filter	Exp. time (sec)	Mag ^c
4602.24	2.06	J	2895.91	17.74±0.03
4605.28	6.09	J	3869.06	17.68±0.03
4612.17	2.09	J	4606.78	17.68±0.02
4615.15	6.08	J	6458.90	17.68±0.02
4618.19	2.19	J	6129.29	17.77±0.03
4632.17	6.04	J	4944.24	17.75±0.04
4602.24	2.06	H	2880.22	17.62±0.06
4605.27	6.09	H	3751.34	17.43±0.06
4612.17	2.09	H	4598.93	17.59±0.06
4615.15	6.08	H	6451.06	17.40±0.04
4618.19	2.19	H	6074.35	17.53±0.05
4632.17	6.04	H	4865.76	17.89±0.11

Note. — PAIRITEL observations were stacked over multiple epochs to increase the S/N.

^aMid-point between the first and last exposures in a single stacked image, reported as JD–2450000.

^bTime between the first and last exposures in a single stacked image.

^cObserved value; not corrected for Galactic extinction.

Optical photometry of SN 2008es was obtained in *BVRI* with the Katzman Automatic Imaging Telescope (KAIT; [Filippenko et al. 2001](#)) and the 1-m Nickel telescope at Lick Observatory beginning 2008 May 30. Point-spread function (PSF)-fitting photometry was performed on the SN and several comparison stars using the *IRAF/DAOPHOT* package ([Stetson 1987](#)) and transformed into the Johnson-Cousins system. Calibrations for the field were obtained with the Nickel telescope on 3 photometric nights. The final photometry from KAIT and the Nickel telescope is given in Tables 2.2 and 2.3, respectively.

Additional optical photometry was obtained in *UBVRI* on 2008 Jun 02 and *BVRI* on 2008 Aug 05 with PFCam on the 3-m Shane telescope at Lick Observatory. The data were reduced using standard techniques and aperture photometry was used to extract the SN flux. The PFCam filters differ slightly from the standard *UBVRI* and therefore we calibrate the SN relative to the SDSS system, which is at a comparable depth to the PFCam images, using the color transformations of [Jester et al. \(2005\)](#). Use of the SDSS system allows us to apply color term corrections to our calibrations while using the maximum number of possible comparison stars. The final PFCam photometry is reported in Table 2.4.

The *Swift* satellite observed SN 2008es during 11 epochs between 2008 May 14 and Aug 03. We downloaded the UVOT data from the quick-look data archive and analyzed the Level 2 sky image data in *U*, *B*, and *V* according to the photometry calibration and recipe by [Li et al. \(2006\)](#). The *Swift* UV filters (*UVW1*, *UVM1*, and *UVW2*) were reduced following [Poole et al. \(2008\)](#). The final *Swift* UVOT photometry is reported in Table 2.5.

Table 2.2: KAIT Observations of SN 2008es

$t_{\text{obs}}^{\text{a}}$ (day)	Filter	Exp. time (sec)	Mag ^b
4620.72	B	360.00	18.36±0.04
4622.73	B	360.00	18.49±0.05
4624.72	B	360.00	18.60±0.04
4626.72	B	360.00	18.64±0.06
4628.72	B	360.00	18.73±0.07
4630.72	B	360.00	18.83±0.06
4632.74	B	360.00	18.93±0.09
4634.77	B	360.00	18.94±0.11
4636.73	B	360.00	19.03±0.09
4639.70	B	360.00	19.00±0.11
4643.74	B	360.00	19.46±0.09
4620.72	V	300.00	18.12±0.06
4622.73	V	300.00	18.07±0.03
4626.72	V	300.00	18.17±0.04
4628.72	V	300.00	18.22±0.04
4630.72	V	300.00	18.33±0.04
4632.74	V	300.00	18.33±0.06
4634.77	V	300.00	18.38±0.09
4636.73	V	300.00	18.55±0.03
4639.70	V	300.00	18.50±0.04
4643.74	V	300.00	18.37±0.05
4616.74	R	300.00	17.81±0.03
4618.76	R	300.00	17.85±0.04
4620.72	R	300.00	17.88±0.04
4622.73	R	300.00	17.91±0.03
4624.72	R	300.00	17.99±0.04
4626.72	R	300.00	18.00±0.03
4628.72	R	300.00	18.03±0.04
4630.72	R	300.00	18.11±0.05
4632.74	R	300.00	18.11±0.03
4634.77	R	300.00	18.20±0.04
4636.73	R	300.00	18.21±0.05
4639.70	R	300.00	18.26±0.05
4643.74	R	300.00	18.44±0.06
4616.74	I	300.00	17.74±0.07
4618.76	I	300.00	17.92±0.16
4620.72	I	300.00	17.72±0.05
4622.73	I	300.00	17.67±0.05
4624.72	I	300.00	17.81±0.05
4626.72	I	300.00	17.88±0.04
4628.72	I	300.00	17.88±0.05
4630.72	I	300.00	17.90±0.07
4632.74	I	300.00	18.01±0.06
4634.77	I	300.00	17.93±0.07
4636.73	I	300.00	18.01±0.08
4639.70	I	300.00	18.24±0.11
4643.74	I	300.00	18.20±0.09

^aExposure mid-point, reported as JD–2450000.

^bObserved value; not corrected for Galactic extinction.

Table 2.3: Nickel Observations of SN 2008es

$t_{\text{obs}}^{\text{a}}$ (day)	Filter	Exp. time (sec)	Mag ^b
4627.75	B	360.00	18.56±0.02
4635.75	B	360.00	19.04±0.07
4638.71	B	360.00	19.05±0.03
4642.67	B	360.00	19.31±0.10
4653.67	B	360.00	19.76±0.09
4655.71	B	360.00	19.76±0.04
4658.67	B	360.00	19.93±0.14
4662.67	B	360.00	20.16±0.09
4627.75	V	300.00	18.22±0.03
4635.75	V	300.00	18.45±0.04
4638.71	V	300.00	18.50±0.03
4642.67	V	300.00	18.77±0.04
4653.67	V	300.00	19.03±0.04
4655.71	V	300.00	19.12±0.04
4658.67	V	300.00	19.13±0.07
4662.67	V	300.00	19.53±0.15
4627.75	R	300.00	18.01±0.02
4635.75	R	300.00	18.19±0.04
4638.71	R	300.00	18.25±0.03
4642.67	R	300.00	18.53±0.12
4653.67	R	300.00	18.62±0.04
4655.71	R	300.00	18.73±0.03
4658.67	R	300.00	18.84±0.11
4662.67	R	300.00	19.08±0.05
4627.75	I	300.00	17.79±0.04
4635.75	I	300.00	17.86±0.09
4638.71	I	300.00	18.04±0.04
4642.67	I	300.00	18.04±0.08
4653.67	I	300.00	18.34±0.11
4655.71	I	300.00	18.42±0.07
4658.67	I	300.00	18.29±0.17
4662.67	I	300.00	18.16±0.13

^aExposure mid-point, reported as JD-2450000.

^bObserved value; not corrected for Galactic extinction.

Table 2.4: PFCam Observations of SN 2008es

$t_{\text{obs}}^{\text{a}}$ (day)	Filter	Exp. time (sec)	Mag ^b
4619.81	U	1230.00	17.72±0.07
4619.83	B	630.00	18.20±0.07
4683.70	B	360.00	21.38±0.16
4619.83	V	930.00	17.90±0.05
4683.71	V	360.00	20.12±0.07
4619.79	R	930.00	17.82±0.05
4683.68	R	600.00	19.66±0.08
4619.85	I	1230.00	17.68±0.06
4683.70	I	360.00	19.32±0.08

^aExposure mid-point, reported as JD-2450000.

^bObserved value; not corrected for Galactic extinction.

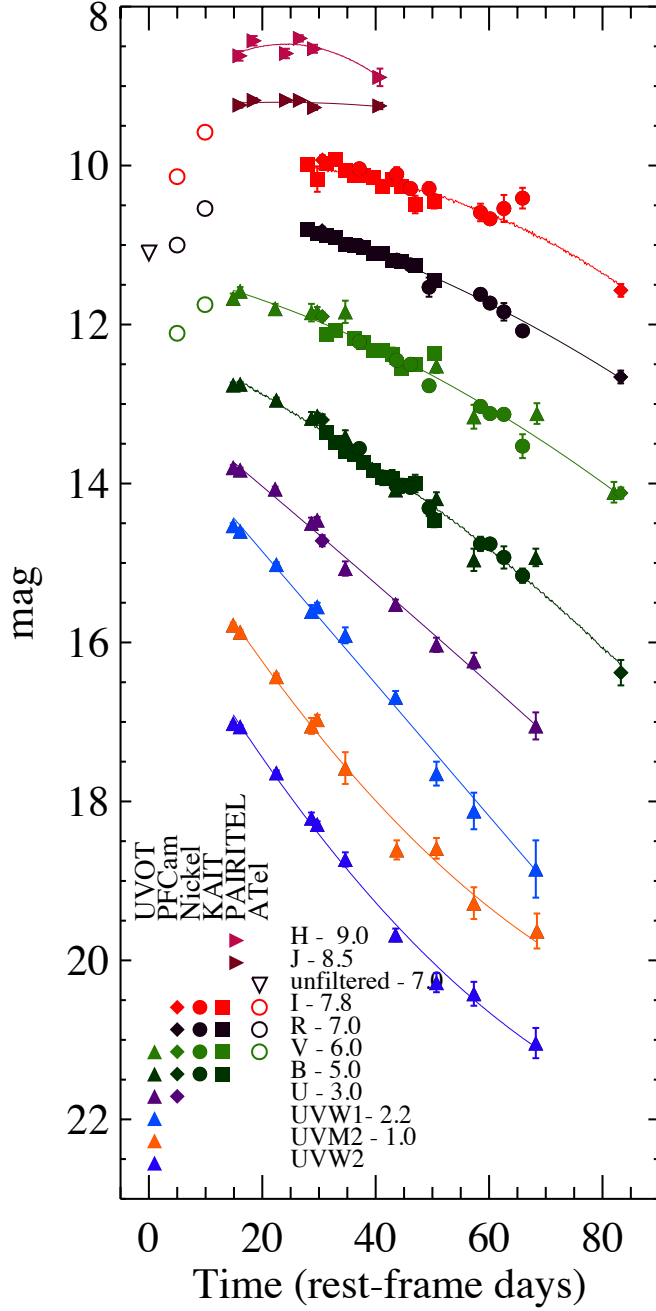


Figure 2.1: Observed UV-optical-NIR light curves of SN 2008es. The data have not been corrected for Galactic or host extinction. We include observations from the literature (open symbols; [Yuan et al. 2008](#)), as well as our optical-NIR observations (filled symbols; KAIT, Nickel, PFCam, and PAIRITEL) and space-based UVOT observations from *Swift* (filled triangles). We adopt the discovery date of SN 2008es, 2008 Apr 26.23, as “day 0” for this SN. Low-order polynomial fits to each band have been overplotted to help guide the eye.

Table 2.5: UVOT Observations of SN 2008es

$t_{\text{obs}}^{\text{a}}$ (day)	Filter	Exp. time (sec)	Mag ^b
4600.75	UVW2	1585.70	17.02±0.02
4602.25	UVW2	1802.20	17.06±0.02
4610.00	UVW2	2119.30	17.64±0.03
4617.50	UVW2	542.40	18.21±0.07
4618.75	UVW2	1731.10	18.29±0.04
4624.75	UVW2	487.70	18.73±0.09
4635.50	UVW2	1664.50	19.68±0.08
4644.25	UVW2	1593.40	20.28±0.12
4652.25	UVW2	1317.80	20.42±0.15
4665.50	UVW2	1765.70	21.04±0.19
4600.75	UVM2	1043.20	16.78±0.03
4602.25	UVM2	1148.40	16.87±0.03
4610.00	UVM2	1523.60	17.43±0.04
4617.50	UVM2	338.60	18.05±0.10
4618.75	UVM2	1110.60	17.97±0.06
4624.75	UVM2	150.30	18.58±0.20
4635.75	UVM2	1149.50	19.61±0.12
4644.25	UVM2	1081.80	19.59±0.13
4652.25	UVM2	938.10	20.28±0.20
4665.75	UVM2	1071.50	20.63±0.22
4600.75	UVW1	792.40	16.78±0.03
4602.25	UVW1	900.70	16.85±0.03
4610.00	UVW1	1058.30	17.27±0.03
4617.50	UVW1	270.70	17.86±0.08
4618.75	UVW1	865.10	17.80±0.05
4624.75	UVW1	243.70	18.16±0.10
4635.50	UVW1	831.80	18.94±0.08
4644.25	UVW1	796.10	19.90±0.15
4652.25	UVW1	790.00	20.37±0.23
4665.50	UVW1	1048.30	21.10±0.36
4600.75	U	395.80	16.80±0.03
4602.25	U	449.90	16.83±0.03
4609.75	U	399.60	17.07±0.03
4617.50	U	134.90	17.50±0.07
4618.75	U	431.90	17.46±0.04
4624.75	U	121.50	18.07±0.09
4635.50	U	415.40	18.52±0.06
4644.25	U	397.40	19.03±0.09
4652.25	U	386.70	19.23±0.10
4665.50	U	523.60	20.05±0.17
4600.75	B	395.80	17.76±0.03
4602.25	B	449.90	17.75±0.03
4610.00	B	527.80	17.95±0.03
4617.50	B	135.00	18.18±0.08
4618.75	B	431.90	18.15±0.04
4624.75	B	121.60	18.41±0.08
4635.50	B	415.40	19.08±0.06
4644.25	B	397.50	19.19±0.08
4652.25	B	328.60	19.96±0.14
4665.50	B	523.70	19.93±0.11
4600.75	V	395.70	17.67±0.06
4602.25	V	449.90	17.58±0.05
4609.75	V	399.50	17.80±0.06

Table 2.5 (*cont'd*): UVOT Observations of SN 2008es

$t_{\text{obs}}^{\text{a}}$ (day)	Filter	Exp. time (sec)	Mag ^b
4617.50	V	134.90	17.85±0.11
4618.75	V	432.00	17.84±0.06
4624.75	V	81.00	17.84±0.14
4635.75	V	415.40	18.41±0.08
4644.25	V	397.60	18.52±0.09
4652.25	V	328.50	19.16±0.15
4665.75	V	398.90	19.12±0.13
4682.22	V	1876.40	20.11±0.13

^aExposure mid-point, reported as JD-2450000.

^bObserved value; not corrected for Galactic extinction.

Simultaneous observations of SN 2008es occurred with the *Swift* XRT, for which we confirm a non-detection of X-ray emission (see also [Gezari & Halpern 2008](#)). To place a limit on the source flux we assume a power-law spectrum with a photon index $\Gamma = 2$, absorbed by Galactic H I. We took an extraction region of radius 64 pixels ($\sim 2.5'$) and fit the PSF model around the centroid of the optical emission. We obtain a 3σ limiting flux of 1.1×10^{-14} erg cm $^{-2}$ s $^{-1}$ in the 0.3–10 keV band for a total exposure of 46.1 ksec. This represents an upper limit to the X-ray luminosity of $\sim 1.5 \times 10^{42}$ erg s $^{-1}$.

We obtained spectra of SN 2008es on 2008 May 16.3, 2008 May 29.3, and 2008 July 7.3 using the Kast spectrograph on the Lick 3-m telescope ([Miller & Stone 1993](#)). Additional spectra were obtained on 2008 June 7.4 and 2008 August 3.3 using the Low Resolution Imaging Spectrometer on the Keck I 10-m telescope ([Oke et al. 1995](#)) and on 2008 June 21.2 and 2008 June 23.2 using the R. C. Spectrograph on the Kitt Peak 4-m telescope, following the approval of our request for Kitt Peak Director's Discretionary Time. The spectra were extracted and calibrated following standard procedures (e.g., [Matheson et al. 2000](#)). Clouds were present during several of the observations, making the absolute flux scales unreliable. The spectrograph slit was placed at the parallactic angle, so the relative spectral shapes should be accurate ([Filippenko 1982](#)), with the exception of the Kitt Peak spectra, which have a small amount of second-order light contamination at wavelengths redward of ~ 8000 Å. The full SN 2008es spectral sequence is plotted in Figure 2.2. The two Kitt Peak spectra show little evolution in the two days that separate them and have been combined to increase the S/N (day 28 in Figure 2.2). A log of our spectroscopic observations is presented in Table 2.6.

We searched our spectra for the possible presence of narrow lines and were unable to positively identify any, either in emission or absorption. Therefore, without a detection of the host galaxy, we determine the redshift of SN 2008es directly from the SN spectrum. As the SN aged, broad P-Cygni spectral features appeared, including an emission feature near 7900 Å that we identify as H α near a redshift of 0.2. Other spectral features are consistent with a Type II SN at about that redshift.

To get a more accurate redshift, we identified two similar reference spectra of the Type

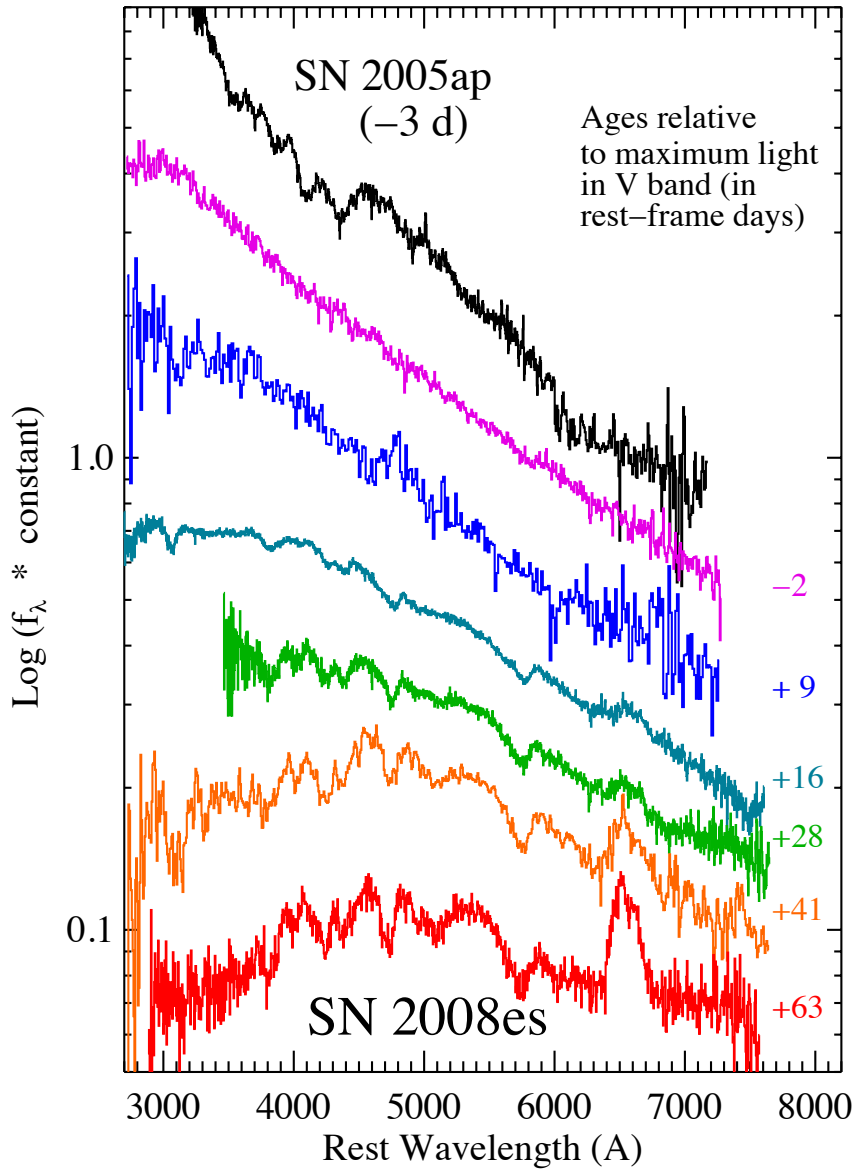


Figure 2.2: Spectral evolution of SN 2008es. Spectra of SN 2008es (in color) are labeled with their ages in the rest frame of the supernova ($z = 0.213$) relative to the observed V -band maximum on May 18.7. The spectra become progressively redder as the SN ages and broad P-Cygni spectral features become more prominent with time. By +63 d, a broad emission feature of $\text{H}\alpha$ is clearly present. The top spectrum (in black) is the earliest spectrum of SN 2005ap, the most luminous observed SN (Quimby et al. 2007a).

Table 2.6: Log of Spectroscopic Observations

Age ^a (days)	UT Date	Instrument ^b	Range (Å)	Exp. Time (s)	Seeing (")	Airmass	Photometric? (y/n)
-2	2008-05-16.345	Kast	3300–8830	1500	2.4	1.3	y
9	2008-05-29.253	Kast	3300–8820	1800	2.3	1.1	n
16	2008-06-07.399	LRIS	3200–9230	1200	1.6	2.0	y
28	2008-06-21.194	RC	4200–9280	1800	2.9	1.3	y
29	2008-06-23.189	RC	4200–9280	2400	1.8	1.3	y
41	2008-07-07.252	Kast	3300–9280	4200	2.5	1.6	y
63	2008-08-03.254	LRIS	3500–9190	877	0.9	2.0	n

^aAge in rest-frame days relative to the observed *V*-band maximum on 2008 May 18.7.

^bKast = Kast spectrograph on Lick 3-m telescope. LRIS = Low Resolution Imaging Spectrometer on Keck-I 10-m telescope. RC = R. C. Spectrograph on Kitt Peak 4-m telescope.

II-L SNe 1979C and 1980K from the literature (Branch et al. 1981; Uomoto & Kirshner 1986). These spectral comparisons are shown in the bottom panel of Figure 2.3. We used the SuperNova IDentification code of Blondin & Tonry (2007) to cross-correlate the day 63 spectrum of SN 2008es with the two reference spectra and derived a weighted-average $z = 0.213 \pm 0.006$, which we adopt throughout this Chapter. For the remainder of this Chapter all spectra are referenced to the date of rest-frame *B*-band maximum light, which we adopt as 2008 May 19 (see §2.3). This redshift agrees with a fit to the broad H α emission line in the day 63 spectrum, which yields a flux centroid of $z = 0.210$. The SN 2008es redshift determined using this method is correlated with the expansion velocity, but we assume that the bias due to this effect is small given that all three SNe have H α emission lines of a similar width.

2.3 Photometric Results

Our dataset provides excellent broad-band coverage of SN 2008es from the UV to the NIR, which allows us to model changes in the spectral energy distribution (SED). In order to sample each photometric band onto a single set of common epochs, we fit low-order polynomials to each light curve, which we then interpolate onto a common grid. NIR observations were only included on or around epochs where we detected the SN. We create an SED at each of the common epochs and fit a single-component blackbody (BB) to the data following the procedure described by Modjaz et al. (2009). Prior to the SED/BB fits we add a systematic term to the uncertainty in the photometric measurement in each band. This term is added in quadrature to the statistical uncertainty, and for the NIR (*JH*) is equal to 2%, in the optical (*BVRI*) we adopt 3%, while for *U*-band we adopt 10%, and the adopted UV (*UVW1*, *UVM2*, *UVW2*) systematic uncertainty is 20%. We assume no host-galaxy extinction (for further details see §2.5.2), and correct our measurements for the modest amount of Galactic reddening $E(B-V) = 0.08$ mag (Schlegel et al. 1998). From the SED/BB fits we derive the temperature, radius, and luminosity of the SN as a function of time, as shown in Figure 2.4. The temperature and luminosity decrease while the radius increases with time, as expected

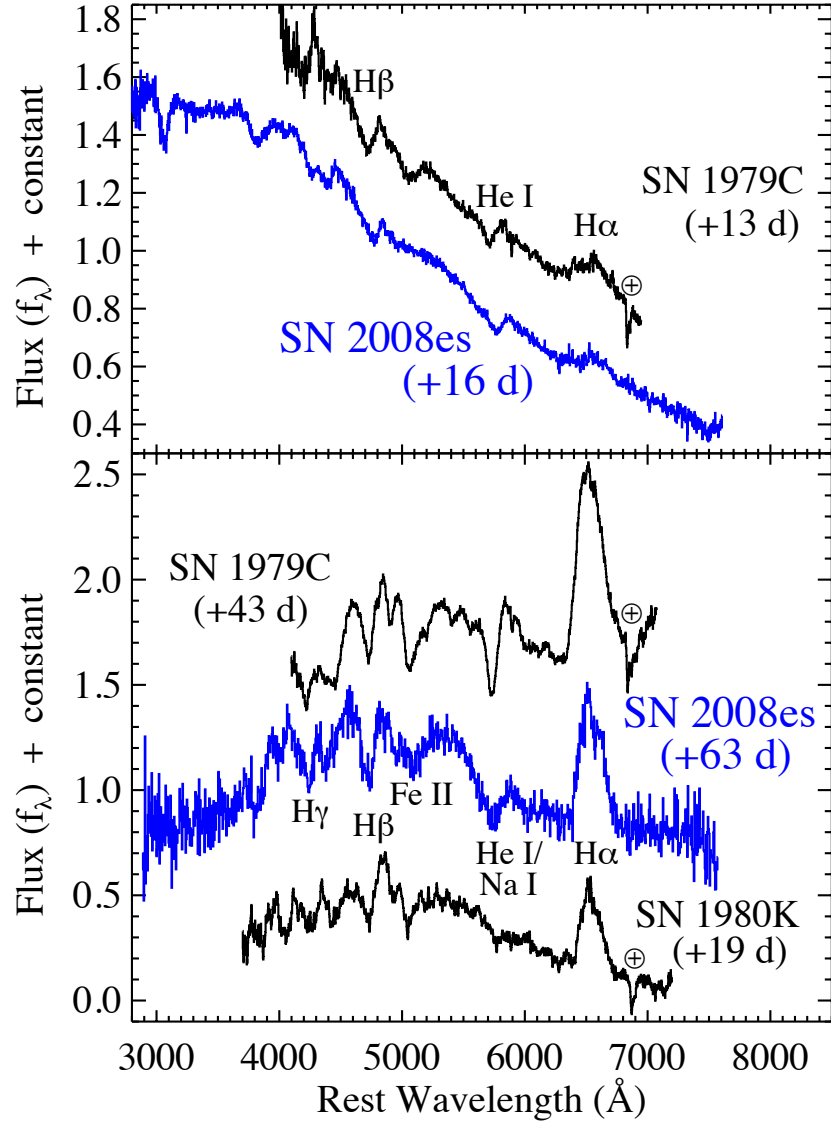


Figure 2.3: Spectral comparisons of SN 2008es to two SNe II-L. All spectra are labeled with their respective ages in rest-frame days relative to maximum light, and prominent spectral features are identified. The zero point of the flux scale is accurate for the SN 2008es spectra (in blue), while the comparison spectra (in black) are vertically offset. The top panel shows a comparison at an early epoch of SN 2008es to SN 1979C from 1979 April 28 (Branch et al. 1981). The bottom panel shows a comparison at a later epoch to SN 1979C from 1979 May 28 (Branch et al. 1981) and SN 1980K (spectra from 1980 November 15 and 17 combined, Uomoto & Kirshner 1986). Telluric absorption bands in the SNe 1979C and 1980K spectra are marked with a \oplus symbol.

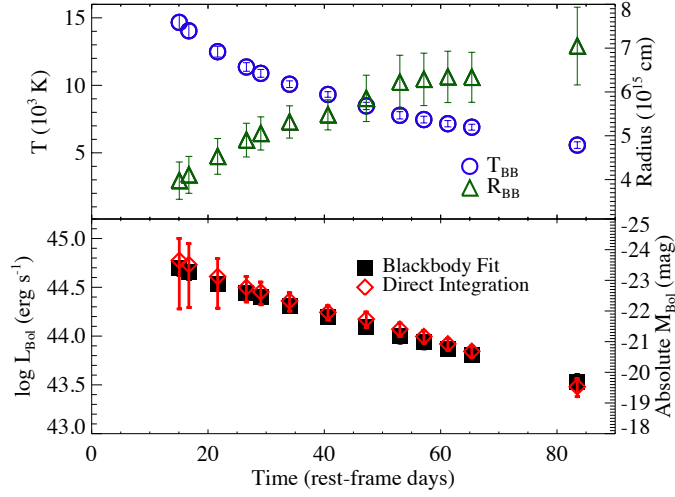


Figure 2.4: Photospheric and bolometric luminosity evolution of SN 2008es. Top: temperature evolution of SN 2008es based on BB fits (open circles) and inferred radius (open triangles). The error bars on the radius are likely to be slightly overestimated because the errors on the BB temperature and luminosity are correlated. Bottom: bolometric luminosity of SN 2008es derived via two independent methods, BB modeling (closed squares) and integration of the total UV+optical (+NIR where available) flux (open diamonds). The two methods agree to within $\lesssim 20\%$.

for an expanding and cooling SN photosphere.

After converting the photometry from [Yuan et al. \(2008\)](#) to *VRI* using the color equations from [Jester et al. \(2005\)](#), we find that the observed *V*-band maximum light, which at the redshift of this SN roughly corresponds to rest-frame *B*, occurred on \sim 2008 May 19, \sim 19 rest-frame days after discovery.

In Figure 2.5 we show two representative fits to the SED of SN 2008es, at 26.6 and 65.4 rest-frame days after discovery. In all epochs we observe excess emission relative to a single BB in the bluest of the *Swift* filters, *UVW2*, while starting around 55 rest-frame days after discovery there is excess emission in both *UVW2* and *UVM2*. This excess was also observed in the Type II-P SN 2006bp, where it was attributed to complex line blanketing by Fe-peak elements ([Immler et al. 2007](#)). The blue excess is readily identified in the UV color curves (e.g., *UVW2*–*UVW1*) of SN 2008es, which evolve toward the red until \sim 50 rest-frame days after discovery at which point the *UVW2*–*UVW1* and *UVM2*–*UVW1* colors become progressively more and more blue. These points were excluded from our SED/BB fits. To confirm that we were not underestimating the bolometric luminosity of the SN, we directly integrated the flux in the SED using the same method as [Modjaz et al. \(2009\)](#). We show the results of this direct integration in the lower panel of Figure 2.4, and in all cases we find that the BB model and direct integration method agree to within $\lesssim 20\%$.

The observed linear decline in the light curve of SN 2008es leads us to classify it as a Type II-L SN. We measure a bolometric photometric decay rate of $0.042 \text{ mag day}^{-1}$, which is slightly faster than the *V*-band (roughly rest-frame *B*) rate of $0.036 \text{ mag day}^{-1}$. This rate is

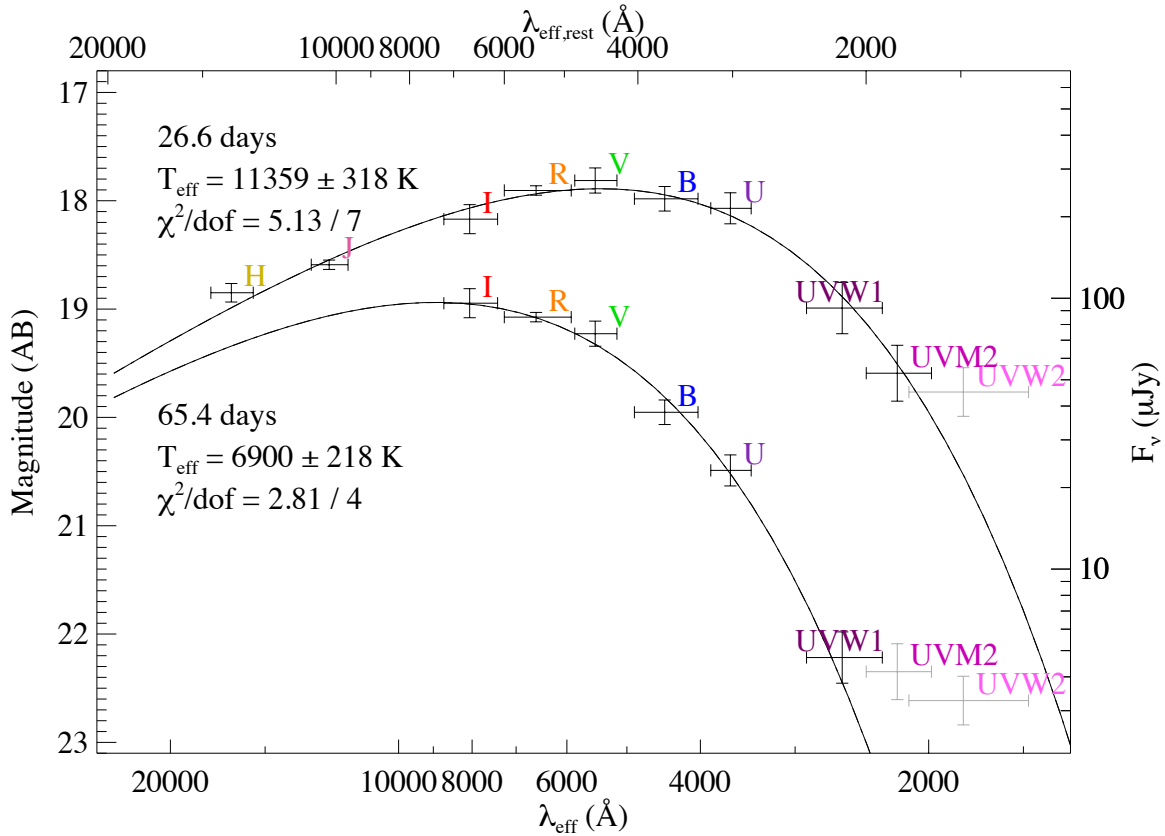


Figure 2.5: SEDs from SN 2008es corrected for Galactic extinction. We show two representative SEDs of SN 2008es at ~ 27 and ~ 65 rest-frame days after discovery. The SEDs are well fit by a single blackbody component. Note that relative to the model blackbody there is excess flux in the $UVW2$ band in both epochs, while the $UVM2$ band shows excess in the later epoch. All UV measurements that exhibit a clear excess relative to a blackbody are shown in gray and are excluded from the fits.

also slightly slower than the rest-frame B -band decay of both SN 1979C (0.046 mag day $^{-1}$; Panagia et al. 1980) and SN 1980K (0.055 mag day $^{-1}$; Barbon et al. 1982). Furthermore, integrating the bolometric light curve from 15 to 83 rest-frame days after discovery yields a total radiated energy of $\sim 9 \times 10^{50}$ erg, comparable to the canonical 10^{51} erg deposited into the kinetic energy of a SN. If we assume the same bolometric correction factor to the observed V -band light curve both pre- and post-peak, and we include the data from Yuan et al. (2008), we find the total radiated energy of SN 2008es over the first 83 days after discovery is $\sim 1.1 \times 10^{51}$ erg.

2.4 Spectroscopy

The SN 2008es spectral sequence plotted in Figure 2.2 is labeled with ages (in the rest-frame) relative to the observed V -band maximum light in order to facilitate comparison with SNe 1979C and 1980K in Figure 2.3. Our first two spectra of SN 2008es (at -2 and $+9$ d relative to maximum light) show a smooth and featureless blue continuum with no identifiable spectral features. In particular, we do not detect an emission feature near 5650 Å (4660 Å in the rest frame) reported in earlier spectra of SN 2008es taken between 2008 May 01 and 2008 May 08 by Yuan et al. (2008). If real, such a transient emission feature would be intriguing, possibly related to the transient emission features seen in the early spectra of some SNe IIn at similar wavelengths due to He II $\lambda 4686$ and the Wolf-Rayet C III/N III $\lambda 4640$ blend (Niemela et al. 1985; Leonard et al. 2000).

In addition, the spectrum of the extremely luminous SN 2005ap from -3 d is shown at the top of Figure 2.2. The SN 2005ap spectrum is also very blue, but has additional spectral features that are not seen in our SN 2008es spectrum from a similar epoch. Quimby et al. (2007a) identified the strongest spectral feature in SN 2005ap, the “W”-shaped feature near 4200 Å, as being due to a blend of C III, N III, and O III with an expansion velocity of about 20,000 km s $^{-1}$.

Our next spectrum, at $+16$ d, is noticeably redder and is the first to show strong spectral features. Both SN 1979C at a similar epoch and SN 2008es show a blue continuum with weak, low-contrast lines of H and He I lines present mostly in absorption (Figure 2.3). However, H α is present only in emission and is weak in SN 2008es. The H α line in SN 2008es has a full width at half-maximum (FWHM) of 10,000 km s $^{-1}$ and an equivalent width of only 22 Å. (Both of these values have large uncertainties due to difficulties in defining the continuum for a line with such a low amplitude.) One difference between the two objects is the lower apparent velocities in SN 2008es. The H β and He I $\lambda 5876$ lines of SN 1979C have absorption minima at velocities of 9700 and 8900 km s $^{-1}$. In SN 2008es, these values are 6000 and 5700 km s $^{-1}$, respectively, although we caution that the exact values are correlated with the assumed value for the redshift.

Over the next two months, the spectra of SN 2008es plotted in Figure 2.2 became redder, reflecting the cooling photospheric temperature evolution discussed above. In addition, the spectral features first seen in the day $+16$ spectrum gradually became more prominent. The

SN features are still muted in amplitude relative to those expected in a normal Type II SN. This may be an example of the “top-lighting” effect described by [Branch et al. \(2000\)](#), where continuum emission from interaction with CSM illuminates the SN ejecta from above and results in a rescaling of the amplitudes of spectral features.

By the time of our day +63 spectrum, the P-Cygni spectral features due to H Balmer lines, Na I, and Fe II become more prominent and the overall appearance starts to resemble that of normal SNe II. The $\text{H}\alpha$ profile lacks an absorption component, which may be common to SNe II-L and not SNe II-P (e.g., [Schlegel 1996](#)). The broad $\text{H}\alpha$ emission extends (at zero intensity) from -9000 to 9000 km s^{-1} , with a FWHM of 9500 km s^{-1} . This velocity width is intermediate between that of the SNe 1979C and 1980K spectra ($\text{FWHM} \approx 10,600$ and $\approx 8200 \text{ km s}^{-1}$, respectively).

Unlike in most core-collapse SNe, the velocity of the minimum of the $\text{H}\beta$ line *increased* over time, from 6000 km s^{-1} at day 16, to 8700 km s^{-1} at day 63, as shown in the bottom panel of Figure 2.6. The exact values of the velocity depend directly on the assumed redshift, however the *trend* is independent of those uncertainties. Unfortunately, the other absorption lines are mostly blended (except for $\text{H}\alpha$, which does not show an absorption component), so we cannot isolate the velocity trend in other spectral features without spectral modeling. The top panel of Figure 2.6 shows the evolution of the He I $\lambda 5876/\text{Na I } \lambda 5892$ blend. At early times He I dominates the blend, and as the ejecta cool at later epochs Na I should dominate, resulting in an $\sim 800 \text{ km s}^{-1}$ redward shift of the rest wavelength. After taking into account that redward shift, the top panel of Figure 2.6 also shows some weak evidence for a blueward shift of the absorption minimum to $\sim 8000 \text{ km s}^{-1}$.

The only supernova known to us to show increasing absorption velocities over time is the peculiar SN Ib 2005bf. The trend of increasing absorption velocities was only visible in the three He I lines, but not in other lines, e.g. Ca II H&K ([Modjaz 2007](#)). [Tominaga et al. \(2005\)](#) explained the effect as being due to progressive outward excitation of He I by radioactive ^{56}Ni in the interior as the ejecta expanded and the density decreased, an effect that seems to be of little relevance to SN 2008es. A more likely possibility is that blending with some unidentified line is shifting the velocity of the apparent absorption minimum. At late times $\text{H}\beta$ dominates its region of the spectrum, but at early times He II $\lambda 4686$ could possibly be contributing emission to the blue wing of the $\text{H}\beta$ absorption profile. Another scenario is that some unusual, but as yet unidentified, radiative transfer effect is affecting the wavelength of the apparent absorption minimum in SN 2008es.

2.5 Discussion

2.5.1 The Physical Nature of SN 2008es

The photometric evolution of SN 2008es (see Figure 2.7) is much faster than other very luminous SNe like SNe 2006gy ([Smith et al. 2007; Ofek et al. 2007](#)), 2006tf ([Smith et al. 2008a](#)), and 2005gj ([Prieto et al. 2007](#)), and its spectrum also betrays no evidence for the

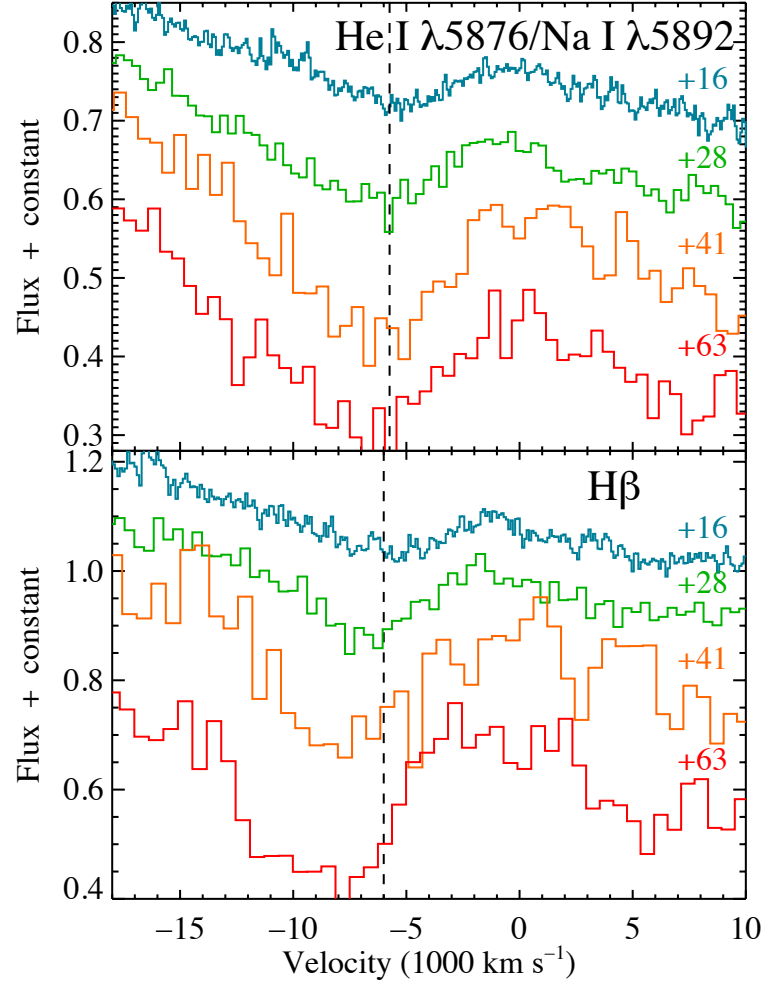


Figure 2.6: Velocity evolution of absorption minima. The spectra are labeled with dates after maximum light in the same manner as in Figure 2.2. In the bottom panel the apparent blueshift of the H β absorption minimum increases over time. A vertical dashed line at -6000 km s^{-1} marks the velocity of the absorption minimum on day 16 to guide the eye. In the top panel, the evolution of the He I $\lambda 5876/\text{Na I } \lambda 5892$ blend is plotted, with $\lambda 5876$ used as the zero point of the velocity scale. The vertical dashed line at -5700 km s^{-1} marks the absorption minimum on day 16 to guide the eye.

strong CSM interaction seen in these other SNe IIn, in the form of narrow lines from the CSM or intermediate-width H α from the post-shock shell. Indeed, considering both its photometric and spectroscopic evolution, we suggest that SN 2008es is most like the over-luminous SN 2005ap (Quimby et al. 2007a) and thereby most closely resembles a Type II-L that is 4–5 mag more luminous than typical SNe II-L (Richardson et al. 2002).

To power the tremendous luminosity of SN 2008es with radioactive decay would require an initial ^{56}Ni mass of $\sim 10 M_\odot$ (see, e.g., Smith et al. 2007). This ^{56}Ni mass would very likely need to be generated in a pair-instability explosion (Barkat et al. 1967; Bond et al. 1984), but this ^{56}Ni mass seems problematic given that it would be larger than the modest envelope mass indicated by the relatively fast rise and decay time (see below). In addition, the photometric decline of 0.042 mag day $^{-1}$ is faster than that of ^{56}Co , 0.0098 mag day $^{-1}$, making radioactive heating unlikely as the dominant source of the energy.

Despite the lack of a Type IIn spectrum, the most likely interpretation seems to be that the high luminosity of SN 2008es is the result of converting shock energy into visual light. This can be accomplished, in principle, if the shock kinetic energy is thermalized throughout a massive envelope, like a normal SN II-P or II-L, but with a much larger initial radius of $(2\text{--}3)\times 10^{15}$ cm (based on the peak luminosity and the evolution in Figure 2.4). The apparent temperature evolution from ~ 15000 to 6000 K over a time period of ~ 66 days (Figure 2.4), reminiscent of other normal SNe II, suggests that the recombination photosphere is receding through a cooling envelope in SN 2008es. In this scenario, the usual narrow/intermediate-width H α emission that is taken as a signpost of CSM interaction might be avoided if the CSM shell is initially very opaque, and if the shock encounters no further CSM material at larger radii (see Smith et al. 2008a). Since the required initial radius exceeds that of the largest known red supergiants (see Smith et al. 2001) by a factor of 20–30, it requires the envelope to be an unbound, opaque CSM shell ejected prior to the SN explosion instead of a traditional bound stellar envelope. Similar models were suggested for SN 2005ap (Quimby et al. 2007a), SN 2006gy (Smith & McCray 2007), and SN 2006tf (Smith et al. 2008a), implying CSM envelope masses of 0.6, ~ 10 , and $18 M_\odot$, respectively. The corresponding CSM mass for SN 2008es would be roughly $\sim 5 M_\odot$ in this scenario, because its evolution and expansion speeds are slower than those of SN 2005ap. This CSM mass of $\sim 5 M_\odot$ allows the observed H α Doppler velocities to remain faster than in SNe 2006gy and 2006tf, where the heavy CSM shells decelerated the shocks to only 4000 and 2000 km s $^{-1}$, respectively (Smith et al. 2007; Smith et al. 2008a). The putative envelope ejection preceding SN 2008es must have occurred 10–100 yr prior to the explosion (for an unknown progenitor wind speed of $V_{\text{CSM}} = 10\text{--}100$ km s $^{-1}$), indicating a progenitor mass-loss rate of order $0.01\text{--}0.1 M_\odot \text{ yr}^{-1}$. This is much larger than any steady stellar wind (see Smith et al. 2007 and references therein), providing another case of impulsive mass ejection in the decades immediately preceding some SNe.

2.5.2 The Host of SN 2008es

Currently there is no conclusive detection of the host galaxy of SN 2008es, so its metallicity and corresponding implications for the pre-SN evolution are not known. From Sloan Digital

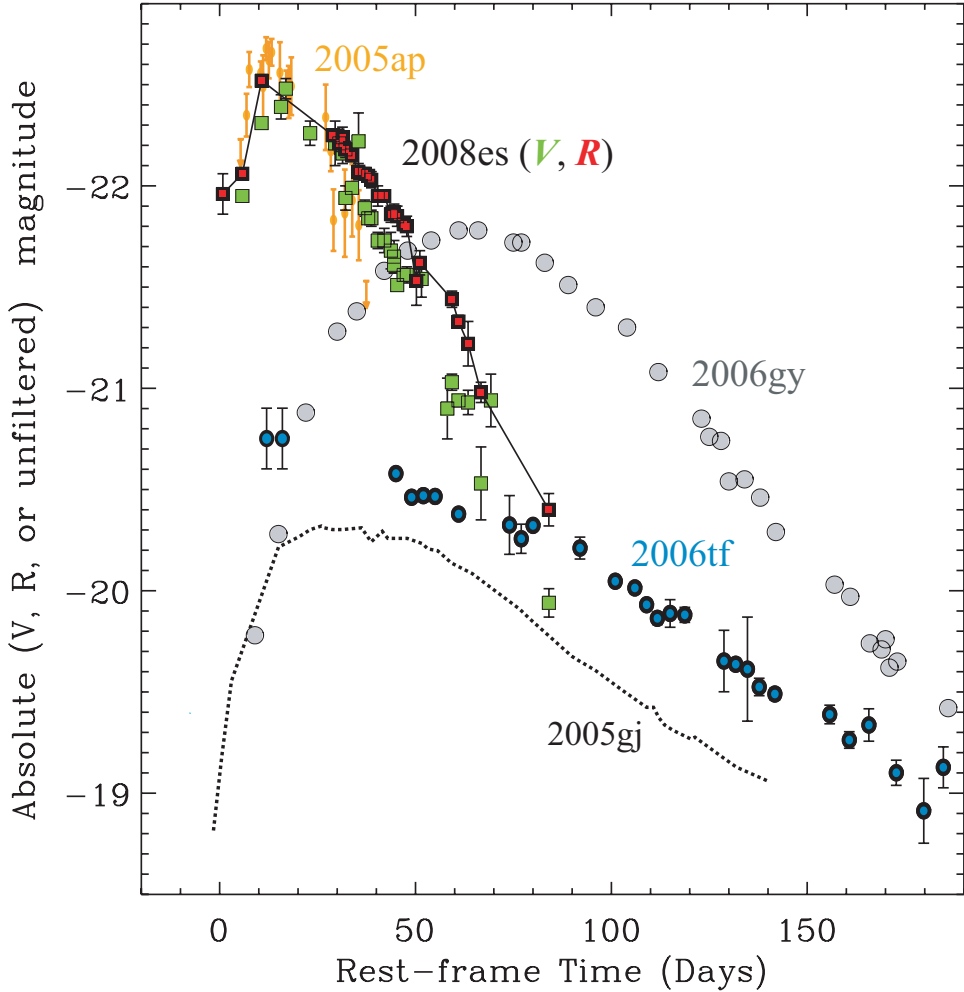


Figure 2.7: Rest-frame brightness evolution of the five most luminous known SNe. For SN 2008es we derive the absolute magnitude using UVOT V -band magnitudes (green squares) and the KAIT/Nickel R -band magnitudes (red squares), assuming that day 0 is the discovery date. The discovery unfiltered magnitude is also shown along with two additional early photometric measurements from [Yuan et al. \(2008\)](#) (red squares). The light curve for SN 2005ap (orange) is derived from unfiltered photometry in [Quimby et al. \(2007a\)](#), and SN 2006gy (gray circles) is also unfiltered from [Smith et al. \(2007\)](#). R -band photometry of SN 2006tf (blue circles) is from [Smith et al. \(2008a\)](#), and r/r' photometry of SN 2005gj (dotted line) is from [Prieto et al. \(2007\)](#). The light curve for SN 2006tf is shifted by +16 days from that in [Smith et al. \(2008a\)](#); since the explosion date is not known, we chose to align its time of peak luminosity with those of SNe 2005ap and 2008es.

Sky Survey DR6 images (Adelman-McCarthy et al. 2008) we derive a 3σ upper limit of $m_{r'} > 22.7$ mag at the SN position, which translates to roughly $M_V > -17.4$ mag at the SN redshift (neglecting any K corrections). Thus, the putative host galaxy is significantly less luminous than an L_* galaxy and could be comparable to or fainter than the Small Magellanic Cloud (with $M_V = -16.9$ mag).¹ In analogy with the under-luminous hosts of SNe 2006tf and 2005ap, deep imaging after the SN has faded may uncover the host galaxy nearly coincident with the SN position.

2.5.3 Rates of Extremely Luminous SN 2008es-like Events

Over the past 3 years the TSS has successfully found tens of SNe with a surprising rate of unusual objects. The list of such SNe includes SN 2005ap, SN 2006gy, SN 2006tf, and now SN 2008es. However, this apparent high anomaly rate is probably the result of combining a huge survey volume with an intrinsically rare class of objects. Following Quimby (2008), we compare the volume probed by the TSS for SNe Ia, and bright core-collapse SNe. The highest redshift of the ~ 30 SNe Ia found by the TSS is $z \approx 0.1$, while SN 2005ap was found at $z \approx 0.3$. The comoving volume scanned by the TSS is therefore ~ 23 times bigger for SN 2008es-like objects than for SNe Ia. Of the 4 bright objects found by the TSS, only two, SN 2005ap and SN 2008es, can be considered together as a class. Thus, the comparative rate is about $30/2 \times 23 \approx 350$ times smaller.

The KAIT SN search (Filippenko et al. 2001) has discovered about 400 SNe Ia in the past 10 years in targeted nearby galaxies, hence the expected number of SN 2008es-like objects is of order 1. This is consistent with the nondetection of any such SN.

Using the light curve of SN 2008es and the accumulated observations of about 10,000 spiral galaxies in the KAIT sample which were observed regularly during the past ten years, we find an upper limit on the rate (per unit K -band luminosity) of such SNe to be about 1/160 times the local type II SN rate (Li et al. 2011b). We therefore conclude that the number of luminous Type II-L SNe, as discovered by the TSS, does not appear to be the result of a statistical fluke, and predict many such detections with future wide-field synoptic surveys.

2.6 Conclusions

We have reported on our early observations of SN 2008es, which at a peak optical magnitude of $M_V = -22.5$ mag is the second most luminous SN ever observed. We argue that the extreme luminosity of this SN was likely powered via a strong interaction with a dense CSM, and that the steep decline in the light curve, $0.042 \text{ mag day}^{-1}$, indicates that the radioactive decay of ^{56}Co is likely not the dominant source of energy for this SN. Integration

¹A galaxy $\sim 9''$ to the NE of the SN position is unlikely to be the host itself even if found to be at a similar redshift as SN 2008es; this would require significant massive star formation at a projected physical distance of ~ 31 kpc.

of the bolometric light curve of SN 2008es yields a total radiated energy output of $\gtrsim 10^{51}$ erg. The spectra of SN 2008es resemble those of the luminous SN 1979C, but with an unexplained increase in the velocity of the H β absorption minimum over time. We also examine the almost astonishing rate of discovery of extremely luminous SNe by the Texas Supernova Search and find that their discovery of the four most luminous observed SNe in the past four years is not a fluke; we suggest that several more such detections are expected in the coming years.

Finally, what behavior can we expect from SN 2008es at late times, roughly 1 yr or more after discovery? Regardless of whether the peak luminosity was powered by radioactive decay or optically-thick CSM interaction (see [Smith et al. 2008c](#)), a SN can be powered by strong CSM interaction at late times if the progenitor had a sufficiently high mass-loss rate in the centuries before exploding. We have seen examples of both: SN 2006tf had strong H α emission indicative of ongoing CSM interaction at late times ([Smith et al. 2008a](#)), whereas SN 2006gy did not ([Smith et al. 2008c](#)). SN 1979C was less luminous at peak than those two SNe, but it has been studied for three decades because its late-time CSM interaction is powering ongoing emission in the radio, optical, and X-rays ([Weiler et al. 1981](#); [Fesen & Matonick 1993](#); [Immler et al. 1998](#)). With such an extraordinarily high peak luminosity, a late-time IR echo like that seen in SN 2006gy ([Smith et al. 2008c](#)) is also likely if SN 2008es has dust waiting at a radius of ~ 0.3 pc. Alternatively, if SN 2008es were powered in whole or in part by radioactivity, a large mass of ^{56}Ni should be evident in the late-time decline rate, provided that SN 2008es can still be detected, since we should expect a H-rich envelope to remain optically thick to the γ -ray heating of radioactive decay.

Acknowledgments

A version of this chapter appears in the *Astrophysical Journal*, 2009, 690, 1303.

During the writing of this chapter I was supported by a UC Berkeley Chancellor's Fellowship, for which I am grateful for the funding.

B. Jannuzzi approved Kitt Peak Director's Discretionary (DD) time observations, which were essential to determining the true classification of SN 2008es. I thank Diane Harmer and David L. Summers for carrying out the DD observations. I thank M. Malkan for accommodating a small telescope time trade, which allowed us to observe SN 2008es one final time before it disappeared behind the sun. Finally, I thank C. V. Griffith, N. Joubert, and B. Macomber for assistance with some of the observations, and P. Nugent for checking for pre-imaging of SN 2008es from DeepSky.

Chapter 3

New Observations of the Very Luminous Supernova 2006gy: Evidence for Echoes

Supernova (SN) 2006gy was a hydrogen-rich core-collapse SN that remains one of the most luminous optical supernovae ever observed. The total energy budget ($> 2 \times 10^{51}$ erg radiated in the optical alone) poses many challenges for standard SN theory. We present new ground-based near-infrared (NIR) observations of SN 2006gy, as well as a single epoch of *Hubble Space Telescope (HST)* imaging obtained more than two years after the explosion. Our NIR data taken around peak optical emission show an evolution that is largely consistent with a cooling blackbody, with tentative evidence for a growing NIR excess starting around day ~ 130 . Our late-time Keck adaptive optics NIR image, taken on day 723, shows little change from previous NIR observations taken around day 400. Furthermore, the optical *HST* observations show a reduced decline rate after day 400, and the SN is bluer on day 810 than it was at peak. This late-time decline is inconsistent with ^{56}Co decay, and thus is problematic for the various pair-instability SN models used to explain the nature of SN 2006gy. The slow decline of the NIR emission can be explained with a light echo, and we confirm that the late-time NIR excess is the result of a massive ($\gtrsim 10 M_{\odot}$) dusty shell heated by the SN peak luminosity. The late-time optical observations require the existence of a scattered light echo, which may be generated by the same dust that contributes to the NIR echo. Both the NIR and optical echoes originate in the proximity of the progenitor, $\sim 10^{18}$ cm for the NIR echo and $\lesssim 10\text{--}40$ pc for the optical echo, which provides further evidence that the progenitor of SN 2006gy was a very massive star.

3.1 Introduction

At the time of discovery, supernova (SN) 2006gy was the most luminous SN ever found (Ofek et al. 2007; Smith et al. 2007). SN 2006gy generated a great deal of interest; in addition

to being \sim 100 times more luminous than a typical Type II (hydrogen-rich, core-collapse) SN at peak, it exhibited a long rise time (\sim 70 day) and slow decline, leading to speculation that it may have been the first observed example of a pair-instability SN (PISN; Ofek et al. 2007; Smith et al. 2007)¹ or a pulsational pair-instability SN (Woosley et al. 2007).

SN 2006gy was classified as a Type IIn SN (see Schlegel 1990 for a definition of the Type IIn subclass and Filippenko 1997 for a review of its spectral properties) based on the relatively narrow emission features present in the early-time SN spectrum. Some Type IIn supernovae (SNe IIn) are known to be over luminous relative to their typical SN II counterparts: $M_R \approx -15.8$ mag for Type II-P with a 1σ scatter of 1.1 mag (Li et al. 2011b), whereas SN 2006gy reached $M_R \approx -21.7$ mag. The enhanced luminosity of some SNe IIn is probably due to the collision of fast-moving SN ejecta with a dense, and possibly clumpy, circumstellar medium (CSM; e.g., Chugai & Danziger 1994). In a companion paper (Smith et al. 2010a), a detailed spectroscopic comparison of SN 2006gy is made to other SNe IIn. SN 2006gy is unique within the SN IIn subclass, however, because typical interaction models cannot explain its early-time behavior, suggesting the need for alternative models for this particular object (Smith et al. 2007; Woosley et al. 2007; Nomoto et al. 2007; Smith et al. 2010a).

Pair-instability SNe (Barkat et al. 1967; Rakavy & Shaviv 1967; Bond et al. 1984) are expected to occur in very massive, low-metallicity stars, such as those that may have been present in the metal-free environment of the very early universe (e.g., Abel et al. 2000). The detection of a pair-instability SN in the comparatively local universe, then, could potentially reveal a great deal about the first generation of stars. The light curves of pair-instability SNe are expected to exhibit a relatively slow rise, followed by a broad turnover after the peak, and a peak luminosity that is considerably larger than that of typical SNe (Scannapieco et al. 2005). Qualitatively, each of these characteristics matches those observed for SN 2006gy.

Other more luminous SNe have been announced since the discovery of SN 2006gy: SNe 2005ap (Quimby et al. 2007a) and 2008es (Miller et al. 2009b; Gezari et al. 2009). This suggests that while these events are rare, there may be a new subclass of very luminous supernovae (VLSNe). The peak luminosity and photometric evolution of both SNe 2005ap and 2008es are difficult to explain via the pair-instability model (Quimby et al. 2007a; Miller et al. 2009b), implying that peak luminosities \gtrsim few $\times 10^{44}$ erg s $^{-1}$ are possible without a pair-instability explosion. There is a wide diversity of alternative models that have been developed to explain the early-time observations of SN 2006gy. Smith & McCray (2007) argue that the peak luminosity and light-curve evolution can be explained via the thermalization of shock energy deposited into a massive ($\sim 10 M_\odot$), optically thick shell. Based on a model of the light curve near peak, Agnoletto et al. (2009) suggest that the combination of ejecta colliding with dense clumps in the CSM and $\sim 1-3 M_\odot$ of ^{56}Ni are responsible for the early-time luminosity of SN 2006gy. Nomoto et al. (2007) are unable to match the light curve with a standard pair-instability SN model; however, they can reasonably reproduce the ($\lesssim 400$ day) light curve of SN 2006gy using a pair-instability model where they artificially reduce the

¹Currently, there is much stronger evidence that SN 2007bi is the first observed example of a PISN (Gal-Yam et al. 2007).

ejecta mass, such that the radioactive heating is less than 100% efficient. The reduction in ejecta mass should lead to a reduction in ^{56}Ni production, as noted by Nomoto et al. (2007); thus, their model with an artificially reduced ejecta mass may not be self consistent. Woosley et al. (2007) use a model of a pulsational pair instability within a massive star to explain the light curve of SN 2006gy.

Some of the models make predictions for the late-time behavior of SN 2006gy. Those with a large yield of ^{56}Ni (Nomoto et al. 2007; Smith et al. 2007) would expect a decline in bolometric luminosity at the rate of ^{56}Co decay, $0.98 \text{ mag} (100 \text{ day})^{-1}$, or faster if the radioactive-decay energy is not converted to optical emission with 100% efficiency. The shell-shock model (Smith & McCray 2007) predicts a rapid decline after ~ 200 day, though the authors note that this decline may be offset by the production of a large amount of ^{56}Ni or continued CSM interaction. The pulsational pair-instability model (Woosley et al. 2007) predicts another SN explosion at the location of SN 2006gy about 9 years after the initial outburst from SN 2006gy.

More than a year after the explosion, Smith et al. (2008c) detected SN 2006gy in the near infrared (NIR) at a luminosity comparable to that of the peak luminosity of most SNe II. This property had not been predicted by any of the models. When coupled with the lack of a detection in the radio and X-rays, this led Smith et al. (2008c) to conclude that the luminosity could not be powered by the continued interaction of the SN ejecta with CSM. Kawabata et al. (2009) draw similar conclusions based on their detection of weak H α emission at a comparable epoch. Smith et al. (2008c) conclude that only two possibilities are able to explain the late-time observations of SN 2006gy: (i) the explosion produced $\gtrsim 2.5 M_{\odot}$ of ^{56}Ni , which is only theoretically expected for PISNe (e.g., Scannapieco et al. 2005), which was heating dust and consequently generating the large NIR excess, or (ii) a massive ($\sim 5\text{--}10 M_{\odot}$), dusty shell, located ~ 1 light year from the site of the SN, was being heated by the radiation produced at peak, and reradiating that energy as a NIR echo (Dwek 1983). For the first case, if the luminosity were powered by radioactive decay, then future observations should indicate a continued decline at the rate of ^{56}Co decay. A dust echo, on the other hand, would result in a NIR light curve that stays roughly constant for $\sim 1\text{--}2$ yr before exhibiting a rapid decline.

Evolved massive stars, such as red supergiants and luminous blue variables (LBVs), are often observed to have massive dust shells, so if these stars explode as SNe IIn one might expect a late-time IR echo. Many SNe IIn have been observed to exhibit a late-time NIR excess (Gerardy et al. 2002) which in some cases lasted > 1 yr. This excess has been attributed to NIR echoes (Gerardy et al. 2002), though we note that the formation of new dust has been argued specifically for SN 1998S (Pozzo et al. 2004) and SN 1995N (Fox et al. 2009). Dusty regions near the SN should also lead to ultraviolet (UV) and optical scattered-light echoes (Chevalier 1986); thus, dust is capable of providing significant optical and NIR emission at late times. The optical decline of SNe IIn at late times is very heterogeneous (Li et al. 2002), and therefore caution must be applied when determining the source of any late-time emission.

In this Chapter we present new NIR observations of SN 2006gy, taken around the peak of optical emission, as well as optical and NIR observations obtained more than two years after SN 2006gy exploded. In §3.2 we describe the observations and data reduction. We discuss the

results in §3.3, and in §3.4 we offer some conclusions. Throughout this Chapter we assume that the distance to NGC 1260 (the host galaxy of SN 2006gy) is 73.1 Mpc, and following Smith et al. (2007) we adopt $E(B-V) = 0.54$ mag as the reddening toward SN 2006gy within the host galaxy, while Galactic extinction accounts for $E(B-V) = 0.18$ mag, leading to a total color excess toward SN 2006gy of $E(B-V) = 0.72$ mag. All spectral energy distributions (SEDs) have been corrected for this color excess assuming $R_V = A_V/E(B-V) = 3.1$ using the reddening law of Cardelli et al. (1989).

3.2 Observations

NIR observations of SN 2006gy were obtained simultaneously in J , H , and K_s with the Peters Automated Infrared Imaging Telescope (PAIRITEL; Bloom et al. 2006) starting on 2006 October 13 UT² (54 days after explosion³). PAIRITEL is a 1.3-m robotic telescope, located on Mt. Hopkins, AZ, which obtained images over the next 24 months for 0.5–1 hr at each of the 124 epochs through normal queue-scheduled operations. All images were processed via an automated pipeline (Bloom et al. 2006).

Analysis of SN 2006gy has proved challenging because the SN is located very close to the nucleus of NGC 1260 (separation $\sim 1''$; Ofek et al. 2007; Smith et al. 2007). PAIRITEL has a large native scale of $2'' \text{ pixel}^{-1}$, precluding spatial resolution of the SN from the nucleus. This necessitates image differencing to obtain the light curve of the SN. Image subtraction was performed with HOTPANTS⁴, and the flux in each difference pair was determined via aperture photometry at the location of the SN. An example subtraction, which clearly shows flux from SN 2006gy after the reference image has been subtracted, is shown in Figure 3.1.

Despite observations extending more than two years past the date of discovery, SN 2006gy has not faded beyond the point of detectability with PAIRITEL. Consequently, all J , H , and K_s images of SN 2006gy contain some flux from the SN. We thus adopted the “NN2 method” of Barris et al. (2005) to determine the relative NIR flux changes of the SN. The NN2 method treats all images equally and does not require a template image with no light from the source of interest, SN 2006gy. It uses the subtraction of all $N(N - 1)$ pairs of images to mitigate against possible errors associated with the use of a single reference template image. The downside to the NN2 method is that it only produces the differential flux between each of the N epochs of observations. To convert these flux differences into magnitudes requires an absolute calibration, which must be obtained independently of the results from the NN2 method. Uncertainties in the individual subtractions were estimated by measuring the scatter in fake SNe inserted at locations having a surface brightness similar to that at the position of SN 2006gy.

Early-time NIR observations of SN 2006gy (defined here as those made before SN 2006gy passed behind the Sun during 2007) show a remarkably flat light curve, as seen in Figure 3.2.

²All dates in this Chapter are UT unless otherwise noted.

³Following Smith et al. (2007), we adopt 2006 August 20 as the explosion date for SN 2006gy.

⁴<http://www.astro.washington.edu/users/becker/hotpants.html>.

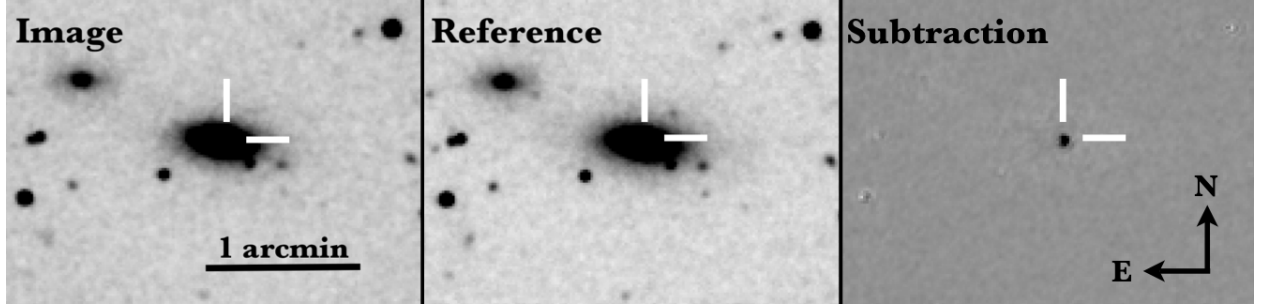


Figure 3.1: Example subtraction of PAIRITEL NIR images of SN 2006gy, which have all been registered to the same coordinate frame. Each image is $\sim 2' \times 3'$ in size. *Left:* PAIRITEL K_s -band image taken on 2006 Nov. 15. *Middle:* PAIRITEL K_s -band image taken on 2007 Jan. 01. *Right:* Image (left panel) minus reference (middle panel) subtraction image. The image subtraction was performed with HOTPANTS, and SN 2006gy is clearly visible in the difference image as a bright point source near the galaxy nucleus.

To transform the relative-flux differences from the NN2 method to an absolute scale, we subtracted the archival Two Micron All Sky Survey (2MASS; [Skrutskie et al. 2006](#)) image from each of the images obtained on 2006 Nov. 13.24, 14.25, 15.38, and 16.37 to determine the J , H , and K_s magnitudes of the SN on these dates. The mean SN flux was then used to transform the relative flux from the NN2 method to the absolute flux of the 2MASS system ([Cohen et al. 2003](#)). PAIRITEL uses the old 2MASS camera and telescope; hence, we do not expect any large systematic effects in the 2MASS subtractions. The final calibrated J , H , and K_s photometry is summarized in Table 3.1.

On 2006 Nov. 01, [Ofek et al. \(2007\)](#) obtained adaptive optics (AO) images in the J and K_s bands with the Palomar Hale (5 m) telescope, clearly resolving SN 2006gy from the host-galaxy nucleus, and measured its flux. In the K_s band our calibration and the [Ofek et al. \(2007\)](#) measurement agree to within 1σ , while the agreement in the J band is somewhat worse ($\sim 2\sigma$). [Ofek et al. \(2007\)](#) had only a single 2MASS star within the field of view of their AO images, whereas >100 2MASS stars were used to calibrate the PAIRITEL images; when coupled with the difficulty associated with photometry of AO images, this may explain the differences between the two measurements. We note that were we to adopt the [Ofek et al. \(2007\)](#) measurements as our calibration, there would be an overall systematic shift of our J and K_s light curves to brighter values, which in turn would lead to worse agreement between the NIR data and early-time optical spectra (see Figure 3.4). This suggests that our calibration method is sufficient. We note that the uncertainties in our photometry are dominated by the uncertainty in the calibration, which is ~ 0.03 mag in J , ~ 0.06 mag in H , and ~ 0.04 mag in K_s . This uncertainty is the same for all epochs, so a change in the calibration would lead to a systematic shift of the entire light curve.

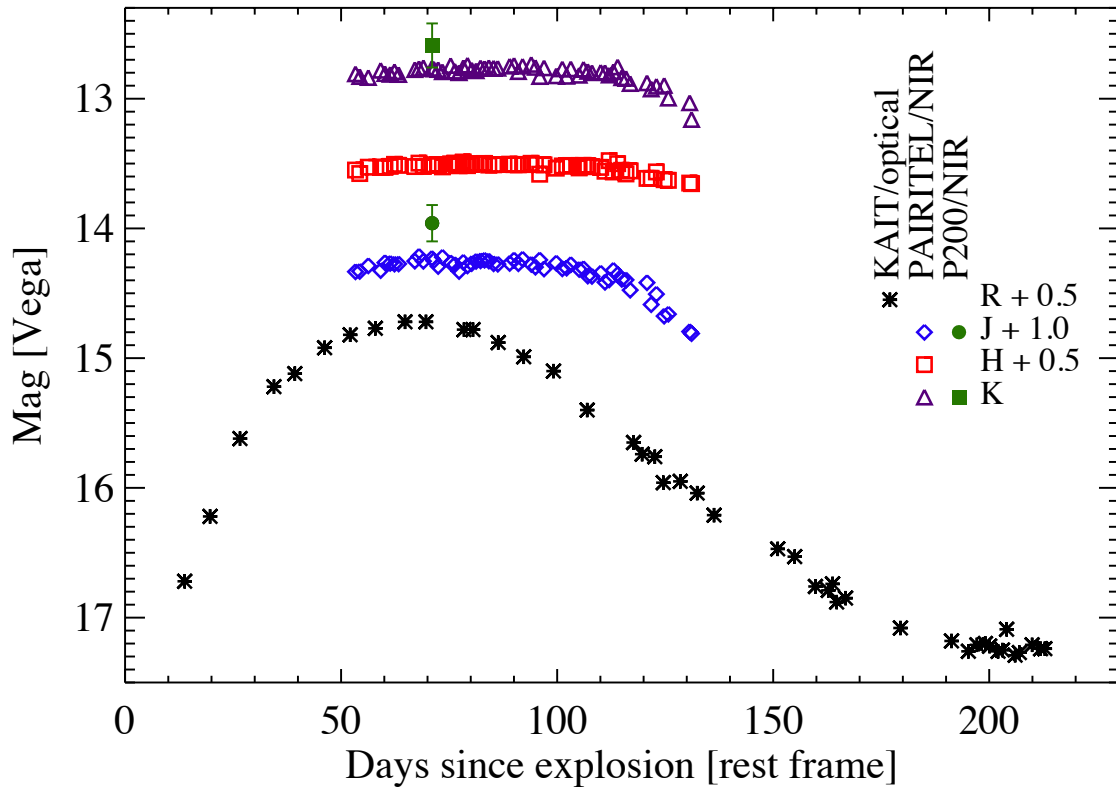


Figure 3.2: Early-time photometric evolution of SN 2006gy. Unfiltered KAIT (roughly R band) observations are taken from Smith et al. (2007). PAIRITEL J , H , and K_s observations are from this work. We also show the Palomar AO photometry from Ofek et al. (2007). The data have not been corrected for extinction in the host or the Galaxy. The NIR evolution is remarkably flat, with the $R - K$ color increasing steadily after day ~ 70 . This behavior is consistent with a cooling blackbody (see text).

Table 3.1: PAIRITEL Observations of SN 2006gy

$t_{\text{mid}}^{\text{a}}$ (MJD)	J mag ^b (Vega)	H mag ^b (Vega)	K_s mag ^b (Vega)
54021.29	13.33 ± 0.04	13.05 ± 0.06	12.81 ± 0.05
54022.28	13.33 ± 0.04	13.08 ± 0.09	12.83 ± 0.05
54024.30	13.29 ± 0.04	13.03 ± 0.06	12.84 ± 0.06
54027.22	13.32 ± 0.04	13.03 ± 0.06	12.78 ± 0.04
54028.23	13.26 ± 0.04	13.03 ± 0.06	12.81 ± 0.05
54029.46	13.27 ± 0.03	13.02 ± 0.06	12.81 ± 0.06
54030.47	13.27 ± 0.04	13.01 ± 0.06	12.79 ± 0.04
54031.45	13.27 ± 0.04	13.01 ± 0.06	12.81 ± 0.05
54035.26	13.25 ± 0.04	13.02 ± 0.06	12.78 ± 0.04
54036.25	13.21 ± 0.05	13.00 ± 0.06	12.77 ± 0.04
54037.28	13.25 ± 0.03	13.02 ± 0.06	12.76 ± 0.04
54039.28	13.23 ± 0.04	13.01 ± 0.06	12.77 ± 0.04
54040.29	13.25 ± 0.04	13.01 ± 0.06	12.77 ± 0.05
54041.31	13.29 ± 0.04	13.01 ± 0.06	12.78 ± 0.04
54042.32	13.22 ± 0.05	13.03 ± 0.08	12.79 ± 0.09
54044.27	13.26 ± 0.04	13.00 ± 0.06	12.74 ± 0.04
54045.27	13.28 ± 0.05	13.00 ± 0.06	12.79 ± 0.05
54046.25	13.33 ± 0.04	13.02 ± 0.07	12.80 ± 0.05
54047.25	13.26 ± 0.03	12.99 ± 0.06	12.76 ± 0.05
54048.23	13.29 ± 0.04	13.02 ± 0.06	12.74 ± 0.05
54049.23	13.27 ± 0.04	13.01 ± 0.06	12.78 ± 0.05
54050.27	13.25 ± 0.03	13.00 ± 0.06	12.78 ± 0.04
54051.31	13.25 ± 0.04	13.00 ± 0.06	12.76 ± 0.04
54052.25	13.24 ± 0.04	13.00 ± 0.06	12.77 ± 0.04
54053.26	13.25 ± 0.03	13.01 ± 0.06	12.76 ± 0.04
54054.38	13.27 ± 0.04	13.01 ± 0.06	12.76 ± 0.04
54055.38	13.28 ± 0.04	13.01 ± 0.06	12.77 ± 0.04
54058.18	13.27 ± 0.03	13.00 ± 0.06	12.75 ± 0.04
54059.19	13.24 ± 0.04	13.01 ± 0.06	12.74 ± 0.05
54060.22	13.27 ± 0.03	13.01 ± 0.06	12.79 ± 0.04
54061.21	13.24 ± 0.04	13.01 ± 0.06	12.75 ± 0.05
54063.24	13.28 ± 0.04	13.00 ± 0.06	12.74 ± 0.05
54064.24	13.30 ± 0.04	13.01 ± 0.06	12.76 ± 0.04
54065.24	13.24 ± 0.07	13.08 ± 0.11	12.83 ± 0.19
54066.25	13.31 ± 0.04	13.01 ± 0.06	12.76 ± 0.05
54069.15	13.27 ± 0.04	13.04 ± 0.06	12.82 ± 0.05
54070.13	13.31 ± 0.04	13.02 ± 0.06	12.77 ± 0.04
54071.15	13.31 ± 0.05	13.02 ± 0.06	12.83 ± 0.05
54072.13	13.28 ± 0.04	13.01 ± 0.06	12.77 ± 0.04
54074.09	13.31 ± 0.04	13.03 ± 0.06	12.82 ± 0.05
54075.13	13.31 ± 0.04	13.01 ± 0.06	12.77 ± 0.05
54076.12	13.37 ± 0.04	13.02 ± 0.06	12.79 ± 0.04
54077.12	13.37 ± 0.04	13.02 ± 0.06	12.80 ± 0.04
54079.18	13.34 ± 0.05	13.03 ± 0.06	12.80 ± 0.05
54080.18	13.41 ± 0.05	13.06 ± 0.06	12.80 ± 0.04
54081.17	13.40 ± 0.04	12.98 ± 0.06	12.82 ± 0.05
54082.15	13.32 ± 0.07	13.07 ± 0.07	12.79 ± 0.05
54083.16	13.36 ± 0.09	13.00 ± 0.06	12.75 ± 0.05
54084.14	13.39 ± 0.05	13.05 ± 0.06	12.84 ± 0.08
54085.13	13.40 ± 0.05	13.08 ± 0.07	12.84 ± 0.05
54086.13	13.48 ± 0.06	13.06 ± 0.07	12.88 ± 0.06
54090.08	13.42 ± 0.04	13.11 ± 0.07	12.88 ± 0.05

Table 3.1 (*cont'd*): PAIRITEL Observations of SN 2006gy

$t_{\text{mid}}^{\text{a}}$ (MJD)	J mag ^b (Vega)	H mag ^b (Vega)	K_s mag ^b (Vega)
54091.08	13.59 ± 0.09	13.11 ± 0.07	12.93 ± 0.05
54092.29	13.51 ± 0.11	13.06 ± 0.06	12.90 ± 0.07
54094.12	13.68 ± 0.11	13.12 ± 0.07	12.90 ± 0.05
54095.12	13.66 ± 0.11	13.13 ± 0.07	13.00 ± 0.16
54100.14	13.79 ± 0.08	13.15 ± 0.07	13.03 ± 0.13
54101.15	13.81 ± 0.07	13.16 ± 0.07	13.16 ± 0.14

^aMidpoint between the first and last exposures in a single stacked image.

^bObserved value; not corrected for Galactic extinction.

As shown by [Smith et al. \(2008c\)](#), and subsequently confirmed by [Agnoletto et al. \(2009\)](#), the NIR evolution of SN 2006gy is very slow at late times. Given the relatively small change in flux, and the reduced signal-to-noise ratio following the fading of the SN, we were unable to recover reliable flux measurements from PAIRITEL data taken after 2007 Sep. Furthermore, unlike the case at early times, the SN had faded below the 2MASS detection limit, which means that the late-time subtractions relative to the 2MASS template image do not yield meaningful results despite the fact that at $K_s \approx 15$ the SN is well above the PAIRITEL detection limit. In principle, if deep PAIRITEL images are obtained after SN 2006gy fades well beyond the detection limit, it should be possible to recover the late-time NIR light curve using template images that contain little or no light from the SN.

We also observed SN 2006gy on 2008 Aug. 25 with the Near-Infrared Camera 2 (NIRC2) using the laser guide star (LGS) AO system ([Wizinowich et al. 2006](#)) on the 10-m Keck II telescope in Hawaii. We have re-reduced the LGS AO images presented by [Smith et al. \(2008c\)](#) from days 398 and 461⁵ and derive revised values for the K' -band magnitudes of SN 2006gy, as summarized in Table 3.2.⁶ The uncertainty on these measurements is large ($\gtrsim 0.17$ mag), and is dominated by the uncertainty in the single calibration star within the field of view. We also present the first measurement of the H -band flux from the AO images taken on 2007 Dec. 2. To obtain this H -band measurement, despite a lack of 2MASS stars in the field, we measured the $H - K'$ color of SN 2006gy relative to the $H - K'$ color of the host galaxy, and calibrated this against the $H - K_s$ color of the galaxy in the archival 2MASS images. The large uncertainty for this measurement reflects the accuracy with which we can determine the color of the galaxy from the 2MASS images.

As part of a *Hubble Space Telescope (HST)* snapshot survey (GO-10877; PI Li), SN 2006gy was observed with the Wide Field Planetary Camera 2 (WFPC2; [Holtzman et al. 1995b](#))

⁵Note that [Smith et al. \(2008c\)](#) refer to these epochs as day 405 and 468, which is the elapsed time in the observed frame. All epochs in the present work are labelled in terms of the elapsed time in the rest frame.

⁶Late-time Keck AO observations were all made in the K' band. The uncertainty associated with the transformation between K' and K_s is small compared to the absolute calibration uncertainty; hence, for the late-time AO images $K' \approx K_s$.

Table 3.2: Keck AO Observations of SN 2006gy

date (UT)	epoch ^a (day)	Filter	mag ^b (Vega)
2007 Sep. 29	398	K'	14.91 ± 0.17
2007 Dec. 02	461	H	16.8 ± 0.3
2007 Dec. 02	461	K'	15.02 ± 0.17
2008 Aug. 25	723	K'	15.59 ± 0.21

^aRest-frame days from the adopted explosion date, 2006 Aug. 20 ([Smith et al. 2007](#)).

^bObserved value; not corrected for Galactic extinction.

Table 3.3: HST day 810 Observations of SN 2006gy

Filter	$\lambda_{\text{cent}}^{\text{a}}$ (Å)	$\Delta\lambda^{\text{b}}$ (Å)	mag ^c (Vega)	Flux ^d (μJy)
<i>F450W</i>	4519	957	22.16 ± 0.03	5.97 ± 0.18
<i>F555W</i>	5397	1226	21.51 ± 0.02	9.31 ± 0.19
<i>F675W</i>	6697	866	21.07 ± 0.03	11.29 ± 0.34
<i>F814W</i>	7924	1500	20.91 ± 0.04	10.80 ± 0.43

^aCentral wavelength of the filter, based on WFPC2 calibrations presented in Table 8 of [Holtzman et al. \(1995a\)](#).

^bFilter width, based on WFPC2 calibrations presented in Table 8 of [Holtzman et al. \(1995a\)](#).

^cObserved value; not corrected for Galactic extinction.

^dObserved flux using the photometric calibrations presented in Table 9 of [Holtzman et al. \(1995a\)](#).

using the *F450W*, *F555W*, *F675W*, and *F814W* filters on 2008 Nov. 22. The data were reduced in the standard fashion using `multidrizzle` ([Koekemoer et al. 2003](#)). NGC 1260 and SN 2006gy were located at the center of the PC chip of WFPC2, which has a native pixel scale of $0.0455'' \text{ pixel}^{-1}$. We follow the recipe of [Dolphin \(2000\)](#) to do charge-transfer efficiency correction and photometric reduction of the WFPC2 images. Our measurements of the SN 2006gy magnitudes are summarized in Table 3.3. A false-color image of this detection is shown in Figure 3.3.

3.3 Discussion

3.3.1 Early-Time NIR Observations

While the early-time evolution of SN 2006gy is remarkably flat in the NIR (see Figure 3.2), we find that these measurements are consistent with radiation from a cooling blackbody. From blackbody fits to optical spectra, [Smith et al. \(2010a\)](#) find that the temperature of SN 2006gy monotonically cools after day ~ 50 , roughly two weeks before optical maximum,

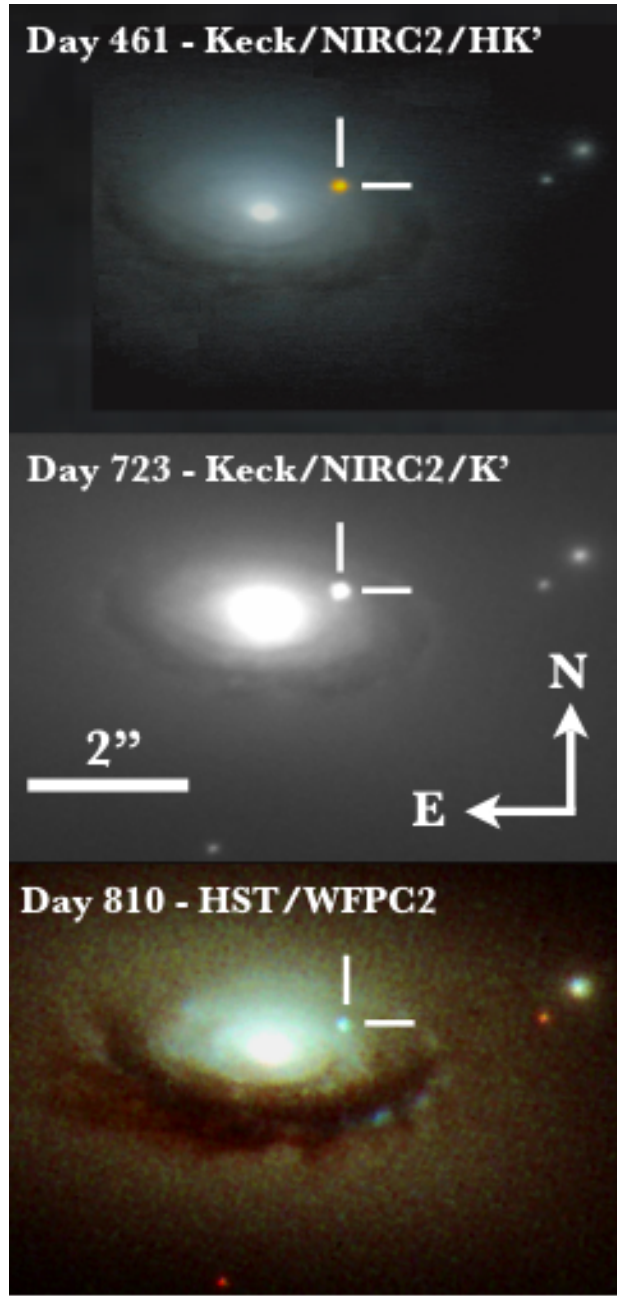


Figure 3.3: Late-time optical and NIR images of SN 2006gy. *Top:* Keck AO H and K' false-color image from Smith et al. (2008c). The SN is clearly red in the NIR. Note that the field of view for this image is slightly smaller than that of the others. *Middle:* Keck AO K' image of SN 2006gy taken on day 723. The SN is still clearly visible in the NIR, and has shown little change since observations taken around day 400. *Bottom:* HST WFPC2 false-color image including the four filters in which we detect SN 2006gy: $F450W$ (corresponding to blue), $F555W$, $F675W$, and $F814W$ (corresponding to red). The SN is clearly blue in the optical compared to the light from the surrounding stars.

until day ~ 165 , where the temperature levels off at ~ 6300 K. In the top panel of Figure 3.4 we show the evolution of the SED of SN 2006gy for three epochs (day 58, 107, and 133) during our early-time NIR observations. These three epochs were chosen as a representative sample covering the full range of our early NIR observations. The evolution of the SED is gradual; the three epochs shown in Figure 3.4 are not more or less statistically significant, in terms of the observed NIR excess (see below), than other epochs from similar times. For each epoch we show the single-component blackbody spectrum, after adopting the temperature from Smith et al. (2010a) and normalizing the spectra to the photometric measurements from Smith et al. (2007). Their photometric observations come from a series of unfiltered observations taken with the Katzman Automatic Imaging Telescope (KAIT; Filippenko et al. 2001), which are best matched by the R band (Riess et al. 1999; Li et al. 2003). However, the scatter in the transformation between KAIT unfiltered and R can be quite large (M. Ganeshalingam 2009, private communication), so we adopt a 0.1 mag uncertainty for the calibration of the blackbody spectra. We also show the NIR flux during these epochs, determined from the absolute calibration of the 2MASS system (Cohen et al. 2003). This shows excellent agreement with an extrapolation of the early-time spectra of SN 2006gy (Smith et al. 2010a). Between day ~ 55 – 135 roughly 2–4% of the bolometric luminosity of SN 2006gy was emitted in the NIR.

In the lower panel of Figure 3.4 we show the fractional excess of the photometric observations relative to the single-component blackbodies (note that by definition the R -band excess is set to zero). For clarity we do not show the uncertainties associated with the excess, but after accounting for the large uncertainty in the R -band calibration, each point is within $\sim 1\sigma$ of zero excess. Nevertheless, there is an apparent trend that the excess is growing in the H and K_s bands as a function of time. The trend may be indicative of radiation from warm dust (see below), though we note that this effect would be small. If this trend toward a NIR excess is created by the same source as the late-time NIR excess, we would expect a K_s -band excess of ~ 0.17 mag, which is comparable to the combined uncertainty from the blackbody calibration and photometric measurements.

3.3.2 Late-Time NIR Observations

With data obtained more than a year after explosion, Smith et al. (2008c) discovered a significant NIR excess from SN 2006gy. Our NIR observations taken 723 days after explosion show that the K' -band flux from SN 2006gy has only faded by a factor of ~ 2 over the course of the previous year. We cannot determine the total IR luminosity at late times, because our NIR data do not cover the peak of the SED. Furthermore, as first noted by Smith et al. (2008c), the very red $H - K'$ color at late times indicates that the IR emission likely peaks in the mid-IR. To place a lower limit on the NIR luminosity we assume that the SED peaks in the K' band. Following this assumption, the NIR excess constitutes a slowly varying luminosity of $\gtrsim 2 \times 10^8 L_\odot$ for > 1 yr.

The most likely explanation for this large luminosity in the NIR is warm dust. The observed $H - K'$ color from day 436 corresponds to a temperature of ~ 1000 K, assuming a single-

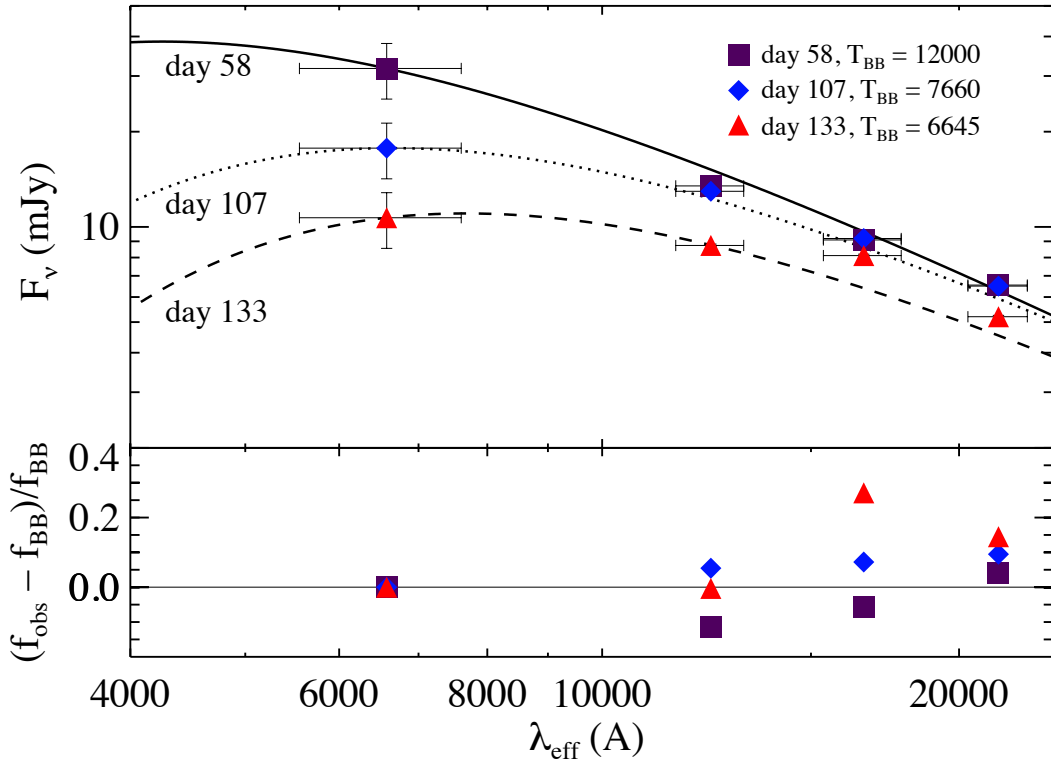


Figure 3.4: SED evolution of SN 2006gy at early times showing a possible trend toward a growing IR excess above a cooling blackbody. *Top:* the solid, dotted, and dashed lines show a single-component blackbody spectrum, normalized to unfiltered observations from Smith et al. (2007), on days 58, 107, and 133, respectively. *Bottom:* the fractional excess emission in J , H , and K_s , relative to the blackbody model. For clarity we do not include the uncertainties in these measurements, which are large and dominated by the uncertainty in the transformation between unfiltered data and the R band (see text). Each point is within $\sim 1\sigma$ of showing no excess; however, the NIR excess does appear to grow with time.

temperature blackbody. If the dust is radiating as a single blackbody with $T_{\text{peak}} = 1000$ K, this would increase the above luminosity to $\gtrsim 3 \times 10^8 L_{\odot}$. We note that our NIR observations are only sensitive to the warmest dust; it is possible that cooler dust with $T \approx 600$ K⁷ could dominate the IR emission, in which case the luminosity could be significantly higher than the values quoted above.

The location of this dust, and whether it is newly formed or pre-existing at the time of the SN explosion, remain to be determined. The dust-cooling time is short, meaning that a prolonged heat source is needed to explain the extended excess. We consider four possibilities for heating the dust: (i) radioactive heating from ^{56}Co decay, (ii) collisional excitation of pre-existing dust, (iii) heating via radiation from circumstellar interaction, and (iv) a late-time IR dust echo, where pre-existing dust is heated by the radiation produced while the SN was near its optical peak.

Radioactive Heating from ^{56}Co

[Smith et al. \(2008c\)](#) noted that the observed K' -band decay between 2007 September and 2007 December could be explained with radioactive heating from a minimum of $2.5 M_{\odot}$ of ^{56}Ni , if a sufficient amount of dust formed in order to move the luminosity into the NIR (though they favored another interpretation; see below). We show the bolometric evolution of SN 2006gy through the first ~ 800 days post explosion, including both optical and NIR detections, in Figure 3.5. From Equation 19 of [Nadyozhin \(1994\)](#), and the fact that the luminosity from ^{56}Co decay dominates over ^{56}Ni decay at times $\gtrsim 2$ weeks after explosion, we arrive at the following expression for the radioactivity-powered luminosity of a SN, assuming 100% trapping of gamma-rays:

$$L_{^{56}\text{Co}} = 1.45 \times 10^{43} \exp^{-t/(111.3 \text{ d})} M_{\text{Ni}} / M_{\odot} \text{ erg s}^{-1}, \quad (3.1)$$

where t is the time since SN explosion in days, and M_{Ni} is the total mass of ^{56}Ni produced. Using Equation 3.1 we also show in Figure 3.5 the expected light curve from $2.5 M_{\odot}$ of ^{56}Ni at times > 400 days. The early-time measurements (< 250 days) come from [Smith et al. \(2010a\)](#). The optical measurement near day 400 comes from photometric measurements by [Kawabata et al. \(2009\)](#), while the optical luminosity on day 810 comes from a direct integration of our *HST* observations (see §3.3.3). The three late-time NIR luminosities represent lower limits based on the measured K' -band flux (see above, §3.3.1). The decay rate of ^{56}Co , $0.98 \text{ mag (100 day)}^{-1}$, is much faster than the observed decay of the K' flux from SN 2006gy, $\sim 0.2 \text{ mag (100 day)}^{-1}$. The late-time NIR excess declines at a rate that is too slow to be explained by ^{56}Co heating alone.

The PISN model of [Nomoto et al. \(2007\)](#), which provided good agreement with the early-time light curve of SN 2006gy after an artificial reduction of the total ejecta mass from their evolutionary calculation, was able to reproduce the late-time NIR luminosity observed

⁷[Smith et al. \(2008c\)](#) show that the combination of the peak luminosity and distance to the dust suggest an equilibrium temperature around 600 K.

by Smith et al. (2008c). This model required less than 100% efficiency in the conversion of gamma-rays (from radioactive decay) to optical/NIR emission, which means that the light curve should decay *faster* than $0.98 \text{ mag (100 day)}^{-1}$. The possibility of a PISN was first invoked to explain the large peak luminosity of SN 2006gy (Ofek et al. 2007; Smith et al. 2007). This scenario would have required the production of $\gtrsim 10 M_{\odot}$ of ^{56}Ni , which in turn would produce a large late-time luminosity that decays at the rate of ^{56}Co . The late-time NIR luminosity is not accounted for in either the general PISN models or the artificial model of Nomoto et al. (2007); it therefore provides a serious challenge to the PISN hypothesis.⁸

Collisional Heating of the Dust

Another possibility is that the dust existed prior to the SN explosion, at large distances from the explosion site, and was heated via collisions with the expanding material in the expanding blast wave. The intense UV/optical output from a SN at its peak vaporizes any dust in the vicinity of the SN (Dwek 1983). This radiation near peak creates a dust-free cavity into which the SN ejecta may expand at early times; however, the ejecta blast wave will eventually reach the edge of the dust-free cavity, at which point collisional excitations of the dust may generate NIR emission.

The large peak luminosity of SN 2006gy, $8 \times 10^{10} L_{\odot}$ (Smith et al. 2010a), provides significant challenges to this collisional heating scenario. Dwek (1983) shows that the radius of the dust-free cavity can be determined from the peak luminosity and the dust vaporization temperature, assuming the grain emissivity Q_v is proportional to $(\lambda/\lambda_0)^{-1}$:

$$R_1(\text{pc}) = 23 \left[\frac{\bar{Q}_v L_0(L_{\odot})}{\lambda_0(\mu\text{m}) T_v^5} \right]^{0.5}, \quad (3.2)$$

where R_1 is the radius of the dust-free cavity, \bar{Q}_v is the mean grain emissivity, L_0 is the peak luminosity, and T_v is the dust vaporization temperature. Following Dwek (1983), if we assume $\bar{Q}_v = 1$ and that $\lambda_0 = 0.2 \mu\text{m}$, we find that $R_1 \approx 1.4 \times 10^{18} \text{ cm}$, for a vaporization temperature $T_v \approx 1000 \text{ K}$. If the absorption coefficient is instead proportional to λ^{-2} , then the cavity becomes even larger. Based on the observed width of the H α line from SN 2006gy, Smith et al. (2007) estimate the speed of the blast wave to be 4000 km s^{-1} , which would mean that this material would take $\sim 112 \text{ yr}$ to reach the edge of the dust-free cavity. Even if there are ejecta traveling at more typical SN velocities of $10,000 \text{ km s}^{-1}$, it would take over 45 yr for this material to reach the edge of the dust-free cavity. Given that the NIR excess is present $\sim 1 \text{ yr}$ following explosion, and that the SN ejecta could not reach the dust in such a short time, collisional heating of dust by SN ejecta cannot explain the observed NIR excess. Large grains will persist at smaller radii than smaller grains according to Equation 3.2, since the size of the dust-free cavity is $\propto \lambda_0^{-0.5}$, while the grain size, $a = \lambda_0/2\pi$. The existence of grains at $R_1 \approx V_{\text{SN}} t_{\text{SN}} = 4000 \text{ km s}^{-1} \times 1 \text{ yr} = 1.26 \times 10^{16} \text{ cm}$, and thus possibly explain

⁸The pulsational pair-instability model of Woosley et al. (2007) has not, however, been excluded; see also Smith et al. (2010a).

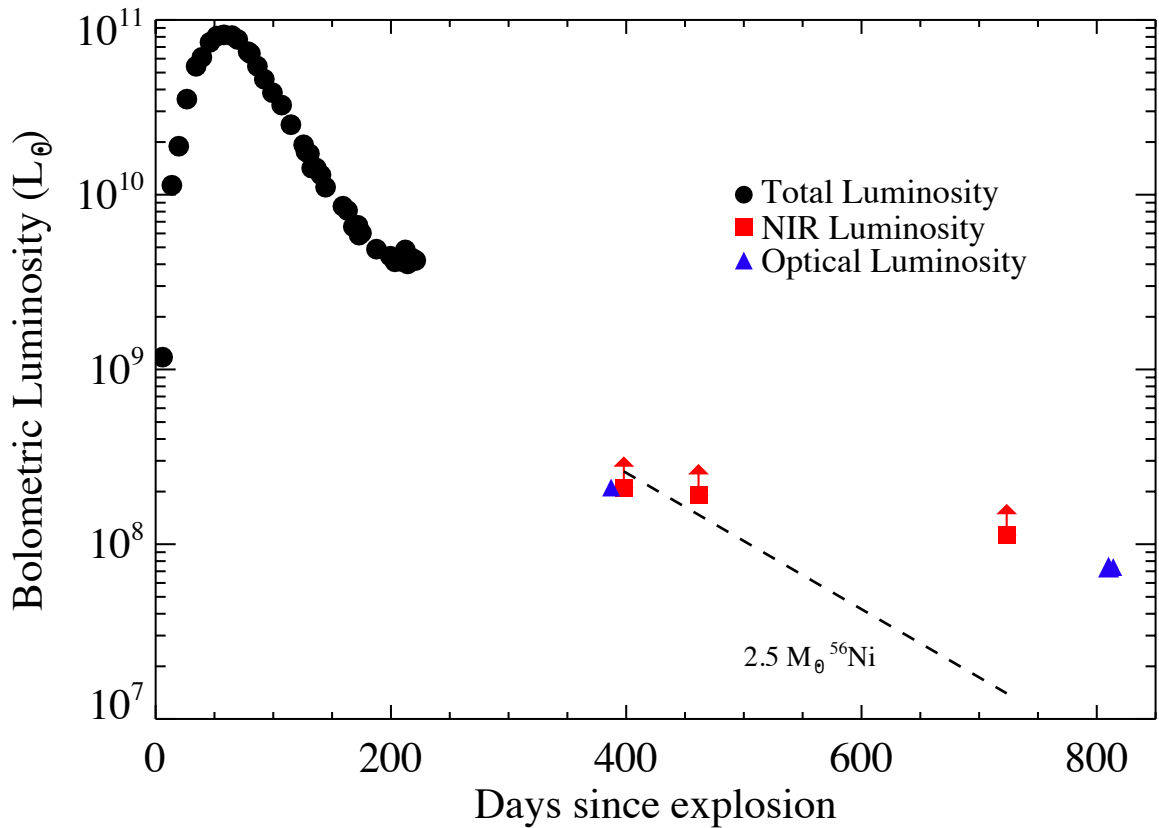


Figure 3.5: Evolution of the bolometric luminosity of SN 2006gy during the first 800 days after explosion. Optical data are shown as black circles, and NIR data are red squares. Early-time data (< 250 days) are from Smith et al. (2010a). The optical detection near day 400 is from Kawabata et al. (2009). All other data are from this work. NIR measurements are only lower limits to the total IR luminosity, because our observations do not sample redward of $2.2 \mu\text{m}$ (see text). The dashed line shows the expected decline if the luminosity were powered by $2.5 M_\odot$ of ^{56}Ni . The flat nature of the light curve indicates that radioactivity is not the primary energy source for the late-time emission.

the NIR excess seen 1 yr after explosion, would require dust particles a factor $\sim 10^4$ larger than those assumed above, roughly corresponding to ~ 1 mm size grains. Such large grains are rare and are inefficient radiators in the NIR (Spitzer 1978); therefore, they are unlikely to explain the observed NIR excess.

Newly Formed Dust

The emission features that arise in SNe IIn, as in SN 2006gy, originate from the interaction of the SN ejecta with a dense CSM. Shocked gas, located between the forward shock which is plowing into the CSM and a reverse shock of the SN ejecta, can cool, and if the density is large enough, it may form new dust grains. The cooling time for such dust is short, and can be estimated in the following manner: $\tau_{\text{cool}} \approx E/L$ where E is the thermal energy of a grain and L is the grain luminosity. We estimate the thermal energy as $Nk_B T_{\text{dust}}$, where N is the total number of particles in a grain and k_B is the Boltzmann constant. We assume the grains radiate as a blackbody: $L = 4\pi a^2 \sigma T_{\text{dust}}^4$, where a is the typical grain size and σ is the Stefan-Boltzmann constant. For graphite grains of size $a \approx 1 \mu\text{m}$, and $\rho \approx 3 \text{ g cm}^{-3}$, we have $N \approx 10^{12}$, meaning $\tau_{\text{cool}} < 1 \text{ s}$. Furthermore, theoretical calculations by Draine & Li (2001) show that the cooling time for PAH and silicate grains at $T \approx 1000 \text{ K}$ is $\lesssim 10 \text{ s}$, for grains of all sizes. Nevertheless, a persistent heat source can generate an extended period of NIR emission. The physical conditions for post-shock dust formation are not necessarily easy to produce: strongly interacting SNe are often X-ray sources, which could prevent the formation of new dust grains in the post-shock gas. Evidence for the formation of dust in the post-shock region has been found for a few SNe, however, including SN 1998S (Pozzo et al. 2004), SN 2006jc (Smith et al. 2008b), and SN 2005ip (Smith et al. 2009b; Fox et al. 2009). This newly formed dust is then heated by the energy from the shock as it continues to propagate into the CSM, which gives rise to the prolonged NIR excess.

This scenario is difficult to reconcile with the case of SN 2006gy, however. Spectra taken around day 200 show a decline in the luminosity of the H α emission line, which indicates a reduction in the CSM interaction at this time (Smith et al. 2010a). Furthermore, as detailed by Smith et al. (2008c), the lack of X-ray, H α , and radio emission a little more than a year after the SN explosion implies that the observed NIR luminosity cannot be explained by shock-heated dust. In fact, the radio nondetection of SN 2006gy continues through day 638 (Bietenholz & Bartel 2008). Kawabata et al. (2009) do claim the detection of very weak H α emission from SN 2006gy on day 394, but the inferred luminosity of $\sim 10^{39} \text{ erg s}^{-1}$ is nearly three orders of magnitude lower than the observed NIR luminosity at this time. Kawabata et al. (2009) also claim an *R*-band detection of 19.4 mag on day 394 (though we note that Smith et al. 2008c report an upper limit of $R > 20$ mag, and Agnoletto et al. 2009 give an upper limit of $R > 20.3$ mag, at a similar epoch), which would constitute an optical luminosity similar to that observed in the NIR. The source of this optical luminosity could potentially be the heat source for newly formed dust at day ~ 400 , though it cannot explain the similar NIR luminosity seen on day 723. While SN 2006gy was detected in the optical at > 800 days to have a luminosity similar to that seen in the NIR, the very blue nature of

optical data suggests that it is a scattered-light echo (see §3.3.3) of UV/optical emission from the SN peak. The light echo must originate *outside* the dust-forming region and therefore cannot heat the dust. While we cannot strongly rule out dust formation in the post-shock region of SN 2006gy, it is implausible to explain the late-time NIR luminosity via new dust, because there are no signs of a heating source that lasts for > 1 yr.

NIR Dust Echo

Perhaps the most natural explanation for the late-time NIR excess is a dust-heated echo, as first discussed by [Smith et al. \(2008c\)](#). In this scenario, the IR emission comes from dust near the explosion site which is heated by the early-time UV/optical emission from the SN. IR echo models by [Dwek \(1983\)](#) predict a fast rise (of order the rise time in the optical of the SN) in the IR, followed by an extended plateau (lasting > 1 yr; see below) before the IR luminosity follows a rapid decline (where the IR flux declines as e^{-t}/t). The extended plateau from an IR echo matches the qualitative behavior of SN 2006gy, which exhibits a very slow decline in the NIR: only a factor of ~ 2 in flux over the course of ~ 1 yr.

Assuming isotropic optical emission from the SN, the plateau occurs because the hottest dust, which exists right at the edge of the dust-free cavity described above, dominates the emission. According to the view of a distant observer, the emitting volume is a series of paraboloid light fronts that expand throughout the dust-free cavity as shown in Figure 3.6 (see also Figure 1 of [Dwek 1983](#)). As a paraboloid expands it continually heats dust at R_1 , which is what gives rise to the plateau in the light curve. After a time $\sim 2R_1/c$, the vertex of a given paraboloid will reach the back edge of the cavity and will no longer be heating dust at R_1 . Emission from the dust will be dominated by the UV/optical radiation produced by the SN at peak, and once this radiation sweeps past the back edge of the cavity the IR luminosity begins to rapidly decline. Therefore, if we know the duration of the plateau phase we can determine the size of the dust-free cavity. Constraints on the cavity size can be determined by assuming that the echo starts at our first K' observation on day 398 and ends on our last observation on day 723. In this case we find that $R_1 \approx 4 \times 10^{17}$ cm; however, it would be contrived if our observations were to perfectly bookend the plateau phase of the echo: the echo almost certainly started prior to day 398 and continued beyond day 723. In fact, the model predicts that the echo should start well before day ~ 400 . There is mild evidence for a NIR echo as early as day ~ 130 : the H -band and K_s -band flux is (respectively) $\sim 2\sigma$ and $\sim 1\sigma$ greater than their expected values based on an extrapolation of optical spectra (see Figure 3.2). If we instead assume that the slight NIR excess seen at day ~ 130 (see Figure 3.2) is the rise of an IR echo, then we find that $R_1 \approx 8 \times 10^{17}$ cm, which shows reasonable agreement with the value we earlier calculated for the dust-free cavity, $R_1 \approx 1.4 \times 10^{18}$ cm, considering the uncertainties in the dust temperature and the likelihood that the plateau extends beyond day 723.

Our NIR observations are only sensitive to the warmest dust, but if we assume that the NIR luminosity peaks in the K' band, then a lower limit to the total energy emitted in the IR is $E_{\text{IR}} \approx 2 \times 10^8 L_\odot \times 600$ days, or $\gtrsim 4 \times 10^{49}$ erg. This is comparable to the canonical

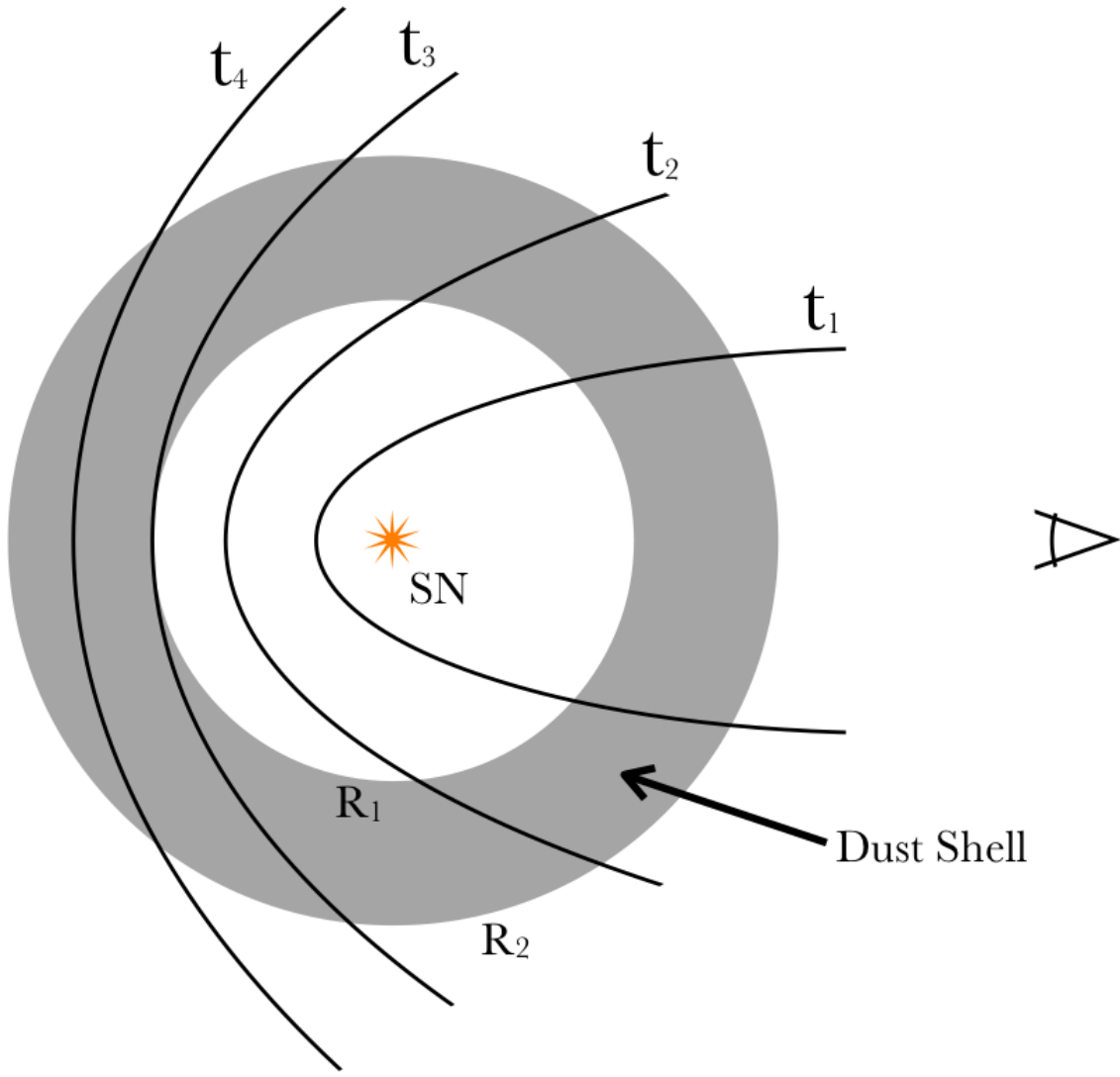


Figure 3.6: Schematic diagram showing the evolution of an IR echo arising from a circumstellar dust shell, shown in the shaded area. The large luminosity from the SN vaporizes a dust-free cavity out to radius R_1 . At early times the dust-emitting volume is small, shown as the area interior to the parabola marked t_1 , as the reradiated light from other portions of the shell has not had sufficient time to reach the observer. As time increases, so does the emitting volume, to the area within t_2 , then t_3 , etc. The echo luminosity is dominated by the warmest dust at $\sim R_1$. As the light parabola sweeps through the shell, new emission from dust at $\sim R_1$ continually becomes observable, leading to a plateau in the NIR light curve. The plateau continues until a time $t_3 \approx 2R_1/c$, at which point the parabola has swept past the inner edge of the shell. Additional emission continues to be observable (t_4); however, this is from more distant, cooler dust and as a result the IR echo falls off the plateau and begins to decline.

optical output of a normal SN II. Typically, this would pose a significant problem for the IR echo hypothesis, as it would require of order unity of the original optical radiation from the SN to be absorbed and reradiated in the NIR. Indeed, this is precisely the argument used by Fox et al. (2009) to argue against the light-echo hypothesis for SN 2005ip. In the case of SN 2006gy this is not a problem, however, because the NIR emission falls well within the available energy budget to heat the dust. After applying a bolometric correction, Smith et al. (2010a) find that $\sim 2.5 \times 10^{51}$ erg were emitted by SN 2006gy during the first ~ 220 days of the light-curve evolution, which means that less than 2% of this energy has been absorbed and reradiated by the dust. This value is comparable to those found by Dwek (1983) for SNe 1979C and 1980K.

If we assume that the dust radiates as a blackbody, we can estimate the optical depth of the dust shell as $\tau \approx E_{\text{IR}}/(E + E_{\text{IR}}) \approx 0.016$. We note that like E_{IR} above, this value constitutes a lower limit for τ . Even if the NIR luminosity is a factor of 10 larger than our lower limits, this would imply $\tau \approx 0.1$, which corresponds to an optical extinction of $A_V = 1.086\tau \approx 0.1$ mag. This is far less than the total observed extinction from the host, $A_{V,\text{host}} \approx 1.67$ mag (Smith et al. 2007), suggesting that the dusty shell responsible for the IR echo cannot produce all of the non-Galactic reddening observed toward SN 2006gy. That there is a considerable amount of dust along the line of sight, which is not in the CSM of SN 2006gy, should not come as a surprise given that there is a prominent dust lane in NGC 1260 (see Figure 3.3).

With this information in hand, it is now possible to estimate the total dust mass of the shell that creates the NIR echo. According to Dwek (1983) for a dust shell with density $n_d \propto r^{-2}$,

$$M_d = 4\pi \left(\frac{4\rho_{\text{gr}}a}{3\bar{Q}_\nu} \right) \tau_d \times \frac{R_1 R_2^2}{R_2 - R_1}, \quad (3.3)$$

where M_d is the total dust mass in the shell, ρ_{gr} is the grain density, a is the grain radius, τ_d is the optical depth, \bar{Q}_ν is the mean absorption efficiency, and R_1 and R_2 are the inner and outer radii of the dust shell, respectively. Above we estimate the inner radius of the dust shell to be $\sim 8 \times 10^{17}$ cm. The value of the outer radius can be deciphered from the decay of the NIR light curve following the plateau. As we have not yet observed the NIR decay, we adopt an outer radius of $2R_1$, which provides a *lower limit* to the dust mass in the shell. Finally, we follow the same assumptions as Dwek (1983) about the dust properties: $\rho_{\text{gr}} = 3 \text{ g cm}^{-3}$, $a = 0.1 \mu\text{m}$, and $\bar{Q}_\nu = 1$. With these assumptions we find a total dust mass of $M_d \approx 0.1 M_\odot$. Assuming a typical value for the dust-to-gas ratio, 1:100, the total mass of the circumstellar shell is $\sim 10 M_\odot$. This value shows good agreement with the initial estimate of 5–10 M_\odot from Smith et al. (2008c), which was based only on observations taken between 400 and 461 days after explosion. We note that $\sim 10 M_\odot$ constitutes a lower limit to the total mass of the shell, because the actual value of the duration of the plateau and E_{IR} could potentially be much larger than the values we adopted above.

At a distance of $\sim 10^{18}$ cm from the SN explosion site, it is not immediately evident whether the dust giving rise to the NIR echo is part of the progenitor's CSM or the local

interstellar medium (ISM). [Smith et al. \(2008c\)](#) argue that the large dust mass needed at $\sim 10^{18}$ cm could be explained if the progenitor passed through a phase of eruptive mass loss $\sim 1000\text{--}1500$ yr prior to explosion, in an event similar to observed outbursts from η Car. Pre-existing dust in the walls of a giant H II region, where a massive star like the progenitor of SN 2006gy might have lived, cannot account for the IR echo because at typical distances of ~ 10 pc or more from the SN, the dust would be far too cold to reproduce the NIR excess.

3.3.3 Observed Color Evolution from HST Observations

[Chevalier \(1986\)](#) predicts that any SN with an IR echo due to pre-existing CSM dust should also show a faint scattered-light echo in the optical as well. He shows that this dust can lead to optical emission characterized by a $\lambda^{-\alpha}$ scattering law, where α is some value between 1 and 2. More than a year after explosion SN 2006gy had faded rapidly in the optical ([Smith et al. 2008c; Agnoletto et al. 2009; Kawabata et al. 2009](#)). Therefore, we obtained *HST* images to search for a possible late-time scattered-light echo.

Our optical detection on day 810 shows a significant change in the optical decline rate of SN 2006gy. During the interval 200–400 days the SN faded by $\gtrsim 3$ mag in the optical ([Smith et al. 2008c](#)), whereas the decline over days 400–810 was only ~ 1 mag. In addition to this reduced rate of decline, the SN underwent significant color evolution. Assuming that *F555W* and *F814W* approximate the *V* and *I* bands, respectively, we find that $V - I = 0.60$ mag on day 810. By contrast, with a 12,000 K color temperature at peak ([Smith et al. 2010a](#)), the observed color of SN 2006gy would have been $V - I \approx 1.01$ mag. Thus, the spectrum on day 810 is *bluer* than the spectrum at peak. Indeed, the ~ 0.4 mag color change shows excellent agreement with a λ^{-1} scattering law. A λ^{-2} scattering law, on the other hand, would predict a -0.83 mag change to the $V - I$ color, or roughly $V - I \approx 0.20$ mag during the late-time epochs.

This behavior is similar to what one would expect from a scattered-light echo: as in the case of an IR echo, when successive paraboloids sweep out to progressively larger radii, dust in the circumstellar (or in some cases the interstellar) environment can scatter that light toward the observer, creating a plateau in the optical light curve of the SN. At the same time, scattering preferentially selects shorter wavelengths, which results in a spectrum that is bluer than that of the SN at peak. This is the precise behavior observed for the Type Ia SNe 1991T ([Schmidt et al. 1994](#)), 1998bu ([Cappellaro et al. 2001](#)), and 2006X ([Wang et al. 2008](#)), which all showed significant departures from the expected decline rate of SNe Ia. Spectra taken roughly two years after maximum, for SNe 1991T and 1998bu, and ~ 10 months after maximum for SN 2006X, show emission features similar to those seen in the spectra near peak superposed on top of a blue continuum for these SNe. Light echoes have also been observed around a number of core-collapse SNe, such as SN 2003gd ([Sugerman 2005; Van Dyk et al. 2006](#)), SN 1993J ([Sugerman & Crotts 2002](#)), and SN 1987A (see [Sugerman et al. 2005](#), and references therein).

In Figure 3.7 we show the late-time SED of SN 2006gy, including our NIR detections on days 461 and 723 and the optical detections from day 810. The solid blue line represents a

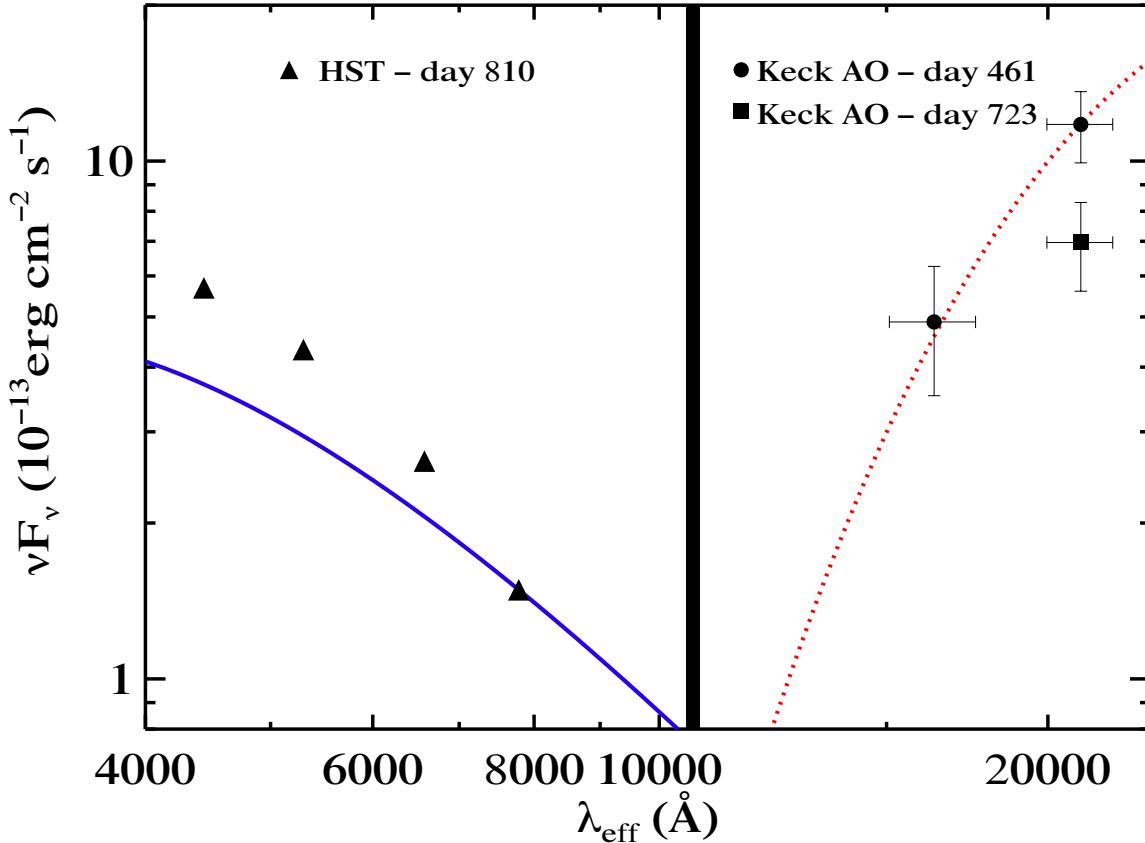


Figure 3.7: Late-time SED of SN 2006gy showing evidence for two distinct emission components. We show the flux in the optical (*HST*, day 810) and NIR (Keck AO, days 461 and 723), corrected for host-galaxy and Milky Way reddening. The vertical solid line is to remind the reader that optical and NIR observations were not taken simultaneously. The solid blue line shows a 12,000 K blackbody, normalized to the *F814W* detection. The red dotted line shows a single-component blackbody fit ($T = 1000$ K) to the *H* and *K'*-band detections from day 461 (note that this fit has zero degrees of freedom). The IR evolution is slow, and the detection from day 723 indicates the degree of fading in the NIR. The SED shows a rapid decline toward the red portion of the optical, as well as a strong rise toward the red within the NIR. These characteristics are precisely those predicted by the IR and scattered-light echo models.

single-component blackbody at $T = 12,000$ K, roughly the peak temperature of SN 2006gy (Smith et al. 2010a), normalized to our $F814W$ detection. The SED clearly shows that the late-time emission is significantly bluer than a blackbody spectrum. We note that the early-time spectra of SN 2006gy show considerable line blanketing blueward of ~ 4000 Å, such that the emission decreases blueward of our $F450W$ detection. The NIR emission rapidly rises toward the IR, suggesting that there is considerable IR emission to which our NIR measurements are not sensitive.

Figure 3.8 illustrates the observed *HST* photometry on day 810, as well as the observed spectrum (grey solid line) of SN 2006gy obtained near peak luminosity (Smith et al. 2010a). The observed late-time photometry is clearly bluer than the spectrum at the time of peak luminosity (note that no correction for reddening has been made to either the observed spectrum or the late-time photometry). The blue colors at late times are difficult to explain with ongoing CSM interaction because SNe IIn typically exhibit relatively constant temperatures of ~ 6000 – 6500 K at late times (e.g., Smith et al. 2010a), which would be redder than the spectrum at peak which had a temperature of $\sim 12,000$ K. A bluer color would be expected, however, if the optical emission at the time of peak luminosity is reflected by dust grains with a size smaller than the observed wavelength, which leads to the spectrum characterized by a $\lambda^{-\alpha}$ scattering law, as mentioned above. Figure 3.8 shows that the observed spectrum from day 71 can be modified by a scattering law with $\alpha = 1.2 \pm 0.15$ to adequately model the late-time *HST* photometry. We do not have a late-time spectrum to confirm that the observed line strengths are consistent with the reflected peak luminosity, and so this precludes a more detailed model of the scattering dust at this time.

3.3.4 Location of the Scattering Dust

The location of the scattering dust is of interest as it can help determine properties of the environment local to SN 2006gy. Earlier, we showed that the CSM dust responsible for the NIR echo cannot account for all the reddening observed toward SN 2006gy, suggesting that the SN light passes through external, non-CSM dusty regions in the host galaxy prior to reaching us. Therefore, the scattered-light echo could originate in a number of different locations.

With only a single epoch of the unresolved scattered-light echo, a precise determination of the location of the scattering dust cannot be obtained. Nevertheless, we can gain some insight into the dust location based on the total optical and NIR emission. For the case where the NIR-echo dust also gives rise to the scattered-light echo, and assuming the SN can be modeled as a single short pulse of UV/optical radiation, the ratio of the scattered-light luminosity (L_s) to the IR luminosity at late times can be shown to be (Chevalier 1986)

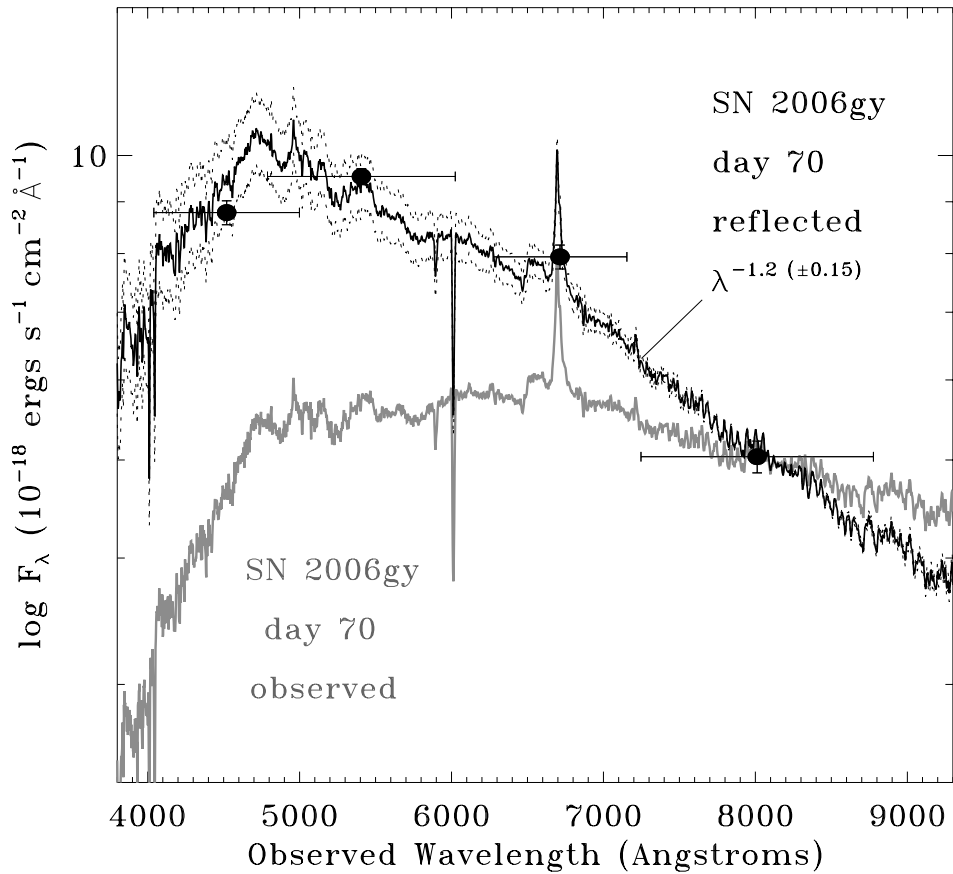


Figure 3.8: Evidence for a scattered-light echo from the blue optical emission from SN 2006gy. The *HST*/WFPC2 photometry of SN 2006gy (black dots) is compared to observed and reflected spectra, both normalized to the *HST* $F814W$ flux density. The gray line is the observed spectrum of SN 2006gy on day 70 during its peak luminosity phase, from Smith et al. (2010a). We plot the observed wavelength (i.e., not corrected for the SN redshift), and the spectrum has no correction for reddening. The black line (and dotted lines above and below) show the same spectrum, but adopting an assumed wavelength dependence for the dust reflectance proportional to $\lambda^{-1.2(\pm 0.15)}$.

$$\frac{L_s}{L_{\text{IR}}} = \frac{\omega}{1-\omega} \left(1 - \frac{(ct)^2}{4R_2^2}\right) \frac{(1-g)^2}{2g^2} \times \left\{ \frac{(1-g)^2 + 2g}{[(1-g)^2 + 4g]^{1/2}} - \frac{(1-g)^2 + gct/R_2}{[(1-g)^2 + 2gct/R_2]^{1/2}} \right\}, \quad (3.4)$$

where ω is the dust albedo, c is the speed of light, t is the time since the SN explosion, R_2 is the outer radius of the dust shell, and g is a measure of the degree of forward scattering. Once again, as in §3.3.2 we have assumed a dust density $n_d \propto r^{-2}$. The case $g = 0$ corresponds to isotropic scattering and $g = 1$ is completely forward scattering. Note that in Equation 3.4 we have assumed that $ct/2 < R_1$, where R_1 is the inner radius of the dust shell, and that the albedo is independent of frequency. Empirical estimates and numerical calculations (White 1979) show $g \approx 0.6$, which we adopt here. Models and observations of interstellar dust show that for near-UV, optical, and NIR emission, which dominate the output from SN 2006gy near peak, the dust scatters light at these wavelengths with $0.4 \lesssim g \lesssim 0.7$ (see Draine 2003, and references therein). For the dust albedo we adopt $\omega \approx 0.6$ (Mathis et al. 1977). For the albedo, models and observations typically constrain $0.5 < \omega < 0.7$, for scattered near-UV, optical, and NIR light (Draine 2003). As mentioned above, we cannot constrain R_2 with our current observations, but we do know that R_2 must be greater than R_1 , and the value of Equation 3.4 does not change when $R_2 \rightarrow \infty$. For reasonable limits to the outer radius, $1.5R_1 < R_2 < \infty$, we find that $L_s/L_{\text{IR}} \approx 0.88\text{--}0.60$.

Direct integration of the *HST* optical flux, which extends from $\sim 4500\text{--}8000$ Å, yields an optical luminosity of $\sim (7.4 \pm 0.5) \times 10^7 L_\odot$. This value is somewhat uncertain because our data do not extend into the UV; however, optical spectra taken near peak show that line blanketing severely reduces the flux blueward of ~ 4000 Å (Smith et al. 2010a), so this uncertainty should not have a significant effect on the total scattered-light luminosity. If we assume that the NIR flux continues to decline at the same rate as that observed between days 398 and 723, then assuming that the NIR emission peaks in the K' band (see §3.3.2), we find a lower limit to the IR luminosity (again, because our NIR observations only probe emission from the hottest dust) of $L_{\text{IR}} > 8.6 \times 10^7 L_\odot$ on day 810. Therefore, on day 810, $L_s/L_{\text{IR}} < 0.86$, consistent with the predicted values above in the case where the scattering dust is the same dust responsible for the IR echo.

The alternative possibility is that the scattering dust is not located in the CSM, instead existing at some other location in NGC 1260 along the line of sight. Cappellaro et al. (2001) inferred that this was the case with SNe 1991T and 1998bu, and like those two SNe we know that SN 2006gy has a significant amount of dust located along the line of sight. As shown by Cappellaro et al. (2001), if we approximate the SN light curve as a short pulse with duration Δt_{SN} , then the scattered-light luminosity is

$$L_{\text{echo}}(t) = L_{\text{SN}} \Delta t_{\text{SN}} f(t), \quad (3.5)$$

where $L_{\text{SN}} \Delta t_{\text{SN}}$ can be obtained via direct integration of the observed light curve, $L_{\text{SN}} \Delta t_{\text{SN}} = \int_0^{+\infty} L_{\text{SN}}(t) dt$, and $f(t)$ is the fraction of light scattered to the observer. Under the assumption

that light is being scattered by dust in a sheet of thickness $\Delta D \ll D$, where D is the distance between the dust and the SN, then (Chevalier 1986; Cappellaro et al. 2001)

$$f(t) = \frac{c}{8\pi} \frac{\omega\tau}{D + ct} \frac{1 - g^2}{\{1 + g^2 - 2g[D/(D + ct)]\}^{3/2}}, \quad (3.6)$$

where τ is the optical depth of the dust. Using the relation $A_V = 1.086\tau_V$, and the fact that A_V outside the dusty CSM is ~ 1.6 mag, we find $\tau \approx 1.5$. From Smith et al. (2010a), we know that $L_{\text{SN}}\Delta t_{\text{SN}} \approx 2.5 \times 10^{51}$ erg. Therefore, using $L_{\text{echo}} \approx 2.9 \times 10^{41}$ erg s $^{-1}$, from the direct integration of the optical SED, we find (from Equation 3.6) that dust located at $D \approx 20$ pc can explain the observed scattered-light luminosity. This value for D is dependent upon our assumptions about the albedo and the degree of forward scattering, g . To show how D changes based on these assumptions, we show D as a function of g for fixed values of the albedo $\omega = 0.3, 0.4, 0.6$, and 0.9 in Figure 3.9. The large red point shows the solution for our assumed values of $g = 0.6$ and $\omega = 0.6$. We also shade the area corresponding to the expected range of values for g and ω mentioned above. This shaded area corresponds to $D \approx 10\text{--}40$ pc, as the location of the scattering dust.

Our observations appear to be consistent with one of two scenarios: either (i) the scattered-light echo is due to CSM dust, which has also been heated and is radiating in the IR, or (ii) a dusty region $\sim 10\text{--}40$ pc from the SN is responsible for the late-time optical luminosity. This latter scenario seems very plausible if the progenitor of SN 2006gy was a very massive star, $\gtrsim 100 M_\odot$ (Smith et al. 2010a). If this were the case, we might expect that the progenitor resides in the center of a giant H II region with multiple dense, dusty clouds nearby. This scenario might be very similar to the Carina nebula surrounding η Car, which has multiple dusty molecular clouds only 10–20 pc from η Car (e.g., Smith & Brooks 2007). If the progenitor of SN 2006gy were surrounded by such a nebula, then our assumption of a single, thin scattering surface would no longer be valid, and the scattering dust could potentially be located at a number of different locations.

With only a single epoch of observations, we cannot distinguish between the two possible dust locations. One additional epoch of optical imaging should prove sufficient to determine which scenario is correct. As long as $D \gg ct$, then $f(t)$ is roughly constant, whereas the models of Chevalier (1986) show a continuous decline in the scattered-light echoes when $g = 0.6$ and the scattering dust is in the CSM. A relatively flat optical light curve would put the dust at ~ 20 pc, whereas significant decline from the observed day 810 flux would suggest CSM dust. Finally, we note that the prospects for fully resolving the SN 2006gy light echo are dim: at a distance of 73 Mpc it would take several decades before the light echo could be resolved with high spatial resolution images (i.e., comparable to *HST* in the optical).

3.4 Conclusions and Future Work

We have presented new observations of SN 2006gy, including early-time NIR data from PAIRITEL, as well as optical and NIR detections more than two years after explosion.

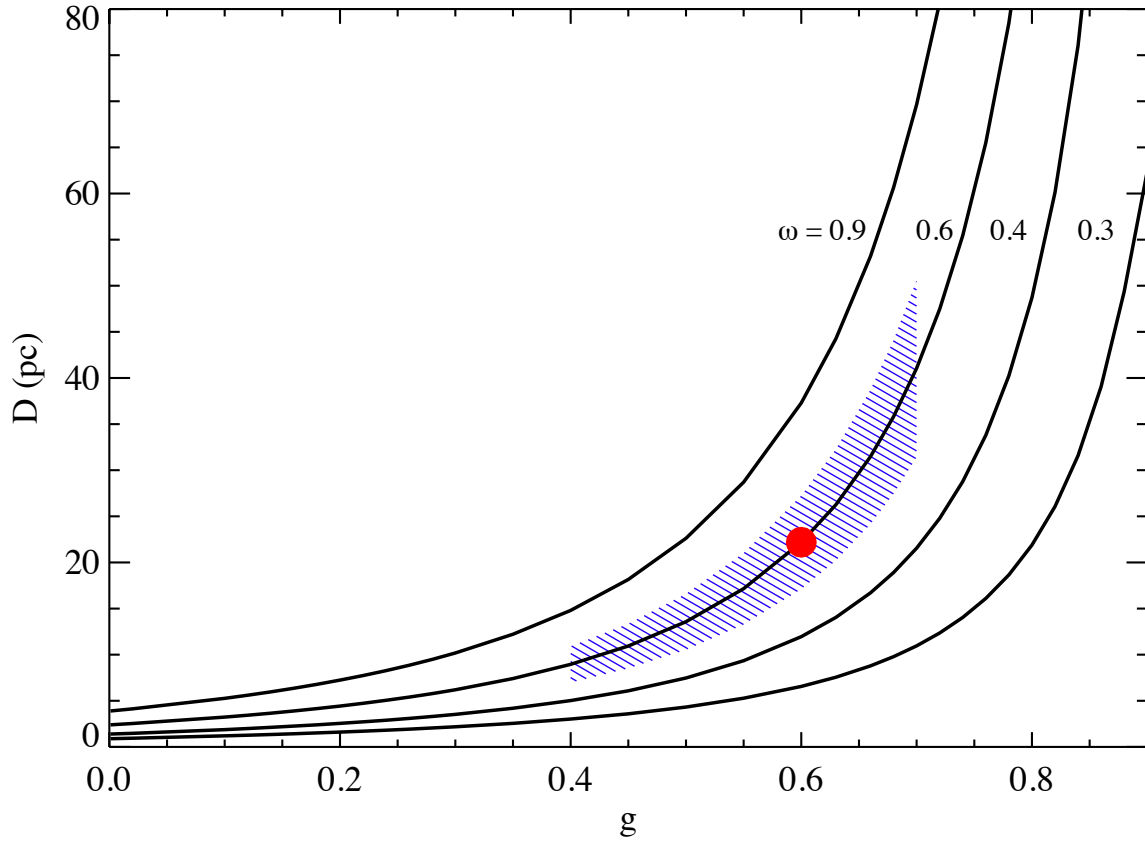


Figure 3.9: Location of the scattering dust, D , as a function of the degree of forward scattering, g , for various values of the albedo, ω . The large red point highlights our adopted values of $g = 0.6$ and $\omega = 0.6$, which corresponds to $D \approx 20$ pc. The shaded area encompasses the full range of values expected for the scattering of near-UV, optical, and NIR light by interstellar dust, $0.4 < g < 0.7$ and $0.5 < \omega < 0.7$ (see text). The shaded area corresponds to $D \approx 10\text{--}40$. Note that this figure only applies to the case where the scattering grains are external, and unrelated, to the dust giving rise to the NIR echo.

These new data, combined with other late-time observations, provide evidence for IR and scattered-light echoes, as follows.

1. There is no radio or X-ray counterpart to SN 2006gy, suggesting that CSM interaction is weak or nonexistent at late times.
2. There is (statistically weak) evidence for a growing NIR excess around day ~ 100 .
3. The decline of both the optical and NIR emission is slower than that of ^{56}Co , which rules out a pair-instability SN as the cause of the extreme peak optical luminosity for SN 2006gy.
4. Emission from warm dust explains the red NIR color, while an IR echo is needed to explain the long-lived NIR emission.
5. The late-time optical emission has a bluer spectrum than the SN at peak optical emission, which can be explained with a scattered-light echo.

Given our interpretation for the late-time optical and NIR emission arising from a dust shell at $\sim 8 \times 10^{17}$ cm from the SN, what might we expect from future observations of SN 2006gy? The IR-echo models of [Dwek \(1983\)](#) show that after a time $t \approx 2R_1/c$, the IR luminosity falls off the plateau and exhibits significant decline. Based on our predicted value for the size of the dust-free cavity (see §3.3.2), we would expect that the plateau phase of the IR echo has ended, and that the IR flux is now in steady decline. Future observations of this decline will place limits on the outer extent of the dust shell, which will in turn provide better limits on the total mass of the dust shell. Our ability to predict the behavior of the scattered-light echo is limited by the current degeneracy concerning the physical location of the scattering dust. If the same dust is responsible for both the IR and scattered-light echoes, then we would expect that the optical emission is now fading, in a manner similar to what ought to be seen in the NIR. Our observations are also consistent with dust located at $\sim 10\text{--}40$ pc from the SN, in which case we might expect the scattered-light echo to continue at roughly a constant flux for several more years. Continued observations with *HST* would allow us to distinguish between these two situations.

The shell-shock model of [Smith & McCray \(2007\)](#) may also explain the peak luminosity of several other VLSNe: SNe 2005ap, 2006tf, 2008es ([Quimby et al. 2007a; Smith et al. 2008a; Miller et al. 2009b; Smith et al. 2010a](#)). This model requires large CSM densities at a distance of a few $\times 10^{15}$ cm, which can be accomplished if the SN progenitor undergoes significant ($\sim 0.1\text{--}1 M_\odot \text{ yr}^{-1}$) mass loss during the few decades prior to explosion. The most luminous LBVs have observed mass shells with $\gtrsim 10 M_\odot$ ([Smith & Owocki 2006](#), and references therein), indicative of giant eruptions ([Humphreys & Davidson 1994](#)) but not LBVs in their more typical state with less violent wind variability (see [Smith et al. 2004](#) for a general reference on LBV winds). The possible connection between large CSM densities and VLSNe may suggest that their progenitors are LBVs ([Smith et al. 2010a](#)). Furthermore, the direct identification of the progenitor of the Type IIn SN 2005gl showed it to be an LBV ([Gal-Yam et al. 2007](#);

([Gal-Yam & Leonard 2009](#)), which strengthens the connection between SNe IIn and LBV progenitors. For the case of SN 2006gy, [Smith et al. \(2008c\)](#) argue that the dusty shell at $\sim 10^{18}$ cm could exist if the progenitor underwent an LBV-like eruptive mass-loss phase ~ 1200 yr prior to the SN. IR echoes for other VLSNe have not been reported to date, but we strongly encourage a search for them. If a substantial fraction of them exhibit late-time characteristics similar to SN 2006gy, this may be suggestive of a common timescale, ~ 1000 yr and ~ 10 yr, for extreme mass loss in the progenitors of VLSNe. The combination of a VLSNe and IR echo would point to multiple phases of eruptive mass loss, which is reminiscent of LBV behavior. The instability driving these eruptions still remains unclear (one possibility is the pulsation pair instability described by [Woosley et al. 2007](#) to explain SN 2006gy), and we encourage future observational and theoretical work to better characterize these systems.

Acknowledgments

A version of this chapter appears in the *Astronomical Journal*, 2010, 139, 2218.

During the writing of this chapter I was supported by a National Science Foundation Graduate Research Fellowship, for which I am grateful for the funding.

I thank Schuyler Van Dyk for his assistance in the preparation of the *Hubble Space Telescope* snapshot proposal, which was essential for acquiring the late-time optical imaging of SN 2006gy. I thank Andy Becker, Maryam Modjaz, Dovi Poznanski, and an anonymous referee for conversations and suggestions that helped to improve this Chapter. I thank Cullen Blake, Dan Starr, and Emilio Falco for their assistance in the operation of PAIRITEL.

Chapter 4

SN 2008iy: An Unusual Type IIn Supernova with an Enduring 400 Day Rise Time

We present spectroscopic and photometric observations of the Type IIn supernova (SN) 2008iy. SN 2008iy showed an unprecedentedly long rise time of ~ 400 days, making it the first known SN to take significantly longer than 100 days to reach peak optical luminosity. The peak absolute magnitude of SN 2008iy was $M_r \approx -19.1$ mag, and the total radiated energy over the first ~ 700 days was $\sim 2 \times 10^{50}$ erg. Spectroscopically, SN 2008iy is very similar to the Type IIn SN 1988Z at late times, and, like SN 1988Z, it is a luminous X-ray source (both supernovae had an X-ray luminosity $L_X > 10^{41}$ erg s $^{-1}$). SN 2008iy has a growing near-infrared excess at late times similar to several other SNe IIn. The H α emission-line profile of SN 2008iy shows a narrow P-Cygni absorption component, implying a pre-SN wind speed of ~ 100 km s $^{-1}$. We argue that the luminosity of SN 2008iy is powered via the interaction of the SN ejecta with a dense, clumpy circumstellar medium. The ~ 400 day rise time can be understood if the number density of clumps increases with distance over a radius $\sim 1.7 \times 10^{16}$ cm from the progenitor. This scenario is possible if the progenitor experienced an episodic phase of enhanced mass loss < 1 century prior to explosion or if the progenitor wind speed increased during the decades before core collapse. We favor the former scenario, which is reminiscent of the eruptive mass-loss episodes observed for luminous blue variable (LBV) stars. The progenitor wind speed and increased mass-loss rates serve as further evidence that at least some, and perhaps all, Type IIn supernovae experience LBV-like eruptions shortly before core collapse. We also discuss the host galaxy of SN 2008iy, a sub-luminous dwarf galaxy, and offer a few reasons why the recent suggestion that unusual, luminous supernovae preferentially occur in dwarf galaxies may be the result of observational biases.

4.1 Introduction

The recent development of synoptic, wide-field imaging has revealed an unexpected diversity of transient phenomena. One such example is the discovery of a new subclass of very luminous supernovae (VLSNe; e.g., Ofek et al. 2007; Smith et al. 2007; Quimby et al. 2007a). While events of this nature are rare (Miller et al. 2009b; Quimby et al. 2011), each new discovery serves to bracket our understanding of the physical origin of well-established classes of SNe and does, in principle, demand an increased clarity in our understanding of the post-main-sequence evolution of massive stars.

Yet another unusual transient was discovered by the Catalina Real-Time Transient Survey (CRTS; Drake et al. 2009), which they announced via an ATel as CSS080928:160837+041626 on 2008 Oct. 07 UT¹ (Drake et al. 2008). The transient was classified as a Type IIn SN with a spectrum taken on 2009 Mar. 27 (Mahabal et al. 2009; see Schlegel 1996 for a definition of the SN IIn subclass, and Filippenko 1997 for a review of the spectral properties of SNe). The SN was later given the IAU designation SN 2008iy (Catelan et al. 2009). Mahabal et al. (2009) noted that the transient was present on CRTS images dating back to 2007 Sep. 13; however, it went undetected by the CRTS automated transient detection software until 2008 because it was blended with a non-saturated, nearby ($\sim 11''$ separation) star.

Here, we present our observations and analysis of SN 2008iy, which peaked around 2008 Oct. 29 (Catelan et al. 2009) and had a rise time of ~ 400 days. This implies that SN 2008iy took longer to reach peak optical brightness than any other known SN. Type II SN rise times are typically $\lesssim 1$ week (e.g., SNe 2004et and 2006bp, Li et al. 2005; Quimby et al. 2007b; see also Patat et al. 1993; Li et al. 2011b), and have never previously been observed to rise $\gtrsim 100$ days, let alone 400, making SN 2008iy another rare example of the possible outcomes for the end of the stellar life cycle. In addition to an extreme rise time, SN 2008iy is of great interest because the unique circumstellar medium (CSM) in which it exploded may provide a link to very long-lived SNe, such as SN 1988Z, and thus provide clues into the nature of their progenitors.

This Chapter is organized as follows. In §4.2 we present the observations. The data are analyzed in §4.3, and the results are discussed in §4.4. We give our conclusions, as well as predictions for the future behavior of SN 2008iy, in §4.5.

4.2 Observations

4.2.1 Photometry

The field of SN 2008iy, which is located at $\alpha = 16^h 08^m 37.27^s$, $\delta = +04^\circ 16' 26.5''$ (J2000), was imaged multiple times by the Palomar Quest survey, and those data have been reprocessed as part of the Deep Sky project² (DS; Nugent 2009). The best constraints on the explosion

¹UT dates are used throughout this Chapter unless otherwise noted.

²<http://supernova.lbl.gov/~nugent/deepsky.html>.

Table 4.1: Deep Sky Observations of SN 2008iy

date (MJD)	mag ^a	σ_{mag} ^b
54618.35	17.37	0.12
54621.35	17.38	0.12
54623.33	17.35	0.12
54626.32	17.34	0.12
54627.36	17.37	0.12
54628.29	17.37	0.12
54629.30	17.36	0.12
54638.21	17.34	0.12
54651.20	17.28	0.12

^aObserved value; not corrected for Galactic extinction.

^bThe calibration uncertainty dominates over the statistical uncertainty with values of ~ 0.12 and ~ 0.01 mag, respectively.

date come from DS imaging: in a coadd of two images from 2007 Jul. 05, we do not detect the SN down to a 3σ limit of $i > 20.9$ mag. DS images are best approximated by the Sloan Digital Sky Survey (SDSS; Adelman-McCarthy et al. 2008) i -band filter. The field of SN 2008iy has well-calibrated SDSS photometry which we use to calibrate the DS images. The observed DS magnitudes are shown in Figure 4.1 and summarized in Table 4.1.

To constrain the rise time of SN 2008iy we visually estimate the possible range of magnitudes for the SN from images on the CRTS website³ based on a comparison to SDSS images. As previously mentioned, SN 2008iy is blended with a nearby star and so the automated photometry produced by the CRTS does not detect the SN on these epochs. On 2007 Sep. 13 the SN was between 18.3 and 19.0 mag, while on 2008 Feb. 19 the SN was observed between 17.9 and 18.3 mag.

Near-infrared (NIR) observations of SN 2008iy were conducted with the 1.3-m Peters Automated Infrared Imaging Telescope (PAIRITEL; Bloom et al. 2006) starting on 2009 Apr. 13. PAIRITEL observes simultaneously in the J , H , and K_s bands. Observations were scheduled and executed via a robotic system, and the data were reduced by an automated pipeline (Bloom et al. 2006). The SN flux was measured via aperture photometry using SExtractor (Bertin & Arnouts 1996), calibrated against the Two Micron All Sky Survey (2MASS; Skrutskie et al. 2006). Filtered photometry of SN 2008iy is shown in Figure 4.2 and summarized in Table 4.2.

Ground-based optical observations of SN 2008iy were obtained using the 1.0-m Nickel telescope located at Lick Observatory (Mt. Hamilton, CA, USA) starting on 2009 Apr. 18. $BVRI$ photometry from the Nickel was measured using the DAOPHOT package (Stetson 1987)

³<http://crtsn.caltech.edu/>.

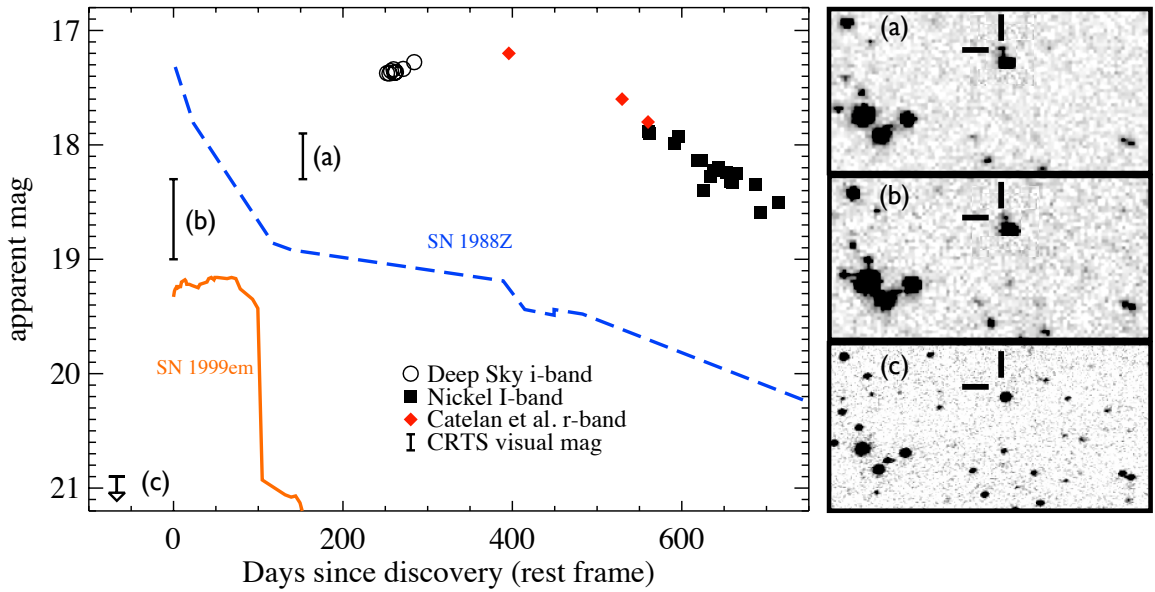


Figure 4.1: Left: Apparent optical light curve of SN 2008iy showing the long rise time of the SN, including data from Deep Sky (this work), the Nickel telescope (this work), [Catelan et al. \(2009\)](#), and the CRTS website. Note: conservatively, we take the start time of the SN ($t = 0$) to coincide with the first epoch where CRTS detects the source; however, the true explosion date is likely prior to 2007 Sep. 13, between the last Deep Sky non-detection and the first CRTS detection. Notice that the light curve is very broad, and almost symmetric about the peak. For comparison we show the light curve of the standard Type II-P SN 1999em (data from [Leonard et al. 2002](#)) and the Type IIn SN 1988Z, which shows many similarities to SN 2008iy at late times (see §4.3.2; SN 1988Z data from [Turatto et al. 1993](#)), as they would have appeared at the redshift of SN 2008iy. Right: Three panels with images of the field of SN 2008iy. Each image is $\sim 2.5' \times 4'$, with north up and east to the left. Black crosshairs mark the location of the SN. The bottom image, marked (c), shows the last non-detection from the Deep Sky data. The middle (b) and top (a) images show the CRTS detections on day 0 and day 153, respectively; SN 2008iy can clearly be seen in each of them. The SN was not flagged as a transient in either the middle or top image by the CRTS software.

Table 4.2: PAIRITEL Observations of SN 2008iy

$t_{\text{mid}}^{\text{a}}$ (MJD)	J mag ^b (Vega)	H mag ^b (Vega)	K_s mag ^b (Vega)
54934.42	16.59 ± 0.05	16.00 ± 0.05	14.98 ± 0.05
54937.43	16.57 ± 0.06	15.99 ± 0.06	15.05 ± 0.05
54941.43	16.57 ± 0.05	16.04 ± 0.08	15.06 ± 0.08
54944.40	16.70 ± 0.05	15.98 ± 0.07	14.98 ± 0.07
54948.40	16.59 ± 0.05	15.87 ± 0.06	14.98 ± 0.06
54951.39	16.55 ± 0.04	15.96 ± 0.06	15.02 ± 0.06
54954.35	16.70 ± 0.04	15.88 ± 0.05	15.00 ± 0.08
54957.37	16.63 ± 0.05	15.91 ± 0.05	14.99 ± 0.10
54959.37	16.68 ± 0.05	15.89 ± 0.06	14.97 ± 0.07
54961.44	16.69 ± 0.06	15.99 ± 0.08	14.83 ± 0.12
54970.30	16.77 ± 0.08	15.98 ± 0.12	...
54975.28	16.66 ± 0.07	15.86 ± 0.05	14.87 ± 0.06
54981.35	16.72 ± 0.04	15.90 ± 0.05	14.93 ± 0.08
54986.29	16.61 ± 0.05	15.85 ± 0.06	15.06 ± 0.12
54990.30	16.68 ± 0.08	16.00 ± 0.11	14.59 ± 0.07
54994.30	16.69 ± 0.05	15.89 ± 0.04	14.84 ± 0.06
54998.31	16.67 ± 0.05	15.92 ± 0.07	14.90 ± 0.07
55003.18	16.86 ± 0.07	15.97 ± 0.05	14.96 ± 0.11
55030.20	16.92 ± 0.19	16.01 ± 0.15	...
55041.18	16.78 ± 0.07	15.94 ± 0.08	14.82 ± 0.10
55091.10	17.08 ± 0.09	15.94 ± 0.07	14.74 ± 0.08

^aMidpoint between the first and last exposures in a single stacked image.

^bObserved value; not corrected for Galactic extinction.

in IRAF⁴, and transformed into the Johnson–Cousins system. Calibrations for the field were obtained on ten photometric nights with the Nickel telescope. The Nickel photometry is shown in Figure 4.2 and summarized in Table 4.3.

SN 2008iy was observed by the space-based *Swift* observatory on 2009 Apr. 15 and 16. *Swift* observed the SN simultaneously with both the X-ray Telescope (XRT; Burrows et al. 2005) and the Ultraviolet/Optical Telescope (UVOT; Roming et al. 2005). We downloaded the Level-2 UVOT images, and measured the U , B , and V photometry using the recipe of Li et al. (2006). The UV filters ($UVM1$, $UVW1$, and $UVW2$) were calibrated using the method of Poole et al. (2008). Our final UVOT photometry is summarized in Table 4.4. The XRT observed the field for a total of 10.71 ks. We extract the 0.3–10.0 keV counts from an extraction region of 64 pixels ($\sim 2.5'$), where we fit the point-spread function model (see Butler & Kocevski 2007) at the centroid of the X-ray emission. From the native XRT astrometry the centroid of the X-ray emission, located at $\alpha = 16^h08^m37.23^s$, $\delta = +04^\circ16'26.7''$ (J2000), with a radial uncertainty of $5''$ (90% confidence interval), coincides with the optical position of SN 2008iy, suggesting that the X-rays are from the SN. In an astrometric fit relative to 2MASS we measure the position of the star $\sim 11''$ from the SN to be $\alpha = 16^h08^m36.98^s$, $\delta = +04^\circ16'16.4''$ (J2000), with a root-mean square scatter of $0.19''$ in α and $0.18''$ in δ for

⁴IRAF is distributed by the National Optical Astronomy Observatory, which is operated by the Association of Universities for Research in Astronomy (AURA) under cooperative agreement with the National Science Foundation.

Table 4.3: Nickel Observations of SN 2008iy

date (MJD)	<i>B</i> mag ⁵ a (Vega)	<i>V</i> mag ⁶ a (Vega)	<i>R</i> mag ⁷ a (Vega)	<i>I</i> mag ⁸ a (Vega)
54939.52	19.06± 0.01	18.59± 0.03	17.86± 0.01	17.87± 0.03
54940.46	19.09± 0.03	18.56± 0.02	17.86± 0.02	17.89± 0.03
54971.37	19.35± 0.06	18.71± 0.04	17.99± 0.04	17.98± 0.11
54975.36	19.25± 0.03	18.75± 0.02	17.96± 0.02	17.92± 0.07
54979.46	19.23± 0.03	18.71± 0.02	17.97± 0.02	...
54999.35	19.36± 0.05	18.79± 0.03	18.07± 0.03	18.12± 0.08
55004.37	19.40± 0.05	18.84± 0.03	18.07± 0.02	18.13± 0.11
55007.43	19.56± 0.11	18.84± 0.10	18.02± 0.04	18.37± 0.13
55015.36	19.43± 0.11	18.95± 0.06	18.10± 0.04	18.26± 0.08
55019.30	19.58± 0.09	19.02± 0.06	18.19± 0.03	18.21± 0.07
55025.36	19.66± 0.24	18.66± 0.10	18.16± 0.08	18.18± 0.12
55034.26	19.52± 0.02	19.02± 0.03	18.19± 0.02	18.23± 0.11
55040.30	19.56± 0.05	18.97± 0.03	18.18± 0.03	18.30± 0.09
55042.24	19.60± 0.07	19.11± 0.06	18.21± 0.03	18.31± 0.11
55047.27	19.43± 0.11	19.21± 0.10	18.22± 0.04	18.24± 0.20
55071.22	19.66± 0.04	19.17± 0.05	18.23± 0.03	18.34± 0.09
55077.23	20.07± 0.24	19.33± 0.17	18.29± 0.03	18.58± 0.17
55100.15	19.75± 0.07	19.25± 0.08	18.35± 0.03	18.49± 0.06

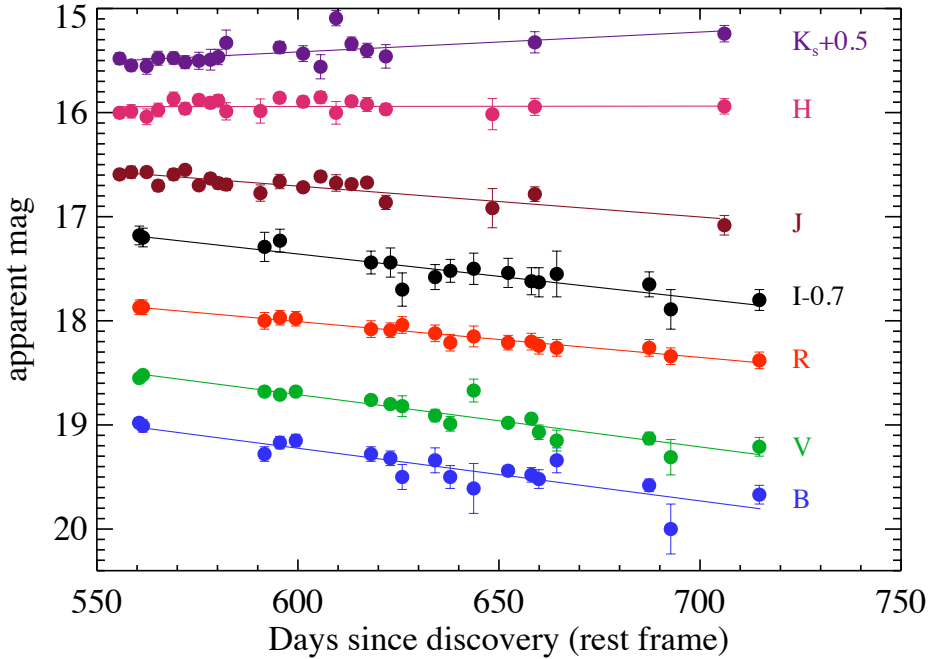
^aObserved value; not corrected for Galactic extinction.

Figure 4.2: Filtered photometry including *BVRJ* from the Nickel telescope and *J, H*, and *K_s* from PAIRITEL, showing the decline rate of SN 2008iy between days ∼560 and 715. To help guide the eye, we illustrate the linear fit to each band used to determine the photometric decline rates (see text). Note that the single epoch of UVOT *B* and *V*-band observations we measured, which agree to $< 1\sigma$ with Nickel data taken < 2 days later, is not shown in this figure.

Table 4.4: UVOT Observations of SN 2008iy

$t_{\text{mid}}^{\text{a}}$ (MJD)	filter	mag ^b (Vega)	σ_{mag}
54936.31	UVW2	19.14	0.06
54936.32	UVM2	18.95	0.08
54936.32	UVW1	18.53	0.07
54936.31	U	18.60	0.06
54937.49	UVW2	19.12	0.04
54937.85	B	19.04	0.06
54937.85	V	18.65	0.08

^aMidpoint between the first and last exposures in a single stacked image.

^bObserved value; not corrected for Galactic extinction.

our astrometric solution. This star is therefore well outside the 90% confidence interval for the location of the X-ray emission. Furthermore, there is no catalogued X-ray source at the position of the SN in the ROSAT catalogue ([Voges et al. 1999](#)), also suggesting that the star located $\sim 11''$ from the SN is not the source of X-ray emission. We measure a background-subtracted 0.3–10.0 keV count rate of $(19 \pm 6) \times 10^{-4}$ counts s⁻¹.

4.2.2 Spectroscopy

Spectra of SN 2008iy were obtained on 2009 Apr. 18, 2009 Apr. 25, and 2009 Jul. 23 with the Kast spectrograph on the Lick 3-m Shane telescope ([Miller & Stone 1993](#)). An additional spectrum was obtained on 2009 Sep. 22 with the Low-Resolution Imaging Spectrometer (LRIS; [Oke et al. 1995](#)) on the 10-m Keck I telescope. To improve the spectral resolution at the location of the H α emission feature from SN 2008iy, we used the 1200 lines mm⁻¹ grating on the red side of the double-arm (blue+red) LRIS system. The spectra were reduced and calibrated using standard procedures (e.g., [Matheson et al. 2000](#)). Clouds were present on the night of 2009 Apr. 25, and the observing setup from that night did not include any wavelength overlap between the red and blue arms of the Kast spectrograph; thus, the absolute flux calibration on this night is less certain than on the other nights. For the Kast spectra, we observed the SN with the slit placed at the parallactic angle, so the relative spectral shapes should be accurate ([Filippenko 1982](#)). LRIS is equipped with an atmospheric dispersion corrector; nevertheless, we observed the SN at the parallactic angle on this night as well. In Figure 4.3 we show the spectral sequence of SN 2008iy, and a summary of our observations is given in Table 4.5.

4.2.3 Host Galaxy

There is no catalogued redshift for the host galaxy of SN 2008iy. To determine the redshift of the SN we examined the LRIS spectrum for the presence of narrow emission lines. Based on a fit to the [O III] $\lambda\lambda 4959, 5007$ doublet we adopt a heliocentric redshift of $z = 0.0411$

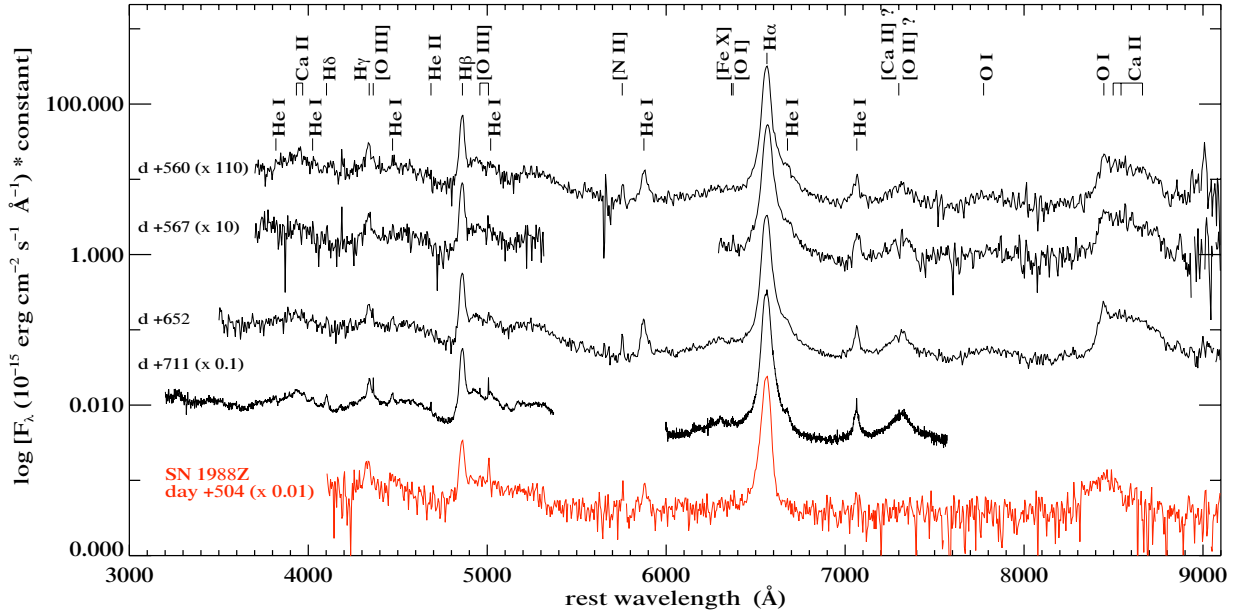


Figure 4.3: Spectral sequence of SN 2008iy (shown in black) and a single, late-time spectrum of SN 1988Z from our spectral database (shown in red), which was observed 504 days after discovery. To the left of the spectra we give the time since discovery, in rest-frame days, at which each spectrum was taken. Prominent spectral features of SN 2008iy are labelled at the top of the figure. The spectra show little evolution between days 560 and 711. Fe II multiplets 42, 48, and 49 can also be seen, though we have not labelled those lines. The spectra have been corrected for Galactic reddening ($E(B - V) = 0.065$ mag; Schlegel et al. 1998). We have assumed no reddening in the SN host galaxy (see §4.2.3).

Table 4.5: Log of spectroscopic observations

Epoch ^a	UT Date	Telescope/ Instrument	Exposure (s)
560	2009-04-18.458	Shane 3-m/Kast	1500
567	2009-04-25.479	Shane 3-m/Kast	1500
652	2009-07-23.274	Shane 3-m/Kast	1800
711	2009-09-22.236	Keck I 10-m/LRIS	600

^aDefined as rest-frame days relative to day 0, 2007 Sep. 13.

for SN 2008iy (not corrected for peculiar motions or Virgo infall). This corresponds to a luminosity distance of $d_L = 179$ Mpc ($H_0 = 71 \text{ km s}^{-1}\text{Mpc}^{-1}$, $\Omega_M = 0.27$, $\Omega_\Lambda = 0.73$), which we adopt throughout the remainder of this Chapter.

The reddening of SN 2008iy by the host galaxy is uncertain. In our Kast spectra we do not detect any absorption from Na I D, and therefore we adopt $A_{\lambda,\text{host}} = 0$ mag.

We confirm the possible detection of the host galaxy by Catelan et al. (2009) in a stack of SDSS g , r , and i -band images of the field. When the $g + r + i$ stack is calibrated to the SDSS r band, we find that the host has $r = 22.75 \pm 0.15 \pm 0.08$ mag in a $2.2''$ diameter aperture, where the two errors represent the statistical and calibration uncertainties, respectively.

As first noted by Catelan et al. (2009), the field of SN 2008iy was observed by the Galaxy Evolution Explorer (GALEX; Martin et al. 2005). On 2004 May 17, the field was imaged as part of the all-sky imaging survey (AIS); the host was not detected to a 5σ limiting magnitude of $FUV \gtrsim 20.2$ and $NUV \gtrsim 20.5$ mag. The field was re-imaged as part of the medium imaging survey on 2008 Jun. 05/06, and SN 2008iy was detected at $FUV = 21.175 \pm 0.094$ mag and $NUV = 19.929 \pm 0.036$ mag.

4.3 Results

4.3.1 Photometric Analysis

At $z = 0.0411$, the absolute peak magnitude of SN 2008iy was a relatively modest $M_r \approx -19.1$ mag. This places SN 2008iy well below the most luminous SNe IIIn, such as SN 2006gy ($M_R = -21.7$ mag; Ofek et al. 2007; Smith et al. 2007) and SN 2008fz ($M_V = -22.3$ mag; Drake et al. 2010), and more in the range of the well-studied SN IIIn 1988Z ($M_R \lesssim -18.9$ mag; Turatto et al. 1993; Stathakis & Sadler 1991). Assuming no bolometric correction, the total integrated optical output from SN 2008iy during the first ~ 700 days after discovery is $\sim 2 \times 10^{50}$ erg. Between day 550 and 720 the SN declines in the optical and the J band, while it actually gets brighter in the H and K_s bands. During this time, the linear decay rates are as follows: $\beta_B = 0.51 \text{ mag (100 day)}^{-1}$, $\beta_V = 0.50 \text{ mag (100 day)}^{-1}$, $\beta_R = 0.34 \text{ mag (100 day)}^{-1}$, $\beta_I = 0.43 \text{ mag (100 day)}^{-1}$, $\beta_J = 0.30 \text{ mag (100 day)}^{-1}$, $\beta_H = -0.03 \text{ mag (100 day)}^{-1}$, and $\beta_{K_s} = -0.19 \text{ mag (100 day)}^{-1}$. These decline rates, all slower than the expected rate of decline for radioactive ^{56}Co , $0.98 \text{ mag (100 day)}^{-1}$, strongly suggest that the SN is still being powered by CSM interaction ~ 700 days after explosion.

For comparison purposes, in addition to the light curve of SN 2008iy, Figure 4.1 shows the light curve of the standard Type II-P SN 1999em (Leonard et al. 2002) as it would have appeared at the redshift of SN 2008iy. As well as illustrating the very long rise time of SN 2008iy, this comparison shows that SN 2008iy was fairly luminous at the time of discovery. Thus, despite the sparse sampling over the first ~ 200 days, this large luminosity suggests that the early detections are not related to a pre-SN outburst, as was observed for SN 2006jc (Foley et al. 2007; Pastorello et al. 2007). CRTS images indicate that the SN was rising over the first ~ 400 days (Mahabal et al. 2009), which provides further evidence against a

pre-SN outburst. Figure 4.1 also shows the light curve of the long lived, interacting, Type IIn SN 1988Z (Turatto et al. 1993). The explosion date of SN 1988Z is not well constrained (see §4.4.3), so we shift the first epoch of detection to day 0. Notice the similarity of the decline rate of SN 2008iy and SN 1988Z around day ~ 600 ; these SNe also have very similar late-time spectra (see §4.4.2).

We were unable to fit the UV through NIR spectral energy distribution (SED) of SN 2008iy to a single-temperature blackbody model. This is not surprising, as SNe II are dominated by emission lines at late times, and single-temperature blackbody models typically apply only to young SNe II (see, e.g., Filippenko 1997). Direct integration of the UV–NIR SED shows that the bolometric correction, relative to the I band, is a factor of ~ 3 in luminosity, corresponding to ~ 1.2 mag, on day ~ 560 . Some features stand out from the SED: there is a strong R -band excess relative to the other optical bands, with $V - R = 0.8$ mag and $R - I = -0.2$ mag on day 715. The red $V - R$ color relative to a blue $R - I$ color can be attributed to the H α emission with large equivalent width. This emission also accounts for the relatively slow decay rate in the R band, as compared to the other optical bands. There is also a NIR excess relative to the I -band flux. In fact, this excess increases with time, $I - K \approx 2.8$ mag on day ~ 560 and $I - K \approx 3.7$ mag on day ~ 710 , which is indicative of the growing importance of dust in the emission from SN 2008iy.

A NIR excess at late times has been observed in many SNe IIn (e.g., Gerardy et al. 2002), and it is the result of either new dust formation (e.g., SN 2005ip; Smith et al. 2009b; Fox et al. 2009) or the presence of a NIR light echo from preexisting dust (Dwek 1983), or both. To distinguish between these two possibilities, which are virtually identical from photometry alone, requires well-sampled optical spectra (see §4.3.2) since line profiles are expected to change with time if new dust is being formed. On day 706, corresponding to our last PAIRITEL observation, the $H - K_s$ color of SN 2008iy was ~ 1.2 mag. Assuming that the dust radiates as a perfect blackbody, this color corresponds to a dust temperature of $T_{\text{dust}} \approx 1320$ K, while the K_s -band measurement corresponds to a dust luminosity $L_{\text{NIR}} \approx 4.8 \times 10^{42}$ erg s $^{-1}$, assuming no bolometric correction as we cannot constrain the emission in the mid-IR. This luminosity is very large, though upon making similar assumptions Gerardy et al. (2002) found NIR luminosities $> 10^{42}$ erg s $^{-1}$ for SNe 1995N and 1997ab at late times. Gerardy et al. also found that the NIR luminosity was roughly an order of magnitude greater than the X-ray emission from SN 1995N, which is also the case for SN 2008iy (see §4.3.3). The $H - K_s$ color of SN 2008iy is bluer than those of the Gerardy et al. sample at a similar epoch, which may be a result of the long rise of SN 2008iy or a contribution to the NIR emission from the SN in addition to the dust. Future NIR observations, as the underlying SN light continues to fade, will place more stringent constraints on the dust near SN 2008iy.

4.3.2 Spectroscopic Analysis

Our spectra of SN 2008iy at ages > 560 days are very similar to those of an unpublished spectrum, from our spectral database, of the Type IIn SN 1988Z taken at a comparable epoch, as shown in Figure 4.3. The general features resemble those of several other SNe IIn

(Filippenko 1997): there are prominent Balmer and He I emission lines, most notably the dominant H α emission, which primarily feature intermediate-width emission components with full width at half-maximum intensity (FWHM) $\sim 1650 \text{ km s}^{-1}$ in the case of SN 2008iy. The higher-resolution Keck spectrum reveals a number of narrow, marginally resolved (FWHM $\lesssim 170 \text{ km s}^{-1}$) emission lines, including H α , H β , [O III] $\lambda\lambda 4363, 4959, 5007$, and He I $\lambda 7065$. The only high-ionization line we detect is [Fe X] $\lambda 6375$. The relative lack of narrow forbidden lines and the low intensity ratio of [O III] $\lambda\lambda 4959, 5007$ to [O III] $\lambda 4363$ suggest a large electron density for the ejecta (Filippenko & Halpern 1984; Filippenko 1989; Stathakis & Sadler 1991). The relative spectral features do not show strong evolution between days 560 and 711.

We can estimate the density of the unshocked emitting material based on the relative intensities of the three [O III] lines mentioned above. Note that [O III] $\lambda 4363$ is only resolved in our day 711 Keck spectrum, so the following estimate of the density is at that epoch only. Following a removal of the underlying continuum, we fit three Gaussian profiles to [O III] $\lambda 4363$ and [O III] $\lambda\lambda 4959, 5007$, and find that $\mathcal{R} = I[\lambda 4959 + \lambda 5007]/I[\lambda 4363] \approx 1.7$. As mentioned above, the strong presence of [O III] $\lambda 4363$ indicates a high density for the emitting material. In fact, with $\mathcal{R} \approx 1.7$, the electron density, n_e , must be $> 10^6 \text{ cm}^{-3}$ regardless of the temperature of the emitting gas. Typically, [O III] emission comes from photoionized regions with $T = 16,000\text{--}20,000$, in which case $n_e \approx 10^7 \text{ cm}^{-3}$ (see Fig. 11 in Filippenko & Halpern 1984). Note that this high-density material is likely only present within clumps in the CSM (see §4.4.3), and that inter-clump portions of the CSM have a lower density.

The H α Profile

As seen in Figure 4.3, the H α emission feature dominates over all the other lines. In the high-resolution Keck spectrum, we see evidence for three distinct emission features: a broad component (FWHM $\approx 4500 \text{ km s}^{-1}$), an intermediate component (FWHM $\approx 1650 \text{ km s}^{-1}$), and a marginally resolved, narrow P-Cygni feature (FWHM $\approx 75 \text{ km s}^{-1}$), as shown in Figure 4.4. The main panel of Figure 4.4 shows a fit to the H α profile (red line) which includes a broad (FWHM $\approx 4500 \text{ km s}^{-1}$) and an intermediate (FWHM $\approx 1650 \text{ km s}^{-1}$) component. Panel (a) in Figure 4.4 shows a close-up view of the narrow emission after the broad and intermediate components have been removed using a spline fit. We fit the spline to the observed H α profile from -1000 km s^{-1} to 1000 km s^{-1} after masking the region between -200 km s^{-1} and 200 km s^{-1} . A narrow absorption minimum such as this, located at $\sim -100 \text{ km s}^{-1}$, has been seen in a number of typical SNe IIIn (e.g., SNe 1997ab, 1997eg, and 1998S, Salamanca et al. 2002; Salamanca 2000; Fassia et al. 2001), and it traces the outflow velocity of the progenitor wind. We note that while the narrow absorption is only marginally resolved, a P-Cygni profile with characteristic speeds of $\sim 10 \text{ km s}^{-1}$, typical of red supergiants (RSGs), would go completely unresolved in the Keck spectrum. Therefore, this P-Cygni profile must be associated with an outflow velocity that is $> 10 \text{ km s}^{-1}$, which will have important consequences for the progenitor (see 4.4.3).

It is interesting that the broad plus intermediate fit overestimates the H α flux out to

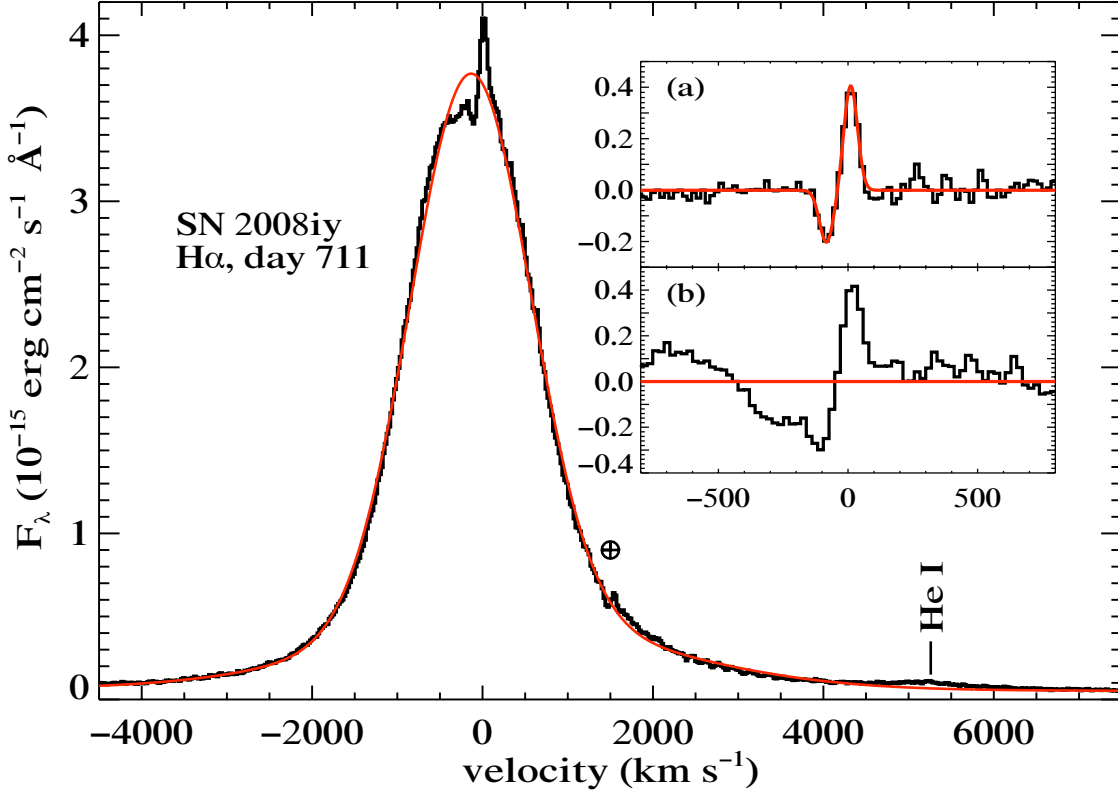


Figure 4.4: Detailed view of the $\text{H}\alpha$ profile from the Keck spectrum taken on day 711. *Main panel:* The black line shows the observed $\text{H}\alpha$ profile, while the smooth red line illustrates a two-Gaussian fit (intermediate, $\text{FWHM} \approx 1650 \text{ km s}^{-1}$; broad, $\text{FWHM} \approx 4500 \text{ km s}^{-1}$) to the profile. Residual emission and absorption from a narrow component to the profile can easily be seen. The location of $\text{He I } \lambda 6678$ has been marked, and the residuals from an imperfect telluric absorption correction have been marked by the \oplus symbol. *Inset (a):* Close-up view of the residual, narrow P-Cygni component. The smooth red line shows a fit to the feature that includes a Gaussian in emission and a Gaussian in absorption (both Gaussians have $\text{FWHM} \approx 75 \text{ km s}^{-1}$). The absorption minimum of the narrow absorption is located at -100 km s^{-1} . Note that for this fit we removed the broad plus intermediate components using a spline fit over the region from -1000 km s^{-1} to 1000 km s^{-1} (see text). *Inset (b):* Residuals following the subtraction of the two-Gaussian broad plus intermediate fit from the observed $\text{H}\alpha$ profile. The absorption minimum still occurs at -100 km s^{-1} , but the BVZI extends to $\sim -450 \text{ km s}^{-1}$, meaning the progenitor wind speed may be $> 100 \text{ km s}^{-1}$ (see text).

about -450 km s^{-1} . In panel (b) of Figure 4.4 we show the residual flux, centered on H α , following the subtraction of our two-Gaussian fit to the broad plus intermediate emission. The blue velocity at zero intensity (BVZI) extends to roughly -450 km s^{-1} , which means that the true wind speed from the progenitor, as traced by the absorbing gas moving directly along the line of sight toward the SN, may be $>100 \text{ km s}^{-1}$ and possibly as high as $\sim 450 \text{ km s}^{-1}$. If this feature represents a true lack of emission, it would be evidence for a two-component CSM: one with velocity $v_{w,1} \approx 100 \text{ km s}^{-1}$ and the other with BVZI $\approx v_{w,2} \approx 450 \text{ km s}^{-1}$. Similar features were seen in SN 1998S (Fassia et al. 2001), which were modeled by Chugai et al. (2002) to be a slow wind accelerated to higher velocities by radiation from the SN photosphere, and in SN 2006gy, which Smith et al. (2010a) argued was the result of a CSM shell that had been ejected from the progenitor in a pre-SN eruption. These two scenarios predict different behavior as the SN evolves.

In the radiatively accelerated scenario, as shown by Chugai et al. (2002) for SN 1998S, the second, faster component to the wind has a negative velocity gradient. Observationally, this effect manifests itself as a BVZI for the second, faster CSM component that decreases with time, as observed in SN 1998S (Fassia et al. 2001). In the shell-ejection scenario, the wind exhibits a positive velocity gradient as the ejected shell is freely expanding, which is thought to be the result of an explosive ($\sim 10^{49} - 10^{50} \text{ erg}$) mass-loss event (see e.g., Chugai et al. 2004). This scenario leads to a BVZI that increases with time, as was observed for SN 2006gy (Smith et al. 2010a). With only a single high-resolution spectrum, we are unable to probe the evolution of this feature, but we note that the velocity of a radiatively accelerated CSM is proportional to t^{-2} (Fransson et al. 1996), so this mechanism is unlikely to be significant at late times ($>$ a few hundred days).

As does the overall continuum, the H α luminosity declines over the course of our observations. In Table 4.6 we summarize the observed properties of the H α profile from our spectra on days 560, 652, and 711. We do not include the spectrum from day 567, as it was taken under cloudy conditions and the overall flux scaling is uncertain, but we do not expect significant spectral evolution between days 560 and 567. The decline in the H α luminosity is accompanied by a rise in the equivalent width over this same time period. For the narrow emission on day 711, we measure $L(\text{H}\alpha) = (2.8 \pm 0.6) \times 10^{39} \text{ erg s}^{-1}$, though we note that this value is likely underestimated because the blue emission wing is probably being partially absorbed. The FWHM of the intermediate component is $\sim 1650 \text{ km s}^{-1}$ at all epochs, while the FWHM of the broad component drops from $\sim 5800 \text{ km s}^{-1}$ on day 560, to $\sim 5200 \text{ km s}^{-1}$ on day 650, to $\sim 4400 \text{ km s}^{-1}$ on day 711. We attribute this change in the broad component to rapid evolution of the spectrum redward of H α between days 560 and 711, as shown in Figure 4.5. The nature of this feature is not currently understood: it could potentially be an absorption feature, or it could be related to a lack of emission from some unidentified species. Similar spectral evolution redward of H α has been seen in the interacting SNe 2005gj and 2006gy (Prieto et al. 2007; Smith et al. 2010a). We do not associate this feature with H α , as the red velocity at zero intensity corresponds to velocities of $\gtrsim 22,000 \text{ km s}^{-1}$, and there are no other emission lines that show evidence for velocities this large.

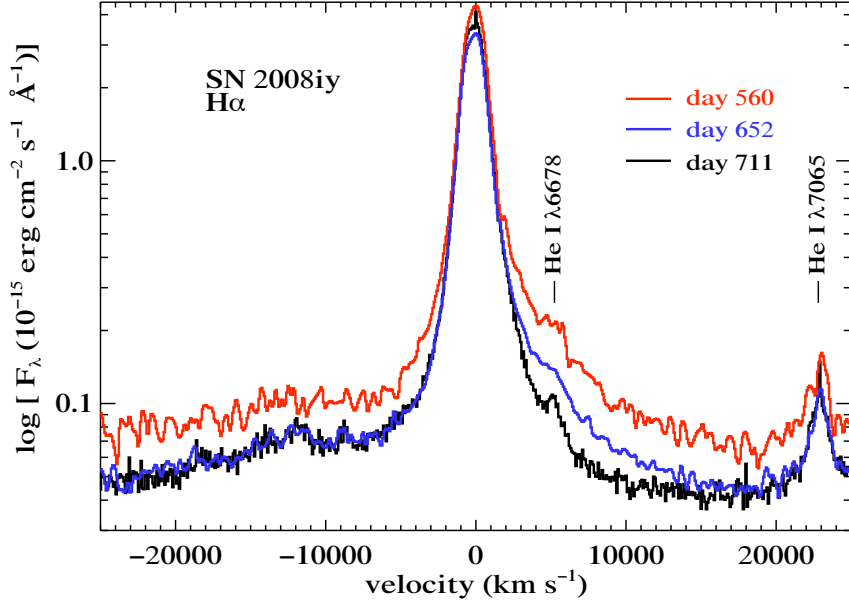


Figure 4.5: Evolution of the H α profile of SN 2008iy between day 560 and day 711. The profile remains largely unchanged, with the exception of a variable spectral feature between $\sim 200 \text{ km s}^{-1}$ and $20,000 \text{ km s}^{-1}$, from day 652 to day 711. Similar spectral features have been observed in other interacting SNe (see text). Emission lines of He I $\lambda 6678$ and He I $\lambda 7065$ are labelled.

Table 4.6: H α line widths, luminosity, equivalent width, and ratio to H β

Epoch ^a	Br. FWHM (km s $^{-1}$)	Int. FWHM (km s $^{-1}$)	Nar. FWHM (km s $^{-1}$)	$L(\text{H}\alpha)^b$ (erg s $^{-1}$)	EW ^b (Å)	H α /H β
560	5774	1641	...	7.86×10^{41}	2122	9.49
652	5162	1685	...	6.10×10^{41}	2386	12.22
711	4405	1639	78	6.50×10^{41}	2786	12.54

^aDefined as rest-frame days relative to day 0, 2007 Sep. 13.

^bUncertainty $\sim \pm 10\%$.

He I Emission

In addition to the prominent Balmer emission lines, SN 2008iy exhibits several He I lines in emission, including $\lambda\lambda 3820, 4026, 4471, 5016, 5875, 6678$, and 7065 . None of these lines show evidence for a broad component, and the intermediate component, $\text{FWHM} \approx 1100\text{--}1400 \text{ km s}^{-1}$, is slightly narrower than that observed for $\text{H}\alpha$. As previously mentioned, He I $\lambda 7065$ has a narrow, marginally resolved emission component in addition to the intermediate component.

A systematic, increasing blueshift in the He I profiles has been argued as evidence for dust formation in the cool, dense shell formed in the post-shock gas of the Type IIn SNe 1998S and 2005ip (Pozzo et al. 2004; Smith et al. 2009b). Newly formed dust in the post-shock region absorbs light from the receding ejecta, resulting in a suppression of flux from the red side of the emission line. Using He I $\lambda 7065$, the strongest He line in our spectra, we searched for changes in the red wing of the profile. The Kast spectra from days 560 and 567 are very noisy, but in the higher signal-to-noise ratio spectra from days 652 and 711 we see no evidence for a change in the red wing of the emission profile. This hints that the observed NIR excess (see §4.3.1) is the result of a NIR echo, rather than newly formed dust, though we caution that with only two spectra separated by ~ 50 days the lack of change in the He I profile does not constitute definitive evidence for this.

4.3.3 X-ray Analysis

To determine the X-ray luminosity of SN 2008iy we assume a thermal plasma spectrum with temperature 0.6 keV (see, e.g., Immler & Kuntz 2005), which has been absorbed by a Galactic column density of $n(\text{H}) = 4.8 \times 10^{20} \text{ cm}^{-2}$ (Kalberla et al. 2005). Using the 0.3–10 keV XRT count rate (see §4.2.1) and PIMMS⁹, we measure the unabsorbed flux, assuming no absorption within the host, to be $(6.1 \pm 1.9) \times 10^{-14} \text{ erg cm}^{-2} \text{ s}^{-1}$. At the adopted distance of SN 2008iy this corresponds to a luminosity of $L_X = (2.4 \pm 0.8) \times 10^{41} \text{ erg s}^{-1}$. Note that Fox et al. (2000) fit the late-time (> 3 yr) X-ray spectra of SN 1995N with a larger temperature of 9.1 keV, which would correspond to a flux and luminosity of $(9.1 \pm 2.9) \times 10^{-14} \text{ erg cm}^{-2} \text{ s}^{-1}$ and $(3.5 \pm 1.1) \times 10^{41} \text{ erg s}^{-1}$, respectively, were we to adopt this value for SN 2008iy. Similar luminosities ($L_X > 10^{41} \text{ erg s}^{-1}$) are observed for other interacting SNe more than 1 year post explosion (e.g., SNe 1988Z and 1995N; Fox et al. 2000).

4.4 Discussion

4.4.1 Mass Loss in the SN 2008iy Progenitor

We assume that the continuum emission traced by the light curve of SN 2008iy is powered solely by CSM interaction. The half life of ^{56}Ni is $\tau \approx 6.0$ days, much too short to power the > 400 day rise of SN 2008iy, while the photometric decay rates are too slow to be powered

⁹<http://heasarc.nasa.gov/Tools/w3pimms.html>.

by ^{56}Co (see §4.3.1), implying that radioactivity contributes minimally to the light curve of SN 2008iy. Furthermore, the SN ejecta will suffer considerable adiabatic losses during the 400 day rise of the light curve, suggesting that interaction is the only viable mechanism for powering SN 2008iy over this entire time.

Following our assumption of interaction-driven luminosity, the expelled gas from the progenitor overtaken by the shock at each epoch can be written as (see Chugai & Danziger 1994)

$$\dot{M} = \frac{2}{\psi} L \frac{v_w}{V_{\text{SN}}^3}, \quad (4.1)$$

where \dot{M} is the mass-loss rate of the progenitor, ψ is an efficiency factor describing the conversion of kinetic energy into radiation, L is the luminosity of the SN, v_w is the wind speed of the progenitor, and V_{SN} is the velocity of the blast wave overrunning the CSM. We adopt $\psi = 0.5$, but this number is likely an overestimate given the optically thin nature of the emission (see §4.4.2). The CSM wind is only probed by our higher-resolution spectrum from day 711, so we adopt $v_w = 100 \text{ km s}^{-1}$ based on the narrow P-Cygni absorption seen in $\text{H}\alpha$, though this may not be valid at all times between days 0 and 700 (see below). We adopt $V_{\text{SN}} = 5000 \text{ km s}^{-1}$ based on the typical widths of the broad $\text{H}\alpha$ emission, which should trace the speed of the blast wave. Unlike our assumption of a constant wind speed, the adoption of a constant-velocity blast wave at all times should at the very least be valid after the peak, at which point the CSM density is decreasing with increasing radius. Hydrodynamic modeling of SNe IIn demonstrates that the blast wave is quickly decelerated to a roughly constant expansion speed as the ejecta sweep up successively more CSM (see, e.g., Chugai et al. 2004). This scenario may not apply to SN 2008iy, however, because the ~ 400 day rise time implies that the CSM density may have been increasing with radius, in which case the blast wave may have been continually decelerated during the rise.

Following the above assumptions we can use Equation 4.1 to determine the mass loss traced by the optical luminosity at a number of different epochs of interest. At each epoch we determine the radius, $R = V_{\text{SN}} t_{\text{SN}} \approx 5000 \text{ km s}^{-1} t_{\text{SN}}$, and the luminosity based on the light curve shown in Figure 4.1. We do not adopt the bolometric correction determined in §4.3.1 for two reasons: (i) it is unclear whether this same correction is valid at early times, and (ii) emission from a NIR echo should not be incorporated into Equation 4.1, as that contribution to the total luminosity is not directly the result of CSM interaction. Thus, the estimates below of the luminosity do not reflect any emission from dust. At early times, day ~ 153 , $L \approx 6.8 \times 10^8 \text{ L}_\odot$, which corresponds to $\dot{M} \approx 1.3 \times 10^{-2} \text{ M}_\odot \text{ yr}^{-1}$ at $R \approx 6.6 \times 10^{15} \text{ cm}$, while at the time of peak $L \approx 1.2 \times 10^9 \text{ L}_\odot$, $R \approx 1.7 \times 10^{16} \text{ cm}$, and $\dot{M} \approx 2.3 \times 10^{-2} \text{ M}_\odot \text{ yr}^{-1}$. On day 563, coincident with our X-ray observations of SN 2008iy the optical luminosity was $L \approx 7 \times 10^8 \text{ L}_\odot$, which corresponds to $R \approx 2.4 \times 10^{16} \text{ cm}$ and $\dot{M} \approx 1.3 \times 10^{-2} \text{ M}_\odot \text{ yr}^{-1}$. On day 714, roughly coincident with our high-resolution Keck spectrum, $L \approx 4 \times 10^8 \text{ L}_\odot$, $R \approx 3.0 \times 10^{16} \text{ cm}$, and $\dot{M} \approx 0.8 \times 10^{-2} \text{ M}_\odot \text{ yr}^{-1}$.

These results are quite remarkable; they suggest that at a time $t \approx V_{\text{SN}} t_{\text{SN}} / v_w \approx 5000 \text{ km s}^{-1} \times 400 \text{ day} / 100 \text{ km s}^{-1} \approx 55 \text{ years}$ prior to the explosion of SN 2008iy, the progenitor

underwent a period of heightened mass loss. This enhanced mass-loss period was then followed by a period of decreasing mass loss leading up to the time of the SN explosion. While the quantitative results for the mass loss discussed above are sensitive to our adopted quantities, most specifically the progenitor wind speed and the speed of the SN blast wave, the fact remains that the continuum luminosity did increase over a period of ~ 400 days after the SN explosion. Rearrangement of Equation 4.1 shows that this luminosity increase is proportional to the wind-density parameter, $w = \dot{M}/v_w$. Thus, w must have *increased* over a distance $R \approx V_{\text{SN}} t_{\text{SN}} \approx 1.7 \times 10^{16}$ cm from the progenitor, regardless of the true wind speed over that distance. An increasing value of w means that during roughly the century prior to the SN, there was a significant change in the wind properties of the progenitor.

Using our X-ray detection of SN 2008iy we have an alternative method to probe the mass-loss history of the progenitor on day ~ 563 . Following [Immler & Kuntz \(2005\)](#), the X-ray luminosity may be written as

$$L_X = \frac{4}{(\pi m)^2} \Lambda(T) \left(\frac{\dot{M}}{v_w} \right)^2 (V_{\text{SN}} t)^{-1}, \quad (4.2)$$

where L_X is the X-ray luminosity, m is the mean mass per particle ($m = 2.1 \times 10^{-24}$ g for a H+He plasma), $\Lambda(T)$ is the cooling function of a plasma heated to temperature T , \dot{M} is the mass-loss rate of the progenitor, v_w is the wind speed of the progenitor (~ 100 km s $^{-1}$, see above), V_{SN} is the speed of the SN blast wave (~ 5000 km s $^{-1}$, see above), and t is the time since explosion, ~ 563 days. Assuming a temperature $T = 10^7$ K, appropriate for an optically thin thermal plasma ([Immler & Kuntz 2005](#)), the effective cooling function is $\Lambda(T) = 3 \times 10^{-23}$ erg cm 3 s $^{-1}$. The X-ray luminosity on day 563 was $L_X \approx 2.4 \times 10^{41}$ erg s $^{-1}$. Substituting these values into Equation 4.2, we find $\dot{M} \approx 0.7 \times 10^{-2}$ M $_{\odot}$ yr $^{-1}$, which shows agreement with the value derived from the optical continuum, $\sim 1.3 \times 10^{-2}$ M $_{\odot}$ yr $^{-1}$, given the uncertainty in a number of the assumptions we have adopted.

An additional estimate of the mass-loss rate of the progenitor comes from the narrow H α emission seen in our Keck spectrum on day 711. [Chugai & Danziger \(2003\)](#) show that the H α emission from the unshocked CSM is related to w :

$$L(\text{H}\alpha) = \frac{1}{4\pi r_1} \alpha_{32} h\nu_{23} (x X w N_A)^2 \left(1 - \frac{r_1}{r_2} \right), \quad (4.3)$$

where r_1 is the inner radius corresponding to the position of the SN blast wave, r_2 is the outer radius related to the fast-moving forward shock, α_{32} is the effective recombination coefficient for H α , $h\nu_{23}$ is the energy of an H α photon, x is the degree of H ionization, X is the hydrogen mass fraction, and N_A is Avogadro's number. We cannot constrain x , X , or r_2 , so we conservatively adopt $x = 1$, $X = 1$, and $r_2 \gg r_1$, all of which have the effect of minimizing w . Assuming Case B H α recombination, $\alpha_{32} = 8.64 \times 10^{-14}$ cm 3 s $^{-1}$, which is appropriate assuming that the narrow emission comes from photoionized gas. Substituting the narrow H α luminosity ($L(\text{H}\alpha) = 2.8 \times 10^{39}$ erg s $^{-1}$) and $r_1 = V_{\text{SN}} t_{\text{SN}} = 3.0 \times 10^{16}$ cm into Equation 4.3, we find that $w \approx 10^{17}$ g cm $^{-1}$. With $v_w = 100$ km s $^{-1}$ on day 711, this corresponds to $\dot{M} \approx 1.6 \times 10^{-2}$ M $_{\odot}$ yr $^{-1}$. At a similar epoch (see above), we find $\dot{M} \approx 0.8 \times 10^{-2}$ M $_{\odot}$ yr $^{-1}$.

based on the optical luminosity. Again, the agreement between these two methods to within a factor of ~ 2 is reasonable given the uncertainties in our adopted parameters.

4.4.2 Late-Time Emission and the Similarity to SN 1988Z

To explain the late-time (i.e., post peak) emission from SN 2008iy we adopt a model that is virtually identical to that developed by Chugai & Danziger (1994) for SN 1988Z: the CSM contains optically thick clumps in addition to a rarefied wind between these clumps (see, e.g., Fig. 1 of Chugai & Danziger 1994). As the SN ejecta sweep through the CSM, they drive a fast-moving forward shock into the rarefied wind. This shocked material forms a cool dense shell between the forward and reverse shocks, and gives rise to the broad emission component seen in H α (FWHM ≈ 5000 km s $^{-1}$ for SN 2008iy). At the same time a slower shock is being driven into the dense clumps, which leads to the intermediate-width emission (FWHM ≈ 1650 km s $^{-1}$ in the case of SN 2008iy) seen in the spectra. The narrow P-Cygni profile results from the pre-shock photoionized wind.

The observed similarities between SN 2008iy and SN 1988Z provide further evidence that comparable models are appropriate for the two SNe. In addition to having similar spectra at late times (see Figure 4.3), SNe 1988Z and 2008iy have large X-ray luminosities (both SNe have $L_X \gtrsim 10^{41}$ ergs $^{-1}$; Fabian & Terlevich 1996, this work), and similar late-time decline rates (~ 0.3 – 0.5 mag (100 day) $^{-1}$ in the optical; Turatto et al. 1993, this work), which in both cases are slower than the expected bolometric decline of radioactive ^{56}Co . Estimates for the mass-loss rate from the progenitor of SN 1988Z vary by roughly an order of magnitude. From X-ray observations Schlegel & Petre (2006) find $\dot{M}_{1988Z} \approx 10^{-3} M_\odot \text{ yr}^{-1}$, while Williams et al. (2002) estimate $\dot{M}_{1988Z} \approx 10^{-4} M_\odot \text{ yr}^{-1}$ based on radio observations, and the models of the optical emission by Chugai & Danziger (1994) yield $\dot{M}_{1988Z} \approx 7 \times 10^{-4} M_\odot \text{ yr}^{-1}$. While these estimates are 1–2 orders of magnitude less than those for SN 2008iy, we note that in each of the above estimates for \dot{M}_{1988Z} a wind speed of 10 km s $^{-1}$ was adopted for the progenitor of SN 1988Z. If SN 1988Z had a progenitor wind speed closer to ~ 100 km s $^{-1}$, a very reasonable possibility given the wind speed of SN 2008iy and other similarities between the two SNe, this would result in an increase in the estimated mass-loss for the progenitor by a factor of ~ 10 , thereby bringing the estimates for the two SNe into accord.

Based on the late-time emission, SN 2008iy seems to belong to the group of SNe IIn that exhibit a slow evolution sustained by long-lived ($\gtrsim 1$ decade) CSM interaction. In addition to SN 1988Z, other members of this group include SN 1986J (Rupen et al. 1987), SN 1995N (Fox et al. 2000; Fransson et al. 2002), and possibly also the VLSN 2003ma (Rest et al. 2011). Both SN 1986J and SN 1995N exhibit evidence for a clumpy progenitor wind, like SN 2008iy and SN 1988Z. Chugai (1993) modeled the X-ray emission from SN 1986J as the interaction between the SN ejecta and a clumpy wind (though note that Houck et al. 1998 prefer a model with a smooth CSM, but they conclude that they cannot rule out the clumpy model). The evidence for a clumpy wind from the progenitor of SN 1995N comes from both the optical spectra (Fransson et al. 2002) and the X-ray emission (Zampieri et al. 2005). Also, the optical decline of both SNe 1986J and 1995N is very slow: SN 1986J declined by $\lesssim 1$ mag

in the optical between 1994 and 2003 (Milisavljevic et al. 2008), while the V -band decline of SN 1995N was only 2.2 mag between 1998 and 2003 (Zampieri et al. 2005).

The duration of the interaction means that the large mass-loss rates from the respective progenitors must have been sustained for at least ~ 100 yr prior to core collapse after the conservative assumption that $V_{\text{SN}} = 1000 \text{ km s}^{-1}$, and $v_w = 100 \text{ km s}^{-1}$. Typically the blast wave continues to expand at $> 1000 \text{ km s}^{-1}$ (SN 1988Z had a broad component that remained nearly constant at $\sim 2000 \text{ km s}^{-1}$ from day ~ 1500 to 3000; Aretxaga et al. 1999), which would make this time period > 100 yr. These very long-lived SNe IIn are therefore connected in that their progenitors experienced lengthy periods with high mass-loss rates. This stands in stark contrast to the Type IIn SN 1994W, which had a light curve with an abrupt drop ~ 100 days post explosion (Sollerman et al. 1998). The mass loss from the progenitor of SN 1994W has been modeled to occur in a short ($\lesssim 1$ yr), violent episode (Chugai et al. 2004), and the sudden drop in the light curve occurs because the SN ejecta have overtaken the dense CSM, thereby halting any interaction luminosity.

4.4.3 Origin of the 400 Day Rise Time and Implications for the Progenitor

With a model to account for the late-time emission from SN 2008iy, we are still left with the puzzle of explaining the 400 day rise time.¹⁰ This rise in the optical is significantly longer than that seen in any other known SN. As previously discussed, this scenario is possible if the progenitor underwent a phase of enhanced mass loss ~ 55 years prior to the SN explosion. The optical luminosity traces the wind-density parameter, w , meaning that during the decades prior to explosion either (i) the mass-loss rate declined, or (ii) the wind speed increased, or (iii) both.

Episodic periods of enhanced mass loss, sometimes in the form of a shell ejection, have been observed for numerous LBVs (see Humphreys & Davidson 1994), though the underlying physics of these eruptions is not currently well understood (see Smith & Owocki 2006). If the progenitor of SN 2008iy had a giant eruption (similar to that of LBVs) $\lesssim 1$ century prior to explosion, this could result in a density profile that peaks $\sim 1.7 \times 10^{16} \text{ cm}$ from the progenitor. In the clumpy-wind scenario described in §4.4.2, this would mean that the ejecta are expanding into a wind where the number density of clumps is increasing with radius. Thus, as more and more clumps are overtaken by the ejecta, the continuum luminosity continues to rise, until after ~ 400 days when the ejecta have reached $\sim 1.7 \times 10^{16} \text{ cm}$, the number density of clumps begins to decline and so does the optical luminosity. Alternatively, the long rise could result from the ejecta expanding into a non-spherical wind, such as a bipolar outflow, though this hypothesis would need to be examined with detailed hydrodynamical models.

The inferred mass-loss rate for SN 2008iy, $\dot{M} \approx 10^{-2} \text{ M}_\odot \text{ yr}^{-1}$, is similar to that for the first LBV, P Cygni, during its great eruption ($\dot{M}_{\text{PCyg}} \approx 10^{-2} \text{ M}_\odot \text{ yr}^{-1}$ during the 1600 AD

¹⁰We have no spectra of the SN while it was still on the rise, thus we have no way of knowing if the SN underwent significant spectral evolution prior to day 560.

eruption; [Smith & Hartigan 2006](#)). Furthermore, the terminal wind speed in the P Cygni nebula is 185 km s^{-1} ([Lamers et al. 1996](#); [Najarro et al. 1997](#)), which is similar to the observed BVZI for the narrow blue absorption seen in SN 2008iy, corresponding to $v_w \approx 160\text{--}450 \text{ km s}^{-1}$. We illustrate these comparisons to show that derived properties of the progenitor wind of SN 2008iy are similar to the giant eruption of a Galactic LBV; we are not insinuating that the great outburst from P Cygni is a direct analogue to the proposed LBV-like eruption from SN 2008iy. Such eruptions are not expected from RSGs.

Further evidence that the progenitor of SN 2008iy could not have had a RSG progenitor comes from the observed narrow P-Cygni H α profile. RSGs have typical wind speeds of $\sim 10 \text{ km s}^{-1}$, with extreme RSG winds reaching 40 km s^{-1} (see [Smith et al. 2007](#)). The observed 100 km s^{-1} wind speed from SN 2008iy is more characteristic of LBVs (e.g., P Cygni, see above) or the escape velocity from a blue supergiant. Similar $\sim 100 \text{ km s}^{-1}$ P-Cygni profiles have been seen in a number of SNe IIn, such as SNe 1997ab ([Salamanca 2000](#)), 1997eg ([Salamanca et al. 2002](#)), 1998S ([Fassia et al. 2001](#)), and 2007rt ([Trundle et al. 2009](#)), implying that the progenitors of each of these SNe may have been in a similar state shortly before core collapse.

The dense CSM and large luminosities associated with many SNe IIn have led a number of authors to suggest that at least some SNe IIn are associated with progenitors that experienced LBV-like mass loss shortly before core collapse (see e.g., [Chu et al. 1999](#); [Salamanca 2000](#); [Chugai & Danziger 2003](#); [Chugai et al. 2004](#)). This possible connection was considerably strengthened following the direct identification of the progenitor of the normal Type IIn SN 2005gl on archival *Hubble Space Telescope* images ([Gal-Yam et al. 2007](#); [Gal-Yam & Leonard 2009](#)). While the diagnostics above are not ubiquitous for all SNe IIn¹¹, many of the signatures (high-density CSM, episodic mass loss with $\dot{M} \approx 10^{-2} \text{ M}_\odot \text{ yr}^{-1}$, and $\sim 100 \text{ km s}^{-1}$ progenitor wind speed) are shared with SN 2008iy, suggesting that it too had an LBV-like progenitor.

As mentioned above, an alternative way to generate a wind-density parameter that is increasing with distance from the progenitor is to increase the progenitor wind speed in the years leading up to the SN event. A relatively mild change in the wind speed by a factor of ~ 3 could, in fact, explain the observed increase in luminosity. During the post-main-sequence evolution of very massive stars a slightly more extreme transition is expected as stars exit the RSG or LBV phase, with wind speeds of $\sim 10\text{--}100 \text{ km s}^{-1}$, to become Wolf-Rayet stars, with typical wind speeds of $\gtrsim 1000 \text{ km s}^{-1}$. As this fast wind expands into the slower wind it will sweep up a thin, dense shell at the interface of the two winds and thus create a wind-blown bubble (e.g., [Dwarkadas 2005](#)). A SN exploding in one of these bubbles will appear as a normal SN until the ejecta reach the edge of the bubble. As the ejecta overtake the thin shell the appearance of the SN will dramatically change as CSM interaction begins to provide a significant contribution to the broad-band luminosity. This is the precise scenario proposed for the Type IIn SN 1996cr, for which [Bauer et al. \(2008\)](#) found an optical luminosity that is clearly decreasing between 1996 and 1999, but the radio emission sharply increases in late

¹¹Note that the low-resolution spectrographs typically employed to observe SNe lack sufficient resolution to resolve narrow ($\text{FWHM} \lesssim 150 \text{ km s}^{-1}$) absorption lines.

1997 while X-ray emission abruptly turns on some time between 1998 Mar. and 2000 Jan. The X-ray emission is especially interesting because after the abrupt initial rise, it continues to rise for at least the next seven years, a feature which had not previously been observed for any X-ray SN. A similar scenario is proposed for SN 2001em, classified as a Type Ic, but which showed unexpectedly strong radio and X-ray emission > 2 yr after explosion, as well as a FWHM ≈ 1800 km s $^{-1}$ H α emission line (Soderberg et al. 2004). Each of these late-time peculiarities can be understood if the progenitor of SN 2001em lost the remainder of its hydrogen envelope during a phase of large mass-loss $\sim (2\text{--}10) \times 10^{-3} M_{\odot}$ yr $^{-1}$, about (1–2) $\times 10^3$ yr prior to core collapse (Chugai & Chevalier 2006). After the hydrogen envelope has been lost, a fast wind from the progenitor sweeps the hydrogen into a shell. The interaction of the Type Ic ejecta with this swept-up shell give rise to the unusual late-time emission.

Can the long optical rise be the result of SN 2008iy exploding inside a wind-blown bubble? There is a somewhat sharp rise in the optical (> 2 mag brightening during the 68 days between the last DS non-detection and the first CRTS detection of the SN) followed by a slow and steady increase over the next ~ 400 days, which may hint that the SN exploded in such a wind-driven cavity. However, we do not favor this model. In the wind-blown bubble scenario, after peak the thin shell has been overtaken by the ejecta, and the luminosity is powered by the interaction of the ejecta with the slower, older wind. To explain this, the wind on day 711 requires $\dot{M} \approx 10^{-2} M_{\odot}$ yr $^{-1}$ and $v_w \approx 100$ km s $^{-1}$, which requires LBV-like mass loss (see above). The wind-blown bubble scenario therefore seems to unnecessarily complicate the scenario discussed above, which is needed to explain the late-time observations, as it requires the transition from a LBV to a Wolf-Rayet star. Yet the addition of this transition does not clearly model any observed properties that could not otherwise be explained.

Additionally, we see no evidence for a normal SN in the years leading up to the initial detection of SN 2008iy as would be expected in the wind-blown bubble scenario. While it would be impossible to completely rule out a SN prior to the first detection of SN 2008iy on 2007 Sep. 13 (for instance, the field is virtually unobservable for ~ 3 months each year while it is behind the Sun), DS images dating to 2004 show no evidence for such an event. These DS images have similar depths to those quoted in §4.2.1, which at the distance of the host galaxy corresponds to an absolute magnitude of $M_i \approx -15.4$ mag. This detection threshold is well below the mean peak magnitude for stripped-envelope SNe: $M_R = -17.01, -16.38$, and -17.04 mag for SNe Ib, Ic, and IIb, respectively (Li et al. 2011b). Stronger constraints on the presence of a stripped-envelope SN prior to 2007 Sep. 13 are based on the individual DS images. There are DS images of the field of SN 2008iy from 2004 Apr. and Jul., 2005 May, Jun., and Jul., 2006 May and Jun., and 2007 Apr., May, Jun., and Jul. Adopting the mean peak magnitudes and mean light curves for stripped-envelope SNe from Li et al. (2011b), we find that on average (note that there is a great deal of dispersion in the peak absolute magnitude and duration of stripped-envelope SNe), SNe Ib and IIb are observable for ~ 70 days above the DS detection threshold, while SNe Ic are observable for only ~ 45 days above the DS detection threshold. In addition to not being detected during any of the months listed above, we can also rule out SNe Ib and IIb in the ~ 2 months prior to those listed above, while SNe Ic can be ruled out in the ~ 1.5 months prior to those above. Therefore, in the

~ 3.5 years prior to SN 2008iy we can rule out SNe Ib or Iib in ~ 21 out of 42 months, while SNe Ic can be ruled out for ~ 18 out of 42 months.

Perhaps the most intriguing points about the progenitor of SN 2008iy are the implications for the progenitors of the very long-lived SNe IIn discussed in §4.4.2, such as SN 1988Z. It is interesting that episodic, LBV-like eruptions, which we argue occurred shortly before SN 2008iy, may be applicable to SNe 1988Z, 1995N, and 1986J, each of which has relatively poor constraints on the actual date of explosion.

SN 1988Z was first observed after peak (Stathakis & Sadler 1991), with an observational constraint on the rise time of < 250 days (Turatto et al. 1993). It was argued by Turatto et al. (1993) that the rise time of SN 1988Z must have been short, in part because at the time no other known SN looked quite like SN 1988Z. SN 2008iy, which is a virtual clone of SN 1988Z at late times, does provide an example of a SN with a long rise time and a peak absolute magnitude that is brighter than the discovery magnitude of SN 1988Z. This negates the necessity of a short rise to peak for SN 1988Z. We submit that it is possible that SN 1988Z had a long rise time, though we note that with no observations during the 250 days prior to discovery, there is no way to definitely prove this claim one way or another. A long rise to peak would, however, further strengthen the similarity of SN 2008iy and SN 1988Z.

Similarly, SNe 1986J and 1995N have poor constraints on the rise time. SN 1986J was discovered in the radio, with constraints on the explosion date ranging from 1982 to 1984; constraints on the optical rise are even worse, owing in part to the large extinction in the host galaxy, $A_V \approx 2$ mag (see Rupen et al. 1987). Typically, ~ 10 months prior to discovery is adopted as the explosion date for SN 1995N (see Fox et al. 2000). However, this age of 10 months is based on the $H\alpha$ profile of SN 1995N, which looked similar to the $H\alpha$ profile of SN 1993N 10 months after SN 1993N had been discovered (Benetti et al. 1995). We note that SNe IIn are a very heterogeneous subclass, and in our experience spectral ages of SNe IIn are not reliable, especially at times greater than a few months. Thus, poor optical constraints mean that SNe 1986J, 1988Z, and 1995N all may have had long rise times, by the standards of typical SNe II whose rise times are $\lesssim 1$ week (Li et al. 2011b).

4.4.4 Similarities to Very Luminous SNe IIn

The long rise time and broad, symmetric evolution of SN 2008iy around peak optical emission is reminiscent of the Type IIn VLSNe 2006gy and 2008fz (Ofek et al. 2007; Smith et al. 2007; Drake et al. 2010). Applying the “shell shock” model of Smith & McCray (2007), which was originally developed to explain the light curve of SN 2006gy, does not provide a physically plausible scenario for SN 2008iy because the relatively low \dot{M} and large radius at peak imply that the CSM shell was not opaque. The “shell shock” model argues that the extreme luminosity of these SNe is powered via a shock running into a dense, optically thick shell. Radiation from the shock is thermalized by the optically thick gas and must diffuse out of the shell.

Nevertheless, SN 2008iy does share a few similarities with the VLSNe IIn. Like SNe 2006gy and 2008fz, SN 2008iy shows evidence for a ~ 100 km s $^{-1}$ pre-shock CSM wind (see Smith

et al. 2007, 2008a), and like SNe 2006gy, 2006tf, and 2008fz, SN 2008iy experienced a period of enhanced mass loss during the decades prior to explosion. The difference between these systems is that the mass-loss rate from SN 2008iy, $\dot{M} \approx 0.01 M_{\odot} \text{ yr}^{-1}$, was less extreme than that from SNe 2006gy, 2006tf, 2008fz, where $\dot{M} \approx 1.0 M_{\odot} \text{ yr}^{-1}$ (e.g., Smith et al. 2010a). Also, the time between the period of enhanced mass loss and the SN was longer for SN 2008iy, ~ 55 years, than for SNe 2006gy and 2006tf, $\lesssim 10$ years (Smith et al. 2010a, 2008a). The result of these differences is that SN 2008iy did not reach as extreme a peak luminosity and took considerably more time to reach peak optical output than the VLSNe IIn. Finally, if the late-time NIR excess is the result of an IR dust echo, this would be similar to SN 2006gy (Smith et al. 2008c; Agnoletto et al. 2009; Miller et al. 2010a). Smith et al. (2008c) and Miller et al. (2010a) argue that a giant eruption $\gtrsim 1000$ year prior to SN 2006gy could potentially create the dust shell giving rise to the echoes, and a similar shell around SN 2008iy may explain the observed NIR excess.

The connection between VLSNe and very massive stars, such as η Car, was first made by Smith et al. (2007) because the large mass-loss rates needed to explain the extreme optical luminosity are reminiscent of η Car during the great eruption of 1843. It is interesting to note that were η Car to explode as a SN today, its appearance would be less like the VLSNe IIn discussed above and more similar to SN 2008iy. The reason for this is that with the eruption happening >150 yr ago, the ejected shell surrounding η Car has had sufficient time to expand ($R \approx \text{few} \times 10^{17} \text{ cm}$) and become clumpy (Morse et al. 1998), with an optical depth that is now near unity (Davidson et al. 2001). Thus, η Car does not have the compact ($R \lesssim \text{few} \times 10^{15} \text{ cm}$), very optically thick shell required to generate an extreme peak luminosity following a SN. Instead, as the SN ejecta sweep through the large shell,¹² they will successively overtake more and more mass within the clumpy CSM. This will likely give rise to a long rise time, similar to what was seen in SN 2008iy.

4.4.5 The Host of SN 2008iy

At the adopted distance to SN 2008iy, our detection of the host galaxy in stacked SDSS images (see §4.2.3) means that the host has an absolute magnitude of $M_r \approx -13.7$ mag. This is significantly fainter than the Small Magellanic Cloud (with $M_V = -16.9$ mag). We do not detect narrow emission lines from the host in our SN spectra in order to make a direct measurement of the metallicity. The prospects for such a measurement in the near future are not good: if SN 2008iy continues to evolve like SN 1988Z, light from the SN may dominate over light from the host galaxy for years to come.

We can, however, estimate the metallicity based on the absolute magnitude of the host. Lee et al. (2006) use 27 dwarf irregular galaxies to determine the luminosity-metallicity relation for low-mass galaxies, and following from their Equation 1, we find $12 + \log(\text{O/H}) \approx 7.7$, assuming $M_B \approx M_r$. The uncertainty in this value is large, perhaps as great as ± 0.3 dex, based both on our assumption of $B - r = 0$ mag for the host and the substantial scatter in

¹²The shell around η Car is much bigger than the one around SN 2008iy because the wind speeds are greater, $v_{w,\eta Car} = 600 \text{ km s}^{-1}$ (Smith 2006), and the nebula is older, ~ 165 yr relative to ~ 55 yr.

the luminosity-metallicity relationship for faint galaxies (Lee et al. 2006 find a scatter of 0.16 dex), yet this nevertheless shows that SN 2008iy occurred in a metal-poor galaxy.

It has recently been suggested that the unusual SNe discovered by the non-targeted transient surveys, such as CRTS, preferentially occur in sub-luminous, possibly metal-poor host galaxies (Miller et al. 2009b; Drake et al. 2010). SN 2008iy is yet another example of an unusual SN in a low-luminosity host. We caution, however, that a number of biases may be skewing initial impressions about the hosts of these unusual SNe. Preliminary calculations show that these VLSNe are rare (Miller et al. 2009b; Quimby et al. 2011). Both the large peak luminosity and slow evolution of SN 2008iy mean that similar SNe would be easily detectable in the galaxies of targeted SN surveys. The lack of other examples of SNe with ~ 400 day rise times suggests that SN 2008iy is also rare. The CRTS, however, does not employ image subtraction during their search for transients; instead they use aperture photometry to find new sources, or sources with large increases in flux, and flag those as possible transients. Consequently, their survey is biased toward the discovery of intrinsically bright SNe in faint host galaxies. From the Lick Observatory Supernova Search (LOSS), we know that SNe IIn are rare, regardless of whether they are very luminous or have long rise times (Li et al. 2011a). Yet, even LOSS, which targets specific galaxies, may be biased in that it observes relatively few sub-luminous galaxies. New and upcoming surveys, such as the Palomar Transient Factory (Law et al. 2009; Rau et al. 2009), which employ image subtraction and survey large, non-targeted fields of view, will not suffer from the same biases discussed above, and hence will be in a better position to address whether these unusual SNe preferentially occur in sub-luminous host galaxies.

4.5 Conclusions

We have reported on observations of the Type IIn SN 2008iy, which took ~ 400 days to reach peak optical output. There are few known SNe with optical rise times $\gtrsim 50$ days, and SN 2008iy is the first with a rise time > 1 year. We argue that this long rise to peak is caused by the interaction of the SN ejecta with a dense CSM; radioactivity is unlikely to drive a 400-day rise. Furthermore, the late-time optical decay, ~ 0.4 mag (100 days) $^{-1}$, is slower than that of ^{56}Co , which provides further evidence that radioactive heating is not a dominant energy source for SN 2008iy. Spectroscopically, SN 2008iy is very similar to SN 1988Z at late times. SN 1988Z is understood to have exploded in a dense, clumpy CSM (Chugai & Danziger 1994), which we argue was also the case for SN 2008iy. We detect SN 2008iy in X-rays with a total luminosity $L_X = (3.7 \pm 1.2) \times 10^{41}$ erg s $^{-1}$, which is similar to that of the Type IIn SNe 1988Z and 1995N (Fox et al. 2000). Similar to other SNe IIn, SN 2008iy has a growing NIR-excess at late times. SN 2008iy had a peak absolute magnitude of $M_r \approx -19.1$ mag and a total radiated energy of $\sim 2 \times 10^{50}$ erg in the optical (assuming no bolometric correction).

The steady increase in optical luminosity over a ~ 400 -day period means that the wind-density parameter, w , increased over a distance of $\sim 1.7 \times 10^{16}$ cm from the SN. We propose

two possible scenarios to explain this increase in w : (i) the progenitor experienced an episode of LBV-like, eruptive mass-loss \sim 55 years prior to the SN, or (ii) the wind speed of the progenitor was increasing during the years leading up to core collapse. We prefer the former scenario, as the later adds unnecessarily complicated pieces to the puzzle without providing a unique solution. Our favored scenario provides yet another piece of evidence that some SNe IIn are connected to LBV-like progenitors (see [Gal-Yam et al. 2007](#), and references therein). We find that the host of SN 2008iy is a sub-luminous dwarf galaxy, though we caution against premature conclusions that unusual SNe, specifically those that are very luminous or have very long rise times, preferentially occur in low-mass dwarf galaxies.

Finally, we close with some predictions for the late-time behavior of SN 2008iy. There are examples of SNe IIn whose luminosity dramatically drops after the SN ejecta overtake the dense CSM (e.g., SN 1994W; [Sollerman et al. 1998](#)). However, the similarities to SN 1988Z suggest that SN 2008iy could continue interacting, and thus remain luminous, for several years. This would allow long-term monitoring in the radio, X-ray, and optical, like SN 1988Z ([Williams et al. 2002](#); [Schlegel & Petre 2006](#); [Aretxaga et al. 1999](#)). We predict that SN 2008iy is a luminous radio source, like SN 1988Z ([van Dyk et al. 1993](#)), though we note that at $z = 0.0411$ deep observations may be necessary for detection. The increasing K_s -band luminosity from day 560 to 710 is likely due to the presence of dust, and we predict that SN 2008iy will also be luminous in the mid-IR (\sim 3–5 μm). The data are insufficient to distinguish between newly formed dust or dust that was present prior to the SN, but future medium- to high-resolution spectroscopy could distinguish between these two cases. If new dust is being formed, it should result in a systematic blueshift in the line profiles, as the dust creates an optically thick barrier to radiation from the receding SN ejecta.

Acknowledgments

A version of this chapter appears in the Monthly Notices of the Royal Astronomical Society, 2010, 404, 305.

During the writing of this chapter I was supported by a National Science Foundation Graduate Research Fellowship, for which I am grateful for the funding.

I would like to thank D. Poznanski for useful discussions that helped improve this Chapter and M. Modjaz for discussions concerning the metallicity of the host galaxy of SN 2008iy. I thank Neil Gehrels for approving the *Swift* ToO request for SN 2008iy, which was submitted by Dave Pooley, and the *Swift* team for scheduling and obtaining those observations. I thank Cullen Blake, Dan Starr, and Emilo Falco for their work operating PAIRTEL. I wish to thank the following Nickel telescope observers: P. Thrasher, M. Kislik, J. Rex, J. Choi, I. Kleiser, J. Kong, M. Kand rashoff, and A. Morton. Finally, I wish to thank the referee for the Monthly Notices manuscript, Nikolai Chugai, for suggestions that helped to improve this chapter.

Chapter 5

Evidence for an FU Orionis-like Outburst from a Classical T Tauri Star

We present pre- and post-outburst observations of the new FU Orionis-like young stellar object PTF 10qpf (also known as LkH α 188-G4 and HBC 722). Prior to this outburst, LkH α 188-G4 was classified as a classical T Tauri star on the basis of its optical emission-line spectrum superposed on a K8-type photosphere, and its photometric variability. The mid-infrared spectral index of LkH α 188-G4 indicates a Class II-type object. LkH α 188-G4 exhibited a steady rise by \sim 1 mag over \sim 11 months starting in Aug. 2009, before a subsequent more abrupt rise of > 3 mag on a time scale of \sim 2 months. Observations taken during the eruption exhibit the defining characteristics of FU Orionis variables: (i) an increase in brightness by \gtrsim 4 mag, (ii) a bright optical/near-infrared reflection nebula appeared, (iii) optical spectra are consistent with a G supergiant and dominated by absorption lines, the only exception being H α which is characterized by a P-Cygni profile, (iv) near-infrared spectra resemble those of late K-M giants/supergiants with enhanced absorption seen in the molecular bands of CO and H₂O, and (v) outflow signatures in H and He are seen in the form of blueshifted absorption profiles. LkH α 188-G4 is the first member of the FU Orionis-like class with a well-sampled optical to mid-infrared spectral energy distribution in the pre-outburst phase. The association of the PTF 10qpf outburst with the previously identified classical T Tauri star LkH α 188-G4 (HBC 722) provides strong evidence that FU Orionis-like eruptions represent periods of enhanced disk accretion and outflow, likely triggered by instabilities in the disk. The early identification of PTF 10qpf as an FU Orionis-like variable will enable detailed photometric and spectroscopic observations during its post-outburst evolution for comparison with other known outbursting objects.

5.1 Introduction

FU Orionis variables are young stellar objects (YSOs) that exhibit large-amplitude optical outbursts ($\Delta m_{\text{visual}} \gtrsim 4$ mag) and remain bright for several decades (Herbig 1977). Models in which the radiation is dominated by a rapid increase in the disk accretion rate have successfully reproduced many of the observational properties of FU Orionis outbursts; see Hartmann & Kenyon (1996) for a review. An alternative interpretation involving a rapidly rotating low-gravity star is presented by Herbig (1989) and Herbig et al. (2003). In the first scenario, the cause of the instability remains uncertain; possible mechanisms include thermal instabilities (Hartmann & Kenyon 1996) and interactions with companion stars on eccentric orbits (Bonnell & Bastien 1992). Accretion instabilities are also believed to give rise to less dramatic YSO flares.¹ These events (e.g., EX Lupi, V1647 Ori, V1118 Ori, Z CMa; see Herbig 1977, Herbig 2007, Aspin et al. 2010, Aspin & Reipurth 2009, Fedele et al. 2007, Rettig et al. 2005, Lorenzetti et al. 2007, Audard et al. 2010, Szeifert et al. 2010, and references therein) are heterogeneous, and it remains to be determined if they should be referred to as a single class (Herbig 2007). These YSO outbursts are nevertheless distinguished from FU Orionis-like outbursts in that their optical spectra are emission-line dominated (whereas FU Ori stars typically show only absorption lines during outburst) and the outbursts have shorter lifetimes, $\tau_{\text{outburst}} \lesssim 2$ yr, than FU Ori stars which remain in outburst for decades (Herbig 1977; Fedele et al. 2007).

YSO outbursts are of great interest given their potential importance to the broader star and planet formation process. Low-mass stars could accrete as much as half their final mass during FU Orionis outbursts (Hartmann & Kenyon 1996), and the strong winds and outflows they are thought to drive likely have a significant impact on the surrounding interstellar medium (Croswell et al. 1987).

One of the major challenges in studying FU Orionis stars is the relatively small sample of known examples. Although ~ 20 FU Orionis candidates have been identified by Reipurth & Aspin (2010) based on a mix of spectroscopic evidence, only a handful (~ 6 –8) of those stars have been observed to rise from their pre-outburst state to their eruptive state. Only one example, V1057 Cyg, has had a pre-outburst spectrum taken; it showed Balmer, Ca II, Fe I, and Fe II lines in emission (Herbig 1977). Herbig noted that these features resembled those of a T Tauri star, but a lack of detected absorption lines precluded a spectral-type classification beyond a late-type star based on the red continuum.

Recently, a new FU Orionis-like variable, associated with LkH α 188-G4, was discovered at $\alpha_{\text{J2000}} = 20^{\text{h}}58^{\text{m}}17\overset{\text{s}}{.}00$, $\delta_{\text{J2000}} = +43^{\circ}53'42''$ in the direction of NGC 7000/IC 5070, also known as the North America/Pelican Nebula. The source was announced as a likely FU Ori-like outburst on 2010 Aug. 17 UT² by Semkov & Peneva (2010a), and was later spectroscopically

¹In the literature, these events are frequently referred to as “EXors”, named for the outbursting star EX Lupi. This nomenclature is confusing, however, as EX Lupi is not part of the Orion constellation and many of the so called EXors seem to have distinct properties (see e.g., Fedele et al. 2007, Herbig 2007, Covey et al. 2011).

²UT dates are used throughout unless otherwise noted.

confirmed as an FU Ori candidate by [Munari et al. \(2010\)](#). Further photometric observations showed that the source became bluer over the course of the outburst and that a reflection nebula was emerging around LkH α 188-G4 ([Semkov & Peneva 2010b](#)). Near-infrared (NIR) photometric observations revealed a \sim 3 mag increase in the J , H , and K_s bands ([Leoni et al. 2010](#)). The variable was independently discovered by our collaboration during the course of regular monitoring of the North America Nebula with the Palomar 48-in telescope. These images were automatically reduced, and new variable and transient sources were found using the software developed for the Palomar Transient Factory (PTF; [Law et al. 2009](#); [Rau et al. 2009](#)). On 2010 Aug. 5 the outburst from LkH α 188-G4 was identified and given the name PTF 10qpf.

Here, we present pre- and post-eruption observations of LkH α 188-G4, an FU Orionis-like star, which we argue was a classical T Tauri star prior to eruption. Shortly before the submission of this article, an independent analysis of LkH α 188-G4 was posted on the arXiv by [Semkov et al. \(2010\)](#), in which they also argue that the 2010 eruption from LkH α 188-G4 is an FU Orionis outburst. In §5.2 we discuss archival observations of LkH α 188-G4 prior to the 2010 eruption. Our new 2009 and 2010 observations are presented in §5.3, and §5.4 contains our analysis of those observations. We discuss our conclusions in §5.5. Throughout this Chapter we designate the 2010 outburst as PTF 10qpf, while we refer to the pre-outburst star as LkH α 188-G4.

5.2 Pre-Outburst Observations of LkH α 188-G4

PTF 10qpf is associated with the previously known optical source LkH α 188-G4 ([Cohen & Kuhi 1979](#)), which was later cataloged by [Herbig & Bell \(1988\)](#) as HBC 722. [Cohen & Kuhi \(1979\)](#) identified the star as an $m_V = 18.9$ mag emission-line object with line equivalent widths of $EW_{H\alpha} = -100.5$ Å and $EW_{H\beta} = -25.8$ Å; [O I] $\lambda 6300$ was also present, and NIR photometry was reported. We are unable to identify the strong emission feature near 4640 Å in the [Cohen & Kuhi \(1979\)](#) spectrum, and the authors themselves do not measure or comment on the feature. It could be related to multiply ionized C or N, or He II (see, e.g., [Sargent & Filippenko 1991](#)), though the absence of a known exact wavelength for the feature precludes a secure identification. The original spectrum is no longer available (M. Cohen, 2010, private communication) and we caution that the feature may be an error in the original data. [Cohen & Kuhi \(1979\)](#) determined a spectral type of K7–M0; they also derived an extinction estimate of $A_V = 3.4 \pm 1.2$ mag and a bolometric luminosity of $\log(L/L_\odot) = 0.43$.

The source is part of a linear chain of young stellar objects that was first designated by [Cohen & Kuhi \(1979\)](#) as the NGC 7000 / IC 5070 LkH α 188 group. *Spitzer* IRAC and MIPS observations presented by [Guieu et al. \(2009\)](#) and [Rebull et al. \(2011\)](#) later revealed that the optically visible stars are only the surface population of a much richer embedded cluster, known as the “Gulf of Mexico” cluster due to its location relative to the North America Nebula. The Two Micron All Sky Survey (2MASS; [Skrutskie et al. 2006](#)) observed the field in the J , H , and K_s bands on 2000 June 10. *BVI* optical photometry obtained with the

Table 5.1: IPHAS Observations of LkH α 188-G4

UT date	<i>r</i> mag (AB)	<i>i</i> mag (AB)	H α mag (AB)
2003/10/15	17.300 \pm 0.010	15.677 \pm 0.006	16.023 \pm 0.007
2003/10/18	17.348 \pm 0.011	15.744 \pm 0.006	16.063 \pm 0.006
2003/11/02	17.283 \pm 0.017	15.608 \pm 0.009	15.975 \pm 0.009
2003/11/14	17.074 \pm 0.009	15.570 \pm 0.005	15.724 \pm 0.006
2005/11/19	17.075 \pm 0.007	15.671 \pm 0.006	15.768 \pm 0.008

Kitt Peak National Observatory 0.9-m telescope was presented by [Guieu et al. \(2009\)](#), while broadband *ri* and narrowband H α imaging of LkH α 188-G4, obtained between 2003 and 2005, is presented in the catalog of the INT/WFC Photometric H α Survey of the Northern Galactic Plane (IPHAS; [González-Solares et al. 2008](#)). We summarize the IPHAS measurements in Table 5.1.

Owing to crowding, there are no *IRAS* measurements of LkH α 188-G4. Additional IR sources are cataloged by the Midcourse Space Experiment (*MSX*; [Mill et al. 1994](#)) and *AKARI* ([Murakami et al. 2007](#)). The *MSX* source has a position ($\alpha_{J2000} = 20^{\text{h}}58^{\text{m}}17\overset{\text{s}}{.}59$, $\delta_{J2000} = 43^{\circ}53'36\overset{\text{s}}{.}24$) which is $\sim 9.2''$ from the optically derived position of LkH α 188-G4. This position has no clear counterpart, to within $\sim 3''$, in the 2MASS catalog, and thus the *MSX* source may represent a blend of emission from several stars in the LkH α 188 group. There are two sources in the *AKARI* MIR catalog ([Ishihara et al. 2010](#)) within $10''$ of the optical position of LkH α 188-G4. Both of these sources are $>4.5''$ from the optical position of LkH α 188-G4, however, so we do not include them here in our analysis of pre-outburst emission from LkH α 188-G4; the photometry of these sources likely does not correspond to LkH α 188-G4 alone. *AKARI* also catalogs a source in the far-infrared (FIR) at $\alpha_{J2000} = 20^{\text{h}}58^{\text{m}}16\overset{\text{s}}{.}809$, $\delta_{J2000} = +43^{\circ}53'41\overset{\text{s}}{.}65$, which is $\sim 2.4''$ from the optical position of LkH α 188-G4. The closest 2MASS counterpart to the *AKARI* FIR source is LkH α 188-G4, though we cannot rule out the possibility that the *AKARI* flux measurements include a contribution from other members of the LkH α 188 group.

The pre-outburst spectral energy distribution (SED) of LkH α 188-G4 is shown in Figure 5.2. The pre-outburst SED of LkH α 188-G4 exhibits a smooth trend with the exception of the two points at ~ 0.75 and $0.9 \mu\text{m}$. These points, corresponding to the IPHAS *i* band and KPNO *I* band, respectively, are not coeval and differ by a factor of $\sim 30\%$ in flux, which is similar to the ~ 0.3 mag variability seen in the multi-epoch IPHAS data.

Direct integration of the pre-outburst SED, excluding the *AKARI* data, results in a total luminosity of $\sim 0.7 L_\odot$, assuming a distance of 600 pc to NGC 7000. Adopting the classification scheme from [Lada & Wilking \(1984\)](#), we fit for the MIR spectral index, defined as

$$\alpha = \frac{d \log \lambda F_\lambda}{d \log \lambda}, \quad (5.1)$$

where α is the spectral index and F_λ is the flux density at wavelength λ . Following a least-squares fit to the *Spitzer*/IRAC data from 3.6 to $8 \mu\text{m}$, we measure $\alpha = -0.40$, indicating that

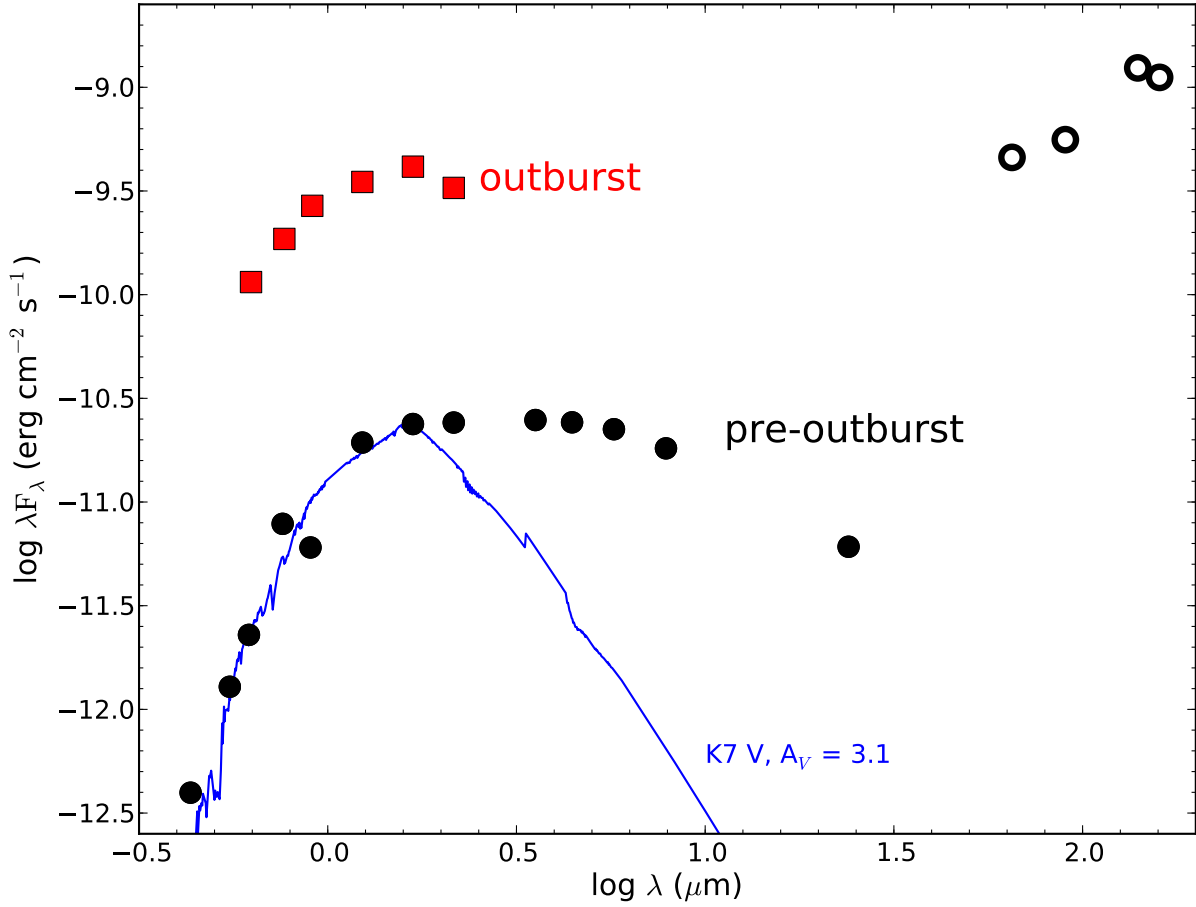


Figure 5.1: Spectral energy distribution of LkH α 188-G4 both before (black circles) and during (red squares) the 2010 outburst. Pre-outburst NIR photometry is from 2MASS, while non-simultaneous optical and MIR photometry is from [Guieu et al. \(2009\)](#), [Rebull et al. \(2011\)](#), and [González-Solares et al. \(2008\)](#). FIR photometry from *AKARI* is shown as open circles because these detections may include light from other members of the LkH α 188 group (see text and figure 5.4). The solid line shows the model spectrum, from [Kurucz \(1993\)](#), of a K7 V star reddened with $A_V = 3.1$ mag, and demonstrates the infrared excess of LkH α 188-G4. The spectral slope in the MIR is consistent with the source being a Class II YSO prior to outburst. NIR outburst photometry was obtained on 2010 Oct. 10 with PAIRITEL, while *riz* photometry was taken on 2010 Oct. 14 with P60.

LkH α 188-G4 was a Class II YSO *prior* to its 2010 outburst. Thus, there was no evidence of either a dense core of infalling material or significant envelope material in the vicinity of the central star. Including the *Spitzer*/MIPS 24 μm detection results in $\alpha = -0.77$, securely establishing this source as a Class II YSO. To demonstrate the MIR excess relative to a stellar photosphere, we also show in Figure 5.2 the model spectrum of a solar metallicity K7 V star, reddened with $A_V = 3.1$ mag, which is consistent with the inferences from Cohen & Kuhi (1979). The model spectrum, taken from the Kurucz (1993) update to the Kurucz (1979) models, has been normalized to match the flux of LkH α 188-G4 in the H band.

Class II YSOs are most commonly associated with classical T Tauri stars (CTTSs; Lada 1987). In addition to being a Class II YSO, we also know from the multi-epoch IPHAS data that LkH α 188-G4 was optically variable between 2003 and 2005, years before the observed PTF outburst, with an amplitude of \sim 0.2–0.3 mag. While some CTTSs show variable amplitudes as large as \sim 2 mag, the majority exhibit low-amplitude variability consistent with what we observe in LkH α 188-G4 prior to eruption (Grankin et al. 2007). The emission-line spectrum, Class II MIR spectral index, and optical variability all point to LkH α 188-G4 being a fairly undistinguished CTTS prior to its 2010 eruption.

5.3 2009 and 2010 Observations

5.3.1 Optical Photometry and an Independent Discovery

During the 2009 and 2010 observing seasons, PTF obtained red optical images of the North America/Pelican Nebula star-forming region with a typical 5-day cadence. These observations were conducted with the main PTF Survey Camera, the former CFHT12K mosaic camera now extensively re-engineered and mounted on the 48-in Samuel Oschin telescope at Palomar Observatory (hereafter P48). The camera is a mosaic of 12 CCDs (one of which is not functional), covering a 7.8 square degree field of view with 1" sampling; typical conditions at Palomar Observatory produce 2.0" full width at half-maximum intensity (FWHM) images (Law et al. 2009). The R_{PTF} filter, a Mould R band, is similar to the Sloan Digital Sky Survey (SDSS) r band in shape but is shifted redward by ~ 27 Å and is ~ 20 Å wider. The typical 5σ limiting magnitudes are $m_R \approx 20.6$ (AB) in 60 s exposures. Representative images of LkH α 188-G4/PTF 10qpf from the 2009 and 2010 observing seasons are shown in Figure 5.4.

Transient sources are detected in the PTF monitoring data by means of automated reduction pipelines, including a nearly real-time image-subtraction pipeline hosted at Lawrence Berkeley National Laboratory (LBNL). Well-detected sources in the difference images are scored (using a human-trained, machine-based classifier) for their likelihood of being truly astrophysical in nature or of spurious origin. Variable sources with larger likelihoods of being nonspurious are passed to an automatic source classifier at UC Berkeley (*Oarical*), which combines PTF measurements with all other available information (e.g., SIMBAD identifications, 2MASS photometry, etc.) to provide probabilistic classifications of PTF

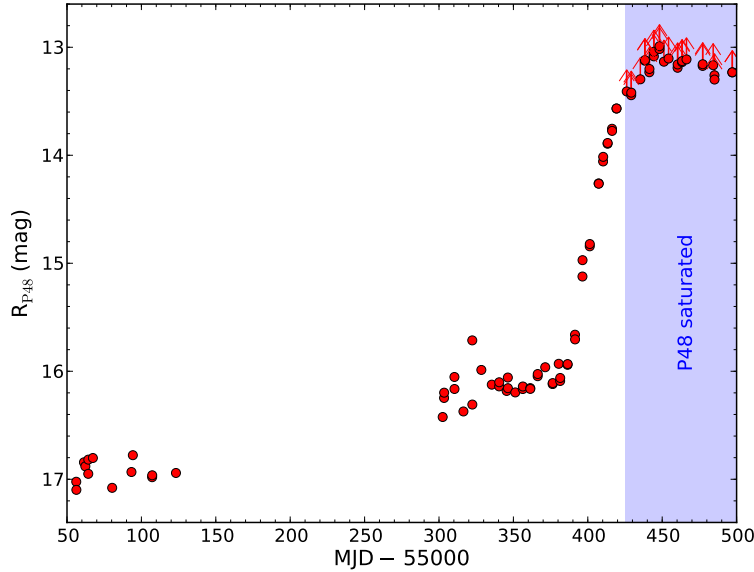


Figure 5.2: P48 light curve showing the outburst of LkH α 188-G4/PTF 10qpf. During the 2009 season PTF 10qpf was variable with typical $\Delta m \approx 0.2$ mag. The source dramatically increased the rate at which it was brightening around 2010 July 13 (day ~ 391 in the figure). P48 saturates on sources brighter than $m_{R_{\text{P}48}} \approx 13.5$ mag. The shaded region shows all data where PTF 10qpf is saturated; these data represent *lower* limits to the true brightness of PTF 10qpf during those epochs.

detections (Bloom et al. 2012). These initial classifications are made available to PTF collaboration members via the PTF Follow-up Marshal, which enables visual inspection of current and reference images, precursor PTF light curves, and any subsequent spectroscopy.

The source reported here was detected by the PTF pipeline and automatically assigned the name PTF 10qpf, following internal PTF naming conventions. Differential photometric measurements are made via aperture photometry, with the aperture size scaled to the seeing in each image, using SExtractor (Bertin & Arnouts 1996), and absolute calibration is relative to the USNO-B1 catalog (Monet et al. 2003) with an uncertainty of ~ 0.15 mag. CCD 3 on the P48 camera saturates at 55,000 counts, roughly corresponding to sources with $R \lesssim 13.5$ mag, given the standard 60 s exposure time. Thus, in all of our observations following those on 2010 Aug. 14, LkH α 188-G4 is saturated and our measurements represent a lower limit to the true brightness of the source. These limits are reflected in the full P48 light curve of LkH α 188-G4, shown in Figure 5.3.1, and the photometry is reported in Table 5.2. We do not include the systematic ~ 0.15 mag calibration uncertainty in this table because this uncertainty represents a constant offset that would be applied to all the data in the same way.

Table 5.2: P48 *R*-Band Photometry of LkH α 188-G4

date (MJD)	mag	σ_{mag}
55056.221	17.023	0.017
55056.295	17.098	0.019
55061.383	16.843	0.012
55062.327	16.880	0.020
55064.286	16.950	0.018
55064.331	16.818	0.021
55067.393	16.803	0.031
55080.361	17.079	0.036
55093.318	16.933	0.016
55094.252	16.777	0.018
55107.222	16.981	0.026
55107.266	16.963	0.025
55123.225	16.942	0.013
55302.479	16.424	0.010
55303.411	16.247	0.012
55303.459	16.198	0.014
55310.370	16.053	0.022
55310.413	16.164	0.010
55316.420	16.372	0.018
55322.359	15.714	0.017
55322.403	16.308	0.009
55328.453	15.988	0.011
55335.477	16.124	0.010
55340.429	16.140	0.008
55340.474	16.102	0.007
55345.470	16.182	0.016
55346.270	16.058	0.015
55346.314	16.157	0.017
55351.271	16.196	0.010
55356.309	16.165	0.013
55356.353	16.141	0.008
55361.311	16.156	0.009
55361.355	16.163	0.011
55366.318	16.046	0.012
55366.362	16.026	0.009
55371.384	15.963	0.011
55376.377	16.119	0.009
55376.420	16.110	0.012
55380.467	15.931	0.009
55381.405	16.090	0.009
55381.455	16.062	0.008
55386.397	15.940	0.007
55386.444	15.933	0.006
55391.400	15.662	0.013
55391.444	15.705	0.011
55396.411	15.123	0.007
55396.466	14.971	0.008
55401.304	14.843	0.012
55401.348	14.822	0.013
55407.294	14.261	0.013
55407.342	14.263	0.011
55410.295	14.057	0.007
55410.340	14.015	0.009

Table 5.2 (*cont'd*): P48 R-Band Photometry of LkH α 188-G4

date (MJD)	mag	σ_{mag}
55413.292	13.893	0.008
55413.336	13.886	0.006
55416.287	13.755	0.009
55416.330	13.774	0.013
55419.282	13.568	0.009
55419.326	13.567	0.011
55426.161	<13.409	...
55429.177	<13.444	...
55429.220	<13.420	...
55435.303	<13.297	...
55438.330	<13.124	...
55438.413	<13.119	...
55441.365	<13.231	...
55441.430	<13.201	...
55444.390	<13.084	...
55444.434	<13.041	...
55448.144	<13.017	...
55448.189	<12.990	...
55451.156	<13.134	...
55454.265	<13.104	...
55460.339	<13.190	...
55460.388	<13.159	...
55463.341	<13.137	...
55463.386	<13.128	...
55466.326	<13.112	...
55477.191	<13.173	...
55477.234	<13.157	...
55484.263	<13.166	...
55485.119	<13.260	...
55485.163	<13.299	...
55497.098	<13.233	...
55497.141	<13.232	...

The PTF also makes use of the robotic Palomar 60-in telescope (P60; [Cenko et al. 2006](#)) to obtain multi-filter photometry for source verification and classification purposes. PTF 10qpf was observed with the P60 on 2010 Oct. 14; Figure 5.3 presents a three-color image constructed from the P60 *riz* frames. Table 5.3 contains the individual photometric measurements. The absolute zero-point calibration was done relative to SDSS photometry ([Adelman-McCarthy et al. 2008](#)) based on other fields observed by the P60 during the same night with the same filter. The uncertainty in the zero point is computed as the standard deviation of the zero points in all other SDSS fields.

5.3.2 Near-Infrared Photometry

Near-infrared observations of PTF 10qpf were conducted with the 1.3 m Peters Automated Infrared Imaging Telescope (PAIRITEL; [Bloom et al. 2006](#)) on Mt. Hopkins, AZ, starting on 2010 Sep. 27. PAIRITEL is a roboticized system using the former 2MASS southern hemisphere survey camera that employs two dichroics to observe simultaneously in the *J*, *H*,

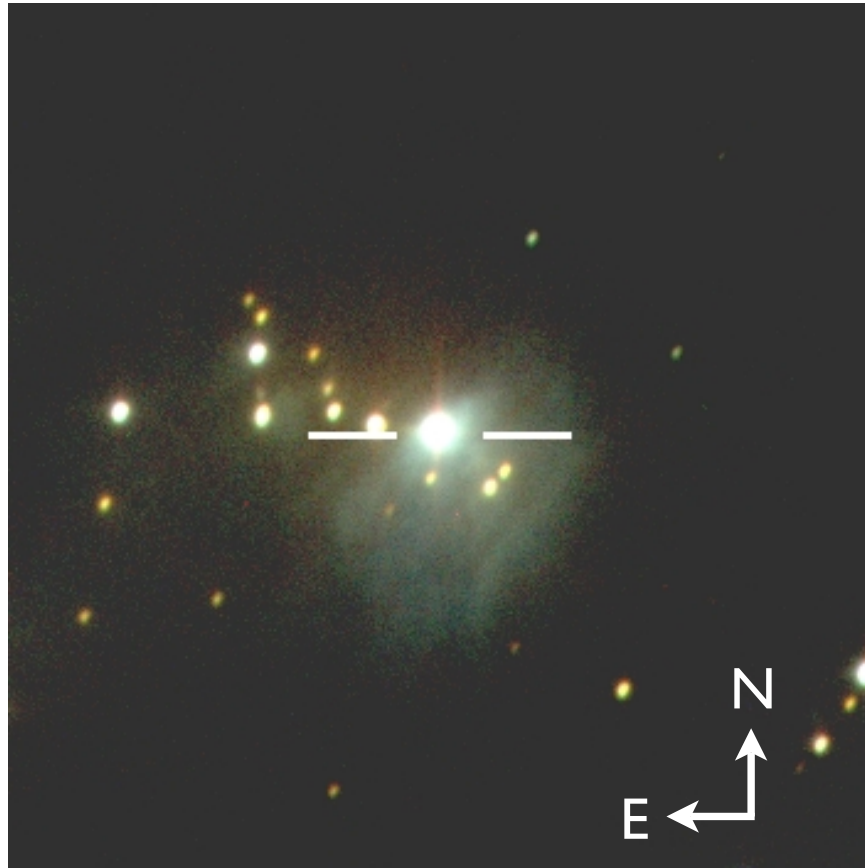


Figure 5.3: False-color *riz* image of PTF 10qpf during the 2010 eruption. The image is $2.2'$ on a side with north up and east to the left. PTF 10qpf is highlighted with crosshairs. Notice the bright reflection nebula to the southwest of PTF 10qpf; this nebula was not present prior to the 2010 eruption.

Table 5.3: P60 Observations of LkH α 188-G4

date (MJD)	filter	mag (AB)	σ_{mag}
55483.127	<i>r</i>	12.948	0.039
55483.127	<i>i</i>	12.207	0.027
55483.128	<i>z</i>	11.623	0.041

Table 5.4: PAIRITEL Observations of LkH α 188-G4

$t_{\text{mid}}^{\text{a}}$ (MJD)	J mag (Vega)	H mag (Vega)	K_s mag (Vega)
55466.137	10.04 ± 0.03	9.14 ± 0.03	8.65 ± 0.03
55468.145	9.99 ± 0.03	9.06 ± 0.04	8.64 ± 0.04
55469.148	10.04 ± 0.03	9.07 ± 0.03	8.70 ± 0.03
55479.109	10.11 ± 0.03	9.11 ± 0.03	8.63 ± 0.04
55504.164	10.20 ± 0.03	9.24 ± 0.03	8.74 ± 0.03
55513.195	10.29 ± 0.03	9.34 ± 0.03	8.79 ± 0.03
55518.168	10.32 ± 0.03	9.34 ± 0.04	8.84 ± 0.03
55527.117	10.35 ± 0.03	9.40 ± 0.03	8.89 ± 0.03
55531.145	10.40 ± 0.03	9.44 ± 0.03	8.97 ± 0.03
55543.066	10.45 ± 0.03	9.48 ± 0.04	9.06 ± 0.04

^aMidpoint between the first and last exposures in a single stacked image.

and K_s bands. Observations were scheduled and executed via a robotic system. PAIRITEL is operated in a fixed observing mode in which 7.8 s double-correlated “images” are created from the difference of a 7.851 s and a 51 ms integration taken in rapid succession (see [Blake et al. 2008](#)). The standard observing procedure involves taking three image pairs prior to dithering the telescope.

The raw data from these images are reduced using standard IR reduction methods via PAIRITEL PIPELINE III and the flux for all sources is measured via aperture photometry using SExtractor ([Bertin & Arnouts 1996](#)), calibrated against 2MASS. In the H and K_s bands, PTF 10qpf saturates the 7.851 s frames; however, PIPELINE III produces “short-frame” mosaics consisting of reduced, stacked 51 ms images (see also [Bloom et al. 2009](#)). The “short-frame” mosaics contain >10 bright 2MASS stars which we use to properly calibrate photometric measurements of PTF 10qpf in these images. PAIRITEL has a systematic uncertainty of ~ 0.02 – 0.03 mag in each of the J , H , and K_s bands (see [Blake et al. 2008](#); [Perley et al. 2010](#)), which, in the case of LkH α 188-G4, is larger than the statistical error in all three bands. Thus, we add a systematic error of 0.03 mag in quadrature with the statistical uncertainty to determine the total uncertainty in each band. PAIRITEL photometry is reported in Table 5.4, and a J , H , and K_s band false-color image of PTF 10qpf is shown in Figure 5.5.

5.3.3 Optical Spectroscopy

Lick Spectroscopy

Low-resolution spectra of PTF 10qpf were obtained on 2010 Sep. 16 and 2010 Nov. 2 with the Kast spectrograph on the Lick 3-m Shane telescope ([Miller & Stone 1993](#)). The spectra were reduced and calibrated using standard procedures (e.g., [Matheson et al. 2000](#)). For the Sep. 16 spectrum, flux calibration for the red arm of the Kast spectrograph was performed using a standard star observed at high airmass, whereas PTF 10qpf was observed at low

Table 5.5: Log of spectroscopic observations

UT Date	Telescope/ Instrument	Exposure (s)	λ (Å)
2010-09-16.24	Shane 3-m/Kast	600	3400–10300
2010-09-23.24	Hale 5-m/TripleSpec	720	9400–24,600
2010-09-25.30	Keck I 10-m/HIRES	560	3640–7990
2010-11-02.21	Shane 3-m/Kast	1200	3400–10300

airmass; thus, the absolute flux calibration is somewhat uncertain in the red portion of the optical spectrum. Furthermore, the noisy features near ~ 9300 Å are likely the result of an imperfect telluric correction and not astrophysical. Since conditions were not photometric on the night of Nov. 2, the absolute flux calibration is again somewhat uncertain. Nevertheless, on both nights we observed PTF 10qpf with the slit placed at the parallactic angle, so the relative spectral shapes should be accurate. The full low-resolution spectra of PTF 10qpf are shown in Figure 5.6, while all of our spectroscopic observations are logged in Table 5.5.

High-Resolution Spectroscopy

PTF 10qpf was observed on 2010 Sep. 25 with the Keck I telescope and HIRES spectrometer (Vogt et al. 1994) using the red cross-disperser and the standard settings of the California Planet Survey (Howard et al. 2010; Johnson et al. 2010). The C2 decker was employed, projecting to $0''.86$ on the sky and providing a resolution $R = \lambda/\Delta\lambda = 55,000$ at 5500 Å. We took advantage of the standard CPS reduction pipeline, which includes flat-fielding, scattered-light subtraction, order tracing, cosmic ray rejection, and spectrum extraction. After extraction, each order is sky-subtracted and summed in the cross-dispersion direction to form the final one-dimensional spectrum. The exposure time of 560 s resulted in a signal-to-noise ratio (S/N) of ~ 20 at 7400 Å.

Near-Infrared Spectroscopy

A NIR spectrum of PTF 10qpf was obtained with the TripleSpec spectrograph on the Palomar 5-m Hale telescope (Herter et al. 2008) on 2010 Sep. 23. TripleSpec has no moving parts and simultaneously acquires 5 cross-dispersed orders covering 1.0–2.4 μm at $R \approx 2700$.

The spectra were reduced with an IDL-based data reduction pipeline developed by P. Muirhead.³ To facilitate the subtraction of the sky and background emission of the total signal, the observations were obtained using an ABBA dither pattern along the slit. Each sky-subtracted exposure was then divided by a normalized flat-field, wavelength calibrated, and optimally extracted (Horne 1986). The spectra were flux-calibrated and corrected for telluric absorption using observations of an A0V star at a similar airmass with the IDL-based code `xteLLcor_general` by Vacca et al. (2003). The full TripleSpec spectrum is shown in Figure 5.11.

³<http://www.astro.cornell.edu/~muirhead/#Downloads>.

5.4 Analysis

5.4.1 Image Morphology and Photometric Analysis

The large-amplitude eruption (~ 4 mag) of LkH α 188-G4/PTF 10qpf qualitatively matches the defining characteristic of FU Orionis eruptions. Such an eruption, however, is not sufficient to prove that a YSO is in an FU Orionis-like state. PTF 10nvg, for example, brightened by ~ 6 mag over the course of a year, yet shows little resemblance to FU Ori-like stars (Covey et al. 2011). Spectroscopy over a broad wavelength range (see below) is required to conclusively classify a source as an FU Orionis-like star.

Over the course of our P48 observations, PTF 10qpf brightened by ~ 1 mag from early August 2009 to early August 2010, before suddenly brightening by ~ 3 mag over a ~ 2 month period (see Figure 5.3.1). Between the start of our observations on 2009 Aug. 13 and 2010 Jul. 9, the initial slow rising phase, PTF 10qpf rose by an average of ~ 0.003 mag d $^{-1}$, while between 2010 Jul. 9 and 2010 Aug. 11, during the rapid rising phase, PTF 10qpf rose by an average of ~ 0.07 mag d $^{-1}$.

After 2010 Aug. 11, PTF 10qpf is saturated in the P48 images and we cannot constrain the rate at which it is increasing; however, [Semkov & Peneva \(2010b\)](#) report that it reached peak brightness on 2010 Aug. 24 with $R = 12.79$ mag. Despite the rather rapid rise at the beginning of the PTF 10qpf optical outburst, the overall light curve is remarkably smooth. The P48 light curve for PTF 10qpf shows fluctuations at the ~ 0.2 mag level about both the pre-outburst slow rise and the sharp rise of the outburst. The long-term trend with low scatter observed prior to 2010 July is somewhat unusual for a standard CTTS, whose year-to-year variability is typically significantly smaller than the intra-year variability ([Grankin et al. 2007](#)). Indeed, the IPHAS photometry of LkH α 188-G4 captures variability that is more characteristic of CTTSs: variability at the ~ 0.3 mag level was observed over the course of 1 month in 2003, with a follow-up observation two years later falling within the same range of magnitudes as observed in 2003. This suggests that the slow rise LkH α 188-G4 demonstrated in 2009 was a prelude to the 2010 outburst, rather than simply standard CTTS variability.

A new reflection nebula, which was not present in 2009, can now clearly be seen around PTF 10qpf (Figure 5.4). Our regular observations over the course of the rise of PTF 10qpf allow us to constrain the appearance of the nebula, similar to the analysis of V1647 Ori/McNeil's Nebula by [Briceño et al. \(2004\)](#). In the P48 subtraction images produced as part of the PTF reduction pipeline, the residual is asymmetric about the point-source centroid on 2010 Aug. 2. The dust responsible for the reflection nebula is offset to the southwest of PTF 10qpf, and the asymmetry in the subtraction image is the result of this dust scattering light into our line of sight. We measure $R \approx 14$ mag for PTF 10qpf on 2010 Aug. 2. The nebula may be present as early as 2010 July 19, however: the faint nebula is difficult to distinguish from the wings of the central star's point-spread function. The optical reflection nebula (Figure 5.3) has an apparent size of $\sim 40''$, which at a distance of ~ 600 pc corresponds to $\sim 24,000$ AU.

In the NIR we have less information than in the optical. Our observations suggest a flat light curve in the J , H , and K_s bands starting on 2010 Sep. 27. Our NIR photometric

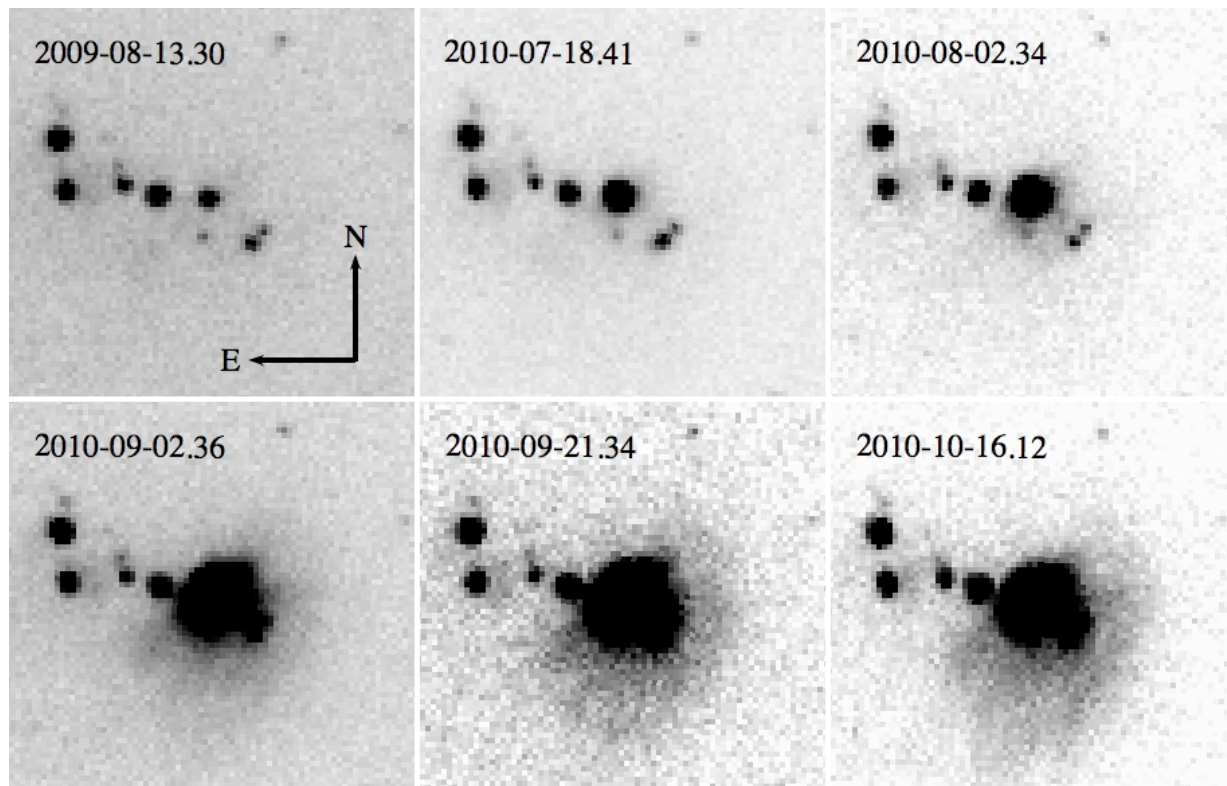


Figure 5.4: P48 *R*-band images of PTF 10qpf showing the emergence of the optical reflection nebula. Each image is centered on PTF 10qpf and is 75'' on a side. As with many other FU Orionis-like variables, the outburst of PTF 10qpf has created an asymmetric reflection nebula. Notice that PTF 10qpf is not located in the center of the reflection nebula which extends to the south west of the pre-outburst point source. All images are registered to the same frame with north up and east to the left. All dates are UT.

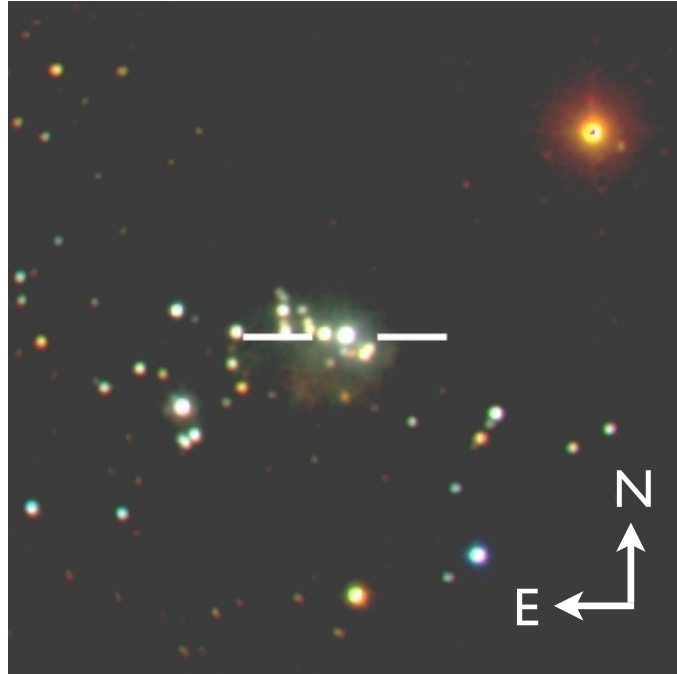


Figure 5.5: False-color JHK_s image of PTF 10qpf during the 2010 eruption. The NIR reflection nebula is less prominent than the optical nebula, but still visible to the southwest of PTF 10qpf. The image is 5' on a side with north up and east to the left. PTF 10qpf is highlighted with crosshairs.

measurements are consistent with those presented by [Leoni et al. \(2010\)](#), and we confirm that PTF 10qpf has brightened by 3.25, 3.07, and 2.81 mag in the J , H , and K_s bands, respectively, since 2MASS observations were obtained on 2000 Jun. 10. The NIR measurements presented by [Cohen & Kuhí \(1979\)](#) are \sim 1.1 mag brighter than those of 2MASS, which may be the result of a larger beam size for the [Cohen & Kuhí \(1979\)](#) measurements. FU Orionis stars are frequently associated with NIR reflection nebulae ([Connelley et al. 2007](#); [Connelley & Greene 2010](#)), and PTF 10qpf is no exception (see Figure 5.5). The NIR nebula is similar in size to the nebula seen in the optical.

The outburst SED is shown in Figure 5.2, and it clearly demonstrates that PTF 10qpf is bluer in the optical/NIR than it was prior to the 2010 outburst. We have limited spectral coverage during the outburst; in particular, we lack any information on how the emission has changed in the MIR. Direct integration of the optical/NIR outburst SED results in a lower limit to the luminosity of at least $4 L_\odot$. Assuming the same bolometric correction to the H band before and after the outburst results in an outburst luminosity of $L_{\text{outburst}} \approx 12 L_\odot$. This luminosity places PTF 10qpf at the bottom of the luminosity scale for FU Ori outbursts, and more than an order of magnitude fainter than FU Ori itself ([Hartmann & Kenyon 1996](#)).

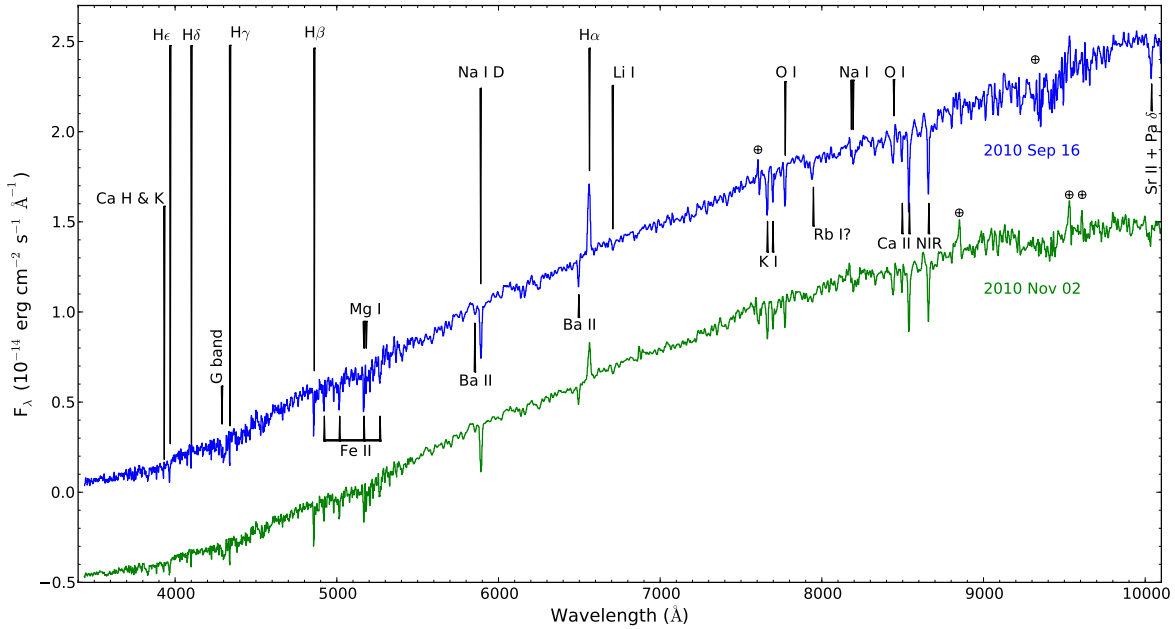


Figure 5.6: Low-resolution spectra of PTF 10qpf. Prominent absorption lines are marked. H α is the only line seen in emission, and it appears to have decreased in strength between our two spectra. Residuals left following an imperfect removal of telluric absorption have been marked with a \oplus , while the noisy features around ~ 9300 Å are also likely telluric (see text). The spectrum from 2010 Nov. 2 has been shifted down by 0.5 for clarity.

5.4.2 Spectroscopic Analysis

Optical spectra of FU Orionis variables share a few defining properties: a late F or G supergiant photosphere, an absorption-dominated spectrum with only H α typically seen in emission, and broad P-Cygni absorption with representative velocities of a few hundred km s $^{-1}$. Figure 5.6 shows that PTF 10qpf exhibits these general properties. Figure 5.8 illustrates our HIRES spectra covering three Balmer transitions. Each of these lines exhibits a strong P-Cygni absorption profile, with absorption minima around -40 km s $^{-1}$. H α is the only line having an emission component, and this emission moves the absorption minimum slightly blueward of the other Balmer lines. The absorption extends to $\lesssim -200$ km s $^{-1}$, suggesting in the classical interpretation that PTF 10qpf is driving a strong outflow (see also Figure 5.8).

In the discussion below, all velocities have been transformed to the local standard of rest (LSR). To our knowledge, a precise radial velocity measurement for LkH α 188-G4 has not been made. Therefore, we adopt a rest velocity of $V_{\text{LSR}} \approx 1.6$ km s $^{-1}$, consistent with ^{13}CO observations of the surrounding molecular gas (Dobashi et al. 1994).

Low-Resolution Optical Spectroscopy

At low resolution, PTF 10qpf exhibits little evolution between our two Kast spectra taken 40 d apart (see Figure 5.6). The strength of the absorption features remains constant to within the uncertainties, while the only major change is in the emission flux from H α . During this 40 d period the H α flux has decreased from $\sim 2.8 \times 10^{30}$ erg s $^{-1}$ to $\sim 1.5 \times 10^{30}$ erg s $^{-1}$. Observing at the parallactic angle allows us to accurately measure the change in the relative color during the 40 d gap between observations. Given the typical uncertainties associated with spectrophotometric measurements with the Kast spectrograph (Silverman et al. 2012), we find that PTF 10qpf does not show significant evidence for a change in color between our two observations.

To constrain the optical spectral type of PTF 10qpf, we use a least-squares minimization procedure to find the best match between the low-resolution Kast spectrum and the low-resolution stellar spectra provided in the Pickles Stellar Spectral Flux Library (Pickles 1998). The spectral type of FU Orionis variables is known to vary as a function of wavelength (Herbig 1977); thus, we divide the spectra into two sections, 4000–6000 Å and 6000–9000 Å. Below 4000 Å, the S/N is low in our Kast spectrum, while above ~ 9000 Å there is an uncertain telluric correction which may add artificial features. Next we redden each of the Pickles star spectra in increments of 0.05 mag from $E(B-V) = 0.00$ to 2.25 mag with $R_V = 3.1$. We mask the region around H α , since emission lines are not expected in normal stellar spectra. We then perform a least-squares fit of the reddened library spectra with our low-resolution spectrum of LkH α 188-G4, where the only free parameter is an overall normalization constant.

We illustrate the results of this procedure in Figure 5.7, where we include the low-resolution spectrum of PTF 10qpf along with the four best matches from our least-squares minimization. The stellar spectra are shown in the order of the quality of the fit, with the best fit on top and the fourth-best fit on the bottom. The adopted reddening has little physical meaning given that the observed flux is not emanating from a stellar photosphere having the standard single-temperature SED; this portion of the procedure merely serves as an automated process to vary the slope of the continuum, which is necessary given that PTF 10qpf has a heavily extinguished spectrum.

The Pickles library is incomplete — it does not include every luminosity class for every spectral type. For this reason we emphasize that our procedure is only illustrative; it does not provide a definitive spectral type for PTF 10qpf in either the blue or red portion of the optical spectrum. Nevertheless, a few trends are readily apparent from Figure 5.7. In the blue portion of the optical, PTF 10qpf most closely resembles the spectra of G supergiants and G giants. In the red portion of the optical, the spectrum resembles that of G and K stars, with no real hint regarding the luminosity class. The adopted values of the reddening are significantly different between the blue and the red, but again we remind the reader that this reddening is only a device with which to match the intrinsic shape of the continuum. Typically, the Mg I $\lambda 5172$ triplet is used to determine the luminosity class of G-type stars, but our high-resolution spectra show that these lines are tracing an outflow (see Figure 5.8) and thus they are unsuitable for providing a luminosity class. Despite this, the procedure

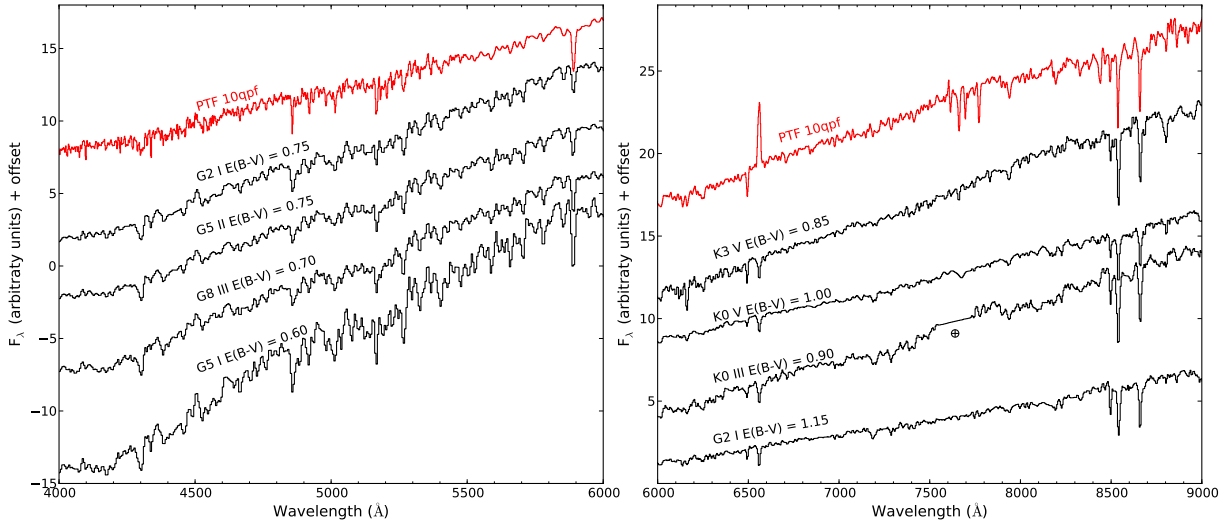


Figure 5.7: Low-resolution optical spectra of PTF 10qpf compared to stellar spectra from the Pickles library (Pickles 1998). The comparison spectra are selected as the best matches to PTF 10qpf following a least-squares minimization procedure (see text). The comparison spectra are shown in order of the goodness of fit, with the best match on top. The reddening values were used as a proxy for removing the overall continuum shape.

does demonstrate that PTF 10qpf is similar to G giants/supergiants in the blue portion of the optical, consistent with observations of other FU Orionis variables (Hartmann & Kenyon 1996). Additionally, as we will show below, the spectrum shifts to later types (K stars in this case) with increasing wavelength, as is also observed in FU Orionis variables (Herbig 1977).

High-Resolution Optical Spectra

The HIRES spectrum of PTF 10qpf is dominated by broadened stellar-like absorption features. The spectral lines are consistent with those of a comparison G2 I star and inconsistent with spectral types later than early K. We note, however, that the diagnostics of G vs. K types are subtle and would become blurred with the large broadening of the PTF 10qpf lines. The line broadening is similar to, but perhaps slightly less than, the 60–100 km s⁻¹ broadening of V1057 Cyg, and significantly more than the 30–40 km s⁻¹ of V1515 Cyg in which some hints of a K-type spectrum can be seen at redder optical wavelengths. A detailed comparison of PTF 10qpf to these two canonical FU Ori objects reveals that the spectrum of PTF 10qpf is similar to both in terms of the relative strength of the common absorption features. However, we note that each object has unique and notable spectroscopic attributes.

Several lines have clear kinematic signatures of winds, specifically Ca II H & K, Fe II $\lambda\lambda$ 5018, the Mg I $\lambda\lambda$ 5167, 5172, 5183 triplet, the Na I D lines, H α , H γ , H δ (H β falls in a gap between the orders in our HIRES setting), and the K I λ 7699 line (its doublet partner at 7665 Å also falls in a gap between orders). The morphology of these lines is illustrated

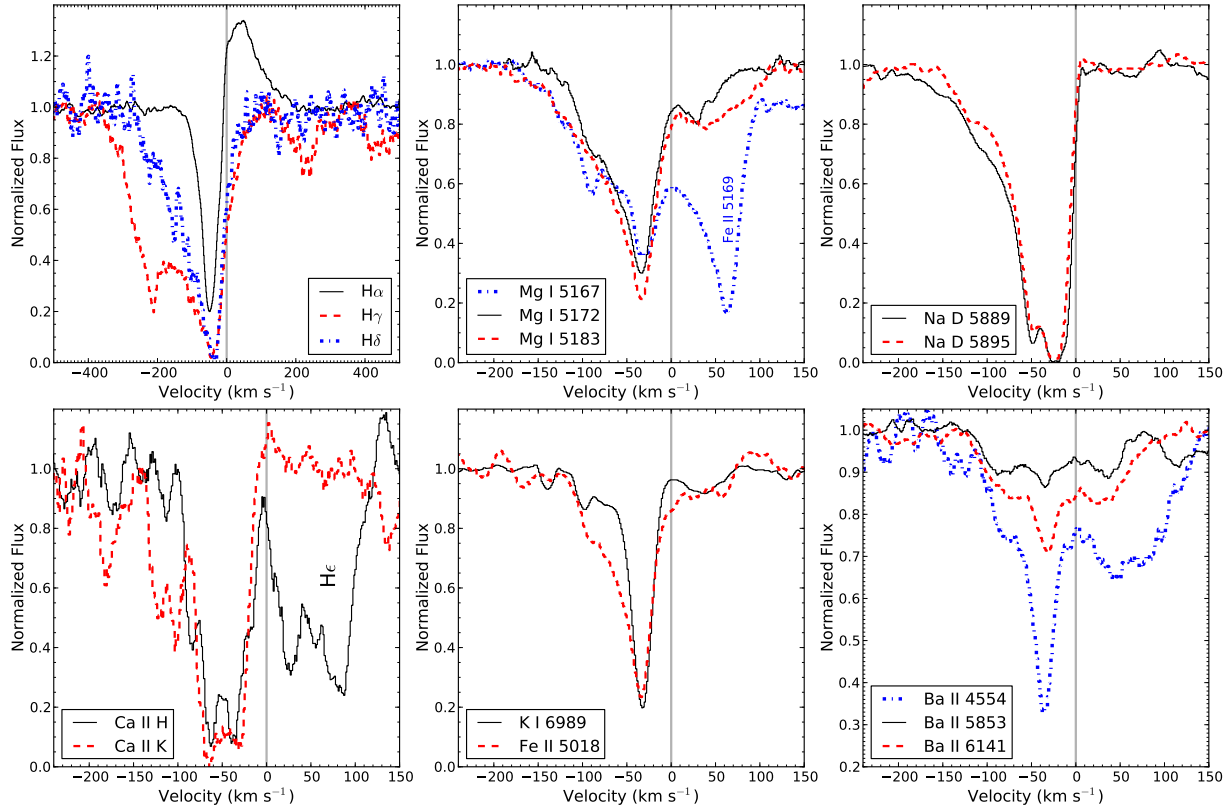


Figure 5.8: Keck HIRES high-resolution profiles of several prominent features showing strong blueshifted absorption, indicative of outflowing material. *Top left:* The Balmer series for PTF 10qpf. H β fell in a gap between echelle orders for our observing setup, and thus is not displayed. PTF 10qpf exhibits strong P-Cygni absorption in the other Balmer lines with outflow speeds of \sim 100–300 km s $^{-1}$. *Top center:* Profiles of the Mg I triplet at 5167, 5172, and 5183 Å. The lines show strong asymmetries, tracing the kinematics of the wind from PTF 10qpf. Fe II λ 5169 is present at about +60 km s $^{-1}$ relative to Mg I λ 5167. *Top right:* Absorption profiles of the Na I D doublet showing similar kinematics as the Mg I lines. *Bottom left:* Absorption profiles of Ca II H & K. He ϵ is also present, offset from Ca H by \sim 100 km s $^{-1}$. *Bottom center:* Absorption profiles of Fe II λ 5018 and K I λ 6989. *Bottom right:* Absorption profiles of Ba II $\lambda\lambda$ 4554, 5853, and 6141. These lines show narrow absorption, FWHM \approx 20 km s $^{-1}$, superposed on broader, shallower profiles extending $\pm \sim$ 60 km s $^{-1}$ from the line center. For clarity, all spectra have been smoothed with a Savitzky-Golay filter, which is similar to a running mean (Savitzky & Golay 1964). Velocities are given relative to the LSR, and the vertical grey line indicates the rest velocity of PTF 10qpf, $V_{\text{LSR}} \approx 1.6$ km s $^{-1}$ (see text).

in Figure 5.8. Notably, the blueshifted absorption troughs are narrower in our early-stage spectrum of PTF 10qpf than exhibited in modern spectra of V1515 Cyg and V1057 Cyg, by at least a factor of two. Although LkH α 188-G4 exhibited [O I] λ 6300 emission in the Cohen & Kuhi (1979) spectrum, it is not apparent post-outburst, even at high spectral resolution, nor do we see other forbidden species in emission (such as [N II] and [S II]) typically associated with outflows in YSOs.

The other line worth noting in PTF 10qpf for its kinematic signatures is Li I λ 6707. Figure 5.9 shows the spectral region containing this line, in comparison to V1515 Cyg and V1057 Cyg as well the G2 I standard. The Li I absorption profile has multiple components including a narrow slightly blueshifted component arising from low-velocity gas and a broader absorption extending to $\pm 60 \text{ km s}^{-1}$ that is reminiscent of the flat-bottomed profiles seen in other metallic lines in the same spectral region. A similar absorption profile is also seen in Ba II (Figure 5.8).

Figure 5.10 illustrates the flat-bottomed nature of many absorption lines in PTF 10qpf. The profiles are reminiscent of those illustrated by Petrov & Herbig (2008) for FU Ori. When the flat-bottomed lines in PTF 10qpf are cross-correlated against a normal G2 I stellar template, the resulting cross-correlation function is broad ($\sim 120 \text{ km s}^{-1}$) with several different peaks. In some spectral regions a central peak can be fit by a Gaussian of width 30 km s^{-1} , and there are two secondary peaks near the full width of the correlation function, each having Gaussian width $\sim 20 \text{ km s}^{-1}$. In other spectral regions, both blue and red, the correlation function has no central peak, but only the double peaks near the limb. To measure the goodness of the cross correlation we adopt the Tonry-Davis R value (Tonry & Davis 1979), which is a ratio of the power in the cross-correlation peak to a measure of the antisymmetry in the correlation. Large R values indicate good cross correlations. Using a G2 supergiant as a template, the Tonry-Davis R value for PTF 10qpf is 4–6 (compared to $R > 5$ to 15 for V1057 Cyg, which shows broadening and flat-bottomed structure similar to PTF 10qpf in some lines, and $R > 20$ for V1515 Cyg, which does not). The cross-correlation results are similar when using V1515 Cyg as a template, rather than the G2 I standard. Employing V1057 Cyg as a template results in a broad and centrally peaked cross-correlation function having width 120–130 km s^{-1} .

Near-Infrared Spectroscopy

NIR spectra of FU Orionis variables resemble the spectra of K and M giants/supergiants, in contrast to their earlier spectral type in the optical (Hartmann & Kenyon 1996). The most prominent features in the NIR spectra of FU Orionis stars are the strong absorption bands from CO at $2.3 \mu\text{m}$ and the H₂O vibration-rotation bands at $1.38 \mu\text{m}$ and $1.87 \mu\text{m}$. These absorption bands are clearly present in the outburst spectrum of PTF 10qpf; see Figure 5.11, which compares spectra from Rayner et al. (2009) of two supergiants (K5 Ib and M5 Ib-II) and a dwarf (M0 V) with PTF 10qpf. There are many prominent absorption features seen in the M0 V spectrum, which are muted or absent in PTF 10qpf and the two supergiant spectra. This is indicative of a low surface gravity environment for PTF 10qpf.

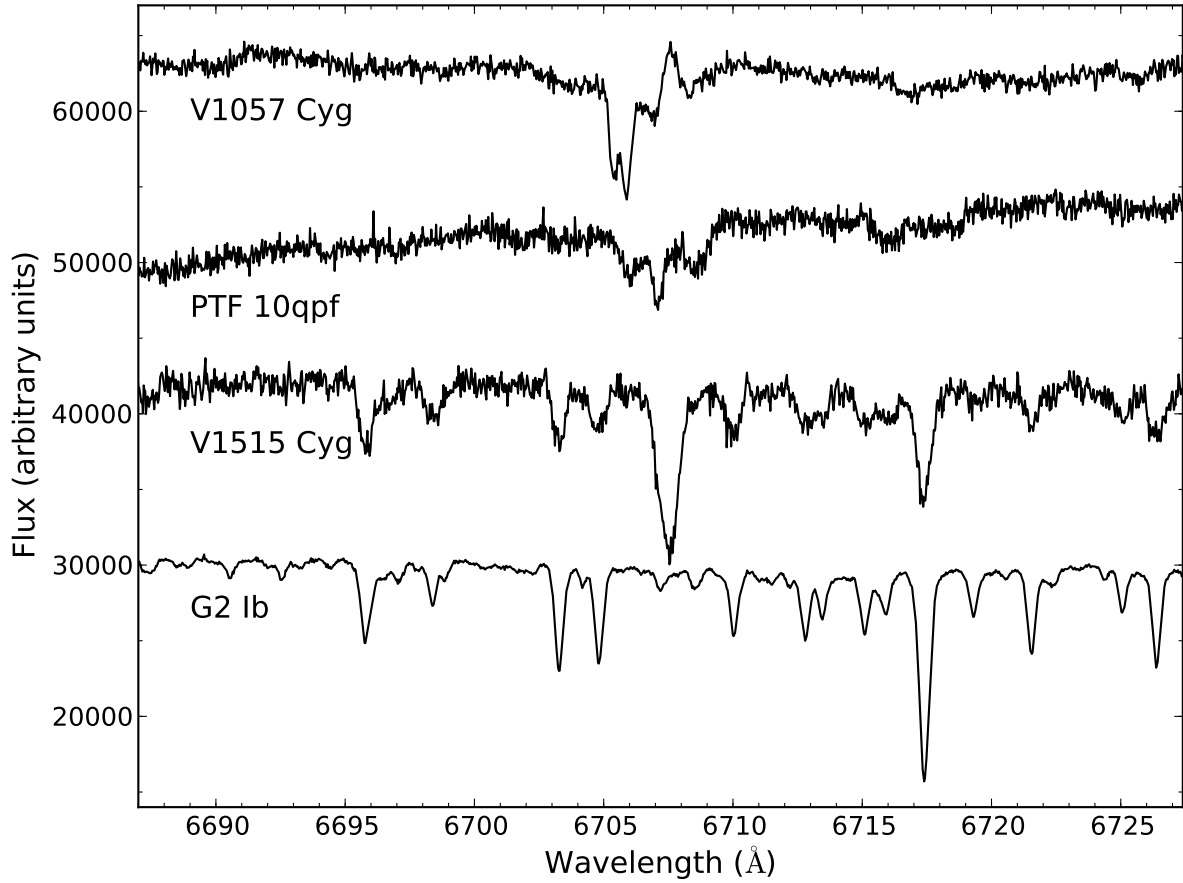


Figure 5.9: Keck HIRES high-resolution spectra of the Li I λ 6706 and Ca I λ 6717 region of PTF 10qpf. For comparison we also show high-resolution spectra of V1057 Cyg, V1515 Cyg, and a G2 Ib spectral standard, all from our unpublished spectral database. In particular, notice the strong Li absorption present in PTF 10qpf and the two canonical FU Orionis objects. The Li line in both V1057 Cyg and PTF 10qpf traces an unusual kinematic structure, possibly similar to that seen in Ba II (see Figure 5.8.)

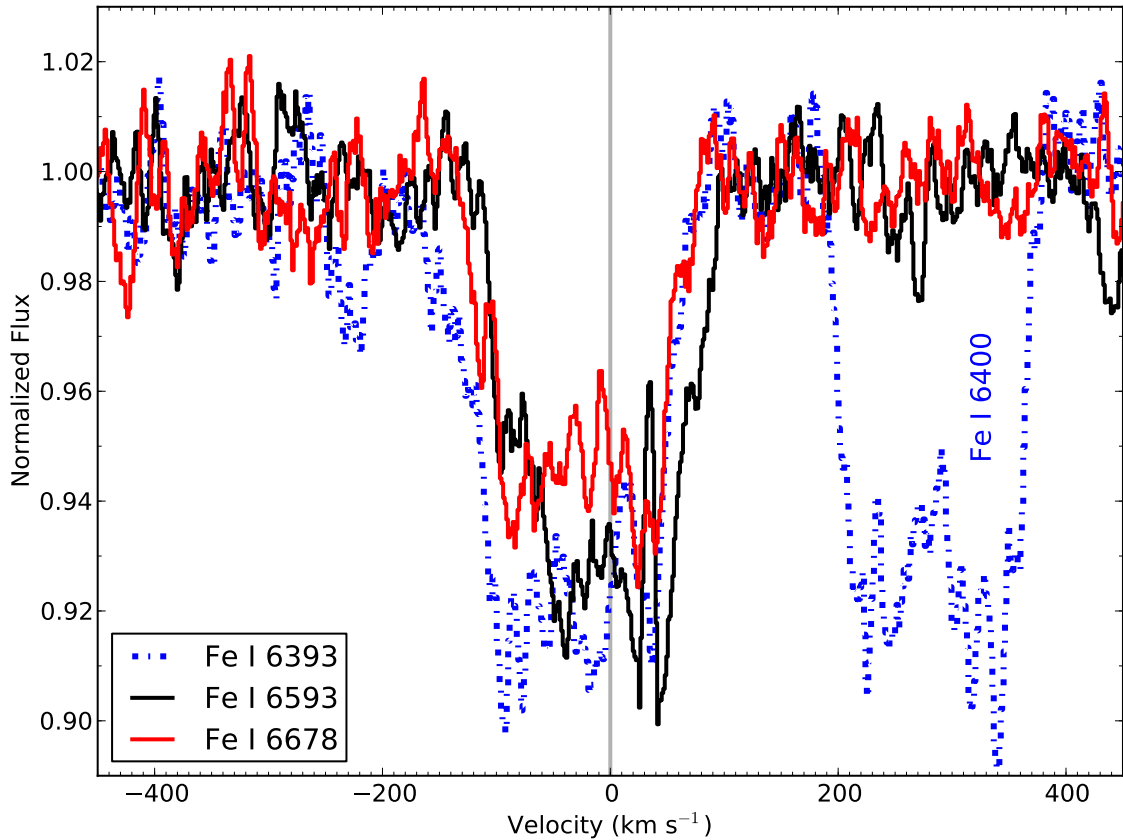


Figure 5.10: Several Fe I line profiles illustrating the flat-bottomed nature typical of the other metallic lines. The Fe I transitions at $\lambda\lambda 6393$, 6593 , and 6678 have been shifted to the same velocity, while Fe I $\lambda 6400$ is offset by $\sim 300 \text{ km s}^{-1}$ relative to $\lambda 6393$. These lines all exhibit a profile with a “flat” bottom similar to those observed in FU Orionis (Petrov & Herbig 2008). For clarity, spectra have been smoothed with a Savitzky-Golay filter, which is similar to a running mean. The vertical grey line is the same as in Figure 5.8.

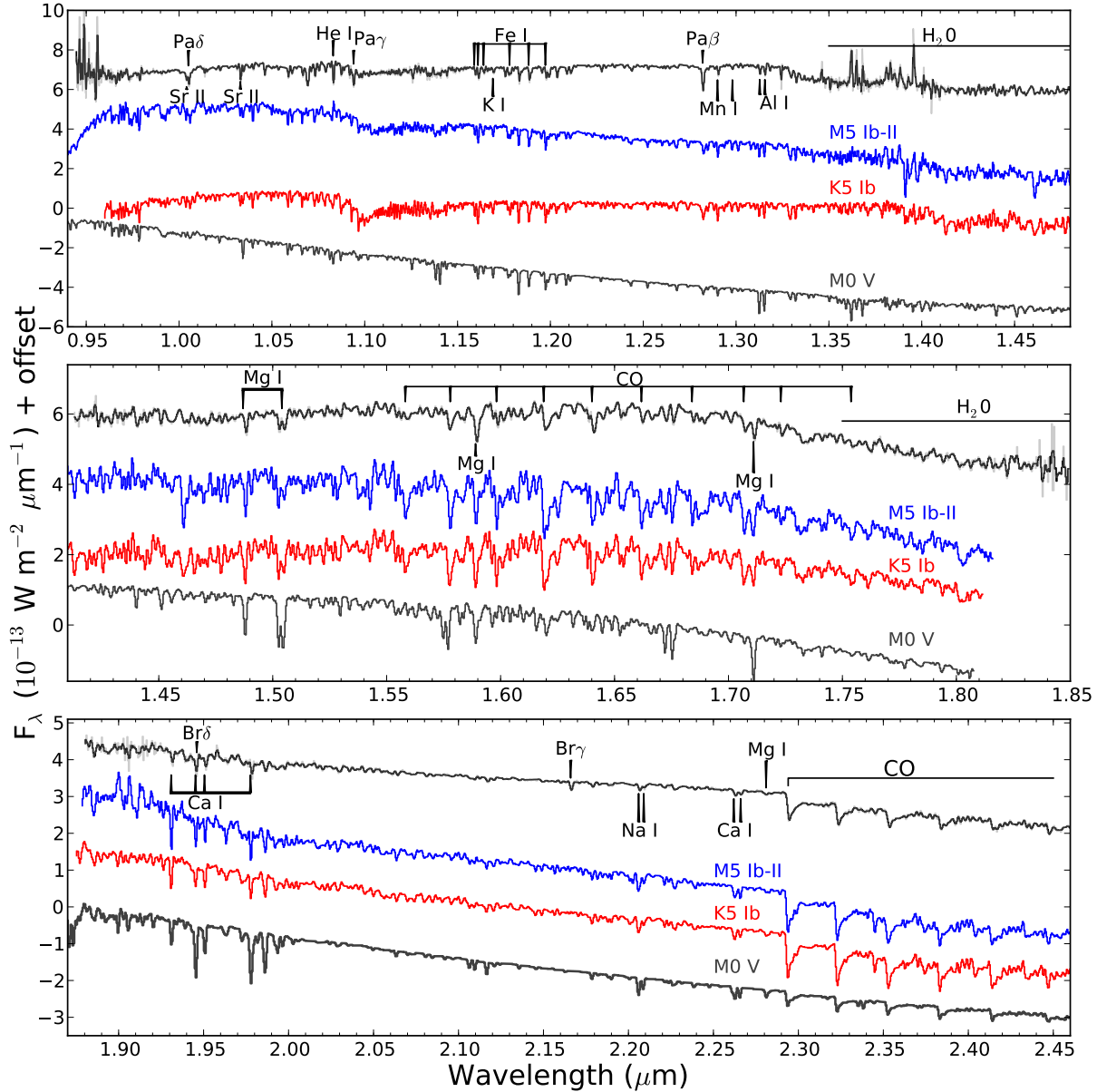


Figure 5.11: TripleSpec NIR spectrum of PTF 10qpf showing from top to bottom the YJ , H , and K -band spectra. Prominent absorption features in the outburst spectrum are identified, while the spectrum shows no clear emission lines. For comparison the spectra of M5 Ib-II and K5 Ib supergiants, and an M0 V dwarf (from Rayner et al. 2009), are also shown. The muted features of PTF 10qpf relative to the M0 V star shows that the NIR emission is from a low surface gravity environment. PTF 10qpf exhibits strong $2.3 \mu\text{m}$ CO absorption and ~ 1.4 and $1.9 \mu\text{m}$ H₂O absorption, similar to other FU Orionis-like sources.

We have attempted to derive a crude NIR spectral type for PTF 10qpf. In addition to its anomalously strong CO features, PTF 10qpf also possesses prominent H₂O absorption in the *H* and *K* bands; the relative strengths of the *H* and *K*-band absorptions are unusual, with PTF 10qpf separated from both the dwarf and giant loci for those features (see, e.g., Figure 4 of Covey et al. 2010). We therefore attempted to characterize the NIR spectral type of PTF 10qpf based on the strengths of several *H*-band absorption features: Mg I (1.51 μm), K I (1.518 μm), Al I (1.67 μm), and a blend at 1.70 μm . We compared the strengths of these features to those measured for a suite of dwarf and giant templates by Covey et al. (2010). While this method is sufficient to derive only a crude NIR spectral type for PTF 10qpf, we find that the source’s outburst spectrum most closely resembles that of K7 III—M2 III giants (see Figure 5.11 for some comparisons). It is important to note that the classification scheme from Covey et al. (2010) does not include supergiants; thus, we conclude that PTF 10qpf has a low surface gravity, but we cannot discriminate among luminosity classes I–III.

While the strength of molecular water absorption is greater than that normally observed in giants, this finding is consistent with observations of other FU Orionis stars. Sato et al. (1992) argue that the unusually strong H₂O absorption seen in FU Orionis stars can be explained if water that has condensed onto dust grains in the midplane of the disk becomes vaporized during the heating of the disk associated with an FU Orionis eruption. Once this evaporated water is flung vertically out of the disk midplane, it will imprint a strong absorption signature in the NIR spectrum.

Connelley & Greene (2010) show that the equivalent width (EW) of CO absorption at 2.3 μm can be used to identify FU Orionis-like stars when compared to the EW of Na (2.206 and 2.209 μm) and Ca (2.263 and 2.266 μm). To compare PTF 10qpf to the stars studied by Connelley & Greene (2010), we measure the EW of Na, Ca, and CO following the prescription of Chalabaev & Maillard (1983) with the correction provided by Vollmann & Eversberg (2006). We measure Na and Ca EWs of 1.56 ± 0.05 and 1.07 ± 0.06 Å, respectively, while the EW of CO is 35.6 ± 0.3 Å. These uncertainties reflect the statistical errors in our measurements, and likely underestimate the systematic effects associated with these measurements (e.g., the precise placement of the continuum). Nevertheless, the systematic uncertainties are not large enough to alter the general conclusions drawn below. The CO absorption is well in excess of what would be expected for both late-type dwarfs and giants based on the strength of the Na and Ca absorption; however, this excess CO absorption is consistent with other FU Orionis-like stars in the sample of Connelley & Greene (see their Figure 4).

Prominent H and He I $\lambda 10830$ absorption lines are also visible in the NIR spectra (see Figure 5.11). However, H and He absorption cannot originate in a simple, single-temperature, cool (late K–M) atmosphere. Thus, these lines, though unresolved in our spectra, likely trace an outflow, similar to the Balmer series in the optical. He I $\lambda 10830$ may be a hot-wind indicator, but high-resolution spectra are needed to confirm this (Edwards et al. 2006; Kwan et al. 2007).

5.5 Discussion and Conclusions

We have shown that the 2010 eruption of LkH α 188-G4 places it within the small family of FU Orionis-like stars having observed outbursts. LkH α 188-G4/PTF 10qpf exhibits the defining observable characteristics of the FU Orionis class as described by [Hartmann & Kenyon \(1996\)](#):

- it exhibited a $\gtrsim 4$ mag increase in its optical light curve;
- it is associated with a star-forming region and shows a bright reflection nebula following its eruption;
- optical spectra of the outburst are consistent with a G-type giant/supergiant;
- during outburst, the Balmer lines exhibit strong P-Cygni profiles, with only H α showing an emission component, and absorption extending to about -200 km s^{-1} ; and
- the NIR spectra during the eruption resemble those of M-type giants/supergiants, with strong absorption seen in the H₂O and CO bands.

In sharp contrast to the class of YSO outbursts referred to as EX Lupi-like or V1647 Ori-like, PTF 10qpf does not exhibit strong optical/NIR emission lines during outburst.

In the IR, unlike typical M and K-type supergiants, PTF 10qpf shows prominent absorption lines of H I (Br γ , Pa β , Pa γ , Pa δ) and He I 1.083 μm . In the optical the H I lines trace an outflow, with clear P-Cygni absorption profiles observed in our HIRES spectrum. Our spectral resolution is insufficient to determine whether a similar P-Cygni profile is observed in the NIR; however, H and He absorption cannot originate in an M-giant/supergiant photosphere. Thus, the H and He lines are likely the result of inner-disk region accretion/wind physics.

LkH α 188-G4 stands out among the currently known group of FU Orionis-like stars in that there are pre-outburst observations with detections from the optical to the MIR, making LkH α 188-G4 the first FU Orionis-like star with a well-sampled SED prior to eruption. This SED shows that LkH α 188-G4 was a Class II YSO, which are commonly associated with CTTSs ([Lada 1987](#)). A pre-outburst optical spectrum reveals a late-type star, K7–M0, with prominent H α and H β seen in emission, again consistent with a CTTS. Multiple epochs of optical imaging prior to the outburst reveal that LkH α 188-G4 exhibited stochastic variability at a level consistent with a CTTS.

One of the most important elements in the study of PTF 10qpf/LkH α 188-G4 is that it is associated with a known, optically revealed and previously studied YSO. The clear identification of LkH α 188-G4 as a CTTS prior to eruption solidifies the interpretation of FU Ori events as enhanced accretion and outflow likely associated with disk-accretion instabilities ([Hartmann & Kenyon 1996](#)). This outburst's association with a previously classified CTTS source shows that FU Ori eruptions are not strictly limited to the most highly embedded Class 0/I phases of pre-main sequence evolution. Indeed, the strong winds associated with these events may play an important role in disrupting a YSO's circumstellar envelope. Such a disruption is thought to be a key component of the Class I/II transition.

Continued photometric and spectroscopic monitoring of PTF 10qpf/LkH α 188-G4 will fully elucidate its nature. As more and more synoptic surveys come online, the rich legacy of IR observations made by several ground- and space-based observatories (e.g., 2MASS, *IRAS*, *MSX*, *Spitzer*, *AKARI*, *WISE*) over the past two decades will enable the discovery of additional FU Orionis outbursts with well characterized pre-outburst SEDs. These discoveries will in turn allow us to determine if the case of LkH α 188-G4 is an outlier or the norm. A better understanding of whether FU Orionis-like eruptions typically occur during the Class I or Class II phase of pre-main sequence evolution will allow us to place stronger constraints on the triggering mechanism and occurrence rates for these events.

Acknowledgments

A version of this chapter appears in the *Astrophysical Journal*, 2011, 730, 80.

During the writing of this chapter I was supported by a National Science Foundation Graduate Research Fellowship, for which I am grateful for the funding.

I thank L. Rebull for providing the *Spitzer*/MIPS data for LkH α 188-G4 in advance of her publication. I am in debt to J. Johnson, J. S. Pineda, and M. Bottom who obtained the HIRES spectrum of PTF 10qpf. I thank Cullen Blake, Dan Starr, and Emilo Falco for their efforts to build and maintain PAIRITEL. I would like to thank Meredith Hughes for a fruitful discussion concerning YSO accretion disks and Ryan Foley for information on the spectrophotometric uncertainty associated with Kast spectra. An anonymous referee provided comments on the ApJ manuscript that have helped improve this chapter.

Chapter 6

Discovery of Bright Galactic R Coronae Borealis and DY Persei Variables: Rare Gems Mined from ACVS

We present the results of a machine-learning (ML) based search for new R Coronae Borealis (RCB) stars and DY Persei-like stars (DYPers) in the Galaxy using cataloged light curves from the All-Sky Automated Survey (ASAS) Catalog of Variable Stars (ACVS). RCB stars—a rare class of hydrogen-deficient carbon-rich supergiants—are of great interest owing to the insights they can provide on the late stages of stellar evolution. DYPers are possibly the low-temperature, low-luminosity analogs to the RCB phenomenon, though additional examples are needed to fully establish this connection. While RCB stars and DYPers are traditionally identified by epochs of extreme dimming that occur without regularity, the ML search framework more fully captures the richness and diversity of their photometric behavior. We demonstrate that our ML method can use newly discovered RCB stars to identify additional candidates within the same dataset. Our search yields 15 candidates that we consider likely RCB stars/DYPers: new spectroscopic observations confirm that four of these candidates are RCB stars and four are DYPers. Our discovery of four new DYPers increases the number of known Galactic DYPers from two to six; noteworthy is that one of the new DYPers has a measured parallax and is $m \approx 7$ mag, making it the brightest known DYPer to date. Future observations of these new DYPers should prove instrumental in establishing the RCB connection. We consider these results, derived from a machine-learned probabilistic classification catalog, as an important proof-of-concept for the efficient discovery of rare sources with time-domain surveys.

6.1 Introduction

R Coronae Borealis (RCB) stars are hydrogen-deficient carbon stars that exhibit spectacular (Δm_V up to ~ 8 mag), aperiodic declines in brightness (for a review on RCB stars see [Clayton 1996](#)). The fading occurs rapidly (\sim one–few weeks) as new dust is formed in the circumstellar environment, and the recovery is slow, sometimes taking several years, as the new dust is dispersed and removed from the line of sight. At maximum light RCB stars are bright supergiants, which in combination with the large-amplitude photometric variability should make them easy to discover. Yet, to date there are only ~ 56 known RCB stars in the Galaxy ([Clayton 1996](#); [Clayton et al. 2002](#); [Zaniewski et al. 2005](#); [Tisserand et al. 2008](#); [Clayton et al. 2009](#); [Kijbunchoo et al. 2011](#)). The rarity of these stars suggests that they reflect a very brief phase of stellar evolution, or a bias in RCB star search methods, or both.

The lack of hydrogen and overabundance of carbon in RCB atmospheres implies that RCB stars are in a late stage of stellar evolution, but no consensus has yet emerged regarding their true physical nature. There are two leading theories for explaining the observed properties of RCB stars: the Double Degenerate (DD) scenario and the final Helium shell flash (FF) scenario (see e.g., [Iben et al. 1996](#)). The double degenerate (DD) scenario posits that RCB stars are the stellar remnant of a carbon-oxygen white dwarf (WD) and helium WD merger. In the FF scenario, a thin layer of He in the interior of the star begins runaway burning, which leads to the rapid expansion of the photosphere shortly before the star becomes a planetary nebula. There are observational properties of RCB stars that both theories have difficulty explaining ([Clayton 1996](#)), and conflicting observational evidence supporting aspects of both (e.g., [Clayton et al. 2007](#); [Pandey et al. 2008](#); [Clayton et al. 2006, 2011](#)). If, as some of the recent observations suggest, the DD scenario proves correct, then a complete census of Galactic RCB stars should be able to calibrate population synthesis models of WD binary systems (e.g., [Nelemans et al. 2001](#)), which may improve our understanding of these systems as the progenitors of Type Ia supernovae. In any event, the enigmatic nature of these rare objects, and the opportunity to elucidate the astrophysics of an important late stage of stellar evolution, motivate us to search for additional benchmark exemplars of the class.

Based on the detection of RCB stars in the Large Magellanic Cloud (LMC), it is argued in [Alcock et al. \(2001\)](#) that there should be ~ 3200 RCB stars in the Galaxy. With the actual number of known RCB stars in the Milky Way roughly two orders of magnitude below this estimate, this suggests that either thousands of RCB stars remain undetected or the differing star formation environments/histories in the LMC and the Milky Way result in highly different RCB populations. An observational bias that preferentially selects warm RCB stars likely contributes to the discrepancy between the predicted and known number of these stars in the Galaxy ([Lawson et al. 1990](#)). Indeed, recent discoveries of RCB stars in the Galactic bulge and Magellanic Clouds (MCs) have uncovered more cool, $T_{\text{eff}} \sim 5000$ K, rather than warm, $T_{\text{eff}} \sim 7000$ K, RCB stars ([Alcock et al. 2001](#); [Zaniewski et al. 2005](#); [Tisserand et al. 2008, 2009](#)). The observed correlation between color and M_V , with bluer RCB stars in the Magellanic Clouds (MCs) being more luminous ([Alcock et al. 2001](#); [Tisserand et al. 2009](#)), clearly shows that any magnitude-limited survey will have an observational bias towards

discovering the intrinsically rarer warm RCB stars.

There may also be a large population of RCB stars that have colder photospheres than the cool RCB stars: there is one known Galactic RCB star, DY Persei (Alksnis 1994), that has $T_{\text{eff}} \sim 3500$ K (Keenan & Barnbaum 1997). Recent observations of the MCs have identified several DY Persei-like stars (DYPers) while searching for RCB stars (Alcock et al. 2001; Tisserand et al. 2009; Soszyński et al. 2009), while Tisserand et al. (2008) discovered the second known DYPer in the Milky Way using observations of the Galactic bulge. In addition to cooler photospheres, DYPers have other properties that differ from RCB stars, which has led to some degree of ambiguity regarding the connection between these two classes (see e.g., Alcock et al. 2001; Tisserand et al. 2009; Soszyński et al. 2009).

DYPers and RCB stars both show an overabundance of carbon in their atmospheres and unpredictable, large-amplitude declines in their light curves. Several properties differ between the two, however, for instance, DYPers: (i) have symmetric declines in their light curves, (ii) clearly show ^{13}C in their spectra, (iii) are on average ~ 10 times fainter than RCB stars, and (iv) may have significant H in their atmospheres. A detailed examination of the differences in the mid-infrared excesses of RCB stars and DYPers in the MCs led to the conclusion in Tisserand et al. (2009) that DYPers are most likely normal carbon stars that experience ejection events rather than an extension of the RCB phenomenon to lower temperature stars. Furthermore, using OGLE-III observations, it is shown in Soszyński et al. (2009) that several carbon-rich asymptotic giant branch stars (AGBs), which have been classified as Mira or semi-regular periodic variables on the basis of their light curves, show evidence for DYPer-like declines in their light curves.¹ This leads to the conclusion in Soszyński et al. that DYPers are heavily enshrouded carbon-rich AGB stars that are an extension of typical variables rather than a separate class of variable stars. Nevertheless, all studies of DYPers to date have cited a need for more observations, in particular high resolution spectra to conduct detailed abundance analyses, to confirm or deny the possibility that DYPers are the low temperature analogs to RCB stars.

Over the past decade the decrease in the cost of large CCDs, coupled with a dramatic increase in computer processing power and storage capabilities, has enabled several wide-field, time-domain surveys. These surveys will continue to produce larger datasets before culminating near the end of the decade with the Large Synoptic Survey Telescope (LSST; Ivezić et al. 2008a). This explosion of observations should enable the discovery of the thousands of “missing” Galactic RCB stars, should they in fact exist. These new discoveries do not come without a cost, however, as the data rates of astronomical surveys are now becoming enormous. While it was once feasible for humans to visually examine the light curves of all the newly discovered variable stars, as the total number of photometric variables grows to 10^6 – 10^7 visual inspection by expert astronomers becomes intractable.

Advanced software solutions, such as machine-learning (ML) algorithms, are required to analyze the vast amounts of data produced by current and upcoming time-domain surveys.

¹We note that the sources included in the study of Soszyński et al. (2009) are photometrically classified as carbon AGB. Thus, the candidates in that study require spectroscopic observations in order to be confirmed as DYPers.

In an ML approach to classification, data from sources of known science class are employed to train statistical algorithms to automatically learn the distinguishing characteristics of each class. These algorithms generate an optimal predictive model that can determine the class (or posterior class probability) of a new source given its observed data.² Richards et al. (2011) presented an end-to-end ML framework for multi-class variable star classification, in which they describe algorithms for feature generation from single-band light curves and outline a methodology for non-parametric, multi-class statistical classification.

In this Chapter we present the results of a search for new RCB stars and DYPers in the Galaxy using version 2.3 of the ML catalog presented in Richards et al. (2012a). In §6.2 we describe the candidate selection procedure, while §6.3 describes the new and archival observations of the candidates. Our analysis of the photometric and spectroscopic data is contained in §6.4. The individual stars are examined in further detail in §6.5, while we discuss the results in §6.6. Our conclusions are presented in §6.7.

6.2 Candidate Selection

6.2.1 Advantages of Machine-Learning Classification

Candidate selection of possible RCB stars was performed using version 2.3 of the machine-learned ACVS classification catalog (MACC; Richards et al. 2012a) of variable sources cataloged from ASAS (Pojmański 1997, 2001). Full details of the classification procedure can be found in Richards et al. (2012b) and Richards et al. (2012a). Briefly, we employ a Random Forest (RF) classifier, which has been shown to provide the most robust results for variable star classification (see e.g., Richards et al. 2011; Dubath et al. 2011), to provide probabilistic classifications for all of the 50,124 sources in ACVS (Pojmański 2000). The classification procedure proceeds as follows: for each source in the ACVS 71 features are computed, 66 from the ASAS light curves (e.g., period, amplitude, skew, etc.; for the full list of features we refer the reader to Richards et al. 2012a and references therein) and 5 color features from optical and near-infrared (NIR) catalogs. A training set, upon which the RF classifications will be based, is constructed using light curves from 28 separate science classes, most of which are defined using well studied stars with high precision light curves from the Hipparcos and OGLE surveys (Debosscher et al. 2007; Richards et al. 2011), as well as some visually classified sources from ACVS for a few of the classes that are not well represented in Hipparcos (Richards et al. 2012b). The same 71 features are calculated for all the sources in the training set, and the RF classifier uses the separation of the 28 science classes in the multi-dimensional feature space to assign probabilistic classifications to each source in the ACVS. In the end, the probability of belonging to each individual science class is provided for each ACVS source and a post-RF procedure is used to calibrate these probabilities (meaning that a source with $P(\text{Mira}) = 0.5$ has a $\sim 50\%$ chance of actually being a Mira).

When searching for RCB stars in time-domain survey data, RF classification provides

²For a primer on machine learning, we refer the reader to Hastie et al. (2009).

a number of advantages relative to the more commonly used method of placing hard cuts on a limited set of a few features. Many studies have focused on light curves with large amplitude variations and a lack of periodic signal (e.g., Alcock et al. 2001; Zaniewski et al. 2005; Tisserand et al. 2008). A few recent studies have noted that additional cuts on NIR and mid-infrared colors can improve selection efficiency (Soszyński et al. 2009; Tisserand et al. 2011; Tisserand 2012). While these surveys have all proven successful, the use of hard cuts may eliminate actual RCB stars from their candidate lists.

Hard cuts are not necessary, however, when using a multi-feature RF classifier, which is capable (in principle) of capturing most of the photometric behavior of RCB stars (including the large-amplitude, aperiodic fades from maximum light as well as the periodic variations that occur near maximum light). Another general disadvantage in the use of hard cuts for candidate selection of rare sources is that the hard cuts are typically defined by known members of the class of objects for which the search is being conducted. Any biases present in the discovery of the known members of a particular class will then be encoded into the absolute (i.e., hard cuts) classification schema. This can exclude subclasses of sources that differ slightly from the defining members of a class. Furthermore, new discoveries will be unable to refine the selection criteria since, by construction, they will fall within the same portion of feature space as previously known examples.

The RF classifier produces an estimate of the posterior probability that a source is an RCB star given its light curve and colors. This allows us to construct a relative ranking of the RCB likelihood for all the sources in ACVS. Instead of making cuts in feature space, we can search down the ordered list of candidates. In this sense the RF classifier identifies the sources that are closest to the RCB training set relative to the other classes. The RF classifier finds the class boundaries in a completely data-driven way, allowing for the optimal use of known objects to search for new candidates in multi-dimensional feature spaces. This helps to mitigate against biases present in the training set, as classifications are performed using the location of an individual source in the multidimensional feature phase-space volume relative to defined classes in the training set.

6.2.2 The Training Set

The MACC RCB training set was constructed using high-confidence positional matches between ACVS sources and known RCB stars identified in SIMBAD³ and the literature. In total there are 18 catalogued RCB stars that are included in the ACVS, which we summarize in Table 6.1. The light curves of the known RCB stars were visually examined for the defining characteristic of the class: sudden, aperiodic drops in brightness followed by a gradual recovery to pre-decline flux levels. All of the known RCB stars but one, ASAS 054503–6424.4, showed evidence for such behavior. ASAS 054503–6424.4 is one of the brightest RCB stars in the LMC ($V_{\max} \approx 13.75$ mag), which during quiescence is barely above the ASAS detection threshold. The light curve for ASAS 054503–6424.4 does not show a convincing decline from

³<http://simbad.u-strasbg.fr/simbad/>.

Table 6.1: Known RCB stars in ACVS

Name	Other ID	DotAstro ^a ID	Training ^b Set?	$P(\text{RCB})^c$	R_{RCB}^d
ASAS 054503–6424.4	HV 12842	220040	N	0.010 ^e	2806 ^e
ASAS 143450–3933.5	V854 Cen	240306	Y	0.914	2
ASAS 150924–7203.8	S Aps	241463	Y	0.934	2
ASAS 154834+2809.4	R CrB	242999	Y	0.430	34
ASAS 162419–5920.6	RT Nor	244506	Y	0.629	10
ASAS 163242–5315.6	RZ Nor	244888	Y	0.944	2
ASAS 171520–2905.6	V517 Oph	247066	Y	0.169	158
ASAS 172315–2252.0	V2552 Oph	247575	Y	0.105	425
ASAS 180450–3243.2	V1783 Sgr	250762	Y	0.642	9
ASAS 180850–3719.7	WX CrA	251121	Y	0.834	2
ASAS 181325–2546.9	V3795 Sgr	251489	Y	0.726	8
ASAS 181509–2942.5	VZ Sgr	251638	Y	0.845	2
ASAS 181851–4632.9	RS Tel	251987	Y	0.951	1
ASAS 184732–3809.6	V CrA	254404	Y	0.804	3
ASAS 190812+1737.7	SV Sge	256072	Y	0.053	859
ASAS 191012–2029.7	V1157 Sgr	256221	Y	0.276	74
ASAS 193222–0011.5	ES Aql	257713	Y	0.044	901
ASAS 220320–1637.6	U Aqr	263740	Y	0.839	3

^aID from the MACC.^bIndicates whether or not (Y/N) this star was included in the RCB training set.^cCalibrated probability of belonging to the RCB class obtained when source is left out of the training set for cross validation.^dRelative rank of RCB likelihood when source is left out of the training set for cross validation.^eSource is not included in the training set, values taken directly from the MACC.

maximum light, and as such we do not include it in the training set.

In addition to the 18 RCB stars in ACVS, 7 additional RCB stars are detected in ASAS with the characteristic variability of the class.⁴ These sources all have clearly variable ASAS light curves; their exclusion from the ACVS means there is some bias in the construction of that catalog. In order to keep this bias self-consistent the training set for the MACC only included sources from Richards et al. (2011) and supplements from ACVS (see Richards et al. 2012b). We note that a future paper to classify all \sim 12 million sources detected by ASAS will include all ASAS RCB stars in its training set (Richards et al., in prep). Therefore the training set includes 17 RCB stars, which is limited by the coverage and depth of ASAS, the selection criteria of the ACVS, and the paucity of known RCB stars in the Galaxy. There are no known DYPers in ACVS: only two are known in the Galaxy and the DYPers in the Magellanic Clouds are fainter than the ASAS detection limits. Nevertheless, the similarity in the photometric behavior of RCB stars and DYPers allows us to use the RCB training set to search for both types of star. As more Galactic RCB stars and DYPers are discovered, we will be able to supplement the training set and improve the ability of future iterations of the RF classifier (see §6.6).

In order to determine our ability to recover known RCB stars using the RF classifier we perform a leave-one-out cross validation (CV) procedure. For the 17 sources in the RCB

⁴They are: SU Tau, UX Ant, UW Cen, V348 Sgr, GU Sgr, RY Sgr, and V532 Oph.

training set, we remove one source and re-run the RF classifier in an identical fashion to that used in Richards et al. (2012a). We then record the RF-determined probability that the removed source belongs to the RCB class, $P(\text{RCB})$, and the ranked value of $P(\text{RCB})$ relative to all other stars that are not included in the training set, R_{RCB} . We repeat the CV procedure for each star included in the training set, and the results are shown in Table 6.1. Since the training set is being altered in each run of the CV, R_{RCB} provides a better measure of the quality of each candidate; R_{RCB} is a relative quantity, whereas the calibration of $P(\text{RCB})$ will differ slightly from run to run. Eight of the 17 sources in the training set have $R(\text{RCB}) \leq 3$, implying that $\sim 50\%$ of the training set would be a top three candidate RCB star had we previously not known about it. 15 of the 17 RCB stars in the training set would be in the top 0.8% of the 50,124 sources in the ACVS, while all the known RCB stars in ACVS, including ASAS 054503–6424.4 (which is not in the training set), are in the top $\sim 6\%$ of RCB candidates. Two sources in the training set, SV Sge and ES Aql, are not listed near the top of R_{RCB} ranking during CV. For ES Aql this occurs because the star is highly active during the ASAS observations showing evidence for at least 6 separate declines during the ~ 10 yr observing period. As a result the light curve folds fairly well on a period of ~ 397 d, and ES Aql becomes confused with Mira and semi-regular periodic variables (see Figure 6.2). SV Sge, on the other hand, shows significant periodicity at the parasite frequency of 1 d, which precludes it from having a high R_{RCB} . The CV procedure allows us to roughly tune the efficiency of our selection criteria; the purity of the selection criteria cannot be evaluated until candidates have been spectroscopically confirmed.

6.2.3 The Candidates

Due to the relative rarity of RCB stars, we elected to generate a candidate list with high efficiency while sacrificing the possibility of high purity. With only ~ 50 Galactic RCB stars known to date, every new discovery has the potential to add to our knowledge of their population and characteristics. To generate our candidate list, we selected all sources from the MACC with $P(\text{RCB}) > 0.1$, which resulted in a total of 472 candidates. The selection criterion was motivated by the CV experiment, which indicates that our candidate list should have an efficiency $\gtrsim 80\%$. To obtain an efficiency close to 1 would require visual examination of roughly 3000 sources.

Since the expected purity of our sample is small by design, we examine the light curves of all sources within our candidate list by eye to remove sources that are clearly not RCB stars. These interlopers are typically semi-regular pulsating variables or Mira variables, often with minimum brightness levels below the detection threshold. We use the ALLSTARS Web interface (Richards et al. 2012b) to examine candidates, which in addition to light curves provides summary statistics (period, amplitude, color, etc.) for each source, as well as links to external resources, such as SIMBAD. We also remove any sources from the candidate list that are spectroscopically confirmed as non-carbon stars.

Following the removal of these stars the candidate list was culled from 472 to 15 candidates we considered likely RCB stars, for which we obtained spectroscopic follow-up observations.

Table 6.2: RCB candidates with $P(\text{RCB}) > 0.1$ from the MACC

Name	Other ID	MACC ^a ID	$\alpha_{\text{J}2000.0}$ ^b (hh mm ss.ss)	$\delta_{\text{J}2000.0}$ ^b (dd mm ss.s)	CGCS ^c ID	$P(\text{RCB})$	R_{RCB} ^d	C ^e
ASAS 060105+1654.7	V339 Ori	220556	06 01 04.65	+16 54 40.8	...	0.466	25	N
ASAS 065113+0222.1	C* 596	223100	06 51 13.31	+02 22 08.6	1429	0.302	73	D
ASAS 073456–2250.1	V455 Pup	225801	07 34 56.24	-22 50 04.2	1782	0.123	283	N
ASAS 095221–4329.7	IRAS 09503–4315	232170	09 52 21.37	-43 29 40.5	...	0.617	10	N
ASAS 153214–2854.4	BX Lib	242289	15 32 13.48	-28 54 21.6	...	0.367	43	N
ASAS 162229–4835.7	IO Nor	244409	16 22 28.84	-48 35 55.8	...	0.950	1	R
ASAS 162232–5349.2	C* 2322	244411	16 22 32.08	-53 49 15.6	3685	0.391	36	D
ASAS 165444–4925.9	C* 2377	245841	16 54 43.60	-49 25 55.0	3744	0.490	22	R
ASAS 170541–2650.1	GV Oph	246478	17 05 41.25	-26 50 03.4	...	0.702	8	R
ASAS 180823–4439.8	V496 CrA	251092	18 08 23.05	-44 39 46.7	...	0.110	389	N
ASAS 182658+0109.0	C* 2586	252675	18 26 57.64	+01 09 03.1	4013	0.115	343	D
ASAS 185817–3543.8	IRAS 18549–3547	255280	18 58 17.19	-35 43 44.7	...	0.127	251	N
ASAS 191909–1554.4	V1942 Sgr	256869	19 19 09.60	-15 54 30.1	4229	0.543	17	D
ASAS 194245–2137.0	...	258411	19 42 45.05	-21 36 59.8	...	0.112	376	N
ASAS 203005–6208.0	NSV 13098	261023	20 30 04.96	-62 07 59.2	...	0.340	52	R

Note. — This table contains only those sources which were selected for spectroscopic follow-up following visual inspection of their light curves.

^aDotAstro ID: internal designation for the MACC.

^bReported coordinates from the Two Micron All Sky Survey point source catalog (Cutri et al. 2003).

^cID from the General Catalog of Galactic Carbon Stars (CGCS; Alksnis et al. 2001).

^dRelative rank of $P(\text{RCB})$ including all sources from version 2.3 of the MACC not in the RCB training set.

^eFlag indicating classification of the source following spectroscopic observations: *R*: RCB, *D*: DYPer, *N*: Neither.

The general properties of the 15 spectroscopically observed candidates, including their names, coordinates, and RF probabilities, are summarized in Table 6.2. Finding charts using images from the Digitized Sky Survey⁵ (DSS) for the spectroscopically confirmed RCB and DYPer candidates can be found in Figure 6.1. Six of the selected candidates for spectroscopic observations are known carbon stars listed in the General Catalog of Galactic Carbon Stars (CGCS; Alksnis et al. 2001; see Table 6.2).

6.2.4 Feature Importance

RF classifiers can provide quantitative feedback about the relative importance of each feature used for classification. The RF feature importance measure describes the decrease in the overall classifier performance following the replacement of a single feature with a random permutation of its values (see Breiman 2001 for further details). We measure the importance of each feature using the average importance from a one-versus-one classifier whereby the RCB class is iteratively classified against each of the 27 other science classes on an individual basis. This procedure is run five times and the average of all runs is taken to reduce the variance present in any single run. Unsurprisingly, we find that `amplitude` is the most important feature. The importance measure does not properly capture the covariance between features and as a result the majority of the important features have to do with

⁵<http://stsdatu.stsci.edu/dss/>.

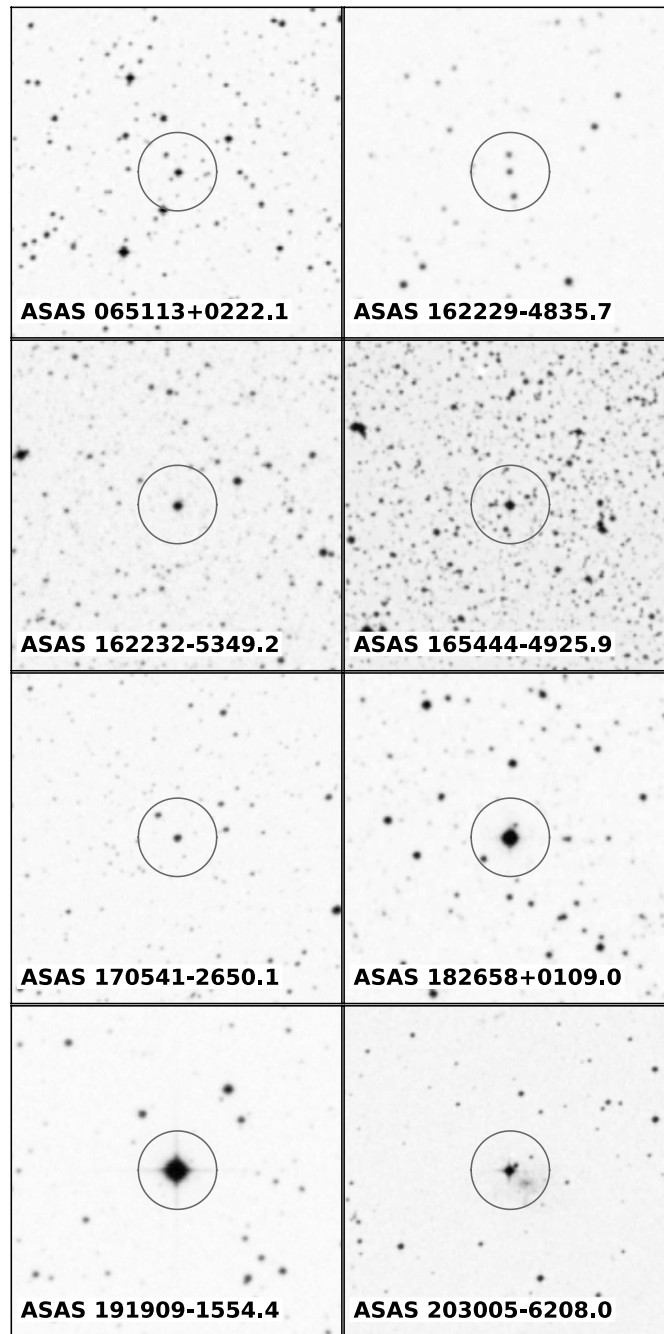


Figure 6.1: Optical finding charts of the newly discovered RCB stars and DYPers. Each finder is $5' \times 5'$ with north up and east to the left. The circles show the location of the targets and have $r = 33.5''$ which is the typical FWHM for ASAS images (Pojmański 1997). The large pixels on the ASAS camera result in PSFs that include the light from several stars, meaning some ASAS light curves underestimate the true variability of the brightest star within the PSF.

amplitude. The second and third most important features that are not highly covariant with amplitude are `qso_log_chi2nuNULL_chi2nu`,⁶ a measure of the dissimilarity between the photometric variations of the source and a typical quasar, and `freq1_harmonics_freq_0`, the best fit period. Interestingly, `freq_signif`, the significance of the best fit period of the light curve, ranks as only the 31st most important out of the 71 features.

We summarize the results of these findings with two-dimensional cuts through the multi-dimensional feature space showing amplitude versus period significance, $\chi_{\text{QSO},\text{False}}^2$, and period in Figure 6.2. We also show amplitude versus $P(\text{RCB})$. In each panel we show the location of the RCB stars in the training set as well as the newly discovered RCBs and DYPers presented in this Chapter, and we use the $P(\text{RCB})$ values from the CV experiment from §6.2.2 for the RCB stars in the training set. We also show the location of cuts necessary to achieve $\sim 80\%$ efficiency (blue dashed line) when selecting candidates using only two features, as well as the cuts necessary to achieve $\sim 100\%$ efficiency (red dashed line). As would be expected based on the results presented above, it is clear that $\chi_{\text{QSO},\text{False}}^2$ and period are far more discriminating than period significance when selecting RCB candidates. To achieve an efficiency near 100%, $P(\text{RCB})$ is vastly superior to any two dimensional slice through feature space. We note that the discretization seen in the distribution of $P(\text{RCB})$ is the result of using a finite number of trials within the RF classifier. The probability of belonging to a class is defined as the total number of times a source is classified within that class divided by the total number of trials. These discrete values are then smeared following the calibration procedure described in §6.2.1.

Many of the known and new RCB stars have very similar measured best periods clustered near ~ 2400 and 5300 d, which for each corresponds to the largest period searched during the Lomb-Scargle analysis in Richards et al. (2012a). Folding these light curves on the adopted periods clearly shows they are not periodic on the adopted periods, despite the relatively high period significance scores (see the upper left panel of Figure 6.2), which suggests some peculiarity in the feature generation process for these sources. We are exploring improved metrics for periodicity to be used in future catalogs. Nevertheless, despite these spurious period measurements, the ML classifier has correctly identified that this feature tends to be erroneous for RCB stars, and as such it is a powerful discriminant for finding new examples of the class.

6.3 Archival Data and New Observations

6.3.1 ASAS Photometry

All optical photometric observations were obtained during ASAS-3, which was an extension of ASAS, conducted at the Las Campanas Observatory (for further details on ASAS and ASAS-3 see Pojmański 1997, 2001). Light curves were downloaded from the ACVS⁷, and

⁶This is the same as the $\chi_{\text{QSO},\text{False}}^2$ statistic, which is defined in Butler & Bloom (2011).

⁷<http://www.astrouw.edu.pl/asas/?page=acvs>

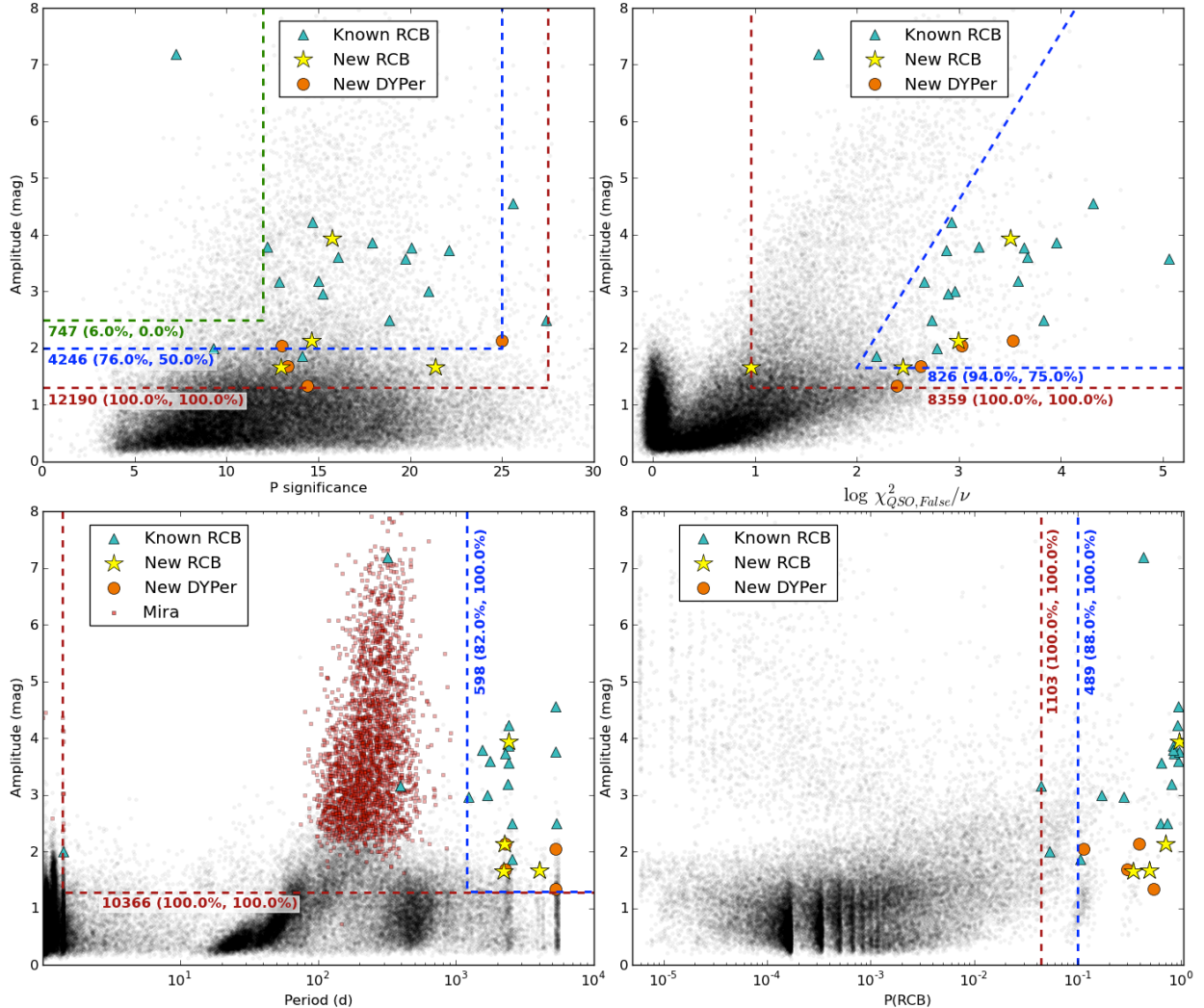


Figure 6.2: Two dimensional cuts through the multi-dimension feature space used to classify sources in version 2.3 of the MACC. Each panel shows the location of all sources in the MACC (black points), as well as the RCB stars in the training set (cyan triangles), newly discovered RCB stars (yellow stars), and new DYPers (orange circles). Also shown are cuts necessary to achieve $\sim 80\%$ (blue dashed line) and $\sim 100\%$ (red dashed line) RCB selection efficiency. Next to these lines are the total number of ACVS sources within the cut region, as well as the efficiency of recovering training set and new detections (shown in parenthesis), respectively. *Upper left:* amplitude versus period significance. *Upper right:* amplitude versus $\chi_{QSO, False}^2 / \nu$. *Lower left:* amplitude versus period. Also shown is the tight cluster of Mira variables (red points), defined here as all ACVS sources with $P(\text{Mira}) > 0.7$. *Lower right:* amplitude versus $P(\text{RCB})$. Note that these are highly covariant as $P(\text{RCB})$ is strongly dependent on amplitude, which is why the cuts presented are shown in a single dimension. The $P(\text{RCB})$ values for the stars used in the training set are taken from the CV experiment from §6.2.2.

imported into our DotAstro.org⁸ astronomical light-curve warehouse for visualization and use with internal frameworks (Brewer et al. 2009). The ACVS provides V -band measurements for a set of 50,124 pre-selected ASAS variables, measured in 5 different apertures of varying size (Pojmański 2002). For each star in the catalog an optimal aperture selection procedure is used to determine the final light curve, as described in Richards et al. (2012a).⁹ The ASAS-3 V -band light curves for the eight new RCB stars and DYPers are shown in Figure 6.3.

6.3.2 Spectroscopy

Optical spectra of the candidate RCB stars were obtained between 2011 Sep. and 2012 May with the Kast spectrograph on the Lick 3-m Shane telescope on Mt. Hamilton, California (Miller & Stone 1993), the Low-Resolution Imaging Spectrometer (LRIS) on the 10-m Keck I telescope on Mauna Kea (Oke et al. 1995), and the RC Spectrograph on the SMARTS 1.5-m telescope at the Cerro Tololo Inter-American Observatory (Subasavage et al. 2010). All spectra were obtained via long slit observations, and the data were reduced and calibrated using standard procedures (e.g., Matheson et al. 2000; Silverman et al. 2012). On each night of observations, we obtained spectra of spectrophotometric standards to provide relative flux calibration for our targets. For queue-scheduled observations on the RC spectrograph, all observations in a single night are conducted with the slit at the same position angle. Thus, the standard stars and targets were not all observed at the parallactic angle, leading to an uncertain flux correction (Filippenko 1982). We note, however, that the uncertainty in the flux correction does not alter any of the conclusions discussed below. A summary of our observations is given in Table 6.3, while the blue portion of the optical spectra are shown in Figures 6.4–6.5.

6.4 Analysis

6.4.1 Spectroscopic Confirmation

While the unique photometric behavior of RCB stars makes them readily identifiable in well sampled light curves taken over the course of several years, there are several examples of high-amplitude variables being classified as RCB stars which are later refuted by spectroscopic observations. Most of the mis-identified candidates are either cataclysmic, symbiotic or semi-regular variables (see e.g., Lawson & Cottrell 1990; Tisserand et al. 2008). RCB stars are a subclass of the hydrogen-deficient carbon stars (HdC). For an RCB candidate to be confirmed as a true member of the class, its spectrum must show the two prominent features of HdC stars: anomalously strong carbon absorption and a lack of atomic and molecular H features.

To confirm the RCB candidates found in the ACVS, we obtained low-resolution spectra of the 15 candidates presented in §6.2. Candidates observable from the northern hemisphere

⁸<http://dotastro.org>.

⁹These optimal aperture light curves can be obtained from DotAstro.org.

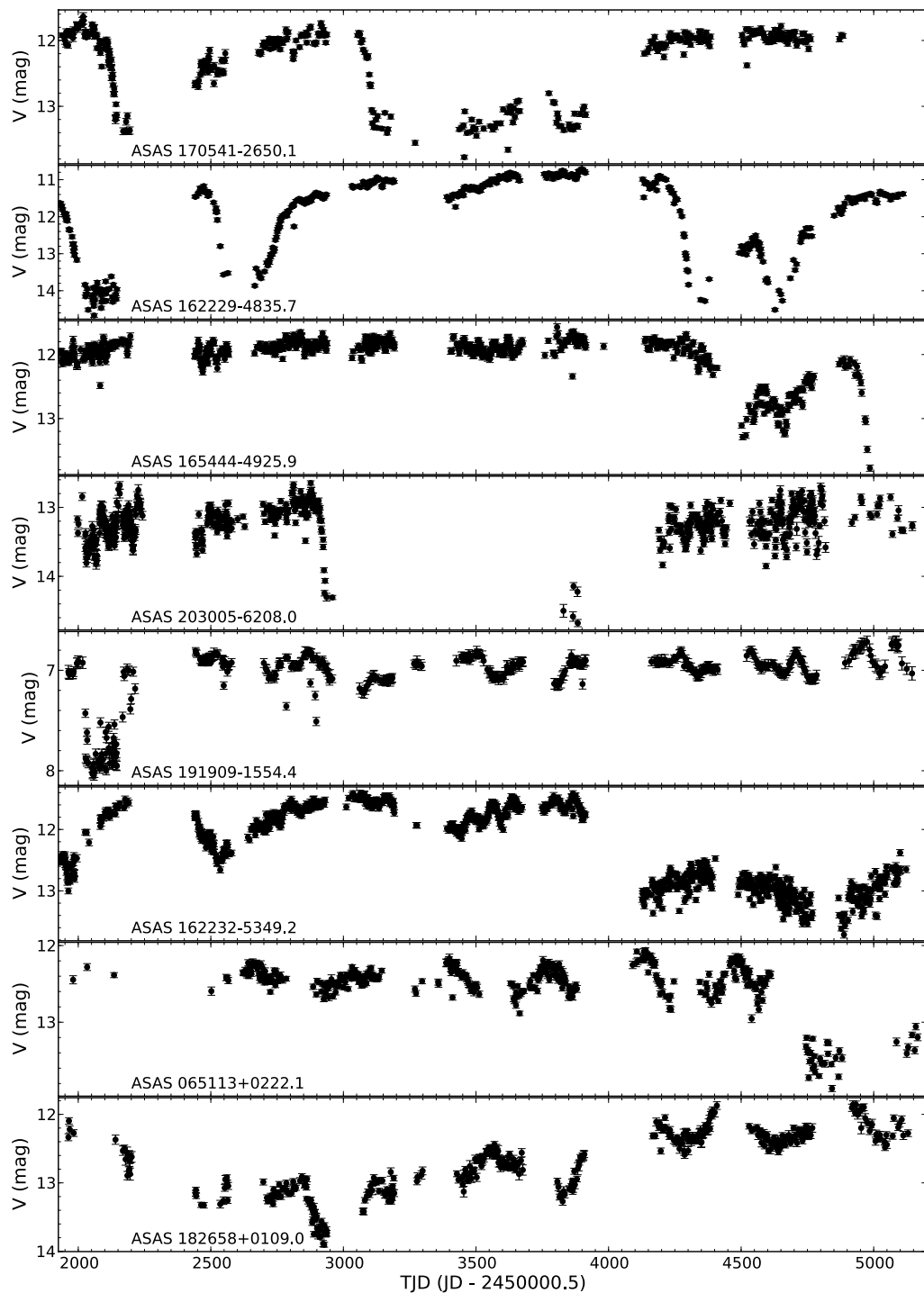


Figure 6.3: ASAS V-band light curves of newly discovery RCB stars and DYPers. Note the differing magnitude ranges shown for each light curve. Spectroscopic observations confirm the top four candidates to be RCB stars, while the bottom four are DYPers.

Table 6.3: Log of spectroscopic observations

Name	UT Date	Instrument ^a	Range (Å)	Res. (Å)	Exp. Time (s)
ASAS 060105+1654.7	2011-08-28.644	LRIS	3300–5630	4	60
ASAS 060105+1654.7	2011-08-28.644	LRIS	5810–7420	2	60
ASAS 170541–2650.1	2011-09-26.206	LRIS	3300–5630	4	60
ASAS 170541–2650.1	2011-09-26.205	LRIS	5720–7360	2	30
ASAS 191909–1554.4	2011-09-26.212	LRIS	3300–5630	4	5
ASAS 191909–1554.4	2011-09-26.212	LRIS	5720–7360	2	2
ASAS 162232–5349.2	2012-01-16.375	RC	3300–9370	17	720
ASAS 095221–4329.7	2012-01-19.151	RC	3300–9370	17	540
ASAS 065113+0222.1	2012-02-01.204	Kast	3450–9850	4 ^b	300 ^c
ASAS 162229–4835.7	2012-02-06.373	RC	3300–9370	17	540
ASAS 162232–5349.2	2012-02-13.325	RC	3660–5440	4	2700
ASAS 162229–4835.7	2012-02-15.348	RC	3660–5440	4	2700
DY Per	2012-02-23.107	Kast	3450–9850	4 ^b	380 ^c
ASAS 073456–2250.1	2012-03-15.225	LRIS	3350–10000	4	60 ^c
ASAS 165444–4925.9	2012-03-15.651	LRIS	3250–10000	4	30 ^c
ASAS 182658+0109.0	2012-03-15.654	LRIS	3250–10000	4	30 ^c
ASAS 185817–3543.8	2012-03-15.667	LRIS	3250–10000	4	30 ^c
ASAS 153214–2854.4	2012-03-15.670	LRIS	3250–10000	4	60 ^c
ASAS 203005–6208.0	2012-03-23.426	RC	3660–5440	4	2160
NSV 11154	2012-04-02.524	Kast	3450–9850	4 ^b	210 ^c
ASAS 194245–2137.0	2012-04-23.513	Kast	3450–9850	4 ^b	120 ^c
ASAS 180823–4439.8	2012-05-17.626	LRIS	5420–10000	4	16

^aKast: Kast spectrograph on Lick 3-m telescope. LRIS: low resolution imaging spectrometer on Keck-I 10-m telescope. RC: RC spectrograph on the SMARTS 1.5-m telescope.

^bThe Kast spectrograph is a dual arm spectrograph with a resolution of ~ 4 Å on the blue side, which is relevant for the spectra shown in Figure 6.4. The typical resolution on the red side is ~ 10 Å.

^cExposure time for the blue arm of the spectrograph. Due to the red nature of the SED the exposure time for the red arm was shorter than the blue.

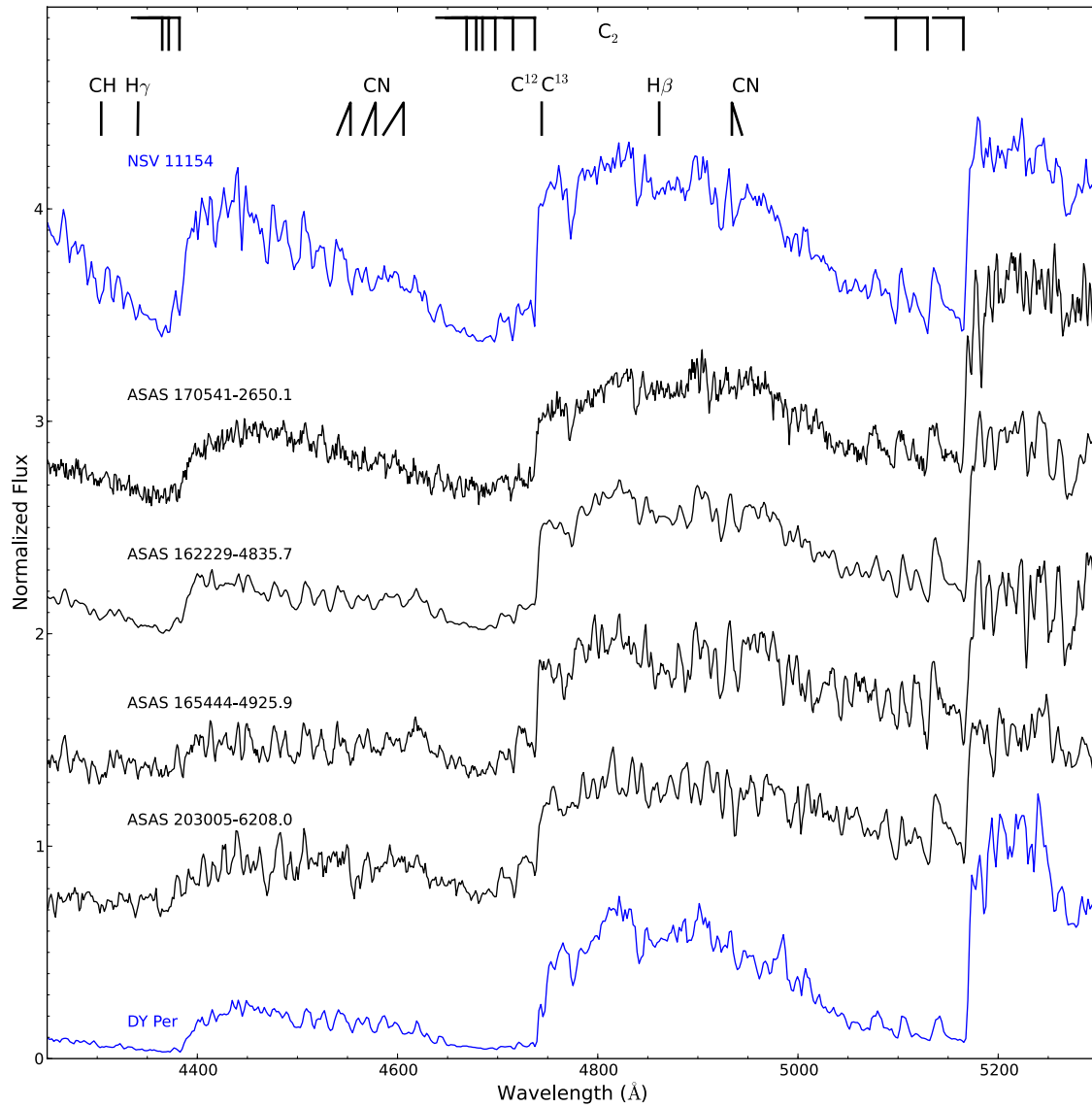


Figure 6.4: Blue optical spectra of the new candidate RCB stars. For reference low-resolution spectra of NSV 11154, a cool RCB star, and DY Per obtained in early 2012 are shown in blue. The new RCB stars all show clear evidence for strong molecular carbon absorption and lack clear evidence for ^{13}C as the $\lambda 4744$ band of $^{12}\text{C}^{13}\text{C}$ is undetected in each. There is also a lack of evidence for strong H absorption as is expected for RCB stars.

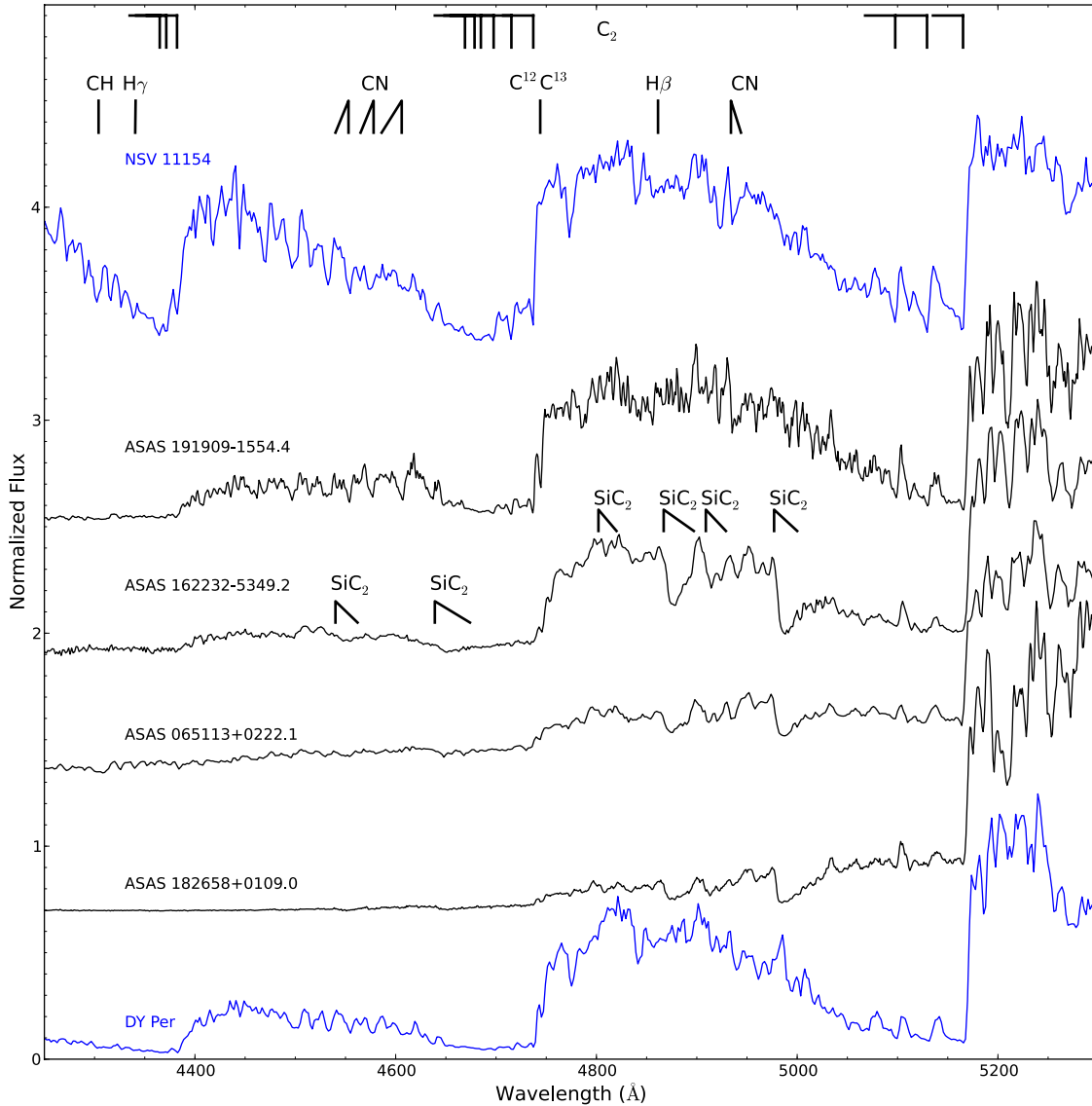


Figure 6.5: Blue optical spectra of the four new DYPer candidates. For reference low-resolution spectra of NSV 11154, a cool RCB star, and DY Per obtained in early 2012 are shown in blue. The new DYPers show strong absorption from the carbon Swan bands and the $\lambda 4744$ band of $^{12}\text{C}^{13}\text{C}$ is clearly detected in each, similar to DY Per. The candidates also show a lack of clear evidence for H absorption. Strong absorption from the Merrill-Sanford bands of SiC_2 is seen in three of the DYPers: ASAS 162232–5349.2, ASAS 065113+0222.1, and ASAS 182658+0109.0.

were observed with Kast and LRIS, while those only accessible from the southern hemisphere were observed with the RC spectrograph. For some of the southern hemisphere targets very low-resolution spectra were obtained first to confirm the presence of C₂ before slightly higher resolution observations were obtained (see Table 6.3).

We searched the spectra for the presence of strong carbon features, primarily C₂ and CN, and a lack of Balmer absorption to confirm the RCB classification for the ACVS candidates. We find these characteristics in eight of the spectroscopically observed stars (see Figures 6.4–6.5), which we consider good RCB and DYPers candidates as summarized in Table 6.4. The remaining candidates were rejected as possible RCB stars based on their spectra, which typically showed strong TiO and VO absorption or clear evidence for H. The properties of the rejected candidates are summarized in Table 6.5. In the remainder of this Chapter we no longer consider these stars candidates and restrict our discussion to the eight good candidates listed in Table 6.4.

In addition to the hallmark traits of overabundant carbon and a lack of Balmer absorption, RCB stars show a number of other unique spectroscopic characteristics. In particular, they show a very high ratio of ¹²C/¹³C and no evidence for G band absorption. To search for the presence of ¹³C, we examined the spectra for the $\lambda 4744$ band head of ¹²C¹³C, which is typically very weak or absent in the spectra of RCB stars. We find evidence for ¹²C¹³C in ASAS 191909–1554.4, ASAS 162232–5349.2, ASAS 065113+0222.1, and ASAS 182658+0109.0 while ASAS 162232–5349.2 shows possible evidence for the ¹³C¹³C band at $\lambda 4752$. The presence of ¹³C suggests that these four stars are likely DYPers. We consider these four stars closer analogs to DY Per and the DYPers found in the LMC and SMC ([Alcock et al. 2001](#); [Tisserand et al. 2009](#)) than they are to classical RCB stars. One of the DYPers, ASAS 065113+0222.1, shows weak evidence for CH $\lambda 4300$ (G band) absorption and possible evidence for H γ , which is sometimes seen in the spectra of DYPers. We note that the signal-to-noise (S/N) ratio of all our spectra in the range between ~ 4300 –4350 is relatively low, making definitive statements about the presence or lack of both CH and H γ challenging. Finally, we note that we see evidence for the Merrill-Sanford bands of SiC₂ in three of our candidates: ASAS 162232–5349.2, ASAS 065113+0222.1, and ASAS 182658+0109.0. To our knowledge this is the first identification of SiC₂ in a DYPER spectrum, though the presence of this molecule should not come as a surprise as RCB stars are both C and Si rich ([Clayton 1996](#)).

6.4.2 Photometric Behavior

In addition to spectral differences, RCB stars and DYPers show some dissimilarities in their photometric evolution as well. The first order behavior is the same: both show deep, irregular declines in their light curves which can take anywhere from a few months to a several years to recover to maximum brightness. Beyond that generic behavior, however, the shape of the decline tends to differ: RCB stars show fast declines with slow recoveries whereas DYPers tend to show a more symmetric decline and recovery.

The photometric properties of our candidates, including decline rates for the most prominent and well sampled declines, are summarized in Table 6.4. As previously noted

Table 6.4: Observational properties of new RCB stars and DYPers

Name	$V_{\text{max}}^{\text{a}}$ (mag)	Δmag	Δt (d)	dm/dt (mag d $^{-1}$)	^{13}C	H/CH	pulse ^b	RCB/ DYPPer
ASAS 170541–2650.1	11.9	1.2	31	0.04	Weak 4744?	None	N ^c	RCB
ASAS 162229–4835.7	10.8	2.8	83	0.03	None	Weak H γ ?, Weak CH	Y	RCB
ASAS 165444–4925.9	11.8	>1.6	>48	0.03	None	Weak H γ ?, H β ?	Y	RCB
ASAS 203005–6208.0	13.2	>1.4	>30	0.05	None	H γ ?, H β ? – blends	Y	RCB
ASAS 191909–1554.4	6.9	1.0	20	0.05	Y	None	Y	DYPPer
ASAS 162232–5349.2	11.5	1.7	<256	>0.007	Y	None	Y	DYPPer
ASAS 065113+0222.1	12.4	1.0	<140	>0.007	Y	Weak H γ ?, Weak CH	Y	DYPPer
ASAS 182658+0109.0	12.1	1.6	960	0.002	Y	None	Y	DYPPer

^aObserved quantity, not corrected for Galactic reddening.^bEvidence for pulsations outside declines: Y/N.^cThe period of ASAS observations covers very little time around maximum light, and as a result there is a relatively short period of data suitable for searching for pulsations. See §6.4.3.

Table 6.5: Rejected RCB candidates

Name	$V_{\text{max}}^{\text{a}}$ (mag)	Remarks
ASAS 060105+1654.7	12.3	No C ₂ ; strong H, G-band
ASAS 073456–2250.1	12.8	C ₂ ; strong H emission
ASAS 095221–4329.7	10.6	strong TiO, VO; H?
ASAS 153214–2854.4	12.3	No C ₂ ; H α emission, strong G band; SRPV ^b
ASAS 180823–4439.8	12.1	strong TiO, VO
ASAS 185817–3543.8	10.9	strong TiO, VO
ASAS 194245–2137.0	12.5	strong TiO, VO

^aObserved quantity, not corrected for Galactic reddening.^bIdentified as a semi-regular periodic variable in the General Catalog of Variable Stars (Samus et al. 2008).

in the caption of Figure 6.1, the full amplitude of the variations of these stars are likely underestimated due to the large PSF on ASAS images. This means that the decline rates should be treated as lower limits, since the true brightness of the star may be below that measured in a large aperture. Nevertheless, the decline rates for the four RCB stars are relatively fast and consistent with those given in Tisserand et al. (2009) for RCB stars in the Magellanic Clouds (MCs), $\sim 0.04 \text{ mag d}^{-1}$. The most telling feature of the light curves is the shape of the declines, however. For the four spectroscopic RCB stars, ASAS 170541–2650.1, ASAS 162229–4835.7, ASAS 165444–4925.9, and ASAS 203005–6208.0 the declines are very rapid. While we do not detect ASAS 165444–4925.9 after its sharp decline on $\text{TJD} \approx 5000$, the other three show slow asymmetric recoveries to maximum light. The four spectroscopic DYPers generally show a slower decline with a roughly symmetric recovery, though we note that the full recoveries of ASAS 065113+0222.1 and ASAS 162232–5349.2 are not observed.

6.4.3 Pulsations

All RCB stars are variable near maximum light, with most and possibly all of the variations thought to be due to pulsation (Lawson et al. 1990; Clayton 1996). Typical periods are $\sim 40\text{--}100 \text{ d}$, and the amplitudes are a few tenths of a magnitude. The pulsational properties of DYPers are not as well constrained, because the sample is both small and only recently identified. Each of the four DYPers identified in Alcock et al. (2001) shows evidence for periodic variability near maximum light, with typical periods of $\sim 100\text{--}200 \text{ d}$.

To search for the presence of pulsations in our candidate RCB stars, we use a generalized Lomb-Scargle periodogram (Lomb 1976; Scargle 1982; Zechmeister & Kürster 2009) to analyze each star (see Richards et al. 2011 for more details on our Lomb-Scargle periodogram implementation). Our analysis only examines data that is well separated from decline phases, and we focus on the portions of light curves where the secular trend is slowly changing relative to the periodic variability. For each star we simultaneously fit for the harmonic plus linear or quadratic long-term trend in the data. The frequency that produces the largest peak in the periodogram, after masking out the 1 day alias, is adopted as the best fit period.

We find evidence for periodicity in the light curves of each star, except for ASAS 162229–4835.7. For most of the observing window ASAS 162229–4835.7 was in or near a decline, and we predict that additional observations of ASAS 162229–4835.7, be they historical or in the future, will show periodic variability near maximum light. The trend-removed, phase-folded light curves of the remaining seven stars are shown in Figure 6.6. Insets in each panel list the range of dates that were included in the Lomb-Scargle analysis, as well as the best fit period for the data.

Some RCB stars are known to have more than a single dominant period (see Clayton 1996 and references therein). We find evidence for multiple periods in ASAS 191909–1554.4, with periods of 120, 175, and 221 d that appear to change every $\sim 1\text{--}2$ years. Evidence for multiple periods also appears to be present in ASAS 165444–4925.9. The best fit periods in this case are 27 and 56 d, which differ by roughly a factor of two. The longer period may in this case simply be a harmonic of the shorter period. Finally, we note that the best fit period

for ASAS 162232–5349.2, 359 d, is very close to one year, and it is possible that the data are beating against the yearly observation cycle. The folded light curve appears to traverse a full cycle over \sim half the full phase cycle. The slight upturn in the folded data around phase 0.15 suggests that the true period is likely \sim 180 d, half the best fit period.

6.4.4 Spectral Energy Distributions

All RCB stars are known to have an infrared (IR) excess due to the presence of circumstellar dust (Feast 1997; Clayton 1996), and all the known DYPers in the MCs also show evidence for excess IR emission (Tisserand et al. 2009). To check for a similar excess in the new ACVS RCB stars and DYPers, broadband spectral energy distributions (SEDs) were constructed with catalog data obtained from USNO-B1 (Monet et al. 2003), the Two Micron All Sky Survey (2MASS; Skrutskie et al. 2006), the *Wide-Field Infrared Survey Explorer* (*WISE*, Wright et al. 2010), *AKARI* (Murakami et al. 2007), the *Mid-Course Space Explorer* (*MSX*; Mill et al. 1994), and the *Infrared Astronomical Satellite* (*IRAS*; Neugebauer et al. 1984).¹⁰ The USNO-B1 catalog contains measurements made on digital scans of photographic plates corresponding roughly to the B , R , and I bands. Repeated B and R plates were taken typically more than a decade apart. To convert the five separate USNO-B1 magnitude measurements to the standard $g'r'i'$ system of the Sloan Digital Sky Survey (SDSS; Fukugita et al. 1996), we invert the filter transformations from Monet et al. (2003) (see also Sesar et al. 2006). The two measurements each for the g' and r' band are then averaged to get the reported SDSS g' and r' magnitudes, unless the two measurements differ by > 1 mag, in which case it is assumed that the fainter observation occurred during a fading episode of the star. Then the final adopted SDSS magnitude is that of the brighter measurement. There is a large scatter in the transformations from USNO-B1 to SDSS (Monet et al. 2003; Sesar et al. 2006), which, leads us to adopt a conservative $1-\sigma$ uncertainty of 40% in flux density on each of the transformed SDSS flux measurements. The 2MASS magnitude measurements are converted to fluxes via the calibration of Cohen et al. (2003) and the *WISE* magnitudes are converted to fluxes via the calibration in Cutri et al. (2011). The remaining catalogs provide flux density measurements in Jy rather than using the Vega magnitude system.

The full SEDs extending from the optical to the mid-infrared for each of the new RCB stars and DYPers are shown in Figure 6.7. All of the candidates but ASAS 203005–6208.0 saturate the W1 (3.5 μm) and W2 (4.6 μm) bands of *WISE*, while of those all but ASAS 170541–2650.1 and ASAS 165444–4925.9 saturate W3 (11.6 μm) as well. ASAS 191909–1554.4 and ASAS 182658+0109.0 saturate all three of the 2MASS filters and are the only candidates detected at either 60 and/or 100 μm by *IRAS*. ASAS 162229–4835.7 and ASAS 191909–1554.4 were the only candidates detected at 90 μm by *AKARI*.

Using RCB stars and DYPers in the MCs, Tisserand et al. (2009) find that the RCB stars typically have SEDs with two distinct peaks, whereas DYPers typically have a single peak. It is argued in Tisserand et al. that the SEDs of both can be understood as emission from

¹⁰Catalog data for each of these surveys can be found at: <http://irsa.ipac.caltech.edu/>.

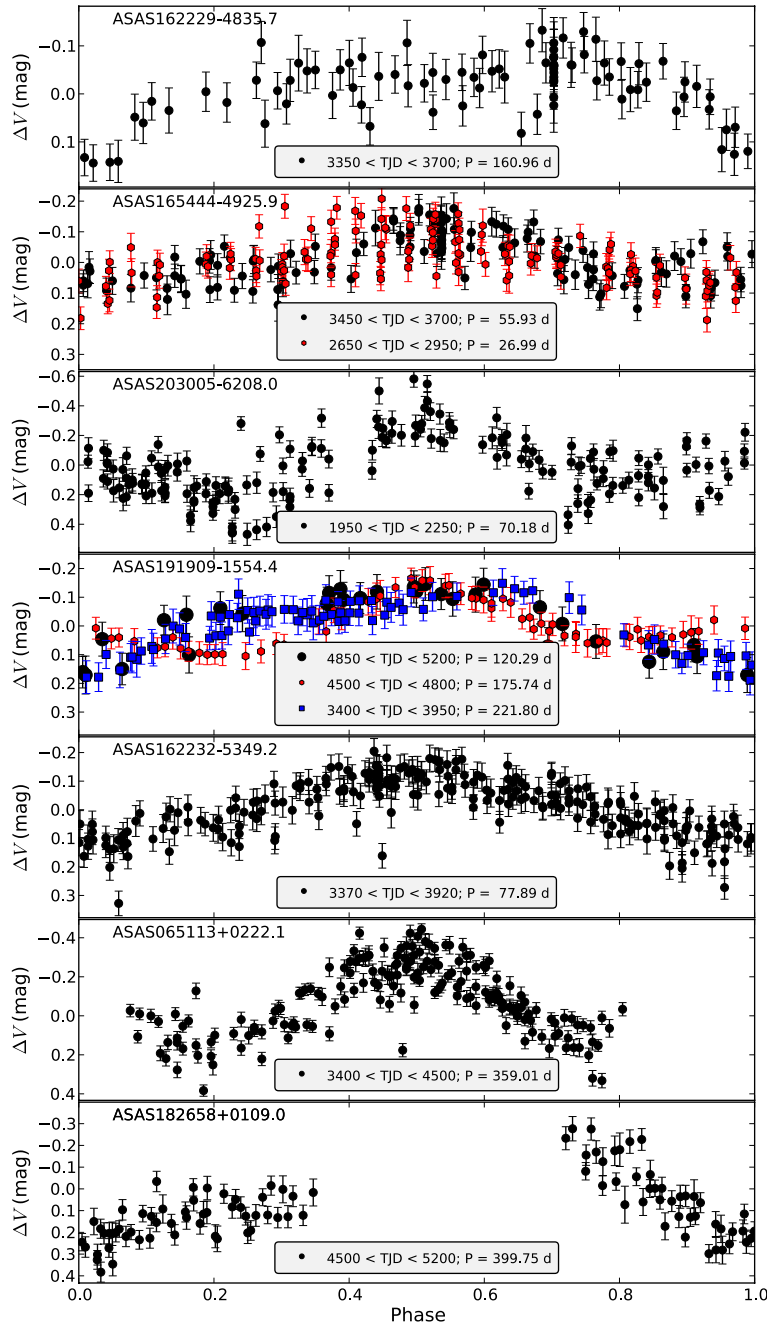


Figure 6.6: Folded light curves showing evidence for periodic variability near maximum light in the new RCB stars and DYPer candidates. The folded light curves only display a portion of the ASAS observations as indicated in the legend for each source. ASAS 165444–4925.9 and ASAS 191909–1554.4 show evidence for multiple dominant periods, which are shown with blue and red points as indicated in their respective legends.

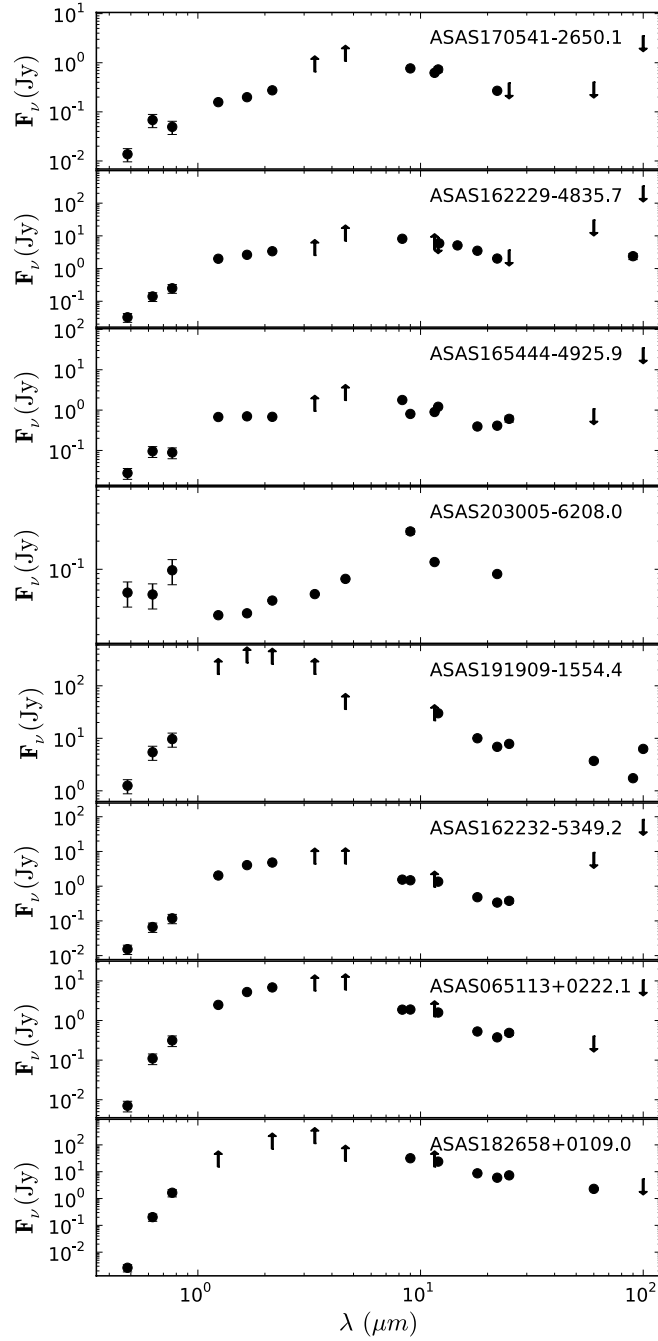


Figure 6.7: Optical through mid-infrared spectral energy distributions for newly discovered RCB stars and DYPers. The observations in the various passbands were not taken simultaneously, thus in some cases the lack of a smooth spectrum is likely the result of intrinsic variability. The reddening towards each star is uncertain.

a stellar photosphere and surrounding dust shell; the cooler photospheric temperatures of DYPers is less distinct relative to the dust emission leading to a single broad peak rather than two. We caution that the reddening towards each of the new Galactic candidates is unknown, which makes a detailed analysis of their SEDs challenging. Furthermore, the observations were not taken simultaneously in each of the various bandpasses. Nevertheless, a few interesting trends can be gleaned from the data. The four stars that spectroscopically resemble RCB stars, ASAS 170541–2650.1, ASAS 162229–4835.7, ASAS 165444–4925.9, and ASAS 203005–6208.0 all show clear evidence for a mid-infrared excess relative to their optical brightness. The peak of emission from ASAS 191909–1554.4 and ASAS 182658+0109.0 is not well constrained because they saturate the detectors between 1 and 6 μm , yet interestingly both show evidence for an infrared excess redward of 50 μm . This suggests that there might be some very cool ($T < 100$ K) dust in the circumstellar environment of these stars, which is observed in some of the bright, nearby RCB stars. For instance, *Spitzer* and *Herschel* observations of R CrB show evidence for a large, ~ 4 pc, cool, $T \sim 25$ K, and diffuse shell of gas that is detected in the far-IR (Clayton et al. 2011). ASAS 162232–5349.2 and ASAS 065113+0222.1 show evidence for a single broad peak in their SED occurring around ~ 2 μm , which is similar to the SEDs of the DYPers observed in the MCs.

6.4.5 Near-Infrared Variability

An overlap in the survey fields between 2MASS and the DEep Near Infrared Southern Sky Survey (DENIS; Epcstein et al. 1994) allows measurements of the NIR variability of four of the newly discovered RCB stars and DYPers. Photometric measurements from 2MASS and the two epochs of DENIS observations for these stars are summarized in Table 6.6. Unfortunately the 2MASS and DENIS observations preceeded the ASAS monitoring, and so we cannot provide contextual information such as the state of the star (near maximum, on decline, during deep minimum, etc.) at the time of the NIR observations. To within a few tenths of a magnitude, ASAS 162229–4835.7 is not variable between the 2MASS and DENIS observations. On timescales of a few weeks–months both ASAS 162232–5349.2 and ASAS 170541–2650.1 show evidence for variations $\gtrsim 1$ mag in the NIR. Similar variations have been observed for several of the RCB stars and DYPers in the MCs (e.g., Tisserand et al. 2004, 2009). The largest variations were observed in ASAS 203005–6208.0, which changed by ~ 4 mag in the J band during the ~ 4 yr between the DENIS and 2MASS observations. ASAS 203005–6208.0 also shows a large variation between the DENIS I band measurement and the I -band measurement from USNO-B1, with $\Delta m \approx 7$ mag. This star is clearly a large amplitude variable, which likely explains its unusual SED. In the DENIS observations, which provide simultaneous optical and NIR measurements, ASAS 203005–6208.0 is always fainter in the optical, suggesting that the unusual shape to its SED (see Figure 6.7) is the result of non-coeval observations.

Table 6.6: 2MASS and DENIS NIR measurements

Name	Epoch _{2MASS} ^a (JD)	<i>J</i> _{2MASS} ^a (mag)	<i>H</i> _{2MASS} ^a (mag)	<i>K_s</i> _{2MASS} ^a (mag)	Epoch _{DENIS} ^b (JD)	<i>I</i> _{DENIS} ^b (mag)	<i>J</i> _{DENIS} ^b (mag)	<i>K_s</i> _{DENIS} ^b (mag)
ASAS 170541–2650.1	2451004.658	10.01	9.28	8.46	2451730.639	11.09	10.18	9.13
					2451749.592	9.94	8.91	7.96
ASAS 162229–4835.7	2451347.541	7.26	6.47	5.73	2451387.540	9.10	6.90	5.40
					2451395.492	8.98	7.13	5.45
ASAS 162232–5349.2	2451347.538	7.24	6.01	5.36	2451387.532	9.12	6.59	4.40
					2451395.485	9.20	6.30	4.28
ASAS 203005–6208.0	2451701.878	11.73	11.20	10.40	2450267.768	17.62	15.66	12.06
					2451003.746	15.82	14.37	11.89

^aCatalog measurement from the 2MASS point source catalog (Cutri et al. 2003).

^bCatalog measurement from the DENIS point source catalog (Epchtein et al. 1999).

6.5 Individual Stars

We discuss the individual stars and whether they should be considered RCB stars or DYPers below. We also use SIMBAD to identify alternate names for these stars and previous studies in the literature (see also Table 6.2).

6.5.1 ASAS 170541–2650.1 (GV Oph)

This star was first identified as a variable source on Harvard photographic plates with the name Harvard Variable 4368, and was cataloged as a likely long period variable based on the large amplitude of variations from 13.9 mag to below the photographic limit of \sim 16.5 mag (Swope 1928). It was later named GV Oph in the General Catalog of Variable Stars (GCVS; Kukarkin et al. 1971; Samus et al. 2008) as a variable of unknown type with rapid variations. The light curve, spectrum, and SED of this star are consistent with it being a RCB star.

6.5.2 ASAS 162229–4835.7 (IO Nor)

This star is listed as a Mira variable in the GCVS with the name IO Nor. In Clarke et al. (2005) it is identified as a star with an IR excess based on MSX observations. On the basis of its NIR and mid-IR colors, it is identified as a RCB candidate in Tisserand (2012), and considered a likely RCB star on the basis of its ASAS light curve.¹¹ We independently identified IO Nor as a likely RCB star on the basis of its light curve (in the MACC it is the

¹¹In Tisserand (2012) two additional stars with IR colors consistent with RCB stars, V653 Sco and V581 CrA, are identified as highly likely RCB stars on the basis of their ASAS light curves. V581 CrA is not included in ACVS and therefore is not included in the MACC. V653 Sco is listed in the GCVS as a Mira variable and classified as a semi-regular periodic variable in the MACC, $P(\text{SRPV}) = 0.55$. It has $P(\text{RCB}) = 0.012$ and $R(\text{RCB}) = 2609$. The light curve is somewhat similar to ES Aql, in that it fades below the ASAS detection limits and it is highly active during the \approx 8 yr it was observed, meaning it folds decently well on a period of \sim 450 d. A spectrum will be needed to disambiguate between an RCB or long period variable classification for V653 Sco.

most likely RCB in ACVS), and our spectrum confirms that it is a genuine RCB star. The previous classification as a Mira variable is likely based on the late spectral type and large amplitude of variability, but Figure 6.3 clearly shows that ASAS 162229–4835.7 is not a long period variable.

6.5.3 ASAS 165444–4925.9 (C* 2377)

The variability of this star has not been cataloged to date, and it is listed in the CGCS as C* 2377 (Alksnis et al. 2001). The spectrum, SED, and pulsations exhibited by this star are consistent with RCB stars. There may be evidence for weak CH absorption, though we caution the S/N is low near \sim 4300 Å. The light curve shows a sharp decline, similar to RCB stars, but the recovery is not observed. Nevertheless, the evidence points to ASAS 165444–4925.9 being a new member of the RCB class.

6.5.4 ASAS 203005–6208.0 (NSV 13098)

This star was first identified as variable by Luyten (1932) with a maximum brightness of 14 mag and a minimum > 18 mag. Luyten assigned it the name AN 141.1932, and it was later cataloged as a possible variable star in the GCVS as NSV 13098. The light curve, spectrum, and SED are all consistent with an RCB classification. Higher resolution and S/N spectra are needed to confirm if H absorption is present, though we note that some RCB stars do show evidence of H in their spectra (e.g., V854 Cen; Kilkenny & Marang 1989), leading us to conclude that ASAS 203005–6208.0 is an RCB star.

6.5.5 ASAS 191909–1554.4 (V1942 Sgr)

This star is listed as a slow irregular variable of late spectral type with the name V1942 Sgr in the GCVS. It is the brightest star among our candidates, and as such it is one of the best studied carbon stars to date. According to SIMBAD ASAS 191909–1554.4 is discussed in more than 50 papers in the literature. In the CGCS it is listed as C* 2721. ASAS 191909–1554.4 is detected by *Hipparcos* (HIP 94940) and has a measured parallax of 2.52 ± 0.82 mas (Perryman et al. 1997). This corresponds to a distance $d = 397 \pm 115$ pc and a distance modulus $\mu \approx 8$ mag. ASAS 191909–1554.4 is one of the few Galactic carbon stars with a measured parallax, and it is important for constraining the luminosity function of carbon stars (Wallerstein & Knapp 1998). In their spectral atlas of carbon stars, Barnbaum et al. (1996) identify ASAS 191909–1554.4 as having a spectral type of N5+ C₂5.5. Relative abundance measurements by Abia & Isern (1997) show that ¹²C/¹³C = 30, which is low relative to classical RCB stars. The proximity of ASAS 191909–1554.4 allows its circumstellar dust shell to be resolved in *IRAS* images (e.g., Young et al. 1993), and Egan & Leung (1991) use ASAS 191909–1554.4 and other carbon stars with resolved dust shells and 100 μm excess to statistically argue that each of these stars must be surrounded by two dust shells, one that is old, \sim 10⁴ yr, and one that is produced by a current episode of mass

loss. Recent H I observations by [Libert et al. \(2010\)](#) have shown evidence for the presence of H in the circumstellar shell of ASAS 191909–1554.4. The shallow, symmetric fade of the light curve, along with the N type carbon star spectrum and presence of ^{13}C in the spectrum, lead us to conclude that ASAS 191909–1554.4 is a DYPer. This is the only candidate within our sample for which we can measure the absolute magnitude, since we have the *Hipparcos* parallax measurement. Adopting a maximum light brightness of $V_{\max} = 6.8$ mag, we find that ASAS 191909–1554.4 has $M_V \approx -1.2$ mag. This is roughly 0.4 mag fainter than the faintest DYPers in the MCs ([Tisserand et al. 2009](#)), suggesting that either the luminosity function extends fainter than that observed in the MCs or there is unaccounted for dust extinction towards ASAS 191909–1554.4.

6.5.6 ASAS 162232–5349.2 (C* 2322)

The variability of this star has not been cataloged to date, and it is listed in the CGCS as C* 2322. The relatively slow, symmetric decline and recovery in the light curve of ASAS 162232–5349.2 lead us to classify it as a DYPer variable. The presence of ^{13}C in the spectrum and the single peak in the SED support this classification.

6.5.7 ASAS 065113+0222.1 (C* 596)

The variability of this star has not been cataloged to date, and it is listed in the CGCS as C* 596. The presence of ^{13}C in the spectrum and the single peak in the SED lead us to classify ASAS 065113+0222.1 as a DYPer variable.

6.5.8 ASAS 182658+0109.0 (C* 2586)

The variability of this star has not been cataloged to date, and it is listed in the CGCS as C* 2586. Based on weekly averages of *DIRBE* NIR observations taken over 3.6 yr, [Price et al. \(2010\)](#) list ASAS 182658+0109.0 as a non-variable source. Low-resolution spectra taken with *IRAS* show 11 μm SiC dust emission, which typically indicates significant mass loss from a carbon star ([Kwok et al. 1997](#)). The light curve shows a \sim 5–6 year symmetric decline, and there is clear evidence for ^{13}C in the spectrum. The *IRAS* detection at 60 μm shows a clear IR excess relative to a single temperature blackbody. While there is no evidence for H α , the S/N in our spectrum is low blueward of \sim 4700 Å. We consider ASAS 182658+0109.0 a likely DYPer, though higher S/N spectra are required for a detailed abundance analysis to confirm this classification.

6.6 Discussion

6.6.1 New Candidates From An Expanded Training Set

Table 6.7: New RCB/DYPer candidates using an augmented training set

Name	Other ID	DotAstro ^a ID	$\alpha_{J2000.0}$ ^b (hh mm ss.ss)	$\delta_{J2000.0}$ ^b (dd mm ss.s)	CGCS ^c ID	$P(RCB)$ ^d new	$R(RCB)$ ^e new	Remarks
ASAS 053302+1808.0	IRAS 05301+1805	219583	05 33 01.72	18 07 59.0	980	0.339	380	1
ASAS 081121−3734.9	C* 1086	227950	08 11 21.39	−37 34 54.2	2106	0.145	492	1
ASAS 125245−5441.6	...	237449	12 52 44.92	−54 41 37.5	...	0.309	394	2
ASAS 160033−2726.3	IRXS J160033.8−272614?	243486	16 00 33.16	−27 26 18.5	...	0.142	498	2,3
ASAS 175226−3411.5	IRAS 17491−3410	249729	17 52 25.50	−34 11 28.2	...	0.166	460	
ASAS 200531+0427.2	V902 Aql	259768	20 05 30.83	04 27 12.8	...	0.382	353	2,4

Note. — Remarks: 1. Known carbon star, shows evidence for multiple declines that may be periodic. Semi-regular variable? 2. Shows evidence for a single partially resolved decline or recovery. 3. This star is ∼9'' from the catalogued X-ray source 1RXS J16033.8−272614. The possible association with an X-ray counterpart suggests that it may be a Be star. 4. This star is listed as having an M spectral type in the GCVS. We were unable to find a published reference listing this spectral type and suggest a new spectrum be taken to determine the spectral type.

^aID from the MACC.

^bReported coordinates from the Two Micron All Sky Survey point source catalog (Cutri et al. 2003).

^cID from the General Catalog of Galactic Carbon Stars (CGCS; Alksnis et al. 2001).

^dProbability of belonging to the RCB class when using the augmented training set.

^eRelative rank of $P(RCB)$ when using the augmented training set.

As mentioned in §6.2.1, one of the major strengths of ML classification is that new discoveries may be fed back into the machinery in order to improve future iterations of the classifier. In an attempt to recover more RCB stars and DYPers in the ACVS that were missed in our initial search of the MACC, we created an augmented RCB training set by adding the 8 new RCB stars and DYPers identified in this Chapter to the 17 sources already included in the training set. This augmented training set should increase the likelihood of discovering new candidates, particularly DYPers, of which there were no examples in the original training set.

Using the augmented training set we re-ran the RF classifier from Richards et al. (2012a) on all the ACVS light curves to search for any additional good candidates. We focus our new search on candidates with a significant change in R_{RCB} , which were not examined in the initial search of the MACC. In particular, we visually examine the light curves of all sources with $R(\text{RCB})_{\text{new}} < 500$, $P(\text{RCB})_{\text{MACC}} < 0.1$, and $R(\text{RCB})_{\text{new}} < R(\text{RCB})_{\text{MACC}}$. There are a total of 96 sources that meet these criteria, which were not included in the 472 visually inspected sources from the original MACC. Of these 96, we conservatively select six as candidate RCB stars or DYPers. One is a highly likely RCB star with multiple declines and asymmetric recoveries, three show evidence for a single decline which is only partially sampled, and two are known carbon stars that are likely semi-regular periodic variables. We list the candidates in Table 6.7 with brief comments on each and show their light curves in Figure 6.8.

6.6.2 Future Improvements to the Classifier

Restricting our search for bright RCB stars to only those sources in the ACVS has biased the results of our search. As was mentioned in §6.2.2, there are 7 known RCB stars that show clear variability in their ASAS light curves yet were not selected for inclusion in the ACVS. This suggests that several large-amplitude ASAS variables are missing from the ACVS, presumably including a few unknown RCB stars. This bias can easily be corrected by searching all of ASAS for RCB stars, however, such a search would include significant new challenges as there are ~ 12 million sources in ASAS. In addition, our existing classification framework is not designed to deal with a catalog where the overwhelming majority of sources are not in fact variable. Nevertheless, both of these challenges must be addressed prior to the LSST era. We have developed frameworks that can ingest millions of light curves and are currently experimenting with methods to deal with non-variable sources, the results of which will be presented in a catalog with classifications for all ~ 12 million sources in ASAS (Richards et al., in prep). Furthermore, it has been shown that the use of mid-infrared colors is a powerful discriminant when trying to select RCB stars (Tisserand et al. 2011; Tisserand 2012). While our use of NIR colors is important for selecting RCB stars (see e.g., Soszyński et al. 2009), adding the mid-infrared measurements from the all-sky *WISE* survey will dramatically improve our purity when selecting RCB candidates as several of the Mira and semi-regular variables that served as interlopers in the current search (§6.2.3) would be eliminated with the use of mid-infrared colors.

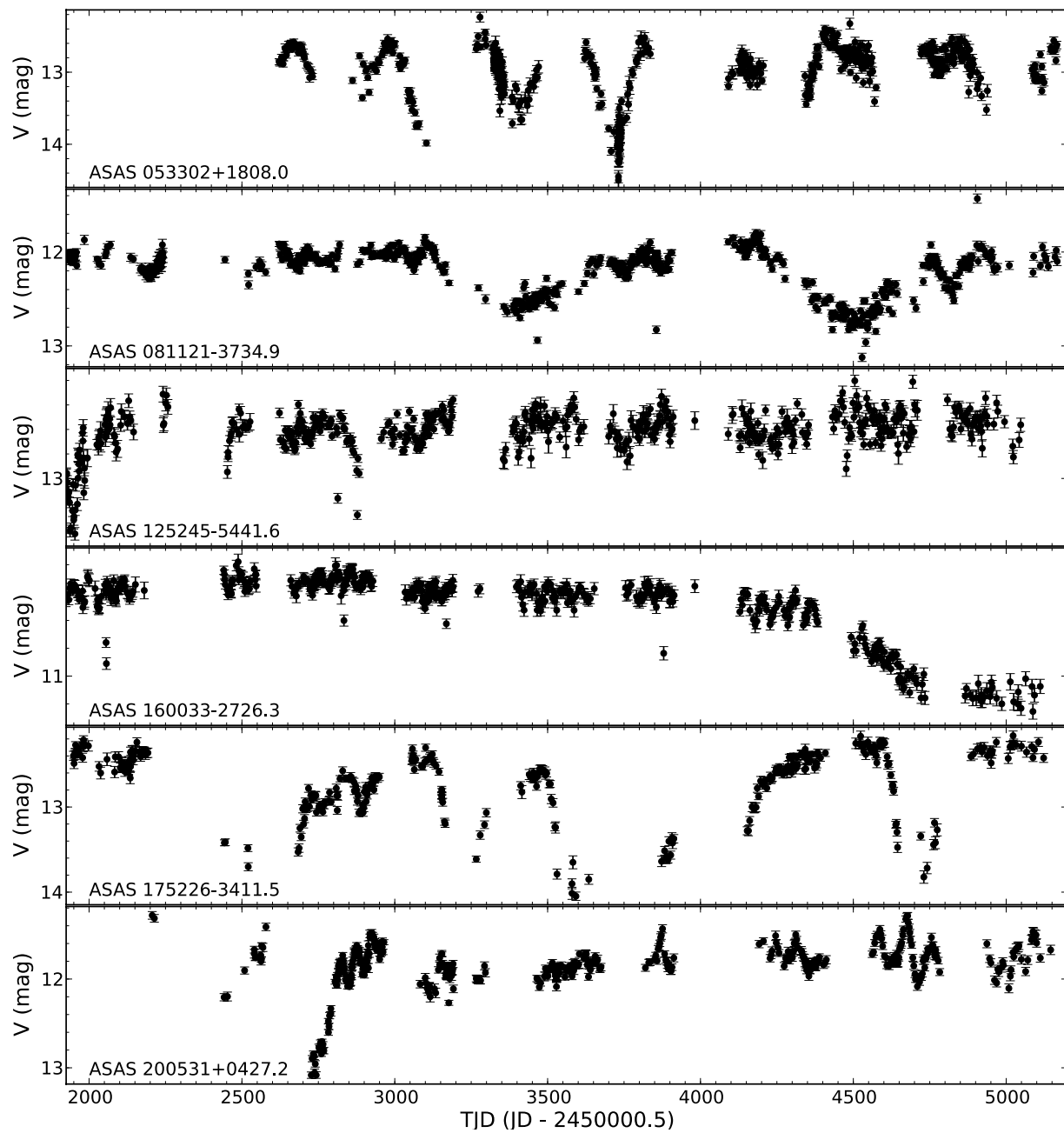


Figure 6.8: ASAS V-band light curves of new RCB candidates found using an augmented training set as described in §6.6.1.

6.7 Conclusions

We have used the 71-feature Random Forest machine-learning ACVS classification catalog from Richards et al. (2012a) to identify likely DYPers and RCB stars in the ACVS catalog. The RF classifier provides several advantages over previous methods to search time-domain survey data for RCB stars and DYPers. Previously successful searches for RCB stars have developed a methodology focused on large amplitude variables that do not show strong evidence for periodicity (e.g., Alcock et al. 2001; Zaniewski et al. 2005; Tisserand et al. 2008). While the RF classifier is capable of capturing the large variations and irregular declines observed in RCB stars, the use of many features allows complex behavior, such as the shape of the decline and recovery, to be captured as well. Another advantage of RF classification is that it does not require hard cuts on any individual light curve feature, which can exclude real RCB stars from the final candidate selection. There are a total of 472 stars with $P(\text{RCB}) > 0.1$ in version 2.3 of the MACC, 15 of which were selected as good RCB or DYPPer candidates after visual inspection and existing spectroscopic information.

Following spectroscopic observations 8 of the good candidates were identified as bona fide RCB stars or DYPers. Four of these, ASAS 170541–2650.1 (GV Oph), ASAS 162229–4835.7 (IO Nor), ASAS 165444–4925.9, and ASAS 203005–6208.0 were confirmed as new RCB stars on the basis of (i) their light curves showing irregular, sharp declines of large amplitude ($\Delta m_V \gg 1$ mag), (ii) carbon rich spectra showing a lack of evidence for H and ^{13}C , and (iii) the mid-infrared excess observed in their SEDs. Four of the candidates, ASAS 191909–1554.4 (V1942 Sgr), ASAS 065113+0222.1, ASAS 162232–5349.2, and ASAS 182658+0109.0 appear to be Galactic DYPers on the basis of (i) shallow, symmetric declines in their light curves occurring at irregular intervals, (ii) carbon rich spectra resembling carbon N stars showing ^{13}C and weak or no H, and (iii) SEDs that show a single peak, but which are too broad to be explained via a single temperature blackbody. With the exception of ASAS 170541–2650.1, all of the new candidates show evidence for periodic variability near maximum light. We incorporate the newly confirmed RCB stars and DYPers into the training set to identify 6 new candidates as likely RCB stars.

Our effort has increased the number of known Galactic DYPers from two to six. While the sample size is small, it appears that DYPers have pulsations with period $P > 100$ d at maximum light, which is longer than the typical timescale for pulsation in RCB stars (see also Alcock et al. 2001). Each of the new RCB stars and DYPers is bright, $V_{\text{max}} \lesssim 12$ mag, which will enable high resolution spectroscopy for future studies of the detailed abundances of these stars. This is particularly important in the case of the four new DYPers, as DY Per itself is the only member of the class which has been observed at high resolution to confirm the lack of H absorption in the spectrum (Keenan & Barnbaum 1997; Začs et al. 2007). If these stars are shown to be H deficient, it would be strong evidence that DYPers are the cool ($T_{\text{eff}} \sim 3500$ K) analogs to RCB stars.

We view the results presented herein as one culmination of a broader effort to extract novel science from the time-domain survey data deluge. Earlier work focused on determining the most suitable ML frameworks for classification and subsequent classification efficiency

(see [Bloom & Richards 2012](#) for review). While production of ML-based catalogs (e.g., ACVS; [Pojmański 2000](#)) have been the norm for over a decade, we know of no concerted effort to validate the predictions of those catalogs. Now having a probabilistic catalog of variable sources ([Richards et al. 2012a](#)) to work with, we can select our demographic priors on classes of interest and also decide just how many false-positives we are willing to tolerate in the name of improved efficiency. In the case of the construction of a new set of very common stars (e.g., RR Lyrae catalog), we might be willing to tolerate a reduced discovery efficiency to preserve a high level of purity. Management of the available resources to follow-up the statements made in a probabilistic catalog becomes the next challenge. We were obviously most interested in finding new exemplars of two rare classes and thus tolerated a high impurity. In the discovery and characterization of several bright RCB stars and DYPers, the payoff of the efficient use of follow-up resources enabled by probabilistic classification is evident.

The classification taxonomy of variable stars clearly conflates phenomenology (e.g., “periodic”) within a physical understanding (“pulsating”) of the origin of what is observed. And while phenomenologically-based mining around an envelope of class prototypes can turn up new class members, we have shown that the diversity of RCB stars and DYPers demands an expanded approach to discovery. We speculate that the richness and connections of the feature set in the ML search may be also capturing some of the phenomenological manifestations of the underlying physics, however nuanced, that we cannot (yet) express.

Acknowledgments

A version of this chapter appears in the *Astrophysical Journal*, 2012, 755, 98.

During the writing of this chapter I was supported by a National Science Foundation Graduate Research Fellowship, for which I am grateful for the funding.

I thank an anonymous referee for comments on the ApJ manuscript that have helped to improve this chapter. I thank A. Filippenko for obtaining the Lick telescope time needed to observe several of the RCB and DYPers, while he and P. Nugent contributed to the Keck proposal and assisted in the observations. I thank K. Clubb, A. Morgan, D. Cohen and I. Shivvers for assisting in the Keck and Lick observations. I thank F. Walter for help with the scheduling and reduction of RC spectrograph data, and I thank R. Hernandez, A. Miranda, and M. Hernandez for carrying out the RC spectrograph observations.

Chapter 7

A Systematic, Spectroscopic Survey of Optical Variability

We present the results of a systematic spectroscopic survey of stellar variability. Variable sources were selected from repeated Sloan Digital Sky Survey (SDSS) observations of Stripe 82, and spectroscopic observations were obtained with Hectospec on the 6.5-m Multi-Mirror Telescope. In sum, spectra were obtained for ~ 8000 stellar variables (4741 observed with Hectospec and 3104 from the SDSS archive), for which we measured T_{eff} , $\log g$, and [Fe/H] using the Segue Stellar Parameters Pipeline (SSPP). Examining the full sample of $\sim 67k$ variables in Stripe 82, we show that the vast majority of photometric variables are consistent with main-sequence stars, even after restricting the search to high galactic latitudes. From the spectroscopic sample we confirm that most of these stellar variables are G and K dwarfs, though there is a bias in the output of the SSPP preventing us from discovering M type variables. We are unable to identify the dominant source of variability for these stars, but eclipsing systems and/or star spots are the most likely explanation. We develop a machine-learning model that can determine T_{eff} , $\log g$, and [Fe/H] without obtaining a spectrum. Instead, the random-forest-regression model uses SDSS color information and light-curve features to infer stellar properties. We detail how the feature set is pruned and the model is optimized to produce final predictions of T_{eff} , $\log g$, and [Fe/H] with a typical scatter of 165 K, 0.42 dex, and 0.33 dex, respectively. We further show that for the subset of variables with at least 50 observations in the g band the typical scatter reduces to 75 K, 0.19 dex, and 0.16 dex, respectively. We consider these results an important step on the path to the efficient and optimal extraction of information from future time-domain experiments, such as the Large Survey Synoptic Telescope. We argue that this machine learning framework, for which we outline future possible improvements, will enable the construction of the most detailed maps of the Milky Way ever created.

7.1 Introduction

The falling costs of large-format CCDs, computational processing power, and digital data storage has driven significant community interest in new astronomical studies of the time-domain. The past \sim decade has seen the creation of several new time-domain surveys exploring everything from extrasolar planets in the local neighborhood (e.g., [Berta et al. 2012](#)) to the most distant observed stellar explosions (e.g., [Jones et al. 2013](#)), and a great deal more in between. These efforts will ultimately culminate with two major observatories, GAIA ([Perryman et al. 2001](#)) and the Large Survey Synoptic Telescope (LSST; [Ivezić et al. 2008a](#)), that will precisely track the motion and variability of billions of stars throughout the Milky Way. While the onslaught of time-domain surveys promises to solve several outstanding questions, the rapidly increasing rate at which we acquire and process observations has already begun to outpace traditional analysis methods. In particular, it is becoming clear that visual inspection of new discoveries must be reserved for only the most interesting sources.¹ In order to remove humans from the discovery and classification process, sophisticated algorithms capable of performing as well or better than human experts must be developed.

Machine-learning methods provide a promising solution for the necessary abstraction of the discovery and classification process.² The algorithms defining these methods are built to learn relationships between observables and parameters of interest. The learning is achieved using objects with known properties (such as a class for variable stars, or a redshift for a galaxy), which is called the training set. Once a machine-learning model has been trained, it can rapidly apply its knowledge to new data providing predictions of the quantities of interest. As more data are obtained, and the quality and scope of the training set is improved, the machine can refine its knowledge and model of the dataset, providing ever more accurate predictions. Furthermore, unlike humans, machine-learning models can instantaneously and automatically produce predictions about new data via a fully reproducible process. Machines can also produce calibrated, probabilistic predictions, which are essential for understanding the confidence of any statements made about sources described via a complex multidimensional space. There is now a growing set of examples whereby machine learning has been successfully applied to the classification (e.g., [Richards et al. 2011](#); [Dubath et al. 2011](#); [Richards et al. 2012a](#)) and discovery (e.g., [Brink et al. 2013](#); [Miller et al. 2012](#)) of sources in astronomical time-domain datasets.

In this Chapter we present the results from the first-ever systematic spectroscopic survey of stellar variability. Our purpose is to explore the demographics of stellar variability, and to develop methods that can infer the spectroscopic properties of stars from their light curves. Candidate variables were selected from the repeated scans of Stripe 82 by the Sloan Digital Sky Survey (SDSS), and observations were obtained using Hectospec on the Multi-Mirror

¹For example, the Palomar Transient Factory (PTF; [Rau et al. 2009](#); [Law et al. 2009](#)) discovers \sim 1 million transient candidates during every night of operations. Visual inspection of these candidates by astronomical experts would prove intractable, instead, the discovery process has been off-loaded to machines ([Bloom et al. 2012](#)).

²For a primer on machine learning we refer the interested reader to [Hastie et al. \(2009\)](#).

Telescope. We detail the design of the survey, and how we measure light-curve properties and the fundamental atmospheric parameters, T_{eff} , $\log g$, and [Fe/H], of our spectroscopic targets. The primary results discussed herein concern the development of a new machine-learned regression model capable of predicting T_{eff} , $\log g$, and [Fe/H] without any spectroscopic observations. We envision these tools will prove extremely valuable for future time-domain surveys.

7.2 Survey Design

7.2.1 Sloan Digital Sky Survey – Stripe 82

The Sloan Digital Sky Survey (SDSS; e.g., Ahn et al. 2013) is a monolithic, static-sky survey that has mapped the northern hemisphere to unprecedented depth in the $ugriz$ optical filters. To date SDSS has imaged $\sim 14,500$ sq. deg. detecting more than 1 billion sources. The SDSS telescope is equipped with a multi-object spectrograph, in addition to its wide-field imager, and the survey has obtained more than 2.5 million spectra, making SDSS truly unique among all existing and planned surveys.

Aiming to construct co-added images that extend significantly fainter than the normal survey, SDSS repeatedly scanned the equatorial Stripe 82 region ($20^{\text{h}}00^{\text{m}} < \alpha_{\text{J2000.0}} < 04^{\text{h}}08^{\text{m}}$, $-01^{\circ}16^{\text{m}} < \delta_{\text{J2000.0}} < 01^{\circ}16^{\text{m}}$) during the first decade of the survey. During the first phase of the survey, known as SDSS-I, Stripe 82 was observed 1–2 times every fall producing a median of 10 observations for the ~ 1.4 million unresolved point sources in the region (Ivezić et al. 2007). In the following 3 years, \sim weekly observations of Stripe 82 were made during four-month long observing seasons as part of the SDSS-II Supernova Survey (Frieman et al. 2008). The ~ 9 yr baseline and observations in the $ugriz$ filters make Stripe 82 the closest existing dataset to what the LSST will eventually produce. Supernova surveys cannot compete with the long time baseline of Stripe 82, while microlensing surveys, which have more observations than Stripe 82 and at higher cadence, are focused on very special locations in the sky such as the Galactic bulge and the Magellanic Clouds. In contrast, Stripe 82 extends from the vicinity of the Galactic plane ($b \approx -15^{\circ}$) to high galactic latitudes ($b \approx -65^{\circ}$).

The combined SDSS-I and II observations of Stripe 82 yield light curves with a median rms scatter $\lesssim 0.02$ mag in the $ugri$ bands to a depth of ~ 19 mag (Sesar et al. 2007). This makes Stripe 82 an extremely useful resource for the study of the variable optical sky enabling a multitude of time-domain studies. While developing a large catalog of standard stars (Ivezić et al. 2007), researchers at the University of Washington also identified variable sources (Sesar et al. 2007) and made their variable point-source catalog (hereafter UW VSC) publicly available.³ The UW VSC contains 67,507 candidate variable sources which were selected based on the following criteria:

³Summary statistics and light curves of the selected variable candidates can be found on the [UW VSC website](#).

1. The source is unresolved and has a photometric uncertainty ≤ 0.05 mag in at least one of the *ugriz* bands.
2. The source is not flagged by the SDSS imaging pipeline as bright, saturated, blended, or being located on the edge of the detector.
3. There are at least 10 observations of the source in the *g* and *r* bands.
4. The median *g* band brightness of the source is ≤ 20.5 mag.
5. The source has a root-mean-scatter > 0.05 mag and the χ^2 per degree of freedom > 3 in *both* the *g* and the *r* bands.

We adopt the UW VSC as the basis for our spectroscopic survey of variability for several reasons: (i) it is one of the largest existing variable star catalogs, (ii) it is the closest existing analog to the dataset that will ultimately be delivered by the LSST, (iii) it covers a large range of galactic latitudes, and (iv) there are several existing studies that have classified RR Lyrae stars, M dwarfs, and quasars which will facilitate comparisons to our spectroscopic and photometric classifications (e.g., [Sesar et al. 2007, 2010](#); [Butler & Bloom 2011](#); [MacLeod et al. 2011](#); [Becker et al. 2011](#); [Davenport et al. 2012](#); [Süveges et al. 2012](#)). Color-color diagrams of all sources in the UW VSC are shown in Figure 7.1. In Table 7.1 we summarize the distribution of all sources in the UW VSC based on their brightness and location in the *u* – *g*, *g* – *r* color-color diagram (*ugr* CC diagram). Similar to [Sesar et al. \(2007\)](#), it is clear from Figure 7.1 that the majority of sources are located in regions II and V (see Table 7.1), which correspond to low-redshift quasars and normal stars, respectively. Interestingly, [Sesar et al.](#) found that the majority of variable sources at the depth of SDSS observations are low-redshift quasars, though only the SDSS-I dataset was available at that time. The joint SDSS-I and II observations show that the overwhelming majority of sources reside within the main stellar locus.

7.2.2 Hectospec

We employed the Hectospec instrument ([Fabricant et al. 2005](#)) on the 6.5-m Multi-Mirror Telescope (MMT) to obtain spectra of a large, systematically-selected sample⁴ of sources in Stripe 82. Hectospec is a 300 fiber-fed, multi-object spectrograph with a circular, 1 degree diameter field of view (FOV). The fibers are positioned in a radial configuration extending inwards from the outer edge of the FOV. Fibers are held in place by magnets following their placement by a pair of high-speed, six axis robots capable of changing from one observing configuration to another in ~ 5 min ([Fabricant et al. 2005](#)). In addition to the rapid field configurations, a major advantage of this system is that mechanical masks, such as those used by SDSS, do not need to be machined prior to observing. The corresponding disadvantage is that the “fisherman on the pond” radial fiber configuration results in a geometry where targets can conflict with one another requiring two fibers to cross, which is not possible. Thus, while 300 fibers are available for observations, if there are only 300 targets within a single FOV it is highly unlikely they can all be observed in a single pointing. As a result it is

⁴See §7.2.3 for further details.

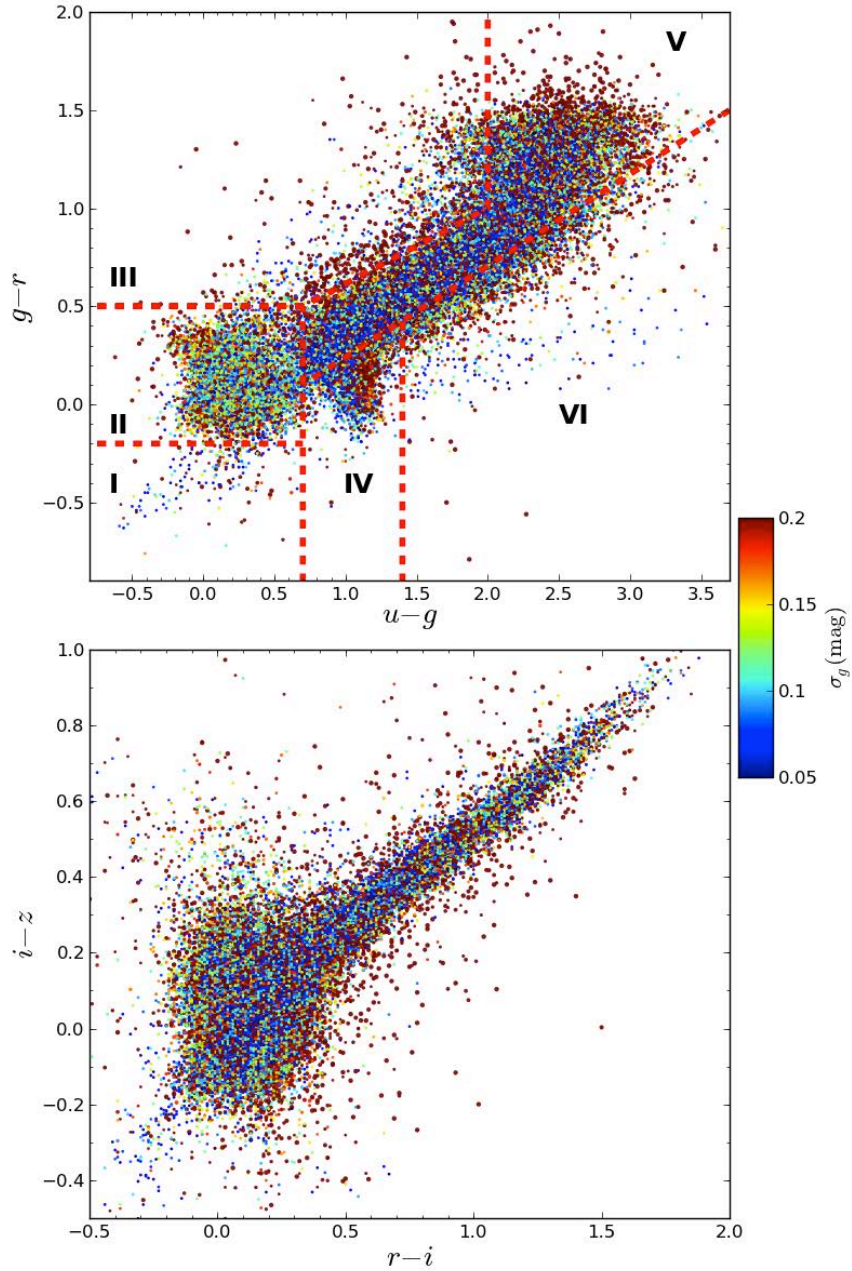


Figure 7.1: Color-color diagrams showing the *de-reddened* mean magnitude of all the Stripe 82 variables identified in the UW VSC. The sources are colored based on the standard deviation of their light curves in the g band. *Top:* $u-g$, $g-r$ color-color diagram. The six regions identified in Sesar et al. (2007) are outlined by the dashed red line. For each region the variability is believed to be dominated by the following: **I** – white dwarfs, **II** – low-redshift ($z \lesssim 2.5$) quasars, **III** – white dwarf-M dwarf binary stars, **IV** – RR Lyrae stars, **V** – normal stars, **VI** – high-redshift ($z \gtrsim 3$) quasars. Most of the high-amplitude variables are located off the main stellar locus. *Bottom* – $r-i$, $i-z$ color-color diagram.

often the case that only \sim 175–200 targets can be observed in a single pointing (N. Caldwell, private communication). Typically, \sim 30 fibers are reserved during any given observation to observe empty patches of sky in order to subtract the sky spectrum from that of the targets, meaning only \sim 270 fibers are available in a single pointing to observe science targets.

The Hectospec detector consists of two E2V model 42-90 4608 \times 2048 CCDs ([Fabricant et al. 2005](#)). Each detector records photons from 150 fibers, which are dispersed along the long axis of the CCDs. The readout noise and dark current for the instrument are low. The CCDs are read out through four amplifiers in 46 s. The spectrograph has two gratings: a 270 groove mm $^{-1}$ grating blazed at 5000 Å and a 600 groove mm $^{-1}$ grating blazed at 6000 Å. The 270 groove mm $^{-1}$ grating, which we will use for spectral classification, provides a dispersion of 1.2 Å pixel $^{-1}$ and a resolution of \sim 6.2 Å FWHM, which is suitable for measuring basic atmospheric properties.

7.2.3 Target Selection

There are numerous factors to consider while selecting targets for a spectroscopic survey, however, to maximize the efficiency of a multi-object spectrograph, such as Hectospec, target density stands out as a primary concern. It would require at least 400 pointings of Hectospec to cover the entire \sim 315 deg 2 area of Stripe 82. Needless to say, such an endeavor would be inefficient and a waste of time. Survey optimization requires that our observations are biased towards the Galactic plane. Fortunately, \sim 40% of all the sources identified in the UW VSC are located in a 10 deg. strip extending from an R.A. of 300° to 310° (see Table 7.1). Thus, we selected this region as the focus of our survey in order to maximize the number of occupied Hectospec fibers per pointing.

Given the dual goals of the survey to obtain a minimally-biased spectroscopic view of variability and to improve photometric classifiers of variable stars we employ additional selection criteria beyond the spatial location of the variable sources. For a fixed observing time, the spectra of brighter sources will have a higher signal-to-noise ratio (SNR) than the spectra of fainter stars. As a result we elect to only observe sources with a mean *observed r* band magnitude < 19 mag, which reduces the total number of potential targets from 26,419 to 14,994. This magnitude cut should provide a SNR \approx 10 for 19th mag sources in a 10 min exposure on the 6.5-m MMT. When classifying light curves the single most powerful discriminant in separating one class from another is the best-fit period ([Richards et al. 2012a](#)). For sources with a random cadence, such as those in the UW VSC, the accuracy of the fit improves as the number of observations increases, and typically $\gtrsim 20$ observations are required to reliably measure the frequency of a periodic variable (C. Klein, private communication). We wish to obtain spectra of the most frequently observed sources, while also having a good chance to measure their periods, so we require all targets to have ≥ 24 observations in each of the *g*, *r*, and *i* bands. This further culls the final target list to 9635 unique sources.

The Hectospec targeting software assigns fibers in each pointing based on the user-supplied relative priority of each individual target. This scheme, which assigns fibers to as many sources in the highest priority category as possible before assigning as many fibers in the

Table 7.1: Summary of Variable Sources in Stripe 82

mag	$N_r \geq 30^a$	$N_{gri} \geq 24^b$	QSO ^c	Per ^d	Amp ^e	I ^f	II ^g	III ^h	IV ⁱ	V ^j	VI ^k
$300^\circ < \text{R.A.} \leq 310^\circ$ (26419 sources total)											
$r \leq 15$	107	153	1	5	19	0	1	0	47	263	41
$15 < r \leq 16$	398	567	2	22	46	0	0	1	61	733	88
$16 < r \leq 17$	825	1193	6	30	143	0	1	10	100	1476	165
$17 < r \leq 18$	1662	2327	12	40	240	1	8	31	121	2907	397
$18 < r \leq 19$	3781	5395	65	27	503	6	57	304	203	7194	778
$19 < r \leq 22$	4985	7036	281	18	735	34	427	310	420	9534	700
$\text{R.A.} > 310^\circ \cup \text{R.A.} \leq 300^\circ$ (41088 sources total)											
$r \leq 15$	543	611	11	78	81	0	1	3	115	849	84
$15 < r \leq 16$	1275	1361	21	182	181	1	2	7	145	1829	123
$16 < r \leq 17$	2630	2742	59	235	309	2	27	33	202	3301	244
$17 < r \leq 18$	4225	4388	205	344	558	12	169	78	261	5333	351
$18 < r \leq 19$	6297	6641	1137	279	902	18	1059	476	249	8020	624
$19 < r \leq 22$	12643	13116	6741	245	2270	124	6994	545	817	8352	638
S82 Total ^l	39371	45530	8541	1505	5987	198	8746	1798	2741	49791	4233

^aNumber of sources with 30 or more observations in the r band and 24 or more observations in both the g and i bands.

^bNumber of sources with 24 or more observations in each of the g , r , and i bands.

^cNumber of sources with quasar-like light curves following the method of Butler & Bloom (2011).

^dNumber of sources with strong periodicity in their light curves.

^eNumber of sources with high-amplitude variability, defined as $r_{\text{MAD}} > 0.15$ mag.

^fNumber of sources with *de-reddened* colors consistent with region I in the $u - g, g - r$ color-color diagram, see Figure 7.1.

^gNumber of sources with *de-reddened* colors consistent with region II.

^hNumber of sources with *de-reddened* colors consistent with region III.

ⁱNumber of sources with *de-reddened* colors consistent with region IV.

^jNumber of sources with *de-reddened* colors consistent with region V.

^kNumber of sources with *de-reddened* colors consistent with region VI.

^lTotal for all of Stripe 82.

second highest category and so on, allows us to ensure that the brightest and best observed sources are the most likely to be observed. In the end, we adopted 11 levels of prioritization, which are summarized in Table 7.2. Generally speaking, we assigned higher rank (priority 1 corresponds to the highest rank) to brighter sources with more observations. We also identified targets of interest, sources that stand out regardless of their brightness or the total number of times they were observed, and elevated their priority as well. The three categories of interest are: (i) high-amplitude sources, which we define as those having a median of absolute deviation (MAD), a robust measure of the scatter about the median, in the r band > 0.15 mag, (ii) sources that are likely periodic,⁵ and (iii) sources with light curves that are consistent with the variability signature of quasars.⁶ This later group is of interest because quasars are difficult to find at low Galactic latitudes (e.g., Butler & Bloom 2011), yet they serve as ideal probes of the interstellar medium. Further, stars that exhibit variability patterns similar to quasars may feature similar physics: namely a compact object surrounded by an accretion disk. For the targets of interest there are 300 high-amplitude sources, 124 likely periodic variables, and 73 quasar-like sources which meet all of our other target criteria. A summary of targets of interest as a function of magnitude can be found in Table 7.1. Finally, we note that the 3 SDSS spectroscopically-confirmed quasars in the UW VSC that match our targeting criterion were excluded from our target list.

Aside from priority 2.5, all targets are exclusively assigned membership to only a single priority class. The detailed criteria for the priorities we assigned to each target are as follows:⁷

- Priority 1 targets are those determined to be quasar-like, likely periodic variables, or bright sources with either mean *observed u, g, or r* ≤ 15 mag, or $i \leq 14.8$ mag, or $z < 14.7$ mag.⁸
- Priority 2 targets are those outside the main stellar locus in color-color space (see Figure 7.2) or those with $ugriz \leq 16$ mag.
- Priority 2.5 targets are either extremely bright, $ugriz \leq 14.6$ mag, or quasar-like, or likely periodic variables, or high-amplitude variables. Note that inclusion as a Priority 2.5 target is the only way a source could be added to the target catalog more than once.
- Priority 3 targets have been observed ≥ 30 times in the r band and have $ugriz \leq 17$ mag.

⁵Periodicity was analyzed using a generalized Lomb-Scargle periodogram (Lomb 1976; Scargle 1982; Zechmeister & Kürster 2009) to analyze each source (see Richards et al. 2011 for more details on our Lomb-Scargle periodogram implementation). Sources with a Lomb-Scargle power spectral density > 16.5 were selected as likely periodic variables.

⁶We identify sources with $\chi_{\text{QSO}}^2/\nu > 5$ as sources similar to quasars (see Butler & Bloom 2011 for a definition of χ_{QSO}^2/ν).

⁷Recall that all targets are required to have an R.A. between 300° and 310° , mean observed $r \leq 19$ mag, and ≥ 24 observations in each of the gri bands.

⁸Magnitude cuts are brighter in the redder bands to prevent an unbalanced selection of very-red objects, which are difficult to classify with low-resolution spectra (e.g., Lee et al. 2008a). For all priorities below the same offsets apply, such that $ugriz \leq m$ mag means that the *observed* mean magnitude in u, g , or $r \leq m$ mag, or $i \leq m - 0.2$ mag, or $z \leq m - 0.3$ mag. A source only needs to be brighter than these limits in a single band for inclusion in a given priority level.

Table 7.2: Summary of Hectospec Target Priorities

Priority	Selection Criteria	Targeted	Observed	%
1	$ugriz < 15 \cup \text{QSO} \cup \text{P}$	423	240	56.7
2	$(ugriz > 15 \cap ugriz < 16) \cup (\textcircled{O}*)$	1189	680	57.2
2.5	$\text{QSO} \cup \text{P} \cup r_{\text{MAD}} > 0.15$	497	149	30.0
3	$ugriz > 16 \cap ugriz < 17 \cap *$	1092	612	56.0
4	$ugriz > 16 \cap ugriz < 17 \cap *$	448	212	47.3
5	$ugriz > 17 \cap ugriz < 18 \cap *$	1930	990	51.3
6	$ugriz > 17 \cap ugriz < 18 \cap *$	758	352	46.4
7	$ugriz > 18 \cap r < 18.5 \cap *$	749	331	44.2
8	$ugriz > 18 \cap r < 18.5 \cap *$	342	160	46.8
9	$ugriz > 18 \cap r > 18.5 \cap *$	1872	734	39.2
10	$ugriz > 18 \cap r > 18.5 \cap *$	829	281	33.9
Total		10129	4741	46.8

Note. — All targets are required to have $300^\circ < \text{R.A.} \leq 310^\circ$, a mean *observed r* band magnitude ≤ 19 mag, and at least 24 observations in each of the *g*, *r*, and *i* bands. The selection criteria symbols mean the following: **QSO** – light curve is consistent with being a quasar following the method of [Butler & Bloom \(2011\)](#); **P** – light curve shows strong periodicity; **rMAD>0.15** – the median absolute deviation in the *r* band is greater than 0.15 mag; **N_r ≥ 30** – there are 30 or more observations in the *r* band; ***** – the *de-reddened* colors are consistent with the stellar locus, this is roughly equivalent to region V in the *u-g*, *g-r* color-color diagram as defined in [Sesar et al. \(2007\)](#), the precise boundaries are shown in Figure 7.2; **∅ *** – colors are outside the main stellar locus; **ugriz < m** – the *observed* mean mag of the source is brighter than *m* mag in the *u* or *g* or *r* bands, or brighter than *m* – 0.2 in the *i* band, or brighter than *m* – 0.3 mag in the *z* band; **ugriz > m** – same as the previous designation except the sources are fainter than *m*. Lastly, note that the targets with priority 2.5 are, by definition, repeated elsewhere in the target list. This was done to provide a test of any systematic issues associated with the reduction pipeline (see text).

- Priority 4 targets have $ugriz \leq 17$ mag.
- Priority 5 targets have been observed ≥ 30 times in the r band and have $ugriz \leq 18$ mag.
- Priority 6 targets have $ugriz \leq 18$ mag.
- Priority 7 targets have been observed ≥ 30 times in the r band and have $r \leq 18.5$ mag.
- Priority 8 targets have $r \leq 18.5$ mag.
- Priority 9 targets have been observed ≥ 30 times in the r band and have $r \leq 19$ mag.
- Priority 10 targets have $r \leq 19$ mag.

While priority 2.5 sources were potentially observed twice, in practice this rarely happened since the observations were not complete for sources with priority 1. Furthermore, the repeated observations of a few targets provides a check of the systematic differences of observations made through different fibers and in some cases on different CCDs. In total there were 10,129 total potential targets selected for Hectospec observations (see Table 7.2). Figure 7.2 shows the distribution of all our potential targets throughout color-color space. The distribution of targets reasonably reflects that of Stripe 82 as a whole (compare with Figure 7.1), with the exception of blue sources in region II of the ugr CC diagram. The magnitude cuts significantly reduce the number of candidate quasars (see Table 7.1), which are additionally more difficult to identify at low Galactic latitudes.

Limited telescope access and fiber conflicts (see §7.2.2) prevent us from possibly obtaining spectra of all 10,129 targets. Optimizing fiber positioning over the 40 pointings we use to cover the survey area we could obtain at most 7038 total spectra; our actual yield was a few thousand lower than this (see Table 7.2 and §7.3.1).

7.3 Observations and Reductions

7.3.1 Hectospec Observations

Hectospec is operated in service mode: observers from each approved program in a given semester travel to the MMT to execute queue observations. In this way time lost to weather can be evenly spread across all programs. While our 40 adopted fields could have been fully observed over the 3 nights allocated to our program, the shared weather losses ensured that some fields would not be observed.

Observations for our program, which are summarized in Table 7.3, were executed during 2011 Jun. and Jul. We observed each field with 2×300 s exposures to facilitate cosmic ray rejection. On one night, at the discretion of the service observers, there were a few fields observed with 3×300 s exposures taken during non-photometric conditions. On another night, the total exposure time was increased to 2×420 s. All observations were made using the 270 grooves mm^{-1} grating, providing a dispersion of 1.2 Å and a wavelength coverage from $\sim 3700\text{-}9200$ Å. In total, there were 26 observed fields for a total of 4741 spectra.

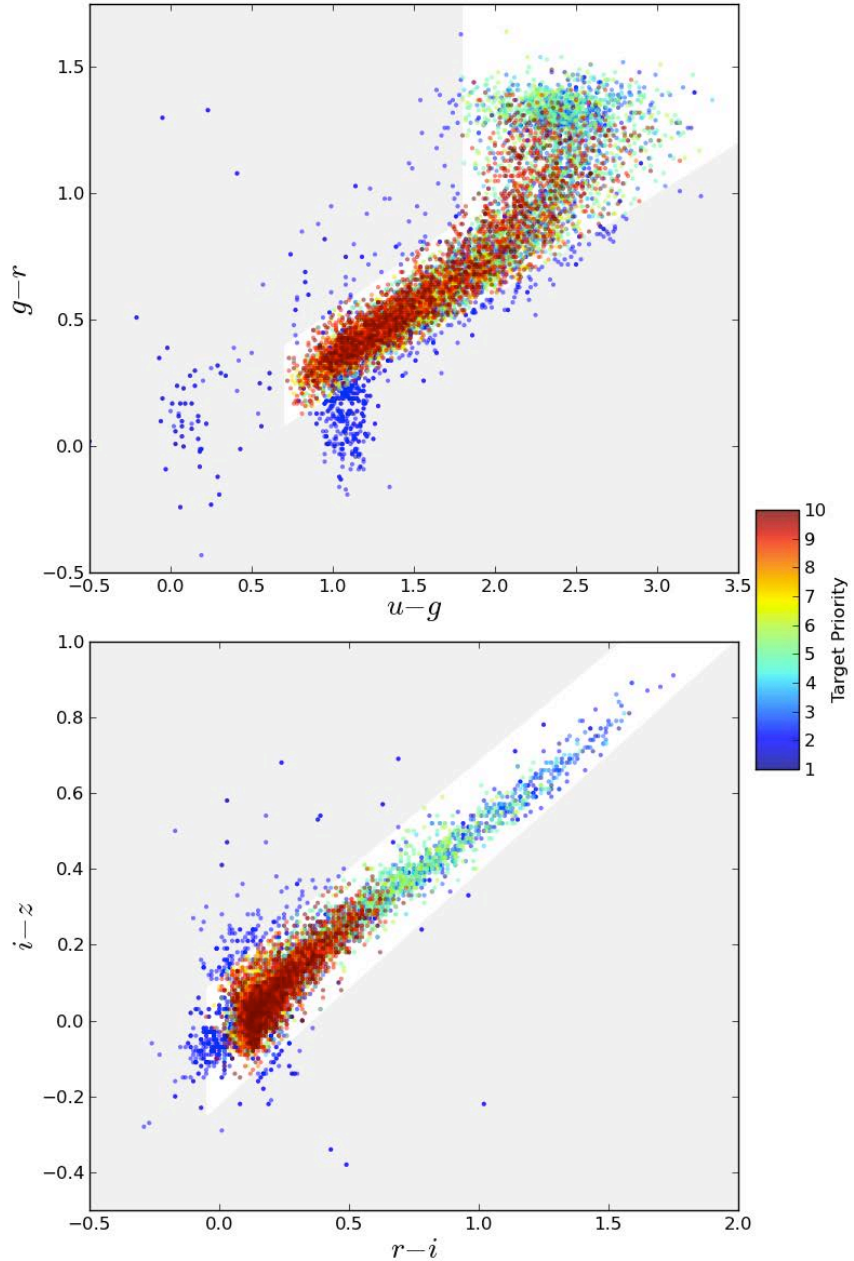


Figure 7.2: Color-color diagrams showing the $\sim 10k$ potential Hectospec targets. The grey shaded area shows the region in color-color space considered outside the main stellar locus for targeting purposes (\ominus * in Table 7.2). All sources in this region have either priority 1 or 2. The distribution of targets reasonably reflects the entire SDSS sample (see Figure 7.1), with the exception of low-redshift quasars, which are less prevalent due to the magnitude cuts and low-galactic latitude of the Hectospec fields. *Top:* ugr CC diagram. *Bottom:* riz CC diagram.

Table 7.3: Summary of Hectospec Observations

UT Date	Field	RA (J2000.0)	Dec (J2000.0)	Exp. Time ^a (s)	Airmass	Seeing (")	N_{spec}
2011-06-08.441	3	20:16:38.47	-00:50:03.32	600.0	1.185	0.65	198
2011-06-08.456	5	20:06:50.02	+00:46:59.29	600.0	1.175	0.65	201
2011-06-09.391	17	20:28:29.76	+00:49:04.43	600.0	1.243	0.86	190
2011-06-09.376	8	20:13:19.60	+00:47:10.78	600.0	1.256	0.86	194
2011-06-10.328	23	20:23:02.66	-00:46:10.10	600.0	1.566	0.91	186
2011-06-10.343	24	20:19:19.46	-00:46:29.35	600.0	1.438	0.91	196
2011-06-10.358	25	20:18:42.43	+00:46:53.25	600.0	1.328	0.91	210
2011-06-10.373	26	20:14:04.20	-00:47:16.61	600.0	1.281	0.91	205
2011-06-10.389	27	20:16:57.74	-00:02:43.31	600.0	1.232	0.91	184
2011-06-10.410	29	20:11:25.30	-00:50:06.78	600.0	1.199	0.77	181
2011-06-10.424	30	20:13:00.47	-00:05:46.31	600.0	1.178	0.77	197
2011-06-10.454	32	20:09:20.93	+00:00:31.04	600.0	1.186	0.77	195
2011-06-11.347	1	20:20:47.66	+00:09:52.50	600.0	1.387	1.11	159
2011-06-11.318	34	20:08:45.75	+00:46:24.12	600.0	1.517	1.11	203
2011-06-11.333	38	20:05:09.17	-00:43:20.15	600.0	1.425	1.11	197
2011-06-12.354	10	20:35:48.40	-00:15:04.47	600.0	1.403	1.01	147
2011-06-12.382	13	20:30:01.50	-00:42:20.61	600.0	1.270	1.01	156
2011-06-12.396	14	20:30:59.07	+00:45:14.06	600.0	1.214	1.01	180
2011-06-12.411	15	20:04:11.70	+00:16:40.64	600.0	1.175	1.01	178
2011-06-12.427	16	20:34:01.51	+00:40:20.90	900.0	1.172	1.01	169
2011-06-12.447	18	20:28:37.06	-00:00:15.05	900.0	1.176	1.01	164
2011-06-12.276	2	20:15:40.00	+00:32:00.15	600.0	2.075	1.01	166
2011-06-14.290	19	20:26:28.18	-00:42:38.26	600.0	1.908	1.01	170
2011-06-14.305	20	20:24:48.79	+00:03:39.71	600.0	1.679	1.01	166
2011-06-14.275	37	20:04:25.10	+00:49:48.15	600.0	1.854	1.01	179
2011-07-08.427	21	20:25:25.79	+00:48:02.16	840.0	1.252	0.89	170

Note. — All observations were obtained with the 270 grooves mm⁻¹ grating, which provides spectroscopic coverage from \sim 3700–9200 Å.

^aThe program called for 2×300 s exposures for each field, however, the service observers elected to increase the exposure times or take 3 exposures on nights with partial cloud cover.

7.3.2 Reductions

Spectroscopic reductions were performed using the **E-specroad** reduction pipeline.⁹ The pipeline begins by bias subtracting, trimming, and correcting bad pixels from the two-dimension science spectra, before correcting for gain variations between the four amplifiers. Apertures to extract each of the 300 spectra are then manually defined using the **IRAF**¹⁰ procedure **apedit**. Following aperture extraction, spectra are flat-fielded and a wavelength solution is applied. Cosmic rays are identified and affected pixels are replaced with values interpolated from unaffected neighboring pixels. At this stage **E-specroad** determines a through-put correction for each aperture, a correction is made for a known red light leak in the instrument (see [Fabricant et al. 2005](#)), and absorption due to the atmospheric A and B bands is corrected. Finally, the background from each fiber spectrum is removed using the average spectrum of nearby sky fibers taken during the observations. As a last step, the **IRAF** task **DOSKYXCSAO** is performed on each of the final extracted spectra to measure the redshift following the cross-correlation of the spectrum against several template spectra of stars, galaxies, and quasars.

We employ a two step procedure to flux calibrate the spectra at this stage. All spectra are flux-calibrated using a spectrum of the spectrophotometric standard star BD+28 4211, which was taken on 2011-06-12. After this initial correction, the spectra are further warped to match their median photometric colors based on the SDSS Stripe 82 observations. It is important to note that the sources selected for this survey have variable spectra, thus, correcting the spectra to the source’s median colors does not necessarily accurately reflect the spectrum on the night the source was observed. That being said, our primary goal is to measure atmospheric parameters from the spectra, which is done after removing the stellar continuum (see below). Thus, the corrections to the median photometric state of the star should not prove detrimental to our program. Visual inspection of the spectra at this stage revealed that several sources had a sharp kink around $\sim 8100 \text{ \AA}$ with continua rising at redder wavelengths. This effect is due to the red light leak in the Hectospec detector, and while the reduction pipeline has a correction procedure, the correction is nonuniform across the focal plane (N. Caldwell, private communication). To correct this effect we define the true stellar continuum as a spline fit to the median photometry of the source. This continuum is then divided by a second order spline fit to the reduced spectrum redward of 8200 \AA , which produces a correction factor. The reduced spectrum is multiplied by the correction factor, after which the entire spectrum is once again warped to its median observed photometric colors. This procedure leaves considerable uncertainty regarding the true continuum redward of 8200 \AA , however, this should not greatly affect the final results as the procedure used to determine the atmospheric parameters relies exclusively on spectral features blueward of

⁹**E-specroad** is based on the **specroad** software package developed by the Harvard Center for Astronomy, which was designed to reduce Hectospec data.

¹⁰IRAF is distributed by the National Optical Astronomy Observatory, which is operated by the Association of Universities for Research in Astronomy (AURA) under cooperative agreement with the National Science Foundation.

8200 Å.

7.3.3 Stellar Atmospheric Parameters Estimation

To estimate stellar parameters, namely effective temperature, surface gravity, and metallicity, we employ an adapted version of the SDSS Segue Stellar Parameters Pipeline (SSPP; Lee et al. 2008a,b; Allende Prieto et al. 2008). The SSPP adopts and combines several methods to determine the fundamental atmospheric parameters, T_{eff} , $\log g$, and [Fe/H], for AFGK-type stars based on medium-resolution spectroscopy and *ugriz* photometry. For high SNR spectra with $4500 \text{ K} \leq T_{\text{eff}} \leq 7500 \text{ K}$, the SSPP measures T_{eff} , $\log g$, and [Fe/H] with typical uncertainties of 157 K, 0.29 dex, and 0.24 dex, respectively (Lee et al. 2008a). The SSPP can also determine the spectral type of stars outside of this temperature range.

For full details on the SSPP procedures see Lee et al. (2008a). Here, we provide a brief overview of the SSPP methodology. The SSPP relies on external measurements of the radial velocity (RV) of a star, though it has been shown that input RVs incorrect by as much as 200 km s⁻¹ do not significantly alter the output of the SSPP. The SSPP uses the RV measurement to shift the spectrum to a zero-velocity rest frame, where it then measures line indices for several prominent stellar absorption features (e.g., H α , H β , Ca II H&K, Na I, etc.). To measure these indices, continuum fits are made both globally, over the entire spectrum, and locally, from a line-free region blueward of the absorption feature to a line-free region redward of the absorption feature. A specific line index is then calculated for each continuum fitting method by integrating the continuum-normalized flux over a pre-defined wavelength interval. The line indices are fed to different parameter estimation methods (e.g., neural networks, synthetic spectral matching, autocorrelation, etc.) to provide multiple estimates of T_{eff} , $\log g$, and [Fe/H]. Each of the estimation methods is tuned to apply only to stars over a restricted range of $g - r$ colors, over which the method is shown to be reliable. Reliable measurements of T_{eff} , $\log g$, and [Fe/H] are robustly combined to provide the final adopted values, and corresponding uncertainties, of the stellar parameters. The number of methods employed to produce the final adopted parameters is also returned. While processing spectra, the SSPP flags stars for which it cannot provide reliable estimates of the stellar parameters, such as very hot stars, white dwarfs and M giants.

The spectra we obtained with Hectospec provide a good match with those obtained by SDSS, making the SSPP an ideal tool for estimating the stellar parameters of our spectra. SDSS spectra cover a wavelength range from 3800–9200 Å with a dispersion of 1 Å pixel⁻¹, while Hectospec covers 3700–9100 Å with a dispersion of 1.2 Å pixel⁻¹. We use a slightly adapted version of the SSPP, which accounts for the lower resolution of Hectospec as compared to SDSS, to estimate T_{eff} , $\log g$, and [Fe/H] for each of the sources observed during our survey. The results from the SSPP are summarized in Table 7.5.¹¹

¹¹This table is exceptionally long (65 pages!), and as such it is relegated to the end of the chapter.

7.4 Analysis of Variable Sources

7.4.1 Photometric Characteristics

In order to characterize the light curves of each of the variables identified in the UW VSC, we measure the 67 light-curve features¹² defined in Richards et al. (2012a) for all sources in each of the *ugriz* filters. Example features include: the best-fit period, amplitude, skew, Stetson-*j* index (Stetson 1996), and standard deviation, for the full list of feature names and descriptions see Richards et al. and references therein.

The variability of quasars in Stripe 82 has been studied extensively (e.g., Butler & Bloom 2011; MacLeod et al. 2010, 2011; Schmidt et al. 2012), while studies of stellar variability have mostly been restricted to sources belonging to a single variability class (Sesar et al. 2010; Becker et al. 2011). Furthermore, within Stripe 82 there has been an extreme bias in spectroscopic surveys toward identifying quasars, as of SDSS data release 9 there are $> 42k$ spectroscopically identified quasars in Stripe 82 compared to only 3,104 spectra of variable stars. Here, we restrict our investigation to the variability characteristics of all stars selected in the UW VSC, while generally (though not completely) ignoring the quasars.

A general study of Stripe 82 variables is presented in Sesar et al. (2007), though that study includes only SDSS-I observations. SDSS-I observations of Stripe 82 were obtained over a ~ 6 yr baseline with a maximum of 28 observations in the *gri* for the most frequently observed sources during that period (Ivezić et al. 2007). Sesar et al. used these observations to identify $\sim 13k$ variable candidates. This study, which includes both the SDSS-I and SDSS-II observations of Stripe 82, increases the number of candidate variables to 67,507 while also increasing the median number of observations per source from 10 to 33.¹³ Broadly speaking, the additional $\sim 54k$ variable candidates do not change the major conclusions in Sesar et al., however, there are a few differences, particularly for the sources located in region V of the *ugr* CC diagram (see Figure 7.1), which warrant an updated discussion.

One of the conclusions presented in Sesar et al. is that, based on the location of variable candidates in the *ugr* CC diagram, the majority ($\sim 63\%$) of variable sources at high galactic latitudes are low-redshift quasars. In the UW VSC the vast majority ($\sim 74\%$) of variable candidates are located in region V of the *ugr* CC diagram, which corresponds to the stellar locus, while only $\sim 13\%$ of sources are likely low-redshift quasars located in region II (see also Table 7.1). Even restricting the sample to include only variables with $|b| > 20^\circ$, as was done in Sesar et al., there are far more candidates in the stellar locus (26484) than there are in the low-redshift quasar region (8403). The number of sources in region II only begins to rival and surpass the number of sources in region V when the UW VSC sample is restricted to faint sources ($r \gtrsim 18.5$ mag) at high galactic latitude ($|b| > 20^\circ$). Thus, the dominant

¹²In machine-learning parlance a “feature” is a real-numbered or categorical metric describing a source. Throughout this Chapter features are based on either the time-series input or physical photometric colors of the source.

¹³Recall from §7.2.1 that sources must be observed at least 10 times in each of the *gr* bands for inclusion in the UW VSC.

variability class for any typical time-domain survey conducted on 1-m class telescopes will be stellar variables, regardless of the survey’s target area. Much deeper surveys (such as LSST, which will have a single observation detection limit of $r \approx 24.5$ mag) will be required for the number of quasars to outnumber the variable stars, and even in these cases this will only be true at high galactic latitudes.

Measurements of light-curve skewness can provide a useful proxy for understanding the physical origins of the variability observed in stars. Light-curve skewness γ provides a measure of the asymmetry of the time-variable brightness relative to the mean brightness of a source. The light-curve skewness is defined as:

$$\gamma = \frac{n^2}{(n-1)(n-2)} \frac{\mu_3}{\Sigma^3}, \quad (7.1)$$

$$\mu_3 = \frac{1}{n} \sum_{i=1}^n (m_i - \langle m \rangle)^3, \quad (7.2)$$

$$\Sigma = \sqrt{\frac{1}{n-1} \sum_{i=1}^n (m_i - \langle m \rangle)^2}, \quad (7.3)$$

where n is the number of source detections, m_i is the source brightness in magnitudes of the i^{th} observation, and $\langle m \rangle$ is the mean magnitude of the source. Sources with positive skew spend most of their time in a brighter state (e.g., eclipsing binaries), while sources with negative skew spend most of their time in a fainter state (e.g., fundamental-mode pulsating RR Lyrae stars). Rotating variables are expected to be symmetric about their mean magnitude, and are thus expected to have $\gamma \approx 0$.

It is found in [Sesar et al. \(2007\)](#) that the majority of stellar variables have positive skew, and that they show a bimodal distribution in the g -band with peaks at $\gamma_g \approx 0.6$ and 2. It is argued that this means there are at least two dominant modes of stellar variability. This, taken in conjunction with predominantly grey flux variations ($\sigma(g)/\sigma(r) \approx 1$), leads to the conclusion in [Sesar et al.](#) that most of the stellar variables detected in Stripe 82 are eclipsing systems. We show the skewness distribution in each of the $ugriz$ bands for all UW VSC main stellar locus sources in Figure 7.3. The strongly bimodal structure reported in [Sesar et al.](#) is not seen in the larger sample of variable stars included in the UW VSC. The peak of the distribution in all filters is greater than zero with a large tail toward positive γ . A minor peak is also clearly present in the gri bands at $\gamma \approx 7$. The specific class of variables giving rise to this peak is unclear: in the entire $\sim 50k$ variable source catalog from the All Sky Automated Survey (ASAS; [Pojmański 2001](#)) there are only 5 sources with $\gamma > 6$. Three of those five are classified as detached eclipsing binaries ([Richards et al. 2012a](#)), each with deep (> 1.5 mag) eclipses, while the other two are not classified with confidence and appear as though the variability may be systematic rather than physical. In the u band the peak is closest to 0, and the asymmetry in the tail is least pronounced. The reason for this is that the observational uncertainties are largest in the u band, which has the effect of smearing out the light curve and driving $\gamma \rightarrow 0$. Additionally, γ does not account for non-detections. The distributions in Figure 7.3 show that as most stars vary away from their mean magnitude

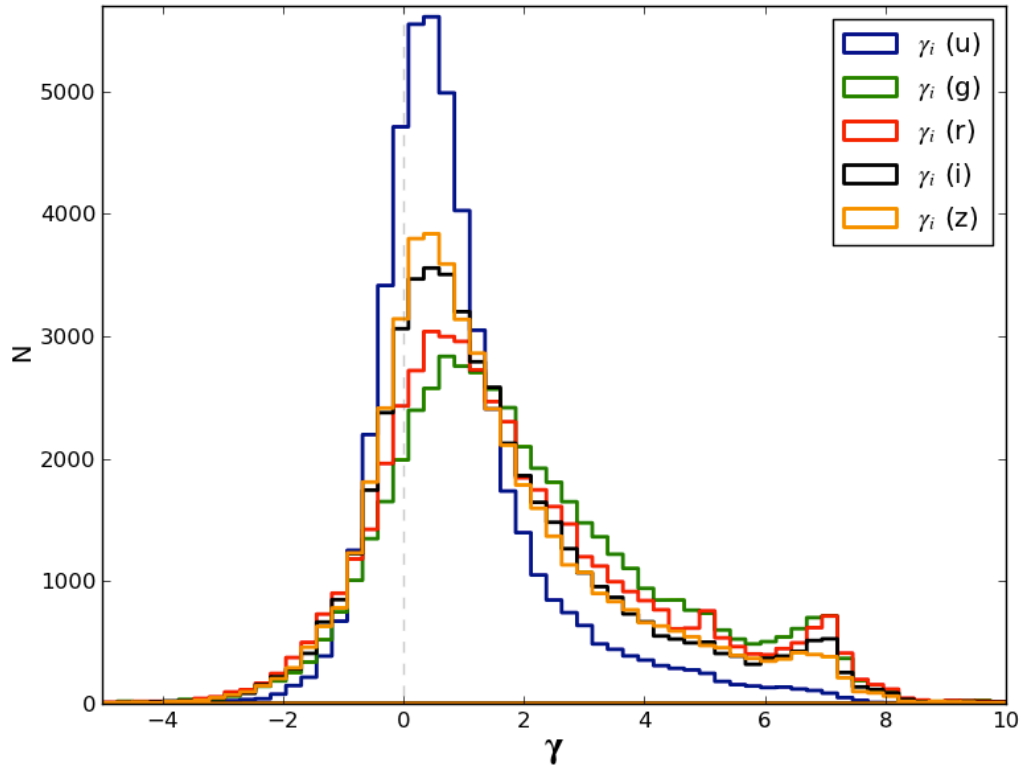


Figure 7.3: Light-curve skewness distribution measured in the *ugriz* bands for each UW VSC source located in the main stellar locus of the *ugr* CC diagram. The distribution is qualitatively similar in each of the *griz* bands. The *gr* bands show the most distinct structure, largely because the uncertainties on individual measurements are smallest in these filters. The *u* band shows a decidedly less asymmetric distribution because the observational uncertainties are larger and most stars are fainter in the *u* band than in the other filters (see text).

they tend to get fainter. Since most stars are fainter in the *u* band than they are in the other filters, as they fade it is most likely that they will be undetected in *u*, which will result in a smaller γ_u . As in Sesar et al., the dual peaks shown in Figure 7.3 suggest that there are at least two dominant physical origins of the observed stellar variability, while the strongly asymmetric distribution suggests that several sources of variability are likely present.

In Figure 7.4 we show the MAD in the *g* band plotted against the MAD in the *i* band for all main stellar locus sources in the UW VSC. MAD provides a robust measure of the typical amplitude of variability, as it is more resistant to outliers than the typically adopted root-mean scatter σ_{rms} metric. Optical flux variations for eclipsing sources are grey, meaning the amplitude of variability is approximately the same in all filters.¹⁴ Thus, if most stellar variables are eclipsing binaries, then they should be strongly clustered around

¹⁴This is not the case when the two eclipsing stars are approximately the same size but very different temperatures. This situation rarely occurs in nature, however.

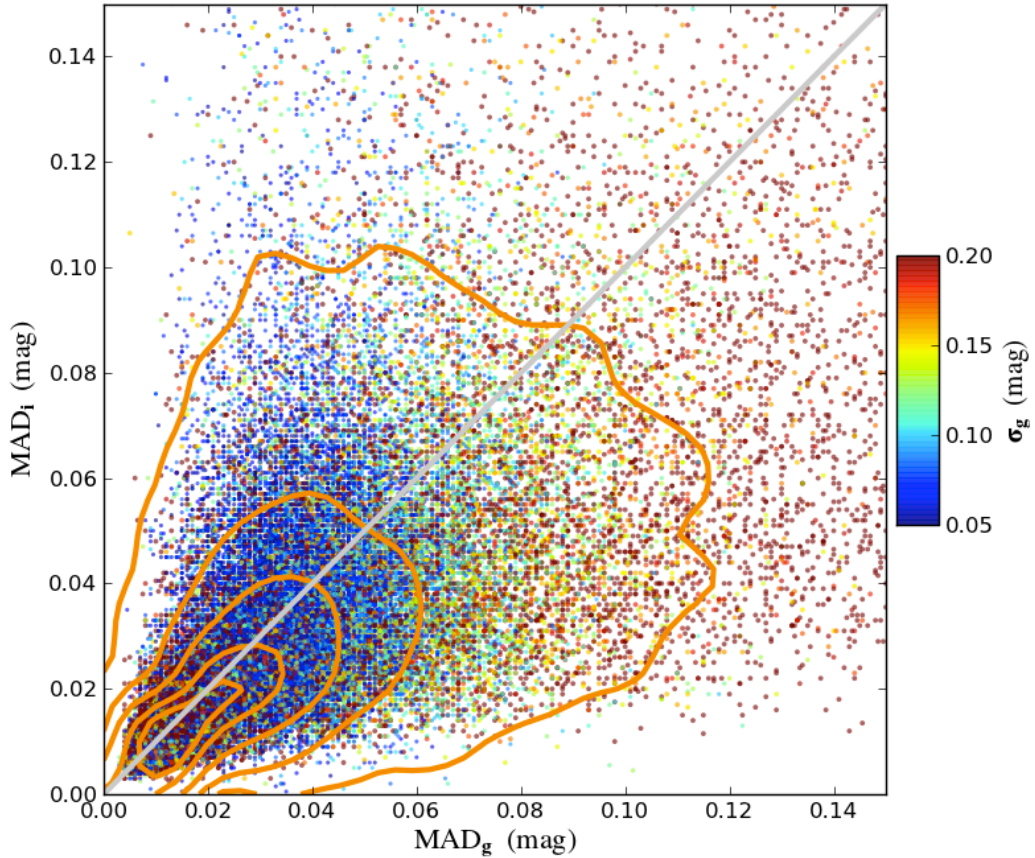


Figure 7.4: The median of absolute deviation (MAD) in the g band against the MAD in the i for all sources in the UW VSC located on the main stellar locus. Sources are color coded by their light curve standard deviation in the g band. The light gray line shows the location of gray-color variations ($MAD_g = MAD_i$). The linearly spaced orange contours show the density of sources, and clearly indicate that for most stars $MAD_g > MAD_i$.

$MAD_g/MAD_i \approx 1$. The contours in Figure 7.4 show that the majority ($\sim 73\%$) of region V variables have $MAD_g > MAD_i$. Furthermore, $\sim 27\%$ of sources clearly show evidence of strong color variations with $MAD_g > MAD_i + 0.02$. There are several classes of variables that show strong color variations, for example: Cepheids, RR Lyrae stars, δ Scuti stars, and rotating RS CVn stars all show temperature fluctuations over their variability cycles. It is unclear, however, how these classes would show such a strongly asymmetric, and positive, light-curve skewness distribution (see Figure 7.3). We conclude that it is impossible to identify a few dominant classes of stellar variability in Stripe 82; an automated, probabilistic, machine-based classification (e.g., Richards et al. 2012a) is likely required to disentangle the different physical origins of the observed variability.

7.4.2 Spectroscopic Characteristics

For most stars a spectrum provides far more insight into its physical properties than a photometric light curve.¹⁵ As noted in §7.3.1, we obtained 4741 spectra of UW VSC sources, which we supplement with 3104 additional spectra of stellar UW VSC sources in the SDSS archive.¹⁶ Each of these 7845 spectra were processed with the SSPP, and estimates of T_{eff} , $\log g$, and $[\text{Fe}/\text{H}]$ were obtained for 5631 of those sources. The remaining sources were either too hot ($T_{\text{eff}} \gtrsim 9000$ K), too cool ($T_{\text{eff}} \lesssim 4000$ K), or had some other peculiarity such that the SSPP could not provide estimates of the fundamental atmospheric properties. No SSPP warning flags were raised for 4086 of the 5631 sources; we consider these 4086 sources our pristine sample, which we will analyze in more detail in §7.5.

In Figure 7.5, we show the distribution of $\log g$ against T_{eff} , sometimes referred to as the “observer’s HR diagram,” for all sources with SSPP estimates of these parameters. Also shown are the loci of dwarf, giant, and supergiant stars, denoted by their respective luminosity classes, V, III, and II. These locations, which are based on the tabulation of Straizys & Kuriliene (1981), are only approximate and serve as a rough guide for any individual source. From Figure 7.5 it is immediately clear that, in a magnitude-limited sample of variable stars, there are few giants and supergiants. For a magnitude limited survey it is not obvious that this should be the case, since giants are several magnitudes brighter than dwarfs. Thus, Stripe 82 probes a much larger volume for giant stars than it does for dwarfs. It is also interesting that most sources have temperatures between ~ 4000 – 6000 K. The pile up on the red end of this range is artificial and the result of the SSPP, which does not provide temperature estimates for stars cooler than 4000 K. From Figure 7.5 we conclude that *the majority of variable stars are G and K dwarfs*, with the caveat that a significant population of even cooler M type stars may constitute a significant fraction of the observed variables (see e.g., Basri et al. 2011).

The sources shown in Figure 7.5 are color coded via their SSPP measured metallicity. There is a general trend for warmer, low-gravity stars to have lower metallicity than the cooler, dwarf stars. We interpret this effect to be a result of the magnitude-limited observations of Stripe 82: low-metallicity dwarf stars in the halo are too faint to be detected, which biases the cooler stars to solar-like $[\text{Fe}/\text{H}]$. SDSS probes a larger volume for giant stars, and given the fixed area of Stripe 82, this means that halo giants will outnumber those found in the disk, biasing low surface gravity sources toward lower metallicities.

In Figures 7.6 and 7.7, we show the fundamental atmospheric parameters plotted against eight of the most important light-curve features for automated variable star classification, as determined in Richards et al. (2012a). The features, each measured from g band observations, are: the amplitude of variations Δg , the best-fit period P_g , the standard deviation σ_g , the MAD of the Lomb-Scargle residuals divided by the MAD of the raw light curves `scatter_res_raw` (see Richards et al. 2012a), the Stetson variability index J (see Stetson 1996), the light-curve skewness γ_g , and the quasar and non-quasar variability metrics, χ^2_{QSO}/ν and $\chi^2_{\text{False}}/\nu$,

¹⁵In §7.5 we will demonstrate that this statement may not actually be true.

¹⁶In addition to these stellar spectra the SDSS archive has 8402 spectra of quasars in the UW VSC.

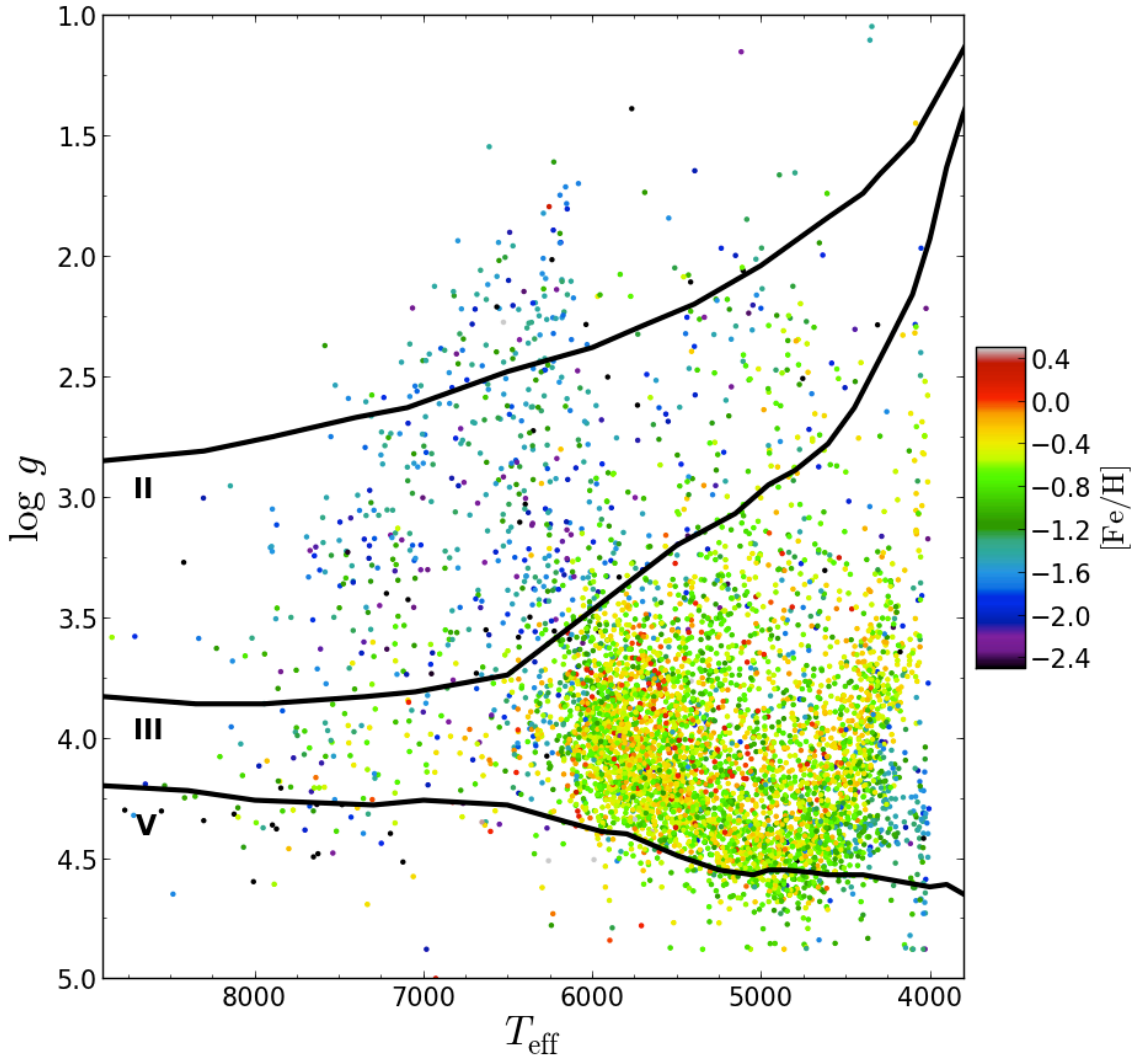


Figure 7.5: T_{eff} versus $\log g$ for all UW VSC sources with atmospheric parameters measured by the SSPP. Sources are color coded by their measured metallicity, as traced by $[\text{Fe}/\text{H}]$. For reference, the approximate locations of the dwarf, giant, and supergiant luminosity classes are shown via solid lines and marked V, III, and II, respectively. Note that the majority of variable stars in a magnitude limited survey are cool ($T_{\text{eff}} \lesssim 6000$ K) with low surface gravity ($\log g \lesssim 3.75$). The apparent trend of $[\text{Fe}/\text{H}]$ against both T_{eff} and $\log g$ is a by-product of the magnitude-limited observations obtained by SDSS.

respectively (see [Butler & Bloom 2011](#)). If it is possible to estimate T_{eff} , $\log g$, and [Fe/H] from light curves alone, then one would expect that at least some of the important light curve features correlate with the atmospheric parameters. From Figures 7.6 and 7.7 it is clear that no obvious one-to-one correlations exist between the light-curve features and the stellar parameters. There are, however, some clear clumps that emerge from the data. For instance, RR Lyrae variables stand out as the warm ($T_{\text{eff}} \approx 7000$ K), low surface gravity ($\log g \approx 2.5 - 3$), low metallicity ([Fe/H] ≈ -2) sources with $\gamma_g \approx -0.4$, $\chi^2_{\text{False}}/\nu \approx 0$, and $P_g \approx 0.7$ d.¹⁷ The existence of these clumps suggest that higher-dimensional models may be capable of parsing the multidimensional light-curve feature space in order to predict fundamental stellar parameters.

7.5 Estimating T_{eff} , $\log g$, and [Fe/H] From Light Curves

7.5.1 Random Forest Regression

As astronomical datasets become larger and successively more information is obtained on individual sources,¹⁸ the necessity of complex models capable of parsing large multidimensional spaces is paramount for keeping pace with the accelerating data streams. Supervised machine learning provides the necessary tools to keep up. Supervised regression describes machine learning methods wherein a training set consisting of objects with known properties of interest are used to describe a relationship, and ultimately build a model, between these properties and observed data. Thus, we endeavor to build a model that will enable accurate predictions of T_{eff} , $\log g$, and [Fe/H] from light-curve features alone. As a training set we will adopt the 4086 subset of spectra described in §7.4.2 for which no flags were raised during SSPP processing. Once a suitable regression model is built, it can be used to predict T_{eff} , $\log g$, and [Fe/H] for any variable star with SDSS photometric colors and a g band light curve.

There are many machine-learning methods that can be used to perform supervised regression, including: artificial neural networks, support vector machines, decision trees, and random forest, which have all been successfully applied to large multidimensional datasets (see [Hastie et al. 2009](#) for detailed examples of the application of these tools). Here, we employ the use of the random forest regression (RFR), because it is computationally fast and the results are easy to interpret. Additionally, random forest has been shown to be the optimal machine learning method for a variety of astrophysical problems (e.g., [Richards et al. 2011](#); [Dubath et al. 2011](#); [Brink et al. 2013](#); [Morgan et al. 2012](#)). A detailed description of random forest can be found in [Breiman \(2001\)](#). Briefly, the random forest method aggregates the results from several decision trees to provide a low-bias, low-variance estimate of the properties of interest. In particular, at each node of the tree the new splitting parameter can only be selected from a random subset of `mtry` features in the entire feature set. For the case

¹⁷[Sesar et al. 2007](#) and [Butler & Bloom 2011](#) show that RR Lyrae stars cluster around these values of γ_g , $\chi^2_{\text{False}}/\nu$, and P_g .

¹⁸A good example of this phenomenon is PTF obtaining variability information for most of the ~ 1 billion photometric sources with *ugriz* measurements in SDSS.

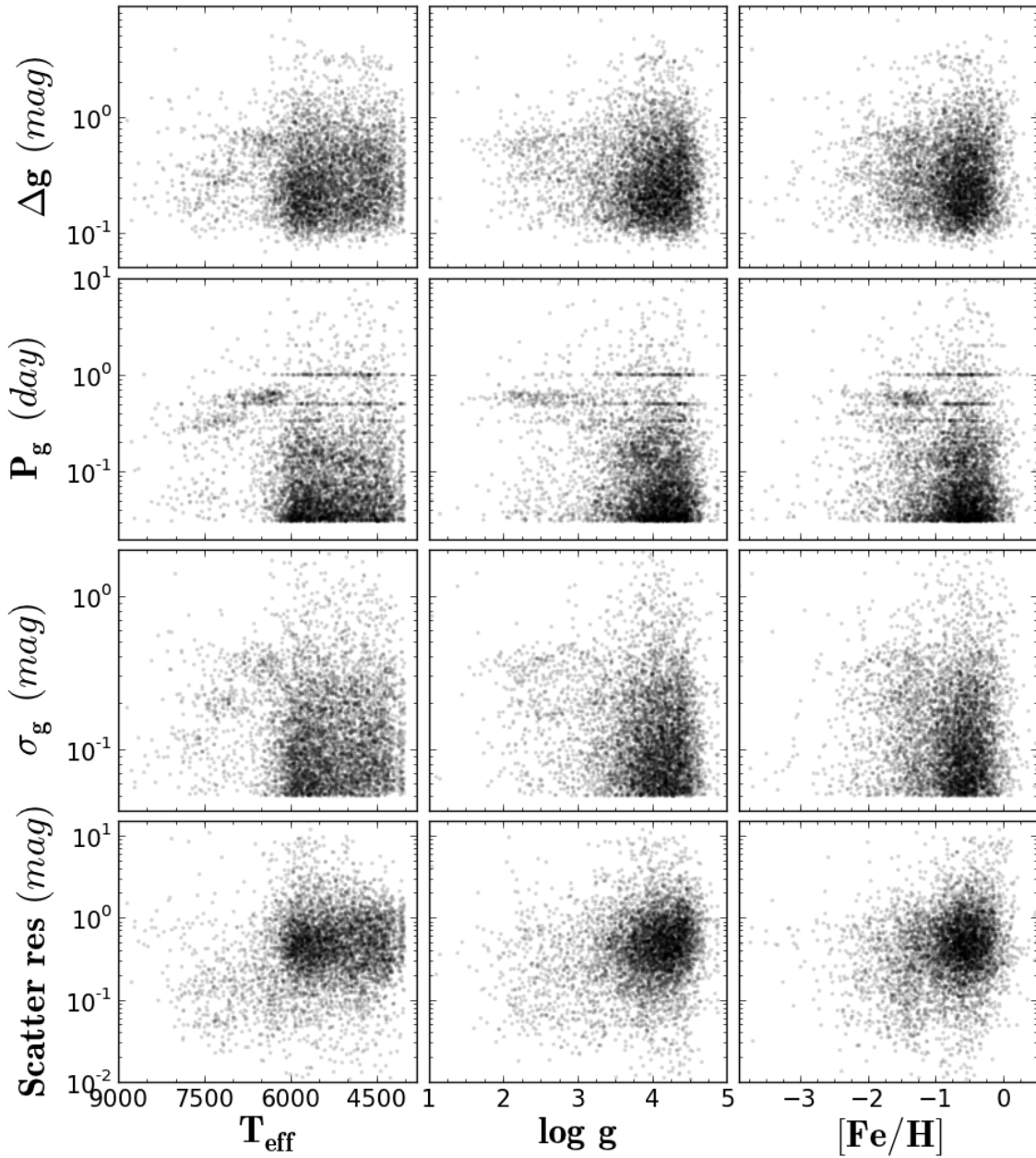


Figure 7.6: The most important light-curve features for automated variable-star classification are plotted against T_{eff} , $\log g$, and $[\text{Fe}/\text{H}]$, as determined by the SSPP. In each case there is a single dominant clump, which consists primarily of main-sequence G and K dwarfs.

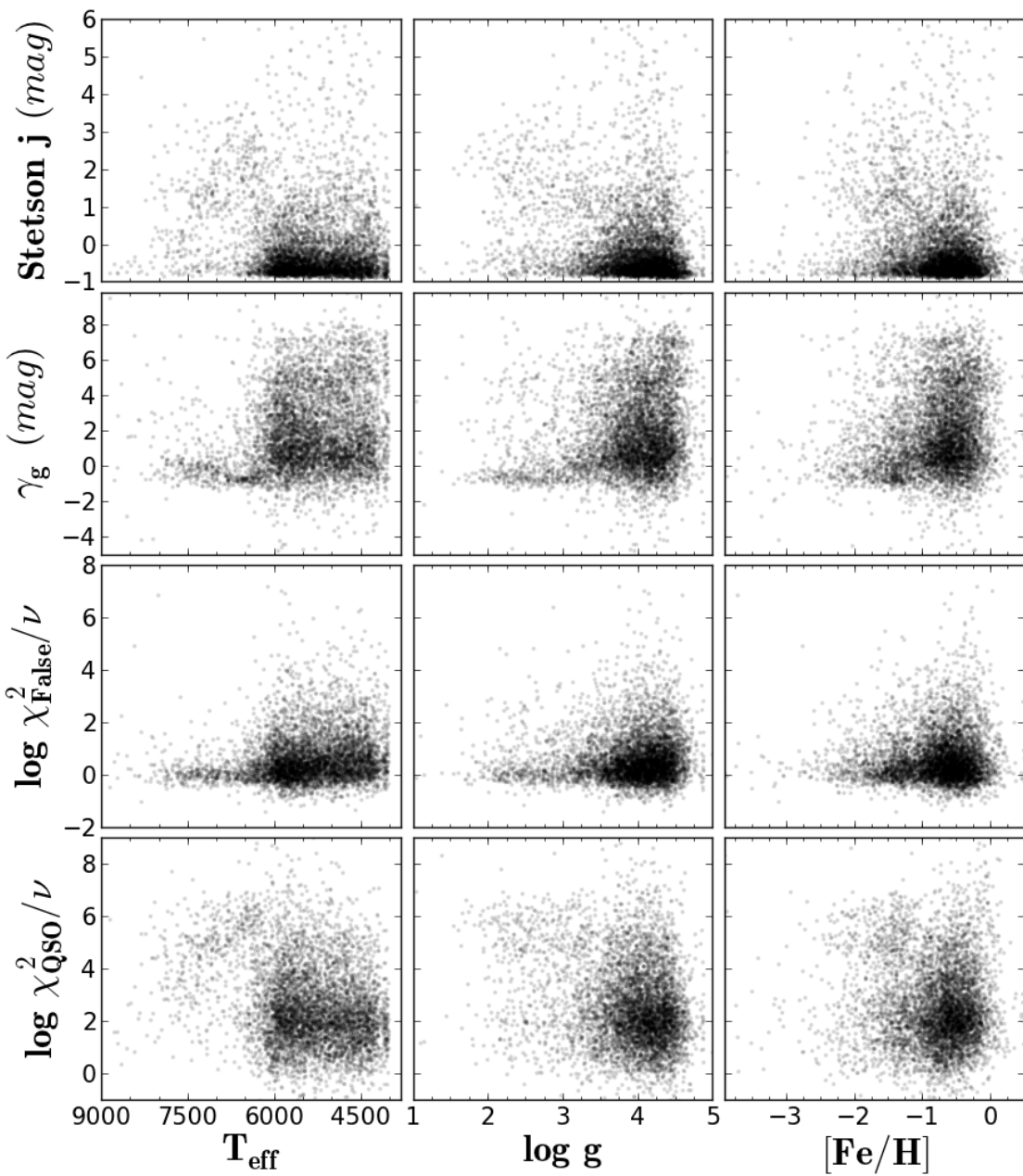


Figure 7.7: Same as Figure 7.6.

described here, after hundreds of trees have been constructed, each with different structure, the output from each of those trees is averaged to provide a robust estimate of T_{eff} , log g , and [Fe/H]. Throughout the remainder of this chapter we use the `WiseRF` (version 1.5.6)¹⁹ implementation of the random forest algorithm.

Ideally, our random forest model would be able to perfectly predict T_{eff} , log g , and [Fe/H] for each of the 67,507 sources in the UW VSC. However, noise in the training set (the SSPP provides estimates with typical uncertainties of ~ 150 K, 0.29 dex, and 0.24 dex for T_{eff} , log g , and [Fe/H], respectively) and in the feature set mean that such an ideal model cannot be constructed. Thus, in order to compare the efficacy of different models we adopt the mean-squared error (MSE) as the figure of merit (FoM) for determining the optimal model. When applied to the training set, the MSE is defined as:

$$\text{MSE} = \frac{1}{n} \sum_i (y_i - x_i)^2, \quad (7.4)$$

where n is the total number of objects in the training set, y_i is the predicted value of the property of interest, and x_i is true value of the property of interest. The splitting parameter of each non-terminal RFR node is optimized to minimize the MSE, making this a natural choice for the FoM. The MSE for the entire training set is measured using k -fold cross validation (CV). In k -fold CV, $1/k$ of the training set is withheld during model construction, and the remaining $(1 - 1/k)$ sources are used to predict the parameters of interest for the withheld data. This procedure is then repeated k times, resulting in every training set source being withheld exactly once, so that predictions are made for each source in the training set enabling a measurement of the MSE. Unless otherwise noted we use $k = 8$ CV throughout the remainder of this Chapter.

7.5.2 Colors vs. Light Curves

We begin by examining the utility of supplementing photometric colors with light-curve features in order to estimate fundamental stellar parameters. While photometric colors are particularly useful for estimating T_{eff} (see e.g., Ivezić et al. 2008b), estimates of log g and [Fe/H] typically prove to be significantly more difficult (e.g., Brown et al. 2011). Since many variable star classes correspond to specific locations within the HR diagram (e.g., RR Lyrae stars, Cepheid stars, Mira variables; see Eyer & Mowlavi 2008), it seems reasonable to expect that light-curve features, in addition to colors, could, at the very least, improve estimates of log g , and possibly [Fe/H] as well. As a basic test of this possibility, for each of the 3 stellar parameters we construct 3 RFR models. The feature set for the first model contains only the median observed SDSS photometric colors ($u - g$, $g - r$, $r - i$, and $i - z$), which have been corrected for reddening according to the dust maps of Schlegel et al. (1998). The feature set for the second model contains only the g band light-curve features described in §7.4.1, while the third model uses both colors and light-curve features. The results of this

¹⁹WiseRF is made available by wise.io.

initial test are shown in Figure 7.8. From the middle column of Figure 7.8, it is obvious that single-band light-curve features are a poor predictor of T_{eff} , log g , or [Fe/H].²⁰ The first column shows colors may be used to estimate T_{eff} with a scatter similar to that produced from SSPP measurements of actual spectra. Colors-only estimates of log g and [Fe/H] are significantly worse than what can be gleaned from low-resolution spectra, however. The third column shows that using both colors and light-curve features only improves the predictive power of the log g model, which still remains somewhat poor (MSE = 0.183). These models have not been optimized, however, and with 67 light-curve features and a median of only 33 observations per source it is likely that these models have been over-fit. Below we examine methods to improve the predictive power of the RFR model.

7.5.3 RFR Model Optimization

When building a machine-learning model there are several decisions that the scientist must make, all of which affect the accuracy of predictions made on new observations. In addition to choosing a specific learning algorithm, choices must also be made in deciding which sources to include and exclude from the training set, which features to use, and how to tune the parameters of the learning algorithm. The importance of these decisions can plainly be seen in Figure 7.8: when using light-curve features and excluding color information to predict [Fe/H], RFR produces very biased results in which almost all sources are predicted to have $[\text{Fe}/\text{H}] \approx -0.5$ dex. Using this model, it would be virtually impossible to identify newly observed low-metallicity stars. Below we describe how we prune the feature sets used to predict T_{eff} , log g , and [Fe/H], and how we adjust the RFR tuning parameters to construct the optimal machine-learning model.

Feature Selection

For variable-star classification, each of the 67 light-curve features described in §7.4.1 provide useful information for discriminating between the various classes (Richards et al. 2012a). As previously noted, for T_{eff} , log g , and [Fe/H], the use of all 67 light-curve features adds noise to the model and reduces its overall accuracy (see the third column of Figure 7.8). The inclusion of too many features can hinder the performance of the model, while also needlessly making it algorithmically more complicated. Faced with a training set of fixed size, 4086 spectra, it is often more difficult to make accurate predictions as the number of features increases due to the increased likelihood of over-fitting the data within the complex multidimensional feature space. Thus, we will prune the feature set with several goals in mind: reducing the complexity of the model and decreasing the total computation time, improving the interpretability of the results, and maximizing the predictive power of the

²⁰We remind the reader that the median number of observations for sources in the UW VSC is 33. We speculate that additional observations obtained at higher-cadence will dramatically improve the efficacy of models built using only light curves.

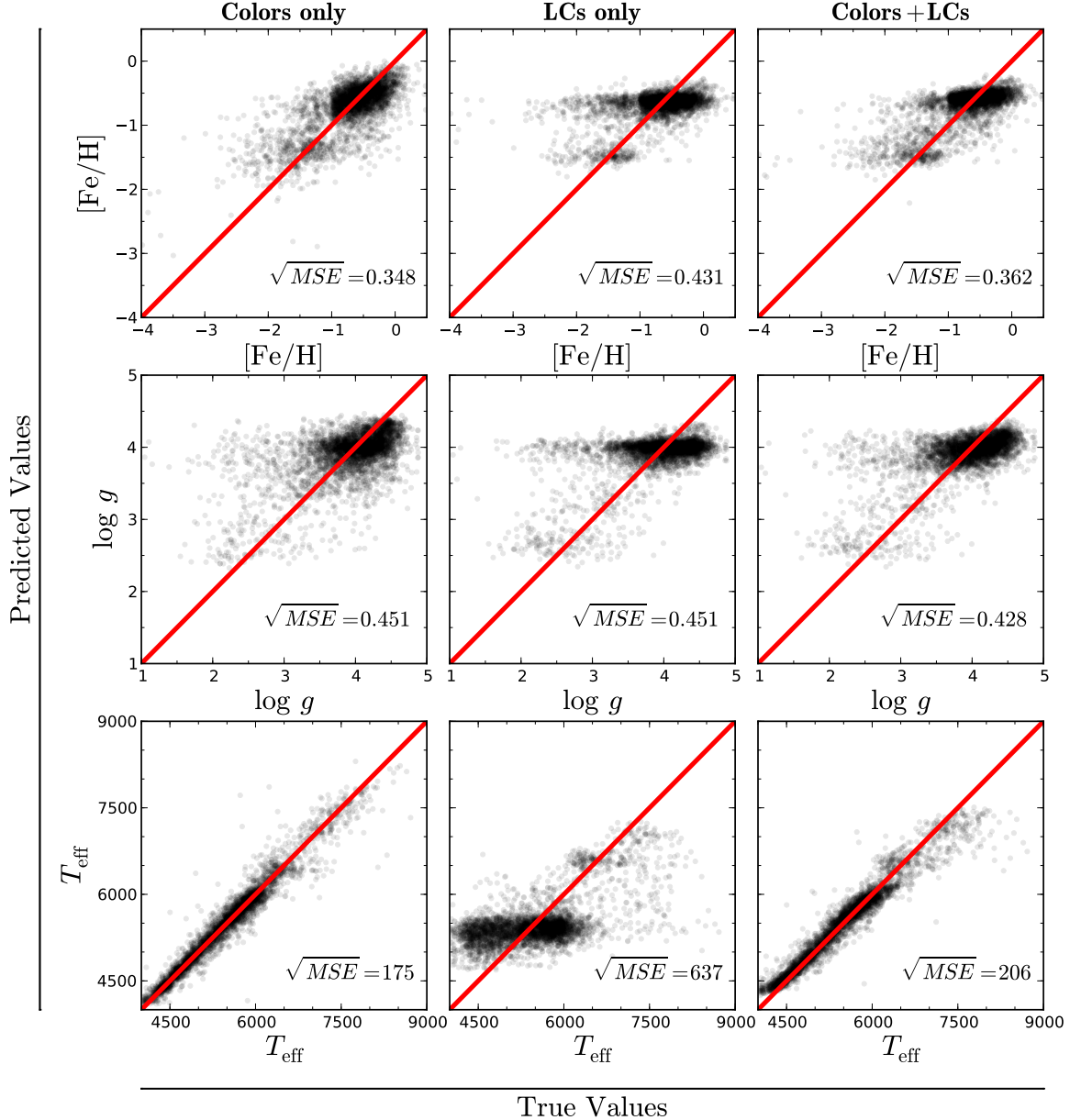


Figure 7.8: Random forest regression predicted stellar parameters vs. true values determined by the SSPP. The top row shows the results for [Fe/H], the middle row shows $\log g$, and the bottom row shows T_{eff} . The columns show models constructed using different feature sets: the first column shows models fit to only SDSS colors, the middle column shows models fit to the g band light-curve features only, and the right column shows models fit using both SDSS colors and light-curve features. For each model the square root of the MSE is shown, which provides an estimate of the average difference between the predicted and true values of [Fe/H], $\log g$, and T_{eff} .

RFR. Selecting only a few light-curve features, instead of all 67, can improve the FoM, while also reducing the overall bias of the predictions (see below).

Feature selection is a challenging problem as there is an exceedingly large number of combinations that include a subset of only some of the 71 total features (4 colors + 67 light-curve features). We wish to determine which subset s of the 71 features produces the best model to predict stellar parameters. Searching over all possible subsets is computationally intractable as this would require us to train $\sum_{s=2}^{71} \binom{n}{s} \approx 2 \times 10^{21}$ RFR models.²¹

Following the method in Brink et al. (2013), we simplify the model selection process using approximation methods. The well-known variations of these methods are the forward and backward feature selection algorithms (Guyon & Elisseeff 2003). The forward feature selection method begins with an empty feature set and iteratively adds features one at a time selecting the feature that best improves the model, as judged by the FoM, at each step. Backwards feature selection begins by using the full feature set and iteratively removes the feature that improves the model the least, or harms the model the most. We adopt the forward feature selection method, since it is clear that the model performs well with as few as 4 features (see Figure 7.8).

Before proceeding with forward feature selection for each of our three models, we must identify one feature that is automatically included in the final feature set. One of the advantages of random forest, over other algorithms, is that during the model construction process the relative importance of each feature is naturally and automatically measured, since a subset of features are excluded as splitting parameters in each non-terminal node of the tree Breiman (2001). Thus, we perform RFR using the full feature set, and adopt the most important feature determined by the random forest algorithm as the initial feature for forward selection. For each of the T_{eff} , log g , and [Fe/H] models the most important feature is $g - r$. From there, we aim to only add features that improve the FoM of the model. To do so, we calculate the cross-validated FoM of all possible models with a single feature added to $g - r$, and select the model with the smallest MSE. We repeat this process until a model with the full feature set has been constructed. This procedure requires the creation of $\sum_{i=1}^{70} 71 - i = 2485$ RFR models, which, though large, can be executed on a normal laptop computer in under 4 hr.

Figures 7.9, 7.10, and 7.11 show the results from the forward feature selection process for T_{eff} , log g , and [Fe/H], respectively. There is a significant improvement in the performance of the RFR model when the feature set is pruned. In particular, there is a $\sim 34\%$, $\sim 6\%$, and $\sim 19\%$ improvement in the FoM for T_{eff} , log g , and [Fe/H], respectively, as compared to a model using all the features. Figures 7.9, 7.10, and 7.11 also show that the addition of light-curve features improves the performance of the RFR models relative to models built with color-information alone.

An important thing to note from Figures 7.9–7.11 is that the feature selection method is robust, since the ordering of features does not change significantly from run to run. The final selected features are selected in most of the runs, while only a few features are selected just

²¹Random forest methods require at least two features to construct a meaningful decision tree. Otherwise, standard linear-least squares methods would provide similar or superior predictions to those made by RFR.

once or twice. The occasional inclusion of a low-ranking feature in an individual run is the result of correlations between the features. The most clear example of this can be seen in Figure 7.9, where the 38th ranked `skew` was selected during one run while `gskew` was not.²² As a result, for T_{eff} , `gskew` ranks lower than other features which were selected fewer times because `gskew` had a very low ranking during one of the runs. These correlations have the most prominent effect for the log g model (see Figure 7.10), since the degradation in the model performance after adding features beyond the optimal feature set is small. Thus, there are a few features that were selected in multiple runs which did not make the final cut for the optimal model.

Similar to Brink et al. (2013), we include an empty feature `empty`, which contains no information (for all sources `empty = 0`). Nevertheless, like Brink et al., we find that this feature is selected in the final feature set for both the T_{eff} and [Fe/H] models. `empty` cannot be used as an actual splitting feature, rather it remains neutral in all iterations of the RFR, thus, the ability of this feature to improve a RFR model following its addition is puzzling. We echo Brink et al. in noting that an improved understanding of this effect is of great interest to future versions of this RFR model and other related astronomical projects.

Another point to notice are the discontinuous jumps showing model improvement following the addition of a single feature in Figures 7.9–7.11. This is prominently seen in Figure 7.9 with the `lcmodel_pos_n_per_day` and `flux_percentile_ratio_mid65` features. These jumps occur after the 25th and 36th features have been added to the feature set. The default value of `mtry`, the number of features used as potential splitting criterion at each tree node, is \sqrt{n} , where n is the total number of features in the feature set. Thus, as the total number of features surpasses integer values of \sqrt{n} , `mtry` increases and the performance of the RFR model improves. It is computationally intractable to optimize the model during every step of the forward feature selection process (model optimization is discussed below), a byproduct of which is the structure in Figures 7.9–7.11 identified here. Below we show that the precise values of the tuning parameters do not have a significant effect on the final results, and thus, there is no reason to believe that the lack of parameter tuning during the forward feature selection process produces a non-optimal final model for stellar parameter prediction.

Model Optimization

All non-parametric regression methods have a set of tuning parameters which affect the rigidity of the model. Adjusting these parameters typically offers a trade-off between variance and bias in the final predictions. Random forest methods feature three important tuning parameters: (i) `ntree`, the total number of decision trees used to construct the forest, (ii) `mtry`, the number of features that are used as potential splitting criterion in each non-terminal node of the tree, and (iii) `nodesize`, the minimum number of training set objects, meaning further splitting is not allowed, in a tree’s terminal nodes. For RFR the “rule-of-thumb”

²²`gskew` is a median-based, rather than mean-based, measurement of the light-curve skewness (see Richards et al. 2012a). Since `gskew` and `skew` are strongly correlated, either, but not both, is likely to be selected as an important feature during an individual run.



Figure 7.9: Results of the forward feature selection process for T_{eff} . We begin by selecting $g - r$ (gr in the figure) and iteratively add the feature that most improves the regression model as measured by the improvement in the FOM. Boxes show the cross-validated range of MSE following the addition of the feature to the model. The vertical dashed line shows the minimum MSE, while the vertical orange line shows the threshold FOM (minimum + 1 σ). Features above the dash-dot line are those that are selected for the optimal feature set. The procedure was rerun 5 times and the feature names are color coded according to the the number of times they were selected in the optimal feature set: 0 (black), 1 (red), 2 (blue), 3+ (green). For brevity, only the first 40 selected features are shown.

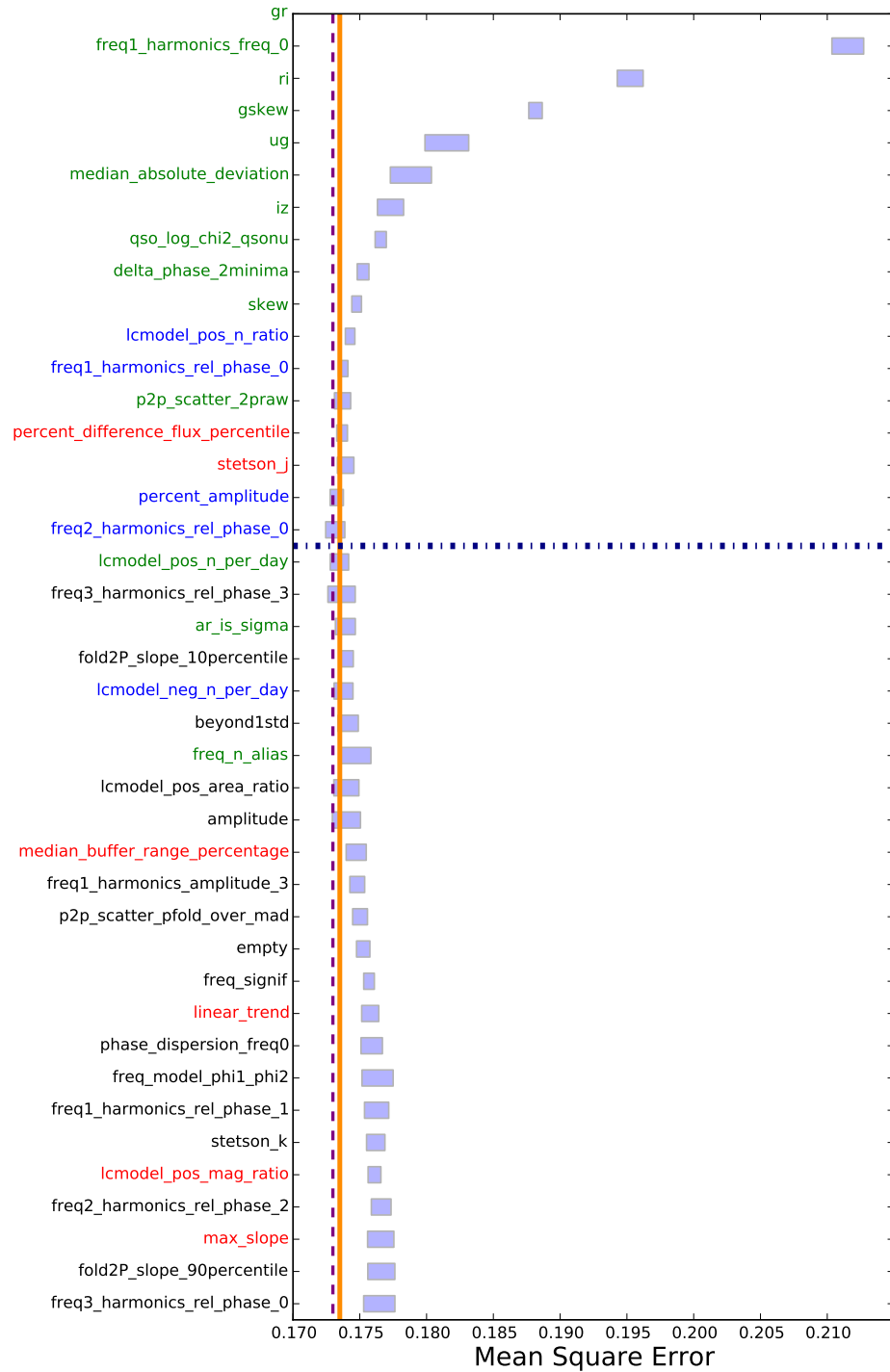


Figure 7.10: Results of the forward feature selection process for $\log g$. The explanation for this figure is the same as Figure 7.9.

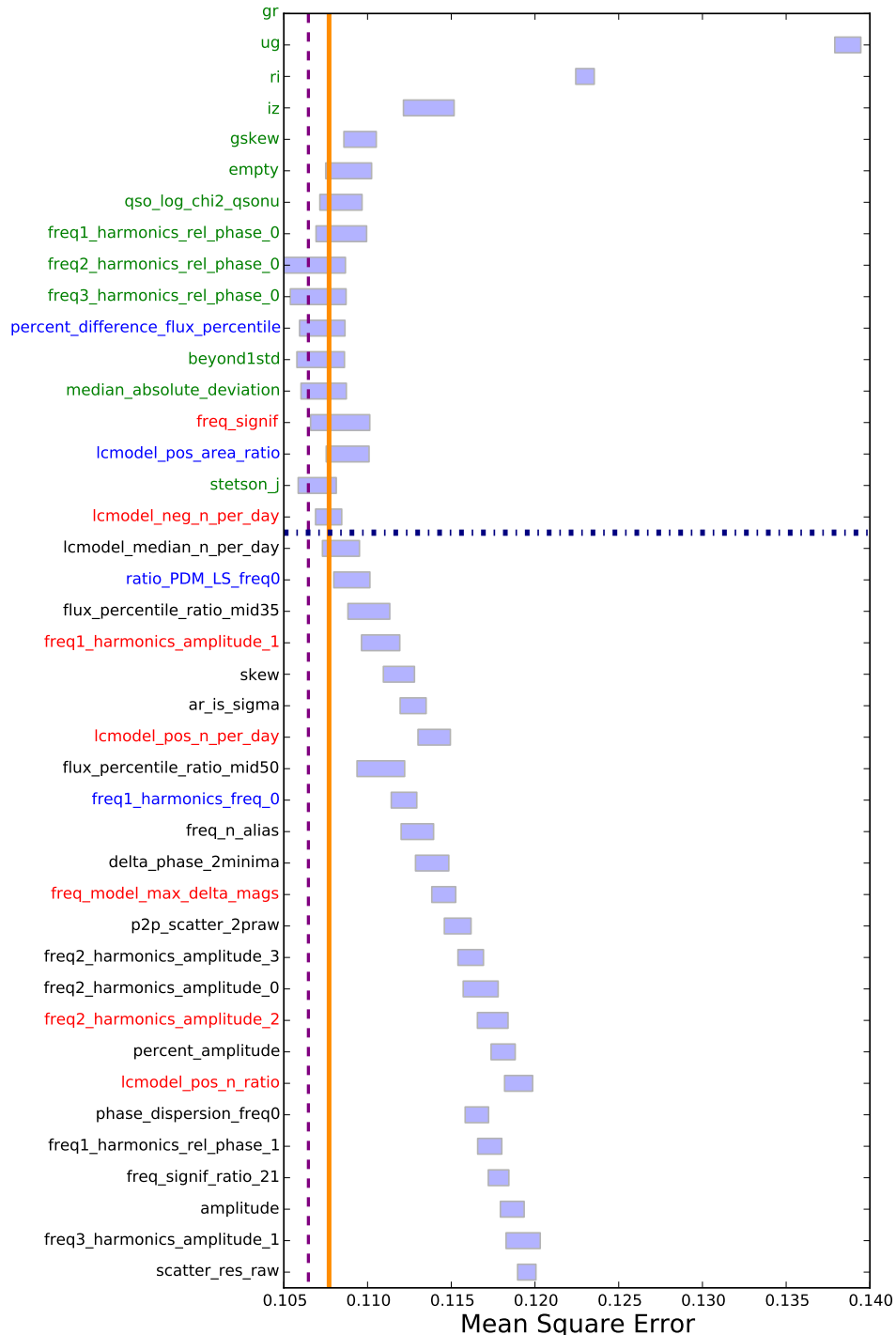


Figure 7.11: Results of the forward feature selection process for [Fe/H]. The explanation for this figure is the same as Figure 7.9

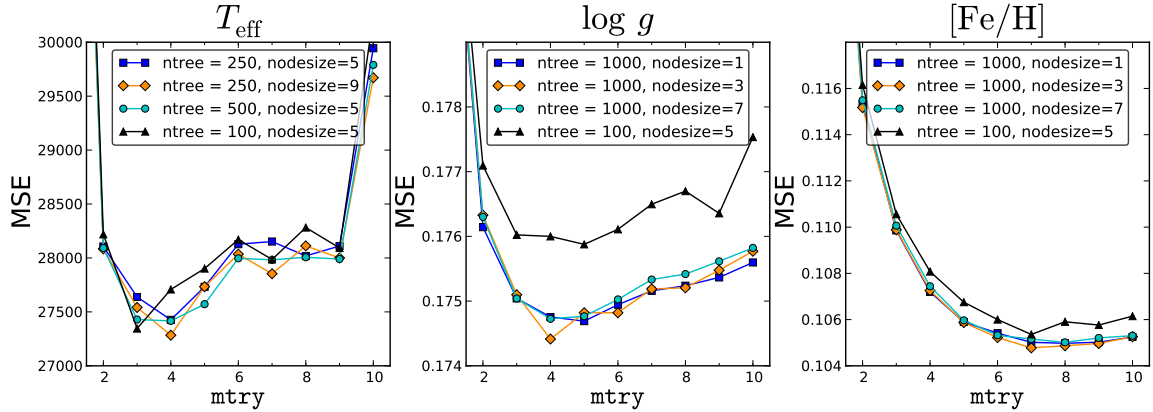


Figure 7.12: Results from a grid search over the three random forest parameters: `ntree`, `mtry`, and `nodesize`. The models are run a total of three times, and the displayed results show the average MSE. Note that the models are not strongly sensitive to the choice of tuning parameters. For T_{eff} , the optimal model is: `ntree` = 250, `mtry` = 4, and `nodesize` = 9. For $\log g$, the optimal model is: `ntree` = 1000, `mtry` = 4, and `nodesize` = 3. For [Fe/H], the optimal model is: `ntree` = 1000, `mtry` = 7, and `nodesize` = 3.

values are $\text{mtry} = \sqrt{n}$, where n is the total number of features used in the model, and `nodesize` = 5. `ntree` is specified by the user, during forward feature selection we selected `ntree` = 100. Broadly speaking, adjusting the tuning parameters adjusts the smoothness of the model, as they affect the complexity of the random forest. Now that we have engineered an optimal feature set, we aim to determine which values of the training parameters will produce the optimal RFR models to predict T_{eff} , $\log g$, and [Fe/H].

To optimize the random forest tuning parameters, we perform a grid search over `ntree`, `mtry`, and `nodesize`. Selected results from this grid search are shown in Figure 7.12. Generally, we find that the precise choice of tuning parameters does not significantly affect the output of the models, as measured by the FoM. For instance, for T_{eff} and $\log g$ adjusting `mtry` from 3 to 6 degrades performance by less than 1%. The same is true for [Fe/H] for `mtry` between 6 and 10. The behavior of the models as `mtry` is adjusted is typical for non-parametric classifiers: small values of `mtry` are over-smoothed, high-bias and low-variance models, while large values of `mtry` lead to under-smoothed, low-bias and high-variance models.

Final Optimized Model

In Figure 7.13 we show the results of the final, optimized RFR models for predicting T_{eff} , $\log g$, and [Fe/H]. The square-root of the MSE, a non-robust measure of the typical distance between the predicted and true values of the parameters of interest, is 165 K, 0.42 dex, and 0.33 dex for T_{eff} , $\log g$, and [Fe/H], respectively. These results represent a significant improvement, \approx 6–7%, over models trained with a colors-only feature set (see Figure 7.8). In addition to having smaller variance, it is also clear that the optimized models shown in

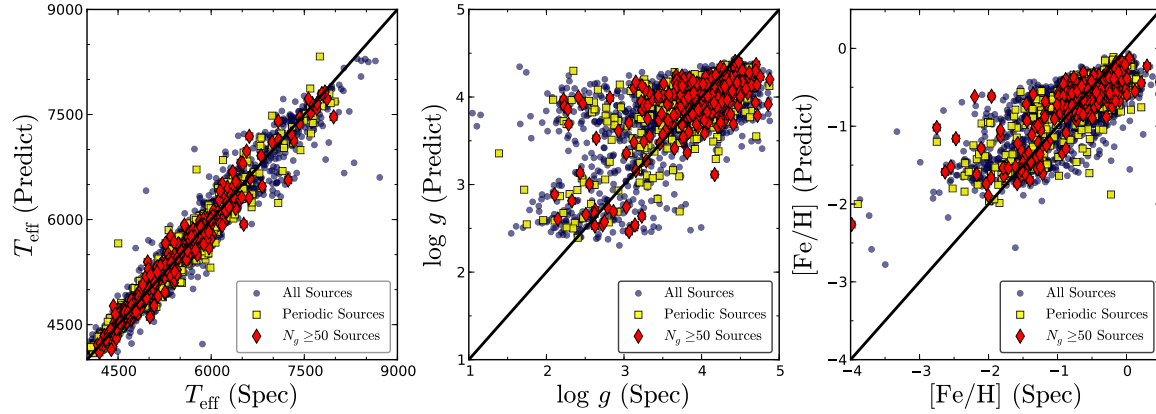


Figure 7.13: Random forest regression results for the optimized models shown in Figure 7.12. The subset of sources with reliably measured periods are shown as yellow squares, while those sources with at least 50 observations in the g band are shown as red diamonds. The optimized models produce less biased predictions of T_{eff} , $\log g$, and [Fe/H].

Figure 7.13 have lower bias than the colors-only models developed earlier.

The predictive power of the models improves significantly, as measured by MSE, when examining subsets of the full training set. In addition to showing the cross-validated predictions for all sources in the training set, Figure 7.13 also shows the predicted values for candidate periodic sources and all sources with at least 50 observations in the g band ($N_g \geq 50$). The improvement in the MSE for these subsets of the training set are summarized in Table 7.4, which shows a factor of $\sim 4\text{--}5$ improvement in MSE. Thus, for sources with $N_g \geq 50$ *the typical scatter in predictions of T_{eff} , $\log g$, and [Fe/H] is smaller than the uncertainties associated with a low-resolution spectrum* (see §7.3.3).

The model performance is poorest for stars with either high temperatures, low surface gravities, or low metallicities. Figure 7.13 shows that there are relatively few examples of such sources in the periodic and well-observed subsets of the data. This suggests that the improvement in MSE for sources with $N_g \geq 50$ may be driven by the exclusion of these sources, which as larger outliers disproportionately inflate MSE. We show in Table 7.4 that both the periodic and $N_g \geq 50$ subsets have a higher fraction of sources with large T_{eff} , low $\log g$, or low [Fe/H] than the full training set. Thus, the improvement in the predictive power of the RFR models for well observed sources appears to be real.

Finally, we note that the poor performance of the models for hot or low surface gravity or low-metallicity stars is, at least in part, due to the imbalance of the training set. The overwhelming majority of sources in our spectroscopic sample have low T_{eff} , dwarf-like $\log g$, and slightly sub-solar [Fe/H], which biases the RFR to predict similar values for all stars. A reduction of the imbalance in the training set would significantly improve the RFR predictive power for the sources that are currently under-represented. We discuss possible strategies to improve the imbalance below.

Table 7.4: Results from the Optimal RFR Models

	N	$T_{\text{eff}}^{\text{a}}$ (K)	$\log g^{\text{b}}$ (dex)	[Fe/H] ^c (dex)	$\sqrt{\text{MSE}}$
All sources	4086	165.7 (5.0, 0.4)	0.42 (7.5, 0.7)	0.33 (7.6, 0.6)	
Periodic	349	163.4 (13.3, 1.1)	0.40 (38.7, 1.8)	0.32 (18.0, 1.8)	
$N_g \geq 50$	900	74.8 (30.1, 1.7)	0.19 (16.8, 4.3)	0.16 (31.5, 1.1)	

^aParentheses show the percentage of sources in the selected subset with $T_{\text{eff}} > 7000$ K and $T_{\text{eff}} > 8000$ K, respectively.

^bParentheses show the percentage of sources in the selected subset with $\log g < 3$ dex and $\log g < 2$ dex, respectively.

^cParentheses show the percentage of sources in the selected subset with [Fe/H] < -1.5 dex and [Fe/H] < -2.5 dex, respectively.

7.6 Discussion

7.6.1 Conclusions

We have presented results from a systematic spectroscopic survey of optical variable stars. Spectroscopic targets were selected from the University of Washington Variable Point-Source Catalog, which was constructed from SDSS *ugriz* observations of Stripe 82. Two small biases were introduced into the targeting criterion of the survey, but we show that one of these does not significantly bias the final sample. The observations were biased towards low galactic latitude to ensure that the density of variable sources was high enough to use as many of the 270 Hectospec science fibers as possible over the full one degree FOV. The low latitude bias significantly reduced the relative number of quasars in our sample, which we view as unimportant given the plethora of existing Stripe 82 quasar variability studies (e.g., [Sesar et al. 2007](#); [MacLeod et al. 2010](#); [Butler & Bloom 2011](#)). The second bias was introduced to ensure that rare targets, defined as those with either unusual colors or atypical variability, had a very high probability of being observed. We demonstrate that this second bias did not significantly alter the demographics of sources included in our survey. In sum, we obtained 4741 Hectospec spectra of variable sources, which we supplemented with 3104 SDSS spectra of variable stars in Stripe 82.

We demonstrated that in a time-domain survey with similar depth as SDSS (variability reliably detected down to $r \approx 20.5$ mag) the variable source population will be overwhelmingly dominated by normal, main-sequence stars. We argue that quasars will only outnumber stellar variables in faint ($r \gg 19$ mag) surveys observing at high galactic latitudes. We confirm the result from [Sesar et al. \(2007\)](#) that the distribution of light-curve skewness is bimodal for stars on the main stellar locus (though the peaks in the distribution occur at different locations). It is hypothesized in [Sesar et al.](#) that the dominant source of variability

in the main stellar locus is eclipsing sources. We present evidence that this is not the case, though we are unable to identify which variable star classes dominate sources within the main stellar locus.

We measure T_{eff} , $\log g$, and $[\text{Fe}/\text{H}]$ for the stars in our spectroscopic sample using the Segue Stellar Parameters Pipeline ([Lee et al. 2008a](#)). From this sample we show that the majority of variable stars in the UW VSC are main-sequence G and K dwarfs with slightly sub-solar metallicity. This suggests that the majority of variables are either eclipsing sources or rotating variables (higher-cadence observations will be needed to disambiguate between the two). We show that light-curve features (e.g., best-fit period, amplitude, skewness) do not correlate with the fundamental stellar properties T_{eff} , $\log g$, and $[\text{Fe}/\text{H}]$.

Finally, we developed a non-parametric, machine-learned regression model to predict T_{eff} , $\log g$, and $[\text{Fe}/\text{H}]$ based on the colors and light-curve features of variable sources. The inclusion of light-curve features produces a \approx 6–7% improvement in the mean square error of the model relative to models trained using only SDSS color information. We found that the full 67 light-curve feature set used in [Richards et al. \(2012a\)](#) over-fit the available data while estimating the stellar atmospheric features. We adopted the forward feature selection method to build an optimal feature set for predicting T_{eff} , $\log g$, and $[\text{Fe}/\text{H}]$, and then tuned the internal random forest parameters to build an optimal random forest regression model. Using an 8-fold cross validated model on a training set containing 4086 stars with reliable measurements of T_{eff} , $\log g$, and $[\text{Fe}/\text{H}]$, we produce predictions with a square root of the mean square error of 165 K in T_{eff} , 0.42 dex in $\log g$, and 0.33 dex in $[\text{Fe}/\text{H}]$. Examining the subset of sources with at least 50 observations in the g band we find that these values drop to 74 K, 0.19 dex, and 0.16 dex, respectively, suggesting that the combination of light curves and photometric colors can produce estimates of T_{eff} , $\log g$, and $[\text{Fe}/\text{H}]$ that are comparable, or superior, to those obtained from low-resolution spectra.

7.6.2 Future Improvements to the Regression Models

While these models demonstrate that light curves can be used to infer stellar parameters, we can identify multiple ways via which the models can be improved. Improved light-curve coverage, i.e. additional observations taken at a more frequent cadence, should provide a significant improvement to the models. We demonstrate this to be the case by examining those sources with at least 50 observations in the g band. The median number of g band observations for Stripe 82 variables is 33, which spread over \sim 9 yr makes period recovery extremely difficult. Within our spectroscopic training set only 349 sources have reliably measured periods. For variable star classification the measured period is the most important light-curve feature ([Richards et al. 2012a](#)), thus, it stands to reason that if periods were determined for more than \sim 9% of the training set this would significantly improve the regression model. Higher cadence observations of Stripe 82 are currently being obtained by the Palomar Transient Factory, which has already observed Stripe 82 more than 100 times. Supplementing the SDSS color information with Palomar Transient Factory light curves should dramatically improve the regression model. The model can further be improved with a more balanced

training set, in particular, there are few sources in the training set with $T_{\text{eff}} > 6500$ K, or $\log g < 3$ dex, or $[\text{Fe}/\text{H}] < -1$ dex. A lack of such sources in the training set produces a bias in the regression model resulting in unknown sources preferentially being identified as slightly sub-solar metallicity, dwarf stars. This bias can be combated via a training set containing more sources near the extremes of the $\log g$ and $[\text{Fe}/\text{H}]$ distributions. Additional candidate sources to balance the training set can be identified using the observed low-metallicity and giant stars in the current training set, obtaining spectra of those candidates should ultimately reduce the bias in the final regression models.

7.6.3 The Future of Time-Domain Surveys

We view the results presented herein as a single, but essential step to extract the maximum amount of useful information from photometric time-domain surveys. SDSS observations of Stripe 82 produced a variable star catalog with $\sim 67k$ sources, in contrast, the Large Synoptic Survey Telescope is expected to discover at least 50 million variable stars (Ivezić et al. 2008a). The vast majority of these sources will be prohibitively faint for spectroscopic observations on anything smaller than a 30-m class telescope, which itself will be extremely expensive.²³ Large spectroscopic surveys of various stellar populations throughout the Milky Way have been the norm for over a decade (e.g., SDSS; the Radial Velocity Experiment – RAVE, Steinmetz et al. 2006), yet the focus of these efforts has largely been placed on the few million stars for which they have obtained spectra. Prior to this current study, significantly less effort has been devoted toward extrapolating the information from the few million spectra to the \gtrsim billion stars that have otherwise only been observed photometrically.

As we embark upon the burgeoning age of celestial cinematography (the LSST will literally make a 10 yr movie, sampled every 3 days, of everything that changes in the southern sky), it is essential that we develop new and advanced tools for discovery. As astronomers we must remember that more data is not always better; more is simply more, and without the necessary algorithmic advances we will be lost within the coming data deluge. Based on the results shown here, it is not unreasonable to think that LSST may be turned into a pseudo-spectrograph, as the 10 yr baseline and *ugrizy* light curves should enable accurate determinations of T_{eff} , $\log g$, and $[\text{Fe}/\text{H}]$ for each of the ~ 50 million expected variable stars. Furthermore, it may be possible to extend such models to all stars (the use of light curves to understand and characterize non-variable stars is completely unexplored at the moment). Once the atmospheric parameters are determined additional fundamental properties, namely mass M_* , luminosity L_* , and radius R_* , can be (probabilistically) inferred. In this way the most detailed maps of the Milky Way ever constructed will be charted, which promises to reveal and solve several mysteries regarding the formation of the Galaxy.

²³And possibly too expensive given the current climate for scientific funding. Fingers crossed the Thirty Meter Telescope actually gets built!

Table 7.5: SSPP Stellar Parameters for Hectospec Targets

UW ID ^a	flags	T_{eff} (K)	$\sigma(T_{\text{eff}})$ (K)	$N(T_{\text{eff}})^{\text{b}}$	$\log g$ (dex)	$\sigma(\log g)$ (dex)	$N(\log g)^{\text{b}}$	[Fe/H] (dex)	$\sigma([\text{Fe}/\text{H}])$ (dex)	$N([\text{Fe}/\text{H}])^{\text{b}}$
4172970	nnnnn	5426.88	96.58	6	3.56	0.14	6	0.14	0.12	5
4583821	Nnnnn	4536.84	149.91	3	4.39	0.48	2	-0.88	0.06	1
4651452	NnnnN	0	0	0
5302673	nnnGn	5902.55	242.59	4	4.02	0.69	2	-1.19	0.21	1
4220866	nnBgn	5135.22	110.15	4	3.42	0.80	4	-1.18	0.14	3
4377727	nnnnn	4912.80	36.81	3	3.37	0.33	4	-0.49	0.10	3
5253630	nnnnn	5797.32	70.61	8	3.78	0.41	6	-0.63	0.07	6
5839217	NCnnN	0	0	0
4305868	NnBnN	0	0	0
4313372	nnnnn	5153.81	104.70	4	4.59	0.13	5	-0.47	0.08	4
4374553	nCnc	0	0	0
4516619	nnnnn	5834.00	27.76	7	4.19	0.11	6	-0.06	0.04	5
4633113	nnBnn	6142.08	169.38	4	4.06	0.81	2	-1.00	0.08	1
4636579	nnnnR	0	0	0
4766649	nnnGn	4039.45	16.03	1	4.46	0.05	1	-1.11	0.08	1
4862820	nCnnn	5936.54	60.31	7	4.36	0.14	6	-0.46	0.01	3
5045025	nnnnn	5036.30	111.66	4	4.37	0.01	5	-0.49	0.04	2
5131032	nnnnn	5301.11	80.42	4	4.56	0.32	4	-0.08	0.05	2
5148546	nnnnn	4863.95	149.34	3	4.43	0.45	2	-1.16	0.21	1
5247052	ICnnR	0	0	0
5412426	nnnnn	4714.93	51.87	3	3.09	0.22	4	-0.73	0.11	3
5440532	nnnnn	5509.38	77.84	7	3.95	0.21	6	-0.49	0.04	4
5609096	nnnnn	5507.63	197.80	4	3.28	0.50	4	0.08	0.10	2
5654824	nnnnn	4982.71	117.24	3	4.29	0.35	2	-0.92	0.06	1
5744826	nnnnn	6394.25	107.13	9	3.83	0.23	7	-1.33	0.09	2
5788205	nnBnn	5824.35	70.28	4	3.55	0.25	2	-0.61	0.05	1
5975305	NnBn	5549.25	92.55	3	4.05	0.34	2	-0.22	0.06	1
4240796	nnnnn	5746.60	171.09	6	3.44	0.58	4	-0.23	0.03	2
4247360	lnnnR	0	0	0
4251687	lnnnR	0	0	0
4351227	nnnnn	5743.09	99.95	4	4.20	0.40	2	-0.51	0.04	1
4374564	nCnnR	0	0	0
4399885	nnnnn	5720.31	89.21	8	4.08	0.05	6	-0.39	0.07	6
4408536	nnnnR	0	0	0
4711930	nnnnn	7089.96	42.91	8	3.84	0.25	6	-0.38	0.06	6
5029422	nnnnn	5721.36	48.22	7	3.91	0.10	6	0.05	0.12	5
5098686	nnnnn	6170.91	151.99	5	2.25	0.89	2	-1.75	0.10	1
5238399	nnnnX	0	0	0
5321004	nnnnn	5518.49	66.61	7	3.94	0.04	6	-0.55	0.02	6
5410925	nnnnn	5081.14	146.66	3	3.69	0.31	3	0.08	0.08	1
5479654	nnnnn	5921.32	105.12	8	4.13	0.18	6	-0.39	0.05	7
5491314	nnnnn	5103.53	91.44	4	2.41	0.15	5	-0.71	0.06	6
5499687	Nnnnn	4248.54	24.07	3	3.78	0.32	2	-0.59	0.06	1
5500750	Nnnnn	4805.01	229.97	3	4.44	0.29	2	-0.29	0.06	1
5723495	nnnnn	6026.87	72.78	8	4.21	0.12	6	-0.76	0.05	6
5991774	NnBnN	0	0	0
5996123	nnnnn	5616.35	85.07	3	3.90	0.02	2	-0.37	0.04	1
6026542	nnBn	5369.39	92.46	4	4.11	0.22	4	-0.61	0.05	1
4423354	nnnnn	5450.60	283.59	5	3.83	0.30	4	-0.82	0.04	2
4450187	NnnnN	0	0	0
4457490	nnnnn	5740.97	73.36	7	4.13	0.11	6	-0.36	0.07	6
4479249	nnnnn	5598.13	130.39	7	3.81	0.14	6	-0.55	0.05	3
4539756	nnnnn	4625.81	129.93	3	4.07	0.15	4	0.16	0.20	1
4555242	nnngn	5494.89	164.31	5	2.83	0.51	2	-1.12	0.05	1
4593408	nnnnn	5812.29	68.68	7	4.02	0.15	6	-0.36	0.04	4
4790621	nCnn	5258.01	166.55	3	4.07	0.07	4	-0.04	0.07	2
4880797	nnnnn	5026.69	81.77	4	4.38	0.10	5	-0.34	0.09	4
5014177	nnnnn	5732.25	97.02	7	3.90	0.05	6	-0.07	0.03	4
5015947	nnnnn	6417.80	127.68	8	3.79	0.08	6	-0.78	0.02	7
5034169	VnnnX	0	0	0
5051552	nnnnn	5090.93	113.44	3	4.11	0.03	4	-0.01	0.17	2
5067963	nnBn	5244.97	99.42	3	4.20	0.32	2	-0.56	0.07	1
5129902	lnnnR	0	0	0
5191359	NnBn	6439.33	421.91	4	3.88	1.00	2	-0.08	0.10	1
5462829	nnnnn	5890.19	121.75	7	3.92	0.18	4	-0.69	0.09	5
5513750	nnnnn	5670.38	73.30	7	4.04	0.06	6	-0.56	0.03	4
5621815	nnnnn	5524.14	71.32	7	3.55	0.05	6	-0.16	0.08	5
6037955	NnnnN	0	0	0
6065428	nnBnN	0	0	0
6086952	Nnnnn	4726.52	100.73	3	4.19	0.12	2	-0.49	0.05	1
4204493	nnnnN	0	0	0
4253967	nnnnn	5962.39	42.17	8	4.22	0.13	6	-0.83	0.06	6
4433701	VnBnX	0	0	0
4577199	nnnnR	0	0	0

Table 7.5 (cont'd): SSPP Stellar Parameters for Hectospec Targets

UW ID ^a	flags	T_{eff} (K)	$\sigma(T_{\text{eff}})$ (K)	$N(T_{\text{eff}})^{\text{b}}$	$\log g$ (dex)	$\sigma(\log g)$ (dex)	$N(\log g)^{\text{b}}$	[Fe/H] (dex)	$\sigma([\text{Fe}/\text{H}])$ (dex)	$N([\text{Fe}/\text{H}])^{\text{b}}$
4615774	NnnnN	0	0	0
4700188	nnnnn	5394.28	130.22	4	4.31	0.16	5	-0.80	0.02	3
5078446	nnnnn	6300.44	84.56	5	3.72	0.22	2	-1.40	0.03	1
5079713	nnngn	4304.63	10.52	2	3.79	0.12	3	-1.22	0.08	1
5292935	nnnnn	5113.65	68.01	6	3.06	0.15	6	-0.81	0.06	4
5296611	nnnnn	5613.20	89.58	7	4.17	0.18	6	-0.61	0.06	7
5355373	nnnnn	5014.41	89.23	3	4.58	0.12	4	-0.56	0.02	2
5383329	nnGn	4098.55	6.85	2	4.88	0.03	1	-1.34	0.06	1
5398376	nnBn	6114.51	222.37	5	3.27	0.25	2	-0.56	0.07	1
5463758	nnnnn	4525.19	90.76	3	4.11	0.14	2	-0.03	0.07	1
5529210	nnnnn	6147.78	100.87	8	3.83	0.63	5	-0.58	0.03	3
5744847	nnBgn	4836.61	232.74	4	3.66	0.13	5	-1.54	0.06	3
5796940	NnnnN	0	0	0
5836847	nnnnn	4813.69	74.06	3	4.45	0.15	2	-0.71	0.08	1
5897424	NnnnN	0	0	0
4370203	nnngn	4639.57	42.82	3	4.15	0.27	2	-1.45	0.09	1
4559372	nnnnn	4874.00	249.03	3	4.20	0.01	2	-0.54	0.07	1
4657927	lnnnR	0	0	0
4695059	nnnnn	4618.65	50.54	3	3.58	0.30	2	-0.35	0.06	1
4739954	nnnnn	6506.82	50.51	8	3.85	0.23	6	-1.26	0.03	4
4777250	nnnnn	4825.81	120.23	3	3.83	0.04	4	-0.96	0.17	4
5069068	nnnnn	4664.01	99.01	3	3.54	0.40	2	-1.10	0.06	1
5113699	nnnnn	5886.57	25.06	6	4.02	0.09	4	-0.37	0.05	5
5203525	nnnnn	4439.83	88.38	3	4.24	0.05	2	-0.39	0.06	1
5321652	nnnnn	5765.13	92.63	4	3.28	0.35	2	-0.58	0.06	1
5383162	lnnnR	0	0	0
5414567	nnnnn	6070.72	263.04	4	4.05	0.73	2	0.06	0.10	1
5423508	nnBnn	5688.23	87.71	4	4.21	0.36	2	-0.57	0.05	1
5526116	nnnnn	5254.96	190.82	4	4.19	0.17	2	-0.73	0.03	1
5895111	nnnnn	4255.62	123.36	2	4.28	0.56	2	-0.53	0.07	1
6004038	NnnnN	0	0	0
4542584	nnngn	5360.20	82.00	6	4.31	0.18	6	-1.06	0.06	6
4641857	ICnnR	0	0	0
4720393	nnnnn	5637.33	105.93	4	4.34	0.51	2	-0.36	0.07	1
4755881	NnnnN	0	0	0
4805741	nnnnn	5600.84	104.96	7	3.97	0.20	6	-0.85	0.04	5
5054408	NnBnN	0	0	0
5160578	nnnnn	6978.65	66.43	7	4.14	0.18	6	-0.63	0.06	4
5177547	nnnnn	7022.98	53.47	8	4.03	0.30	6	-0.94	0.04	4
5230603	nnBgn	5375.99	64.46	3	4.33	0.50	2	-1.01	0.15	1
5402668	nnnnn	5595.31	151.36	7	3.89	0.09	6	-0.21	0.05	3
5485671	ICnnR	0	0	0
5515925	nnnnn	5743.58	146.27	5	3.89	0.14	4	-0.53	0.09	4
5548276	nnnnn	5019.46	122.98	3	4.54	0.17	4	-0.60	0.11	1
5811329	nnnnR	0	0	0
4300388	ICnnR	0	0	0
4339178	nCnnR	0	0	0
4789942	nnnnn	6328.47	25.94	9	3.85	0.09	7	-0.83	0.05	6
4795572	nnnnn	5028.26	107.76	4	4.18	0.39	4	-0.73	0.20	1
5073887	lnnnn	4147.68	57.51	2	3.30	0.13	1	-0.28	0.07	1
5092261	nnnnn	4308.25	66.46	3	3.88	0.19	4	-0.62	0.08	1
5132587	ICnnR	0	0	0
5177616	VnBnX	0	0	0
5476420	nnnnn	5702.98	88.36	8	3.75	0.08	6	-0.57	0.05	6
5604247	nnnnn	4952.93	165.79	4	4.68	0.13	5	-0.59	0.09	3
5770510	nnnnn	5911.96	104.26	8	3.88	0.10	6	-0.56	0.04	6
5791747	NnnnR	0	0	0
5975721	nCnnR	0	0	0
7909350	nnnnn	4720.73	64.61	3	4.43	0.12	4	-0.74	0.20	2
4394923	nnnnn	4885.31	153.38	3	4.39	0.17	4	-0.67	0.14	3
4616357	nnnnn	4450.54	79.32	3	4.57	0.15	4	-0.82	0.12	2
4857209	lnnnR	0	0	0
4871597	nCnnn	5207.71	232.86	3	3.29	0.13	4	-0.36	0.05	2
5054747	nnGn	5603.98	162.78	4	2.76	0.45	2	-1.19	0.07	1
5135140	lCnnR	0	0	0
5163339	nnnnn	5626.74	74.39	7	3.96	0.07	6	-0.46	0.03	3
5242156	nnnnn	5931.10	44.84	8	3.96	0.04	6	-0.24	0.03	6
5315030	nnnnn	5932.73	54.95	7	3.87	0.08	6	-0.46	0.04	6
5356240	nnnnR	0	0	0
5439874	nnngn	5193.68	7.28	5	4.27	0.11	4	-1.03	0.09	4
5758279	NnnnN	0	0	0
5820176	nnnnn	5993.88	48.43	7	3.64	0.41	4	-1.08	0.01	2
5841778	nnnnn	6105.07	180.97	4	3.98	0.15	2	-0.32	0.06	1
4442716	nnnnn	4339.30	49.69	3	4.33	0.24	4	-0.54	0.01	2

Table 7.5 (cont'd): SSPP Stellar Parameters for Hectospec Targets

UW ID ^a	flags	T_{eff} (K)	$\sigma(T_{\text{eff}})$ (K)	$N(T_{\text{eff}})^{\text{b}}$	$\log g$ (dex)	$\sigma(\log g)$ (dex)	$N(\log g)^{\text{b}}$	[Fe/H] (dex)	$\sigma([\text{Fe}/\text{H}])$ (dex)	$N([\text{Fe}/\text{H}])^{\text{b}}$
4878058	lnnnR	0	0	0
5018848	VnnnX	0	0	0
5080469	nCnnX	0	0	0
5196862	nnnnR	0	0	0
5197961	nnnnn	6107.54	32.52	8	3.75	0.06	6	-0.19	0.04	6
5233597	nnnnn	4969.99	115.04	3	3.14	0.26	4	-0.78	0.10	2
5937436	nnnnn	4393.54	44.83	3	4.48	0.21	4	-0.64	0.07	1
4672775	nnnnR	0	0	0
4841172	nnnnn	5515.28	181.99	7	4.10	0.25	6	-0.40	0.09	3
4843409	nnBnn	5352.39	90.90	4	4.09	0.15	4	-0.74	0.14	3
5037367	nnnnn	4601.40	51.78	3	3.51	0.64	2	-0.35	0.15	1
5119284	nnBnn	5208.43	79.52	6	4.14	0.29	6	-0.98	0.03	6
5160946	nnnnn	5684.39	249.40	3	4.15	0.19	2	-0.50	0.06	1
5181850	lnnnR	0	0	0
5241036	nnnnn	5547.42	34.00	6	3.60	0.09	6	-0.47	0.05	4
5270369	nnnnn	5794.33	75.85	7	4.17	0.12	6	-0.27	0.02	5
5589534	Nnnnn	5791.44	207.48	4	4.03	0.01	2	0.46	0.05	1
5736581	NnnnN	0	0	0
5968934	NnnnR	0	0	0
4202889	nnnnn	4614.24	85.94	3	4.21	0.34	2	-1.54	0.14	1
4283050	nnnnn	5487.26	16.90	4	3.97	0.07	5	-0.17	0.07	4
4309627	lnnnn	4078.36	57.02	2	3.15	0.27	2	-0.20	0.27	1
4553877	nnnnn	5793.76	55.08	7	4.08	0.12	6	-0.51	0.05	6
4553920	nnnGn	5372.76	24.52	6	3.13	0.14	6	-1.02	0.03	5
4591458	nnnnn	4772.76	90.34	3	4.43	0.13	4	-0.49	0.15	3
4700246	nnnnn	5921.05	54.77	8	4.62	0.19	6	-0.35	0.12	6
4847565	nnBnn	5586.11	329.13	3	4.43	0.25	4	-0.11	0.14	3
4857244	nCnnR	0	0	0
4871978	NnnnN	0	0	0
5056378	nnnnn	4557.20	66.48	3	4.47	0.20	4	-1.06	0.23	2
5130508	NnnnN	0	0	0
5153184	nnBnn	5539.18	26.69	4	4.39	0.49	2	-0.33	0.04	1
5158699	nnnnn	4548.62	64.73	3	4.45	0.17	4	-0.70	0.07	1
5183206	nnnnn	4864.66	141.11	3	4.37	0.51	2	-1.12	0.12	1
5318314	nnnnR	0	0	0
5413217	nnnnn	5397.73	66.40	6	3.85	0.12	6	-0.87	0.05	6
5417566	lnnnn	4201.40	91.84	2	3.75	0.16	1	-0.68	0.07	1
5446697	nnnGn	5757.44	133.76	8	3.70	0.32	6	-1.11	0.00	5
5504431	nnnnn	5780.06	67.66	4	3.47	0.04	2	-0.30	0.04	1
5563194	nnnGn	5841.45	145.99	5	3.20	0.15	2	-1.22	0.04	1
6017407	nCnnR	0	0	0
6024676	nnnnn	5122.95	258.95	3	3.21	0.19	4	-0.98	0.00	2
4195014	nnnnN	0	0	0
4195293	NnBnN	0	0	0
4266206	nnnnn	6053.33	534.90	3	4.29	0.31	4	-0.34	0.15	1
4288208	nnnnn	5123.98	107.30	4	4.47	0.13	5	-0.67	0.11	4
4383313	nnnnn	5548.39	53.06	7	3.94	0.14	6	-0.46	0.06	4
4590325	nCnnn	4768.40	142.41	3	3.95	0.12	4	-0.20	0.11	2
4623189	NnnnN	0	0	0
4628612	nnnnn	5265.11	54.95	6	3.72	0.06	6	-0.53	0.05	4
5026666	NnnnN	0	0	0
5148669	nnnnn	5559.23	67.69	7	4.27	0.09	6	-0.38	0.02	5
5167915	nnnnn	4488.73	61.13	3	4.14	0.08	4	-1.07	0.09	1
5246072	nnnnn	5842.17	55.55	8	3.89	0.08	6	-0.22	0.04	7
5311806	nnnnn	5602.44	55.27	4	3.94	0.07	2	-0.29	0.06	1
5325849	nnnnR	0	0	0
5359363	nnnnn	5920.78	289.36	7	4.23	0.24	4	-0.30	0.24	3
5393126	nnnnn	6441.83	79.53	7	4.08	0.15	4	-0.76	0.05	4
5541650	nnnnn	5882.13	81.43	5	3.82	0.13	2	-0.94	0.02	1
5562004	nnnnn	5107.60	158.73	4	3.93	0.22	5	-0.51	0.04	2
5608516	nnnnn	6146.52	81.79	9	2.16	0.36	7	-1.29	0.08	6
5761480	nnnnn	4779.52	77.18	3	2.35	0.22	4	-0.50	0.02	4
5830807	NnBnN	0	0	0
4216674	nnBGn	5286.69	115.94	3	3.73	0.23	2	-1.02	0.08	1
4339330	NCnnR	0	0	0
4489920	nnnnn	4856.52	264.56	3	4.24	0.55	2	-0.63	0.10	1
4881611	nnnnn	4776.47	93.65	3	4.41	0.11	4	-0.78	0.16	3
5044360	nCnnR	0	0	0
5080483	NnBnN	0	0	0
5245580	nnnnn	7796.46	102.27	4	4.46	0.23	3	-0.21	0.03	1
5250274	nnnnn	4588.90	73.20	3	2.87	0.29	3	-0.84	0.04	2
5252851	nnnnn	5694.30	84.43	6	3.01	0.26	4	-0.98	0.04	5
5275857	nnnnn	5810.05	56.58	7	3.72	0.32	4	-0.57	0.03	4
5355815	nnnnn	5906.02	133.59	5	4.39	0.45	2	-0.76	0.06	1

Table 7.5 (cont'd): SSPP Stellar Parameters for Hectospec Targets

UW ID ^a	flags	T_{eff} (K)	$\sigma(T_{\text{eff}})$ (K)	$N(T_{\text{eff}})^{\text{b}}$	$\log g$ (dex)	$\sigma(\log g)$ (dex)	$N(\log g)^{\text{b}}$	[Fe/H] (dex)	$\sigma([\text{Fe}/\text{H}])$ (dex)	$N([\text{Fe}/\text{H}])^{\text{b}}$
5487379	lnnnR	0	0	0
5749023	nnnnn	5799.86	64.45	8	3.86	0.06	6	-0.43	0.02	4
5811416	nnnnn	4686.75	94.43	3	4.19	0.16	3	-0.31	0.09	1
5825873	nnnnn	5427.90	85.95	6	3.68	0.16	6	-0.48	0.02	3
4222163	nnnnn	4678.97	70.92	3	4.10	0.13	4	-0.63	0.16	3
4333984	NnnnnN	...	0	0	0
4368667	nnnnn	5637.12	60.26	7	3.74	0.09	6	-0.13	0.06	5
4555631	nnBnn	5005.50	52.47	3	4.36	0.01	2	-0.64	0.07	1
4564534	VnnnN	...	0	0	0
4578569	nnnnn	5589.13	126.83	6	4.45	0.18	6	-0.50	0.10	4
4707627	nnnnn	4628.17	50.43	3	4.13	0.09	4	-0.28	0.09	2
4803295	nnnnn	5616.64	116.99	5	3.45	0.16	4	-0.58	0.07	3
5025331	nnnnn	4563.08	107.60	3	4.32	0.52	2	-0.93	0.13	1
5035253	nnnnn	5273.37	53.90	6	4.38	0.09	6	-0.10	0.01	4
5062125	nnnnn	5974.35	115.23	5	3.88	0.22	2	-0.17	0.05	1
5078666	nnngn	4307.19	42.58	3	3.30	0.35	4	-1.23	0.16	2
5088283	Nnnnn	5756.35	206.37	4	4.10	0.45	2	-0.51	0.08	1
5122898	NnnnnN	...	0	0	0
5229237	nnnnn	5971.68	53.03	8	4.00	0.12	6	-0.55	0.02	5
5569550	nnnnn	4921.68	230.39	3	4.72	0.15	4	-1.12	0.03	2
5571930	nnnnn	4929.85	92.50	3	4.13	0.14	2	-0.67	0.06	1
5851896	lnnGn	4086.37	21.93	1	4.13	0.12	1	-1.31	0.11	1
5955416	nnnnn	4889.25	105.17	3	4.48	0.11	4	-0.49	0.09	3
6023667	nnnnn	4683.97	408.16	2	4.10	0.04	2	-0.62	0.07	1
4443887	nnnnn	4310.18	66.67	3	3.99	0.19	3	-0.47	0.07	1
4450751	nnnnn	4809.57	72.58	3	3.38	0.13	3	-0.21	0.06	1
4505210	nnnnn	5744.69	144.02	7	3.51	0.20	4	-0.86	0.04	3
4679565	nnnnc	...	0	0	0
5108461	nnnnn	5966.48	133.56	5	2.17	0.92	2	-0.41	0.07	1
5138790	nCBgn	4262.78	153.07	2	4.18	0.49	2	-1.18	0.23	1
5143110	nnnnn	6022.01	231.04	3	3.93	0.21	3	-0.59	0.07	1
5227320	nnnnn	4551.91	87.48	3	3.46	0.34	3	-0.08	0.07	1
5245615	nnnnn	4776.86	62.38	3	2.45	0.23	4	-0.69	0.08	6
5481272	nnnnn	5338.74	98.00	4	4.35	0.10	5	-0.51	0.10	3
5493626	nnnnn	4319.05	166.46	2	4.43	0.41	2	-0.60	0.10	1
5706167	nnnnn	4735.17	74.55	3	4.53	0.13	3	-0.37	0.06	1
5810711	nnnnn	5816.25	89.01	8	3.73	0.08	6	-0.35	0.03	7
5895233	nnnnn	5810.99	38.91	8	3.44	0.08	6	-0.33	0.02	5
4173760	NnBnN	...	0	0	0
4272800	lCnnR	...	0	0	0
4286946	nnngn	5048.33	141.79	6	3.19	0.21	6	-1.27	0.02	5
4318560	nnBnn	4899.51	142.40	3	4.44	0.14	4	-0.66	0.12	3
4452152	NnBnN	...	0	0	0
4491503	VnBnX	...	0	0	0
4578179	nnnnn	4262.09	45.41	3	4.29	0.38	2	-1.44	0.09	1
4804774	nnnnn	6051.30	66.92	8	3.45	0.27	6	-0.43	0.01	2
4877852	NnnnnN	...	0	0	0
5098569	nnBnn	5602.15	40.08	5	4.07	0.17	4	-0.14	0.08	4
5194792	nnnnn	5278.59	109.94	4	4.26	0.07	5	-0.40	0.05	5
5211439	nnnnn	4477.84	56.60	3	3.77	0.15	4	-1.04	0.11	1
5227414	nnnnn	5550.10	101.89	6	4.21	0.11	6	-0.32	0.08	4
5333534	nnnnn	6032.50	70.25	5	3.90	0.23	2	-0.46	0.07	1
5354133	lnnnN	...	0	0	0
5482237	nnnnn	5018.68	18.96	4	3.26	0.03	5	-0.73	0.06	5
5731978	nnnnn	5792.02	82.08	6	3.78	0.48	4	-0.54	0.01	5
5921579	NnnnR	...	0	0	0
5958372	nnnnn	4686.16	155.77	3	4.60	0.28	2	-0.63	0.04	1
6033429	nnnnn	4910.30	6.19	3	2.61	0.08	4	-0.70	0.03	3
4256125	nnnnn	5667.79	58.34	7	4.18	0.11	6	-0.47	0.06	6
4284627	NnnnN	...	0	0	0
4634192	lnnnn	4398.15	41.07	3	3.69	0.15	4	-0.23	0.15	2
4655872	Nnnn	4630.82	145.27	3	4.19	0.16	2	-0.32	0.07	1
4805306	nnnnn	5892.32	78.47	8	3.95	0.17	6	-0.57	0.03	3
5041771	NCBnN	...	0	0	0
5081675	nnnnn	7415.21	74.38	6	3.36	0.31	4	-1.99	0.11	2
5141506	nnBnN	...	0	0	0
5232071	lCnnR	...	0	0	0
5389459	nnBnn	5462.65	46.00	4	3.64	0.45	2	-0.47	0.04	1
5414603	nnBnn	4925.98	41.97	3	4.18	0.29	3	-0.66	0.11	1
5429770	nnnnn	5560.98	387.88	3	3.94	0.16	4	0.01	0.12	3
5456839	nnnnn	5542.03	94.65	6	4.06	0.08	6	-0.07	0.09	5
5579091	NnnnN	...	0	0	0
5718058	nnnGn	4274.02	21.05	2	4.05	0.14	2	-1.67	0.07	1
5864498	lnnnR	...	0	0	0

Table 7.5 (cont'd): SSPP Stellar Parameters for Hectospec Targets

UW ID ^a	flags	T_{eff} (K)	$\sigma(T_{\text{eff}})$ (K)	$N(T_{\text{eff}})^{\text{b}}$	$\log g$ (dex)	$\sigma(\log g)$ (dex)	$N(\log g)^{\text{b}}$	[Fe/H] (dex)	$\sigma([\text{Fe}/\text{H}])$ (dex)	$N([\text{Fe}/\text{H}])^{\text{b}}$
5981080	nnnnn	5699.30	49.13	7	4.04	0.07	6	-0.14	0.06	5
6044337	nnnnn	5985.88	82.62	7	4.13	0.28	6	-0.48	0.02	5
4201494	nnBGN	5923.58	149.65	4	3.27	0.41	2	-1.72	0.15	1
4288324	nnnnn	4190.22	95.52	3	3.01	0.47	3	-0.51	0.07	1
4300586	nnBnn	5832.33	181.71	7	4.25	0.30	6	-0.20	0.07	5
4657713	nnnnn	4546.23	120.76	3	4.36	0.16	4	-1.21	0.21	2
4704774	1CnnR	0	0	0
5035690	nnnnR	0	0	0
5102233	nnnnR	0	0	0
5112358	nnngn	5674.02	198.97	5	4.04	0.22	4	-1.65	0.17	3
5147407	Nnnnn	5122.49	212.32	3	4.53	0.18	2	-0.55	0.13	1
5234044	nnnnn	4799.41	121.72	3	4.18	0.07	4	-0.67	0.04	2
5305507	nnBnn	5627.13	310.21	3	4.17	0.69	2	-0.79	0.06	1
5439923	nnnnn	5722.29	165.30	7	4.20	0.25	6	-0.71	0.07	6
5538831	nnnnn	6175.71	55.57	9	3.19	0.32	7	-2.17	0.04	4
5569358	nnBnn	5278.96	54.68	5	4.32	0.20	4	-0.63	0.03	2
5703605	nnnnn	6235.63	93.04	7	4.06	0.44	4	-1.71	0.04	2
5714172	nCnnn	4906.39	94.73	3	4.35	0.14	4	-0.35	0.14	2
6050244	NnnnN	0	0	0
4156019	nnBnn	5263.33	77.38	3	4.05	0.11	2	-0.34	0.06	1
4215881	nCnnn	6004.54	174.83	8	3.73	0.47	6	0.12	0.04	2
4394591	1CnnR	0	0	0
5148889	nnBnn	5820.58	135.94	4	3.47	0.81	2	-0.35	0.07	1
5180650	nnnnn	5823.35	77.48	7	4.08	0.27	6	-0.62	0.04	6
5282226	nnBnn	4866.47	136.68	3	4.03	0.38	2	-0.82	0.07	1
5688551	nnnnn	5654.59	19.17	5	2.59	0.32	2	-0.57	0.06	1
5851213	VnBnN	0	0	0
4481653	IlnnnR	0	0	0
4676874	NnnnN	0	0	0
4713672	nnnnn	5999.62	181.92	6	3.83	0.14	4	0.09	0.05	2
5191138	NnnnN	0	0	0
5240272	nnnnn	7672.64	82.77	3	4.28	0.33	2	-1.80	0.13	1
5712181	nnnnn	6276.83	86.77	8	2.47	0.23	6	-1.80	0.01	5
6024010	nnnnn	5300.42	130.04	4	3.57	0.09	5	-0.73	0.13	3
4176982	nnnnn	5070.51	144.82	4	4.41	0.11	5	-0.36	0.10	4
4297181	nnnnn	5820.32	169.21	4	3.99	0.89	2	-0.39	0.10	1
4381391	nnnGn	4029.85	26.81	1	4.14	0.11	2	-1.74	0.17	1
4433741	nnnnn	5673.29	131.05	3	4.20	0.23	2	-0.85	0.12	1
4523840	nnnnn	5547.11	78.83	6	4.10	0.31	4	-0.56	0.10	3
4524626	nnnnn	4793.78	82.85	3	3.77	0.11	4	-0.46	0.13	3
4527954	NnBnN	0	0	0
4594666	nnnnn	5042.35	143.04	3	3.98	0.21	4	-0.84	0.11	2
4777250	nnBnn	4864.36	83.03	3	3.86	0.08	4	-0.90	0.02	4
4847242	nnnnn	6195.31	139.41	8	3.80	0.12	6	-0.65	0.04	6
5092240	nnBGN	5952.49	100.26	4	4.03	0.65	2	-1.01	0.07	1
5097716	nnnnn	5249.67	78.11	6	4.54	0.11	6	-1.00	0.09	5
5124936	nnnnn	5086.14	126.00	3	4.17	0.13	4	0.15	0.04	3
5168706	VnBnX	0	0	0
5223440	nnnnn	5728.03	71.34	6	3.88	0.28	4	-0.34	0.07	5
5251967	nnnnn	5867.29	32.62	8	3.87	0.13	6	-0.73	0.02	4
5501922	nnnnn	5622.07	48.51	6	3.96	0.05	6	-0.07	0.08	6
5684132	NnBnN	0	0	0
5698089	nnnnn	6122.19	173.78	6	3.75	0.05	6	-0.51	0.06	4
6058853	nnnnn	5976.96	38.98	8	4.04	0.02	6	-0.18	0.03	3
4265567	nnnnn	5708.20	177.32	5	4.14	0.34	4	-1.28	0.06	2
4398079	nnnnX	0	0	0
4472791	NnnnN	0	0	0
4546569	1CnnR	0	0	0
4598821	1CnnR	0	0	0
4634355	nnnnn	5638.10	257.92	6	3.99	0.23	4	-0.74	0.03	5
4762022	nnnnn	4990.27	229.12	3	4.23	0.04	2	-0.24	0.11	1
4765867	Nnnnn	4751.84	159.76	3	4.51	0.37	2	-0.73	0.06	1
5030626	1CnnR	0	0	0
5051006	NnnnN	0	0	0
5108562	nnnnn	4548.73	62.63	3	4.35	0.11	4	-0.61	0.15	2
5278003	nnnGn	4202.82	79.87	2	4.25	0.25	4	-1.39	0.15	2
5305835	nnnnn	5617.72	156.05	5	3.65	0.34	4	-0.46	0.05	2
5439858	nnnnn	5060.77	130.61	4	4.37	0.06	5	-0.22	0.05	4
5708529	nnnnn	4492.71	75.64	3	4.49	0.19	4	-0.80	0.04	1
5794703	nnnnn	6101.26	48.20	8	4.05	0.04	6	-0.25	0.04	5
5871910	nnnnn	5600.22	130.72	6	4.14	0.09	6	-1.18	0.07	6
5962667	NnnnN	0	0	0
6064462	nnnnn	6174.30	293.85	7	3.60	0.57	4	-0.93	0.09	1
6078393	nnBnn	4864.32	180.25	4	3.92	0.45	4	-1.15	0.08	2

Table 7.5 (cont'd): SSPP Stellar Parameters for Hectospec Targets

UW ID ^a	flags	T_{eff} (K)	$\sigma(T_{\text{eff}})$ (K)	$N(T_{\text{eff}})^{\text{b}}$	$\log g$ (dex)	$\sigma(\log g)$ (dex)	$N(\log g)^{\text{b}}$	[Fe/H] (dex)	$\sigma([\text{Fe}/\text{H}])$ (dex)	$N([\text{Fe}/\text{H}])^{\text{b}}$
4252416	NCnnR	0	0	0
4376054	nnnnn	5179.57	87.89	6	3.49	0.15	6	-0.96	0.04	6
4379344	nnnnn	5861.61	39.65	7	3.67	0.06	6	-0.00	0.07	7
4423949	nnBnc	0	0	0
4545549	nnnGn	5915.42	368.96	5	3.44	0.48	2	-1.04	0.11	1
4615430	nnnnn	5924.59	106.45	6	3.48	0.66	4	-0.33	0.07	1
4797050	nnnnn	5147.87	115.81	4	4.39	0.10	5	-0.29	0.07	4
4815726	nCnnN	0	0	0
4875870	lCnnR	0	0	0
5134327	nnnnn	5409.60	126.81	6	3.38	0.17	6	-0.31	0.07	5
5206647	nnnnn	6061.37	119.66	9	4.34	0.14	7	-0.33	0.10	3
5222798	nnnnn	5975.56	70.22	5	2.92	0.33	2	-0.78	0.12	1
5258688	nnnnn	4159.39	34.24	2	2.33	0.17	1	-0.31	0.09	1
5282413	nnnnn	6499.13	155.78	5	3.64	0.46	2	-0.58	0.09	1
5300051	nnnnn	4600.83	117.82	3	4.28	0.33	2	-0.62	0.09	1
5309573	nnBnn	5629.61	60.88	4	4.09	0.29	2	-0.50	0.05	1
5493909	nnnnn	4473.53	59.59	3	4.53	0.20	4	-0.69	0.05	1
5536045	nnnnn	4799.17	78.14	3	4.53	0.08	4	-0.73	0.00	2
5714921	nnnnn	5469.05	62.53	6	3.94	0.08	6	-0.15	0.06	5
5789854	NCBnN	...	0	0	0
5940153	nnnnn	5363.54	78.29	4	3.97	0.08	5	-0.11	0.06	4
4195966	nnnnn	5143.79	220.86	3	4.03	0.28	4	-0.29	0.08	2
4253621	nnnGn	6271.88	150.88	6	3.83	0.28	3	-1.39	0.05	1
4256023	nnnnN	...	0	0	0
4264015	NCBnN	...	0	0	0
4340749	nnnnn	5441.81	102.12	7	3.95	0.17	6	-0.86	0.05	5
4356497	nnnnn	5208.19	333.81	4	3.74	0.62	5	-0.42	0.15	1
4465410	lnnnN	...	0	0	0
4575156	nnnnn	5275.84	200.16	3	4.08	0.80	2	-0.85	0.07	1
5021574	lnnnR	...	0	0	0
5033395	nnnnn	5205.27	189.20	6	4.10	0.10	6	-0.76	0.12	4
5040882	nnnnn	5425.61	171.57	3	4.21	0.24	2	-0.32	0.06	1
5152874	Nnnnn	4524.93	170.53	3	3.69	0.05	2	-0.36	0.07	1
5225408	nnnnn	5784.45	288.65	3	3.37	0.12	2	-0.77	0.07	1
5296877	lnnnR	...	0	0	0
5476527	nnnnn	5254.46	168.71	4	3.58	0.15	4	-0.16	0.04	1
5577503	nnnnn	4810.42	167.72	3	2.13	0.18	4	-1.23	0.08	5
5661695	nnnnn	5578.98	50.68	6	3.76	0.03	6	0.14	0.03	4
5687675	nnBGN	5397.53	35.53	3	4.12	0.74	2	-1.04	0.12	1
5740448	nnBnn	5515.81	61.37	4	4.40	0.06	2	-0.78	0.06	1
5806472	nnnGn	5535.74	222.78	4	4.11	0.77	2	-1.41	0.21	1
6028899	NnnnN	...	0	0	0
4258589	NnnnN	...	0	0	0
4304866	nnnnn	5839.13	47.11	7	3.51	0.17	6	-0.63	0.05	4
4340143	NnnnN	...	0	0	0
4382078	Nnnnn	4590.32	66.63	3	3.90	0.20	2	-0.41	0.07	1
4440418	lnnnN	4081.24	18.38	1	2.29	0.18	1	-0.64	0.15	1
4635485	nnnnn	5674.43	187.28	4	4.23	0.23	2	-0.80	0.07	1
4699308	nnnnn	5268.58	86.22	6	4.38	0.25	6	-0.74	0.04	4
4749871	nnnnn	7940.76	367.99	3	3.86	0.28	2	-1.43	0.07	1
4762445	nnnnn	5223.09	92.21	3	4.31	0.57	2	-0.89	0.16	1
4830012	lnnnR	...	0	0	0
5042955	nnnnn	5565.98	106.89	6	3.96	0.18	4	-0.63	0.06	4
5101509	nnnnn	4602.77	93.95	3	4.46	0.15	4	-0.27	0.04	1
5123151	nnnnn	4270.41	78.79	3	4.21	0.31	4	-0.66	0.09	1
5197889	nnnnn	5607.59	79.91	7	4.23	0.14	6	-0.70	0.06	6
5250859	nnnnn	5096.87	121.69	4	4.38	0.14	5	-0.78	0.05	4
5301278	nnBnn	5498.55	84.08	3	3.85	0.08	2	-0.71	0.07	1
5317713	NnnnN	...	0	0	0
5369945	nnnnn	4566.97	37.16	3	4.34	0.14	4	-0.89	0.06	2
5618520	nnBnn	5798.40	143.87	4	3.62	1.02	2	-1.31	0.06	1
6030062	nnnnn	5209.45	103.87	4	4.28	0.17	4	-0.83	0.04	3
4185977	nnnnn	7365.37	72.80	6	3.65	0.30	4	-2.01	0.05	1
4390427	nnngn	5925.94	152.43	5	3.74	0.51	2	-1.02	0.05	1
4609421	nnBnn	5478.98	61.39	6	3.99	0.14	4	-0.71	0.02	3
4839757	nnnnn	6445.87	53.34	8	2.86	0.15	6	-2.17	0.05	5
5032946	lnnnR	...	0	0	0
5037579	nnnnn	5618.39	60.66	7	3.83	0.11	6	-0.57	0.03	6
5237929	Nnnnn	4673.79	163.97	3	4.31	0.15	2	-0.74	0.11	1
5251855	nnnnR	...	0	0	0
5329778	nnnnn	5589.00	65.85	7	3.67	0.09	6	-0.67	0.02	4
5407561	nnnnn	5938.43	74.12	8	4.29	0.14	6	-0.56	0.04	6
5792253	nnnnn	5812.96	60.48	7	4.00	0.04	6	-0.24	0.05	6
5916743	nnnnn	5487.85	154.72	3	3.41	0.15	2	-0.67	0.12	1

Table 7.5 (cont'd): SSPP Stellar Parameters for Hectospec Targets

UW ID ^a	flags	T_{eff} (K)	$\sigma(T_{\text{eff}})$ (K)	$N(T_{\text{eff}})^{\text{b}}$	$\log g$ (dex)	$\sigma(\log g)$ (dex)	$N(\log g)^{\text{b}}$	[Fe/H] (dex)	$\sigma([\text{Fe}/\text{H}])$ (dex)	$N([\text{Fe}/\text{H}])^{\text{b}}$
5946369	nnnnn	5245.16	12.05	4	3.78	0.07	5	-0.78	0.07	5
4182596	nnnnn	5112.94	68.59	4	4.38	0.21	4	-0.60	0.06	2
4283452	nnBnn	5387.92	263.27	4	4.31	0.22	5	-0.24	0.07	2
4465913	nnnnn	4346.05	26.53	3	4.22	0.05	3	-0.87	0.06	1
4691014	nnnGn	4096.02	22.69	1	4.31	0.03	2	-1.57	0.09	1
4822615	nnnnn	4305.14	29.92	2	3.83	0.53	2	-0.22	0.24	1
5079828	nnnnn	4991.79	116.00	3	4.19	0.61	2	-0.93	0.08	1
5090771	nnBnn	5555.06	98.51	3	4.25	0.56	2	-0.52	0.08	1
5106348	nnnnn	6585.13	92.05	8	3.77	0.19	6	-0.73	0.05	6
5318377	nnngn	5083.61	333.91	3	1.85	1.64	2	-1.25	0.15	2
5320444	lnnnR	0	0	0
5407501	nnnnn	4664.16	119.82	3	4.46	0.42	2	-0.78	0.09	1
5787235	nnnnn	5373.98	66.15	6	4.02	0.17	6	-0.33	0.06	5
5874684	nnnnn	5953.69	88.63	7	3.93	0.24	4	-0.61	0.10	4
5933717	nnnnn	6570.91	195.04	5	3.23	0.61	3	-1.96	0.04	1
5955075	nnBnn	5171.96	36.44	4	3.74	0.17	2	-0.88	0.08	1
4249764	nCnnR	0	0	0
4455432	nnnnn	7833.18	108.00	3	4.30	0.23	2	-0.88	0.08	1
4594323	nnnnN	0	0	0
4876133	nnnnn	5022.65	122.48	6	3.54	0.14	6	-0.69	0.03	3
5087856	lnnnR	0	0	0
5137130	nnnnn	5455.85	17.27	4	3.84	0.12	2	-0.78	0.06	1
5167968	nnnnn	6337.93	64.61	8	3.39	0.23	6	-1.64	0.03	4
5210648	nCBnn	4659.64	255.46	3	3.49	0.15	3	-1.35	0.36	2
5294720	nnnnn	5708.44	97.92	8	4.10	0.25	6	-0.65	0.04	5
5344540	nnnGn	7317.16	127.84	8	2.97	0.21	6	-1.99	0.08	3
5690716	nnnnn	4273.90	62.74	3	3.87	0.12	2	-0.46	0.09	1
5777417	nnnnn	5255.58	142.86	3	4.05	0.02	2	0.12	0.06	1
5894605	nnnnn	5903.84	102.62	8	3.93	0.18	6	-0.37	0.06	6
5952357	nnnnn	5385.37	50.87	6	4.37	0.13	6	-0.22	0.05	4
6056528	nnnnn	5959.51	62.57	7	4.10	0.14	6	-0.52	0.03	5
4173777	nnnnn	6149.88	57.58	7	3.92	0.49	4	-0.68	0.09	1
4272248	nnnnn	5491.59	35.87	5	4.19	0.12	4	-0.71	0.04	3
4410097	nCnnR	0	0	0
4464618	nCnnR	0	0	0
4756281	nnngn	5274.80	42.67	6	3.36	0.14	6	-1.10	0.05	7
4848616	nnnnn	4631.03	98.76	3	4.01	0.17	2	-0.26	0.06	1
5151245	nnnnn	6478.81	242.20	7	3.76	0.38	4	-0.49	0.09	5
5158350	nnBnn	5702.08	219.87	3	4.06	0.18	2	-0.66	0.08	1
5281873	nnnnn	4410.91	55.51	3	4.10	0.13	3	-0.31	0.07	1
5286814	nnnnn	4407.56	53.08	3	2.44	0.22	4	-0.48	0.07	5
5303046	nnnnn	5041.46	97.81	4	3.69	0.14	5	-0.75	0.06	4
5381294	nCnnn	5044.91	54.01	4	4.00	0.52	2	-0.55	0.07	1
5761527	nCnnn	4588.85	73.70	3	3.62	0.07	4	-0.59	0.08	1
5900657	nnnnn	4897.31	127.43	3	4.64	0.27	3	-0.63	0.05	1
5984459	nnnnn	5226.31	195.10	4	3.87	0.22	5	-0.21	0.12	1
6003291	nnnnn	4977.69	75.60	3	4.52	0.14	4	-0.53	0.06	2
6031977	NnnnN	0	0	0
4186243	nnnnn	5625.19	100.75	7	3.76	0.04	6	-0.30	0.07	6
4237111	nnnnn	5852.91	112.43	7	3.64	0.12	4	-0.27	0.04	4
4378671	nnbn	0	0	0
4463558	nnnnn	7833.82	407.03	3	3.89	0.10	2	-1.78	0.19	1
4544790	lnnnR	0	0	0
4669069	nnnnn	5442.04	43.06	6	3.37	0.15	6	-0.98	0.02	6
4705494	NCnnR	0	0	0
5014990	nnnnn	8064.43	73.89	3	4.46	0.19	2	-1.21	0.12	1
5027830	NnnnN	0	0	0
5160491	nnnnn	5800.75	300.62	4	3.59	0.06	4	-0.93	0.05	1
5223023	nnnnn	5480.83	54.48	6	4.29	0.11	6	-0.68	0.04	7
5311114	nnngn	4464.69	13.93	3	4.62	0.16	4	-1.36	0.02	2
5324727	nnnnn	4232.05	135.98	2	3.44	0.09	1	-0.64	0.07	1
5400521	nnnnn	6379.76	139.17	5	3.54	0.05	2	-0.89	0.07	1
5405834	nnnnn	5804.14	119.47	4	3.98	0.16	2	-0.42	0.04	1
5502153	nnnnn	4709.94	67.06	3	4.34	0.19	2	-0.98	0.05	1
6066262	DCnnn	5345.25	703.80	3	4.88	0.02	4	-0.69	0.16	1
4433339	nnnnn	4953.42	99.06	3	2.57	0.15	4	-0.59	0.10	2
4500443	lnnnR	0	0	0
4539320	lnnnR	0	0	0
4651019	nnnnn	5679.07	56.82	7	4.09	0.14	6	-0.24	0.06	5
4756967	nnnnn	5654.29	23.41	7	3.67	0.05	6	-0.61	0.04	3
4766955	NnBnN	0	0	0
4776345	nCnnR	0	0	0
4786480	nnBnn	5055.27	90.58	3	3.79	0.19	4	-0.49	0.08	2
5091162	nnnnn	6350.66	79.03	5	2.20	0.95	2	-1.85	0.16	1

Table 7.5 (cont'd): SSPP Stellar Parameters for Hectospec Targets

UW ID ^a	flags	T_{eff} (K)	$\sigma(T_{\text{eff}})$ (K)	$N(T_{\text{eff}})^{\text{b}}$	$\log g$ (dex)	$\sigma(\log g)$ (dex)	$N(\log g)^{\text{b}}$	[Fe/H] (dex)	$\sigma([\text{Fe}/\text{H}])$ (dex)	$N([\text{Fe}/\text{H}])^{\text{b}}$
5151577	nnnnn	4711.02	107.42	3	3.80	0.07	4	-0.64	0.18	3
5157787	NnBnN	0	0	0
5171552	nnnnn	5641.24	83.58	7	4.07	0.13	6	-0.38	0.03	4
5304517	nnnnn	5855.42	59.09	8	4.14	0.22	6	-0.46	0.05	5
5359231	lnnnR	0	0	0
5557692	nnnnR	0	0	0
5741488	nnnnn	5334.83	16.18	6	3.35	0.15	6	-0.86	0.03	6
4174708	nnnnn	6245.78	44.74	9	4.12	0.16	7	-1.04	0.03	5
4616736	nnnnn	5407.80	213.52	3	4.32	0.08	4	-0.51	0.05	3
4652527	nnBnn	5104.33	66.88	3	4.54	0.10	2	-0.85	0.05	1
4704684	nnnnn	6030.33	122.31	5	3.58	0.47	2	-1.49	0.07	1
4811997	nnnnn	4719.71	328.59	3	4.32	0.56	2	-0.92	0.09	1
4877207	nnnnn	6286.31	70.56	8	3.93	0.13	6	-1.53	0.06	5
5080327	nnnnn	4730.53	52.33	3	2.27	0.47	4	-1.23	0.11	3
5090344	nnnnn	4703.62	66.17	3	4.04	0.12	4	-0.60	0.25	2
5137280	nnnnn	4501.35	81.08	3	4.06	0.04	4	-0.49	0.30	2
5223488	nGn	4053.04	22.28	2	4.49	0.08	1	-1.37	0.09	1
5271243	nnnnn	4605.92	106.39	3	4.16	0.03	3	-0.36	0.09	1
5389408	nnnnn	5575.88	83.34	7	4.16	0.14	6	-0.47	0.04	6
5561470	nnnnn	4901.34	96.47	3	4.41	0.05	4	-0.15	0.10	2
5657137	nnnnn	5864.00	53.74	6	3.91	0.08	4	-0.70	0.01	4
5708769	nnnnn	4190.37	117.77	2	3.68	0.27	2	-0.53	0.09	1
6009060	nnnnn	5574.74	62.13	6	3.77	0.06	6	-0.02	0.06	4
4254976	NnBnN	0	0	0
4331940	NnnnN	0	0	0
4348730	nnBnn	5812.96	48.00	4	4.18	0.70	2	-0.97	0.05	1
4384976	lCnnR	0	0	0
4432698	nCnnn	6041.11	70.76	8	3.99	0.13	6	-0.90	0.03	6
4604393	nnngn	5954.94	60.98	7	3.25	0.11	3	-1.13	0.01	3
4776306	lnnnR	0	0	0
4798788	nnBnn	5382.05	99.77	3	3.92	0.50	2	-0.70	0.10	1
4818670	nnnnR	0	0	0
5138364	VnBnN	0	0	0
5177287	nnnnn	4697.09	70.38	3	3.94	0.13	2	0.00	0.09	1
5183266	nCBnn	6145.82	105.31	3	3.26	0.52	2	-2.04	0.09	1
5413792	nnnnn	5602.21	128.62	5	3.95	0.16	4	-0.70	0.08	4
5426614	nnnnn	6501.98	62.81	8	2.62	0.24	6	-1.18	0.07	6
5615114	lnnnR	0	0	0
5803584	nnnnn	7566.20	150.31	4	3.97	0.19	3	-1.37	0.07	1
5974736	nnnnn	5518.79	21.38	6	4.31	0.22	6	-0.69	0.05	7
6009113	nnnnn	5664.30	51.26	7	4.33	0.14	6	-0.74	0.05	6
7909416	nnnnn	5658.97	81.19	7	4.11	0.15	6	-0.80	0.03	5
4243964	nnnnn	5851.20	53.49	8	4.51	0.04	6	-1.65	0.01	4
4274785	lnnnR	0	0	0
4290479	nnnnn	5089.23	48.69	4	4.38	0.12	5	-0.62	0.04	4
4586205	nnnnn	5010.24	214.57	4	4.00	0.21	5	-0.50	0.10	1
4781441	nnnnR	0	0	0
4808227	lCnnR	0	0	0
5112935	nnBnn	5353.75	60.48	5	4.22	0.25	4	-0.38	0.08	3
5326697	nnBGn	5888.46	76.16	7	3.26	0.04	4	-1.84	0.03	2
5340306	nnnnn	5980.75	62.86	8	4.19	0.18	6	-0.66	0.07	6
5373525	nnnnn	6571.30	75.94	8	4.11	0.08	6	-0.66	0.03	5
5477197	nnnnn	5199.12	102.43	6	2.18	0.14	6	-0.83	0.06	7
5562506	nnnnn	6296.28	178.61	7	3.57	0.27	4	-0.71	0.07	2
5729607	nnnnn	4830.40	156.43	3	4.55	0.11	4	-0.22	0.00	2
5877802	nnBnn	5110.44	114.99	3	4.15	0.04	4	-0.18	0.11	2
4189356	nnnnn	4795.80	142.62	3	4.50	0.10	4	-0.79	0.14	3
4255078	lnnnN	0	0	0
4293628	lnnnn	4283.19	106.42	2	3.25	0.07	1	-0.13	0.06	1
44494283	NnnnN	0	0	0
4491459	VnBnN	0	0	0
4513926	nCnnR	0	0	0
4606998	nnnnn	5080.50	117.10	3	4.45	0.07	4	-0.73	0.01	2
4660470	nnnnn	4763.97	106.12	3	4.25	0.04	4	-0.28	0.11	3
4831437	nnnGn	6167.46	52.01	8	3.62	0.23	6	-1.44	0.03	3
4865026	nnnnn	6352.12	40.25	8	3.11	0.20	6	-2.35	0.04	4
5045819	nnBnn	6033.30	182.64	6	3.55	0.24	4	-0.63	0.04	2
5067800	nnnnn	6093.84	42.41	8	3.74	0.02	6	0.04	0.05	3
5140178	nnnnn	4406.22	40.89	3	3.80	0.00	2	-0.27	0.09	1
5185320	nnnnn	5142.37	123.91	4	4.20	0.01	5	-0.12	0.06	4
5323374	lnnnR	0	0	0
5323614	nnngn	6046.71	101.45	5	3.58	0.42	2	-1.03	0.11	1
5327824	nnnnn	5679.88	90.54	6	3.58	0.12	6	-0.40	0.05	5
5505279	nnngn	4943.41	37.74	3	3.83	0.15	4	-1.44	0.13	3

Table 7.5 (cont'd): SSPP Stellar Parameters for Hectospec Targets

UW ID ^a	flags	T_{eff} (K)	$\sigma(T_{\text{eff}})$ (K)	$N(T_{\text{eff}})^{\text{b}}$	$\log g$ (dex)	$\sigma(\log g)$ (dex)	$N(\log g)^{\text{b}}$	[Fe/H] (dex)	$\sigma([\text{Fe}/\text{H}])$ (dex)	$N([\text{Fe}/\text{H}])^{\text{b}}$
5605647	NCnnR	0	0	0
5688551	nnnnN	0	0	0
5867691	nnnnn	4765.64	254.86	4	3.32	0.26	5	-0.60	0.10	1
6072004	nnnnn	5863.25	45.26	8	4.13	0.13	6	-0.58	0.05	7
4201034	lnnnR	0	0	0
4368170	nnnnn	6078.31	43.86	8	3.70	0.15	6	-1.13	0.02	5
4399695	nnnnn	6053.14	99.02	8	3.78	0.12	6	-0.64	0.10	6
4548777	nnnnn	4576.96	97.57	3	3.58	0.13	4	-1.09	0.10	2
4582630	nnnnn	5732.39	114.46	3	3.83	0.19	2	-0.56	0.05	1
4660035	lCnnR	0	0	0
4720858	nnBnn	5137.68	48.54	4	4.51	0.20	4	-0.92	0.10	1
473370	nnnnn	4711.38	64.81	3	4.30	0.11	2	-0.85	0.05	1
5019542	nnnnn	6150.27	31.04	8	3.84	0.03	6	-0.32	0.04	6
5022707	nnnnn	4765.82	91.72	3	4.27	0.04	2	-0.61	0.05	1
5111328	nnBnn	5222.27	97.82	4	4.16	0.33	4	-0.67	0.13	2
5120244	nnnnn	4909.05	102.09	3	3.06	0.20	4	-0.18	0.13	2
5122636	lCnnR	0	0	0
5251744	nnBnn	5164.06	93.37	4	4.23	0.12	5	-0.41	0.08	5
5403842	nnnnn	4447.59	86.55	3	4.32	0.17	4	-0.66	0.06	1
5474939	nnnnn	6753.44	33.84	9	4.00	0.07	7	-0.18	0.05	3
5577646	nnnnn	5039.91	87.17	4	4.42	0.14	5	-0.48	0.08	4
5650248	nnnnn	6438.91	40.43	8	3.97	0.03	6	0.02	0.02	4
5820107	nnnnn	4796.73	250.87	3	4.25	0.55	2	-0.77	0.12	1
5929618	nnBnn	5078.37	81.42	3	4.07	0.07	4	0.08	0.06	1
5993437	NnnnN	0	0	0
4253226	NnnnN	0	0	0
4375852	nnnnn	4675.79	44.65	3	3.33	0.11	4	-0.52	0.11	2
4408934	nnBnN	0	0	0
4513591	nnnnn	5243.09	51.75	6	4.00	0.20	6	-0.68	0.08	6
5018778	nnBgn	5455.01	37.81	4	3.42	0.25	2	-1.11	0.08	1
5270692	nnnnn	5490.98	103.99	6	3.94	0.08	6	-0.07	0.05	6
5559708	nnBnn	6044.27	75.58	4	4.18	0.56	2	-0.68	0.06	1
5608743	ncngn	5432.20	110.47	3	4.12	0.74	2	-1.62	0.53	1
4612744	lCnnR	0	0	0
4736060	VnBnN	0	0	0
4758374	nnnnn	6018.10	164.87	3	4.01	0.55	2	-0.96	0.08	1
4776453	nnnnn	4646.55	48.08	3	3.11	0.23	3	-0.65	0.05	1
5121387	lnnnR	0	0	0
5240448	nnnnn	4937.33	116.15	3	4.29	0.11	3	-0.29	0.03	2
5386527	nnnnn	4467.35	80.96	3	4.14	0.01	4	-0.38	0.08	2
4535185	lnnnR	0	0	0
4795169	nnnnR	0	0	0
5082814	nnnnn	6652.10	103.70	9	4.08	0.26	7	-0.37	0.08	6
5163920	nnnnn	5520.82	43.75	7	4.14	0.10	6	-0.48	0.04	6
5179071	nnnnn	5489.42	79.64	6	4.21	0.17	4	-0.58	0.03	4
5333793	nnnnn	5667.81	105.48	6	3.92	0.08	6	-0.01	0.09	6
5360389	lCnnR	0	0	0
5461160	lnnnR	0	0	0
5482367	lnnnR	0	0	0
5763943	lnnnN	0	0	0
5785071	lnnnR	0	0	0
5795274	lnnnR	0	0	0
5980741	nnnnn	4715.01	151.68	3	4.19	0.07	2	-0.08	0.07	1
4353134	nnnnn	6520.53	32.79	8	3.77	0.07	6	-0.40	0.04	6
4439228	nnnnn	5868.32	65.69	7	4.27	0.11	6	-0.46	0.06	6
4508044	nnnnn	4283.98	46.51	3	3.82	0.11	2	-0.90	0.06	1
4590258	nnnnn	5576.73	27.94	6	3.89	0.03	6	0.01	0.06	4
4744761	nnnnn	6275.84	55.46	9	3.55	0.07	7	-0.81	0.01	3
4759644	nnnnn	6339.35	49.80	9	3.69	0.26	7	-2.02	0.07	5
4861086	lCnnR	0	0	0
5014824	VnnnX	0	0	0
5095140	lnnnn	4081.07	6.48	2	3.14	0.09	1	-0.33	0.07	1
5339576	nnnnn	4773.69	140.92	3	4.49	0.27	3	-0.75	0.08	1
5388797	nnnnn	5676.14	67.05	7	4.07	0.04	6	-0.12	0.05	4
5400668	nnnnn	4525.76	108.26	3	4.47	0.18	4	-0.43	0.03	2
5533056	Nnnnn	4501.10	37.72	3	4.15	0.05	2	-0.37	0.06	1
5603083	nnnnn	4349.49	7.40	3	4.12	0.16	3	-0.36	0.07	1
5857754	nnnnn	4410.95	58.70	3	4.48	0.17	4	-0.87	0.00	2
5881730	nnnnn	4118.05	13.38	2	3.68	0.64	2	-0.48	0.11	1
4173387	nnnnn	5095.02	32.78	3	3.84	0.13	4	-0.71	0.11	3
4183590	nnBnn	5240.30	207.99	4	3.35	0.20	5	-0.43	0.06	3
4222703	NnnnN	0	0	0
4289515	lnnnR	0	0	0
4440334	NnBnN	0	0	0

Table 7.5 (cont'd): SSPP Stellar Parameters for Hectospec Targets

UW ID ^a	flags	T_{eff} (K)	$\sigma(T_{\text{eff}})$ (K)	$N(T_{\text{eff}})^{\text{b}}$	$\log g$ (dex)	$\sigma(\log g)$ (dex)	$N(\log g)^{\text{b}}$	[Fe/H] (dex)	$\sigma([\text{Fe}/\text{H}])$ (dex)	$N([\text{Fe}/\text{H}])^{\text{b}}$
4494521	nnnnn	4026.01	15.60	1	4.73	0.02	1	-1.35	0.07	1
4560409	nnnnn	4612.52	90.33	3	3.37	0.18	4	-0.30	0.15	3
4729653	nnBnn	5352.40	76.87	4	4.39	0.09	5	-0.33	0.09	4
5110692	nnnnn	4814.11	191.69	3	4.44	0.30	2	-0.53	0.06	1
5249662	nnnnn	4634.82	53.94	3	4.46	0.16	4	-0.66	0.22	2
5709364	lnnnR	0	0	0
5911838	Nnnnn	4506.68	89.95	3	4.18	0.11	2	-0.24	0.11	1
6058724	nnBnN	0	0	0
6093797	NnnnN	0	0	0
4233081	nnnnn	5761.43	13.57	7	4.08	0.29	6	-0.59	0.05	5
4276210	NnnnN	0	0	0
4332107	NnBnN	0	0	0
4368792	lnnnn	4231.10	96.57	2	3.47	0.07	1	-0.21	0.07	1
4570024	nnnnn	6295.50	135.26	8	4.62	0.04	6	-0.37	0.09	6
4674263	nnnnn	4924.81	67.56	3	3.74	0.08	2	-0.56	0.08	1
4682321	VnnnX	0	0	0
4793306	nnnnn	5536.66	94.05	4	4.87	0.02	5	-0.82	0.03	5
4864287	lCnnR	0	0	0
5059173	nnngn	5855.12	94.85	4	2.76	0.80	2	-1.48	0.06	1
5192944	nnnnn	4372.37	26.08	3	3.81	0.29	2	-0.34	0.08	1
5254867	nnnnn	5343.25	65.84	3	4.33	0.36	2	-0.85	0.05	1
5312211	nnnnn	4386.29	48.92	3	4.28	0.35	2	-0.47	0.07	1
5385097	nnnnn	5404.43	104.56	6	4.31	0.07	6	-0.19	0.04	5
5544012	nnnnn	5407.26	67.29	4	4.10	0.18	5	0.10	0.12	2
5927948	nnnnn	5029.29	63.16	3	3.53	0.11	4	-0.13	0.05	3
6020110	nnnnn	6141.47	173.74	5	4.04	0.63	2	-1.44	0.02	1
4162071	nnBnn	6926.04	428.92	6	5.00	0.12	4	0.11	0.12	1
4320005	nnnnn	6260.39	78.12	9	3.07	0.33	7	-1.42	0.08	5
4344670	NnnnN	0	0	0
4365444	nnnGn	5755.92	83.56	7	3.95	0.16	6	-1.00	0.04	6
4417121	nnnnn	5691.75	287.25	4	4.48	0.29	5	-0.07	0.07	3
4428625	nnnnR	0	0	0
4434033	nnnnR	0	0	0
4570895	Nnnnn	4643.85	233.69	3	4.01	0.76	2	-1.05	0.07	1
4740289	nnnnn	5853.39	75.09	8	3.90	0.12	6	-0.47	0.05	5
5156408	nnnnN	0	0	0
5160251	nnnnN	0	0	0
5218290	nnnnn	5797.05	43.65	4	4.29	0.21	2	-0.65	0.05	1
5269279	nnnnn	6249.73	72.98	8	3.94	0.27	5	-1.55	0.06	4
5309858	nnnnn	6231.18	73.19	8	4.22	0.24	5	-1.11	0.07	2
5566289	nnnnn	5905.48	66.97	8	3.72	0.07	6	-0.52	0.02	4
5811877	nnnnN	0	0	0
4317549	nnnnn	5874.26	248.86	4	4.27	0.50	2	-0.38	0.06	1
4450132	nnngn	5018.70	77.02	6	3.27	0.22	6	-1.03	0.07	6
4454833	nnnnn	4732.71	154.97	3	4.87	0.26	3	-0.54	0.06	1
4705198	NnBnN	0	0	0
4750328	nnnnn	4920.43	108.97	3	4.50	0.09	4	-0.34	0.16	1
5121412	nnnnn	5822.47	128.67	6	4.09	0.08	4	-0.45	0.06	4
5142183	nnnnn	5879.28	57.41	7	3.83	0.05	6	0.01	0.06	4
5202894	nnnnn	6381.14	94.78	6	4.15	0.43	3	-1.36	0.09	1
5349833	nnnnn	6022.81	290.39	3	4.03	0.51	2	-0.22	0.10	1
5392845	lnnnn	4075.25	17.92	2	3.77	0.80	2	-0.36	0.13	1
5493836	nnnGn	6001.62	90.41	9	3.79	0.25	7	-1.07	0.07	5
5657058	lnnnR	0	0	0
5927629	lnnnR	0	0	0
6027560	nnBnn	5460.80	61.94	7	4.18	0.09	6	-0.38	0.06	6
6069151	nnnnn	4954.13	155.26	4	2.29	0.22	5	-0.67	0.07	6
4215856	nnnnn	5799.31	199.71	3	4.23	0.64	2	-0.39	0.06	1
4295303	nnnGn	4382.55	81.56	3	4.02	0.11	4	-1.90	0.20	1
4383743	nnnnn	7068.28	96.75	8	3.89	0.14	6	-1.38	0.05	4
4598156	NnBnN	0	0	0
4728827	nnBnn	5397.38	85.80	6	4.04	0.07	6	-0.81	0.01	6
4733648	VnnnX	0	0	0
5022615	nnnnn	6023.33	110.95	8	2.56	0.51	5	-1.38	0.04	5
5030166	nnnnn	7757.39	130.92	4	3.98	0.14	3	-1.33	0.07	1
5164725	nnngn	4687.46	89.45	3	4.54	0.18	3	-1.17	0.05	1
5170724	nnnnn	5495.14	45.16	6	3.82	0.26	4	-0.39	0.02	3
5209990	nnngn	4441.52	46.86	3	2.52	0.32	4	-1.17	0.06	3
5399491	nnBnn	5899.13	330.27	4	4.39	0.47	2	-0.31	0.04	1
5450912	nCBGn	4296.02	216.39	1	4.03	0.49	2	-1.58	0.11	1
5625365	nnnnn	5653.71	64.48	6	3.93	0.15	4	-0.34	0.02	3
5677354	NnnGn	4442.35	52.47	3	4.43	0.45	2	-1.41	0.05	1
5933222	nnBnn	5237.09	89.52	4	3.50	0.24	5	-0.82	0.08	4
5958635	NnnnN	0	0	0

Table 7.5 (cont'd): SSPP Stellar Parameters for Hectospec Targets

UW ID ^a	flags	T_{eff} (K)	$\sigma(T_{\text{eff}})$ (K)	$N(T_{\text{eff}})^{\text{b}}$	$\log g$ (dex)	$\sigma(\log g)$ (dex)	$N(\log g)^{\text{b}}$	[Fe/H] (dex)	$\sigma([\text{Fe}/\text{H}])$ (dex)	$N([\text{Fe}/\text{H}])^{\text{b}}$
4160644	nnnnR	0	0	0
4176793	lnnnR	0	0	0
4295340	NnBnN	0	0	0
4350904	nnnnn	5924.45	162.72	4	4.10	0.15	5	-0.68	0.07	2
4370911	nnnnn	4445.43	28.38	3	3.90	0.10	2	-0.62	0.10	1
4437607	nCBnX	0	0	0
4633054	nnnnn	5606.03	144.85	7	3.77	0.16	6	-0.91	0.02	3
4665114	lnnnR	0	0	0
4691099	nnnnn	5866.43	19.83	4	3.66	0.09	2	-0.62	0.13	1
4750698	nnnnn	5457.62	89.50	6	2.09	0.34	6	-0.51	0.03	3
5160577	nnnnn	5683.99	100.66	4	3.34	0.61	2	-0.70	0.08	1
5198342	Nnnnn	4680.67	99.68	3	4.50	0.38	2	-0.97	0.06	1
5230402	nnnnn	5704.23	139.06	4	4.10	0.15	2	-0.42	0.05	1
5247423	nnnnn	5734.06	179.29	4	4.00	0.57	2	-0.63	0.06	1
5272186	nnnGn	4115.17	72.14	3	4.31	0.32	2	-1.34	0.09	1
5384051	nnnnn	5834.43	57.99	7	3.93	0.11	6	-0.33	0.07	6
5560403	nnnnn	5633.11	70.00	6	4.05	0.03	6	-0.16	0.05	5
5594575	nnnnn	5242.07	26.40	6	3.49	0.07	6	-0.90	0.03	6
5686673	NnnnN	0	0	0
5922869	nnnnn	5551.18	56.89	6	3.68	0.07	6	-0.10	0.08	4
6093532	nnnnN	0	0	0
4166144	nnBnn	7898.52	357.86	3	3.21	0.38	2	-1.51	0.09	1
4402191	nnnnn	6129.78	51.21	7	2.64	0.39	4	-1.71	0.18	2
4402472	nnnnn	6011.92	114.43	8	4.04	0.19	6	-0.53	0.04	3
4417365	nnngn	5693.68	118.42	6	3.75	0.11	4	-1.07	0.09	3
4440857	nnnnn	5886.62	94.07	7	3.90	0.16	4	-0.76	0.11	4
4788691	nnnnn	5667.17	186.91	6	4.52	0.19	6	-0.34	0.05	4
5081590	nnnnn	5653.52	77.78	6	4.07	0.09	4	-0.24	0.08	4
5273135	nnnnn	4653.40	155.51	3	4.18	0.13	2	-0.10	0.07	1
5287841	Nnnnn	4068.36	18.72	1	4.38	0.05	1	-1.42	0.06	1
5892706	nnnnn	5994.12	49.23	8	3.79	0.12	6	-0.61	0.10	3
4325501	nnBnn	5282.32	114.23	5	3.89	0.31	4	-1.16	0.03	3
4727757	nnnnn	5346.33	327.60	3	4.04	0.22	4	-0.87	0.07	1
4786779	nnnnn	5176.85	114.97	4	3.77	0.13	5	-0.77	0.06	5
5313185	nnngn	4335.29	60.66	3	4.34	0.20	4	-1.35	0.22	2
5418496	nnnnn	5590.62	72.34	6	4.21	0.27	4	-0.71	0.07	3
5987468	nnnnn	5653.08	101.64	4	4.43	0.45	2	-0.63	0.04	1
4359968	nnnnn	5621.47	99.87	7	4.27	0.11	6	-0.81	0.09	6
5191160	lnnnN	0	0	0
5330327	nnnnn	5122.91	223.73	3	4.48	0.40	2	-0.37	0.07	1
5379089	nnngn	4157.10	62.52	2	4.25	0.14	1	-1.44	0.08	1
4231996	nnnnn	6054.09	204.11	4	4.04	0.74	2	-0.67	0.07	1
4807480	nnnnn	5796.17	118.22	4	3.91	0.38	2	-0.14	0.06	1
5188393	nnnnn	6315.74	107.78	7	3.83	0.28	4	-0.82	0.01	5
5239063	nnnnn	5584.69	85.43	5	3.71	0.13	4	-0.61	0.01	3
5344461	NnnnN	0	0	0
5405593	nnnnn	5610.99	52.03	7	4.13	0.07	6	-0.47	0.04	5
5590150	nnBgn	4936.31	57.62	3	3.58	0.03	2	-1.05	0.11	1
5714783	nnnnn	5248.71	175.81	3	4.41	0.47	2	-0.65	0.07	1
4152720	nnnGn	7670.76	351.12	6	3.22	0.19	6	-2.29	0.11	3
4165727	lnnnR	0	0	0
4252491	nnnnn	4959.88	109.25	3	4.40	0.09	4	-0.56	0.11	3
4310921	NCnnN	0	0	0
4316990	nnnnn	4351.66	45.42	3	3.60	0.30	4	-0.43	0.24	1
4499038	nnBnn	5236.74	141.23	4	4.02	0.18	5	-0.79	0.02	5
4627672	nnnnn	4508.79	137.53	3	4.19	0.17	4	-0.06	0.11	2
5075064	NnnnN	0	0	0
5132934	nnnnn	5223.44	120.05	3	4.53	0.27	2	-0.39	0.09	1
5158679	nnngn	4704.88	17.71	4	3.50	0.18	4	-1.25	0.09	3
5172653	NnnnN	0	0	0
5227382	nnnnR	0	0	0
5257408	nnngn	4269.60	68.20	3	4.26	0.17	4	-1.39	0.14	1
5331042	nnnnn	6611.15	98.13	5	3.62	0.29	2	-1.53	0.06	1
5470994	nnnnn	5945.67	107.86	8	4.05	0.13	6	-0.60	0.04	6
5530621	nnnnn	4669.93	58.04	3	4.39	0.09	4	-0.71	0.03	2
5935530	nnBnN	0	0	0
5972418	nnnnn	7702.34	103.46	4	3.97	0.16	3	-0.88	0.09	1
6069188	nnBnn	5647.59	62.20	7	4.24	0.18	6	-0.83	0.07	5
4204879	nnnnn	4957.59	122.51	3	3.68	0.16	3	-0.64	0.14	2
4208862	Nnnnn	4485.93	136.26	3	4.60	0.28	2	-0.90	0.09	1
4242377	nnnnn	5928.03	23.16	4	3.89	0.04	2	-0.88	0.05	1
4353763	nnnnR	0	0	0
4533159	nnnnn	4334.26	62.04	2	4.48	0.21	4	-1.21	0.01	2
4675831	nnngn	5757.82	141.41	7	4.25	0.25	6	-1.12	0.06	2

Table 7.5 (cont'd): SSPP Stellar Parameters for Hectospec Targets

UW ID ^a	flags	T_{eff} (K)	$\sigma(T_{\text{eff}})$ (K)	$N(T_{\text{eff}})^{\text{b}}$	$\log g$ (dex)	$\sigma(\log g)$ (dex)	$N(\log g)^{\text{b}}$	[Fe/H] (dex)	$\sigma([\text{Fe}/\text{H}])$ (dex)	$N([\text{Fe}/\text{H}])^{\text{b}}$
4786366	NnBnN	0	0	0
4852347	nnnnn	5373.68	30.59	6	4.11	0.03	6	-0.51	0.05	5
5101148	lnnnn	4192.12	87.74	2	3.70	0.56	2	-0.41	0.13	1
5206727	nnnnn	5401.37	108.72	4	3.88	0.12	5	0.34	0.05	2
5226538	nnnnn	5223.58	83.37	6	3.85	0.09	6	-0.03	0.08	5
5357611	nnBnn	5054.91	62.26	3	4.15	0.73	2	-1.48	0.13	1
5377648	nnnnn	5761.95	77.58	8	3.82	0.10	6	-0.40	0.05	6
5498983	nnnnn	5837.14	49.74	7	3.78	0.08	6	-0.15	0.09	6
5761347	lnnnR	0	0	0
5993235	nnnnn	5232.68	221.29	4	3.72	0.34	5	-0.74	0.09	2
6015012	LnnnR	0	0	0
4162497	Nnnnn	6116.38	86.08	5	4.15	0.73	2	-0.11	0.06	1
4450450	nnnnn	5757.41	86.25	7	4.31	0.25	6	-1.37	0.03	7
4570571	nnnnn	5170.99	126.23	4	4.47	0.10	5	-0.66	0.04	2
4682185	nnnnn	4459.95	66.99	3	4.09	0.01	2	-0.66	0.05	1
4711829	nnnnn	8014.37	215.94	4	3.59	0.30	3	-1.29	0.19	1
4800805	nnnnn	5311.37	99.90	6	3.59	0.06	6	-1.14	0.00	4
5035933	nnGn	6827.61	201.78	6	3.59	0.35	3	-1.35	0.04	1
5041842	nnnnn	4676.49	132.82	3	4.51	0.14	4	-0.67	0.16	2
5173236	nnnnn	5722.07	142.69	6	4.12	0.21	4	-0.47	0.06	2
5204845	nnBgn	5591.34	33.94	4	3.44	0.23	2	-1.21	0.07	1
5248825	nnngn	5331.10	125.47	7	4.44	0.14	6	-1.20	0.08	4
5354099	NnnnN	0	0	0
5375429	lCnnR	0	0	0
5423689	nnnnn	4368.19	91.28	3	4.22	0.17	4	-0.67	0.10	2
5468235	nnnnn	4482.79	76.32	3	4.16	0.12	4	-0.84	0.02	2
5473513	nnnnn	4845.98	45.31	3	4.63	0.15	4	-0.71	0.03	2
5531243	nnnnn	5567.37	68.84	6	3.80	0.13	6	-0.06	0.02	2
5800395	nnnnn	5787.73	76.38	6	3.58	0.40	4	-0.51	0.01	4
5801177	nnBnn	5025.71	192.57	3	4.43	0.29	3	-0.27	0.07	1
4393937	nnnnn	4449.71	35.43	3	3.65	0.20	4	-0.20	0.20	2
4425206	nnnnn	4949.41	110.85	3	2.82	0.18	4	-0.83	0.07	3
4540172	nnBnc	0	0	0
4674898	nnnnn	5690.69	60.62	7	3.93	0.03	6	-0.20	0.05	7
4709564	nnngn	5472.56	199.00	6	2.86	0.00	4	-1.89	0.04	4
4791760	nnnnn	4583.12	72.18	3	4.33	0.13	4	-0.98	0.08	2
5118317	NnnnN	0	0	0
5151813	NnnnN	0	0	0
5152431	nnnnn	5909.38	44.46	8	4.03	0.10	6	-0.32	0.04	5
5170849	nnnnn	5355.22	193.48	3	3.59	0.37	2	-1.02	0.08	1
5202812	nnnnn	6352.56	71.45	8	2.79	0.12	6	-1.22	0.05	6
5291667	nnnnn	4247.59	130.24	2	3.51	0.14	1	-0.64	0.08	1
5343472	nnnnn	4623.34	98.74	3	4.19	0.13	2	-0.90	0.13	1
5519133	nnnnn	5348.91	30.40	3	4.26	0.42	2	-0.78	0.05	1
5768843	nnnnn	5036.65	109.27	3	3.57	0.05	4	-0.82	0.02	2
5905048	nnnnn	5944.51	90.74	8	3.85	0.15	6	-1.12	0.03	5
5929514	nnnnn	4689.33	59.17	3	4.12	0.13	3	-0.73	0.10	1
4623264	NnnnN	0	0	0
4625355	NnnnN	0	0	0
4849237	nnnnn	5413.87	44.84	6	3.94	0.05	6	-0.72	0.03	4
5097806	Dnnnn	4337.20	130.12	3	3.71	0.01	2	-0.27	0.11	1
5197434	nnnGn	6108.34	69.42	7	3.85	0.16	4	-1.28	0.11	4
5241553	nnnnn	5518.53	142.48	6	4.01	0.14	4	-0.27	0.05	3
5249819	nnnnn	5740.52	104.29	7	4.19	0.12	6	-0.84	0.05	5
5291611	Nnnnn	4231.40	190.04	2	3.35	0.05	1	-0.78	0.04	1
5313481	nnnnn	5571.91	47.09	6	4.39	0.20	4	-0.59	0.07	3
5339113	nnnnn	5351.96	96.16	6	3.73	0.13	6	-0.78	0.02	5
5415015	nnnnn	6262.70	53.53	9	3.85	0.04	7	-0.59	0.07	7
5437119	NCnnn	4565.78	161.21	3	4.30	0.31	2	-0.50	0.07	1
5686136	nnnGn	5578.46	153.69	6	4.23	0.28	4	-1.12	0.09	2
5978929	NnnnR	0	0	0
4240029	nnnnn	5216.89	148.76	3	4.32	0.08	4	-0.84	0.02	3
4373884	nnngn	5672.26	80.56	7	3.28	0.07	6	-1.73	0.03	3
4573945	nnnnn	4742.57	93.88	3	3.96	0.34	3	-0.85	0.06	1
4633577	lCnnR	0	0	0
4634542	nnnnn	4616.37	162.82	3	3.86	0.13	4	-0.48	0.11	1
4792688	Nnnnn	4812.50	154.65	3	4.53	0.32	2	-0.90	0.08	1
5104783	nnnnn	5782.46	84.48	7	3.91	0.01	6	-0.52	0.03	4
5129533	nnngn	4807.55	35.80	3	2.93	0.12	4	-1.23	0.05	2
5199563	NnBnN	0	0	0
5219275	nnnnn	5530.88	118.67	4	3.87	0.25	2	-0.65	0.03	1
5232141	nnnnn	5646.82	103.27	6	3.85	0.27	4	-0.42	0.02	3
5251812	NnBnN	0	0	0
5301927	nnnnn	5295.86	82.68	6	3.63	0.07	6	-0.87	0.04	7

Table 7.5 (cont'd): SSPP Stellar Parameters for Hectospec Targets

UW ID ^a	flags	T_{eff} (K)	$\sigma(T_{\text{eff}})$ (K)	$N(T_{\text{eff}})^{\text{b}}$	$\log g$ (dex)	$\sigma(\log g)$ (dex)	$N(\log g)^{\text{b}}$	[Fe/H] (dex)	$\sigma([\text{Fe}/\text{H}])$ (dex)	$N([\text{Fe}/\text{H}])^{\text{b}}$
5338337	lnnGn	4199.58	33.17	1	4.17	0.14	2	-1.53	0.16	1
5458065	nnnnn	4532.24	119.26	3	4.42	0.39	2	-0.73	0.09	1
5528862	NnnnnN	0	0	0
5752724	nnnnn	4367.78	14.15	3	3.84	0.34	2	-0.20	0.06	1
5790789	nnnnn	5446.20	126.05	6	3.63	0.40	4	-0.82	0.10	5
5863912	Nnnnn	0	0	0
4193894	1CnnR	0	0	0
4363623	nnnnn	5273.92	97.00	4	4.37	0.06	5	-0.04	0.01	2
4466327	nnnnnc	0	0	0
4792782	nnnnn	5874.74	236.52	5	3.91	0.19	3	0.74	0.20	1
4808519	nmmN	0	0	0
5020075	nnnnn	5419.96	163.38	4	4.50	0.03	4	-0.93	0.08	1
5083154	nnnnn	5855.67	85.04	4	3.87	0.26	2	-0.33	0.04	1
5168319	nnngn	4267.94	79.03	3	3.57	0.25	4	-1.66	0.13	2
5192922	nnnnn	6449.03	106.68	5	4.14	0.44	2	0.06	0.09	1
5241612	nnnnn	5792.40	151.16	3	3.71	0.35	2	-0.64	0.07	1
5414511	nnnnn	4700.24	86.39	3	4.38	0.14	4	-0.73	0.06	2
5426648	nnBnn	5435.76	77.12	7	2.94	0.27	6	-0.78	0.08	5
5675591	nCnnR	0	0	0
5702628	nnBnn	5675.77	69.29	3	4.29	0.34	2	-0.37	0.06	1
5973462	nnnnn	5252.17	35.36	6	3.33	0.01	6	-0.95	0.04	5
4178308	nCnnR	0	0	0
4215869	nmmN	0	0	0
4487742	nnBnn	5439.42	122.70	4	4.37	0.33	2	-0.64	0.05	1
4554016	nnnnn	5865.67	79.92	8	3.73	0.21	6	-0.78	0.03	4
4579098	Dnnnn	4228.57	115.43	3	4.68	0.04	4	-0.95	0.31	1
4733474	nnnnn	4664.53	108.37	3	4.35	0.09	4	-0.51	0.01	2
4875317	nnmmn	5989.82	142.33	5	3.92	0.12	2	-0.83	0.05	1
5035179	nnBnn	5689.01	115.76	3	4.02	0.16	2	-0.47	0.10	1
5035438	lmmGn	4042.93	18.28	1	4.52	0.05	1	-1.01	0.13	1
5172595	nnnnnc	0	0	0
5176667	nnnnn	6112.88	53.69	8	3.98	0.12	6	-0.65	0.03	4
5203288	nnnnn	5664.64	50.52	7	4.14	0.14	6	-0.39	0.05	6
5308102	nnnnn	5880.16	30.83	8	4.09	0.13	6	-0.49	0.04	4
5394277	nnnnn	5747.55	72.96	7	4.00	0.16	6	-0.62	0.02	5
5509835	nnBnn	5689.56	106.46	4	3.82	0.01	2	-0.55	0.04	1
5604937	nnBnn	5962.72	130.75	7	3.50	0.58	4	-0.49	0.09	4
5808561	nnnnn	4906.03	82.17	3	4.14	0.07	2	-0.42	0.07	1
5961397	nnnnn	5943.84	33.66	8	3.96	0.09	6	-0.72	0.03	4
4301848	nnnnn	5455.16	247.03	4	3.05	0.09	2	-0.31	0.10	1
4548214	nnnnn	4922.54	140.47	4	4.23	0.17	5	-0.87	0.03	3
5149348	nnBnn	4737.84	145.75	3	3.92	0.03	2	-1.51	0.11	1
5411052	lmmR	0	0	0
5594367	nnnnn	5025.94	198.27	3	2.16	0.22	4	-1.63	0.07	2
7906333	nnnnn	4278.14	105.26	2	3.92	0.11	1	-0.49	0.10	1
4230023	nnnnn	4808.03	77.76	3	3.86	0.11	2	-0.88	0.06	1
4605744	nnnnn	5558.86	56.98	7	4.04	0.05	6	-0.38	0.03	5
4637676	nnnnn	4204.68	86.93	2	3.84	0.41	2	-0.63	0.14	1
5023669	nnBnn	6077.47	509.80	4	4.33	0.24	4	0.11	0.04	2
5095459	nnBnn	5034.13	162.47	3	4.44	0.44	2	-0.81	0.07	1
5216472	nnnnn	6148.65	105.52	8	3.26	0.29	6	-2.30	0.14	4
5360401	nnBnn	4864.91	130.47	3	4.26	0.28	3	-0.26	0.06	1
5356141	NnnnR	0	0	0
4252499	nnnnN	0	0	0
4313256	nnnnn	5604.11	53.65	4	4.09	0.03	2	-0.63	0.05	1
4422110	nnnnnc	0	0	0
4483759	nnnnn	5956.70	114.82	9	3.99	0.05	7	-0.19	0.04	4
4567620	nnnnn	4408.24	63.76	3	3.76	0.13	4	-0.46	0.12	1
4606328	nnnnn	6112.48	96.50	5	4.09	0.38	2	-0.04	0.08	1
4676198	lmmGn	4354.06	12.96	3	4.33	0.55	2	-1.22	0.08	1
4721933	nnnnn	4528.78	74.36	3	4.03	0.08	4	-0.29	0.14	2
4814966	nnnnn	5082.12	79.37	4	4.04	0.14	5	-0.00	0.12	2
5068600	nnngn	4366.65	313.31	2	4.83	0.01	2	-1.12	0.17	1
5074938	nnnnn	5805.49	62.42	7	4.05	0.05	6	-0.16	0.07	5
5225722	NnBgn	5562.68	126.92	4	3.66	0.19	2	-1.24	0.12	1
5326941	nnnnn	5889.36	142.63	4	3.58	0.29	2	-0.28	0.08	1
5343234	nnnnn	5158.66	226.96	3	4.15	0.53	3	-0.86	0.09	1
5360941	nnnnn	4645.50	52.23	3	4.35	0.16	2	-1.28	0.08	1
5523850	nnnnn	4498.61	102.20	3	4.20	0.12	4	-0.37	0.17	2
5542585	nnnnN	0	0	0
5726724	nnnnn	4196.54	130.00	2	3.76	0.37	2	-0.56	0.16	1
5897013	nnBnn	6080.79	190.85	4	4.07	0.50	2	-0.84	0.07	1
5960847	nnnnn	4850.71	39.54	3	4.10	0.09	3	-0.38	0.07	1
6098080	nnnnnc	0	0	0

Table 7.5 (cont'd): SSPP Stellar Parameters for Hectospec Targets

UW ID ^a	flags	T_{eff} (K)	$\sigma(T_{\text{eff}})$ (K)	$N(T_{\text{eff}})^{\text{b}}$	$\log g$ (dex)	$\sigma(\log g)$ (dex)	$N(\log g)^{\text{b}}$	[Fe/H] (dex)	$\sigma([\text{Fe}/\text{H}])$ (dex)	$N([\text{Fe}/\text{H}])^{\text{b}}$
6099995	nnnnn	5410.38	388.33	3	4.14	0.33	3	-0.23	0.05	1
4301106	VnnnX	0	0	0
4305492	NnnnN	0	0	0
4325061	nnnnn	4188.81	49.23	2	3.45	0.12	1	-0.60	0.09	1
4338779	nnnnn	5793.14	87.36	6	4.15	0.14	4	-0.46	0.03	3
4380553	nnnnn	4470.46	30.03	3	3.32	0.13	4	-0.66	0.24	1
4495694	nnBgn	4768.90	110.23	3	3.15	0.39	4	-1.44	0.12	3
4628729	NNnnn	4256.93	15.60	3	3.61	0.28	2	-0.18	0.08	1
4830564	nnnnn	6350.56	93.81	9	2.80	0.21	7	-1.47	0.05	5
5026557	nnnnn	6016.05	248.79	4	3.02	0.20	2	-1.53	0.09	1
5170653	nnnnn	5024.32	106.71	4	3.57	0.14	5	-0.50	0.07	4
5194891	nnnnR	0	0	0
5253672	nnnnn	4580.93	180.09	3	2.45	0.40	4	-1.91	0.13	1
5372368	nnnnn	5405.55	45.38	4	4.11	0.07	4	-0.54	0.05	2
5412113	NnnnN	0	0	0
5481008	nnnnn	5720.17	76.90	7	4.03	0.10	6	-0.47	0.06	6
5526898	nnnnn	4868.33	59.98	3	3.50	0.11	3	-0.23	0.08	1
5640671	nnnnn	4866.24	48.93	3	2.31	0.26	4	-0.51	0.08	7
5773638	NnnnN	0	0	0
5911959	nnnnn	5273.11	234.87	5	3.93	0.18	4	-1.22	0.09	1
6077612	nnnnn	5968.10	149.26	4	4.24	0.47	2	-0.66	0.04	1
4263452	Nnnnn	5256.12	76.91	3	4.16	0.35	2	-0.87	0.06	1
4282211	nnnnn	6299.60	151.72	9	2.94	0.43	7	-0.23	0.00	2
4339441	VCnnN	0	0	0
4717200	nnnnn	4971.50	89.46	3	4.21	0.27	3	-0.62	0.09	1
4879619	nnngn	4731.25	125.52	3	4.88	0.04	4	-1.32	0.10	2
5016434	nnnnn	4859.34	147.20	3	4.05	0.10	2	-0.09	0.09	1
5017624	nnnnn	6094.20	147.24	7	4.04	0.27	6	-0.62	0.04	5
5075171	nnnnn	6050.14	110.32	5	4.20	0.50	2	-0.94	0.05	1
5143160	nnnnn	5814.22	71.13	7	4.13	0.15	6	-0.55	0.06	6
5147597	nnnnn	5280.14	90.91	4	4.17	0.01	5	-0.11	0.10	5
5163379	nnnGn	6178.32	203.96	4	4.04	0.83	2	-1.03	0.07	1
5207433	nnnnn	4311.55	109.85	2	3.79	0.10	1	-0.58	0.06	1
5486585	NnBnN	0	0	0
5522052	nnnnn	4561.23	61.36	3	4.18	0.11	4	-0.49	0.15	3
5601477	LnnnR	0	0	0
5637848	nnnnn	5949.30	86.66	7	3.74	0.08	6	-0.24	0.06	5
5670767	nnnnn	5729.78	41.28	7	4.00	0.07	6	-0.43	0.09	6
5729416	NnnnN	0	0	0
6096281	nnnnn	5701.50	87.25	8	3.66	0.12	6	-0.27	0.03	7
4293263	NnBnN	5119.29	96.33	3	3.91	0.04	2	-0.39	0.09	1
4429177	NnnnN	0	0	0
4481281	ICnnR	0	0	0
4604368	nnnnn	4938.68	67.21	3	4.47	0.03	3	-0.60	0.06	1
5075375	nnnnn	5875.21	58.72	8	3.85	0.07	6	-0.84	0.05	3
5219645	nnBnn	5029.86	104.10	4	4.51	0.13	5	-0.76	0.03	4
5250102	nnnnn	5492.24	68.00	7	4.09	0.18	6	-0.94	0.03	5
5289121	nnnnn	5188.97	83.20	4	4.34	0.08	5	-0.59	0.10	3
5299214	nnngn	4057.15	17.86	2	3.59	0.33	2	-1.26	0.11	1
5312766	nnBnn	4954.12	164.38	4	3.73	0.14	5	-0.59	0.17	1
5386078	nnnnn	5179.46	140.84	4	4.30	0.12	5	-0.23	0.08	4
5424950	NnnGn	4275.81	16.97	3	4.29	0.33	3	-1.33	0.12	1
5489400	nnnnn	5764.66	117.34	6	4.11	0.36	3	-0.33	0.04	2
5968404	nnnnn	5731.62	47.48	6	4.05	0.41	4	-0.36	0.19	3
6054980	nnnnn	6110.98	63.91	8	3.73	0.06	6	-0.98	0.02	6
6086019	nnnnn	5298.45	63.88	3	4.18	0.14	2	-0.05	0.08	1
4155699	nnnnn	5488.88	99.62	6	3.88	0.22	6	-0.86	0.02	4
4205838	Lnnn	4637.45	151.99	3	4.32	0.16	4	-0.22	0.05	3
4309593	nnBnX	0	0	0
4416432	nnngn	5829.19	99.28	7	4.47	0.09	6	-1.42	0.13	6
4459588	nnnnn	4431.16	66.94	3	3.66	0.21	4	-0.58	0.18	3
4728094	nnBnn	5118.06	88.47	3	3.95	0.34	2	-0.29	0.07	1
4869319	VnnnX	0	0	0
5111808	nnnnn	4939.07	74.84	3	4.62	0.18	3	-0.77	0.06	1
5132978	NCnnR	0	0	0
5133588	nnnnn	5748.90	140.57	6	3.57	0.21	4	-0.44	0.07	1
5332491	nnnnn	5503.07	36.88	6	3.87	0.10	6	-0.35	0.05	3
5366649	nnnnn	5643.73	74.49	6	4.04	0.01	6	-0.14	0.06	5
5388733	nnnnn	5828.06	69.03	8	3.90	0.09	6	-0.41	0.07	4
5575058	nCnnR	0	0	0
5746541	nnnnn	5812.94	64.42	7	4.01	0.12	6	-0.28	0.06	6
5816586	NnnnR	0	0	0
6054710	nnnnn	5184.71	124.78	5	3.98	0.17	4	-0.47	0.04	3
4250465	NnnnN	0	0	0

Table 7.5 (cont'd): SSPP Stellar Parameters for Hectospec Targets

UW ID ^a	flags	T_{eff} (K)	$\sigma(T_{\text{eff}})$ (K)	$N(T_{\text{eff}})$ ^b	$\log g$ (dex)	$\sigma(\log g)$ (dex)	$N(\log g)$ ^b	[Fe/H] (dex)	$\sigma([\text{Fe}/\text{H}])$ (dex)	$N([\text{Fe}/\text{H}])$ ^b
4257308	nnnnn	5633.20	77.57	8	4.02	0.08	6	-0.33	0.08	4
4321631	nnnnn	5908.00	36.95	8	3.92	0.10	6	-0.13	0.02	6
4554204	NnBnN	0	0	0
4560977	nnnnn	5413.71	32.45	6	3.49	0.05	6	-0.50	0.03	6
4732676	nnnnn	4694.31	73.21	3	2.76	0.28	4	-0.53	0.11	3
4799881	nnnnR	0	0	0
4857420	nCnnP	4387.43	356.18	2	0.73	0.84	3	-3.04	0.01	1
5141569	nnnnn	4980.41	74.80	4	4.46	0.17	5	-0.94	0.02	3
5170481	nnnnn	5359.52	7.94	5	4.11	0.27	4	-0.92	0.05	3
5228985	NnnnN	0	0	0
5231261	nnnnN	0	0	0
5233888	nnnnn	4749.06	102.50	3	4.33	0.18	2	-0.83	0.05	1
5437060	VnnnX	0	0	0
5484171	nnngn	6266.65	252.97	5	4.02	0.68	2	-1.48	0.05	1
5772277	nnnnn	4980.94	89.97	3	4.19	0.07	4	-0.14	0.08	3
5774574	nnnnn	5909.83	73.63	7	4.23	0.25	4	-0.61	0.03	4
5809732	nnnnn	4426.72	42.54	3	4.53	0.15	4	-0.81	0.15	3
5943990	nnnnn	4769.73	98.83	3	4.38	0.09	4	-0.63	0.04	2
4210340	nnnnn	5125.17	79.87	4	3.84	0.12	5	-0.85	0.17	4
4224631	nnnnn	4327.87	19.04	3	3.76	0.17	4	-0.78	0.07	1
4284121	nnnnn	4945.02	99.32	3	4.61	0.25	3	-0.76	0.04	2
4364710	NnBnN	0	0	0
4469643	nnnnn	4549.94	57.44	3	4.21	0.19	4	-0.64	0.02	2
4616450	nnnnn	5351.78	107.46	7	3.56	0.16	6	-0.04	0.01	4
4647874	nnnGn	5900.40	120.61	5	4.00	0.78	2	-1.21	0.06	1
4841641	nnnnn	5886.65	95.99	7	4.31	0.24	4	-0.79	0.06	3
5076105	nnBnn	5543.06	126.08	4	3.88	0.16	2	-0.76	0.05	1
5103144	nnnnn	4718.40	133.37	3	4.69	0.18	4	-0.32	0.05	3
5128398	nnnnn	6039.21	209.89	5	3.38	0.55	2	-0.43	0.06	1
5178231	nnnnC	0	0	0
5203880	VnnnX	0	0	0
5255182	nnnnn	5421.62	194.07	3	4.33	0.54	2	-0.81	0.07	1
5306555	nnnnn	4937.26	42.14	3	3.51	0.04	4	-0.97	0.07	3
5325367	nnnnn	4637.67	3.40	3	3.96	0.12	2	-0.80	0.08	1
5515363	VnBnX	0	0	0
5641042	nnBnn	5275.19	82.16	6	4.29	0.12	6	-0.96	0.07	4
5843828	nnBnn	5319.63	22.99	3	4.31	0.30	2	-0.65	0.06	1
5966063	nnBnn	5533.64	103.16	6	4.19	0.09	6	-0.20	0.06	4
4260685	nnnnn	6245.95	38.96	9	3.78	0.04	7	-0.58	0.03	7
4276566	nnnnn	4884.49	95.66	3	4.13	0.19	4	-0.95	0.18	2
4421045	nnnnn	4957.09	121.88	3	4.59	0.15	4	-0.48	0.04	2
4619525	nnngn	4260.41	128.10	2	4.26	0.16	4	-1.50	0.14	1
4643058	nnnnn	5754.50	206.46	4	3.81	0.32	2	-0.47	0.10	1
4707507	NnnnN	0	0	0
5066709	nnnnn	4901.64	188.60	3	4.68	0.28	3	-0.49	0.09	1
5068885	nnnnn	5850.65	113.76	5	3.89	0.00	2	-0.44	0.08	1
5195313	nnnnn	4631.12	96.61	3	4.05	0.14	2	-1.00	0.09	1
5228899	nCnnR	0	0	0
5311755	nnnnn	4349.07	77.47	3	3.55	0.20	3	-0.42	0.07	1
5473070	VnBnX	0	0	0
5495944	nnnnn	5494.01	32.60	3	3.77	0.39	2	-0.73	0.06	1
5529360	nnnnn	5877.93	127.14	6	3.90	0.17	4	-0.44	0.00	2
5601654	nnBnn	5812.59	55.87	6	3.90	0.09	4	-0.57	0.10	4
5731635	nnnnn	5431.11	102.39	6	3.80	0.09	6	-0.59	0.06	4
6089859	NnBnN	0	0	0
4157427	nnBnn	5613.90	109.08	3	3.59	0.12	2	-0.51	0.06	1
4214096	nnnnn	5537.19	70.90	5	4.43	0.31	4	-0.66	0.10	1
4234908	nnBnN	0	0	0
4664434	lnnnR	0	0	0
4667110	nnnnn	6595.43	131.65	6	3.91	0.29	3	-2.16	0.11	2
4731234	ICnnR	0	0	0
4808587	nnnnn	6038.18	32.71	8	3.85	0.04	6	-0.07	0.06	5
5062448	nnngn	5841.12	80.30	7	4.27	0.38	4	-1.44	0.09	1
5137168	nnnnn	5516.83	114.97	6	3.96	0.09	6	-0.40	0.10	4
5148317	nnnnn	5904.46	106.51	8	3.81	0.11	6	-0.76	0.06	4
5216505	nnnnn	5327.17	286.74	4	4.29	0.33	4	-0.23	0.15	3
5219890	nnnnn	4291.25	66.42	3	4.09	0.23	3	-0.66	0.07	1
5317519	nnnnn	6075.44	87.41	8	4.20	0.18	6	-0.57	0.04	4
5335540	nnnnn	5544.42	121.77	6	4.14	0.27	4	-0.86	0.05	4
5364554	NnnnN	0	0	0
5470212	nnnnn	5730.66	78.91	8	4.21	0.04	6	0.08	0.06	4
5577617	nnnnn	5843.57	61.96	6	3.44	0.12	4	-0.43	0.10	5
5674117	nnnGn	5243.85	218.94	4	3.78	0.32	4	-1.02	0.10	3
6032356	nnnnn	5536.86	26.14	4	3.24	0.14	4	-1.00	0.11	3

Table 7.5 (cont'd): SSPP Stellar Parameters for Hectospec Targets

UW ID ^a	flags	T_{eff} (K)	$\sigma(T_{\text{eff}})$ (K)	$N(T_{\text{eff}})^{\text{b}}$	$\log g$ (dex)	$\sigma(\log g)$ (dex)	$N(\log g)^{\text{b}}$	[Fe/H] (dex)	$\sigma([\text{Fe}/\text{H}])$ (dex)	$N([\text{Fe}/\text{H}])^{\text{b}}$
6086920	nnnnn	4220.31	64.69	3	3.28	0.28	4	-0.47	0.00	2
4279122	nnnnn	5423.25	110.67	6	3.65	0.08	6	-0.73	0.08	5
4368562	nnnnn	4533.80	116.62	3	3.39	0.32	3	-0.49	0.07	1
4465610	Nnnnn	4601.75	163.58	3	4.21	0.47	2	-0.68	0.06	1
4469608	Nnngn	4226.41	73.42	2	4.05	0.17	2	-1.39	0.07	1
4481235	nnnnn	5859.72	34.71	1	3.64	0.50	2	-0.65	0.05	1
4712017	nnngn	4023.65	20.76	1	4.59	0.04	1	-1.86	0.09	1
4842850	NnBnN	0	0	0
5017568	NnnnN	0	0	0
5026401	nnnnC	0	0	0
5026969	NnnnR	0	0	0
5128265	nnngn	4915.21	93.33	3	4.36	0.18	3	-1.14	0.04	1
5147370	nnnnn	5230.30	54.38	6	3.13	0.11	6	-0.67	0.05	5
5158147	nnnnn	5562.57	105.03	4	3.85	0.28	2	-0.65	0.04	1
5186024	nnnnn	5494.25	51.77	7	3.91	0.11	6	-0.22	0.06	6
5354784	nnnnn	5919.87	46.42	8	3.78	0.10	6	-0.59	0.01	4
5406507	nnnnn	4716.00	233.64	3	3.64	0.51	4	-1.69	0.23	1
5501175	nnnnn	4706.83	67.65	3	4.47	0.12	4	-0.57	0.06	1
5732250	nnnnn	5342.19	107.43	4	4.26	0.14	5	-0.59	0.12	2
5752976	nnnnn	4824.91	125.29	3	4.54	0.12	4	-0.80	0.21	2
5831509	nnnnn	5954.08	82.25	7	3.85	0.14	6	-0.79	0.02	4
6002099	nnnnn	4925.52	85.57	4	4.54	0.14	5	-0.82	0.08	3
4254146	nnnnn	6143.25	108.83	7	3.76	0.26	4	-1.23	0.03	2
4298876	nnnnn	6310.89	26.60	5	3.87	0.43	2	-1.51	0.05	1
4324088	nnnnn	4748.42	186.78	3	4.75	0.19	4	-0.64	0.10	3
4434065	1CnnR	0	0	0
4489980	NCBnN	0	0	0
4563473	nnnnn	6023.73	32.89	8	4.15	0.07	6	-0.53	0.01	4
4721053	VnnnX	0	0	0
4792139	lnnnR	0	0	0
4802616	lnnnR	0	0	0
5107540	nnnnn	5756.72	41.20	7	3.54	0.04	6	-0.07	0.05	4
5132751	Nnnnn	4368.96	90.85	3	3.95	0.26	3	-0.23	0.06	1
5303344	NnnnR	0	0	0
5335542	nnnnn	5089.80	116.01	4	2.46	0.16	5	-0.75	0.05	5
5419214	nnnnn	5832.68	124.10	6	3.96	0.18	4	-0.48	0.10	3
5456640	nnnnn	6301.30	90.01	7	2.48	0.69	4	-1.19	0.02	4
5525990	nnBnn	5186.81	231.24	4	4.71	0.25	3	-0.44	0.19	2
5897335	nnnnn	5263.08	86.12	4	4.25	0.01	5	-0.17	0.04	2
5898064	NnnnN	0	0	0
5967207	nnnnn	5411.07	249.96	4	3.88	0.14	5	-0.71	0.01	5
4158571	nnnnn	5734.71	73.43	6	4.17	0.31	4	-0.55	0.00	3
4250672	nnnnn	6080.47	77.93	8	3.87	0.07	6	-0.76	0.05	7
4365238	1CnnR	0	0	0
4423055	nnnnn	5879.89	52.08	8	3.68	0.12	6	-0.33	0.04	6
4550097	nnnnn	5966.35	120.94	7	4.42	0.44	4	-0.46	0.09	1
4621384	nnnnn	6251.44	56.21	8	3.13	0.19	6	-1.44	0.06	4
4658121	nnnnn	5770.47	78.97	4	3.81	0.35	2	-0.93	0.06	1
4705241	nnnnn	5567.53	69.23	7	4.32	0.17	6	-0.68	0.05	5
4837526	nnngn	5948.33	111.77	5	3.61	0.51	2	-1.24	0.05	1
5134299	nnnnn	6214.41	74.56	8	2.92	0.22	6	-1.50	0.06	4
5190823	lnnnR	0	0	0
5351086	nnnnn	5657.11	59.83	4	4.59	0.29	2	-0.96	0.03	1
5440263	NnnnN	0	0	0
5627463	nnnnn	7514.67	113.68	4	4.39	0.18	3	-0.85	0.03	2
5638442	NnnnN	0	0	0
5676361	nnBnn	5102.78	149.33	4	3.08	0.28	5	-0.97	0.13	4
5698234	nnnnn	6042.76	85.85	5	3.51	0.06	2	-0.84	0.08	1
5728121	nnnnR	0	0	0
5837097	DnBnn	7217.99	828.94	3	3.40	0.45	2	-2.93	0.26	1
4372695	LnnnR	4212.71	128.85	2	4.20	0.64	2	-0.45	0.14	1
4713280	NnnnR	0	0	0
5037623	NnnnN	0	0	0
5173509	nnnnn	6049.90	80.81	7	3.81	0.35	4	-1.46	0.06	4
5230089	nnnnn	5186.37	111.78	4	4.40	0.09	5	-0.17	0.07	3
5245675	nnnnn	5684.51	90.13	4	4.42	0.23	2	-0.34	0.05	1
5443948	nnnnn	4296.50	45.80	3	3.74	0.27	2	-0.46	0.07	1
5561862	nnBnn	5569.24	40.86	7	3.78	0.11	6	-0.71	0.06	5
5699114	nnngn	5908.14	129.03	6	3.83	0.21	4	-1.23	0.04	5
5708650	nnnnn	5624.22	124.61	7	3.50	0.23	4	-0.43	0.06	4
5966246	nnnnn	4660.54	126.97	3	4.62	0.15	4	-0.21	0.13	2
4314402	nnBnn	4815.92	98.69	3	3.92	0.13	3	-0.52	0.13	1
4378425	nnBnn	5246.93	131.11	4	4.11	0.15	3	-0.60	0.17	2
4397873	nnnnn	5207.25	66.01	6	4.17	0.09	6	-0.03	0.08	6

Table 7.5 (cont'd): SSPP Stellar Parameters for Hectospec Targets

UW ID ^a	flags	T_{eff} (K)	$\sigma(T_{\text{eff}})$ (K)	$N(T_{\text{eff}})^{\text{b}}$	$\log g$ (dex)	$\sigma(\log g)$ (dex)	$N(\log g)^{\text{b}}$	[Fe/H] (dex)	$\sigma([\text{Fe}/\text{H}])$ (dex)	$N([\text{Fe}/\text{H}])^{\text{b}}$
4426501	lCnnR	0	0	0
4431456	nnnGn	7214.09	220.88	7	3.05	0.19	4	-1.30	0.01	2
4541745	NnBnN	0	0	0
4558815	nnBnn	5418.67	121.18	6	3.44	0.59	4	-0.86	0.00	2
4638268	nnnnn	5566.85	65.70	6	3.78	0.08	6	-0.23	0.10	4
4722742	nnnnn	6167.50	165.01	7	4.15	0.27	6	-0.11	0.05	5
4847232	nnnnn	4481.31	97.36	3	4.48	0.18	4	-1.32	0.10	2
5096098	nnnnn	6189.10	45.11	6	3.77	0.35	3	-1.25	0.11	2
5120218	nnBnn	4937.38	83.22	3	4.04	0.12	2	-0.44	0.07	1
5126005	nnnnn	5498.57	23.04	6	4.34	0.23	6	-0.94	0.03	4
5253180	NnBnN	0	0	0
5290928	nnnnn	5803.00	56.31	8	3.81	0.10	6	-0.56	0.02	5
5427905	NnnGn	4227.60	56.04	2	4.25	0.31	2	-1.34	0.08	1
5474724	NnnnN	4393.14	205.51	3	4.25	0.39	2	-0.76	0.11	1
5515787	lnnnN	0	0	0
5684740	nnnnn	5633.32	71.39	7	4.16	0.13	6	-0.22	0.04	6
5747617	nnBnn	5108.95	15.46	4	3.31	0.14	5	-0.49	0.08	4
5854635	NnnnR	0	0	0
4253988	nnnnn	5559.93	171.37	4	3.95	0.56	2	-0.33	0.08	1
4397456	nnnnn	6130.59	36.00	8	3.81	0.09	6	-0.73	0.06	6
4448584	NnnnN	0	0	0
4465268	nnnnn	5450.44	95.40	5	3.94	0.41	4	0.48	0.09	1
4468428	NnBnN	0	0	0
4507265	lnnnR	0	0	0
4749603	nnnnn	4673.01	53.23	3	4.12	0.21	4	-0.51	0.09	1
4866884	nnnnn	4709.05	88.50	3	4.61	0.08	4	-0.84	0.16	2
5143348	nnnnn	5954.91	77.26	7	3.99	0.24	4	-0.69	0.07	4
5159778	nnnnn	5937.62	75.38	8	4.06	0.13	6	-0.58	0.07	6
5168312	CnnnN	6183.59	18.30	8	3.87	0.08	6	-0.14	0.07	4
5172613	lCnnR	0	0	0
5240800	nnnnn	4621.31	35.38	3	3.23	0.23	4	-0.94	0.24	2
5296619	NnBnn	5390.87	192.75	3	4.36	0.13	2	0.37	0.07	1
5445533	nnnnn	5987.93	183.73	7	3.42	0.33	4	-1.38	0.08	4
5645531	nnnnN	0	0	0
5843070	nnngn	5676.15	153.55	6	2.49	0.21	4	-1.86	0.09	3
5912671	nnnnn	4707.24	95.44	3	4.47	0.10	4	-0.49	0.05	2
5985829	nnnnn	4957.20	187.66	4	2.55	0.16	5	-0.91	0.04	4
6087484	NnnGn	6009.74	75.93	8	3.76	0.20	6	-1.03	0.04	6
7912702	nnngn	5233.35	41.05	3	4.14	0.31	2	-1.07	0.08	1
4177967	nnnnn	6044.93	90.02	8	3.65	0.19	6	-0.59	0.00	2
4230230	nCnnR	0	0	0
4248039	LnnnR	0	0	0
4276700	nnnGn	5890.39	98.78	7	3.77	0.18	4	-1.11	0.05	3
4319344	nnnnn	4640.53	92.95	3	4.12	0.15	4	-0.38	0.02	2
4492102	nnnGn	6213.80	151.96	5	3.31	0.12	2	-1.25	0.04	1
4742088	NnBnN	0	0	0
4853634	NnBnn	5394.02	117.56	3	4.43	0.43	2	-0.74	0.07	1
5052581	nnnnn	5716.94	43.97	7	4.22	0.04	6	-0.31	0.00	7
5082495	NCnn	4387.51	93.36	3	3.68	0.09	2	-0.21	0.24	1
5108746	nnnnn	6177.82	61.80	9	2.11	0.21	7	-1.28	0.06	7
5118953	nnnnn	4637.34	94.57	3	4.16	0.16	3	-0.69	0.07	1
5291413	nnnnn	5564.50	63.33	5	3.97	0.09	4	0.04	0.06	3
5323978	NnnnN	0	0	0
5329320	nnnnn	5266.13	114.98	6	4.44	0.18	6	-0.13	0.04	5
5797880	nnnnn	4902.33	113.28	4	3.80	0.13	5	-0.85	0.18	3
5813527	NnnGn	5787.40	123.66	6	2.98	0.18	3	-1.02	0.25	1
6023462	NnBnn	5238.48	158.80	4	4.68	0.11	4	-0.39	0.06	1
6046972	VnBnX	0	0	0
6075646	nnnnn	5226.71	70.07	4	4.46	0.01	5	-0.43	0.10	4
4330744	NnnnN	0	0	0
4708655	nnnnR	0	0	0
4733613	nnnnn	4883.51	49.49	3	2.62	0.10	4	-0.80	0.02	3
5099799	lCnnR	0	0	0
5418751	nnngn	5432.08	219.61	4	3.77	0.33	2	-1.16	0.11	1
6076359	nnnnn	5944.22	89.56	7	4.06	0.34	4	-0.35	0.02	2
4282938	lnnnC	0	0	0
4470815	NCBnN	0	0	0
5032835	nnnnn	5442.37	150.65	6	3.79	0.23	6	-0.68	0.04	4
5051863	nnnnn	5841.29	71.01	8	4.01	0.12	6	-0.21	0.04	5
5487425	nnnnn	5030.93	129.23	4	4.44	0.21	5	-0.84	0.08	3
5642622	nnnnN	0	0	0
5717538	nnnnn	5872.14	80.96	8	4.33	0.09	6	-0.62	0.07	6
5784957	nnnnn	5017.85	63.80	3	2.96	0.12	4	-0.47	0.14	2
4314132	nnnnR	0	0	0

Table 7.5 (cont'd): SSPP Stellar Parameters for Hectospec Targets

UW ID ^a	flags	T_{eff} (K)	$\sigma(T_{\text{eff}})$ (K)	$N(T_{\text{eff}})^{\text{b}}$	$\log g$ (dex)	$\sigma(\log g)$ (dex)	$N(\log g)^{\text{b}}$	[Fe/H] (dex)	$\sigma([\text{Fe}/\text{H}])$ (dex)	$N([\text{Fe}/\text{H}])^{\text{b}}$
4387062	nnBnn	5590.60	178.88	4	3.71	0.03	2	-0.13	0.09	1
4478489	nnnnn	5052.81	283.72	3	4.47	0.10	4	-0.58	0.06	3
4487123	nCnnR	0	0	0
4848200	NnnnN	0	0	0
5139465	VnnnX	0	0	0
5182435	nnnnn	4447.82	46.95	3	4.08	0.05	4	-0.67	0.17	3
5212400	nnnnn	5899.69	64.15	8	4.46	0.13	6	-0.59	0.03	6
5415779	nnnnN	0	0	0
5472337	nnnnn	4817.06	164.24	3	4.57	0.18	4	-0.54	0.00	2
5478408	nnnnn	5886.42	77.67	7	4.22	0.18	6	-0.47	0.04	6
5668624	nnnnn	5127.70	52.32	4	3.74	0.16	5	-0.94	0.02	3
5741322	nnnnn	5170.71	79.61	6	4.43	0.08	6	-0.64	0.06	5
5816512	nnngn	4187.82	147.46	2	3.87	0.11	4	-1.52	0.07	2
5956426	nnnnn	4625.94	48.50	3	2.81	0.32	4	-0.57	0.17	3
4346244	nnBnn	5405.44	49.00	5	4.00	0.25	4	-0.42	0.03	3
4398429	nnnnn	5977.95	52.30	6	4.02	0.06	6	-0.23	0.02	4
4436011	nnnnn	5843.13	42.96	7	4.14	0.00	6	-0.32	0.07	5
4440580	NCBnN	0	0	0
4522359	nnnGn	5247.08	29.14	5	3.50	0.18	4	-1.02	0.15	2
4584659	nnngn	5427.75	95.72	6	2.99	0.19	6	-1.21	0.00	5
4634314	NCnnR	0	0	0
4743652	nnnnn	4389.85	55.64	3	4.20	0.19	4	-0.40	0.24	1
4818802	nnBnc	0	0	0
5067665	nnnnn	4822.10	146.93	3	4.33	0.26	3	-1.35	0.15	1
5090317	nnnnn	5789.92	103.84	8	4.13	0.17	6	-0.45	0.08	4
5098239	nnnnn	5511.67	106.23	7	3.75	0.17	6	-0.62	0.04	4
5221605	nnnnn	5838.11	94.91	8	3.79	0.09	6	-0.47	0.03	4
5377106	nCnnR	0	0	0
5433082	Nnnnn	4674.64	121.50	3	4.58	0.28	2	-0.75	0.05	1
6007487	nnnnN	0	0	0
6083236	nnBnn	5746.21	107.51	3	4.34	0.54	2	0.49	0.08	1
4314846	NnnnR	0	0	0
4331454	NBnN	0	0	0
4467667	nnBnn	5503.45	35.48	6	3.67	0.08	6	-0.14	0.03	4
4498518	nnnnn	5520.87	129.77	6	3.91	0.33	6	-0.80	0.10	6
4557243	nnnnn	5944.43	186.22	5	4.40	0.31	4	-0.03	0.13	4
4557632	NnBnN	0	0	0
5066054	nnnnn	5046.34	101.35	3	4.60	0.11	4	-0.55	0.16	2
5097490	nnnnn	5806.24	68.18	7	3.73	0.18	6	-0.47	0.05	5
5178699	nnnnn	7303.31	99.97	6	3.78	0.51	4	-0.62	0.08	3
5363796	nnnnn	5692.56	104.03	6	4.17	0.32	4	-0.34	0.03	3
5364757	nnngn	4121.68	73.55	3	2.81	0.71	2	-1.06	0.10	1
5401948	nnnnn	6088.71	292.82	4	4.19	0.58	2	-0.89	0.04	1
5423907	nnnnn	5043.59	52.47	4	4.40	0.10	5	-0.47	0.08	3
5627909	nnnnn	5909.75	117.39	4	3.60	0.10	2	-0.42	0.09	1
5651828	nnnnn	5853.17	121.76	8	4.12	0.19	5	0.00	0.04	5
5699926	nnnnn	4675.62	72.36	3	4.21	0.16	4	-0.79	0.01	2
6066270	NnnnN	0	0	0
6085797	nnnnN	0	0	0
4272309	nnnnn	5254.53	77.53	4	4.34	0.17	5	-0.16	0.06	3
4277367	nnnnn	5755.09	34.71	7	4.01	0.12	6	-0.21	0.02	5
4356459	NnBnN	0	0	0
4414371	nnngn	4764.44	85.17	3	4.50	0.38	2	-1.25	0.04	1
4433701	VnBnX	0	0	0
4482014	InnnR	0	0	0
4537547	nnBnn	4917.80	168.94	3	4.08	0.56	2	-0.64	0.10	1
4603056	nnnnn	5330.98	76.44	6	4.36	0.22	6	-0.57	0.11	5
4713633	lCnnR	0	0	0
5071021	nnnnn	5680.09	103.92	7	4.02	0.17	6	-0.51	0.01	5
5166934	nnnnn	5739.51	129.31	6	4.16	0.17	4	-0.42	0.01	2
5215716	nnnnn	4620.10	144.20	3	4.16	0.17	3	-0.51	0.08	1
5252295	Nnnnn	4291.25	48.86	3	4.42	0.46	2	-1.19	0.05	1
5266769	nnnnn	5432.01	66.24	6	3.73	0.15	4	-0.64	0.07	3
5341452	nnnnn	5736.19	118.13	7	3.78	0.18	6	-0.74	0.04	4
5417541	nnnnR	0	0	0
5523795	lnnnR	0	0	0
5545366	nnnnn	5874.49	70.71	8	4.14	0.12	6	-0.54	0.06	5
4234957	nnnnR	0	0	0
4395224	nnnnn	6637.64	343.30	4	2.68	0.72	3	-1.23	0.11	1
4432090	nnnnn	5705.06	99.26	6	3.97	0.05	4	-0.49	0.09	4
4576482	nnBnn	5823.69	64.83	7	3.69	0.07	6	-0.64	0.07	6
4598005	VnnnN	0	0	0
4732529	NnnnN	0	0	0
4795431	nnnnn	5295.93	134.11	6	3.87	0.18	6	-0.31	0.02	3

Table 7.5 (cont'd): SSPP Stellar Parameters for Hectospec Targets

UW ID ^a	flags	T_{eff} (K)	$\sigma(T_{\text{eff}})$ (K)	$N(T_{\text{eff}})$ ^b	$\log g$ (dex)	$\sigma(\log g)$ (dex)	$N(\log g)$ ^b	[Fe/H] (dex)	$\sigma([\text{Fe}/\text{H}])$ (dex)	$N([\text{Fe}/\text{H}])$ ^b
4872856	nnnnn	5589.41	151.24	5	4.52	0.35	4	-0.56	0.08	3
5186449	nnnnn	6570.81	56.78	8	3.72	0.26	6	-1.33	0.02	5
5278073	nnnnn	5792.91	87.85	6	3.74	0.38	4	-0.62	0.01	3
5339011	lnnGn	4270.76	30.29	1	0.68	0.25	1	-2.65	0.20	1
5407041	nnnnn	7086.57	182.90	5	3.85	0.58	2	0.05	0.13	1
5548565	nnnnn	6183.56	38.55	9	3.92	0.13	7	-0.37	0.04	5
5592116	nnnnn	5606.19	34.22	7	4.28	0.16	6	-0.23	0.06	4
5784332	nnnnN	0	0	0
6080801	nnnnn	5477.51	111.61	6	4.33	0.09	6	-0.39	0.06	3
4235887	nnnnn	5742.49	61.46	7	4.03	0.18	6	-0.78	0.04	6
4335381	nnBnn	5306.98	125.08	4	4.70	0.03	5	-0.70	0.11	2
4423544	nnnnn	4583.09	61.03	3	4.42	0.18	4	-0.66	0.04	2
4441274	nnnnn	4404.99	77.10	3	3.60	0.21	4	-0.60	0.10	2
4567938	Nnnnn	4519.48	85.17	3	3.84	0.18	2	-0.23	0.07	1
4594129	NnnnR	0	0	0
4609308	nnnnn	5775.21	84.22	8	3.75	0.13	6	-0.40	0.03	5
4726782	nnnnn	5912.77	53.33	8	4.10	0.04	6	-0.22	0.03	6
4821974	nnnnn	5564.31	64.96	7	3.91	0.08	6	0.11	0.03	3
5035633	VnnnX	0	0	0
5164112	nnnnn	5413.05	33.36	4	4.47	0.11	5	-0.13	0.04	3
5208720	nnnnn	5290.26	88.67	6	4.40	0.07	6	-0.63	0.04	6
5210130	nnnnn	5368.19	210.85	4	4.19	0.31	4	-0.63	0.07	2
5248187	nnnnn	5979.46	101.11	8	4.30	0.12	6	-0.49	0.04	5
5267990	lnnnR	0	0	0
5283567	nnnnn	5707.98	221.32	6	4.78	0.19	5	0.05	0.08	3
5357385	nnnnn	5484.47	128.47	3	3.75	0.77	2	-0.75	0.07	1
5363013	nnnnn	6061.97	15.56	5	3.56	0.04	2	-0.33	0.06	1
5413707	nnnnc	0	0	0
5718234	nnnnn	4651.93	64.56	3	2.74	0.24	4	-0.82	0.02	2
6032150	nnnnn	6030.50	67.03	5	3.76	0.28	2	-0.98	0.05	1
4304743	nnnnn	4536.11	80.79	3	4.47	0.17	4	-0.67	0.04	2
4324784	nnnnn	4547.20	15.98	3	4.17	0.45	2	-0.85	0.19	1
4368883	Nnnnn	5666.41	207.24	3	4.16	0.72	2	-0.18	0.09	1
4468499	ICnnR	0	0	0
4506910	nnnnn	7541.32	52.15	5	4.02	0.22	4	-0.66	0.02	2
4659735	ICnnR	0	0	0
4742043	nnnnc	0	0	0
4822124	nCnGn	5264.45	443.93	5	2.89	0.59	3	-1.15	0.06	1
4833054	nnnGn	5412.20	135.96	7	3.43	0.13	6	-1.00	0.05	1
5046420	NnnnR	0	0	0
5066638	nnnnn	5895.10	68.50	8	4.38	0.32	6	-0.55	0.08	5
5268715	nnnnn	5873.93	71.87	8	3.61	0.11	6	-0.69	0.06	6
5288047	nnBgn	4703.90	172.09	4	4.27	0.30	5	-1.20	0.15	4
5314290	nnBnn	6093.63	229.78	6	4.23	0.26	4	0.25	0.05	2
5321540	nnnnn	4644.35	184.93	3	4.24	0.64	2	-0.45	0.14	1
5325201	VnnnX	0	0	0
5422663	nnnnn	4767.13	91.68	3	4.35	0.05	2	-0.76	0.06	1
5621361	nnnnn	4936.44	118.12	4	2.95	0.17	5	-0.82	0.07	4
5666776	nnnnn	5081.90	184.32	3	4.32	0.35	3	-0.44	0.24	1
5746133	nnnnn	6099.74	60.36	9	3.98	0.02	7	-0.14	0.04	5
5968066	nnnnn	5269.06	202.35	4	3.26	0.14	5	-0.79	0.01	3
5997985	nnnnn	5780.65	118.69	5	3.63	0.23	2	-0.65	0.09	1
4282220	nnBnc	0	0	0
4361529	nnnnn	4545.18	95.15	3	3.84	0.12	3	-0.43	0.12	1
4415656	NnnnN	0	0	0
4472910	NnnnN	0	0	0
4564212	nnBnn	4964.75	168.44	4	4.01	0.12	4	-0.39	0.17	2
4619712	nnnnn	5880.45	129.68	8	4.79	0.05	5	-1.24	0.16	2
4701221	nnnnn	7233.43	140.40	7	2.59	0.23	4	-1.86	0.14	3
4759889	nnnnn	5408.79	90.13	3	4.06	0.29	2	-0.94	0.10	1
4831017	nnnnn	5703.33	67.96	8	4.17	0.10	6	-0.57	0.04	5
5063155	nnnnn	6358.57	107.02	6	3.94	0.30	3	-1.46	0.03	2
5130136	nnnnn	5024.70	91.00	3	4.59	0.15	3	-0.43	0.07	1
5133674	nnnnn	6096.49	121.78	7	4.28	0.36	4	-0.78	0.02	2
5424488	NnnnN	0	0	0
5428351	nnnnn	5481.77	105.71	6	4.08	0.06	6	-0.33	0.04	5
5443433	nnnnn	5694.03	92.43	6	3.54	0.16	6	-0.83	0.08	6
5486190	nnnnn	5301.46	149.32	7	3.82	0.20	6	-0.76	0.05	6
5600337	nnnGn	5259.09	173.54	4	3.35	0.30	2	-1.52	0.10	1
5914113	nnnnn	5639.83	80.77	6	4.10	0.20	4	-0.60	0.04	5
6052552	nnnnn	4679.68	77.67	3	3.20	0.09	4	-0.81	0.11	1
4390402	nnnGn	6108.78	111.53	7	3.51	0.13	4	-1.01	0.04	1
4761200	nnnnn	5930.03	39.43	7	3.73	0.05	6	0.03	0.07	6
4761433	NnnnN	0	0	0

Table 7.5 (cont'd): SSPP Stellar Parameters for Hectospec Targets

UW ID ^a	flags	T_{eff} (K)	$\sigma(T_{\text{eff}})$ (K)	$N(T_{\text{eff}})^{\text{b}}$	$\log g$ (dex)	$\sigma(\log g)$ (dex)	$N(\log g)^{\text{b}}$	[Fe/H] (dex)	$\sigma([\text{Fe}/\text{H}])$ (dex)	$N([\text{Fe}/\text{H}])^{\text{b}}$
4822386	nnBnc	0	0	0
5077641	nnnnn	4354.84	13.99	3	3.93	0.18	4	-1.17	0.07	2
5247089	nnnnn	5723.05	54.70	6	3.61	0.05	6	0.04	0.04	3
5405059	lnnnR	0	0	0
5486680	nnnnn	5960.38	105.63	7	4.05	0.37	4	-0.63	0.08	1
5542014	nnnnn	5798.84	143.63	6	3.73	0.22	4	-0.36	0.05	2
4188591	nnnnn	6157.47	111.26	9	4.00	0.16	7	-0.95	0.06	4
4592699	NnBnN	0	0	0
4643437	nCnnn	5200.18	173.87	3	3.00	0.03	4	-0.50	0.06	3
5139538	nnnnn	5596.66	21.35	7	4.33	0.08	6	-0.86	0.06	6
5339240	nnBnn	6008.23	94.86	7	4.12	0.35	6	-0.44	0.01	4
5486863	nnnnn	6050.45	90.42	7	4.06	0.05	4	-0.35	0.06	4
5512754	nnBnn	5032.96	83.43	3	3.33	0.17	4	-0.54	0.06	3
5574178	nnngn	5291.72	78.90	3	4.06	0.04	2	-1.25	0.04	1
6090939	nnnnn	5116.11	75.31	4	4.30	0.12	5	-0.19	0.08	3
4397336	nnnnn	5435.39	72.10	6	4.16	0.08	6	-0.55	0.06	5
4649302	NnnnN	0	0	0
5074174	NnBnn	4979.03	15.72	3	3.99	0.09	3	-0.96	0.12	1
5485720	nCnnn	5391.07	76.17	2	4.25	0.05	2	-0.80	0.04	1
5617922	nnnnn	4410.92	78.32	3	4.06	0.06	4	-0.57	0.05	1
4185973	nnnnn	6692.99	81.87	5	2.22	1.07	2	-1.99	0.06	1
4575342	nnnnn	6309.47	49.42	9	2.44	0.22	7	-1.34	0.08	7
4831107	NnBnN	0	0	0
5423792	nnnnn	6723.88	125.54	8	3.08	0.19	6	-1.45	0.02	2
5457591	lnnnR	0	0	0
5538010	nnnnn	4424.39	74.65	3	4.15	0.17	4	-0.43	0.07	1
6010410	nnnnn	5434.64	71.48	6	3.82	0.13	6	-0.69	0.00	3
7906161	nnmn	4243.40	104.40	2	4.15	0.23	3	-1.50	0.07	2
4378545	nnBnn	4939.42	100.81	4	4.38	0.28	4	-0.88	0.26	2
4410488	LnnnR	0	0	0
4550646	nnBnn	5715.09	103.04	7	3.82	0.12	6	-0.81	0.03	5
4576803	nnnnn	6135.10	44.87	4	4.01	0.10	2	-0.15	0.06	1
4594594	nnnnn	5954.60	76.59	9	3.12	0.23	7	-0.75	0.06	4
4722465	nCnnR	0	0	0
4774000	NnBnN	0	0	0
4815281	nnnnn	5415.06	35.30	6	4.27	0.06	6	-0.26	0.01	5
5023982	nnnnn	5604.72	64.03	6	4.31	0.12	6	-0.18	0.05	5
5033513	nnnnn	4937.58	105.82	3	4.11	0.08	2	-0.21	0.05	1
5096294	nnBnn	6231.87	137.31	7	4.73	0.15	6	-0.07	0.01	3
5165817	nnnnn	5897.71	147.51	6	4.68	0.37	4	-0.46	0.13	2
5198178	NnBnN	0	0	0
5284185	nnnnn	5410.28	26.94	6	4.44	0.17	6	-0.71	0.05	6
5335583	NnnnR	0	0	0
5641590	nnnnn	5320.19	48.59	6	3.25	0.01	6	-0.69	0.06	5
5819910	nnBnn	5075.53	121.63	4	4.46	0.08	5	-0.56	0.08	4
5828944	nnnnn	4610.91	84.12	3	4.35	0.12	4	-0.60	0.03	1
5829837	ICnnR	0	0	0
5872990	Nnnnn	4893.68	109.79	3	4.45	0.05	2	-0.34	0.07	1
5921721	nnnnn	6173.00	136.94	7	3.37	0.19	4	-0.84	0.04	1
4232870	nnnnn	6081.50	15.13	5	4.07	0.53	2	-0.66	0.07	1
4529429	nnnnn	5029.56	64.14	4	2.01	0.18	5	-1.35	0.07	3
4668755	nnnnn	5515.36	108.83	7	3.79	0.11	6	-0.47	0.02	4
4684395	nnnnn	4706.42	131.81	3	4.48	0.18	4	-0.27	0.26	1
4711173	nnnnn	5686.34	59.49	7	3.81	0.07	6	-0.43	0.07	6
4793695	nnnnn	5493.78	65.85	7	4.06	0.03	6	-0.19	0.06	7
5103345	nnnnn	5468.75	185.05	4	4.29	0.25	4	-1.11	0.02	2
5253857	nnnnn	4510.02	69.09	3	4.63	0.20	4	-1.26	0.10	2
5308578	nnnnn	6090.54	49.91	8	3.95	0.05	6	-0.40	0.02	4
5318426	nnBnn	5540.87	93.81	3	3.60	0.37	2	-0.42	0.05	1
5349901	nnnnn	5366.92	134.84	3	4.01	0.00	2	-0.78	0.06	1
5433591	nnnnn	5751.94	54.76	7	4.00	0.08	6	-0.46	0.03	4
5456963	nCnnn	4644.86	37.24	1	3.98	0.05	2	-0.15	0.14	1
5513680	nnnnn	6563.38	138.07	9	2.08	0.27	7	-1.54	0.09	5
5878357	VCnnR	0	0	0
5966729	nnnnn	5179.39	24.89	3	4.27	0.07	2	-0.92	0.05	1
6013312	nnnnn	4278.11	116.03	3	3.74	0.07	2	-0.53	0.07	1
6038286	ICnnR	0	0	0
4159102	NCnnN	0	0	0
4167983	Nnnnn	4343.63	47.23	3	3.45	0.41	2	-0.53	0.07	1
4566633	nnnnN	0	0	0
4584480	nnnnn	5407.62	7.58	5	3.99	0.30	4	-0.44	0.11	2
4628612	nnnnn	5323.71	79.38	6	3.86	0.12	6	-0.49	0.07	5
4691265	nnnnn	5661.96	56.60	7	4.03	0.08	6	-0.70	0.04	5
4863592	nnnnn	6085.15	161.38	7	4.31	0.31	6	0.14	0.05	3

Table 7.5 (cont'd): SSPP Stellar Parameters for Hectospec Targets

UW ID ^a	flags	T_{eff} (K)	$\sigma(T_{\text{eff}})$ (K)	$N(T_{\text{eff}})^{\text{b}}$	$\log g$ (dex)	$\sigma(\log g)$ (dex)	$N(\log g)^{\text{b}}$	[Fe/H] (dex)	$\sigma([\text{Fe}/\text{H}])$ (dex)	$N([\text{Fe}/\text{H}])^{\text{b}}$
5038448	nnnnn	5645.18	40.25	7	4.30	0.11	6	-0.65	0.07	4
5042036	Nnnnn	4671.77	126.97	3	3.87	0.14	2	-0.76	0.07	1
5225674	NnBnN	0	0	0
5319972	nnBnn	5357.74	95.75	5	4.26	0.07	4	-0.74	0.01	3
5352485	nnnnn	5334.37	49.13	5	4.43	0.23	4	-0.68	0.05	4
5379602	nnnnn	5686.36	50.62	6	3.73	0.01	4	-0.71	0.08	5
5690123	nnnnn	5885.11	45.12	7	4.05	0.11	6	-0.17	0.06	6
5712159	nnnnn	5767.85	52.40	4	4.17	0.54	2	-0.86	0.03	1
5955329	nnBnn	5739.96	181.40	4	3.90	0.70	2	-0.45	0.04	1
6084956	nnnGn	6267.56	89.40	6	3.12	0.91	3	-1.00	0.09	1
4351608	nnnGn	4455.68	100.36	3	4.65	0.19	4	-1.59	0.25	1
4448899	nnnnn	4301.66	56.85	3	3.80	0.24	4	-0.40	0.16	1
4529148	nnnnn	4291.25	10.96	3	4.18	0.24	2	-1.22	0.07	1
4551199	nnnnn	4760.87	120.88	3	4.13	0.05	2	-0.17	0.08	1
4645636	nnnnn	5647.81	128.21	7	3.86	0.20	6	-0.66	0.07	3
4824467	nnnnn	5177.75	35.62	3	4.16	0.10	2	-0.28	0.06	1
5018082	VCnnR	0	0	0
5064453	NnBnN	0	0	0
5205976	nnnnn	5924.13	52.71	8	4.16	0.09	6	-0.35	0.03	4
5274513	lnnnR	0	0	0
5290328	nnnnn	5741.70	39.91	7	3.75	0.09	6	-0.32	0.04	6
5377341	nnnnn	5867.62	44.12	8	3.84	0.07	6	-0.08	0.05	5
5423606	nnnnn	5292.03	163.78	3	4.43	0.45	2	-0.80	0.08	1
5464428	nnnnn	5663.77	81.47	7	4.14	0.13	6	-0.43	0.03	5
5663153	lCnnR	0	0	0
5932235	VnnnX	0	0	0
4159219	nnnnn	6593.85	166.57	5	3.75	0.71	2	-1.50	0.06	1
4168047	DnBnn	5003.04	18.10	3	4.06	0.24	4	-0.38	0.31	1
4188200	nnBnn	4832.68	122.49	3	3.73	0.06	4	-0.11	0.01	2
4196055	nnnnn	5917.76	27.70	8	4.19	0.14	6	-0.45	0.04	5
4454736	NnnnN	0	0	0
4648602	NnnnN	0	0	0
4719832	nnnnn	6096.02	165.96	7	2.88	0.13	4	-1.97	0.10	1
4724400	nnnnn	4520.41	50.54	3	4.12	0.13	4	-0.70	0.17	2
5029040	nnBgn	6031.13	330.01	4	3.97	0.91	2	-2.41	0.15	1
5058729	nnnnn	5966.28	41.54	7	3.76	0.05	6	-0.21	0.07	5
5124517	nnnnn	5288.61	48.29	3	3.85	0.12	2	-0.79	0.04	1
5286680	nnnnn	5079.98	92.36	3	4.38	0.44	2	-0.89	0.09	1
5313731	lCnnR	0	0	0
5362530	nnnnN	0	0	0
5568770	nnnnn	5956.38	49.99	5	3.90	0.08	2	-0.83	0.05	1
5618891	nnBnn	5389.88	81.84	3	4.12	0.19	2	-0.57	0.07	1
5638560	nnnnn	4295.29	164.15	2	3.67	0.11	1	-0.38	0.11	1
5881217	lCnnR	0	0	0
5943965	nnnnn	5888.45	212.24	6	3.65	0.08	4	-0.65	0.03	3
4165593	NnBnN	0	0	0
4186471	nnnnn	6046.92	39.38	8	4.18	0.07	6	-0.42	0.05	7
4193963	nnnnn	6428.64	71.18	8	2.87	0.25	6	-1.23	0.25	1
4277855	nnnnn	5720.13	154.45	7	3.61	0.40	6	-0.70	0.05	6
4417185	nnnnn	4225.04	86.56	2	3.87	0.40	2	-0.59	0.10	1
4514223	nnnnn	4891.69	85.03	3	4.54	0.10	4	-0.49	0.11	1
4664223	nnnnn	5327.45	76.36	5	4.14	0.14	4	-0.69	0.04	2
4664783	NnnnR	0	0	0
5021505	lnnnN	0	0	0
5044435	nnnGn	5734.93	87.57	6	4.09	0.22	4	-1.14	0.06	3
5148276	nnnnn	5890.56	101.73	4	3.69	0.25	2	-0.40	0.09	1
5194977	nnnnn	4978.88	76.95	3	4.36	0.07	3	-0.39	0.06	2
5284792	nnnnn	4383.91	57.98	3	4.07	0.27	4	-0.44	0.09	1
5296568	NnBnN	0	0	0
5306262	nnnnn	5063.07	170.63	4	4.48	0.04	5	-0.33	0.07	1
5344385	nnnnn	4549.02	89.22	3	4.34	0.26	2	-0.65	0.15	1
5436213	nnnnn	4503.81	24.46	3	3.15	0.22	2	-0.74	0.10	1
5608708	nnnnn	5804.21	61.60	4	4.17	0.28	2	-0.69	0.04	1
5705779	nnnnn	5718.10	108.50	7	3.98	0.08	6	-0.31	0.03	4
5779839	nnBnn	5027.31	212.94	4	3.92	0.28	5	-0.56	0.03	2
5790453	nnnnR	0	0	0
6066071	lCnnR	0	0	0
4413570	nnnnn	5541.31	41.77	6	3.90	0.10	6	0.04	0.08	6
4415539	nnBnn	5298.98	78.20	6	3.72	0.17	6	-0.72	0.11	4
4577237	lnnnR	0	0	0
4778078	nnBnn	5226.68	28.92	3	4.02	0.18	2	-0.51	0.15	1
4818914	lnnnR	0	0	0
5101748	nnBnn	5314.90	7.17	4	4.35	0.35	4	-1.28	0.22	3
5158420	nnnnn	5247.72	683.95	2	4.77	0.04	1	-0.41	0.05	1

Table 7.5 (cont'd): SSPP Stellar Parameters for Hectospec Targets

UW ID ^a	flags	T_{eff} (K)	$\sigma(T_{\text{eff}})$ (K)	$N(T_{\text{eff}})^{\text{b}}$	$\log g$ (dex)	$\sigma(\log g)$ (dex)	$N(\log g)^{\text{b}}$	[Fe/H] (dex)	$\sigma([\text{Fe}/\text{H}])$ (dex)	$N([\text{Fe}/\text{H}])^{\text{b}}$
5163980	nnnnn	5060.50	96.66	4	3.19	0.11	5	-0.57	0.06	5
5186974	nnnnn	5249.03	29.56	6	3.69	0.05	6	-0.77	0.03	5
5233603	nnnnn	5227.67	191.20	3	4.26	0.62	2	-0.73	0.12	1
5236918	nnnnn	5810.62	336.69	5	4.04	0.57	2	-0.68	0.09	1
5286421	nnBnn	6360.31	332.08	4	4.11	0.77	2	-0.42	0.07	1
5425211	nnBnn	5000.71	73.47	3	4.41	0.23	3	-0.32	0.06	1
5569043	nnnnn	7059.21	96.37	7	4.58	0.20	6	-0.32	0.07	4
5629516	nnnnn	6286.13	76.63	6	3.37	0.30	3	-1.58	0.09	1
5996010	nnnnn	5410.66	95.70	6	3.99	0.13	4	-0.65	0.10	5
6060414	lnnnR	0	0	0
4195504	NnBnN	0	0	0
4251928	nnnnn	5209.22	56.00	4	4.49	0.09	5	-0.43	0.08	5
4318560	nnBnn	4978.66	120.27	3	4.47	0.19	4	-0.64	0.05	2
4371615	nnnnn	4641.91	37.92	3	4.11	0.17	4	-0.62	0.20	2
4594311	nnnnn	5393.48	54.71	3	4.34	0.28	2	-0.39	0.14	1
4812869	nnnnn	5868.97	58.79	8	3.96	0.24	6	-0.61	0.02	4
5194657	nnnnn	4745.06	83.45	3	4.40	0.10	4	-0.64	0.16	2
5199139	nnnnn	5024.69	108.23	3	4.42	0.05	4	-0.20	0.06	3
5228513	nnnnn	5957.98	124.39	4	4.34	0.54	2	-0.58	0.05	1
5341644	nnBnn	5890.65	254.16	5	4.18	0.53	3	-0.49	0.50	3
5441341	nnnnn	5714.86	114.42	7	4.05	0.08	6	-0.64	0.06	5
5469684	nnnGn	5633.94	144.90	4	3.83	0.41	2	-1.03	0.10	1
5495921	lnnnn	4358.99	188.04	2	3.82	0.07	1	-0.27	0.06	1
5681734	nnnnn	4550.15	218.43	3	2.47	0.44	4	-0.67	0.10	4
6047535	nnnnn	4581.55	87.63	3	4.29	0.28	2	-0.46	0.13	1
5024031	Nnnnn	4322.65	16.10	3	3.32	0.42	2	-0.58	0.10	1
5312153	nnnnn	6781.88	97.51	6	3.46	0.21	4	-1.75	0.05	2
5465780	nnnnn	5480.76	170.24	4	3.93	0.57	2	-0.53	0.05	1
5585569	nnnnn	5860.13	366.03	3	4.18	0.69	2	-0.84	0.08	1
6027747	nnnnn	5778.33	37.15	7	4.11	0.03	6	-0.15	0.06	5
4276832	NnBnn	5520.60	119.81	3	4.16	0.31	2	-0.54	0.05	1
4287889	nnBnn	4981.34	52.88	3	3.89	0.06	3	-0.73	0.07	1
4409163	nnnnN	0	0	0
4704750	nnBnn	5697.17	208.56	6	4.28	0.29	4	-0.11	0.14	2
5058392	nnBnn	5441.94	37.29	4	4.39	0.23	2	-0.70	0.05	1
5103008	VnBnX	0	0	0
6037175	nnnnn	6711.04	24.47	8	2.45	0.31	6	-1.33	0.02	6
6063081	nnnnn	5890.45	68.45	7	4.01	0.11	6	-0.24	0.02	4
4177307	nnnnn	5334.21	93.16	3	4.13	0.09	2	-0.34	0.06	1
4245192	nnnnC	0	0	0
4363252	nnnnn	5887.08	87.68	4	4.02	0.34	2	-0.73	0.07	1
4644315	nnnnn	6177.97	71.59	9	2.26	0.37	7	-1.56	0.07	5
4667060	NnBnN	0	0	0
4750898	nNnGn	6352.65	83.42	7	2.63	0.20	4	-1.31	0.01	2
5079500	NCBnN	0	0	0
5080073	nnnnn	4842.80	198.96	4	3.84	0.13	5	-0.21	0.10	3
5108577	nnnnn	5948.72	149.43	5	3.56	0.28	2	-0.44	0.06	1
5192858	nnnnn	6166.92	229.09	4	4.10	0.78	2	-0.43	0.12	1
5272331	nnnnn	5792.95	45.49	7	3.96	0.04	6	-0.43	0.05	4
5414313	nnngn	4543.08	48.61	3	4.29	0.07	3	-1.25	0.06	1
5440884	nnnnR	0	0	0
5480935	nnnnn	4396.16	60.43	3	3.84	0.09	2	-0.41	0.08	1
5529383	nnnnn	6011.40	97.76	7	4.33	0.10	6	-0.06	0.01	3
5719827	lnnnR	0	0	0
5751409	nnnnn	5566.43	124.08	7	3.72	0.11	6	-0.33	0.00	2
6087257	nCBnN	0	0	0
4229956	lCnnR	0	0	0
4235717	nnnnn	4294.59	138.81	3	2.75	0.59	3	-0.92	0.19	1
4289559	VnBnX	0	0	0
4574875	nnBnc	0	0	0
4594522	NnBnN	0	0	0
4789415	nnnnn	6001.35	98.82	8	3.77	0.07	6	-0.45	0.06	4
5040652	NCBnN	0	0	0
5101256	nCnnR	0	0	0
5112334	nnnnn	5543.82	72.73	7	4.18	0.10	6	-0.31	0.07	5
5130445	nCnnn	5418.15	459.41	3	3.35	0.12	4	-0.17	0.07	1
5135772	nnnnn	5825.52	68.97	7	3.57	0.31	4	-0.47	0.07	4
5277776	nnBnn	5142.61	89.00	4	4.39	0.16	4	-0.86	0.06	4
5433856	nnnnn	5953.77	51.71	8	4.24	0.08	6	-0.71	0.04	4
5703343	lCnnR	0	0	0
5784059	nnnnn	5771.45	89.39	7	4.35	0.11	6	-0.55	0.04	4
5880968	nnnnn	4825.25	75.05	3	2.91	0.22	4	-0.67	0.08	3
5895182	lCnnR	0	0	0
4181371	NnnnN	0	0	0

Table 7.5 (cont'd): SSPP Stellar Parameters for Hectospec Targets

UW ID ^a	flags	T_{eff} (K)	$\sigma(T_{\text{eff}})$ (K)	$N(T_{\text{eff}})^{\text{b}}$	$\log g$ (dex)	$\sigma(\log g)$ (dex)	$N(\log g)^{\text{b}}$	[Fe/H] (dex)	$\sigma([\text{Fe}/\text{H}])$ (dex)	$N([\text{Fe}/\text{H}])^{\text{b}}$
4455265	nnnnn	5659.20	66.84	8	4.16	0.05	6	-0.31	0.05	6
4482995	Nnnnn	4533.83	55.56	3	4.20	0.03	2	-0.60	0.06	1
4581415	nnnnn	4643.42	190.28	3	3.39	0.13	4	-1.46	0.17	1
4656980	nnngn	4380.16	42.66	3	4.36	0.52	2	-1.43	0.14	1
5173769	nnnnn	5659.42	58.27	4	4.27	0.12	2	-0.57	0.04	1
5186562	nnnnn	6083.32	82.07	5	3.94	0.30	2	-0.83	0.01	1
5227403	nnnnn	4325.48	118.06	3	3.81	0.38	2	-0.66	0.06	1
5295330	lnnnR	0	0	0
5444812	nnnnn	5842.42	126.62	6	3.94	0.06	6	-0.80	0.05	4
5451526	nnBnn	6167.61	271.73	6	4.35	0.33	4	-0.96	0.20	1
5682082	NnnnR	0	0	0
6040613	NnBnN	0	0	0
6079007	nnnnn	5546.13	46.88	7	4.12	0.14	6	-0.31	0.01	5
6099618	nnnnn	6030.44	22.09	7	3.72	0.09	6	0.12	0.05	4
4584506	lCnnR	0	0	0
4637034	nnnnn	4446.88	75.68	3	4.33	0.24	4	-0.70	0.13	1
4755999	nnnnn	5665.60	377.29	3	4.53	0.18	4	-0.65	0.01	2
5016812	nnnnn	5737.28	125.03	7	4.17	0.15	4	-0.55	0.03	3
5117912	nnnnn	4849.50	133.15	3	3.80	0.25	3	-1.00	0.10	1
5155630	nnnnn	5267.52	55.62	4	4.33	0.12	5	-0.39	0.09	4
5322804	nCnn	4504.91	416.31	2	0.63	0.03	4	-3.03	0.03	1
5334379	nnnnn	5599.37	63.83	7	3.50	0.25	6	-0.72	0.01	2
5349228	nnnnn	5070.43	102.56	4	2.51	0.23	5	-0.83	0.04	4
5350871	nnnnn	4758.00	99.20	3	4.50	0.09	4	-0.39	0.08	2
5353394	nnnnn	4367.24	168.41	3	3.89	0.53	2	-0.95	0.13	1
5372054	nnngn	5661.87	165.14	3	3.76	0.43	2	-1.22	0.03	1
5594111	nnnnn	5635.85	134.84	6	3.88	0.24	6	0.30	0.11	5
5763028	nnnnn	5577.36	47.86	7	4.16	0.08	6	-0.34	0.05	5
5895011	VnBnX	0	0	0
6064938	nnnnn	6032.99	40.58	5	3.97	0.04	2	-0.49	0.05	1
4539684	nnnnn	5565.34	164.77	6	4.00	0.13	6	-0.29	0.02	4
4861383	nnnnn	5982.24	41.85	8	3.86	0.08	6	-0.84	0.04	6
4869606	nnnnn	5961.44	78.53	8	4.24	0.25	6	-0.63	0.00	3
4881593	nnnnc	0	0	0
5018210	nnnnn	4932.57	170.41	3	4.52	0.24	2	-0.61	0.05	1
5227686	nnnnn	6005.50	141.20	8	4.06	0.10	5	-0.71	0.07	4
5351923	nnngn	4843.78	101.49	3	4.78	0.11	4	-1.06	0.12	2
5362578	nnnnn	4334.85	73.48	3	3.64	0.16	3	-0.43	0.07	1
5396912	nnnnn	4948.39	120.45	3	4.64	0.18	3	-0.26	0.06	1
5565500	nnnnn	8096.69	135.99	3	4.33	0.21	2	-0.52	0.05	1
5597572	nnnnn	4447.72	68.30	3	4.10	0.05	4	-0.43	0.09	1
5678749	nnBnn	4931.98	205.65	4	4.54	0.05	5	-0.64	0.09	3
5894032	nnnnn	6319.28	34.19	9	4.01	0.04	7	-0.24	0.03	5
5979104	lnnnR	0	0	0
4195394	NnnnN	0	0	0
4231118	nnnnn	5985.24	156.94	8	3.84	0.17	6	-0.33	0.07	5
4524916	nnnnN	0	0	0
4854565	lnnnR	0	0	0
5083814	nnnnn	5309.16	51.26	5	4.20	0.09	4	-0.90	0.02	4
5107251	nnnnn	5523.45	92.83	6	3.71	0.11	6	-0.74	0.04	6
5124762	nnnnn	5870.85	72.88	8	4.25	0.01	6	-0.55	0.06	5
5177700	nnBnn	6199.23	167.75	8	4.07	0.27	5	-0.09	0.18	3
5268973	NnnnR	0	0	0
5288698	nnnnn	6015.35	195.80	5	4.07	0.40	2	-0.69	0.03	1
5645575	nnnnn	5411.91	61.30	6	3.51	0.06	6	-0.04	0.08	5
5769472	nnnnn	5015.80	136.97	4	4.36	0.18	5	-0.53	0.00	3
4251511	lCnnR	0	0	0
4260594	lCnnR	0	0	0
4288986	nnnnn	5361.31	121.25	7	3.71	0.09	6	-0.78	0.06	6
4399673	nnBnn	5457.08	63.52	3	3.88	0.19	2	-0.23	0.06	1
4419934	nnnnn	4304.55	69.13	3	3.92	0.06	2	-0.47	0.06	1
4554998	nnnnn	5507.07	42.07	7	3.47	0.05	6	-0.74	0.00	4
4641172	nnnnN	0	0	0
4670373	nnnnn	5738.59	52.29	8	4.29	0.11	6	-0.62	0.06	5
5023906	Nnnnn	4574.75	142.81	3	4.34	0.33	2	-1.49	0.12	1
5108348	nnnnn	5198.81	77.99	3	4.47	0.27	2	-0.74	0.06	1
5114213	nCbnn	0	0	0
5239492	nnnnn	5455.96	94.71	6	4.08	0.16	4	-0.58	0.07	4
5325366	nnnnn	5489.01	146.23	6	3.59	0.10	4	-0.77	0.03	3
5406280	nnnnn	5923.53	67.29	8	4.02	0.06	6	-0.75	0.03	6
5480414	nnnnn	5965.15	115.23	7	4.16	0.13	6	-0.29	0.04	5
5505541	nnnnn	4744.25	61.24	3	4.66	0.12	4	-0.96	0.10	3
5513939	nnBnn	5500.19	85.61	6	4.20	0.13	6	-0.41	0.02	3
5656154	nnnnn	4427.70	101.19	3	3.72	0.29	3	-0.19	0.07	1

Table 7.5 (cont'd): SSPP Stellar Parameters for Hectospec Targets

UW ID ^a	flags	T_{eff} (K)	$\sigma(T_{\text{eff}})$ (K)	$N(T_{\text{eff}})^{\text{b}}$	$\log g$ (dex)	$\sigma(\log g)$ (dex)	$N(\log g)^{\text{b}}$	[Fe/H] (dex)	$\sigma([\text{Fe}/\text{H}])$ (dex)	$N([\text{Fe}/\text{H}])^{\text{b}}$
5731202	nnnnn	5788.55	124.91	5	4.37	0.51	2	-0.81	0.04	1
5837419	nnnnn	5915.47	37.95	8	3.70	0.06	6	-0.43	0.03	6
4210120	nnnnn	5264.91	129.36	7	3.50	0.22	6	-0.71	0.05	4
4258483	nnnnn	5675.45	119.11	8	4.07	0.21	6	-0.67	0.04	4
4722860	lnnnn	4270.17	48.05	3	4.03	0.22	3	-0.45	0.10	1
4790644	lnnnN	0	0	0
5233551	nCnnn	4395.32	238.47	1	3.74	0.33	2	-0.79	0.24	1
5288622	lCnnR	0	0	0
5443829	nnnnn	4609.98	98.10	3	4.28	0.10	2	-0.67	0.04	1
5658959	lCnnR	0	0	0
5675965	nnnGn	5621.08	122.56	4	2.52	0.52	2	-1.54	0.13	1
5749937	NCnnN	0	0	0
6068191	nnnnn	4896.70	15.82	3	2.96	0.11	4	-0.76	0.06	1
4165330	NnnnN	0	0	0
4290549	nnnnnc	0	0	0
4310849	nnnnn	5503.96	71.58	6	4.16	0.08	6	-0.24	0.04	4
4433155	nnnnn	4684.75	25.08	3	4.35	0.31	3	-1.54	0.10	1
4440798	nnnnn	4862.74	148.60	3	3.47	0.09	4	-0.14	0.15	1
4460395	nnBnn	5035.13	14.76	3	4.34	0.23	2	-0.48	0.10	1
4501756	lCnnR	0	0	0
5022437	nnngn	4051.07	20.30	1	4.22	0.07	1	-1.60	0.07	1
5102495	nnnnn	5470.58	183.58	7	3.86	0.23	6	-0.33	0.02	2
5158972	nnnnn	5831.60	35.75	8	4.17	0.17	6	-0.79	0.05	4
5213252	nnnnn	4270.04	124.57	3	4.18	0.39	2	-1.02	0.15	1
5278896	nnnnn	5799.01	108.34	7	4.48	0.15	4	-0.67	0.05	5
5398059	nCnnR	0	0	0
5401396	nnnnn	5525.37	81.91	7	3.55	0.06	6	-0.06	0.05	3
5592200	nnnnn	5820.22	139.19	7	3.96	0.10	4	-0.41	0.05	3
5774268	nnnnn	5668.42	59.09	7	4.16	0.04	6	-0.30	0.05	6
5939394	nnnnn	6000.03	149.00	5	3.31	0.39	3	-0.51	0.12	2
6043863	nnnnn	5456.01	119.30	6	3.88	0.13	6	-0.29	0.05	3
4244564	VnnnX	0	0	0
4340755	nnnnN	0	0	0
4529755	NnnnN	0	0	0
4597174	lCnnR	0	0	0
4763954	NnnnN	0	0	0
5016285	nnnnn	5776.45	212.03	5	3.99	0.39	4	-0.97	0.04	3
5173344	nnnnn	6145.43	39.23	8	4.03	0.02	6	-0.19	0.04	6
5315527	lCnnR	0	0	0
5324238	nnnnc	0	0	0
5338611	nnBnn	5229.35	55.48	6	3.80	0.06	6	-0.39	0.06	4
5360297	nnnnn	5212.54	128.59	3	3.76	0.08	4	-0.52	0.10	3
5454565	nnnnn	5476.68	138.51	7	4.06	0.13	6	-0.62	0.09	6
5495975	nnnnn	5909.13	72.77	4	3.72	0.43	2	-0.44	0.05	1
5605091	VnnnX	0	0	0
5605515	nnBnn	5125.19	137.63	7	3.72	0.06	6	-0.77	0.10	4
5967217	nnnnn	5813.05	65.05	7	4.21	0.04	6	-0.11	0.06	6
6015524	lCnnR	0	0	0
6021358	nnnnn	5063.77	143.50	4	2.51	0.21	5	-0.65	0.07	3
4175052	nnnnn	4725.85	121.89	3	4.51	0.17	4	-0.50	0.17	2
4253264	nnBnN	0	0	0
4618030	nnnnn	5094.61	53.17	4	4.00	0.08	5	-0.24	0.10	3
4798626	nnnnn	5761.29	114.46	6	4.36	0.28	4	-0.92	0.02	4
4811830	nnnnn	5780.81	185.82	5	3.83	0.50	2	-0.92	0.08	1
5213709	nnnnn	5687.63	85.04	6	3.66	0.09	6	-0.17	0.05	3
5339190	nnnnn	5042.08	105.10	4	4.52	0.06	5	-0.45	0.00	5
5383723	nnnnn	5529.98	319.44	3	4.26	0.39	2	0.21	0.08	1
5488424	nCnnR	0	0	0
5496986	nnnnn	6129.84	35.56	8	3.73	0.02	6	-0.03	0.04	6
5639897	nnnnn	5072.17	8.80	3	4.15	0.03	2	-0.79	0.06	1
5886870	nnngn	6172.84	119.11	8	4.08	0.23	6	-1.12	0.06	4
5888607	NnnnN	0	0	0
5904672	nnnnn	4295.01	152.25	2	3.56	0.12	1	-0.63	0.07	1
5932633	nnnnn	5775.85	76.41	7	3.88	0.07	6	-0.08	0.05	6
6086465	nnnnn	7866.09	102.04	4	3.46	0.36	3	-0.93	0.08	1
4404434	NnBnn	5143.92	177.74	3	3.78	0.34	2	-0.80	0.07	1
4572721	nnnnn	5935.56	63.90	7	3.62	0.11	6	-0.57	0.07	4
4635945	nnnnn	5917.20	186.73	5	3.52	0.39	2	-0.57	0.06	1
4674911	nnnnn	4734.58	193.66	3	4.71	0.05	4	-0.46	0.01	2
4757726	nnnnn	5954.29	86.74	7	4.44	0.10	6	-0.34	0.03	4
5018527	nnngn	4400.58	76.43	3	4.03	0.26	4	-1.43	0.10	1
5087883	nnnnn	6651.91	220.83	8	4.35	0.17	6	0.46	0.03	3
5116641	lnnnR	0	0	0
5266196	nnnnn	7288.93	51.25	8	4.15	0.34	6	-1.62	0.02	4

Table 7.5 (cont'd): SSPP Stellar Parameters for Hectospec Targets

UW ID ^a	flags	T_{eff} (K)	$\sigma(T_{\text{eff}})$ (K)	$N(T_{\text{eff}})^{\text{b}}$	$\log g$ (dex)	$\sigma(\log g)$ (dex)	$N(\log g)^{\text{b}}$	[Fe/H] (dex)	$\sigma([\text{Fe}/\text{H}])$ (dex)	$N([\text{Fe}/\text{H}])^{\text{b}}$
5292262	nnBnn	6097.82	315.05	4	4.11	0.77	2	-0.13	0.09	1
5351153	nnnnn	5176.31	187.85	4	4.66	0.25	5	-0.91	0.12	3
5707844	nnBnn	5035.63	45.80	3	4.43	0.16	4	-0.66	0.07	3
5925234	nnnnn	5928.81	40.77	8	3.79	0.05	6	-0.66	0.05	6
6066347	ICnnR	0	0	0
4326553	nnnc	0	0	0
4515171	nnngn	4350.70	74.36	3	4.58	0.21	4	-1.56	0.07	3
4680534	nnnnR	0	0	0
4705683	nnnnn	5923.91	60.48	8	3.70	0.16	6	-0.72	0.02	5
4787871	nnnnn	5492.24	56.12	6	4.48	0.11	6	-0.60	0.03	7
4839654	nnnnn	4520.60	102.99	3	4.10	0.24	3	-1.24	0.16	1
5044743	NCBnN	0	0	0
5059743	NnBnn	6053.55	92.85	4	3.97	0.73	2	-0.43	0.06	1
5106853	nnnnn	5478.89	106.33	6	4.25	0.13	6	-0.19	0.06	4
5273102	nnnnn	5769.55	91.45	6	4.44	0.19	4	-0.67	0.05	4
5362144	nnnnn	4603.18	155.11	3	4.17	0.25	3	-0.70	0.06	1
5437119	nCnn	4618.86	150.17	3	4.30	0.17	3	-0.04	0.07	1
5458243	DnBnn	5680.95	185.26	3	3.70	0.08	2	-0.43	0.07	1
5470506	nnBnn	6227.31	306.64	7	4.31	0.27	5	-0.30	0.41	1
5636822	nnBnn	5354.46	56.60	3	3.96	0.10	2	-0.49	0.08	1
5819292	nCnn	5801.33	69.32	7	4.25	0.11	6	-0.75	0.01	3
5838101	nnngn	5438.04	112.36	7	2.25	0.30	6	-1.89	0.04	4
5991159	nnnnn	4920.94	105.80	3	3.52	0.10	4	-0.27	0.04	2
6096597	nnnnn	5850.23	39.08	8	4.02	0.10	6	-0.62	0.04	6
7912513	nnnnn	5979.41	89.96	8	3.96	0.12	6	-0.51	0.00	4
4186418	nCnn	4352.22	104.51	2	3.87	0.22	2	-0.71	0.09	1
4231309	nnnnn	4566.72	58.96	3	4.52	0.20	3	-0.87	0.06	1
4349916	nnnnn	4872.43	44.73	3	4.40	0.27	3	-0.56	0.23	2
4383049	nCnnR	0	0	0
4417334	nnnnn	7286.43	98.63	3	4.17	0.71	2	-1.39	0.07	1
4604360	nnnnR	0	0	0
5159058	nnnnn	5978.52	157.98	5	3.55	0.04	2	-0.58	0.06	1
5221525	nnnnn	5314.31	38.81	6	3.63	0.18	6	-0.66	0.07	5
5302279	Nnnnn	4298.91	75.36	3	3.53	0.23	2	-0.93	0.08	1
5342465	nnnnn	5688.64	69.79	7	4.15	0.12	6	-0.26	0.03	5
5554833	VnnnX	0	0	0
5636985	VnBnX	0	0	0
5876619	nnnnn	4814.63	123.94	3	3.46	0.14	4	0.11	0.10	2
5899301	nnnnn	5767.16	74.92	7	3.84	0.16	6	-0.58	0.07	6
5940195	nnnnn	5842.49	86.57	7	4.01	0.18	6	-0.49	0.10	3
4169193	nnBnn	4974.50	22.89	3	4.02	0.03	2	-0.33	0.07	1
4235081	nnnnn	5022.82	197.25	3	4.45	0.23	3	-0.60	0.16	3
4286650	nnBnn	5462.53	49.73	6	4.15	0.18	6	-0.50	0.06	6
4314741	nnBnn	6162.01	270.18	7	3.66	0.11	6	-0.61	0.07	5
4367822	nnnnn	5837.60	75.02	8	4.03	0.09	6	-0.35	0.02	6
4731375	nnnnR	0	0	0
4817517	NCnN	0	0	0
5084213	nnnnn	4860.52	105.17	3	4.18	0.02	3	-0.37	0.06	1
5090106	nnnnn	5321.31	75.89	6	3.68	0.07	6	-0.35	0.05	7
5230589	nnnnn	6400.86	125.45	8	2.79	0.44	5	-1.49	0.04	1
5297186	nnBgn	5040.37	129.72	3	4.14	0.57	2	-1.16	0.04	1
5300863	nnnnn	5471.34	28.67	5	4.20	0.36	4	-0.63	0.04	3
5328210	nnnnn	6118.53	70.06	8	3.78	0.10	6	-1.65	0.02	6
5360415	Nnnnn	4453.69	137.41	3	4.08	0.09	2	-0.39	0.06	1
5383420	nnnnn	5187.90	137.98	4	3.95	0.21	5	-0.73	0.14	3
5394533	nnnnn	5480.29	109.70	7	3.63	0.23	6	-0.83	0.05	5
5840644	nnnnn	5826.85	168.52	7	3.94	0.17	6	-0.25	0.08	6
5847606	NnnnN	0	0	0
5964012	nnnnn	5028.53	94.13	4	3.47	0.10	5	-0.67	0.05	3
6009921	nnnnn	5872.36	38.80	8	3.90	0.08	6	-0.31	0.04	6
6030468	nnnnn	5828.91	75.95	8	4.10	0.03	6	-0.56	0.03	6
4302730	ICnnR	0	0	0
4330222	nnnnN	0	0	0
4367640	nnnnn	5357.64	36.14	6	3.96	0.24	6	0.06	0.06	3
4678834	nnnnn	6278.05	52.59	9	3.72	0.04	7	-0.34	0.06	6
5059607	nnnnn	5996.04	31.00	4	4.08	0.45	2	-0.79	0.07	1
5096882	nnnnn	4981.13	72.81	3	4.45	0.43	2	-1.42	0.11	1
5104870	nnnnn	5819.29	90.65	8	4.11	0.19	6	-0.95	0.04	4
5259883	nnngn	5603.30	67.19	4	2.63	0.47	2	-1.78	0.08	1
5305382	nnBgn	5638.72	142.84	3	3.68	0.82	2	-1.04	0.05	1
5363632	nnnnn	5552.98	54.53	6	3.76	0.07	6	-0.40	0.05	6
5389680	nnnnR	0	0	0
5524848	nnnnn	5453.00	78.39	6	4.08	0.16	6	-0.31	0.06	3
5553721	nnnnn	4607.20	60.38	3	4.08	0.01	4	-0.43	0.14	1

Table 7.5 (cont'd): SSPP Stellar Parameters for Hectospec Targets

UW ID ^a	flags	T_{eff} (K)	$\sigma(T_{\text{eff}})$ (K)	$N(T_{\text{eff}})^{\text{b}}$	$\log g$ (dex)	$\sigma(\log g)$ (dex)	$N(\log g)^{\text{b}}$	[Fe/H] (dex)	$\sigma([\text{Fe}/\text{H}])$ (dex)	$N([\text{Fe}/\text{H}])^{\text{b}}$
5613983	nnnnn	5753.57	40.15	8	4.21	0.17	6	-0.84	0.05	7
5624216	nnBnn	5449.35	42.48	6	4.32	0.12	6	-0.17	0.08	5
5822086	VnnnN	0	0	0
6029852	nnnnn	6195.12	121.94	5	3.99	0.39	2	-0.86	0.07	1
4255341	nnnnn	5293.43	79.19	5	4.24	0.37	4	-0.98	0.14	1
4669135	nnnnn	5601.86	116.94	6	3.79	0.37	5	0.38	0.07	3
4681463	NnnnN	0	0	0
5180862	nnnnn	4949.46	116.96	3	4.29	0.11	3	-0.00	0.09	1
5233960	nnnnn	4334.88	293.65	3	3.90	0.49	2	-1.67	0.11	1
5276286	lCnnR	0	0	0
5495014	nngn	5235.08	101.71	6	1.97	0.18	6	-1.93	0.04	4
4230295	nnnnn	5341.92	24.21	4	3.78	0.19	5	-0.17	0.08	4
4453373	nnnnn	4972.87	220.97	3	4.45	0.11	4	-0.13	0.08	2
5065161	nnBnn	4809.23	82.78	3	4.63	0.13	3	-0.93	0.06	1
5320175	nnnnX	0	0	0
5515281	nnnnn	5711.60	59.68	6	3.57	0.06	6	-0.01	0.06	4
5612944	nnnnn	5274.30	120.21	4	4.07	0.07	2	-0.50	0.06	1
6092902	nnngn	5656.52	155.67	5	3.21	0.13	4	-1.07	0.26	2
4189939	nnBnn	6731.79	118.10	8	2.78	0.18	6	-1.24	0.04	4
4299785	nnngn	5993.86	58.50	5	3.88	0.31	2	-1.11	0.06	1
4341234	NCnnN	0	0	0
4608947	nnnnn	5096.08	58.37	6	4.48	0.08	5	-0.32	0.04	4
4655439	NnnnN	0	0	0
4683149	nnBnn	5197.71	69.98	3	4.46	0.08	4	-0.43	0.00	2
4762117	nnnnn	4734.82	129.69	3	4.58	0.20	4	-0.90	0.15	1
4877302	nnnnn	4627.28	96.88	3	3.06	0.25	4	-0.98	0.15	2
5079979	nnBnn	4670.96	69.46	3	4.00	0.00	2	-0.39	0.08	1
5174630	nnBnn	5275.77	15.24	6	4.32	0.16	6	-0.69	0.03	5
5221424	nnnnn	5409.62	163.63	4	4.04	0.27	4	-0.41	0.08	1
5285698	nnnnn	5582.30	87.08	6	4.04	0.31	4	-0.72	0.10	4
5294331	nnnnn	5049.05	93.56	3	4.59	0.09	4	-0.67	0.12	3
5317331	NnnnN	0	0	0
5325286	nnnnn	5750.09	117.19	4	4.08	0.43	2	-0.43	0.05	1
5336694	lnnnR	0	0	0
5582781	nnnnn	5273.96	160.65	4	4.10	0.11	5	0.04	0.06	2
5674917	nnBnn	4912.57	146.15	3	4.61	0.11	4	-0.32	0.11	3
5729944	nnBnn	5346.28	155.79	3	3.68	0.73	2	-0.91	0.07	1
6008592	nnnnn	6321.56	42.88	8	3.97	0.10	6	-0.25	0.06	5
6041707	Nnnnn	5459.65	249.40	3	4.04	0.14	2	-0.28	0.07	1
4167434	nnnnn	7650.10	100.81	4	4.50	0.21	3	-2.75	0.12	1
4226781	VnnnX	0	0	0
4299295	VnnnX	0	0	0
4492766	lCnnR	0	0	0
4517660	nnnnn	6208.89	99.00	9	3.27	0.17	7	-0.91	0.05	2
4541224	NnnnN	0	0	0
4779400	nnnnn	5246.45	143.86	6	3.57	0.17	6	-0.32	0.08	4
5069700	nnnnn	4819.47	81.70	3	4.38	0.13	4	-0.52	0.00	2
5160450	nnbn	0	0	0
5178189	nnnnn	4122.05	35.45	2	3.66	0.64	2	-0.46	0.07	1
5198959	nnBGn	5033.76	39.68	3	3.20	0.01	2	-1.34	0.23	1
5283999	nnnnn	5036.39	111.84	3	4.46	0.24	3	-0.61	0.06	2
5866035	nnnnn	5202.46	124.87	3	4.36	0.40	2	-0.63	0.09	1
5993606	VCnnR	0	0	0
6027779	nnnnn	5765.34	93.49	7	3.74	0.11	6	-0.29	0.05	7
4170061	nnnnR	0	0	0
4376544	nnnnn	5975.11	57.86	8	3.94	0.10	6	-0.20	0.03	7
4484407	nnnnn	4957.55	117.37	3	3.91	0.17	2	0.28	0.08	1
4715343	nnnnn	6476.30	43.66	8	3.73	0.03	6	-0.76	0.04	5
5056751	Dnnnn	6981.09	113.95	5	4.88	0.44	3	-2.07	0.30	1
5158128	nnnGn	6170.70	161.91	7	3.95	0.36	4	-1.30	0.18	2
5257104	nnBnn	5086.37	96.52	4	4.38	0.16	4	-0.77	0.26	3
5283233	nnnnn	5845.91	108.01	8	3.98	0.27	6	-0.56	0.06	6
5368650	nnnnn	5706.98	85.44	7	3.81	0.12	6	-0.37	0.00	5
5472877	nnngn	4471.03	16.27	3	4.19	0.05	3	-1.07	0.07	1
5500316	lCnnR	0	0	0
5557502	nnnnn	6295.66	57.64	6	4.19	0.51	3	-1.52	0.06	1
5592726	nnnnn	5923.05	51.64	8	3.86	0.06	6	-0.13	0.03	6
6002792	nnnnn	5631.43	92.06	7	4.28	0.11	6	-0.27	0.03	5
4420854	nnnnn	5696.42	66.07	7	3.86	0.23	6	-0.28	0.03	6
4502372	nnnnn	5041.00	77.45	3	3.99	0.06	4	-0.04	0.15	3
4572320	lnnnR	0	0	0
4586274	lnnnN	0	0	0
4769146	nnnnn	4836.28	75.08	4	2.92	0.13	5	-0.25	0.05	3
4865778	NnnGn	4343.82	34.76	3	4.13	0.14	2	-1.02	0.07	1

Table 7.5 (cont'd): SSPP Stellar Parameters for Hectospec Targets

UW ID ^a	flags	T_{eff} (K)	$\sigma(T_{\text{eff}})$ (K)	$N(T_{\text{eff}})^{\text{b}}$	$\log g$ (dex)	$\sigma(\log g)$ (dex)	$N(\log g)^{\text{b}}$	[Fe/H] (dex)	$\sigma([\text{Fe}/\text{H}])$ (dex)	$N([\text{Fe}/\text{H}])^{\text{b}}$
5081098	nnnnn	4952.01	31.89	3	4.13	0.05	2	-0.70	0.06	1
5304478	nnnnn	5765.34	48.69	7	3.90	0.14	6	-0.82	0.02	7
5338276	nnnnn	5305.85	109.75	6	4.03	0.05	6	-0.64	0.07	6
5364395	nnnnn	5902.85	264.96	4	3.89	0.12	5	-0.27	0.02	3
5378990	nnnnn	5879.17	64.66	7	4.19	0.12	6	-0.61	0.03	6
5379235	nnnnn	5811.75	130.07	4	4.34	0.31	2	-0.57	0.03	1
5640876	NCnnN	0	0	0
5716099	nnnnR	0	0	0
5926817	nnnnn	5992.15	90.51	7	3.35	0.14	4	-0.59	0.06	5
5928866	nnnnn	5630.15	105.52	6	3.76	0.07	6	-0.15	0.06	5
6005046	nnnnn	4246.91	20.55	3	4.39	0.17	3	-1.24	0.11	1
4241538	nnnnn	4698.67	95.88	3	3.54	0.12	4	-0.12	0.20	1
4252560	nnnnn	5325.29	136.96	4	4.43	0.22	4	-0.50	0.07	1
4532138	lnnnR	0	0	0
4617363	NnnN	0	0	0
4744078	nnnnn	5939.54	58.79	7	3.74	0.17	6	-0.40	0.05	5
4852167	nnnnn	4933.61	119.29	3	4.40	0.07	4	-0.33	0.04	2
5158200	nnnnn	5210.96	121.79	3	4.47	0.11	2	-0.42	0.08	1
5247655	nnnnn	5542.75	49.77	7	4.06	0.03	6	-0.01	0.07	4
5375357	nnnnn	5911.96	57.24	8	3.93	0.13	6	-0.94	0.03	6
5421365	nnnnn	5014.46	77.03	3	3.41	0.16	4	-0.55	0.10	3
5450956	nnBnn	5876.02	37.41	8	4.42	0.18	6	-0.21	0.02	5
5464619	lnnnR	0	0	0
5618708	nnnnn	4371.51	74.30	3	4.02	0.11	3	-0.60	0.07	1
5707301	nnnnn	5404.56	29.62	6	4.30	0.10	6	-0.62	0.03	5
5932887	nnnnn	5509.60	27.29	6	4.04	0.03	6	0.11	0.03	4
5986757	Nnnnn	4671.27	165.60	3	4.39	0.16	2	-1.13	0.12	1
6017457	nnnnn	6075.96	51.05	8	3.97	0.10	6	-1.02	0.03	5
4241899	nnnnn	5970.40	59.20	8	4.20	0.14	6	-0.65	0.03	5
4284762	nnnnn	5858.31	92.46	7	4.00	0.19	4	-0.36	0.06	2
4290669	nnngn	4560.60	51.33	3	4.50	0.13	4	-1.10	0.06	2
4373327	nnnnn	6083.35	102.21	6	3.26	0.80	3	-0.73	0.25	1
4392207	lnnnn	4561.65	118.62	3	4.56	0.19	4	-0.39	0.05	1
4429799	nnnnn	5956.81	132.43	7	4.10	0.22	6	-0.23	0.07	5
4501821	lnnnn	4341.47	26.34	3	3.87	0.16	4	-0.53	0.02	2
4694985	nnnnn	5653.72	101.24	7	3.87	0.17	6	-0.17	0.03	5
5031056	nnnnn	5467.90	79.26	6	3.70	0.05	6	-0.30	0.00	5
5099036	nnnnn	6090.96	68.59	5	4.16	0.63	2	-1.57	0.06	1
5161985	nnngn	5511.12	121.03	4	4.17	0.70	2	-1.19	0.08	1
5168288	nnnnn	6276.64	60.44	8	3.91	0.15	6	-1.58	0.04	5
5257379	VnBnN	0	0	0
5260273	nnnnn	5437.01	24.29	3	4.04	0.12	2	-0.71	0.07	1
5360335	NnnnN	0	0	0
5459941	nnnnn	5490.62	62.21	6	3.56	0.09	6	-0.28	0.05	5
5611410	NnnnR	0	0	0
5635694	nnnnn	5986.11	99.46	5	3.68	0.25	2	-0.40	0.08	1
5718934	VCnnN	0	0	0
5784285	nnnnn	4579.27	80.16	3	4.37	0.14	4	-0.60	0.05	1
5941141	VnnnX	0	0	0
4229311	nnnnn	4547.38	50.90	3	4.33	0.14	4	-0.64	0.07	1
4259392	nnnnn	5402.22	125.21	4	4.10	0.48	2	-0.50	0.05	1
4294263	NCnnN	0	0	0
4367351	nnngn	4226.81	208.12	2	3.37	0.10	1	-1.04	0.07	1
4471803	NnnnN	0	0	0
4554125	ICnnR	0	0	0
4745467	NCBnN	0	0	0
4806378	nnnnn	4604.45	113.23	3	4.71	0.03	4	-0.39	0.03	3
5015943	nnBnn	5515.29	31.24	4	4.03	0.63	2	-1.00	0.11	1
5025244	nnnnn	5804.24	69.29	7	3.95	0.09	6	-0.41	0.02	6
5072500	nnnnn	5593.59	70.97	7	3.72	0.12	6	-0.60	0.03	5
5244458	nnnnn	5344.07	80.80	3	4.23	0.47	2	-0.60	0.08	1
5426020	nnBnn	5518.22	93.58	3	4.30	0.16	4	-0.55	0.12	3
5439056	nnnnn	5333.05	113.64	4	4.00	0.48	3	-0.67	0.06	1
5472914	nnnnn	5990.67	55.81	5	4.00	0.01	2	-0.44	0.07	1
5651514	nnBnn	5476.50	125.42	4	4.24	0.29	4	-0.18	0.08	2
5665249	nnBnn	5110.72	4.19	4	2.05	0.15	5	-0.64	0.07	3
5808429	NnBnN	0	0	0
5841807	nnnnn	5745.47	24.65	7	3.92	0.04	6	-0.26	0.04	4
5935003	nnnnn	5763.11	41.38	7	4.09	0.07	6	-0.26	0.04	5
4212577	nnnnn	5356.44	87.52	3	3.64	0.11	2	-0.93	0.07	1
4287651	nnngn	4996.15	38.90	4	1.97	0.57	5	-1.26	0.07	3
4349117	NnnnN	0	0	0
4381250	nnBnn	5649.83	40.41	6	3.77	0.09	4	-0.38	0.01	2
4584052	nnnnn	6190.44	51.24	9	1.95	0.32	7	-1.69	0.07	6

Table 7.5 (cont'd): SSPP Stellar Parameters for Hectospec Targets

UW ID ^a	flags	T_{eff} (K)	$\sigma(T_{\text{eff}})$ (K)	$N(T_{\text{eff}})^{\text{b}}$	$\log g$ (dex)	$\sigma(\log g)$ (dex)	$N(\log g)^{\text{b}}$	[Fe/H] (dex)	$\sigma([\text{Fe}/\text{H}])$ (dex)	$N([\text{Fe}/\text{H}])^{\text{b}}$
4649735	nnnnn	0	0	0
4757082	NnBnN	0	0	0
4768112	nnnnN	0	0	0
4866935	nnnnn	5683.16	101.63	7	4.01	0.25	4	-0.45	0.06	3
5039902	nnnnn	5285.30	53.77	6	4.43	0.11	6	-0.78	0.00	5
5041351	nnnnn	4492.77	84.29	3	4.01	0.00	2	-0.90	0.10	1
5051023	nnnnn	4684.79	64.20	3	4.23	0.29	2	-0.94	0.13	1
5139391	nnnnn	6029.84	219.84	4	4.38	0.49	2	-0.26	0.06	1
5321708	nCnnR	0	0	0
5393525	nnnnn	5130.68	78.11	3	4.41	0.14	2	-0.56	0.08	1
5436500	NnnnN	0	0	0
5527732	nnnnn	5614.84	26.39	6	3.90	0.04	6	-0.23	0.05	6
5787545	lnnnR	0	0	0
5958635	nnGn	5060.08	264.39	3	4.37	0.51	2	-1.54	0.10	1
6037444	nnnnn	4357.46	93.08	3	3.72	0.06	4	-0.77	0.01	2
4785747	nnnnn	4283.25	39.80	3	3.74	0.37	4	-0.39	0.08	1
5084441	nnnnn	4989.16	139.25	3	4.52	0.12	4	-0.18	0.17	2
5133485	nCnc	0	0	0
5272292	nnBnn	5220.72	101.56	5	4.61	0.05	4	-0.82	0.02	4
5364316	Nnnn	4416.32	157.10	3	3.74	0.04	2	-0.31	0.07	1
5803211	nnBnn	5206.37	96.13	4	4.23	0.21	2	-0.68	0.06	1
5946709	nnngn	4723.24	79.84	3	4.45	0.10	4	-1.03	0.02	2
4198096	nnnnn	5029.63	96.35	3	4.28	0.04	4	-0.33	0.06	2
4598642	nnnnn	5308.58	105.53	7	3.70	0.05	6	-0.16	0.07	5
4623241	nnnnn	5708.21	14.86	7	3.81	0.10	6	-0.37	0.08	5
5444299	VnnnX	0	0	0
5449653	nnnnn	4794.95	157.59	3	4.54	0.33	2	-0.90	0.08	1
5992818	ICnnR	0	0	0
4457649	NnnnN	0	0	0
4528820	nCnnR	0	0	0
4664303	nnnnn	5668.30	138.60	6	3.92	0.19	4	-0.14	0.04	5
4869177	nnnnn	7388.61	88.04	7	2.99	0.31	5	-1.44	0.07	5
5092294	nnnnn	4645.84	76.35	3	4.46	0.21	2	-0.79	0.06	1
5093929	nnBnn	5907.35	297.32	8	2.50	0.45	6	-2.72	0.09	1
5283983	nnnnn	5553.95	131.94	4	4.11	0.03	2	-0.56	0.04	1
5999842	nnnnn	5144.73	128.72	4	4.47	0.09	5	0.03	0.11	1
6041809	NnnnR	0	0	0
4864088	nnnnn	4295.58	59.52	3	3.84	0.21	4	-0.40	0.20	1
4866861	NCBnX	0	0	0
5033774	nnnnn	5721.86	65.29	8	4.20	0.09	6	-0.21	0.01	4
5180633	nnnnn	5492.36	60.01	6	4.19	0.05	6	-0.44	0.06	6
5333632	nnBnn	4725.23	101.36	3	4.21	0.14	2	-1.03	0.10	1
5973188	nnBnn	5345.11	86.09	3	4.27	0.36	2	-0.69	0.06	1
4358342	nCnnN	0	0	0
4374708	nnnnn	5792.07	233.20	3	3.33	0.06	2	-0.50	0.05	1
4431507	nnnnn	5610.04	29.31	6	3.81	0.08	4	-0.25	0.04	4
4601580	ICnnR	0	0	0
4637589	nnnnn	5249.66	105.90	4	3.88	0.16	5	0.22	0.02	3
4655292	nnnnn	5367.87	61.43	6	4.51	0.19	6	-0.79	0.08	2
4668255	nnnnn	5697.71	142.03	7	3.93	0.19	5	-0.02	0.02	3
4700089	nnnnn	4273.88	30.64	3	3.78	0.15	2	-0.43	0.05	1
4827299	LnnnR	0	0	0
5048764	nnnnn	4412.82	59.79	3	4.12	0.12	2	-0.83	0.06	1
5097328	nnnnR	0	0	0
5145871	nnnnn	5270.86	70.39	4	4.40	0.07	5	-0.31	0.10	4
5169192	LnnnR	0	0	0
5353492	nnnnn	4528.91	109.61	3	4.23	0.19	2	-0.24	0.06	1
5402674	nnnnn	4497.99	18.26	3	4.56	0.18	4	-0.83	0.03	1
5417613	lCnnR	0	0	0
5749369	nnnnn	5766.72	92.16	7	4.01	0.12	6	-0.07	0.05	4
5768860	nnnnn	4842.81	91.18	3	4.41	0.01	4	-0.67	0.02	2
5978416	NnnnN	0	0	0
6078284	nnnnn	4857.42	140.29	3	4.46	0.08	4	-0.07	0.00	2
6101278	NnnnN	0	0	0
4211588	NnnnN	0	0	0
4294719	nnnnN	0	0	0
4570573	nnnnn	4627.13	78.49	3	4.34	0.15	4	-0.57	0.01	2
4727368	nnnnn	5404.87	317.18	4	3.74	0.11	5	-0.89	0.10	4
4807809	NnnnN	0	0	0
4819512	nnnnn	6461.80	28.81	8	4.05	0.05	6	-0.09	0.04	6
4820692	nnnnn	4566.89	87.66	3	4.29	0.36	2	-0.87	0.14	1
5067569	nnnnc	0	0	0
5073280	nnnnn	7432.48	135.14	7	4.08	0.29	4	-0.81	0.09	3
5108383	Lnnn	4102.87	20.31	1	4.88	0.02	1	-0.97	0.07	1

Table 7.5 (cont'd): SSPP Stellar Parameters for Hectospec Targets

UW ID ^a	flags	T_{eff} (K)	$\sigma(T_{\text{eff}})$ (K)	$N(T_{\text{eff}})^{\text{b}}$	$\log g$ (dex)	$\sigma(\log g)$ (dex)	$N(\log g)^{\text{b}}$	[Fe/H] (dex)	$\sigma([\text{Fe}/\text{H}])$ (dex)	$N([\text{Fe}/\text{H}])^{\text{b}}$
5179425	nnnnn	5753.54	101.74	8	4.16	0.10	6	-0.31	0.03	5
5330316	nnBnn	5778.31	227.93	4	4.02	0.36	2	-0.92	0.03	1
5415593	nnnnn	5130.98	82.43	3	4.34	0.15	2	-0.28	0.09	1
5455007	nnnnn	5885.44	59.44	8	4.10	0.10	6	-0.71	0.04	7
5823173	nnnnn	5753.91	55.01	6	4.02	0.07	6	-0.10	0.03	4
5904964	Nnnnn	4519.70	44.90	3	3.87	0.36	2	-0.76	0.06	1
5979843	nnnnn	4699.35	72.34	3	4.40	0.08	3	-0.76	0.06	1
4412307	nCBnN	0	0	0
4425844	nnnnn	5774.30	99.31	7	4.21	0.24	6	-0.51	0.14	6
4465765	nnnnn	5701.16	122.49	6	4.30	0.13	4	-0.62	0.04	2
4547053	nnnnn	5321.45	102.58	6	3.57	0.18	6	-0.79	0.02	6
4588147	nnnnn	5723.94	172.09	7	4.36	0.24	5	-0.62	0.10	3
4595248	lnnnR	0	0	0
4613269	nnnnn	5636.88	64.78	6	3.86	0.08	6	-0.15	0.04	3
4849757	NnnNN	0	0	0
4857249	nnBnn	5072.16	238.81	4	4.56	0.23	4	-0.64	0.07	1
5020900	nnnnn	6056.20	68.20	8	4.04	0.07	6	-0.67	0.04	5
5031379	nnngn	5089.53	175.21	3	4.25	0.45	2	-1.31	0.10	1
5124676	nnnnn	5368.90	137.29	3	4.11	0.76	2	-0.61	0.10	1
5129342	nnngn	4758.73	98.39	3	4.18	0.21	4	-1.02	0.18	3
5201747	nnnnn	5169.37	146.83	3	3.42	0.05	2	-0.56	0.07	1
5233295	nnnnn	4188.43	146.84	2	4.44	0.06	1	-1.52	0.07	1
5349129	nnnnn	4287.61	63.02	3	4.21	0.14	3	-1.35	0.11	1
5363043	nnnnn	5661.76	46.16	6	3.99	0.07	4	-0.78	0.06	6
5410944	nnBnn	4526.25	84.05	3	3.90	0.21	2	-1.02	0.05	1
5631760	nnnnn	5624.90	52.19	7	4.23	0.10	6	-0.61	0.01	5
5837478	NnnGn	4236.25	80.79	2	3.88	0.21	2	-1.53	0.16	1
5946744	nnngn	5955.60	64.03	8	3.53	0.21	6	-1.16	0.05	7
6058998	nnngn	4996.24	158.53	4	4.21	0.13	4	-1.00	0.04	5
4256051	nnnnn	5778.05	41.96	7	3.82	0.08	6	-0.20	0.06	5
4325306	nCngn	4357.58	69.88	3	3.63	0.25	4	-1.27	0.25	1
4339073	nnnnn	4768.02	149.49	3	4.03	0.15	3	-0.68	0.02	2
4345679	nCnnR	0	0	0
4561691	nnnnn	5346.85	22.79	6	3.75	0.11	6	-0.16	0.06	4
4582398	nnnnn	5331.57	56.91	4	4.06	0.05	5	-0.13	0.09	3
4798413	nnnnn	6104.96	124.19	5	3.67	0.05	2	-0.53	0.04	1
5147345	nnnnn	5606.07	38.40	6	3.78	0.08	6	0.10	0.07	6
5208282	VnnnX	0	0	0
5248122	nnnnn	4651.41	186.74	3	3.48	0.14	2	-0.93	0.12	1
5301449	nnnGn	6124.69	152.16	4	3.16	0.15	2	-2.30	0.06	1
5341888	nnBnn	4860.59	121.39	3	4.44	0.26	3	-0.74	0.07	1
5631180	nnnnn	7330.82	43.11	7	4.69	0.16	6	-0.34	0.07	3
5846935	Nnnnn	5091.93	152.97	3	4.54	0.34	2	-0.55	0.07	1
5924096	nnnnn	4873.65	132.21	3	3.24	0.16	4	0.07	0.09	2
6021575	nnnnn	5157.83	129.71	6	4.47	0.13	6	-0.81	0.09	6
6025798	nnnnn	4524.89	101.75	3	3.97	0.38	2	-0.02	0.07	1
4285751	nnnnn	5623.68	127.15	5	3.81	0.67	4	-0.55	0.07	2
4294474	NnnnN	0	0	0
4523052	nnBnn	5415.46	88.19	5	4.45	0.14	4	-0.55	0.08	2
4591362	nnnnn	5978.18	35.09	8	3.62	0.09	6	-0.43	0.04	6
4615056	nnBnn	5173.14	78.57	3	4.11	0.12	2	-0.62	0.05	1
4800059	nCnnn	4685.68	448.19	2	4.50	0.04	1	-1.03	0.06	1
4806082	nCnnn	4752.02	310.33	1	2.51	0.44	2	-3.05	0.14	1
4826685	nnnGn	4037.25	10.47	1	4.73	0.03	1	-1.66	0.10	1
5076098	nnnnn	6067.72	75.71	8	3.90	0.24	5	-0.91	0.06	3
5220730	nnnnn	5080.57	103.07	4	4.87	0.22	4	-0.82	0.16	3
5316898	nnnnn	4808.27	79.57	3	3.92	0.12	2	-0.49	0.09	1
5318026	nnnnn	5704.79	164.56	4	4.18	0.41	2	-0.26	0.06	1
5408481	nnnnn	5696.07	73.21	7	4.23	0.12	6	-0.54	0.00	5
5547828	nnnnn	4603.56	59.78	3	4.26	0.15	4	-0.42	0.18	2
5855728	LnnnR	0	0	0
6072721	nnnnn	4614.04	47.06	3	4.37	0.13	4	-0.97	0.01	2
4206511	nnnnn	4079.19	21.37	2	3.94	0.46	2	-0.49	0.24	1
4295128	nnnnn	5066.06	182.78	3	4.45	0.06	2	0.16	0.09	1
4326248	VnnnN	0	0	0
4330990	Nnnnc	0	0	0
4465239	nnnnn	5832.47	89.28	5	4.19	0.25	2	-0.57	0.04	1
5061719	nnnnn	5988.12	26.38	7	3.88	0.08	4	-0.45	0.03	3
5160122	nnnnn	5270.66	253.11	4	4.35	0.10	5	-0.48	0.03	3
5190254	nnnnn	5087.01	98.06	3	4.37	0.09	4	-0.22	0.07	3
5233989	LnnnR	4254.12	52.46	3	3.84	0.35	2	-0.42	0.07	1
5276313	nnnnn	5971.93	57.04	8	4.05	0.12	6	-0.89	0.01	6
5349969	ICnnR	0	0	0
5471482	nnnnn	5588.67	44.64	7	4.28	0.15	6	-0.48	0.03	5

Table 7.5 (cont'd): SSPP Stellar Parameters for Hectospec Targets

UW ID ^a	flags	T_{eff} (K)	$\sigma(T_{\text{eff}})$ (K)	$N(T_{\text{eff}})^{\text{b}}$	$\log g$ (dex)	$\sigma(\log g)$ (dex)	$N(\log g)^{\text{b}}$	[Fe/H] (dex)	$\sigma([\text{Fe}/\text{H}])$ (dex)	$N([\text{Fe}/\text{H}])^{\text{b}}$
5535336	NnnnN	0	0	0
5606432	nnnnn	5457.35	156.87	3	4.22	0.66	2	-0.60	0.16	1
5606604	nCnnn	4911.36	97.63	3	3.40	0.26	3	-0.60	0.14	1
5722362	nnnnn	6085.39	81.08	5	3.88	0.18	2	-0.44	0.07	1
5913973	lnngn	4016.33	20.40	1	4.36	0.08	2	-1.74	0.10	1
4247050	nnnnn	5690.58	98.89	5	3.74	0.01	2	-0.92	0.05	1
4488586	NnnGn	5185.89	81.66	3	4.24	0.64	2	-1.00	0.12	1
4715687	nnnnn	5469.95	138.16	6	4.26	0.11	6	-0.38	0.03	4
4808050	nnnnn	5862.88	52.60	7	4.20	0.28	4	-0.46	0.04	2
5037993	nnnnn	6077.33	58.97	5	4.00	0.28	2	-0.96	0.03	1
5147189	nnnnR	0	0	0
5151180	nnBnn	5280.27	76.26	4	3.98	0.22	5	-0.14	0.07	3
5159952	nnnnn	6769.41	87.67	8	4.33	0.14	6	-0.48	0.05	4
5360477	nnnnn	4269.72	68.68	2	3.06	0.15	1	-0.52	0.09	1
5644293	nnBnn	5504.15	32.14	3	3.58	0.49	2	-0.97	0.06	1
5717380	lnnnR	0	0	0
5807776	nnnnn	5624.35	31.31	4	3.36	0.45	2	-0.57	0.06	1
5970687	nnnGn	6013.26	111.41	8	3.46	0.26	5	-1.02	0.03	4
6080998	nnnnc	0	0	0
4222952	nnBnn	5405.90	61.38	6	3.69	0.09	6	-0.69	0.00	4
4299393	nnnnR	0	0	0
4341696	nnnGn	6130.70	91.81	8	4.01	0.38	5	-1.01	0.04	4
4354650	nnngn	4690.06	62.01	3	4.52	0.16	4	-1.06	0.07	1
4383494	NnnnN	0	0	0
4433728	nnnnn	5602.00	66.02	6	4.47	0.18	6	-0.00	0.06	5
4647336	lnnnn	4269.18	100.14	3	3.81	0.07	3	-0.53	0.06	1
4721053	VnnnX	0	0	0
4766997	nnnnn	4872.99	190.03	3	4.40	0.23	4	-0.65	0.20	1
5051899	nnnnn	5014.57	120.34	3	2.47	0.24	4	-0.44	0.05	4
5081632	nnnnn	4535.91	169.82	3	3.43	0.26	3	-0.36	0.10	1
5491878	lnnGn	4049.66	18.04	1	4.34	0.05	1	-1.52	0.08	1
5607098	Nnnnn	4654.79	98.66	3	3.81	0.18	2	-0.09	0.08	1
5717528	nnnnn	5917.00	64.13	8	3.33	0.12	6	-0.82	0.06	5
5745530	nnnnn	5820.93	97.34	7	3.94	0.16	6	-0.14	0.06	7
4385528	nnnnn	5887.37	46.10	8	4.11	0.10	6	-0.51	0.03	6
4467347	nCBnn	4307.82	192.09	3	3.23	0.02	2	-0.99	0.30	1
4821080	nnnnn	5293.48	99.63	3	4.61	0.27	2	-0.90	0.06	1
6047167	nnnnn	4939.68	120.80	4	2.87	0.18	5	-0.51	0.06	2
4415171	nnnnN	0	0	0
4626606	NnBnN	0	0	0
4634853	nnnnn	5112.21	148.97	4	4.21	0.19	4	-0.82	0.12	1
4716539	nnnnn	5439.42	71.95	7	3.93	0.07	6	0.02	0.05	7
5346198	nnnGn	7521.37	122.17	7	2.54	0.26	6	-1.48	0.07	1
5413281	nnnnn	5246.87	134.44	5	4.29	0.30	4	-0.73	0.02	2
5776611	nnnnn	6159.44	106.42	4	3.87	0.23	2	-0.65	0.04	1
5899735	nnnnn	4883.47	76.20	3	3.22	0.04	4	-0.91	0.15	3
4298350	lnnnR	0	0	0
4324403	nnnnn	5400.46	39.10	6	4.64	0.09	6	-0.77	0.04	4
4616607	nnBnn	5784.25	16.92	6	4.28	0.08	4	-0.71	0.07	2
4652060	nnBgn	4959.16	234.64	3	4.38	0.50	2	-1.17	0.12	1
4717200	nnBnn	5288.08	230.58	3	4.43	0.24	4	-0.24	0.08	2
4856735	nnnnn	4747.33	50.49	3	4.34	0.13	4	-0.86	0.03	2
5093048	nnngn	4652.36	91.40	3	4.59	0.15	4	-1.32	0.13	3
5152510	nnnnn	5613.13	37.16	7	3.98	0.22	6	-0.71	0.03	3
5159544	nnnnn	5200.47	62.26	3	4.51	0.07	4	-0.31	0.09	1
5222842	nnnnn	5281.09	52.25	6	4.38	0.21	6	-0.98	0.03	6
5299450	nnnnn	4932.10	79.32	3	4.27	0.14	4	-0.64	0.06	3
5323787	nnnnN	0	0	0
5445826	nnnnn	5568.78	70.62	7	4.18	0.21	6	-0.41	0.00	2
5483113	ICnnR	0	0	0
5552859	nnnnn	4508.40	35.22	3	4.57	0.16	4	-0.93	0.09	1
5570713	nnnnn	4780.85	151.51	3	4.22	0.06	2	-0.30	0.08	1
5793852	nnnnn	5709.79	181.20	6	4.20	0.29	4	-0.88	0.05	3
5853366	nnBnn	4908.75	114.05	4	4.60	0.06	5	-0.58	0.06	3
4202293	nnnGn	4038.02	28.98	1	4.32	0.25	2	-1.85	0.19	1
4213491	nnnnn	5307.04	52.06	4	4.59	0.15	5	-0.62	0.03	4
4307018	lnnnN	0	0	0
4326523	nnnnn	4483.17	40.32	3	4.46	0.18	4	-0.84	0.07	1
4475846	nnnnn	5627.94	50.21	7	3.72	0.07	6	0.11	0.03	5
4508926	ICnnR	0	0	0
4748813	nnBnn	5596.65	106.67	4	2.87	0.14	2	-0.57	0.05	1
4846400	nnnnn	5655.80	79.77	7	4.14	0.01	6	-0.19	0.01	6
5030714	nnBnn	4975.72	105.24	4	3.97	0.09	5	-0.42	0.13	3
5163929	nnnnn	5357.79	29.72	6	4.07	0.05	6	-0.26	0.06	6

Table 7.5 (cont'd): SSPP Stellar Parameters for Hectospec Targets

UW ID ^a	flags	T_{eff} (K)	$\sigma(T_{\text{eff}})$ (K)	$N(T_{\text{eff}})^{\text{b}}$	$\log g$ (dex)	$\sigma(\log g)$ (dex)	$N(\log g)^{\text{b}}$	[Fe/H] (dex)	$\sigma([\text{Fe}/\text{H}])$ (dex)	$N([\text{Fe}/\text{H}])^{\text{b}}$
5205664	nnnnn	6086.38	100.17	8	4.04	0.33	6	-0.30	0.03	5
5246038	nnBnn	6457.55	148.88	7	3.25	0.06	4	-1.78	0.28	2
5263116	nnnnn	5568.13	137.16	4	3.99	0.31	2	-0.79	0.05	1
5273504	nnnnn	5101.07	108.72	6	4.31	0.12	6	-0.72	0.05	4
5279573	lnnnR	0	0	0
5386501	nnnnn	5599.87	106.04	4	4.29	0.06	2	-0.55	0.04	1
5441556	nnBnn	5234.04	149.97	3	4.14	0.29	2	-1.00	0.12	1
5648542	NCnnN	0	0	0
5659058	nnnnR	0	0	0
5765463	nnnnn	4506.35	183.22	3	4.04	0.26	4	-0.70	0.04	2
5855092	nnnnn	4338.40	79.27	3	3.56	0.10	3	-0.77	0.08	1
6064402	nnnnn	5797.51	55.99	6	3.92	0.17	4	-0.65	0.06	4
6079126	1CnnR	0	0	0
4324545	nnnnn	7410.33	42.72	6	3.98	0.44	4	-1.28	0.04	3
4610691	nnnnn	5198.76	102.83	4	4.22	0.08	5	-0.15	0.07	4
4631751	Nnnnn	4529.44	126.16	3	3.96	0.14	2	-0.38	0.06	1
4794516	nnngn	4471.87	45.58	3	4.57	0.17	4	-1.26	0.00	2
5085090	nnnnn	5674.86	69.29	7	3.68	0.06	6	-0.24	0.04	7
5286331	nnnnn	4349.87	105.21	3	4.12	0.27	4	-0.20	0.11	1
5315032	nnnnn	5721.55	139.75	6	4.30	0.12	4	-0.34	0.03	3
5346055	lnnnn	4045.26	13.86	2	2.69	0.10	1	-0.42	0.10	1
5374464	nnnnn	5460.22	76.44	6	4.34	0.21	6	-0.72	0.08	4
5734866	nnnnn	5267.17	93.25	4	4.22	0.13	5	0.02	0.05	2
5785211	nnnnR	0	0	0
5916057	nnnnn	5190.78	37.65	4	3.67	0.13	5	-0.54	0.10	5
6081723	nnnnn	5936.76	193.30	4	4.35	0.51	2	-0.45	0.11	1
4160126	nnnnn	5802.11	70.47	7	4.11	0.09	6	-0.10	0.06	5
4203270	nnBnn	5493.75	84.72	7	4.07	0.16	6	-0.87	0.05	6
4310931	nnBnn	5643.00	81.77	4	3.87	0.43	2	-0.85	0.11	1
4552329	nnnnn	4685.92	158.65	3	4.43	0.15	3	-0.33	0.18	1
4634991	NnnnN	0	0	0
4706509	nnnnn	5431.09	67.92	6	4.13	0.09	6	-0.72	0.06	5
4733975	VnnnN	0	0	0
4807423	NnBnN	0	0	0
4812924	nnnnR	0	0	0
4824401	VnBnX	0	0	0
5031461	nnnnR	0	0	0
5047295	nnnnn	4764.46	98.23	3	4.20	0.11	2	-0.45	0.07	1
5095006	nnngn	4159.94	80.69	3	3.54	0.10	2	-1.86	0.25	1
5203756	1CnnR	0	0	0
5298334	nnnnn	5116.44	48.15	4	3.65	0.09	5	-0.57	0.05	2
5351102	nnnnn	5142.51	44.41	3	4.31	0.20	2	-0.57	0.11	1
5370208	nnnnn	5382.47	69.08	3	4.05	0.32	2	-0.55	0.08	1
5427330	NnBnN	0	0	0
5490884	nnngn	4539.59	152.39	3	4.60	0.28	2	-1.06	0.08	1
5598807	nnnnn	5145.24	48.29	4	4.46	0.16	4	-0.78	0.01	2
5605875	nnnnn	5901.49	106.10	8	4.08	0.14	6	-0.57	0.04	5
5785463	nnBnn	5270.15	71.72	3	4.12	0.36	2	-0.92	0.09	1
5939807	NCnnN	0	0	0
4288198	nnnGn	4256.38	29.23	3	3.94	0.34	4	-1.22	0.15	2
4401782	nnnnn	4866.36	50.22	3	3.30	0.26	4	-1.00	0.02	4
4478295	nnnGn	4294.30	40.98	2	4.24	0.64	2	-1.12	0.10	1
4579015	nnnnn	5893.41	111.45	4	3.72	0.11	2	-0.21	0.06	1
4607648	nnnnn	4930.69	110.69	3	4.28	0.26	3	-0.51	0.14	1
4715428	nnnnn	5803.30	140.66	5	4.02	0.17	4	-0.22	0.01	2
4848298	VnnnX	0	0	0
5083657	nnnnn	5218.09	101.17	3	4.59	0.09	4	-0.41	0.06	3
5090161	nnnnn	5676.48	73.14	5	4.01	0.15	2	-0.58	0.04	1
5159061	lnnnR	0	0	0
5182372	nnBgn	4742.69	154.37	4	3.09	0.18	5	-1.33	0.09	3
5311049	nnnnn	5752.11	73.36	6	4.22	0.07	6	-0.42	0.01	5
5379263	NnBnN	0	0	0
5408876	nnnnn	4771.67	85.04	3	4.59	0.10	4	-0.63	0.01	2
5571736	nnngn	5445.31	29.34	5	3.75	0.48	4	-1.01	0.10	2
5694976	nnnnn	5511.35	98.66	6	4.31	0.10	6	-0.38	0.03	5
5700867	nnnGn	5835.20	155.28	5	3.99	0.69	2	-2.22	0.06	1
5961962	nnnnn	5046.37	124.16	4	3.68	0.10	5	-0.55	0.07	4
4461017	nnnnn	6253.21	224.36	6	3.22	0.18	4	-0.37	0.02	2
4593348	nnnnn	6086.15	138.28	8	3.77	0.26	6	-0.48	0.09	5
4596026	lnnGn	4050.29	29.22	1	4.50	0.01	2	-1.28	0.20	1
4704767	nnnnn	4956.73	84.58	3	3.89	0.18	4	-0.67	0.02	2
4705634	nnnnn	4565.91	105.56	3	4.43	0.11	4	-0.62	0.02	2
5030390	nnngn	4495.92	80.07	3	4.36	0.25	2	-1.21	0.07	1
5039616	nnnnn	6000.65	61.76	8	4.12	0.12	6	-0.71	0.02	7

Table 7.5 (cont'd): SSPP Stellar Parameters for Hectospec Targets

UW ID ^a	flags	T_{eff} (K)	$\sigma(T_{\text{eff}})$ (K)	$N(T_{\text{eff}})^{\text{b}}$	$\log g$ (dex)	$\sigma(\log g)$ (dex)	$N(\log g)^{\text{b}}$	[Fe/H] (dex)	$\sigma([\text{Fe}/\text{H}])$ (dex)	$N([\text{Fe}/\text{H}])^{\text{b}}$
5115822	nnnnn	5562.85	42.11	4	4.13	0.26	2	-0.39	0.06	1
5117868	nnnnn	4448.62	21.95	3	4.25	0.22	2	-0.98	0.07	1
5130856	nnnnn	5769.24	115.19	7	3.63	0.09	6	-0.19	0.03	6
5137286	nnnnn	5919.42	31.36	7	3.70	0.08	4	-0.29	0.02	2
5470264	nnngn	4009.09	19.62	1	3.77	0.10	1	-1.83	0.08	1
5656204	nnnnn	5302.32	73.05	6	2.78	0.26	6	-0.72	0.05	6
5733490	nnnnn	6041.38	134.06	6	4.12	0.39	4	-0.64	0.07	2
5947429	nnnnn	5679.78	267.89	4	3.35	0.09	2	-0.96	0.06	1
5991455	nnnGn	6379.90	160.14	5	3.30	0.03	2	-1.31	0.08	1
4205737	nnnnn	5898.96	86.39	7	3.90	0.07	6	-0.80	0.04	6
4340847	nnnnn	5915.77	79.64	8	3.94	0.07	6	-0.30	0.07	6
4509372	nnnnn	4406.77	101.34	3	3.90	0.03	4	-0.25	0.07	1
4526963	lnnnN	0	0	0
4617820	nnnnn	5640.84	81.89	7	4.40	0.13	6	-0.50	0.05	7
4718708	nnBnn	4944.84	162.45	4	4.86	0.01	5	-0.91	0.02	3
4814890	nnnnc	0	0	0
4831127	lnnnR	0	0	0
4832742	nnnnn	4388.08	259.29	2	4.37	0.22	2	-1.00	0.17	1
5065474	nnnnn	5699.94	40.90	4	4.35	0.39	2	-0.91	0.04	1
5207393	nnnnn	5205.26	24.42	5	4.24	0.11	4	-0.44	0.03	3
5226307	nCnnR	0	0	0
5348123	nnnnn	5295.56	103.15	4	4.20	0.24	4	-0.70	0.00	2
5383218	lnnnR	0	0	0
5482549	nnngn	5040.37	108.38	6	4.03	0.16	6	-1.05	0.06	6
5724782	nnnnn	5989.91	52.44	8	3.96	0.16	6	-0.86	0.08	4
6026133	NnnnN	0	0	0
6060174	nCnnN	0	0	0
4213324	NnBnN	0	0	0
4277156	nnnne	0	0	0
4277698	Dnnnn	4579.89	68.74	3	4.03	0.15	4	-0.31	0.20	1
4339249	nnnnn	6032.48	83.65	8	4.08	0.14	6	-0.59	0.03	4
4381209	nnnnn	5816.36	79.95	8	4.28	0.15	6	-0.54	0.05	6
4544565	nnngn	5189.82	53.31	6	2.66	0.16	6	-1.13	0.05	4
4743160	nnnnn	5861.95	88.82	8	4.31	0.11	6	-0.42	0.10	3
5066903	nnnnn	5442.14	55.88	4	3.94	0.18	2	-0.56	0.10	1
5117418	nCnnX	0	0	0
5153139	nnnnn	5345.20	33.87	4	3.68	0.12	5	-0.59	0.06	4
5184680	nnnnn	5880.74	81.21	8	4.03	0.10	6	-0.29	0.04	3
5213759	nnnnn	5590.19	58.85	7	4.00	0.21	6	-0.57	0.05	6
5238395	nnnnn	5608.38	88.10	6	3.66	0.15	6	-0.46	0.07	6
5301925	nnnnn	5043.24	120.51	4	3.13	0.27	5	-0.70	0.05	3
5541862	nnnnn	5645.49	110.58	6	3.99	0.11	6	-0.55	0.08	7
5582015	NnnnN	0	0	0
5740429	lnnnR	0	0	0
6006465	NCnnR	0	0	0
6096049	nnnnn	5635.84	38.19	6	3.85	0.08	6	-0.07	0.08	4
4152895	NnnnN	0	0	0
4169136	nnnnn	4322.94	53.99	3	4.08	0.20	4	-0.41	0.20	1
4263105	nnnnn	5533.66	79.65	6	4.24	0.10	6	-0.25	0.03	5
4272303	nnngn	5688.14	166.39	7	1.74	0.32	4	-1.15	0.13	1
4322008	ICnnR	0	0	0
4412887	Nnnnn	4917.76	133.81	3	4.64	0.24	2	-0.84	0.05	1
4586636	nnnnn	4252.82	116.29	3	3.58	0.14	4	-1.14	0.11	2
5051538	nnnnn	5809.25	130.74	5	3.88	0.02	2	-0.46	0.04	1
5100921	nnnnn	4926.77	121.43	3	4.02	0.05	2	-0.25	0.06	1
5189400	nnnnR	0	0	0
5277817	nnnnn	5426.88	80.98	4	4.27	0.34	2	-0.43	0.07	1
5303137	nnnnn	5449.74	130.28	3	3.92	0.27	2	-0.66	0.06	1
5417477	nnnnn	6145.88	49.75	7	3.54	0.04	4	-1.38	0.05	4
5472204	nnnnn	5504.69	209.22	4	4.37	0.24	4	0.18	0.17	2
5998989	nnnnn	5904.90	78.00	5	3.87	0.01	2	-0.61	0.15	1
6062061	nnnnn	4417.38	294.04	2	4.41	0.26	2	-0.99	0.13	1
6088645	nnnnn	6247.46	33.89	9	3.91	0.06	7	-0.49	0.01	4
4216087	nnnnn	5567.81	51.74	6	4.12	0.07	6	-0.48	0.04	6
4248131	nnnnn	4824.69	65.22	3	4.02	0.27	3	-0.73	0.05	1
4371650	nnnGn	4027.65	24.92	2	4.33	0.10	2	-1.40	0.28	1
4615005	nnnnn	5425.42	163.79	3	2.47	0.79	2	-1.45	0.13	3
4690163	nnnnn	5904.24	132.19	7	4.10	0.08	6	0.13	0.08	5
4693467	nnnnn	4828.22	145.25	3	4.08	0.12	3	-0.48	0.11	1
5028028	nnnnn	5196.01	225.93	3	3.80	0.06	4	-0.10	0.09	2
5056229	nnnnn	4760.35	82.74	3	4.50	0.08	4	-0.60	0.01	2
5061287	nnnnn	4892.05	120.55	3	4.47	0.03	4	-0.21	0.09	3
5092034	nnnnn	5443.07	102.64	7	4.35	0.11	6	-0.43	0.08	6
5266754	lnnGn	4021.84	14.77	1	2.22	0.15	1	-2.35	0.10	1

Table 7.5 (cont'd): SSPP Stellar Parameters for Hectospec Targets

UW ID ^a	flags	T_{eff} (K)	$\sigma(T_{\text{eff}})$ (K)	$N(T_{\text{eff}})^{\text{b}}$	$\log g$ (dex)	$\sigma(\log g)$ (dex)	$N(\log g)^{\text{b}}$	[Fe/H] (dex)	$\sigma([\text{Fe}/\text{H}])$ (dex)	$N([\text{Fe}/\text{H}])^{\text{b}}$
5351777	nnnnn	5917.88	75.21	8	4.26	0.17	6	-0.51	0.02	4
5415839	nnnnn	4649.71	37.50	3	4.44	0.44	2	-1.34	0.15	1
5505264	ICnnR	0	0	0
5522900	nnnnn	5691.36	47.24	7	4.12	0.14	6	-0.69	0.04	6
5755556	NnnnN	0	0	0
5995338	nnnnn	5458.46	90.76	6	4.38	0.20	6	-0.53	0.05	6
6058913	nnnnn	6983.88	179.17	6	2.43	0.45	4	-1.43	0.02	2
4174409	nnnnn	4877.53	121.07	3	4.35	0.10	4	-0.08	0.07	2
4303986	ICnnR	0	0	0
4528409	nnnnN	0	0	0
4639557	nnnnn	6038.36	185.10	3	4.27	0.60	2	-0.70	0.05	1
4788672	nnnnn	5465.97	104.05	7	4.35	0.17	6	-0.47	0.05	4
4791189	nnnnn	4766.83	126.27	3	4.12	0.14	4	-0.04	0.36	1
4840106	nnnnn	6333.00	80.31	8	2.52	0.23	6	-1.12	0.09	5
4852419	NnBnN	0	0	0
5048567	nnnnn	5700.37	84.26	4	3.65	0.15	2	-0.42	0.08	1
5052248	nnBnN	5793.13	167.20	4	3.99	0.56	2	-0.32	0.05	1
5067176	nnnnn	4765.65	191.14	3	4.27	0.02	3	-0.23	0.08	1
5112553	nnnnn	4559.68	112.26	3	3.89	0.14	4	-0.78	0.05	2
5319691	nnnnn	5182.40	209.36	4	4.51	0.13	4	-0.26	0.01	2
5351235	LnnnR	0	0	0
5401176	nnnnn	4840.18	123.03	3	2.41	0.31	4	-0.69	0.20	2
5499462	nnnnn	5566.72	49.90	6	4.24	0.06	6	-0.26	0.05	5
5689417	nnnnn	5353.02	162.97	6	4.05	0.18	4	-0.48	0.04	5
6009762	nnBnN	4937.01	158.35	3	4.21	0.26	3	-1.06	0.30	3
6083867	nnBnN	0	0	0
6098833	nnnnN	0	0	0
4177889	NnnnR	0	0	0
4232340	nnnnn	4149.49	46.30	1	4.86	0.02	2	-0.78	0.17	1
4331293	nnnnn	5622.61	65.57	6	3.75	0.02	6	0.07	0.04	3
4342752	nnnnn	5417.58	16.79	3	3.91	0.38	2	-0.67	0.08	1
4389226	nnnnn	5509.49	37.31	5	3.92	0.54	4	-0.92	0.25	1
4451954	nnngn	5346.98	122.18	7	0.55	0.32	4	-2.57	0.07	4
4544579	nnnnn	4481.21	70.38	3	3.93	0.14	4	-0.26	0.11	2
4814175	nnngn	5955.89	42.95	7	4.14	0.20	4	-1.26	0.05	3
5053650	nnnnn	5659.91	64.49	6	4.40	0.14	4	-0.57	0.07	4
5115290	nnnnn	5847.67	56.90	6	3.52	0.10	4	-0.47	0.02	2
5164129	NnnnN	0	0	0
5266791	nnnnn	4429.30	112.95	3	4.19	0.30	3	-0.21	0.10	1
5271772	nnnnn	5369.69	49.13	6	4.19	0.07	6	-0.14	0.06	6
5375051	nnnnn	4531.26	53.00	3	4.11	0.10	3	-0.40	0.08	1
5492993	nnnnn	4955.29	93.87	3	4.51	0.08	3	-0.59	0.07	1
5526230	nnnnn	4874.47	34.49	3	2.49	0.17	4	-0.60	0.07	4
5589249	LnnnR	0	0	0
5648450	nnBnN	5280.93	38.54	6	3.93	0.14	6	-0.89	0.02	5
4204662	nnnnn	5213.57	122.95	4	4.04	0.01	5	-0.34	0.04	2
4576678	nnnnn	6683.72	75.95	7	3.80	0.16	4	-1.80	0.06	2
4605756	NnnnN	0	0	0
4654071	nnBnN	5404.03	107.80	6	4.45	0.11	6	-0.65	0.03	7
4749407	nnnnn	6125.42	62.31	7	3.74	0.35	4	-1.25	0.04	2
4800798	nnBnN	4855.34	81.82	3	3.57	0.26	3	-1.71	0.14	1
4873250	nnnnn	5553.94	63.29	6	4.14	0.12	6	-0.46	0.04	4
5092081	nnnGn	5973.50	189.51	4	3.78	0.41	2	-1.10	0.13	1
5121444	nnnnn	5825.96	42.32	8	3.96	0.10	6	-0.25	0.05	7
5287188	ICnnR	0	0	0
5363811	nnnnn	6777.84	53.36	8	4.22	0.17	6	-1.05	0.07	3
5432477	ICnnR	0	0	0
5537094	nnnnn	5750.48	138.31	4	3.80	0.17	2	-0.54	0.06	1
5687502	nnnGn	6164.80	95.59	6	3.87	0.17	4	-1.09	0.08	5
5714887	nnnnn	6325.57	93.32	8	3.99	0.11	6	-0.38	0.06	6
5869508	nnnnn	5989.02	46.84	8	4.09	0.15	6	-1.38	0.03	6
5896911	nnnnn	4825.19	208.28	4	4.19	0.30	4	-0.61	0.11	3
4345936	ICnnN	0	0	0
4437110	ICnnR	0	0	0
4439296	nCnnR	0	0	0
4501142	nnnnn	5261.53	109.63	5	4.07	0.10	4	-0.25	0.01	2
4605935	nnnnn	5813.71	44.57	8	3.83	0.05	6	-0.58	0.03	5
4698535	nnnnn	5781.30	64.18	7	4.16	0.17	6	-0.40	0.05	5
4867844	nnnnn	5367.48	75.93	6	4.28	0.01	6	-0.21	0.02	4
5021737	nnnnn	5926.65	142.16	4	3.79	0.23	2	-0.31	0.08	1
5143880	NnBnN	0	0	0
5200726	nnBnN	5380.24	91.25	6	3.90	0.12	6	-0.30	0.02	3
5219763	nnnnn	5904.71	23.07	8	3.88	0.06	6	-0.43	0.04	6
5283782	nnBnN	5448.51	158.18	3	3.77	0.09	2	-0.41	0.08	1

Table 7.5 (cont'd): SSPP Stellar Parameters for Hectospec Targets

UW ID ^a	flags	T_{eff} (K)	$\sigma(T_{\text{eff}})$ (K)	$N(T_{\text{eff}})^{\text{b}}$	$\log g$ (dex)	$\sigma(\log g)$ (dex)	$N(\log g)^{\text{b}}$	[Fe/H] (dex)	$\sigma([\text{Fe}/\text{H}])$ (dex)	$N([\text{Fe}/\text{H}])^{\text{b}}$
5301318	nnnnn	5963.14	5.05	7	3.52	0.14	4	-0.32	0.04	4
5355469	nnnnn	8482.23	65.60	3	4.65	0.20	2	-1.66	0.09	1
5371227	nnnnn	4707.26	79.47	3	4.51	0.15	4	-0.56	0.09	2
5411901	nnnnn	4433.82	79.37	3	3.79	0.09	4	-0.85	0.09	2
5469120	nnnnn	5503.13	68.28	7	4.17	0.14	6	-0.25	0.07	6
5552148	nnnnn	6081.98	44.24	8	3.82	0.11	6	-0.41	0.06	7
5875626	nnngn	5260.30	93.19	6	2.18	0.17	6	-1.61	0.02	5
5971521	NnnnR	0	0	0
4186846	NnnnN	0	0	0
4313233	1CnnR	0	0	0
4370007	nnngn	4425.49	65.56	3	4.37	0.30	3	-1.54	0.15	1
4535804	nnnnn	7298.20	39.56	6	3.60	0.45	4	-0.36	0.05	3
4559649	nnnnn	5302.01	23.91	4	3.63	0.13	5	-0.66	0.10	4
4639043	NnnnN	0	0	0
4740074	nnnnn	5942.60	74.94	4	4.22	0.52	2	-0.76	0.03	1
4806553	NnBnN	0	0	0
4808120	NnnnN	0	0	0
5169324	nnnnR	0	0	0
5175409	lnnnR	0	0	0
5229703	nnBnn	5711.41	306.18	4	3.88	0.47	2	-0.68	0.07	1
5268458	NnnnN	0	0	0
5360730	nnnnn	5759.74	144.03	7	4.13	0.18	6	-0.66	0.11	4
5365520	nnnnn	4735.48	139.26	3	4.49	0.23	3	-0.15	0.08	1
5372446	Nnnnn	4468.42	107.25	3	4.22	0.26	2	-0.30	0.08	1
5383528	nnnnn	5739.15	124.51	3	3.45	0.30	2	-0.70	0.07	1
5415273	nnnnn	7149.35	48.02	8	3.50	0.24	6	-0.98	0.05	4
5810291	Nnnnn	4868.33	259.87	3	4.26	0.58	2	-0.97	0.05	1
5991759	nnnnn	5876.27	43.57	6	2.91	0.29	4	-0.63	0.05	5
6015826	nnnnn	5897.47	66.96	7	4.16	0.14	6	-0.31	0.05	4
6085660	nnnGn	4947.01	169.10	3	4.25	0.63	2	-1.00	0.07	1
6088446	lnnnR	0	0	0
4310283	nnnnn	6127.91	69.38	8	4.26	0.25	5	-0.48	0.06	4
4349534	NnnnN	0	0	0
4471608	nnnnn	4379.74	63.92	3	4.20	0.24	3	-0.54	0.07	1
4554802	nnBnn	5787.61	130.94	5	4.25	0.15	4	-0.31	0.14	2
4563191	nnnnn	5850.83	52.88	8	4.34	0.13	6	-0.59	0.04	4
4578957	nnngn	5756.58	66.75	7	3.27	0.24	6	-1.10	0.04	5
4662618	nnnnn	6283.80	73.52	9	2.58	0.13	7	-1.37	0.07	6
4800423	nnngn	5105.64	144.81	4	2.44	0.07	5	-1.35	0.08	4
5029627	nnnnn	5946.51	73.36	4	4.17	0.42	2	-0.49	0.06	1
5113222	nnngn	5335.21	282.20	3	2.25	0.23	2	-2.23	0.05	4
5160531	Nnnnn	4710.77	78.52	3	4.09	0.15	2	-0.39	0.07	1
5183980	nnnnR	0	0	0
5220618	nnnnn	5953.05	72.48	7	2.16	0.64	4	-1.00	0.03	3
5327173	nnnnn	5870.65	101.22	7	3.55	0.15	4	-0.39	0.06	5
5417502	nnnnn	4743.61	54.31	3	4.15	0.15	3	-0.62	0.09	1
5508248	nCnnR	0	0	0
5692668	nnBnn	4888.35	97.46	3	3.64	0.17	2	-0.42	0.07	1
5889399	nnBnn	5721.40	64.68	4	3.88	0.01	2	-0.61	0.04	1
5916861	nnBnn	5231.48	144.52	4	3.78	0.13	4	-0.85	0.02	2
6031170	nnnnn	5484.72	68.86	4	4.01	0.09	5	0.21	0.03	3
4523729	lnnnn	4307.31	19.17	3	3.77	0.19	4	-0.52	0.19	3
4571539	nnnnn	6059.26	76.75	7	3.15	0.42	4	-0.57	0.21	1
4597928	nnnnn	4639.53	87.94	3	4.44	0.33	2	-1.24	0.08	1
4816051	nnnnn	5206.48	96.95	4	4.46	0.14	5	-0.43	0.07	4
5114261	nnnnn	4606.67	50.38	3	4.42	0.17	4	-0.75	0.06	2
5338270	nnnnn	6349.28	96.72	8	2.93	0.28	6	-1.11	0.07	6
5409281	nnnnn	5799.91	83.13	5	3.49	0.17	2	-0.70	0.05	1
5462435	nnngn	5680.33	43.59	8	4.13	0.11	6	-1.98	0.06	6
5850118	NnnnN	0	0	0
6040436	nCnnR	0	0	0
6042651	nnBnn	5472.70	49.92	6	3.99	0.16	6	-0.35	0.04	4
5489451	nnBnn	5512.61	154.69	4	4.40	0.42	2	-0.96	0.04	1
4224014	nnBGn	5521.75	89.46	4	3.74	0.38	2	-1.15	0.07	1
4269536	lCnnR	0	0	0
4325991	nnnnN	0	0	0
4387964	nnnnn	5803.34	63.85	7	3.95	0.13	6	-0.46	0.04	6
4480410	nnnnR	0	0	0
4531022	VnBnX	0	0	0
4750903	nnnnn	5892.40	125.36	7	3.77	0.12	6	-0.26	0.03	3
4799871	nnnnn	5123.57	50.95	3	4.07	0.06	2	-0.21	0.08	1
5070833	nCnnR	0	0	0
5193332	Lnnnn	4066.56	12.87	2	3.07	0.23	1	-0.81	0.10	1
5384418	nnnnn	5380.95	198.64	3	4.10	0.78	2	-0.64	0.06	1

Table 7.5 (cont'd): SSPP Stellar Parameters for Hectospec Targets

UW ID ^a	flags	T_{eff} (K)	$\sigma(T_{\text{eff}})$ (K)	$N(T_{\text{eff}})^{\text{b}}$	$\log g$ (dex)	$\sigma(\log g)$ (dex)	$N(\log g)^{\text{b}}$	[Fe/H] (dex)	$\sigma([\text{Fe}/\text{H}])$ (dex)	$N([\text{Fe}/\text{H}])^{\text{b}}$
5426442	nnnnn	4949.14	112.98	3	4.50	0.24	3	-1.02	0.07	1
5504730	nnnnn	4907.76	48.04	3	3.99	0.09	2	-0.55	0.05	1
5638340	lnnnn	4173.78	51.56	2	3.86	0.53	2	-0.32	0.22	1
5742701	1CnnR	0	0	0
5772213	NnnnN	0	0	0
4213962	nnnnn	4855.20	128.61	3	4.32	0.12	4	-0.16	0.01	2
4215359	nnnnn	5845.48	40.57	8	4.12	0.16	6	-0.57	0.00	5
4216159	nnnnn	5182.75	55.13	6	4.38	0.14	6	-0.62	0.11	5
4254728	nnnnn	7783.63	66.96	4	3.50	0.04	3	-1.30	0.05	1
4734920	nnnnn	5861.39	103.94	7	4.09	0.14	4	-0.79	0.10	3
4830131	NnnnN	0	0	0
5100865	nnnnn	5760.90	51.09	8	4.04	0.03	6	-0.39	0.06	4
5222268	nnnnn	5231.01	76.58	4	4.14	0.14	5	-0.28	0.12	3
5332367	nnngn	5545.54	224.77	4	3.62	0.35	2	-1.43	0.05	1
5350035	nnnnn	4599.73	33.17	3	4.32	0.20	3	-0.51	0.10	1
5367623	1CnnR	0	0	0
5372555	nnnnn	5719.23	37.42	7	4.08	0.07	6	-0.47	0.04	5
5391926	nnnGn	5618.45	92.03	8	3.76	0.25	6	-1.52	0.07	5
5405162	nnnnn	4586.53	88.98	3	4.35	0.11	4	-0.71	0.11	2
5575160	nCnnN	0	0	0
5580198	nnBnn	5693.63	59.09	6	4.26	0.33	4	-0.56	0.06	3
5860823	NnnnR	0	0	0
5866726	nnnnn	5326.05	67.85	6	4.23	0.07	6	-0.02	0.06	5
4331966	nnnnn	5566.34	61.82	7	4.30	0.09	6	-0.59	0.04	5
4553243	NnnnN	0	0	0
4562947	nnnnn	5433.97	77.72	7	4.31	0.10	6	-0.83	0.05	5
4706547	nnnnn	4234.83	74.51	2	3.86	0.46	2	-0.40	0.18	1
4715353	nnnnn	5088.24	113.60	4	3.14	0.12	5	-0.82	0.02	3
4767817	nnnnn	6679.80	162.07	9	4.03	0.19	7	-0.55	0.06	5
4789005	nnBgn	5368.34	92.81	7	3.86	0.26	6	-1.28	0.06	4
4840880	nnnnn	6015.02	71.87	8	3.44	0.27	6	-0.99	0.01	3
5023273	nnnnn	4654.97	108.82	3	4.62	0.24	3	-0.81	0.10	1
5096035	nnnnn	4406.06	27.23	3	3.93	0.18	3	-0.56	0.05	1
5119540	lnnnR	0	0	0
5279711	nnnnn	4693.77	106.49	3	4.40	0.10	4	-0.75	0.05	2
5367857	nnnnn	6310.48	91.68	5	3.86	0.31	2	-1.03	0.08	1
5485242	1CnnR	0	0	0
5680062	NnnnN	0	0	0
5893683	lnngn	4026.25	4.88	2	4.65	0.04	1	-1.29	0.07	1
5969299	nnBnN	0	0	0
4227754	nnnnn	5340.80	360.68	3	4.12	0.36	2	-0.60	0.05	1
4332646	nnnnN	0	0	0
4429528	NCBnN	0	0	0
4497859	nCnnR	0	0	0
4549725	nnnnn	5704.89	7.79	7	4.06	0.10	6	-0.39	0.06	6
4597207	lnnnR	0	0	0
5051315	nnnnn	5538.90	55.75	7	4.06	0.05	6	-0.32	0.07	5
5094281	nnnnn	4080.28	37.95	2	2.99	0.12	1	-0.29	0.12	1
5103254	nnnnn	4702.46	70.62	3	4.28	0.20	4	-0.24	0.12	2
5259441	1CnnR	0	0	0
5281330	nnnnn	5600.41	95.54	4	4.12	0.11	2	-0.76	0.07	1
5288649	nnnnn	6222.61	168.47	5	3.35	0.18	2	-0.98	0.09	1
5313203	nnnnn	5340.03	85.68	6	3.99	0.02	6	-0.23	0.09	5
5336990	NnnnR	0	0	0
5345340	nnngn	5643.52	64.69	6	3.74	0.36	4	-1.49	0.05	2
5345738	nnnGn	5571.04	56.20	7	4.42	0.20	6	-1.10	0.02	3
5594004	nnnnn	5667.30	249.12	6	3.68	0.22	4	-0.31	0.05	4
5778246	nCnnN	0	0	0
5806347	nnngn	4412.53	84.50	3	4.48	0.24	4	-1.24	0.08	2
5816306	nnnnn	6307.92	62.26	9	3.97	0.13	7	-0.50	0.09	5
6072853	nnBnn	5338.77	10.67	6	3.92	0.21	6	-0.71	0.05	5
7906183	nnnnn	4064.71	34.73	2	3.22	0.45	2	-0.44	0.18	1
4425715	nnBgn	5021.44	92.23	6	4.51	0.15	6	-1.32	0.13	4
4548417	nnnnn	5666.38	12.85	5	3.21	0.04	4	-0.82	0.06	3
4659030	NnBnN	0	0	0
4708105	nnBnn	5424.62	26.91	6	4.21	0.08	6	-0.62	0.03	6
4765635	nnngn	5959.19	59.19	7	3.81	0.08	4	-1.15	0.17	3
4769099	VnnnN	0	0	0
4803335	nnnnn	4995.08	111.38	3	4.14	0.04	4	-0.34	0.01	2
4878490	nnnnn	6360.71	138.83	9	3.24	0.14	7	-0.22	0.07	4
5024539	nnngn	4357.46	129.99	1	4.47	0.29	4	-1.57	0.03	2
5066141	nnBnn	5160.09	100.11	3	4.44	0.44	2	-0.85	0.06	1
5080427	nnnnn	6010.02	212.67	5	4.16	0.72	2	-0.15	0.08	1
5410615	nnnnn	5599.19	115.01	4	4.05	0.50	2	-0.70	0.06	1

Table 7.5 (cont'd): SSPP Stellar Parameters for Hectospec Targets

UW ID ^a	flags	T_{eff} (K)	$\sigma(T_{\text{eff}})$ (K)	$N(T_{\text{eff}})^{\text{b}}$	$\log g$ (dex)	$\sigma(\log g)$ (dex)	$N(\log g)^{\text{b}}$	[Fe/H] (dex)	$\sigma([\text{Fe}/\text{H}])$ (dex)	$N([\text{Fe}/\text{H}])^{\text{b}}$
5468373	lnnnR	0	0	0
5484297	nnnnn	5360.53	114.81	3	4.47	0.29	2	-0.34	0.11	1
5497590	nnnnn	4823.58	181.35	3	3.47	0.11	4	-1.37	0.16	3
5522456	nnnGn	5879.15	57.25	8	3.67	0.15	6	-1.32	0.10	5
5523831	nnnnn	4248.83	114.83	2	3.76	0.38	2	-0.43	0.13	1
6039438	NnnnN	0	0	0
6053355	nnnnn	5673.32	96.17	6	3.97	0.14	6	-0.30	0.05	5
6095198	nnnnn	4791.88	91.44	3	2.35	0.26	4	-0.17	0.08	2
6098912	nnnnn	4851.16	93.69	3	4.34	0.14	2	-0.40	0.14	1
4261362	nnngn	5920.31	51.34	7	4.36	0.13	6	-1.06	0.07	6
4283885	LnnnR	0	0	0
4329199	nnnnn	4579.28	71.64	3	4.13	0.00	2	-0.64	0.05	1
4389709	nnnnn	4614.68	60.29	3	4.41	0.12	4	-0.65	0.22	2
4644573	CnnnR	4748.57	45.63	3	3.57	0.13	4	-0.63	0.16	1
4654281	lCnnR	0	0	0
4662395	nnngn	4309.84	54.46	3	4.08	0.17	4	-1.06	0.06	1
5027359	nnnnn	5856.73	55.67	8	3.61	0.10	6	-0.42	0.02	4
5064057	nnnnn	4345.45	41.85	3	3.78	0.31	2	-0.43	0.09	1
5249614	nnnnn	5562.45	148.16	3	4.13	0.57	2	-0.30	0.07	1
5340681	nnnnn	5334.73	95.59	3	3.96	0.21	2	0.55	0.04	1
5346815	nnBnn	5404.46	109.56	3	4.06	0.66	2	-0.57	0.05	1
5564049	nCnnN	0	0	0
5776944	nnnnn	4508.17	322.11	2	4.54	0.06	1	-0.62	0.10	1
5959412	nnnnn	6420.88	49.81	7	4.24	0.29	4	-0.95	0.17	3
6001789	NnnnN	0	0	0
4228167	nnnnR	0	0	0
4286898	NnnnR	0	0	0
4562751	NnnnN	0	0	0
4567747	lnnnn	4192.54	21.98	2	3.88	0.58	2	-0.29	0.14	1
4690982	Dnnnn	4529.91	38.87	3	4.33	0.05	4	-0.30	0.28	1
4809210	nnngn	4035.99	37.21	1	4.22	0.08	2	-1.65	0.24	1
4833879	nnnnn	4481.65	88.78	3	4.14	0.16	4	-0.75	0.20	3
5018848	VnnnX	0	0	0
5099992	nnnnn	4975.38	250.59	3	4.22	0.39	2	-0.78	0.12	1
5202931	nnnnn	4373.08	57.46	3	3.26	0.21	2	-0.93	0.08	1
5269276	nnnnn	5742.76	156.55	3	4.09	0.66	2	-0.51	0.09	1
5320941	nnngn	4549.87	66.42	3	4.30	0.12	4	-1.06	0.12	2
5403910	nnnnn	4185.45	91.23	3	3.62	0.28	4	-0.73	0.18	1
5475188	nnnnn	4641.73	73.04	3	4.26	0.09	4	-0.43	0.19	2
5627070	nnnnN	0	0	0
5710822	nnBnn	4777.01	114.29	3	4.41	0.15	4	-0.75	0.08	2
5768805	nnnnn	5270.40	54.77	4	3.23	0.27	4	-0.57	0.02	3
5837478	nnnnn	4217.52	69.93	2	4.13	0.44	2	-1.71	0.08	1
6096788	nnnnn	5318.18	78.35	4	4.03	0.34	5	-0.14	0.09	2
4173109	nnnnn	5936.57	52.11	7	3.40	0.38	4	-0.83	0.13	3
4284154	nnnnN	0	0	0
4325288	nnnnn	4087.94	76.26	2	2.32	0.09	1	-0.27	0.06	1
4391287	nnnnn	5687.62	46.42	6	3.65	0.03	4	-0.78	0.12	3
4482492	nnnnn	5837.97	54.57	6	4.09	0.20	4	-0.90	0.01	2
4590014	nnnnn	4468.03	55.84	3	4.49	0.21	4	-0.99	0.20	2
4864289	nnBnc	0	0	0
5064073	NnnnN	0	0	0
5082981	nnnnn	4882.02	65.00	3	4.66	0.10	4	-0.79	0.09	3
5133889	nnnnn	5112.80	75.35	4	4.23	0.09	5	-0.50	0.11	3
5166801	LnnnR	0	0	0
5240224	nnnnn	4759.34	207.09	3	4.29	0.53	2	-0.73	0.10	1
5337526	nnnnn	5113.21	76.58	4	3.11	0.15	5	-0.77	0.04	4
5366031	nnnnn	4506.55	56.09	3	4.47	0.12	4	-0.99	0.03	2
5545949	nnngn	4862.92	157.34	4	4.34	0.12	5	-1.10	0.04	3
5641326	nnnGn	4146.89	68.15	2	4.06	0.22	2	-1.74	0.20	1
5721229	nnnnn	6837.96	104.56	3	3.56	0.17	2	-1.09	0.18	1
5798093	nnnGn	5687.80	28.97	4	4.17	0.71	2	-1.11	0.16	1
5904857	nnnnn	5600.25	55.03	6	3.96	0.02	6	-0.16	0.05	5
4153579	nnnnn	4479.53	357.14	2	3.02	0.45	2	-1.94	0.06	1
4218179	nnBnn	5412.59	56.30	5	3.77	0.23	4	0.53	0.17	1
4248360	nnnnn	5839.30	64.17	7	4.16	0.15	6	-0.84	0.04	5
5112072	nnnnn	5956.73	176.88	6	3.05	0.48	3	-1.50	0.08	1
5157921	nnnnn	5481.78	62.66	7	4.36	0.08	6	-0.51	0.03	5
5219842	nnBnn	4747.19	64.42	3	3.84	0.37	2	-0.99	0.09	1
5235927	LnnnR	0	0	0
5361389	nnngn	4787.39	167.49	4	3.92	0.17	5	-1.09	0.09	2
5879075	nnnnn	5968.23	57.32	5	3.94	0.23	2	-1.11	0.08	1
4213227	nnnnN	0	0	0
4697062	nnnnn	4568.51	119.47	3	3.27	0.31	3	-0.72	0.11	3

Table 7.5 (cont'd): SSPP Stellar Parameters for Hectospec Targets

UW ID ^a	flags	T_{eff} (K)	$\sigma(T_{\text{eff}})$ (K)	$N(T_{\text{eff}})^{\text{b}}$	$\log g$ (dex)	$\sigma(\log g)$ (dex)	$N(\log g)^{\text{b}}$	[Fe/H] (dex)	$\sigma([\text{Fe}/\text{H}])$ (dex)	$N([\text{Fe}/\text{H}])^{\text{b}}$
4790997	NnnnN	0	0	0
5380188	nnnnn	6156.87	84.58	9	1.71	0.29	7	-1.67	0.03	6
5757283	Dnnnn	4083.33	6.73	2	1.45	0.19	2	-0.29	0.17	1
6027784	nnBnn	5714.18	141.81	6	4.09	0.26	4	-0.51	0.08	1
5215128	nnnnn	4578.65	99.23	3	4.29	0.14	4	-0.16	0.16	2
5375014	Nnnnn	4823.38	125.04	3	4.37	0.04	2	-0.24	0.07	1
5577612	lnnnR	0	0	0
5678960	lnnnR	0	0	0
6025422	nnnnn	5714.62	44.74	7	4.24	0.22	6	-0.43	0.05	5
4252905	NnBnN	0	0	0
4286313	nnnnR	0	0	0
5025880	nnnnn	4246.32	94.72	3	3.41	0.24	3	-0.86	0.10	1
5113589	nnnnn	6537.79	220.84	5	2.88	0.80	2	-1.54	0.08	1
5285170	nnnnn	4490.21	44.63	3	3.89	0.16	2	-0.60	0.10	1
5796625	nnnnn	5888.27	65.38	7	3.87	0.18	4	-0.37	0.10	5
4175365	nnBnn	4987.06	85.77	4	4.79	0.02	5	-0.86	0.04	3
4205453	NnnnN	0	0	0
4351875	nnnnn	5593.56	44.43	7	4.27	0.07	6	-0.20	0.05	5
4568087	nnnnn	5943.56	5.24	7	3.99	0.08	6	-0.26	0.03	5
4599178	nnnnn	5694.41	36.78	7	4.29	0.07	6	-0.38	0.03	4
4627975	nnnnn	5868.39	346.85	4	3.98	0.14	5	0.10	0.06	2
4812273	nnnnn	4105.43	21.66	1	0.30	0.13	2	-1.41	0.07	2
5056202	nnngn	4326.46	85.34	3	3.99	0.29	4	-1.13	0.19	2
5184909	nnnnn	5411.68	29.58	6	4.01	0.10	6	-0.11	0.08	5
5201427	nnBnn	5643.27	90.81	3	4.05	0.13	2	-0.65	0.05	1
5298684	NnBnN	0	0	0
5305052	nnGn	6181.93	88.61	8	4.06	0.22	6	-1.09	0.04	6
5381639	nnnnn	4922.19	49.03	3	4.02	0.14	4	-0.57	0.13	3
5465075	nnnnn	5099.51	99.67	3	3.60	0.11	4	0.15	0.14	2
5479328	nnnnn	4874.50	115.72	3	4.43	0.08	4	-0.28	0.06	3
5497317	nnnnn	6337.10	159.89	5	4.06	0.82	2	-0.88	0.09	1
5538410	nnBnn	5194.73	91.61	3	4.36	0.13	2	-0.57	0.06	1
5742825	lCnnR	0	0	0
5905612	nnBgn	5780.84	128.45	4	3.42	0.49	2	-1.62	0.08	1
5997567	nnnnn	4954.87	25.45	3	3.28	0.05	4	-0.17	0.06	3
6016949	lnnnn	4012.54	10.85	1	2.58	0.11	1	-0.49	0.09	1
4293585	nnnnn	5487.08	235.26	4	4.10	0.20	4	-0.61	0.35	3
4411279	lnnnR	0	0	0
4421232	nnnGn	5726.63	82.99	6	3.88	0.67	4	-1.18	0.02	3
4475936	nnnnn	5758.30	92.38	7	4.17	0.14	6	-0.65	0.04	6
4500374	nnnnn	5978.40	63.45	8	3.93	0.16	6	-0.81	0.04	5
4581620	nnnnn	7192.24	184.16	7	2.74	0.18	4	-1.36	0.01	2
4661989	nnnnn	7056.31	230.95	8	3.46	0.31	6	-2.36	0.05	4
4806466	nnnnn	5364.14	343.75	3	3.46	0.72	2	-0.49	0.06	1
5058609	nnnnn	5443.28	400.34	4	3.76	0.96	2	-0.59	0.06	1
5332476	nnnnn	5779.31	138.87	4	3.53	0.53	2	-0.54	0.08	1
5336728	nnnnn	4506.53	59.63	3	3.67	0.07	2	-0.49	0.12	1
5427372	nnnnn	5827.46	62.18	4	3.89	0.07	2	-0.46	0.07	1
5453873	nnnnn	4380.69	17.82	3	3.62	0.34	2	-0.11	0.07	1
5470371	nnnnn	4704.62	103.86	3	4.06	0.10	2	-0.26	0.06	1
5474220	nnBgn	5153.83	109.43	4	3.38	0.60	4	-1.04	0.12	2
5482605	nnngn	6084.96	23.77	8	3.88	0.14	6	-1.08	0.07	5
5525841	nnngn	4214.32	123.77	3	4.61	0.19	4	-1.27	0.14	1
5559432	nnnnn	7081.60	78.18	8	4.06	0.37	6	-0.71	0.05	4
5795306	nnngn	4010.45	27.10	1	4.40	0.20	2	-1.57	0.17	1
5824726	nnnnn	4982.59	135.49	3	2.64	0.32	4	-0.15	0.12	3
4318357	nnnnn	5712.12	38.63	6	3.58	0.04	6	-0.16	0.05	5
4490135	NnBnN	0	0	0
4544299	nnnnc	0	0	0
4568412	nnnnn	0	0	0
4583761	nnnnn	4304.46	48.04	3	3.58	0.13	2	-0.43	0.08	1
4781928	nnnnn	5402.92	76.40	6	3.42	0.23	6	-0.89	0.06	6
4791158	nnnnn	5759.92	66.57	7	3.67	0.10	6	0.08	0.06	5
4877746	nnnnn	5166.56	114.02	3	4.39	0.37	2	-0.84	0.06	1
5189026	nnnnn	5957.72	117.24	4	3.63	0.19	2	-0.35	0.06	1
5269627	nnnnn	7544.66	412.56	3	3.24	0.44	2	-1.23	0.11	1
5283053	nnnnn	5975.75	84.09	9	4.15	0.11	7	-0.35	0.08	5
5299329	lCnnR	0	0	0
5306488	nnnnn	5150.40	166.35	3	2.00	0.29	4	-2.01	0.06	4
5410425	nnnnn	5452.37	64.78	6	3.67	0.05	6	0.00	0.07	3
5479187	nnnnn	5796.45	81.71	3	3.83	0.60	2	-0.68	0.08	1
5597583	nnBnn	4893.02	55.15	3	3.97	0.08	4	-0.80	0.17	3
5740902	nnnnc	0	0	0
6076694	nnnnn	5280.75	64.83	6	4.34	0.05	6	-0.37	0.05	5

Table 7.5 (cont'd): SSPP Stellar Parameters for Hectospec Targets

UW ID ^a	flags	T_{eff} (K)	$\sigma(T_{\text{eff}})$ (K)	$N(T_{\text{eff}})^{\text{b}}$	$\log g$ (dex)	$\sigma(\log g)$ (dex)	$N(\log g)^{\text{b}}$	[Fe/H] (dex)	$\sigma([\text{Fe}/\text{H}])$ (dex)	$N([\text{Fe}/\text{H}])^{\text{b}}$
6086097	nnnnn	5291.80	43.68	3	3.84	0.04	2	-0.29	0.09	1
4168900	nnnnn	5628.47	47.63	6	4.35	0.12	6	-0.43	0.02	5
4179388	NnnnnN	0	0	0
4185442	nnnnn	5917.79	89.13	8	4.04	0.10	6	-0.68	0.05	5
4453302	nnnnn	5128.50	100.58	3	4.06	0.29	2	-1.16	0.09	1
4570909	nnnnc	0	0	0
4636337	nnnnn	5027.16	75.88	3	3.27	0.12	4	-0.36	0.10	3
4754899	lnnnR	0	0	0
4783355	nnnnn	5314.38	74.63	6	3.95	0.07	6	-0.11	0.07	5
4840346	nnnnn	7608.80	100.74	5	3.63	0.43	4	-2.15	0.08	1
5070797	nnnnn	4397.53	71.56	3	4.12	0.05	3	-0.45	0.11	1
5156097	nnnnn	5310.95	68.04	6	4.34	0.11	6	-0.41	0.05	6
5265003	nnnnn	5971.72	17.25	5	3.88	0.49	2	-0.71	0.08	1
5308880	nnnnn	5219.43	58.84	4	3.51	0.14	5	-0.68	0.04	3
5309820	nnnnR	0	0	0
5732369	NCBnN	0	0	0
5776101	nnnnn	5670.92	74.72	6	3.73	0.18	4	-0.55	0.02	2
5909223	nnnnn	5347.01	92.33	3	3.82	1.06	2	-0.99	0.06	1
5936196	NnnnR	0	0	0
5958408	nnnnn	6039.78	61.08	7	4.11	0.10	6	-0.02	0.05	4
4181310	nnBnN	5449.82	159.38	4	3.68	0.16	4	-0.49	0.01	2
4213941	nCnnn	6302.09	610.98	3	3.82	0.01	4	-0.54	0.18	2
4365663	nnnnn	5803.31	121.86	4	3.81	0.21	2	-0.71	0.14	1
4472148	nnnnn	5008.10	119.39	4	4.43	0.05	5	-0.50	0.11	4
4724082	nnnnX	0	0	0
4783868	VnBnN	0	0	0
4833579	nnnnn	5258.73	135.13	4	4.15	0.14	5	-0.27	0.04	2
4869087	NCBnN	0	0	0
5278026	nnnnn	4363.55	338.36	2	3.76	0.14	1	-0.54	0.13	1
5374161	lnnnn	4060.79	19.39	1	4.42	0.12	1	-1.28	0.10	1
5416271	nnnnn	5984.59	67.03	8	3.95	0.06	6	-0.90	0.06	7
5467685	nnnnn	5809.20	203.25	5	4.14	0.30	4	-0.70	0.01	6
5631079	nnnnn	6417.87	31.15	8	2.68	0.16	6	-1.69	0.05	6
5717328	nnnnn	4995.13	84.30	3	4.18	0.08	2	0.21	0.08	1
5727259	nnnnn	5258.24	140.11	6	3.10	0.18	4	-0.73	0.10	3
5917586	nnnnn	5690.62	53.52	7	4.11	0.04	6	-0.29	0.03	6
5960762	nnnnn	5182.95	78.35	4	4.14	0.09	5	0.01	0.11	1
4180900	nCnnR	0	0	0
4356083	nnnnn	5937.57	50.11	8	4.39	0.08	6	-0.69	0.01	6
4397885	nnnnn	5206.75	100.34	4	4.40	0.04	5	-0.20	0.05	3
4419214	nnnnN	0	0	0
4474304	lnnnR	0	0	0
4622305	nnnnn	6185.45	114.12	9	2.80	0.29	7	-0.23	0.04	2
4629665	lnnnR	0	0	0
4649719	nnnnN	0	0	0
5020175	nnnnn	4901.23	67.04	3	2.88	0.19	4	-0.27	0.03	2
5027363	NnBnN	4895.15	81.21	3	4.63	0.25	2	-0.61	0.05	1
5175225	nnnnn	4642.91	37.36	3	3.78	0.40	2	-0.48	0.07	1
5179807	nnnnn	4388.29	210.02	2	4.05	0.10	1	-0.32	0.08	1
5192825	nnnnn	6143.61	83.28	5	3.57	0.11	2	0.18	0.09	1
5301384	nCnnn	5081.15	493.41	3	4.38	0.12	3	-0.65	0.02	1
5547784	nnnnn	5670.25	39.36	7	4.17	0.05	6	-0.41	0.06	6
5741009	nnnnn	5274.98	102.22	4	2.49	0.13	5	-0.77	0.04	6
5844582	NnBnN	0	0	0
5919589	nnnnn	5868.85	32.60	8	4.03	0.04	6	-0.28	0.04	4
6076566	nngnGn	6569.78	118.38	7	2.95	0.03	4	-1.54	0.16	2
4167243	nnnnn	5224.13	111.65	3	3.47	0.10	2	-0.56	0.06	1
4228487	nnnnn	5503.01	123.75	4	4.44	0.44	2	-0.45	0.10	1
4296821	nnnnn	7318.75	85.33	6	3.20	0.21	4	-1.96	0.03	3
4297330	nCnnR	0	0	0
4611535	nnnnn	5946.22	48.26	8	3.89	0.06	6	-0.16	0.03	6
4652901	nnnnn	5679.59	34.72	6	4.47	0.19	4	-0.72	0.06	4
4666431	nnnnn	4998.33	96.19	4	4.45	0.06	5	-0.35	0.07	3
5118901	nnnnn	5293.96	76.42	3	3.52	0.31	2	-0.96	0.05	1
5133806	nnnnn	5873.43	58.68	8	4.10	0.22	6	-0.69	0.02	5
5153227	nnnnn	5523.36	132.55	4	3.97	0.08	4	-0.42	0.05	3
5156520	nnngn	5031.36	258.78	3	3.72	0.12	2	-1.37	0.06	1
5322474	VnnnX	0	0	0
5440753	lnnnn	4232.31	178.64	2	4.21	0.35	2	-0.71	0.18	1
5482198	nnnnn	5593.67	24.86	7	3.62	0.01	6	-0.03	0.06	4
5534721	lnnnN	0	0	0
5917179	nnngn	5674.25	109.92	4	3.51	0.27	2	-1.18	0.18	1
5936501	nnnnn	5943.00	75.91	8	4.15	0.13	6	-0.95	0.05	4
6053603	nnnnn	4621.01	80.70	3	4.45	0.14	4	-0.87	0.04	2

Table 7.5 (cont'd): SSPP Stellar Parameters for Hectospec Targets

UW ID ^a	flags	T_{eff} (K)	$\sigma(T_{\text{eff}})$ (K)	$N(T_{\text{eff}})^{\text{b}}$	$\log g$ (dex)	$\sigma(\log g)$ (dex)	$N(\log g)^{\text{b}}$	[Fe/H] (dex)	$\sigma([\text{Fe}/\text{H}])$ (dex)	$N([\text{Fe}/\text{H}])^{\text{b}}$
4310155	nnnnn	4443.75	139.33	3	3.62	0.10	3	-0.27	0.09	1
4334811	nnnnn	5768.09	68.51	8	3.98	0.03	6	-0.54	0.04	6
4529677	nnnnn	4205.01	106.53	3	3.81	0.23	4	-0.66	0.07	1
4562892	nnnnR	0	0	0
4665172	LnnnR	0	0	0
4701571	nnnnN	0	0	0
4793522	nnnnR	0	0	0
5018244	nnngn	5628.05	103.19	4	3.43	0.92	2	-1.36	0.18	1
5026362	nnnnn	4348.39	67.00	3	3.93	0.37	4	-1.40	0.14	1
5048699	nCnnR	0	0	0
5341191	lCnnR	0	0	0
5354429	nnnnn	6009.70	95.37	7	3.36	0.42	4	-0.91	0.02	5
5440766	nnnnn	5416.31	42.91	6	4.01	0.07	6	0.07	0.08	5
5519369	lCnnR	0	0	0
5619051	nnnnn	5999.24	66.66	7	3.90	0.18	4	-0.50	0.08	4
5685938	nnnnn	6123.83	72.86	8	3.80	0.15	6	-0.34	0.02	3
6065457	nnBnn	4980.27	170.12	3	4.12	0.04	2	-0.23	0.08	1
4181156	nCnnR	0	0	0
4185861	nnnnn	5553.84	88.56	6	4.33	0.15	6	-0.85	0.04	5
4221578	nnnnn	5795.31	175.49	6	3.53	0.78	4	-0.42	0.15	3
4630822	nnBnn	4789.89	108.65	3	4.34	0.22	3	-0.33	0.06	1
5015808	nnnnn	5592.03	105.21	6	4.29	0.11	6	-0.41	0.08	5
5080261	nnnnn	4835.73	18.54	3	2.25	0.20	4	-0.61	0.09	5
5491448	nnngn	4438.41	38.14	3	4.46	0.25	3	-1.45	0.10	1
5523473	nnnnn	5464.73	79.71	6	4.16	0.15	6	-0.31	0.06	5
5584584	nnnnn	4419.77	46.27	3	4.04	0.24	3	-0.49	0.08	1
4263341	nnnnn	5962.53	113.92	4	4.33	0.55	2	-0.58	0.05	1
4649457	NnBnn	5211.37	74.50	3	3.21	0.78	2	-0.55	0.07	1
4691314	nnnnn	5790.08	39.15	7	3.56	0.04	6	-0.07	0.05	6
4793729	lnnnn	4081.49	13.38	2	3.57	0.66	2	-0.38	0.31	1
4851079	nnnnn	4785.95	167.88	3	4.63	0.20	2	-0.33	0.06	1
4853321	nnnnR	0	0	0
5124522	nnnnn	5927.95	99.41	5	3.45	0.17	2	-0.71	0.05	1
5169332	nnnnn	5691.63	59.58	7	4.36	0.12	6	-0.83	0.03	5
5256230	nnnnn	5445.98	122.55	4	3.65	0.11	2	-0.88	0.06	1
5439796	nnnnn	6489.68	35.47	8	2.66	0.40	6	-1.81	0.07	5
5551868	nnnnn	4413.54	32.44	3	4.10	0.01	3	-1.06	0.08	1
5554713	nnngn	4036.03	27.98	1	4.42	0.22	2	-3.17	0.14	1
4535705	nnnnn	4433.19	116.55	3	4.29	0.21	4	-0.62	0.07	1
4554840	nnnnn	5635.00	59.16	7	3.64	0.05	6	-0.48	0.02	5
4579723	nnngn	4135.58	75.95	3	4.43	0.25	4	-1.36	0.02	2
4584426	nnnnn	6150.37	60.61	7	3.86	0.18	4	-0.53	0.03	2
4610054	lCnnR	0	0	0
4647683	nnnnn	6647.36	61.71	5	3.71	0.05	2	-0.95	0.03	1
4718860	nnnnn	5862.48	53.11	7	4.14	0.08	6	-0.55	0.05	6
4849621	NnnnN	0	0	0
4864466	nnnnn	4940.68	118.08	3	4.53	0.20	3	-0.88	0.06	1
5037004	nnnnn	6223.19	59.17	8	3.68	0.13	5	-0.64	0.08	5
5076661	nnnnn	5828.38	31.43	7	4.04	0.06	6	-0.15	0.06	6
5114226	nnnnn	5553.18	78.44	6	4.33	0.11	6	-0.38	0.06	7
5215024	nnnnn	4349.73	36.46	3	3.65	0.40	2	-0.37	0.09	1
5276995	nnngn	5635.35	66.45	7	3.59	0.33	6	-1.55	0.07	6
5345107	Nnnnn	4379.69	116.47	3	3.41	0.49	2	-0.40	0.08	1
5398059	nCnnR	0	0	0
5461556	nnnnn	4356.79	101.06	3	3.84	0.28	2	-0.55	0.10	1
5661404	nnnnn	5857.30	198.53	5	4.28	0.25	4	-0.56	0.09	2
5733092	nnnnn	5605.88	61.86	6	3.73	0.11	6	0.06	0.06	3
5860130	nnnnn	4897.51	125.11	4	3.30	0.11	5	-0.94	0.06	4
6036344	VCBnN	0	0	0
4232654	NnnnN	0	0	0
4268040	nnnnn	4920.70	133.82	3	4.66	0.08	4	-0.66	0.07	2
4286504	VnBnX	0	0	0
4480578	nnnnn	5231.10	153.69	3	4.39	0.17	2	-0.44	0.10	1
4483579	nnnnn	4893.16	90.21	3	3.95	0.43	2	-0.43	0.10	1
4628186	nnnnn	6893.21	51.47	8	3.91	0.27	6	-0.74	0.05	6
4685580	nnnnn	6169.71	168.15	5	3.70	0.64	2	-0.61	0.08	1
4698034	nnnnn	4627.56	81.44	3	4.54	0.16	4	-0.92	0.01	2
5028200	nnnnn	4948.44	252.10	3	4.13	0.75	2	-0.59	0.10	1
5031354	NnnnN	0	0	0
5043799	nnnnn	4622.22	181.97	3	4.13	0.29	2	-0.61	0.13	1
5112722	nCnnn	6380.79	370.59	3	4.02	0.86	2	-0.73	0.08	1
5191975	nnnnn	4444.66	82.03	3	4.37	0.19	3	-0.54	0.07	1
5219621	nnnnn	6095.63	52.07	4	4.37	0.40	2	0.14	0.09	1
5230680	nnnnn	5646.20	110.09	4	3.54	0.11	2	-0.14	0.06	1

Table 7.5 (cont'd): SSPP Stellar Parameters for Hectospec Targets

UW ID ^a	flags	T_{eff} (K)	$\sigma(T_{\text{eff}})$ (K)	$N(T_{\text{eff}})^{\text{b}}$	$\log g$ (dex)	$\sigma(\log g)$ (dex)	$N(\log g)^{\text{b}}$	[Fe/H] (dex)	$\sigma([\text{Fe}/\text{H}])$ (dex)	$N([\text{Fe}/\text{H}])^{\text{b}}$
5280426	nnnnn	5704.04	63.87	3	4.09	0.79	2	-0.81	0.07	1
5448390	lnnnR	0	0	0
5486093	nnnnn	5816.45	215.72	4	4.01	0.47	2	-0.77	0.03	1
5499866	nnnnn	5313.56	392.32	3	4.46	0.23	4	-0.69	0.06	1
5674059	nnnnn	4656.11	67.41	3	4.17	0.14	4	-0.55	0.02	2
5915318	nnnnn	6010.77	83.28	7	3.99	0.24	4	-0.52	0.02	5
5959950	NnBnN	0	0	0
4270052	VCBnN	0	0	0
4331009	nngng	4653.56	129.65	3	4.20	0.25	4	-1.23	0.05	2
4583407	nnnnn	6214.73	80.19	8	2.26	0.33	6	-1.45	0.02	5
4773771	nnBnN	0	0	0
4797816	nnnnn	4667.20	121.57	3	4.37	0.21	3	-0.19	0.08	1
5040394	nnnnn	4900.60	113.10	3	4.53	0.11	4	-0.31	0.08	2
5198001	nngng	4800.24	48.22	3	3.25	0.18	4	-1.22	0.02	4
5356472	nnnnn	5131.59	129.68	3	4.13	0.56	2	-0.58	0.16	1
5407370	nnBnn	5525.10	191.87	4	4.24	0.57	3	-0.31	0.12	1
5471440	nnnnn	4753.00	213.65	3	4.18	0.12	3	-0.46	0.09	1
5491927	nnnnn	7317.13	71.16	6	3.96	0.60	4	-0.40	0.12	3
5522980	nnnnn	6428.66	46.10	9	4.08	0.08	7	-0.11	0.05	4
5664870	NnnnN	0	0	0
5683237	nnnnN	0	0	0
5915511	nnnnn	5298.55	43.34	6	4.34	0.09	6	-0.40	0.03	6
6057917	nnnnn	5805.75	47.06	7	4.02	0.08	6	-0.26	0.02	4
4158698	nCnnR	0	0	0
4231688	nnnnn	4816.01	99.50	3	4.54	0.13	4	-0.37	0.15	2
4250356	nnnnn	4426.66	205.58	3	4.23	0.53	2	-2.20	0.24	1
4276118	lCnnR	0	0	0
4418350	Nnnnc	0	0	0
4472398	nmmnR	0	0	0
4703649	nnnnn	4395.92	51.94	3	3.93	0.19	4	-0.32	0.14	2
5038641	nnnnn	4376.37	157.56	2	3.96	0.04	2	-1.46	0.08	1
5038768	nnnnn	4431.03	86.81	3	3.95	0.19	3	-0.41	0.06	1
5045383	nCnnR	0	0	0
5065072	nngng	4860.42	118.95	3	4.71	0.22	3	-1.22	0.26	2
5261270	nnnnn	5190.65	72.83	3	3.62	0.30	2	-0.60	0.12	1
5323750	nnnnc	0	0	0
5334589	nnnnn	5901.93	29.59	8	3.84	0.08	6	-0.52	0.01	6
5413265	NnnnN	0	0	0
5786048	NCnnN	0	0	0
5959316	nnnnn	5292.65	68.47	6	3.76	0.15	6	-0.76	0.05	6
6063206	nnnnn	4624.27	112.02	3	2.66	0.05	4	-0.31	0.04	3
6076874	nnnnR	0	0	0
4167684	nnnnn	4132.50	1.34	2	3.75	0.67	2	-0.39	0.11	1
4262570	nnnnn	6436.87	29.95	8	3.98	0.07	6	-0.31	0.02	3
4329201	nnnnn	6097.50	69.42	9	4.23	0.11	7	-0.55	0.04	4
4479070	nngng	4088.87	20.39	1	4.62	0.04	1	-1.22	0.08	1
4561917	nnnnX	0	0	0
4671501	NnnnN	0	0	0
4734515	nnnnn	5153.54	106.00	4	4.31	0.26	5	-0.83	0.06	3
5023175	nnnnn	4626.81	104.98	3	3.87	0.24	2	-0.31	0.09	1
5048033	nnnnn	4712.69	154.12	3	3.77	0.66	2	-0.87	0.10	1
5127399	nnnnn	4303.71	180.56	2	3.91	0.07	1	-0.50	0.06	1
5200227	nnnnn	5478.84	83.65	6	3.44	0.07	6	-0.22	0.06	5
5223380	nnnnn	5405.31	179.29	4	3.36	0.14	2	-0.40	0.06	1
5367846	Nnnnn	4560.52	123.20	3	4.04	0.07	2	-0.35	0.09	1
5485470	nnnnn	5767.09	59.78	8	4.08	0.05	6	0.12	0.05	5
5575154	nnnnR	0	0	0
5582085	NCnnN	0	0	0
5877004	nnnnn	5442.86	71.09	6	3.95	0.17	6	-0.69	0.02	5
6058985	lCnnR	0	0	0
4171607	nnnnn	5905.23	28.01	8	3.93	0.09	6	-0.58	0.05	6
4303640	nnnnn	5955.46	77.42	8	4.24	0.14	6	-0.65	0.05	3
4531457	NnnnN	0	0	0
4579750	lCnnR	0	0	0
4827230	nnnnn	4877.87	180.02	3	4.39	0.39	3	-0.56	0.11	1
4827455	NnnnN	0	0	0
5020769	nnnnn	5085.03	255.18	3	4.49	0.39	2	-0.43	0.08	1
5152068	nnnnn	5989.60	40.36	5	4.07	0.81	2	-0.66	0.04	1
5214865	VnnnX	0	0	0
5231223	nnnnn	5459.19	111.27	4	4.33	0.15	5	-0.68	0.06	4
5287463	nnBnn	5380.89	72.92	3	4.28	0.09	2	-0.61	0.09	1
5293770	Nnnnn	4245.63	61.20	3	4.20	0.31	2	-1.32	0.11	1
5318045	nnnnn	5307.03	73.86	6	4.17	0.18	6	-0.56	0.06	5
5340121	lnnnn	4055.07	12.02	2	3.43	0.72	2	-0.65	0.11	1

Table 7.5 (cont'd): SSPP Stellar Parameters for Hectospec Targets

UW ID ^a	flags	T_{eff} (K)	$\sigma(T_{\text{eff}})$ (K)	$N(T_{\text{eff}})^{\text{b}}$	$\log g$ (dex)	$\sigma(\log g)$ (dex)	$N(\log g)^{\text{b}}$	[Fe/H] (dex)	$\sigma([\text{Fe}/\text{H}])$ (dex)	$N([\text{Fe}/\text{H}])^{\text{b}}$
5672875	nnnnn	5926.07	53.90	7	3.94	0.03	6	-0.48	0.02	6
6039430	Nnnnn	5405.27	70.86	3	4.19	0.12	2	-0.44	0.09	1
6075152	nnnnn	5184.40	201.37	4	4.44	0.15	5	-0.74	0.08	3
4156215	VnnnX	0	0	0
4181367	NnBnN	0	0	0
4213051	nnnnR	0	0	0
4669237	NnnnN	0	0	0
4671220	nnnnn	5688.20	70.46	7	4.46	0.12	6	-0.45	0.01	5
4697484	nnngn	5219.64	151.56	6	4.35	0.24	6	-1.02	0.04	3
4715112	nnnnn	6207.03	75.93	9	4.01	0.13	7	-1.12	0.05	5
4753521	nnnnn	5961.71	32.75	8	3.97	0.11	6	-0.53	0.01	3
5092359	lCnnR	0	0	0
5120415	nnnnn	5266.86	137.95	5	4.41	0.22	4	-0.48	0.03	2
5234205	nnnnn	6155.37	114.18	7	3.75	0.12	4	-1.17	0.06	4
5295530	nnBnn	5670.79	34.33	4	3.83	0.20	2	-0.70	0.05	1
5329488	nnnnn	4655.00	87.34	3	4.36	0.09	2	-0.63	0.05	1
5426020	nnnnn	5494.71	65.86	3	4.35	0.08	4	-0.50	0.07	3
5434961	nnnnn	5438.65	57.89	7	4.26	0.02	6	-0.26	0.02	5
5468249	nnngn	5726.56	75.74	6	3.71	0.16	4	-1.04	0.04	5
5628885	nnBnn	5101.19	136.97	3	4.17	0.14	4	0.09	0.11	1
5774721	lCnnR	0	0	0
5993462	lnnnR	0	0	0
6093694	nnnnn	4613.48	84.15	3	4.12	0.19	3	-0.21	0.08	1
4201113	nnnnn	4788.67	119.33	3	4.39	0.06	3	-0.17	0.06	1
4363138	nnnnn	4390.45	37.47	3	3.93	0.20	4	-0.22	0.20	1
4440611	nnngn	4551.20	81.12	3	4.48	0.15	4	-1.09	0.03	2
4575178	lnnnN	0	0	0
4767238	nnnnn	5596.41	142.11	7	3.91	0.23	6	-0.69	0.05	4
4779804	nnnnn	6012.82	76.65	5	3.52	0.52	2	-1.20	0.09	1
5170049	nnnnn	5240.87	216.11	3	3.25	0.81	2	-1.23	0.16	1
5182870	nnBnn	6078.88	74.56	4	3.95	0.80	2	-0.88	0.05	1
5222669	nnnnn	5911.11	46.73	8	3.78	0.04	6	-0.15	0.03	5
5223320	nnngn	5346.60	91.59	6	3.65	0.12	6	-1.13	0.01	5
5327678	nnnnn	4606.26	60.82	3	4.03	0.01	2	-0.50	0.08	1
5328925	nnnnn	5979.45	73.90	8	3.70	0.05	6	-0.34	0.02	4
5393047	NnnnN	0	0	0
5475809	nnnnn	4496.07	204.40	3	3.97	0.47	2	-1.80	0.29	1
5713115	nnnnn	6137.46	71.61	8	3.65	0.58	5	-0.90	0.16	2
5840701	NnnnR	0	0	0
5844389	nnnnn	6064.77	62.34	4	3.50	0.50	2	-0.48	0.06	1
5864714	nnnnn	4781.73	110.11	3	4.45	0.09	4	-0.42	0.06	1
6001143	VnnnN	0	0	0
4251181	lnnnn	4087.08	23.19	1	4.32	0.08	2	-0.96	0.15	1
4301093	nnnnn	7167.53	65.81	9	3.31	0.18	7	-2.12	0.08	4
4588341	nnnnn	6083.45	139.21	4	3.78	0.33	2	-0.41	0.10	1
4621450	nnnnn	5988.70	255.28	6	4.51	0.08	6	0.59	0.00	2
4784551	nnnnn	5637.01	83.85	6	2.70	0.45	4	-1.23	0.09	2
5155139	nnnnn	5049.87	130.21	3	4.26	0.19	2	-0.12	0.07	1
5250576	nnnnn	5397.46	58.42	5	4.24	0.09	4	-0.73	0.05	4
5298579	nnnnn	4981.71	139.46	3	3.65	0.02	4	0.06	0.17	2
5311211	lnnnR	0	0	0
5430492	nnnnn	5877.37	98.60	6	3.84	0.24	4	-0.75	0.03	3
5621156	nnBnn	5069.21	72.34	4	3.34	0.11	5	-0.32	0.11	4
5760106	nnnnn	5715.66	82.65	7	3.86	0.11	6	0.08	0.04	3
4507424	nnnnn	4478.86	75.07	3	4.15	0.01	3	-0.32	0.10	1
4551171	NnnnN	0	0	0
4634148	nnnnn	6007.17	45.12	6	2.94	0.61	3	-1.26	0.01	2
4779745	nnnnn	7858.82	152.89	5	4.18	0.39	5	-1.16	0.10	3
5024028	nnnnn	5912.92	231.06	3	4.10	0.38	2	-0.32	0.04	1
5109704	nCnnR	0	0	0
5148542	nnnnn	5494.36	70.78	6	3.89	0.08	6	-0.26	0.08	4
5221582	nnnnn	5801.43	391.35	3	3.80	0.11	4	-0.75	0.06	2
5278664	nCnnR	0	0	0
5396522	nnBnn	5359.92	148.77	3	4.54	0.33	2	-0.55	0.08	1
5425638	nnnnn	6116.49	129.28	5	4.24	0.32	2	-0.20	0.07	1
5487181	nnnnn	4481.66	50.42	3	4.11	0.25	3	-0.28	0.07	1
5517851	NnnnN	0	0	0
5684279	nnnnn	4685.20	209.04	3	2.30	0.24	4	-0.89	0.05	2
5691195	nnnnn	5506.16	148.99	6	4.08	0.27	4	-0.95	0.06	5
5827824	lnnnn	4102.16	38.54	2	3.65	0.64	2	-0.62	0.12	1
4207496	nnnnn	4492.44	119.82	3	3.69	0.03	4	-1.24	0.15	1
4352263	nnnnn	4083.40	12.75	2	3.75	0.55	2	-0.57	0.12	1
4371706	nnnnn	5411.25	67.12	6	3.92	0.07	6	-0.31	0.04	4
4454223	lnnnn	4351.12	112.40	3	3.39	0.52	2	-0.14	0.12	1

Table 7.5 (cont'd): SSPP Stellar Parameters for Hectospec Targets

UW ID ^a	flags	T_{eff} (K)	$\sigma(T_{\text{eff}})$ (K)	$N(T_{\text{eff}})^{\text{b}}$	$\log g$ (dex)	$\sigma(\log g)$ (dex)	$N(\log g)^{\text{b}}$	[Fe/H] (dex)	$\sigma([\text{Fe}/\text{H}])$ (dex)	$N([\text{Fe}/\text{H}])^{\text{b}}$
4671488	nnnnn	4753.74	165.37	3	4.54	0.15	4	-0.66	0.01	2
4765216	Dnnnn	4778.58	97.36	3	3.18	0.25	4	-0.31	0.00	2
5063357	nnnnR	0	0	0
5081763	NnBnN	0	0	0
5121169	nnnnn	5786.16	33.65	7	4.34	0.17	6	-0.55	0.06	7
5160762	nnnnn	4552.47	115.81	3	4.29	0.22	4	-0.55	0.12	1
5196513	nnnnn	6321.77	48.29	9	3.87	0.09	7	-0.41	0.02	6
5338660	nnnnn	7160.73	75.51	7	3.28	0.24	5	-0.96	0.01	3
5497059	ICnnR	0	0	0
5497391	nnnnn	5754.21	51.59	6	4.07	0.05	6	-0.07	0.06	5
5892957	NnnnN	0	0	0
6003779	nCnnN	0	0	0
4296051	nnnnn	5259.68	55.35	6	4.40	0.14	6	-0.76	0.03	6
4350446	nnnnn	5086.58	132.28	3	4.62	0.12	4	-0.06	0.13	2
4594448	nnnnn	4112.62	20.50	1	2.65	0.11	1	-0.38	0.10	1
4595639	nCnGn	5128.92	74.38	6	4.21	0.32	6	-1.43	0.11	1
4663790	nnnnn	4832.06	57.91	3	3.17	0.01	4	-0.71	0.11	3
4740705	nnBnn	5016.15	62.55	3	4.38	0.18	4	-0.26	0.20	1
5034632	nnnnn	4543.62	77.52	3	3.75	0.05	2	-0.78	0.08	1
5113491	nnnnn	5789.60	103.92	8	4.24	0.12	6	-0.41	0.05	3
5242984	nnnnn	5889.94	68.16	7	3.75	0.07	6	-0.15	0.07	5
5339584	NnnGn	4465.29	39.39	3	3.59	0.07	2	-1.09	0.09	1
5344540	nnBGn	7000.02	175.84	8	3.89	0.35	6	-2.13	0.07	4
5369342	nnnnn	5774.15	55.41	8	4.13	0.13	6	-0.49	0.03	7
5388057	nnnnn	6054.72	49.07	6	3.42	0.58	3	-0.54	0.01	2
5429184	nnBgn	4886.81	197.39	3	3.66	0.19	2	-1.26	0.06	1
5801202	nnBgn	5229.73	30.55	4	3.38	0.22	5	-0.57	0.06	4
5901161	NnBnN	0	0	0
5944472	nnnnn	4361.53	83.20	3	3.56	0.26	3	-0.41	0.06	1
5987745	ICnnR	0	0	0
6049004	nnnnn	5719.62	117.45	7	4.29	0.14	6	-0.56	0.06	2
4179546	nnngn	4310.52	46.09	3	4.19	0.29	4	-1.16	0.21	2
4269397	nnnnn	5883.16	38.62	5	3.91	0.68	2	-0.73	0.04	1
4293494	nnnnN	0	0	0
4497526	nnnnn	4367.14	94.85	3	4.09	0.15	4	-0.39	0.03	2
4507321	nnBnn	6472.42	233.91	5	3.45	0.13	2	-1.50	0.06	1
4624403	lnnnR	0	0	0
4784589	nCBnn	4932.52	455.99	3	4.10	0.66	2	-0.95	0.06	1
5173173	nnBnn	5216.42	87.11	4	3.72	0.30	4	-0.79	0.20	2
5262182	nnnnn	5645.52	54.51	4	3.90	0.24	2	-0.65	0.05	1
5294278	Nnnnn	4491.67	72.64	3	4.14	0.02	2	-0.50	0.06	1
5315154	nnBnn	5022.85	53.80	3	3.94	0.13	2	-1.11	0.07	1
5407021	nnnnn	7860.49	40.97	4	3.80	0.35	3	-1.15	0.08	1
5627757	VnnnN	0	0	0
5643257	nnnnn	5684.67	160.53	4	4.03	0.31	2	-0.85	0.05	1
5651296	VCBnX	0	0	0
5797904	nnnnn	7167.80	48.65	8	4.23	0.39	6	-0.58	0.03	6
4206445	nnBnn	5127.87	181.41	3	4.40	0.48	2	-0.55	0.07	1
4206526	nnnnR	0	0	0
4206887	lnnnn	4269.94	44.56	3	3.60	0.31	2	-0.17	0.13	1
4272197	nnnnn	6432.31	46.20	8	3.62	0.07	6	-1.00	0.01	5
4282392	nnnnn	4393.77	60.61	3	4.61	0.37	3	-0.87	0.09	1
4502185	NnnnN	0	0	0
4630901	ICnnR	0	0	0
4771332	NCnnR	0	0	0
5053165	nnnnn	5325.05	55.03	6	4.35	0.11	6	-0.18	0.05	5
5130311	nnnnn	5377.68	178.62	6	4.24	0.11	4	-0.87	0.12	3
5141965	Nnnnn	4482.20	86.06	3	4.44	0.44	2	-0.99	0.05	1
5199565	lnnnR	0	0	0
5246095	nnnnn	4279.21	58.69	3	3.50	0.14	4	-0.80	0.18	3
5320667	nnngn	4225.77	119.65	2	3.73	0.11	1	-1.04	0.06	1
5407991	nnnnn	5572.27	68.65	7	4.23	0.10	6	-0.33	0.05	5
5453551	nnnnn	5615.85	50.20	7	4.18	0.14	6	-0.83	0.04	5
5624886	nnnnn	5969.91	54.98	8	4.13	0.08	6	-0.54	0.01	4
5805875	NCnnN	0	0	0
5829601	nnnnn	5175.46	8.72	4	3.42	0.10	5	-0.78	0.06	4
6021103	NnBnN	0	0	0
4243407	NnnnN	0	0	0
4272883	nnnnn	6254.38	239.01	7	1.79	0.35	6	0.24	0.05	3
4349342	nnBnn	5344.13	80.63	6	4.37	0.14	6	-0.72	0.04	6
4454531	nnngn	4538.84	99.27	3	4.58	0.21	4	-1.21	0.11	1
4585657	NnBnN	0	0	0
4598723	nnnnn	5959.40	81.40	7	3.95	0.10	6	-0.62	0.03	6
4823871	nCnnR	0	0	0

Table 7.5 (cont'd): SSPP Stellar Parameters for Hectospec Targets

UW ID ^a	flags	T_{eff} (K)	$\sigma(T_{\text{eff}})$ (K)	$N(T_{\text{eff}})^{\text{b}}$	$\log g$ (dex)	$\sigma(\log g)$ (dex)	$N(\log g)^{\text{b}}$	[Fe/H] (dex)	$\sigma([\text{Fe}/\text{H}])$ (dex)	$N([\text{Fe}/\text{H}])^{\text{b}}$
4831252	nnBnn	5135.11	55.74	3	4.29	0.18	2	-0.73	0.07	1
4856793	nCnnn	4959.94	107.55	3	4.61	0.12	4	-0.74	0.01	2
5135121	nnnnn	5706.63	40.95	7	3.87	0.04	6	-0.16	0.06	7
5221401	nnnnn	5191.50	153.20	4	3.32	0.20	5	-0.70	0.03	2
5277832	nnnnn	5548.06	63.13	7	4.16	0.06	6	-0.30	0.02	5
5304582	nnnnn	4860.59	97.05	3	3.31	0.11	4	-0.10	0.08	3
5355823	nnnnn	5616.15	62.09	6	4.18	0.11	4	-0.55	0.06	5
5423335	nnnnn	6138.67	119.17	5	3.47	0.17	2	-0.46	0.07	1
5452290	nnnnn	5973.19	86.98	8	4.08	0.16	6	-0.49	0.06	7
5454673	nnBnn	5510.99	75.74	7	3.95	0.03	6	-0.52	0.07	6
5578948	nnnnR	0	0	0
5721197	lnnnR	0	0	0
5740448	NnnnN	0	0	0
5851213	VnnnX	0	0	0
5859425	nnngn	4608.79	46.66	3	4.56	0.19	4	-1.07	0.18	1
4193073	nnnGn	4819.56	36.13	3	3.30	0.03	4	-1.02	0.04	3
4253326	lCnnR	0	0	0
4301266	nnBnn	4885.08	115.35	3	4.47	0.11	4	-0.97	0.07	3
4333676	NCBnN	0	0	0
4388570	VnnnX	0	0	0
4399568	lCnnR	0	0	0
4617576	nCnnN	0	0	0
5047074	nnnnn	5670.78	197.86	5	3.89	0.21	2	-0.73	0.07	1
5072009	nnBnN	0	0	0
5101284	nnnnn	5678.92	94.49	6	3.98	0.09	4	-0.52	0.20	3
5145048	nnnnn	6277.22	50.89	6	3.53	0.55	3	-1.26	0.04	1
5188908	nnnnn	6084.47	72.59	8	3.88	0.18	6	-0.81	0.07	3
5228913	nnnnn	5788.97	62.59	8	3.45	0.13	6	-0.25	0.04	5
5427787	nnnnn	5644.27	67.31	7	4.27	0.11	6	-0.43	0.03	5
5486031	nnnnn	5836.66	148.57	4	3.84	0.32	2	-0.50	0.05	1
5486074	nnnnn	5565.69	60.06	7	4.17	0.12	6	-0.29	0.06	6
5527492	nnnnn	4425.09	63.80	3	4.11	0.20	4	-1.09	0.03	2
5751409	nnnnn	5695.83	110.17	7	3.58	0.06	6	-0.09	0.02	3
5839958	nnnnn	5407.78	146.52	3	4.21	0.66	2	-0.48	0.07	1
5907315	nnngn	4355.53	13.96	3	4.08	0.03	4	-1.05	0.10	1
4177794	nnnnn	4415.85	57.47	3	4.31	0.20	4	-0.90	0.04	2
4247914	lnnnR	0	0	0
4517743	nnnnn	4639.66	119.58	3	4.23	0.14	4	-0.92	0.07	2
5308025	LnnnR	0	0	0
5336609	nnnnn	7155.53	14.46	6	3.74	0.31	4	-1.60	0.05	1
5394853	NnBnn	5486.37	96.77	3	3.07	0.07	2	-0.63	0.05	1
5710229	nnnnn	5705.08	45.50	6	3.81	0.19	4	-0.73	0.05	3
5743515	nnnnn	5391.67	111.53	4	3.33	0.17	5	-0.40	0.06	4
5792618	NnnnN	0	0	0
4165544	nnnnn	5711.74	40.63	8	4.11	0.11	6	-0.50	0.06	5
5095823	nnnnn	5891.53	115.94	7	3.72	0.03	4	-0.45	0.08	3
5449759	nnnnn	5873.61	92.76	6	4.35	0.31	4	-0.90	0.04	3
5644394	nnnnn	5958.12	87.50	6	4.07	0.35	4	-0.65	0.10	4
4199866	nnnnn	6143.11	67.78	5	3.74	0.23	2	-0.37	0.07	1
4210125	nnnnn	7438.19	81.74	6	3.71	0.48	4	-1.32	0.10	2
4235313	nnngn	4010.90	17.26	1	4.50	0.04	1	-1.48	0.08	1
4295801	nnnnn	5894.96	351.96	4	4.84	0.43	3	-0.01	0.01	2
4601262	lnnnX	0	0	0
4770073	nnBnn	5470.88	186.94	6	3.79	0.21	4	-0.22	0.04	4
4786424	nnnnn	5186.20	86.77	4	4.33	0.09	5	-0.16	0.10	3
4823731	nnnnn	5969.43	121.66	4	4.40	0.42	2	-0.35	0.05	1
5151881	nnnnn	4477.46	143.25	3	3.84	0.14	2	-0.29	0.07	1
5151952	nnnnn	5650.60	392.86	3	3.99	0.62	2	-0.26	0.05	1
5321780	nnnnn	6931.36	52.50	8	4.14	0.10	6	-0.41	0.04	6
5489534	nnnnn	5816.36	150.21	4	4.22	0.59	2	-0.59	0.06	1
5566386	nnnnn	5709.60	34.16	6	3.73	0.20	4	-0.37	0.13	4
5639640	nnnnn	7302.02	73.77	5	4.26	0.23	3	-0.03	0.07	2
5939385	nnnnn	5467.69	73.39	5	3.95	0.11	4	-0.79	0.04	4
5986904	NnnnR	0	0	0
4215781	nnnnn	5319.57	78.20	6	4.36	0.05	6	-0.30	0.03	5
4251951	nnnnn	4246.76	78.20	3	3.44	0.42	2	-0.55	0.09	1
4418211	nnnnn	4308.43	51.03	3	3.56	0.17	4	-0.52	0.22	2
4452929	nnbnn	0	0	0
4470713	NCnnR	0	0	0
4545616	NnBnn	0	0	0
4778692	nnnnn	4742.91	73.03	3	4.62	0.14	4	-0.96	0.08	3
4866431	nnnnn	5029.46	96.69	3	3.42	0.10	4	0.35	0.14	2
5170239	nnBnn	5080.61	58.79	4	4.44	0.10	5	-0.28	0.08	3
5205970	nnnnn	4739.74	91.73	3	4.41	0.17	3	-0.23	0.10	1

Table 7.5 (cont'd): SSPP Stellar Parameters for Hectospec Targets

UW ID ^a	flags	T_{eff} (K)	$\sigma(T_{\text{eff}})$ (K)	$N(T_{\text{eff}})^{\text{b}}$	$\log g$ (dex)	$\sigma(\log g)$ (dex)	$N(\log g)^{\text{b}}$	[Fe/H] (dex)	$\sigma([\text{Fe}/\text{H}])$ (dex)	$N([\text{Fe}/\text{H}])^{\text{b}}$
5264082	nnnnn	5483.33	82.25	6	4.17	0.02	6	-0.26	0.06	7
5335251	nnBgn	5356.01	138.56	3	4.30	0.50	3	-1.36	0.06	1
5415976	nnnnn	5535.00	95.86	3	3.90	0.38	2	-0.48	0.06	1
5438193	nnnnn	4569.18	54.10	3	3.96	0.21	2	-0.21	0.08	1
5536726	nnnnn	4421.59	202.50	2	3.91	0.09	1	-0.40	0.07	1
5601177	nnnnn	5583.47	100.42	7	3.97	0.11	6	-0.40	0.02	4
5935951	1CnnR	0	0	0
6031888	Dnnnn	4758.03	134.41	3	4.36	0.15	2	-0.24	0.14	1
4156287	Nnnnn	4937.85	164.47	3	4.03	0.25	2	-0.13	0.07	1
4286668	VCBnN	0	0	0
4492296	nnnnn	4305.05	63.63	3	4.39	0.30	3	-0.88	0.11	1
4539980	nnnnn	5164.91	78.51	4	4.58	0.08	5	-0.32	0.11	2
4721332	nnnnn	4742.75	81.61	3	4.13	0.14	4	-0.37	0.09	2
4876038	NnnnN	0	0	0
5066236	nnnnn	5502.65	43.35	6	3.87	0.16	6	-0.20	0.05	5
5083903	nnnnn	6357.65	33.65	9	3.97	0.07	7	-0.10	0.02	4
5138226	nnnnn	4991.15	195.47	3	4.69	0.12	4	-0.72	0.12	2
5177468	nnnnn	4798.14	132.44	3	3.97	0.03	4	-0.22	0.11	1
5204041	nnnnn	5945.48	49.10	8	4.09	0.09	6	-0.61	0.04	7
5372130	NnBnN	0	0	0
5408442	NnnnN	0	0	0
5472550	nnngn	4938.99	80.16	3	4.56	0.32	2	-1.28	0.08	1
5496387	nnnnn	4739.01	130.43	3	4.30	0.17	4	-0.58	0.11	1
5500045	NnnnN	0	0	0
5705109	nnnnn	5012.52	57.34	3	3.80	0.08	4	-0.59	0.09	3
5756509	nnnnn	5682.60	229.57	4	3.97	0.20	2	-0.52	0.05	1
5978231	nnnnn	6166.18	108.89	5	4.09	0.66	2	-0.56	0.07	1
4215736	nnnnn	4301.24	84.23	3	3.77	0.06	2	-0.85	0.08	1
4271742	nnnnn	5597.95	135.26	7	3.65	0.15	6	-0.58	0.03	4
4350964	nnnnnc	0	0	0
4359532	nnnnn	5461.48	35.53	6	3.61	0.08	6	-0.38	0.00	5
4423548	nnnnn	5224.76	57.66	3	4.28	0.11	4	-0.56	0.07	3
4496027	nnnnn	4231.72	92.14	3	3.37	0.45	2	-0.47	0.10	1
4808354	nnnGn	4010.91	17.00	1	3.17	0.16	1	-2.36	0.13	1
4822466	nnnnn	5438.88	31.19	5	4.09	0.12	4	-1.37	0.06	2
4862793	nnnnn	4669.46	34.78	3	4.19	0.12	4	-0.31	0.03	2
5033582	nnBnn	5811.50	85.83	6	3.91	0.27	4	-0.43	0.06	5
5144032	lnnnR	0	0	0
5207755	nCnnn	4721.16	95.88	3	2.48	0.26	4	-0.28	0.13	1
5265529	nnBnn	5251.55	147.98	3	4.52	0.07	4	-0.31	0.08	3
5278624	lnnnR	0	0	0
5350993	nnbnn	0	0	0
5381837	nnnnn	5808.61	154.05	5	3.81	0.30	2	-0.54	0.08	1
5402428	nnnnn	5075.61	127.62	3	4.39	0.49	2	-0.82	0.07	1
5404890	1CnnR	0	0	0
5638079	nnnnn	4627.86	84.46	3	4.46	0.13	4	-0.44	0.01	2
5732452	NnBnN	0	0	0
5958505	nnBnn	4937.63	92.43	3	4.38	0.44	3	-0.90	0.07	1
6013611	nnnnn	6129.14	28.41	5	3.89	0.17	2	-0.81	0.07	1
4287548	nnnnR	0	0	0
4375085	Nnnnn	4512.44	68.68	3	4.27	0.20	2	-1.22	0.05	1
4424074	nnnnR	0	0	0
4556384	nnnnR	0	0	0
4630445	nnnnR	0	0	0
4682846	nnBnn	4540.33	150.96	3	2.51	0.60	3	-0.64	0.09	1
5084981	nnnnR	0	0	0
5222741	nnBnn	5345.89	113.80	3	3.85	0.29	2	-0.69	0.04	1
5234043	Nnnnn	4725.76	186.98	2	4.11	0.06	1	0.16	0.06	1
5360699	nnnnn	6356.36	82.49	8	3.12	0.13	6	-2.33	0.03	5
5370596	nCnnR	0	0	0
5394663	nnnnn	5476.50	34.47	4	4.11	0.16	5	-0.90	0.08	3
5460151	nnnnn	5593.30	74.15	7	4.14	0.11	6	-0.31	0.04	5
5551525	nnnnn	5600.51	101.23	3	3.93	0.31	2	-0.72	0.22	1
5716124	NnnnN	0	0	0
5788086	nnnnn	4851.44	111.15	3	4.51	0.15	4	-0.91	0.09	3
4174087	nnnnn	4898.42	51.70	3	3.72	0.06	4	-0.65	0.10	4
4265895	nnnnn	5061.58	146.49	5	4.03	0.19	4	-1.07	0.05	1
4648541	nnnnn	6383.25	144.88	5	3.54	0.03	2	-0.64	0.04	1
4690890	nnnnn	6068.80	39.77	8	3.88	0.03	6	-0.04	0.03	6
4719546	nnnnn	5847.04	51.73	7	4.22	0.12	6	-0.65	0.07	5
4789551	nnnnn	5811.08	93.49	7	4.15	0.13	6	-0.24	0.07	4
4810447	Nnnnn	4684.97	143.80	3	4.06	0.21	2	-0.02	0.08	1
5114966	nnngn	5904.92	85.14	4	2.90	0.08	2	-1.06	0.09	1
5165337	nnBnn	5304.57	85.59	4	4.77	0.18	4	-0.90	0.05	3

Table 7.5 (cont'd): SSPP Stellar Parameters for Hectospec Targets

UW ID ^a	flags	T_{eff} (K)	$\sigma(T_{\text{eff}})$ (K)	$N(T_{\text{eff}})^{\text{b}}$	$\log g$ (dex)	$\sigma(\log g)$ (dex)	$N(\log g)^{\text{b}}$	[Fe/H] (dex)	$\sigma([\text{Fe}/\text{H}])$ (dex)	$N([\text{Fe}/\text{H}])^{\text{b}}$
5230035	1CnnR	0	0	0
5273190	NCBnN	0	0	0
5343910	nnnnn	4339.97	34.04	3	3.98	0.16	4	-0.91	0.04	2
5360716	nnnnn	7939.74	100.42	4	3.65	0.08	3	-1.04	0.06	1
5383358	nnBnn	5155.24	80.98	4	4.38	0.08	5	-0.33	0.13	2
5399864	nnnnn	6608.51	31.53	8	4.09	0.13	6	-0.08	0.02	6
5474989	NnnnR	0	0	0
5689371	nnnnn	4980.81	65.46	3	4.55	0.08	4	-0.52	0.12	2
5694605	lnnnR	0	0	0
5719716	nnnnn	4996.23	69.37	4	4.26	0.26	4	-0.45	0.05	1
5957334	nCnnN	0	0	0
4164314	nGnGn	4270.00	98.11	2	4.43	0.21	4	-1.11	0.10	1
4188154	NnBnN	0	0	0
4330811	1CnnR	0	0	0
4387950	nGnGn	6109.85	176.84	7	3.82	0.58	4	-1.11	0.01	2
4388794	nnnnn	6017.06	103.92	5	3.68	0.33	2	-0.90	0.04	1
4483416	nnnnn	4750.89	86.01	3	4.28	0.16	4	-0.14	0.09	3
4519835	nnnnn	4624.70	101.04	3	3.40	0.09	4	-0.85	0.10	1
4604373	NCBnN	0	0	0
4680902	nnnnn	4388.91	34.94	3	4.15	0.28	4	-0.34	0.10	1
4796789	Nnnnc	0	0	0
4830348	nnnnn	4550.80	87.05	3	2.87	0.03	2	-0.83	0.06	1
5072432	nnnnn	5602.94	114.45	3	4.03	0.18	2	-0.53	0.05	1
5162460	nnnnn	7745.79	42.80	4	3.99	0.30	3	-1.24	0.10	1
5311376	nnnnn	4709.06	59.68	3	4.35	0.23	3	-0.12	0.07	1
5382596	nnnnn	4419.99	107.39	3	4.11	0.18	4	-0.75	0.04	2
5752827	nnnnn	4342.98	19.74	3	3.76	0.20	3	-0.52	0.08	1
5772026	nnnnN	0	0	0
5826280	nnnnn	5868.87	39.21	7	4.09	0.06	6	0.03	0.05	6
5836188	nnBnN	5713.20	98.57	4	3.60	0.03	2	-0.87	0.18	1
5882064	nnnnn	4772.13	69.13	3	2.53	0.26	4	-1.11	0.10	3
5933526	nnnnR	0	0	0
4186874	nCnn	4868.07	89.73	6	3.98	0.07	6	-0.76	0.08	4
4292547	nnnnn	6660.69	120.62	5	3.46	0.24	2	-2.10	0.38	1
4302757	nnnnn	5887.54	72.55	7	3.59	0.42	4	-0.47	0.04	4
4596440	NnnnN	0	0	0
4625435	nnnnn	4558.88	48.96	3	4.18	0.26	3	-1.30	0.09	1
4626372	nnnnn	5838.88	37.57	7	3.85	0.08	6	-0.29	0.02	6
4681235	nnnnn	6446.66	98.78	8	3.33	0.12	5	-2.25	0.08	4
4706650	NnnnN	0	0	0
5051154	nnnnn	4381.84	19.09	3	4.34	0.18	4	-0.91	0.04	1
5091390	lCnnR	0	0	0
5099132	nnnnn	5300.56	129.67	5	3.24	0.31	4	-0.61	0.03	3
5169850	nnnnn	5676.39	66.30	4	4.04	0.03	2	-0.71	0.06	1
5443831	nnnnn	5955.04	25.86	7	4.20	0.12	6	-0.73	0.07	3
5884395	nnnnn	5887.01	89.37	8	3.78	0.14	6	-0.77	0.05	6
6035940	nnnnn	5370.84	32.65	6	3.93	0.04	6	-0.44	0.04	6
6080141	1CnnR	0	0	0
4179634	nnnnn	4505.36	91.41	3	4.09	0.07	3	-0.70	0.10	1
4194247	nnnnn	4558.89	129.84	3	4.35	0.13	3	-0.64	0.07	1
4408709	nnnGn	5058.94	113.09	3	3.75	0.21	2	-1.06	0.12	1
4428830	NCnnR	0	0	0
4638381	nnnnn	5326.07	56.51	6	4.36	0.06	6	-0.36	0.02	6
5029357	nnnnn	4991.34	134.79	3	4.41	0.11	3	-0.20	0.07	1
5391125	nnngn	4750.59	95.32	3	4.57	0.11	4	-1.03	0.07	3
5478542	nGnGn	4092.95	37.03	1	4.36	0.13	2	-1.27	0.27	1
5557266	nnnnn	5770.12	65.16	7	4.33	0.14	6	-0.33	0.05	6
5914357	NnnnN	0	0	0
4683866	VnBnX	0	0	0
4779344	nnnnn	5040.26	133.19	4	4.56	0.30	5	-0.86	0.05	2
5227940	nnnnn	5833.64	80.08	8	4.03	0.11	6	-0.10	0.03	5
5326104	nnnnn	7098.62	102.82	8	3.74	0.24	6	-2.07	0.06	4
5886061	nnnnn	4598.94	139.79	3	4.38	0.50	2	-1.13	0.08	1
4668708	lCnnR	0	0	0
4880732	nnnnn	6213.12	171.86	4	3.58	0.20	2	-0.67	0.06	1
5057197	nnnnn	5761.05	53.02	7	3.75	0.01	6	-0.03	0.06	5
5236714	nnBnn	5104.47	68.77	6	3.03	0.20	6	-0.74	0.08	6
5251860	nnnnn	4882.35	99.85	3	4.41	0.10	4	-0.47	0.03	1
5883698	nnBnn	5503.87	107.66	4	4.19	0.20	5	-0.34	0.05	3
5038837	nnnnn	5927.80	56.63	5	3.71	0.26	2	-0.69	0.12	1
5050238	nnBnn	5288.80	56.11	3	4.08	0.26	4	-0.51	0.14	3
5292648	nnnnn	4369.08	52.85	3	3.84	0.02	2	-0.62	0.07	1
5374523	nnnnn	5525.30	81.44	6	3.83	0.24	6	-0.25	0.03	3
5486150	nnnnn	4716.37	28.16	3	3.42	0.23	4	-0.54	0.13	3

Table 7.5 (cont'd): SSPP Stellar Parameters for Hectospec Targets

UW ID ^a	flags	T_{eff} (K)	$\sigma(T_{\text{eff}})$ (K)	$N(T_{\text{eff}})^{\text{b}}$	$\log g$ (dex)	$\sigma(\log g)$ (dex)	$N(\log g)^{\text{b}}$	[Fe/H] (dex)	$\sigma([\text{Fe}/\text{H}])$ (dex)	$N([\text{Fe}/\text{H}])^{\text{b}}$
4184861	nnnnn	5694.26	244.41	3	4.06	0.14	4	-0.47	0.04	3
4197023	nnBnn	5974.79	152.37	4	3.50	0.00	2	-0.44	0.05	1
4198140	nnnnn	6524.93	271.75	8	2.28	0.50	6	0.59	0.00	2
4227143	nnnnn	5833.43	163.47	5	2.08	0.73	2	-0.81	0.09	1
4294038	nCnnR	0	0	0
4323871	nnnnn	5104.78	42.97	3	3.92	0.10	2	-0.26	0.08	1
4490989	nnnnn	4419.55	74.27	3	4.01	0.09	4	-0.51	0.06	1
4538520	nnnnn	5927.06	129.97	4	3.84	0.25	2	-0.88	0.06	1
4771978	nnBnn	5684.29	89.05	6	4.12	0.12	4	0.11	0.07	4
4798324	nnnnn	6466.98	92.52	5	4.21	0.67	2	-1.26	0.05	1
4862886	nnnnn	4343.94	74.23	3	3.88	0.27	4	-0.45	0.09	1
5092477	nnnnn	5356.90	25.72	5	3.82	0.28	4	-0.95	0.11	4
5104640	nnnnn	6036.53	70.57	7	4.29	0.31	4	-0.54	0.12	5
5185001	nnBnn	5678.68	363.05	3	4.32	0.56	2	-0.33	0.06	1
5241235	Nnnnn	4612.43	112.39	3	4.31	0.19	3	-0.20	0.08	1
5252961	nnnnn	5097.57	79.99	6	4.33	0.10	6	-0.52	0.06	5
5389606	nnnnn	4832.03	99.36	3	4.14	0.20	3	-0.22	0.08	1
5393288	nnngn	5901.68	102.14	6	4.09	0.21	4	-1.05	0.12	4
5708973	nnnnn	5402.54	119.82	5	3.84	0.19	4	-0.63	0.08	2
5753507	nnnnn	4030.04	9.36	2	2.75	0.10	1	-0.61	0.08	1
5779710	LnnnN	0	0	0
5820135	nnngn	4424.24	137.16	3	4.49	0.37	2	-1.17	0.14	1
4198331	nnnnn	4473.08	19.25	3	4.03	0.13	3	-0.40	0.06	1
4285875	nnnnn	6377.87	46.99	8	3.07	0.17	6	-2.05	0.07	4
4340700	nnnnn	4116.18	29.61	2	3.59	0.71	2	-0.49	0.14	1
4394723	nnnnn	5594.77	81.95	6	4.04	0.14	4	-0.48	0.03	4
4440104	NnnnN	0	0	0
4536611	nnnnN	0	0	0
4643251	nnnnn	4760.95	144.00	3	4.49	0.10	4	-0.32	0.01	2
4706809	nCnn	5410.76	79.97	6	2.40	0.08	6	-0.26	0.06	6
4837152	nnBnn	5538.96	49.97	3	3.40	0.46	2	-0.26	0.08	1
5053406	ICnnR	0	0	0
5066943	nnnnn	5630.56	65.62	7	3.91	0.11	6	-0.40	0.02	5
5074645	nnnnn	5009.15	39.69	8	3.93	0.17	6	-0.64	0.03	5
5130518	nnnnn	5207.23	80.31	6	4.25	0.10	6	-0.67	0.02	4
5245180	nnnnn	4385.85	80.44	3	3.59	0.38	3	-0.10	0.10	1
5392400	nCnnR	0	0	0
5418163	nnnnn	5612.62	51.60	6	4.13	0.11	4	-0.56	0.03	3
5422567	nnnnn	5146.69	65.40	4	3.89	0.10	4	-0.31	0.09	2
5490286	nnnnn	4751.25	72.70	3	4.27	0.07	3	-0.52	0.09	1
5541677	nnnnn	5863.72	74.12	7	4.06	0.10	6	-0.40	0.04	3
5603624	NnnnN	0	0	0
5854453	nnnnn	5168.91	131.66	3	4.16	0.00	2	0.06	0.08	1
4185302	nnnnn	4026.37	17.88	1	4.04	0.00	2	-1.17	0.12	1
4212859	ICnnR	0	0	0
4336218	LnnnR	0	0	0
4450457	nnnnn	5013.21	147.92	4	4.50	0.17	5	-0.89	0.02	2
4528088	NnnGn	4231.75	66.15	3	3.35	0.34	2	-1.15	0.05	1
4571023	nnnnn	5134.55	99.97	3	4.35	0.08	3	-0.58	0.06	1
4768090	nnnnn	5774.50	68.32	8	3.67	0.05	6	-0.41	0.01	4
5106145	nnnnn	5944.41	31.57	8	4.04	0.08	6	-0.36	0.05	6
5239818	nnBnn	5556.10	6.65	3	4.14	0.02	2	-0.58	0.04	1
5256882	nnnnR	0	0	0
5322327	nnnnn	5747.11	205.12	6	4.38	0.08	6	-0.09	0.05	4
5334464	nnnnn	4627.34	98.57	3	4.38	0.13	4	-0.37	0.17	2
5668906	nnnnn	4723.42	94.99	3	4.37	0.13	4	-0.58	0.04	1
6015155	NCnnN	0	0	0
4306405	nnnnn	5659.80	133.82	4	4.03	0.04	2	-0.06	0.05	1
4474812	ICnnN	0	0	0
4493553	nnnnn	5828.02	217.37	6	3.93	0.15	6	0.05	0.10	3
4573011	NCnn	4703.24	37.91	2	4.60	0.04	1	-0.72	0.07	1
4751728	nnnnn	5800.73	33.82	7	4.31	0.27	6	-0.65	0.02	4
4870522	nnBnn	4975.98	32.56	3	4.16	0.04	2	-0.76	0.11	1
5024112	nnnnn	5488.00	41.06	3	3.91	0.06	2	-0.58	0.07	1
5169791	nnnnn	6256.17	57.09	8	3.43	0.43	5	-1.36	0.05	3
5335123	nnnnn	6019.03	107.19	4	3.21	0.04	2	-1.03	0.09	1
5356193	LnnnR	0	0	0
5429093	nnnnn	7873.21	188.39	2	3.51	0.06	1	-1.50	0.05	1
5444299	VnnnX	0	0	0
5736121	NnBnN	0	0	0
6005624	nnnnn	6151.19	77.26	8	3.53	0.06	6	-0.66	0.03	3
4196557	nnnnn	5607.66	19.26	6	3.75	0.19	4	-0.21	0.06	2
4250581	nnnnn	4987.39	110.22	3	4.51	0.13	4	-1.09	0.07	2
4442477	nnnnn	5708.46	112.89	4	4.36	0.34	2	-0.71	0.01	1

Table 7.5 (cont'd): SSPP Stellar Parameters for Hectospec Targets

UW ID ^a	flags	T_{eff} (K)	$\sigma(T_{\text{eff}})$ (K)	$N(T_{\text{eff}})^{\text{b}}$	$\log g$ (dex)	$\sigma(\log g)$ (dex)	$N(\log g)^{\text{b}}$	[Fe/H] (dex)	$\sigma([\text{Fe}/\text{H}])$ (dex)	$N([\text{Fe}/\text{H}])^{\text{b}}$
4465390	NnBnn	5437.52	156.16	3	3.01	0.30	2	-0.26	0.04	1
4574795	nnnnn	4646.04	84.76	3	4.18	0.06	4	-0.25	0.12	2
5084589	nnnnn	5842.65	166.14	4	3.85	0.65	2	-0.85	0.06	1
5208221	nnnnn	5814.36	89.43	7	4.15	0.11	6	-0.29	0.03	6
5412001	nnngn	5912.39	198.75	4	3.63	0.21	2	-1.49	0.02	1
5451382	nnnnn	5929.55	122.30	7	4.35	0.15	6	-0.92	0.05	3
5461947	nnnnn	5107.63	121.97	3	4.50	0.10	3	-0.20	0.08	1
5467747	nnGn	6038.98	167.07	5	3.92	0.95	2	-1.78	0.15	1
5884266	nnnnn	5646.00	41.38	6	3.99	0.09	6	-0.23	0.05	5
5994122	nnnnn	6081.31	248.88	5	2.76	0.06	2	-1.26	0.28	1
4165934	NCnnR	0	0	0
4296264	Nnnnn	4444.56	100.14	3	3.79	0.10	2	-0.63	0.09	1
4524098	nnnnn	4964.74	186.24	3	4.14	0.04	2	-0.26	0.08	1
4674112	nnnnn	5538.96	232.21	3	4.22	0.35	2	-0.21	0.09	1
4766994	lnnnn	4767.71	57.75	3	4.30	0.23	4	0.03	0.05	2
4814426	nnnnn	4103.26	21.23	1	4.73	0.11	2	-0.95	0.12	1
5217333	nnBnn	5349.06	152.87	3	4.25	0.45	2	-0.60	0.04	1
5224861	nnnnn	5725.42	39.92	7	3.80	0.08	6	-0.16	0.04	4
5230589	nnnnn	6288.25	112.44	8	1.82	0.01	5	-1.54	0.10	5
5290377	nnnnn	5209.67	17.37	5	3.26	0.17	4	-0.57	0.06	3
5291298	nnnnn	4923.56	112.98	3	4.58	0.06	4	-0.35	0.06	2
5398463	nnnnn	5799.69	107.05	4	3.57	0.15	2	-0.80	0.04	1
5426933	nnnnn	5296.61	45.95	6	4.35	0.09	6	-0.51	0.02	6
5652205	nnnnn	5202.74	42.34	4	4.46	0.10	5	-0.78	0.02	4
5972833	nnnnn	5482.92	40.98	3	3.83	0.19	2	-0.46	0.05	1
4268493	nnBnc	0	0	0
4382840	lCnnR	0	0	0
4383422	nnnnn	5456.09	109.38	7	3.73	0.10	6	-0.40	0.03	4
4391319	NnBnN	0	0	0
4479464	nnnnn	5466.17	61.06	6	4.25	0.17	6	0.15	0.08	4
4505113	nnnnn	5799.93	24.77	4	3.67	0.27	2	-0.88	0.05	1
4606866	NnnnR	0	0	0
4775171	nnnnn	5041.10	54.26	4	4.50	0.10	5	-1.05	0.09	4
5020698	nnnGn	5602.40	125.39	4	4.19	0.25	2	-1.06	0.06	1
5070735	nnnnn	5807.80	65.86	8	3.97	0.10	6	-0.43	0.06	6
5164442	nnnnn	5580.73	126.48	7	4.24	0.19	6	-0.33	0.02	2
5256822	nnnnn	4464.10	71.46	3	3.87	0.12	2	-0.27	0.09	1
5375718	nnnnn	4584.16	85.92	3	4.00	0.23	3	-0.30	0.10	1
5469716	NnnnN	0	0	0
5586889	nnnnn	5337.99	33.22	3	2.95	0.11	2	-0.11	0.10	1
5791663	nnnnn	5461.54	67.95	6	4.22	0.13	6	-0.51	0.05	5
6015136	nnnnn	6191.52	91.77	6	3.60	0.50	3	-1.13	0.11	1
4200042	nnBnn	5527.75	135.35	4	4.30	0.36	4	-0.91	0.20	1
4569873	nnngn	5442.25	74.74	6	3.40	0.63	4	-1.89	0.04	3
4774504	lnnnN	0	0	0
4811830	nnnnn	5744.64	136.12	8	3.92	0.09	6	-0.86	0.05	7
4842903	NnBnN	0	0	0
5048004	nnnnR	0	0	0
5212364	NnnnN	0	0	0
5242269	lCnnR	0	0	0
5262999	nnnnn	5658.92	107.22	4	4.25	0.39	2	-0.50	0.04	1
5263594	nnnnR	0	0	0
5381906	nnnnn	6313.62	86.74	8	2.25	0.38	6	-1.43	0.05	4
5439023	nnngn	4769.94	163.60	3	4.38	0.50	2	-1.32	0.10	1
5472596	nnnGn	7547.19	251.26	6	2.75	0.17	6	-1.71	0.03	4
5639027	nnnnn	5790.39	91.30	5	3.46	0.60	2	-0.20	0.09	1
6041817	nnnnn	5404.35	262.53	4	4.08	0.28	4	-0.83	0.06	1
4197458	NnnnN	0	0	0
4352969	nnnnn	5322.50	66.08	4	4.03	0.05	5	-0.00	0.00	2
4495340	lnnnn	4034.10	10.84	2	2.82	0.09	1	-0.39	0.09	1
5169524	NCnnR	0	0	0
5285956	nnnnN	0	0	0
5645576	lnnnR	0	0	0
5663466	nnnnn	6046.74	22.14	8	3.98	0.04	6	-0.17	0.05	7
4414296	nnBnn	6083.99	220.55	6	3.66	0.04	4	-0.24	0.07	1
4471479	nnnnn	7338.21	81.71	8	3.46	0.24	6	-1.51	0.04	3
4592360	nnnnn	5635.03	144.11	6	4.42	0.19	6	-0.24	0.05	4
5015148	nnngn	5909.74	62.29	5	3.60	0.69	2	-1.31	0.03	1
5126923	nnngn	6076.35	74.19	5	3.84	0.26	2	-1.38	0.03	1
5284660	nnnnn	5954.44	46.32	8	4.00	0.12	6	-0.57	0.05	5
5482602	nnBnn	4937.11	88.23	4	4.49	0.07	5	-0.54	0.01	2
5689076	NCBnN	0	0	0
5942121	NnBnN	0	0	0
4174223	nnnnn	4738.36	150.23	3	4.41	0.21	4	-0.88	0.09	1

Table 7.5 (cont'd): SSPP Stellar Parameters for Hectospec Targets

UW ID ^a	flags	T_{eff} (K)	$\sigma(T_{\text{eff}})$ (K)	$N(T_{\text{eff}})^{\text{b}}$	$\log g$ (dex)	$\sigma(\log g)$ (dex)	$N(\log g)^{\text{b}}$	[Fe/H] (dex)	$\sigma([\text{Fe}/\text{H}])$ (dex)	$N([\text{Fe}/\text{H}])^{\text{b}}$
4239466	nnnnn	5964.87	77.63	7	4.07	0.08	6	-0.82	0.03	6
4379608	nCnnn	4940.73	395.83	3	4.48	0.13	4	-0.51	0.06	2
4526140	nnnnn	7785.23	49.58	4	4.21	0.36	3	-0.99	0.07	1
4539671	nnnnN	0	0	0
4546768	Nnnnn	0	0	0
4555096	nnnnn	5021.50	120.39	3	4.51	0.09	4	-0.63	0.13	3
4555649	nnnnn	4915.26	113.77	3	4.61	0.05	4	-0.52	0.03	2
4837996	nnnnn	5693.03	98.01	7	4.36	0.15	6	-0.43	0.05	6
5026853	nnnnn	5896.51	69.18	8	4.10	0.07	6	-0.46	0.04	6
5044471	nnnnn	5674.42	50.53	7	4.34	0.07	6	-0.18	0.04	5
5070815	nnnnn	5353.52	59.86	6	3.34	0.11	6	-0.64	0.02	6
5371585	ICnnR	0	0	0
5385620	nnnnn	5002.10	161.93	4	4.58	0.07	5	-0.45	0.09	4
5398585	nnBnN	0	0	0
5447280	nnnnn	5664.49	69.48	7	4.26	0.11	6	-0.37	0.00	5
5454061	nnnnn	4316.20	69.71	3	3.51	0.49	2	-0.26	0.07	1
5526220	nnnnn	5299.29	73.83	4	4.17	0.18	5	-0.17	0.06	1
5825112	nnnnn	5842.77	123.81	7	3.65	0.12	6	-0.54	0.07	5
5919901	nnBnn	4950.51	60.56	3	3.15	0.10	4	-0.02	0.05	3
5992340	lnnnR	0	0	0
7909641	nnnnn	5115.88	92.56	3	4.40	0.47	2	-0.83	0.09	1
4213547	nnnnn	5116.12	129.19	3	4.48	0.19	4	-0.55	0.23	3
4293219	nnnnn	4284.93	125.47	3	4.02	0.35	2	-2.06	0.06	1
4333493	Dnnnn	4481.03	303.73	2	3.40	0.17	4	-0.59	0.29	2
4532889	nnnnn	6149.64	33.14	4	3.62	0.36	2	-0.62	0.07	1
4612239	nnnnn	6104.91	68.15	8	4.05	0.14	6	-0.58	0.01	4
4739936	nnnnN	0	0	0
4787944	nnngn	4068.84	8.20	1	3.43	0.07	1	-1.92	0.06	1
4813711	nnnnn	5697.21	61.33	6	3.75	0.41	4	-1.42	0.04	3
5017460	nnnnn	6868.90	46.79	8	3.55	0.24	6	-0.80	0.05	5
5023116	nnnnn	5729.94	99.29	4	4.19	0.29	2	-0.46	0.04	1
5118299	nnnnn	6071.12	35.69	8	4.22	0.12	6	-0.45	0.05	5
5183097	nnnnn	5333.72	282.70	3	4.05	0.14	2	-0.94	0.04	1
5257417	nnnnn	5561.46	32.62	7	4.46	0.14	6	-0.99	0.04	7
5342999	nnnnn	4481.09	78.67	3	4.19	0.24	4	-0.43	0.11	1
5358656	nnnnn	5679.29	98.27	6	3.92	0.13	4	-0.44	0.06	4
5452405	nnnnn	5796.77	133.00	7	3.40	0.15	4	-0.22	0.01	4
5731635	nnnnn	5448.58	50.31	6	3.76	0.24	6	-0.68	0.10	1
5952932	nnnnn	5758.51	73.79	7	4.30	0.11	6	-0.33	0.04	6
6088311	nnnnn	5471.96	155.02	5	4.22	0.18	4	-0.13	0.15	1
6100866	NnBnN	0	0	0
4226990	nnnnn	5007.13	80.04	3	3.65	0.11	4	-0.16	0.08	3
4261375	NnBnc	0	0	0
4366627	nnnnn	5234.34	212.78	3	3.53	0.36	2	-0.74	0.08	1
4391003	LnnnR	0	0	0
4396774	nnnnn	5778.56	161.62	3	3.45	0.06	2	-0.64	0.05	1
4496005	Nnnnn	5595.20	149.11	3	4.22	0.06	2	0.18	0.05	1
4601127	nnnnn	5723.46	105.81	7	4.33	0.19	6	-0.65	0.04	3
4713759	NCnnN	0	0	0
5078200	nnnnn	6183.76	63.58	9	3.61	0.01	7	-0.74	0.03	6
5100476	NnnnN	0	0	0
5153426	Dnnnn	4313.71	41.63	3	3.69	0.19	2	-0.42	0.07	1
5266525	ICnnR	0	0	0
5303263	nnnnn	5927.55	85.39	7	4.02	0.21	6	-0.66	0.04	4
5489798	nnnnn	5148.11	82.52	4	3.62	0.12	5	-0.78	0.04	4
5588235	nnnnn	6674.47	59.44	8	3.41	0.29	6	-1.00	0.02	5
5829312	nnnnn	5761.02	45.16	7	4.03	0.06	6	-0.24	0.03	6
5939519	nnBnn	5247.65	111.59	4	3.19	0.05	5	-0.65	0.01	4
6090619	nnnnn	5756.51	195.18	5	4.49	0.41	4	-0.67	0.10	1
4311215	Nnnnn	4598.61	107.84	3	3.76	0.22	2	-0.29	0.07	1
4451001	nnnnn	4689.70	119.02	3	4.30	0.18	4	-1.36	0.17	1
4654864	nnnnn	5706.86	74.12	7	4.00	0.06	6	-0.12	0.06	6
4748917	nnnnn	0	0	0
4798412	nnnnn	5516.26	41.49	4	3.77	0.20	2	-0.64	0.06	1
4809164	nnnnn	0	0	0
4845893	LnnnR	0	0	0
5104821	nnnnn	5877.71	62.78	8	3.91	0.12	6	-0.90	0.05	6
5143590	nnnnn	5710.64	85.07	7	4.05	0.12	6	-0.36	0.10	4
5260014	nnnnn	4814.83	112.06	3	4.14	0.15	2	-0.31	0.07	1
5302536	nnnnn	5457.29	14.97	5	4.11	0.12	4	-0.71	0.04	4
5404270	nnnnn	4334.32	49.90	3	3.75	0.03	2	-0.91	0.06	1
5438107	nnnnn	5367.20	31.76	6	3.47	0.09	6	-0.92	0.03	7
5878441	nnnnn	6030.17	172.60	4	3.97	0.19	2	-0.42	0.06	1
4211234	nnnnn	5548.46	112.04	3	3.75	0.02	2	-0.46	0.06	1

Table 7.5 (cont'd): SSPP Stellar Parameters for Hectospec Targets

UW ID ^a	flags	T_{eff} (K)	$\sigma(T_{\text{eff}})$ (K)	$N(T_{\text{eff}})^{\text{b}}$	$\log g$ (dex)	$\sigma(\log g)$ (dex)	$N(\log g)^{\text{b}}$	[Fe/H] (dex)	$\sigma([\text{Fe}/\text{H}])$ (dex)	$N([\text{Fe}/\text{H}])^{\text{b}}$
4257238	nnnnn	5854.89	77.18	7	3.66	0.04	4	-0.74	0.04	4
4260588	nnnnR	0	0	0
4368291	lnnnR	0	0	0
4413081	nnngn	4760.29	59.26	3	3.84	0.17	4	-1.70	0.19	3
4547951	nnnnn	5794.19	77.11	8	3.46	0.10	6	-0.47	0.04	5
4576642	nnnnn	5690.53	39.06	7	3.84	0.07	6	-0.42	0.02	4
4584052	nnnnn	6228.99	65.50	9	2.44	0.22	7	-1.71	0.04	7
4604446	NnnnN	0	0	0
4771620	Nnnnn	4528.80	110.91	3	4.11	0.02	2	-0.36	0.06	1
5105990	nnBnn	5911.00	362.25	5	3.02	0.16	3	-0.86	0.25	1
5160594	nnnnn	5198.79	58.01	3	3.91	0.04	4	-0.47	0.13	2
5271563	nnnnn	5706.46	102.49	7	3.64	0.05	6	-0.62	0.04	3
5342441	nnnnn	5362.46	68.22	3	4.39	0.28	2	-0.86	0.05	1
5422547	nnnGn	6610.88	123.48	5	3.57	0.45	2	-2.06	0.08	1
5463036	nnnnn	5779.85	77.20	7	3.95	0.12	6	-0.40	0.03	6
5648124	nnngn	4710.87	145.20	3	4.66	0.30	3	-1.00	0.06	1
5737554	nnnnn	4763.47	100.39	3	4.29	0.09	4	-0.52	0.23	2
5815025	nnBnn	4801.91	80.88	3	3.93	0.11	3	-0.44	0.09	1
4152881	NnnnN	0	0	0
4182852	nnnnn	5676.18	66.07	7	3.94	0.07	6	-0.42	0.04	6
4423997	nnnnn	4840.47	160.03	3	4.48	0.27	3	-1.21	0.43	3
4446334	nnnnn	4611.35	118.35	3	4.13	0.31	3	-0.66	0.07	1
4464622	NnBnN	0	0	0
4534435	lCnnR	0	0	0
4684903	NnnnN	0	0	0
5035866	nnnnn	4982.22	105.34	3	3.88	0.17	2	-0.27	0.06	1
5083310	nnnnn	5855.75	46.02	7	3.74	0.13	4	-0.59	0.11	4
5117170	nnnnn	5308.80	79.39	4	3.50	0.05	5	-0.17	0.08	3
5320553	nnnnn	5171.55	140.19	3	3.57	0.32	2	-0.89	0.05	1
5417972	nnBnn	5069.76	274.08	5	3.15	0.49	4	-0.81	0.06	1
5470145	nnnnn	5300.79	2.81	5	3.93	0.44	4	-0.86	0.08	4
5475375	nnnnn	5807.14	61.48	7	3.85	0.07	6	-0.26	0.02	2
5511699	NnnnN	0	0	0
5640675	nnnnN	0	0	0
6037141	nnnnn	4876.38	61.35	3	4.02	0.11	4	-0.87	0.14	4
4338283	nnnR	0	0	0
4342289	lnnnR	0	0	0
4356588	nnnnn	5921.93	92.40	5	3.90	0.25	2	-0.39	0.06	1
4600603	nnBnc	0	0	0
4623936	NnBnN	0	0	0
4715107	nnnnn	5497.67	69.83	7	4.34	0.07	6	-0.46	0.00	7
4834136	nnnnn	5794.95	86.28	7	3.85	0.08	6	-0.32	0.04	5
5024274	NnBnN	0	0	0
5151160	nnnnn	4825.27	65.89	3	4.49	0.07	4	-0.48	0.06	1
5155344	NnnnN	0	0	0
5176896	lnnnn	4186.65	92.72	2	3.35	0.09	2	-0.23	0.09	1
5179541	nnnnn	5134.83	215.03	4	4.28	0.13	4	-0.92	0.09	3
5194644	nnnnn	5183.97	95.63	3	3.68	0.23	2	-0.94	0.07	1
5196293	NCnn	4801.88	56.51	3	2.88	0.23	4	-0.62	0.09	3
5303892	nnnnn	5981.55	128.60	8	4.08	0.20	5	-0.70	0.14	3
5337149	lnnnR	0	0	0
5529328	Nnngn	4307.34	96.25	3	4.47	0.41	2	-1.00	0.09	1
5919706	nnnnn	4906.48	85.67	3	4.23	0.02	2	-0.31	0.06	1
6042712	nnnnn	4787.05	77.17	3	4.02	0.05	4	-0.67	0.03	2
4408697	lnnnR	0	0	0
4551394	nnnnn	5265.01	74.85	6	4.64	0.13	6	-0.83	0.06	6
4556853	nnnnn	4422.23	17.94	3	4.10	0.01	2	-0.56	0.07	1
4559874	VnnnN	0	0	0
4703884	nnnnn	6052.11	59.44	9	3.88	0.26	7	-0.81	0.06	5
4865398	nnnnn	5957.11	51.74	8	3.79	0.07	6	-0.17	0.05	5
5087972	nnnnn	4654.26	47.86	3	4.03	0.11	3	-0.33	0.11	1
5144822	nnngn	5510.35	64.31	7	2.05	0.10	6	-1.23	0.09	5
5195884	nnnnn	4844.25	114.28	3	4.04	0.09	3	-0.28	0.07	1
5231635	nnnnn	5839.35	115.28	7	4.50	0.35	4	-0.77	0.10	1
5307261	nnnnn	5808.65	81.60	7	4.35	0.06	6	-0.77	0.05	5
5432830	lCnnR	0	0	0
5442572	nnngn	5310.48	53.64	4	4.30	0.38	4	-1.18	0.02	2
5529799	nnnnn	5950.23	125.75	9	4.08	0.22	7	-0.19	0.08	6
5669455	nnnnn	5853.17	75.99	4	3.72	0.14	2	-0.39	0.07	1
5776046	NnBnn	5013.19	115.91	3	4.17	0.53	2	-0.93	0.11	1
6065787	NnBnN	0	0	0
4184398	nnnnn	5867.92	426.09	3	3.84	0.51	2	-0.14	0.09	1
4240029	NnnnN	0	0	0
4303291	nnBnn	5280.96	184.44	3	4.44	0.12	4	-0.42	0.04	3

Table 7.5 (cont'd): SSPP Stellar Parameters for Hectospec Targets

UW ID ^a	flags	T_{eff} (K)	$\sigma(T_{\text{eff}})$ (K)	$N(T_{\text{eff}})^{\text{b}}$	$\log g$ (dex)	$\sigma(\log g)$ (dex)	$N(\log g)^{\text{b}}$	[Fe/H] (dex)	$\sigma([\text{Fe}/\text{H}])$ (dex)	$N([\text{Fe}/\text{H}])^{\text{b}}$
4431470	nnnGn	5927.84	66.57	8	4.10	0.11	6	-1.10	0.05	6
4459088	nnBnn	5460.37	93.04	7	4.18	0.05	6	-0.21	0.09	5
4506041	nnnnn	5792.41	70.14	7	4.16	0.09	6	-0.62	0.02	6
4626627	nnnnn	5628.36	111.11	6	4.36	0.09	6	-0.30	0.03	6
4717476	nnnnc	0	0	0
5018563	lnnnR	0	0	0
5127976	nnnnn	6199.06	120.05	7	3.82	0.39	4	-1.98	0.25	2
5132609	nnnnn	6233.44	34.63	8	3.96	0.02	6	-0.24	0.01	5
5403376	nnnnn	5936.53	74.13	6	3.58	0.32	4	-0.39	0.05	3
5443060	nnnGn	5680.85	27.15	7	4.31	0.15	6	-1.01	0.05	4
5681962	nnngn	5136.76	110.97	6	3.96	0.15	6	-1.12	0.07	5
5791135	Nnnnn	5388.38	413.94	3	4.17	0.68	2	-0.71	0.06	1
5948213	NnnnN	0	0	0
4253307	nnnnn	5687.43	85.99	7	3.97	0.20	6	-0.31	0.07	5
4294757	nGnnn	6429.95	94.35	8	2.35	0.37	6	-2.21	0.25	1
4524695	nnngn	5429.12	31.78	6	2.08	0.13	6	-1.03	0.08	5
4551804	nnnnn	4578.69	120.04	3	4.35	0.12	4	-0.82	0.03	2
4552045	nnngn	4071.64	12.88	2	2.93	0.05	2	-1.26	0.10	1
4617414	nnnnn	5449.83	91.64	6	4.22	0.05	6	-0.20	0.05	5
4733489	nnnnn	4875.57	178.25	3	4.18	0.23	4	-0.82	0.03	2
5175183	nnBnn	5635.22	64.42	6	3.70	0.08	6	-0.62	0.02	4
5230614	nnBGn	5141.92	31.95	4	3.96	0.21	5	-1.08	0.16	4
5271152	lnnnR	0	0	0
5399597	nnnnn	6032.79	50.05	7	3.71	0.06	6	-0.09	0.05	6
5405657	lnnnR	0	0	0
5457857	lnnnn	4072.68	21.78	2	3.57	0.78	2	-0.49	0.11	1
5507001	nnnnn	5722.79	101.05	4	3.67	0.02	2	0.01	0.09	1
5629515	nnnnn	5698.76	150.56	4	3.71	0.13	2	-0.46	0.06	1
5870153	nnnnn	4976.30	53.07	3	3.92	0.04	2	-0.80	0.07	1
4207930	nnnnn	4609.33	151.83	3	4.43	0.45	2	-0.78	0.08	1
4630204	nnnnn	4344.00	85.89	3	3.73	0.22	3	-0.29	0.08	1
4633524	1CnnR	0	0	0
4671307	nnBnN	0	0	0
4683511	nnnnn	5736.32	38.62	7	3.71	0.13	6	-0.21	0.05	6
4691196	nCnnR	0	0	0
4762898	nnnnn	5714.58	138.85	6	4.17	0.23	6	-0.25	0.06	4
4813534	NnnnR	0	0	0
5043137	nnnnn	5970.67	38.52	8	4.21	0.11	6	-0.51	0.03	6
5058474	nnnnn	5872.67	151.51	6	2.90	0.36	4	-0.68	0.01	2
5127864	nnnnn	5905.92	96.81	7	4.00	0.11	4	-0.45	0.07	4
5390807	nnnnn	4423.20	59.73	3	3.69	0.43	2	-0.17	0.08	1
5583321	nnnnR	0	0	0
5674333	nnnnn	7627.51	64.69	4	3.71	0.06	3	-1.65	0.07	1
5703878	nnnnn	4436.07	118.11	3	3.46	0.23	3	-0.41	0.13	1
5878357	VnBnN	0	0	0
6090734	nnnnn	5715.72	205.81	3	4.09	0.29	2	-0.18	0.06	1
4244940	nnnnn	5134.15	9.31	4	3.42	0.11	5	-0.52	0.05	2
4265479	nnnnn	5482.21	51.69	6	3.82	0.12	6	-0.45	0.05	4
4367008	nnnnn	5788.68	132.85	6	3.94	0.60	4	-0.37	0.04	2
4373799	NnBnN	0	0	0
4453691	nnngn	4749.47	208.08	4	3.46	0.34	4	-1.71	0.10	1
4665556	nnnnn	5480.68	249.41	4	2.96	0.21	5	-0.86	0.06	5
4752599	nnngn	6042.93	150.72	4	3.69	0.23	2	-1.05	0.05	1
4803254	nnnnn	5198.22	71.15	4	4.54	0.01	5	-0.32	0.04	3
4812371	nGnnn	7032.67	219.40	9	2.88	0.25	7	-1.62	0.00	2
5044401	Dnnnn	4532.92	40.74	3	3.92	0.15	3	-0.32	0.11	1
5151780	nnnnn	4894.03	66.39	3	4.54	0.02	4	-0.40	0.06	1
5154103	nnnnn	4590.27	82.37	3	4.52	0.11	4	-0.71	0.10	2
5283690	Nnnnn	4823.97	128.81	3	4.21	0.13	2	-0.27	0.07	1
5293726	nnnnN	0	0	0
5322606	nnnnn	5801.70	46.33	7	4.09	0.12	6	-0.51	0.05	5
5773179	nnnnn	4711.70	87.18	3	4.26	0.02	4	-0.28	0.17	2
5777427	nnnnn	4511.42	34.06	3	4.02	0.21	2	-0.80	0.11	1
5796935	NnBnN	0	0	0
4207161	nnngn	5642.22	182.40	4	3.73	0.18	2	-1.11	0.07	1
4243430	nnnnn	5468.38	91.33	6	3.74	0.16	6	-0.42	0.05	7
4251718	nnnnn	7575.76	157.25	4	3.78	0.27	3	-1.64	0.07	1
4280974	nnnnn	6473.74	87.67	9	3.81	0.18	7	-0.50	0.03	4
4364169	nnnnn	5507.05	38.31	7	4.22	0.15	6	-0.32	0.06	4
4461047	nnnnn	5495.09	106.12	6	3.06	0.16	6	-0.65	0.06	6
4698585	nnnnn	4928.65	107.22	3	4.13	0.24	3	-0.33	0.10	2
4750955	nnnnR	0	0	0
5033827	1CnnR	0	0	0
5038896	NnnnN	0	0	0

Table 7.5 (cont'd): SSPP Stellar Parameters for Hectospec Targets

UW ID ^a	flags	T_{eff} (K)	$\sigma(T_{\text{eff}})$ (K)	$N(T_{\text{eff}})$ ^b	$\log g$ (dex)	$\sigma(\log g)$ (dex)	$N(\log g)$ ^b	[Fe/H] (dex)	$\sigma([\text{Fe}/\text{H}])$ (dex)	$N([\text{Fe}/\text{H}])$ ^b
5050993	nnnnn	5971.35	42.83	5	3.41	0.11	2	-0.64	0.07	1
5087502	nnnGn	4096.48	93.37	3	3.38	0.53	2	-1.29	0.06	1
5094272	nnnnn	5488.90	167.81	6	4.29	0.15	6	-0.57	0.09	5
5135658	nnnnR	0	0	0
5357683	nnnnn	5355.41	76.21	6	3.24	0.14	6	-0.71	0.02	5
5632075	NnnnN	0	0	0
6090012	Nnnnn	4918.54	69.27	3	3.80	0.18	2	-0.54	0.07	1
4199385	nnnnn	5664.81	118.09	5	3.86	0.14	2	-0.55	0.05	1
4239903	nnnnn	5521.97	85.64	7	3.87	0.09	6	-0.51	0.02	6
4744079	Nnngn	4285.66	11.74	3	4.38	0.50	2	-1.55	0.10	1
4774000	nnBnn	5375.49	68.44	5	4.03	0.05	4	-0.40	0.04	5
4833283	nnnnn	5538.18	66.42	4	3.37	0.65	2	-0.32	0.06	1
4875903	nnnnn	6029.59	27.58	8	3.56	0.08	6	-1.15	0.03	6
5082863	nnnnn	7752.49	82.66	4	3.72	0.33	3	-1.07	0.06	1
5096418	NnnnN	0	0	0
5112072	nnnnn	6259.92	51.51	6	3.81	0.35	3	-1.24	0.04	2
5286585	NCnnN	0	0	0
5320785	nnnnn	5494.16	26.43	6	4.24	0.13	6	-0.67	0.02	5
5638625	lnnnR	0	0	0
5749026	nnnnn	4781.96	48.72	3	2.75	0.18	4	-0.41	0.13	1
6016608	nnnnn	5320.56	27.40	6	3.43	0.08	6	-0.35	0.06	4
6020785	nnnnn	5497.32	235.19	4	4.01	0.27	5	-0.84	0.10	3
6098890	nnBnn	5357.59	68.52	6	4.50	0.07	6	-0.44	0.07	4
4190114	VnnnX	0	0	0
4226040	nnBnn	5082.07	123.12	4	3.40	0.12	5	-0.80	0.06	4
4245106	NnnnN	0	0	0
4246379	NnnGn	4270.98	173.37	2	4.27	0.61	2	-1.64	0.18	1
4484163	nnnnn	5822.89	93.89	7	3.83	0.11	4	-0.51	0.02	4
4637149	nnnnn	4400.51	110.17	3	3.99	0.25	3	-0.23	0.08	1
4653980	nnnnn	5386.88	78.99	3	3.44	0.10	2	0.03	0.07	1
4732816	nnnnn	5844.23	187.86	4	4.19	0.69	2	-0.69	0.06	1
4750995	nnnnn	5634.72	46.71	4	3.53	0.21	2	-0.63	0.09	1
5204240	nnnnn	4529.27	51.24	3	4.11	0.04	4	-0.48	0.08	1
5232943	nnnnn	4324.71	105.61	3	4.23	0.31	2	-0.37	0.08	1
5256633	nnnnn	5000.85	57.05	3	3.00	0.11	4	-0.44	0.12	3
5353715	nnnnN	0	0	0
5401947	nnnnn	7925.76	252.87	3	4.10	0.15	2	-0.23	0.08	1
5424353	nnnnn	6307.01	151.74	5	3.82	0.32	2	-1.38	0.04	1
5426565	nnnnn	4832.67	177.73	3	4.65	0.11	4	-0.73	0.09	3
5541936	nnnnn	6079.78	59.41	8	4.09	0.11	6	-0.96	0.02	3
5633229	nnnnn	4562.72	51.84	3	3.78	0.19	2	-0.84	0.07	1
5914739	nnnnn	5930.28	154.61	4	3.77	0.23	2	-0.45	0.07	1
5972653	nnnnn	5043.84	27.48	4	4.38	0.10	5	-0.88	0.09	3
5988601	nnBnn	5049.44	57.73	4	3.47	0.21	5	-0.61	0.05	3
4339701	nnBnn	5219.76	68.46	3	4.32	0.16	2	-0.84	0.10	1
4359532	nnnnn	5566.01	51.72	6	3.21	0.21	6	-0.39	0.05	3
4518676	NnnnN	0	0	0
4530823	nnngn	5082.11	104.04	4	4.46	0.15	5	-1.30	0.13	1
4771435	VnnnX	0	0	0
4777406	lnnnR	0	0	0
5045101	nCnnR	0	0	0
5075510	nnnnn	4381.69	56.96	3	3.70	0.03	3	-0.50	0.06	1
5084422	nnnnn	5749.42	38.46	4	3.81	0.30	2	-0.36	0.07	1
5090198	nCnnR	0	0	0
5248093	nnnnn	5745.51	72.00	5	3.95	0.05	2	-0.92	0.04	1
5371999	lnnnn	4337.20	45.80	3	3.72	0.22	2	-0.43	0.08	1
5454637	nnnnn	6902.41	46.37	8	3.65	0.13	6	-0.67	0.04	6
5683698	nnnnn	5276.26	353.25	3	4.46	0.26	3	-1.18	0.06	1
5730779	nnnnn	5959.07	70.04	6	3.69	0.23	4	-0.76	0.05	3
5753580	nnnnR	0	0	0
5840474	lnnnR	0	0	0
5995929	nnnnn	4489.54	89.97	3	4.25	0.13	3	-0.58	0.10	1
6025988	Nnnnn	4410.95	151.72	3	4.43	0.45	2	-0.45	0.08	1
4390320	nnnnn	5430.16	38.97	6	4.35	0.09	6	-0.44	0.05	4
4511504	nnBnc	0	0	0
4741417	nnnnn	4961.64	159.82	4	4.44	0.24	5	-0.66	0.04	5
5399186	nnnnn	4353.93	306.82	2	3.70	0.08	1	-0.54	0.07	1
5535448	nnBnn	5697.62	222.03	4	4.16	0.40	2	-0.72	0.07	1
4171734	NnnnN	0	0	0
4200072	nnnnn	5916.66	44.20	8	3.66	0.19	6	-0.65	0.06	4
4272813	NnnnN	0	0	0
4476095	nnBnn	4844.47	97.31	3	4.34	0.54	2	-1.27	0.07	1
5166521	NnnnN	0	0	0
5479252	nnnnn	5829.44	94.26	7	4.14	0.16	6	-0.36	0.07	5

Table 7.5 (cont'd): SSPP Stellar Parameters for Hectospec Targets

UW ID ^a	flags	T_{eff} (K)	$\sigma(T_{\text{eff}})$ (K)	$N(T_{\text{eff}})^{\text{b}}$	$\log g$ (dex)	$\sigma(\log g)$ (dex)	$N(\log g)^{\text{b}}$	[Fe/H] (dex)	$\sigma([\text{Fe}/\text{H}])$ (dex)	$N([\text{Fe}/\text{H}])^{\text{b}}$
5758090	nnnnn	6477.22	74.98	8	2.86	0.39	6	-1.69	0.05	4
6010784	NnnnR	0	0	0
6047256	Nnnnn	4555.09	114.73	3	4.44	0.33	2	-0.23	0.11	1
4154981	nnnnn	5702.02	113.01	7	4.38	0.20	6	-0.36	0.03	4
4287836	nnnnn	5385.31	39.77	6	4.13	0.09	6	0.03	0.06	3
4302398	nnnnn	5418.26	74.06	6	4.26	0.09	6	-0.26	0.06	4
4340615	lnnnn	4202.35	137.74	2	4.17	0.68	2	-0.64	0.17	1
4528525	nnnnnc	0	0	0
4723578	nnnnn	6312.58	25.16	9	3.53	0.06	7	-0.18	0.05	5
4816883	VnBnN	0	0	0
4816967	NCmnN	0	0	0
5027705	nnnnn	4719.79	60.59	3	4.10	0.09	2	-0.93	0.09	1
5124871	VnBnX	0	0	0
5161488	nnBnn	5067.35	207.58	4	3.80	0.27	5	-0.65	0.07	1
5320932	nnnnn	5016.62	130.05	4	3.10	0.14	5	-0.63	0.10	5
5385340	NnBnN	0	0	0
5635137	nnnnn	5490.64	55.74	6	4.16	0.13	6	0.07	0.07	3
5723118	Nnnnn	0	0	0
5790109	nnBnn	5400.19	820.63	3	4.55	0.33	2	-0.99	0.07	1
6044130	nnnnn	4962.14	142.50	3	4.40	0.24	3	-0.23	0.03	2
4256122	nnBgn	4999.85	143.05	6	2.22	0.22	5	-1.79	0.08	5
4398432	nnnGn	4083.45	27.42	1	4.24	0.06	2	-1.59	0.18	1
4433736	nnnnn	4611.31	112.72	3	4.32	0.56	2	-1.11	0.15	1
4455333	nnnnn	5144.30	57.79	4	4.08	0.18	5	-0.95	0.07	4
4608755	VnnnN	0	0	0
4770405	nnB Gn	5447.15	52.95	3	3.43	0.07	2	-1.55	0.30	1
4808963	Nnnnn	4443.56	34.00	3	4.22	0.28	2	-1.04	0.16	1
5051373	Nnnnn	0	0	0
5067758	nnnnn	5856.42	75.95	6	3.89	0.18	4	-0.43	0.11	4
5365098	nnnnn	4693.84	78.41	3	2.77	0.31	4	-0.47	0.08	2
5428357	nnnnn	4988.06	45.39	3	4.02	0.06	2	-1.18	0.04	1
5483443	nnnnR	0	0	0
5506953	nnnnn	5656.24	54.96	7	4.06	0.08	6	-0.31	0.04	5
5749796	nnnnn	5928.44	121.24	4	3.45	0.18	2	-0.76	0.05	1
5765074	nnBnn	5487.53	116.75	3	3.84	0.29	2	-0.21	0.09	1
5778732	nnngn	4525.06	33.01	3	4.51	0.19	4	-1.01	0.21	2
4482486	lnnnn	4524.59	325.64	2	4.46	0.26	2	-0.61	0.20	1
4533902	nnnnn	5503.41	96.66	5	3.51	0.13	4	-0.03	0.12	2
4568624	nnnnn	5816.02	72.65	7	3.90	0.18	6	-0.69	0.05	6
4726130	nnnnn	5669.05	33.37	4	3.89	0.12	2	-0.39	0.07	1
4822449	nnBnn	5227.07	81.65	6	3.33	0.12	6	-0.86	0.04	5
5029626	nnnnn	4407.04	137.18	3	4.68	0.28	3	-0.73	0.11	1
5119328	NCBnn	4906.37	399.88	3	4.23	0.19	2	-0.51	0.14	1
5219766	nnnnn	5911.74	79.63	6	3.76	0.26	4	-0.32	0.08	3
5237849	nnnnn	4892.24	92.96	3	4.42	0.29	3	-1.21	0.00	2
5435151	nCnnR	0	0	0
5551274	nnnnn	5999.70	95.42	8	3.58	0.04	6	-0.65	0.04	5
5786430	nnnnn	5410.57	48.37	6	4.38	0.09	6	-0.58	0.03	5
5818949	nnnnn	5299.26	163.72	5	3.53	0.24	4	-0.74	0.06	4
5928283	nnnnn	5411.87	94.00	3	4.53	0.29	2	-0.44	0.04	1
4176776	Nnnnn	0	0	0
4180928	nnngn	4312.54	37.36	3	3.80	0.10	2	-1.13	0.19	1
4361422	nnnnn	6174.86	35.25	8	3.87	0.05	6	-0.57	0.02	4
4477792	lnnnR	0	0	0
4490470	nnngn	5549.47	126.53	7	2.69	0.21	6	-2.05	0.06	4
4571184	nnnnn	4975.59	97.74	3	4.42	0.41	2	-0.78	0.08	1
4683510	nnnnn	5685.34	58.08	7	3.73	0.08	6	0.09	0.02	3
5040790	nnnGn	4108.43	27.57	1	4.25	0.15	2	-1.58	0.13	1
5047609	nnnnn	5826.91	49.57	7	3.75	0.08	6	-0.28	0.03	4
5235832	lnnnR	0	0	0
5245421	nnnnn	5200.73	48.60	4	3.65	0.10	5	-0.52	0.08	3
5704887	nnBnn	5075.32	36.59	4	2.89	0.15	5	-0.88	0.03	3
5804238	nnBnn	5596.80	133.77	4	4.43	0.44	2	-0.89	0.05	1
5826637	nnnnn	4381.50	58.50	3	4.30	0.18	4	-0.26	0.14	1
5830764	nnnnn	5968.50	66.64	7	3.97	0.05	6	-0.28	0.00	5
5972322	nnnnn	5592.20	152.40	5	3.82	0.18	4	-0.33	0.05	3
6099556	nnBnn	5563.14	131.96	4	3.16	0.40	2	-0.05	0.14	1
4171894	nnnnnc	0	0	0
4229149	nnBnn	5696.96	411.05	4	4.55	0.32	5	-0.24	0.18	2
4303285	nnnnn	4758.58	96.36	3	4.50	0.04	3	-0.47	0.07	1
4359692	nnnnn	5111.80	132.08	3	4.21	0.17	3	0.04	0.10	1
4454734	nnnnn	6806.61	47.74	8	3.69	0.30	6	-0.45	0.05	7
4535330	nnnnn	6233.69	34.23	9	3.39	0.16	7	-1.22	0.06	6
4868580	nnnnn	4719.08	111.19	3	4.76	0.04	4	-0.77	0.03	2

Table 7.5 (cont'd): SSPP Stellar Parameters for Hectospec Targets

UW ID ^a	flags	T_{eff} (K)	$\sigma(T_{\text{eff}})$ (K)	$N(T_{\text{eff}})^{\text{b}}$	$\log g$ (dex)	$\sigma(\log g)$ (dex)	$N(\log g)^{\text{b}}$	[Fe/H] (dex)	$\sigma([\text{Fe}/\text{H}])$ (dex)	$N([\text{Fe}/\text{H}])^{\text{b}}$
5073828	lnnnR	0	0	0
5117094	nnnnn	4078.54	17.74	2	2.71	0.08	2	-0.63	0.08	1
5229594	nnnnn	5873.00	21.00	7	3.79	0.04	6	-0.28	0.04	6
5244610	nnnnn	6260.92	108.18	5	4.18	0.48	2	-0.41	0.07	1
5302940	nnnnn	6121.01	56.36	8	3.57	0.14	6	-1.56	0.05	7
5395210	nnnnn	4744.07	84.48	3	4.46	0.12	4	-0.87	0.07	3
5420151	nnnnn	4392.14	125.28	3	4.02	0.36	3	-0.36	0.11	1
5736892	ICnnR	0	0	0
5859705	nnnnn	4888.86	179.73	3	4.13	0.01	2	-0.41	0.07	1
6053987	nnnnn	5410.43	100.12	6	3.40	0.17	6	-0.73	0.00	4
4381751	nCnnR	0	0	0
4435341	nnnnn	5329.75	85.54	4	3.99	0.14	5	-0.32	0.07	3
4456841	nnnnn	4262.34	39.59	3	3.71	0.19	2	-0.20	0.12	1
4533226	nnnnn	4617.67	66.66	3	3.65	0.32	3	-0.31	0.07	1
4548468	nnnnn	5846.07	63.33	5	3.79	0.64	2	-2.01	0.06	1
4664662	nnnnn	4861.49	88.60	4	4.35	0.26	5	-0.96	0.10	3
5067068	nnnnN	0	0	0
5132122	nnnnn	4852.62	24.66	4	4.26	0.06	5	-0.84	0.38	1
5153322	nnnnn	5004.63	78.56	4	3.24	0.01	5	-0.67	0.04	2
5219687	nnnnn	4919.62	118.20	3	4.63	0.05	4	-0.45	0.01	2
5256766	nnBnn	5084.96	117.10	3	4.48	0.40	2	-0.57	0.09	1
5317115	nnnnn	5845.75	60.28	8	4.27	0.11	6	-0.47	0.05	4
5351581	nnnnn	4195.69	95.57	3	3.48	0.44	2	-1.11	0.09	1
5397401	nnnnn	5079.10	185.29	3	4.26	0.28	3	-0.47	0.08	1
5485093	ICnnR	0	0	0
5490313	nnnnn	5613.00	49.57	4	4.20	0.68	2	-0.10	0.09	1
5546089	nnBgn	6151.82	125.91	9	3.10	0.32	7	-2.04	0.06	1
5627835	NnnnN	0	0	0
5680286	nnnnR	0	0	0
5806326	nnBnn	5826.27	92.48	6	3.63	0.03	4	-0.34	0.10	4
4340749	nnBgn	5305.27	128.86	7	3.74	0.28	6	-1.00	0.05	5
4341729	NnBnn	4776.44	188.78	3	4.22	0.65	2	-0.87	0.08	1
4403618	lnnnn	4198.85	53.19	2	3.66	0.40	2	-0.38	0.27	1
4427633	nnnnn	5488.24	42.47	6	3.66	0.08	6	-0.46	0.04	5
4537865	nnnnn	5646.07	34.37	7	3.87	0.03	6	-0.06	0.05	4
4668417	nnBnn	5323.65	65.78	5	3.91	0.38	4	-1.30	0.09	5
4678302	nnnnn	5721.86	108.75	7	3.71	0.17	6	-1.09	0.07	7
4778593	nnnnR	0	0	0
4801118	nnnnn	4621.73	86.67	3	3.89	0.09	3	-0.25	0.07	1
4860558	nnnnn	5742.08	30.40	4	3.67	0.15	2	-0.97	0.05	1
5120176	nnnnn	5618.80	92.83	6	3.74	0.41	4	-0.97	0.04	2
5182771	nnnnc	0	0	0
5247200	nnngn	4230.03	59.32	2	4.36	0.27	4	-1.37	0.15	1
5295458	nnnnn	5702.14	121.74	6	4.32	0.16	6	-0.48	0.03	2
5303749	nnnnn	4734.92	102.43	3	4.30	0.17	2	-0.85	0.10	1
5335200	nnnnn	5728.24	49.17	7	4.01	0.04	6	-0.54	0.05	6
5483325	lnnnR	0	0	0
5681140	nnnnn	4833.10	73.76	3	4.65	0.10	4	-0.94	0.02	4
5831181	nnnnn	4762.35	210.72	3	4.05	0.36	4	-0.07	0.03	2
6038085	nnBnn	4493.96	123.83	3	3.60	0.36	2	-0.14	0.14	1
6066682	nnBnn	5435.69	31.88	5	3.51	0.73	4	-0.69	0.01	2
4161125	VnnnR	0	0	0
4199420	ICnnR	0	0	0
4298737	nnnnn	4465.97	57.67	3	4.49	0.18	4	-1.23	0.01	2
4360504	nnnnn	4890.56	70.88	4	1.66	0.20	5	-1.24	0.00	4
4393764	Nnnnn	4250.47	175.33	2	3.65	0.09	1	-0.47	0.08	1
4483967	nnnnn	5403.82	116.31	7	4.36	0.09	6	-0.26	0.05	4
4505618	nnnnn	5635.73	82.69	6	3.89	0.16	4	-0.55	0.03	2
4548913	NnnnN	0	0	0
4560415	nnnnn	5712.00	56.69	7	4.52	0.05	6	-0.65	0.05	5
4589953	ICnnR	0	0	0
5161098	NnnnN	0	0	0
5258502	nnnnn	4721.96	175.51	3	4.79	0.03	4	-0.62	0.03	2
5330663	nnnnn	5921.63	388.92	3	4.53	0.24	3	-0.43	0.04	1
5390555	nnnnn	5383.30	84.85	7	4.30	0.09	6	-0.55	0.04	5
5396700	ICnnR	0	0	0
5429675	nnnGn	6033.60	8.40	5	3.65	0.41	2	-1.15	0.04	1
5449400	nnnnn	5048.83	70.91	3	4.40	0.04	4	-0.22	0.00	2
5665040	nnnnN	0	0	0
5678974	nnnnn	5402.69	52.91	6	3.93	0.08	6	-0.06	0.07	5
5938443	nnBnn	5424.43	76.32	5	4.43	0.19	4	-0.44	0.00	4
5965330	nnngn	4471.62	179.88	3	4.37	0.27	4	-1.33	0.23	2
6017576	nnnnn	6050.90	65.02	8	4.25	0.24	6	-0.98	0.02	5
4428394	nCnnn	6466.73	103.01	8	2.67	0.22	6	-1.43	0.02	5

Table 7.5 (cont'd): SSPP Stellar Parameters for Hectospec Targets

UW ID ^a	flags	T_{eff} (K)	$\sigma(T_{\text{eff}})$ (K)	$N(T_{\text{eff}})^{\text{b}}$	$\log g$ (dex)	$\sigma(\log g)$ (dex)	$N(\log g)^{\text{b}}$	[Fe/H] (dex)	$\sigma([\text{Fe}/\text{H}])$ (dex)	$N([\text{Fe}/\text{H}])^{\text{b}}$
4671629	nnnnn	5840.36	95.81	7	3.69	0.17	6	-0.21	0.03	6
5053890	nnnnn	5856.04	47.64	8	3.91	0.10	6	-0.68	0.03	6
5415779	nnnnn	4977.69	23.82	3	3.95	0.04	2	-0.63	0.07	1
4326447	nnnnn	5766.59	220.02	4	4.46	0.41	2	-0.46	0.09	1
4427534	nnnnn	4762.27	142.77	3	4.45	0.09	4	-0.35	0.12	1
4484017	nnnnn	4763.90	163.97	3	4.34	0.46	2	-0.52	0.11	1
4516006	nnnnn	5464.89	42.52	6	4.14	0.12	6	-0.40	0.04	6
5398403	nnnnn	6159.02	136.00	7	3.79	0.33	4	-1.38	0.14	3
5473721	nnnnn	4220.13	99.04	2	3.84	0.44	2	-0.65	0.08	1
5874518	nnnnn	5592.01	124.55	7	3.75	0.13	6	-0.26	0.05	5
5975268	NCnnR	0	0	0
4729516	nnBnn	5603.73	250.67	3	4.45	0.35	2	-0.89	0.08	1
4822927	nnnnn	5767.21	34.59	7	4.01	0.11	6	-0.39	0.04	6
5641731	nnngn	4069.96	23.02	1	4.14	0.07	1	-2.08	0.08	1
5908032	nnBnn	5213.24	131.73	4	4.39	0.23	5	0.11	0.07	1
6088216	nnnnn	5314.26	15.63	6	4.31	0.11	6	-0.53	0.04	6
4433491	VnBnX	0	0	0
4445012	nnnnn	5896.63	41.25	7	3.89	0.26	4	-0.92	0.05	4
4835605	nnnnn	4359.15	116.63	3	4.41	0.47	2	-1.00	0.12	1
5014139	nnnnn	4795.01	138.87	3	4.64	0.19	3	-0.27	0.09	1
5432008	nnnnn	4380.90	64.37	3	3.75	0.16	3	-0.64	0.08	1
5906528	nnnnn	5189.08	108.83	3	4.09	0.04	4	-0.22	0.05	2
4180266	NnBnX	0	0	0
4263229	nnnnn	4967.48	172.25	3	4.53	0.20	3	-0.16	0.13	2
4338775	NnnnN	0	0	0
4339291	nnBnn	5285.83	108.61	3	4.39	0.49	2	-0.67	0.05	1
4428042	nnnnn	4275.39	79.88	3	3.64	0.03	2	-0.98	0.08	1
4429748	nnBnn	5763.66	125.09	4	4.01	0.51	2	-0.97	0.04	1
4505256	ICnnR	0	0	0
4574474	nnnnR	0	0	0
4589755	nnBnn	5254.55	61.89	4	4.50	0.14	4	-0.43	0.09	3
4682164	nnnnn	6023.76	64.65	8	3.87	0.13	6	-0.88	0.06	6
4742716	nnnnn	7096.19	55.77	9	3.99	0.17	7	-0.39	0.06	6
4811779	nnBnn	5561.66	178.21	4	3.60	0.04	2	-0.54	0.10	1
5062729	Nnnnn	5019.23	108.56	3	4.22	0.13	2	-0.13	0.06	1
5137031	NnnnR	0	0	0
5138205	nnnnn	5156.73	158.21	3	4.08	0.14	2	-0.76	0.07	1
5173342	NCnnR	0	0	0
5308419	nnnnn	5919.30	35.42	7	3.76	0.03	6	-0.00	0.06	6
5311548	nnnnn	4947.17	204.73	3	4.38	0.49	2	-0.74	0.06	1
5467523	nnnnn	4060.74	9.60	2	3.58	0.75	2	-0.69	0.09	1
5505007	nnnnn	4892.06	150.21	4	3.30	0.09	5	-0.95	0.00	2
5746409	nnnnn	5840.22	42.85	7	3.82	0.05	6	-0.35	0.05	7
5850215	nnnnn	5967.40	236.15	4	4.15	0.30	2	-0.56	0.10	1
5883517	DCnn	5516.85	18.64	1	4.77	0.07	2	-0.37	0.07	1
5994975	nnnnn	5804.06	25.30	7	4.08	0.09	6	-0.60	0.03	2
4197320	nnnnn	6063.47	170.08	3	3.76	0.58	2	-1.37	0.04	1
4468205	nnBgn	4843.71	156.94	3	3.51	0.25	3	-1.62	0.19	3
4472742	lnnnR	0	0	0
4582128	VnBnX	0	0	0
4620669	nnnnn	4954.65	204.06	3	3.55	0.27	4	-0.27	0.06	1
4667731	nnnnn	5845.72	6.06	7	4.01	0.06	6	-0.38	0.05	6
4684030	nnBnn	5216.05	56.37	5	4.23	0.14	4	-0.74	0.02	2
4758449	nnnnR	0	0	0
4783320	nnBnn	5449.20	114.44	3	4.01	0.33	2	-0.96	0.06	1
4804494	nCnnR	0	0	0
5053458	nnnnn	5385.25	62.75	6	4.30	0.13	6	-0.70	0.05	6
5130597	nnnGn	5491.98	93.77	6	3.51	0.18	4	-1.03	0.08	3
5166360	NnnnN	0	0	0
5252765	lnnnn	4149.86	49.47	2	3.72	0.63	2	-0.38	0.08	1
5395641	nnnnR	0	0	0
5598801	nnngn	4290.75	62.33	3	3.75	0.15	4	-1.06	0.13	2
5669255	nnnnn	4608.21	63.10	3	4.08	0.12	4	-0.19	0.22	2
5884312	nnnnn	4774.76	58.58	3	4.28	0.28	3	-0.49	0.07	1
6012747	nnnnn	6021.85	34.73	8	3.89	0.03	6	-0.10	0.05	7
6047970	nnBnn	5068.30	100.13	3	3.26	0.03	3	-0.41	0.06	1
4174385	nnnnn	4634.64	154.16	3	4.27	0.19	2	-0.95	0.10	1
4240465	lnnnN	0	0	0
4252195	nCnnR	0	0	0
4466700	nnnnn	5373.06	121.31	7	3.66	0.06	6	-0.64	0.01	4
4467533	nnnnn	4674.86	116.04	3	4.32	0.12	4	-0.27	0.09	2
4635653	DnnGn	4352.21	89.47	3	4.49	0.22	4	-1.62	0.20	1
4651310	nnnnn	5004.93	104.75	3	4.50	0.07	4	-0.46	0.13	3
4653392	nnnnn	5750.04	50.96	6	4.12	0.27	4	-0.81	0.11	3

Table 7.5 (cont'd): SSPP Stellar Parameters for Hectospec Targets

UW ID ^a	flags	T_{eff} (K)	$\sigma(T_{\text{eff}})$ (K)	$N(T_{\text{eff}})^{\text{b}}$	$\log g$ (dex)	$\sigma(\log g)$ (dex)	$N(\log g)^{\text{b}}$	[Fe/H] (dex)	$\sigma([\text{Fe}/\text{H}])$ (dex)	$N([\text{Fe}/\text{H}])^{\text{b}}$
4834369	nnnnn	5692.33	54.83	7	3.57	0.12	6	0.14	0.06	4
5286714	nnnnR	0	0	0
5324553	nnnnR	0	0	0
5422825	nnnnn	5749.53	69.12	4	4.09	0.35	2	-0.64	0.02	1
5423835	nnnnn	4844.17	94.42	3	4.72	0.10	4	-0.79	0.04	3
5490655	nnnnn	5416.63	44.36	3	4.40	0.29	2	-0.75	0.06	1
5497104	nnnnn	4673.09	87.17	3	3.90	0.20	4	-0.30	0.07	1
5500526	NnBnn	5284.27	68.08	3	3.93	0.06	2	-0.03	0.11	1
5517610	nnnnn	5213.19	30.23	6	3.69	0.13	6	-1.16	0.07	3
5588497	lnnnN	0	0	0
5853340	nnnnn	6128.93	37.13	8	3.91	0.12	6	-0.66	0.04	6
5958771	nnnnn	5652.62	46.06	7	3.69	0.05	6	0.03	0.05	4
6071106	nCnnR	0	0	0
4201181	nnnnn	5754.91	151.96	4	4.24	0.63	2	-0.82	0.02	1
4251575	nnnnn	6008.81	88.83	8	4.22	0.18	6	-0.66	0.06	7
4342677	nCnnP	4311.43	306.69	2	0.72	0.80	3	-3.51	0.23	2
4493974	nnnnn	4668.17	107.61	3	4.46	0.27	4	-0.51	0.18	1
4535142	nnnnn	4797.17	139.02	3	4.07	0.16	2	-0.50	0.08	1
4639010	nnnnn	5620.58	75.32	6	4.19	0.24	6	-0.71	0.03	4
4729223	nnGn	4059.69	26.09	1	3.94	0.11	2	-1.53	0.21	1
4732833	Nnnnn	4383.73	55.81	3	3.88	0.10	2	-0.14	0.08	1
4795802	nnngn	5412.63	54.01	7	3.85	0.17	6	-1.31	0.02	5
5043991	nnnnn	5644.12	71.10	8	3.68	0.07	6	-0.47	0.04	4
5351088	nnnnn	4978.81	115.32	3	4.54	0.10	4	-0.28	0.08	2
5421366	nnnnn	6144.46	144.90	4	4.20	0.55	2	-0.07	0.10	1
5450894	nnnnn	4707.96	68.42	3	4.16	0.33	4	-0.59	0.13	1
5496074	nnnnn	6500.10	122.84	6	3.49	0.03	3	-1.83	0.04	2
5932235	VnBnX	0	0	0
6006609	nnnnn	5381.27	58.99	3	4.40	0.22	2	-0.32	0.10	1
6049728	nnBnG	5589.51	310.40	4	4.43	0.32	4	-1.04	0.06	3
6091269	nnnnn	5823.53	34.62	7	3.78	0.06	6	-0.01	0.06	6
4160988	nnnnn	5531.18	79.96	7	4.56	0.04	6	-0.96	0.03	4
4216535	nnnnn	4534.68	111.52	3	3.97	0.01	2	-0.39	0.08	1
4445411	nnnnn	5680.43	50.05	4	4.31	0.33	2	-0.70	0.05	1
4556323	lnnnR	0	0	0
4700788	nCnn	4844.10	66.64	3	4.46	0.09	4	-0.39	0.09	2
4717861	nnnnn	5876.79	82.21	8	4.23	0.22	6	-0.62	0.00	4
4741386	nnnnN	0	0	0
4810394	nnnnn	5762.50	33.02	7	3.61	0.08	6	-0.01	0.07	6
5428366	nnnnn	5722.26	38.38	7	3.73	0.12	6	-0.18	0.06	6
5457082	nnnnn	4815.19	118.50	3	3.90	0.03	4	-0.33	0.14	2
5464637	nnnnn	6026.03	27.95	8	3.86	0.05	6	-0.23	0.04	5
5539336	nnnnn	5947.82	59.80	7	3.72	0.17	4	-0.94	0.10	5
5867943	nnnnn	5495.77	45.75	4	4.26	0.29	5	-0.46	0.07	2
6037417	NnnnN	0	0	0
4171099	nnGn	5333.38	62.62	6	3.15	0.16	6	-1.14	0.03	4
4227645	nnnnn	5657.50	139.06	6	3.76	0.12	6	-0.33	0.06	5
4246809	nnnnn	5861.27	39.01	7	3.92	0.06	6	-0.29	0.01	5
4455743	nnnnn	5665.39	83.05	7	4.24	0.17	4	-0.62	0.07	4
4562519	VnBnX	0	0	0
4668433	NnBnN	0	0	0
4733187	nnnnn	4548.45	177.14	3	3.60	0.49	2	-0.37	0.06	1
4835513	nnnnR	0	0	0
5143749	nnnnn	5057.22	150.86	5	4.47	0.21	4	-0.80	0.13	4
5178138	ICnnR	0	0	0
5309596	nnnnn	4275.62	34.57	3	3.23	0.32	3	-0.30	0.09	1
5401306	nnnnn	5725.85	44.26	6	3.69	0.12	4	-0.67	0.07	4
5541342	nnnnn	4703.77	61.74	3	3.88	0.07	2	-0.19	0.09	1
5548390	nnnnn	5870.44	79.71	6	4.09	0.17	4	-0.64	0.02	5
5757531	nnnnn	4726.91	116.39	3	4.33	0.20	2	-0.90	0.09	1
5817314	NnnnN	0	0	0
6066696	Nnnnn	4474.49	94.04	3	4.02	0.01	2	-0.76	0.06	1
4235698	nnnnR	0	0	0
4315702	nnnnn	4940.41	95.51	3	4.10	0.08	2	-0.56	0.11	1
4319785	nnngn	4980.38	202.46	3	4.41	0.30	4	-1.34	0.32	1
4378585	lnnnR	0	0	0
4607382	nnnnn	4468.68	83.13	3	4.19	0.28	3	-0.22	0.09	1
4636460	nnnnn	6052.34	32.33	8	3.78	0.01	6	-0.04	0.06	5
4665549	ICnnR	0	0	0
5091256	nnnnn	5234.97	55.41	5	4.37	0.19	4	-1.24	0.03	3
5176479	NnnnR	0	0	0
5195896	nnnnn	5648.07	11.64	5	4.28	0.16	4	-0.56	0.04	3
5243374	nnnnn	6061.04	76.79	5	3.97	0.21	2	-0.48	0.06	1
5394351	nnnnn	6045.37	114.18	5	3.96	0.26	2	-0.11	0.05	1

Table 7.5 (cont'd): SSPP Stellar Parameters for Hectospec Targets

UW ID ^a	flags	T_{eff} (K)	$\sigma(T_{\text{eff}})$ (K)	$N(T_{\text{eff}})^{\text{b}}$	$\log g$ (dex)	$\sigma(\log g)$ (dex)	$N(\log g)^{\text{b}}$	[Fe/H] (dex)	$\sigma([\text{Fe}/\text{H}])$ (dex)	$N([\text{Fe}/\text{H}])^{\text{b}}$
5407031	nnnnn	5257.58	293.15	3	3.76	0.11	4	-0.90	0.10	3
5494018	nnnnn	5761.45	56.56	7	4.04	0.25	4	-0.75	0.05	2
5566583	nnnnn	0	0	0
5624176	nnnGn	7247.16	32.83	4	2.73	0.30	2	-1.38	0.13	1
5735201	nnnnn	5715.68	111.70	4	4.36	0.52	2	-0.95	0.04	1
5863634	lnnnR	0	0	0
6085909	nnBnn	5294.63	67.12	6	3.99	0.10	6	-0.27	0.02	5
4175102	nnBnn	5714.14	54.23	6	4.12	0.12	4	-0.39	0.02	3
4505131	nnnnn	5178.18	83.02	6	3.67	0.07	6	-0.82	0.05	7
4534874	nnnGn	5700.77	339.43	4	3.30	0.25	2	-1.97	0.07	1
4620945	nnnnn	6838.37	43.40	9	3.99	0.09	7	-0.39	0.05	8
4767305	nnnnn	4522.32	54.33	3	4.32	0.15	4	-0.90	0.24	3
4783549	nnnnn	5607.46	172.11	5	4.14	0.45	4	-0.27	0.21	2
4840346	nnnnn	7127.19	55.77	7	3.18	0.35	5	-2.29	0.11	3
4841792	NnBnN	0	0	0
5033307	nnnnn	5976.94	203.04	6	3.74	0.45	4	-0.41	0.07	2
5070112	nnnnn	7654.12	143.53	5	3.51	0.31	5	-1.83	0.08	4
5109159	nnBnn	5182.66	51.84	6	4.05	0.17	6	-0.54	0.06	4
5136447	nnnnn	5835.24	139.83	6	3.83	0.19	4	-0.76	0.05	5
5276998	nnnnn	5080.97	63.77	3	4.39	0.16	4	-0.51	0.05	2
5278892	nnnnn	5528.05	114.45	4	4.01	0.37	2	-0.90	0.05	1
5299876	lnnnR	0	0	0
5363761	nnBnn	5337.93	167.46	6	4.29	0.20	4	-0.85	0.08	3
5399608	nnnnn	6440.80	84.45	6	4.02	0.49	3	-1.60	0.06	1
5584370	nnnnn	5573.33	81.14	7	4.11	0.19	6	-0.32	0.04	5
5835347	nnnnn	5269.16	83.43	4	4.44	0.07	5	-0.26	0.08	4
5925534	nnnnn	7046.32	75.11	7	3.26	0.30	5	-1.59	0.06	3
6075772	lnnnR	0	0	0
5141451	lnnnn	4347.73	19.35	3	3.79	0.30	2	-0.04	0.09	1
5260752	NnnGn	4175.24	144.67	2	3.64	0.25	2	-2.57	0.09	1
5392137	nnnnn	6027.77	87.97	5	3.70	0.00	2	-0.72	0.04	1
5549501	nnnnn	5976.23	99.75	6	2.62	0.52	4	-1.46	0.10	4
6085661	nnnnn	5292.05	109.16	5	4.40	0.09	4	-0.45	0.08	3
4299751	nnnnn	5463.47	82.82	6	4.27	0.13	6	-0.43	0.04	4
4460003	NnnnN	0	0	0
4726207	nnnnn	5373.33	37.75	6	3.87	0.13	6	-0.11	0.07	5
5044789	lnnnR	0	0	0
5250151	nnnnn	4710.96	104.73	3	4.28	0.21	4	-1.59	0.43	2
5289948	nnnnn	5769.88	72.18	7	3.63	0.15	4	-0.78	0.00	2
5293945	nnnnn	5613.01	142.49	3	3.98	0.38	2	-0.75	0.04	1
5458706	NnnGn	5452.80	88.38	4	4.17	0.27	2	-1.39	0.05	1
5718459	nnnnn	5887.51	129.08	6	3.18	0.18	4	-0.87	0.06	5
6051829	nnnnn	5921.61	151.99	5	3.56	0.06	2	-0.87	0.03	1
4197416	nnnnn	5876.70	55.34	8	3.83	0.13	6	-0.67	0.06	5
4248911	nnnnn	6002.96	20.89	8	3.91	0.03	6	-0.18	0.01	5
4249010	NnBnN	0	0	0
4268819	nnnnn	4886.59	2.96	3	4.10	0.12	4	-0.71	0.04	2
4343737	nnBnn	5241.53	95.88	3	4.07	0.10	2	-0.62	0.08	1
4383838	nCBnN	0	0	0
4504235	NnnnN	0	0	0
4604861	lnnnn	4374.56	153.14	2	4.58	0.04	1	-0.52	0.07	1
4634667	NnnnN	5018.03	82.87	3	3.89	0.35	2	0.04	0.09	1
4775165	nnBnn	5375.33	246.72	3	4.03	0.85	2	-1.03	0.06	1
5020463	nnnnn	4796.06	118.46	3	4.00	0.27	2	-0.58	0.06	1
5131557	ICnnR	0	0	0
5186549	NnnnN	0	0	0
5387875	nnnnn	4814.00	116.07	3	4.31	0.11	2	-0.20	0.07	1
5467276	nnnnn	4823.11	114.78	3	4.63	0.25	2	-0.44	0.07	1
5516853	nnnnn	5351.47	57.74	4	4.14	0.08	5	-0.05	0.02	2
5922470	nnnnn	5636.81	119.96	6	4.12	0.14	6	-0.51	0.06	5
5962158	nnnnn	5899.28	29.93	8	3.95	0.02	6	-0.14	0.03	6
5972578	NnBnN	0	0	0
6008985	nnnnn	5912.13	47.43	8	3.91	0.11	6	-0.72	0.05	5
4235861	nnnnn	5753.85	92.00	7	4.17	0.16	6	-0.03	0.03	5
4490010	DnnGn	4324.71	79.96	3	4.18	0.20	4	-1.39	0.17	1
4509576	Nnnnn	5463.90	64.92	3	3.59	0.60	2	-0.54	0.08	1
4535271	nnnnn	5235.85	87.08	6	3.32	0.06	6	-0.61	0.05	4
4559967	nnnnR	0	0	0
4604097	nnnnn	4491.01	55.91	3	4.06	0.29	4	-0.46	0.09	1
4717317	nnnnn	5238.98	74.83	3	4.11	0.01	2	-0.76	0.06	1
4819597	lnnnR	0	0	0
4868796	NnnnN	0	0	0
5065974	nnnnn	5337.71	146.77	8	3.50	0.19	6	-0.99	0.15	3
5140747	nnnnn	5676.05	59.97	7	4.28	0.11	6	-0.43	0.04	6

Table 7.5 (cont'd): SSPP Stellar Parameters for Hectospec Targets

UW ID ^a	flags	T_{eff} (K)	$\sigma(T_{\text{eff}})$ (K)	$N(T_{\text{eff}})^{\text{b}}$	$\log g$ (dex)	$\sigma(\log g)$ (dex)	$N(\log g)^{\text{b}}$	[Fe/H] (dex)	$\sigma([\text{Fe}/\text{H}])$ (dex)	$N([\text{Fe}/\text{H}])^{\text{b}}$
5158089	Nnnnn	5024.31	111.33	3	3.73	0.10	2	-0.10	0.06	1
5182303	nnnnn	5928.13	52.23	8	4.20	0.10	6	-0.79	0.06	5
5207519	nnBnn	5662.80	95.34	4	4.40	0.36	2	-0.55	0.04	1
5322309	nnnnn	5948.51	164.58	4	4.37	0.28	2	-0.87	0.05	1
5338130	nnBgn	4442.96	224.12	4	2.30	0.44	4	-2.15	0.07	2
5436171	nnnnn	5481.15	89.35	6	3.88	0.12	6	-0.54	0.02	6
5751763	NnnnR	0	0	0
5891377	nnnnn	4397.59	43.29	3	4.50	0.22	4	-0.97	0.12	1
6021488	nnnnR	0	0	0
4160774	nnnnn	4642.67	89.91	3	4.36	0.20	4	-0.58	0.13	1
4225960	nnnnn	6846.24	51.19	9	3.59	0.34	7	-0.88	0.03	7
4279631	nnnnn	5216.89	30.20	6	3.37	0.08	6	-0.89	0.04	6
4367710	nnnnn	5590.96	153.35	7	3.79	0.17	6	-0.97	0.03	5
4490359	nnnnn	6042.55	62.56	7	4.00	0.24	4	-0.48	0.05	3
4533882	nnnnN	0	0	0
4736929	nnnnn	7546.60	79.31	6	4.01	0.28	5	-1.33	0.06	3
5044528	nnnnn	5378.34	238.04	3	4.10	0.09	2	-0.91	0.04	1
5121325	nnnnn	5705.03	85.40	6	4.27	0.14	6	-0.39	0.05	6
5183168	nnnnn	7989.75	106.78	5	4.35	0.15	4	-0.64	0.05	1
5243827	nnnnn	5909.60	55.10	8	4.09	0.13	6	-0.91	0.05	5
5337546	nnnnn	5914.06	235.19	5	3.53	0.19	4	-0.96	0.08	2
5360966	nnnnn	5429.54	197.32	3	3.89	0.27	2	-0.45	0.09	1
5766774	nnBnn	5114.14	96.39	4	4.25	0.13	4	-0.53	0.08	3
5768051	NnnnN	0	0	0
5835769	nnnnn	5821.71	86.26	7	4.20	0.16	6	-0.86	0.03	5
5865250	nnnnn	6027.62	45.10	8	3.94	0.06	6	-0.14	0.03	6
6037061	NnnnN	0	0	0
6053852	nnnnn	5738.71	57.04	8	3.96	0.06	6	-0.12	0.03	4
4160472	ICnnR	0	0	0
4332532	nnBnn	5305.80	48.72	6	4.20	0.11	6	-0.65	0.05	4
4361284	nnnnn	4546.99	95.83	3	4.32	0.20	4	-0.47	0.06	2
4650230	nnBnn	4806.97	170.55	3	3.84	0.33	2	-0.55	0.09	1
4705540	nnnnn	5688.95	390.30	3	3.51	0.64	2	-0.67	0.10	1
4742528	nnngn	4004.68	21.67	1	4.30	0.10	1	-1.85	0.11	1
5097107	nnngn	4651.62	44.77	3	4.68	0.16	4	-1.03	0.10	2
5105195	nnnnn	5788.70	435.79	3	3.98	0.08	4	-0.88	0.01	2
5106012	nnnnn	5847.32	91.39	8	4.28	0.04	6	-0.58	0.04	5
5174565	nnnnn	5477.81	35.72	6	3.99	0.07	6	-0.03	0.06	6
5284525	nnnnn	5523.32	58.99	7	4.26	0.08	6	-0.47	0.04	6
5308321	nnnnn	5792.54	65.16	7	3.70	0.16	4	-0.43	0.08	1
5337384	nnngn	5707.24	74.41	7	3.94	0.15	6	-0.16	0.05	5
5490864	nnngn	4670.80	213.37	4	4.30	0.33	4	-1.24	0.10	2
5519111	nnnnn	4708.84	128.17	3	4.44	0.09	2	-0.41	0.05	1
5617328	nnBnn	5029.28	224.89	4	4.59	0.14	5	-0.86	0.06	1
5855696	nnBnn	4778.05	93.71	3	4.10	0.05	2	-0.81	0.06	1
5897834	nnnnn	6027.16	171.77	5	4.31	0.57	2	-0.94	0.07	1
5968591	nnnnn	5049.98	6.64	4	3.24	0.21	5	-0.38	0.07	4
6037990	nCBnN	0	0	0
4208784	NnBnN	0	0	0
4244703	nnnnn	6416.04	4.14	8	3.78	0.01	6	-0.65	0.03	4
4369815	nnnnn	4428.34	33.48	3	3.87	0.11	3	-0.76	0.09	1
4509613	nnnnn	4486.63	69.71	3	4.33	0.24	4	-0.76	0.05	2
4594010	nnnnn	5317.13	67.12	6	3.88	0.06	6	-0.44	0.04	6
4791181	NnnnN	0	0	0
5042780	nnnnn	5376.15	147.30	4	4.26	0.11	5	-0.42	0.06	1
5153522	nnnnn	5949.06	122.36	6	4.16	0.14	4	-0.63	0.01	4
5296200	nnnnR	0	0	0
5345581	Nnnn	4440.40	69.26	3	4.13	0.01	2	-0.72	0.06	1
5384884	lnnnR	0	0	0
5398554	Dnnnn	4056.68	20.74	1	4.20	0.11	1	-1.11	0.13	1
5469581	nnnnn	5003.97	84.94	3	3.24	0.04	4	-0.49	0.11	2
5744070	nnnnn	4779.96	70.83	3	4.41	0.09	4	-0.82	0.05	1
5756364	nnBnN	0	0	0
5807589	nnBnn	4862.90	63.93	3	4.04	0.12	2	-0.35	0.07	1
5840056	nnnnn	5535.63	85.86	7	4.19	0.14	6	-0.47	0.06	6
5869851	nCnnR	0	0	0
5920450	nnnnN	0	0	0
4307712	nnnnC	0	0	0
4382260	nnngn	5597.34	114.50	5	4.18	0.25	4	-1.12	0.15	4
4455770	nnnnn	4977.64	111.52	3	4.09	0.16	4	-0.16	0.00	2
4552522	VnnnX	0	0	0
4627992	nnnnn	5852.60	57.14	8	3.96	0.09	6	-0.25	0.05	5
4631287	nnnnn	4464.99	123.92	3	3.83	0.15	3	-0.22	0.06	1
4771866	NnBnN	0	0	0

Table 7.5 (cont'd): SSPP Stellar Parameters for Hectospec Targets

UW ID ^a	flags	T_{eff} (K)	$\sigma(T_{\text{eff}})$ (K)	$N(T_{\text{eff}})$ ^b	$\log g$ (dex)	$\sigma(\log g)$ (dex)	$N(\log g)$ ^b	[Fe/H] (dex)	$\sigma([\text{Fe}/\text{H}])$ (dex)	$N([\text{Fe}/\text{H}])$ ^b
4834314	nnnnn	4468.15	54.93	3	4.12	0.16	2	-0.55	0.09	1
5158679	nnnGn	5143.92	267.77	9	3.41	0.30	7	-1.30	0.04	6
5176972	nnnnn	5774.79	77.68	4	3.76	0.30	2	-0.06	0.05	1
5211996	nnnnn	5821.14	72.58	7	4.16	0.07	6	-0.43	0.08	7
5238054	nnnnn	5910.62	52.02	4	3.97	0.29	2	-0.67	0.04	1
5479247	nCnnR	...	0	0	0
5573980	nCnnR	...	0	0	0
5721978	lnnGn	4057.80	18.54	1	4.67	0.03	1	-1.11	0.10	1
5774426	Nnnnn	4829.73	113.82	3	4.65	0.16	2	-0.39	0.09	1
5867006	nnnnn	4447.48	93.25	3	3.72	0.11	4	-0.56	0.03	2
5993614	nnnnn	5567.99	1.33	7	4.35	0.12	6	-0.63	0.04	5
4247480	nnnnn	5645.04	127.00	4	4.39	0.21	4	0.48	0.02	2
4428097	nnnnR	...	0	0	0
4534624	nnnnn	7411.90	63.44	5	4.11	0.15	5	-0.40	0.08	5
4550137	nnnnn	5084.32	99.14	4	4.23	0.09	5	-0.86	0.09	3
4570339	Nnnnn	4640.07	113.17	3	4.15	0.10	3	-0.21	0.06	1
4703364	nngn	5135.14	59.81	4	4.58	0.10	5	-1.20	0.05	4
5014056	nnnnn	5098.87	170.67	3	3.82	0.13	2	-0.70	0.04	1
5050486	nnnnn	5491.14	66.92	6	4.25	0.15	4	-0.64	0.03	2
5080927	nnnnn	5685.62	84.59	7	4.15	0.07	6	-0.29	0.04	6
5102608	nnnnn	5669.26	288.42	3	4.10	0.24	4	-0.66	0.02	2
5218307	nnnnn	5195.54	81.43	4	4.29	0.20	4	-0.61	0.09	3
5516601	Nnnnn	4835.06	88.27	3	4.17	0.00	2	-0.94	0.24	1
5607780	nnnnn	5657.93	118.16	6	3.63	0.26	4	-0.73	0.02	2
5944680	NnBnN	...	0	0	0
5986924	nngn	5729.33	148.25	5	3.58	0.08	4	-1.08	0.04	4
6085650	nnnnn	4856.64	113.36	3	4.58	0.06	4	-0.45	0.02	2
4166087	nnnnn	5977.64	140.09	6	4.13	0.44	3	-0.52	0.04	1
4200230	nCnn	4178.85	121.21	2	3.81	0.50	2	-0.43	0.09	1
4289484	nnnnn	6243.58	134.96	5	4.31	0.57	2	-0.57	0.08	1
4317562	nnnnn	5985.22	133.38	6	3.98	0.21	4	-0.93	0.05	2
4496219	1CnnR	...	0	0	0
4497072	NCnnR	...	0	0	0
4514956	nnnnn	5442.23	6.43	4	4.06	0.11	4	-0.33	0.07	1
4606071	nnnnR	...	0	0	0
4642632	nnnnn	5126.29	214.35	3	4.35	0.53	2	-0.57	0.07	1
4754272	nnnnn	5949.57	73.17	8	3.89	0.02	6	-0.52	0.02	3
5099831	nnnGn	5979.92	119.72	5	3.78	0.25	2	-1.09	0.04	1
5145218	nnnnn	5958.96	51.82	8	3.97	0.01	6	-0.50	0.04	4
5200105	nngn	4342.15	41.49	2	3.73	0.34	3	-1.71	0.14	1
5352028	nnBnn	5275.49	135.18	4	4.44	0.32	4	-0.05	0.10	1
5390257	NnnnN	...	0	0	0
5690168	NnnnN	...	0	0	0
5702115	nnnnn	6573.78	74.43	8	4.30	0.12	6	-0.41	0.03	5
5795840	nnnnn	5424.58	62.78	6	4.63	0.10	6	-0.61	0.00	5
5856163	nngn	4758.83	181.79	3	4.24	0.50	3	-1.27	0.53	2
6087331	NnnnN	...	0	0	0
4427338	nnnnR	...	0	0	0
4551604	nnnnn	5569.07	66.32	7	4.00	0.09	6	-0.15	0.07	6
4582014	nnBgn	5935.02	211.33	4	4.03	0.70	2	-1.11	0.07	1
4793377	nnnnn	6212.77	126.59	6	3.59	0.35	3	-0.45	0.10	2
5025584	nngn	4504.19	56.10	3	4.58	0.12	4	-1.36	0.06	2
5049257	nnnnn	5307.95	31.10	6	3.94	0.06	6	-0.33	0.05	5
5212991	nCnnR	...	0	0	0
5243207	nnBnn	5304.89	23.27	3	4.41	0.30	2	-0.87	0.06	1
5506510	lnnnc	...	0	0	0
5712022	nnnnn	4923.71	50.09	3	4.24	0.09	3	-0.46	0.05	1
4157148	nnnnn	6007.66	30.94	8	3.60	0.14	6	-0.78	0.05	6
4414129	nnnnn	6058.28	61.93	8	3.78	0.10	6	-0.60	0.05	5
5249935	nnnGn	5523.15	250.13	4	3.98	0.65	2	-1.50	0.20	1
5375369	nnnnn	4862.52	505.35	2	4.88	0.04	1	-0.26	0.09	1
5393011	nnnnn	4363.72	75.02	3	3.72	0.44	2	-0.30	0.07	1
5419168	nnnnn	5784.46	52.21	7	4.03	0.03	6	-0.29	0.05	5
6013872	nnnnn	5843.55	81.92	5	3.53	0.44	2	-0.46	0.07	1
4313909	nnnnn	5159.15	179.84	3	4.35	0.25	2	-0.64	0.07	1
4343406	nnnnn	4640.06	83.41	3	4.44	0.11	4	-0.54	0.22	1
4417800	nnnnn	5413.28	55.84	6	4.19	0.05	6	-0.14	0.05	6
4422870	nnnnn	4884.68	173.77	3	4.40	0.17	3	-0.78	0.25	3
4426169	1CnnR	...	0	0	0
4594498	1CnnR	...	0	0	0
4701006	nnnnn	5533.76	30.49	3	3.99	0.08	2	-0.50	0.06	1
4731882	nCnnR	...	0	0	0
4739295	nnnnn	4673.07	106.93	3	4.22	0.14	4	-0.38	0.10	1
4812003	nnnnn	4990.63	113.49	3	4.41	0.07	4	-0.52	0.10	3

Table 7.5 (cont'd): SSPP Stellar Parameters for Hectospec Targets

UW ID ^a	flags	T_{eff} (K)	$\sigma(T_{\text{eff}})$ (K)	$N(T_{\text{eff}})^{\text{b}}$	$\log g$ (dex)	$\sigma(\log g)$ (dex)	$N(\log g)^{\text{b}}$	[Fe/H] (dex)	$\sigma([\text{Fe}/\text{H}])$ (dex)	$N([\text{Fe}/\text{H}])^{\text{b}}$
5021164	nnnnn	5482.41	35.70	6	4.25	0.11	6	-0.80	0.04	5
5087529	nnnnn	5940.81	205.88	4	3.82	0.28	2	-0.72	0.05	1
5088799	NnnnnN	0	0	0
5221270	1CnnR	0	0	0
5227680	nnnnn	4632.89	138.76	3	3.96	0.11	3	-0.16	0.07	1
5259655	1CnnR	0	0	0
5299617	lnnnR	0	0	0
5484320	nnnnn	5693.26	47.07	7	3.80	0.07	6	0.07	0.07	6
5558317	nnnnn	4708.40	343.05	3	4.15	0.71	2	-0.70	0.12	1
5691570	nnnnn	5959.30	107.83	8	3.78	0.07	6	-0.64	0.02	5
5771531	nnnnn	5009.01	172.87	3	4.71	0.09	4	-0.93	0.02	2
5851460	NnnnnN	0	0	0
5855774	nnnnn	4338.77	46.53	3	4.01	0.27	3	-0.46	0.07	1
4171787	NCnnN	0	0	0
4256082	lnnnn	4372.69	193.25	2	4.12	0.09	1	-0.62	0.08	1
4284597	1CnnR	0	0	0
4321316	nnnnn	5544.60	250.36	4	3.99	0.04	4	-0.93	0.29	2
4381791	nnnnn	5526.67	103.06	7	4.03	0.12	6	-0.23	0.06	7
4499787	nnnnn	4332.51	104.67	3	4.18	0.16	3	-0.56	0.06	1
4592920	nnnnn	5680.58	31.74	7	3.49	0.07	6	-0.07	0.10	5
4667202	nnBnn	5519.48	28.82	7	4.01	0.02	6	-0.45	0.03	5
4705761	nnnnn	5141.73	32.74	3	4.43	0.14	4	-0.46	0.04	3
5033228	nnnnn	5215.11	95.56	4	3.96	0.06	5	0.21	0.00	2
5045867	nnnnn	4611.32	56.05	3	4.48	0.17	4	-0.71	0.13	1
5114414	NnnnnN	0	0	0
5168415	1CnnR	0	0	0
5268750	nnnnn	5419.26	47.96	3	4.08	0.13	2	-0.46	0.05	1
5335638	nnnnn	4918.89	129.50	4	4.67	0.09	5	-0.90	0.09	3
5352389	nCnnn	5304.59	93.93	1	3.68	0.15	2	-0.44	0.08	1
5401063	nnnnn	4751.26	113.51	3	4.35	0.06	3	-0.40	0.06	1
5644835	nnngn	5265.88	43.88	6	2.18	0.14	6	-1.01	0.06	5
5693231	nCnnR	0	0	0
5764126	nnngn	5948.02	96.92	4	4.02	0.19	2	-1.11	0.04	1
5798914	nnBnn	5114.04	75.33	4	4.28	0.07	5	-0.19	0.07	4
5891718	NnnnnN	0	0	0
6032673	NCnnR	0	0	0
4213623	nnnnn	4881.40	131.53	3	4.40	0.21	4	-0.28	0.14	1
4404441	nnnnn	5550.78	60.90	4	4.02	0.20	5	-0.29	0.08	2
4510934	lnnnN	0	0	0
4533058	nnnnn	5885.96	115.19	7	3.94	0.12	4	-0.35	0.10	4
4634261	nnnnnR	0	0	0
4791667	nCnnn	5187.04	119.06	4	4.33	0.19	4	-0.43	0.04	1
4845559	nnnnn	5111.71	107.51	4	4.25	0.18	5	-0.87	0.10	4
5103491	nnBnn	5098.02	105.58	4	3.37	0.19	4	-0.61	0.01	2
5143432	nnnnn	4785.82	65.90	3	2.90	0.15	4	-0.22	0.09	2
5151567	nnnnc	0	0	0
5193595	nnBnn	5495.52	57.79	3	4.04	0.27	2	-0.63	0.05	1
5209742	nnBnn	5003.12	83.41	4	4.22	0.15	5	-0.57	0.05	2
5407028	nnnnn	4897.75	110.99	3	4.40	0.07	4	-0.42	0.01	2
5422761	nnnnn	5491.89	161.08	3	4.00	0.20	2	-0.60	0.08	1
5539361	nnnnn	5843.33	32.64	7	4.16	0.03	6	-0.26	0.04	6
5593868	nnnnn	5966.77	36.21	7	3.98	0.20	4	-0.86	0.02	2
5790798	NnnnnN	0	0	0
5830112	Nnnnn	5154.98	219.37	3	3.46	0.01	2	-0.59	0.10	1
4221496	nnnnn	5293.91	69.08	6	4.37	0.08	6	-0.36	0.03	6
4502850	nnnnn	5138.98	91.08	6	4.08	0.12	6	-0.91	0.05	4
4590143	1CnnR	0	0	0
4679914	nnnnn	5061.27	111.88	3	4.88	0.26	3	-0.57	0.15	3
4749834	NnnnR	0	0	0
5305811	nnnnn	5712.34	40.41	7	4.01	0.06	6	-0.05	0.07	6
5314662	nnnnn	8137.38	169.90	5	3.96	0.20	4	-1.73	0.12	1
5324408	nnnnn	4213.14	42.50	3	3.53	0.27	2	-0.75	0.06	1
5351794	nnngn	5463.16	59.74	7	4.13	0.19	6	-1.05	0.05	5
5356183	NnnnR	0	0	0
5500830	Nnnnn	5197.21	97.99	3	4.15	0.53	2	-0.92	0.04	1
5619046	nnnnn	4834.00	88.73	3	3.27	0.09	3	-0.47	0.10	1
5817274	nnnnn	4900.16	85.52	3	3.54	0.07	4	-0.61	0.18	3
5856047	nnBnn	5603.32	193.28	6	4.21	0.15	4	-0.22	0.03	2
6037816	nnngn	4273.16	41.50	3	4.08	0.28	4	-1.28	0.11	1
6051865	nnnnn	7248.50	79.24	8	4.44	0.22	5	-1.89	0.02	2
4163416	nnngn	5729.01	76.10	6	2.32	0.34	4	-1.22	0.07	4
4468848	Nnnngn	4591.19	123.76	3	4.33	0.34	2	-1.01	0.06	1
4486804	NCnnR	0	0	0
4509314	nnnnn	5567.15	228.06	3	4.38	0.19	4	-0.86	0.01	2

Table 7.5 (cont'd): SSPP Stellar Parameters for Hectospec Targets

UW ID ^a	flags	T_{eff} (K)	$\sigma(T_{\text{eff}})$ (K)	$N(T_{\text{eff}})^{\text{b}}$	$\log g$ (dex)	$\sigma(\log g)$ (dex)	$N(\log g)^{\text{b}}$	[Fe/H] (dex)	$\sigma([\text{Fe}/\text{H}])$ (dex)	$N([\text{Fe}/\text{H}])^{\text{b}}$
4551709	lCnnR	0	0	0
4657600	nnnnn	5176.26	55.71	4	3.14	0.25	5	-0.92	0.02	3
4732843	nnnnn	5571.04	86.13	7	3.89	0.08	6	-0.36	0.04	6
4743508	nnnnn	4960.25	111.97	3	4.43	0.12	4	-0.34	0.06	3
5130447	nnnnn	5446.05	18.49	7	3.94	0.08	6	-0.16	0.05	6
5165629	lCnnR	0	0	0
5167239	nCnnn	5483.01	431.65	3	4.45	0.10	4	-0.40	0.09	2
5189964	nnnnn	5204.88	149.93	4	4.61	0.08	5	-0.85	0.07	3
5213451	nnnnn	6107.21	65.34	8	4.07	0.13	6	-0.53	0.01	4
5292050	nnnnn	6362.94	168.32	5	3.89	0.53	2	-0.18	0.12	1
5449955	nnnnn	6248.47	56.12	8	3.76	0.08	6	-0.30	0.00	4
5535356	lCnnR	0	0	0
5614419	nnnnn	4873.35	109.11	3	4.36	0.10	4	-0.32	0.01	2
5870498	nnnnn	5407.91	156.78	4	3.53	0.15	5	-0.11	0.02	2
5897704	nnnnn	5404.41	123.25	5	3.41	0.22	4	-0.81	0.09	3
6019656	nnnnn	5483.80	61.96	6	4.30	0.13	6	-0.11	0.05	5
6041112	lnnnR	0	0	0
4155231	lCnnR	0	0	0
4174554	nnnnn	5892.17	44.55	7	3.97	0.10	4	-0.51	0.06	4
4289635	NCnnN	0	0	0
4477874	nnBGn	5801.16	122.51	4	3.63	0.11	2	-1.27	0.07	1
4502825	nCnnR	0	0	0
4516464	nnnnn	5192.99	14.36	4	3.55	0.11	5	-0.77	0.05	5
4733489	nnBnn	4757.57	115.37	3	3.98	0.13	4	-0.33	0.05	2
4801113	nnnnn	4344.81	75.04	3	4.22	0.02	3	-0.92	0.10	1
4818488	nnnnn	6434.60	162.69	7	3.76	0.34	4	-0.12	0.05	1
5091009	nnnnn	5119.05	67.24	4	3.89	0.03	5	-0.68	0.07	5
5165086	nnnnn	5365.10	68.01	3	4.19	0.26	2	-0.74	0.05	1
5169791	nnnnn	6398.54	146.18	6	3.05	0.61	3	-1.32	0.10	2
5320614	lnngn	4027.39	18.62	1	4.09	0.12	2	-1.22	0.14	1
5406178	nnBnn	5009.41	56.29	3	4.45	0.15	4	-0.32	0.04	3
5450871	nnnnn	5819.96	40.16	4	3.84	0.07	2	-0.57	0.02	1
5465035	nnnnn	5415.97	28.01	6	2.23	0.11	6	-0.94	0.08	7
5465291	nnnnN	0	0	0
5779810	nnnnn	5401.92	93.99	5	4.29	0.12	4	-0.63	0.08	3
5937331	nnnnn	5302.58	66.36	6	4.00	0.13	6	-0.58	0.06	5
5972664	nnnnn	5897.81	51.92	7	3.63	0.09	6	-0.69	0.04	7
5981254	nnnnn	5500.33	49.16	6	4.28	0.16	6	-0.64	0.05	5
6019448	lCnnR	0	0	0
4205188	nnBnn	0	0	0
4226095	nnnnn	5790.83	92.56	7	4.11	0.18	6	-0.33	0.05	6
4236112	nnnnn	4337.94	56.37	3	3.58	0.16	3	-0.29	0.08	1
4239636	nnnnn	5966.05	58.83	7	3.86	0.12	6	-0.48	0.04	6
4326777	NnnnR	0	0	0
4360657	nCnGn	4180.26	175.27	2	4.17	0.24	2	-1.04	0.18	1
4391692	nnnnn	5506.59	134.66	4	3.97	0.21	2	-0.70	0.09	1
4863910	nnnnn	5750.52	46.68	7	4.01	0.09	6	-0.17	0.03	5
5170009	nnGn	6325.19	59.50	8	3.89	0.12	5	-1.00	0.05	5
5254848	lnnnR	0	0	0
5274235	nnnnN	0	0	0
5298860	lnnnR	0	0	0
5380596	nnnnn	6057.74	37.35	8	3.85	0.07	6	-0.22	0.04	6
5630505	nnnnn	4903.26	105.83	3	2.72	0.26	4	-0.86	0.10	3
5763835	NnBnN	0	0	0
5780838	nnBnn	5587.48	118.11	4	3.53	0.08	2	-0.45	0.09	1
5830616	nnnnn	5641.86	43.30	7	4.31	0.06	6	-0.40	0.07	6
6042287	nnBnn	5102.16	201.73	4	3.33	0.14	5	-0.68	0.05	4
4195055	lnnnN	0	0	0
4429493	nnnnn	5636.27	104.06	5	4.20	0.24	4	-0.29	0.02	2
4450832	NCnnN	0	0	0
4630534	nnnnn	4679.83	39.95	3	2.66	0.15	4	-0.34	0.01	2
4708537	nnnGn	6093.55	116.44	8	4.18	0.43	5	-1.41	0.03	2
4714900	nnnnn	6023.84	74.87	6	3.93	0.57	4	-0.55	0.01	2
4780484	nnnnn	4698.92	116.55	3	4.67	0.02	4	-0.14	0.22	1
4844030	nnBnn	5179.02	122.82	4	3.95	0.35	5	0.50	0.12	1
5250995	nCnnR	0	0	0
5257406	NnnnN	0	0	0
5447181	nnnGn	4209.92	104.76	3	4.40	0.15	4	-1.06	0.08	1
5464221	nnnnn	6134.91	182.88	5	4.01	0.46	2	-0.23	0.09	1
5468661	VCBnX	0	0	0
5611828	nnnnn	5982.82	40.38	8	4.01	0.10	6	-0.49	0.01	5
5843739	nnBnn	5346.66	10.02	6	4.03	0.26	6	-0.64	0.05	6
5933069	nnnnX	0	0	0
5985240	NnnnN	5581.19	72.33	3	4.28	0.46	2	-0.61	0.03	1

Table 7.5 (cont'd): SSPP Stellar Parameters for Hectospec Targets

UW ID ^a	flags	T_{eff} (K)	$\sigma(T_{\text{eff}})$ (K)	$N(T_{\text{eff}})^{\text{b}}$	$\log g$	$\sigma(\log g)$ (dex)	$N(\log g)^{\text{b}}$	[Fe/H]	$\sigma([\text{Fe}/\text{H}])$ (dex)	$N([\text{Fe}/\text{H}])^{\text{b}}$
6057858	nnnnn	7441.24	61.89	6	4.02	0.20	5	-0.40	0.02	3
4757146	NnnnR	0	0	0
4803561	lnnnN	0	0	0
5406849	nnnnn	5568.10	184.97	3	3.98	0.16	2	-0.67	0.03	1
4170078	Nnnnn	5640.91	29.01	3	3.90	0.16	2	-0.56	0.05	1
4239654	nnnnn	6006.18	64.58	5	3.99	0.23	2	-0.77	0.05	1
4341049	ICnnR	0	0	0
4694201	NnBnN	0	0	0
5541672	nnnnn	7215.59	83.05	7	3.63	0.54	5	-2.41	0.08	2
6071650	nnnnn	4912.96	77.02	3	4.52	0.12	4	-0.95	0.03	2
4252424	NnnnN	0	0	0
4256744	nnnnn	6114.06	135.88	7	4.13	0.29	4	-0.58	0.08	4
4448675	NnBnn	4719.08	34.64	3	3.62	0.03	2	-0.90	0.06	1
4594666	nnnnn	4895.51	93.45	3	3.94	0.37	3	-0.99	0.06	1
4633680	nCnnR	0	0	0
4760356	nnnnn	5765.41	29.83	7	4.14	0.04	6	-0.36	0.06	6
5060995	LnnnR	0	0	0
5126388	nnnnn	5658.37	101.46	6	4.30	0.08	4	-0.54	0.03	2
5180358	nnnnn	4985.65	113.91	3	4.18	0.14	4	-0.61	0.13	2
5210273	nnnGn	4201.14	66.88	3	3.46	0.33	2	-1.09	0.17	1
5279423	nnnGn	6263.00	30.97	6	3.61	0.55	3	-1.09	0.09	1
5337915	nnnnn	5516.94	88.76	6	4.16	0.20	6	-0.59	0.06	4
5365961	nnnnn	4413.24	43.63	3	4.37	0.21	4	-1.31	0.07	1
5425336	nnnnn	5283.23	168.29	4	3.76	0.15	5	-0.27	0.09	4
5432980	nnnnn	5864.63	67.24	4	3.49	0.17	2	-0.36	0.05	1
5493187	nnnnn	5521.35	33.17	6	4.11	0.03	6	-0.18	0.06	5
5629355	nnnnn	5663.35	23.42	4	3.78	0.40	2	0.06	0.15	1
5633383	nnnnn	6076.14	87.12	5	4.06	0.43	2	-0.30	0.08	1
5671550	nnnnn	7014.16	160.03	3	3.20	0.06	2	-1.86	0.06	1
4160299	nnnnn	5922.27	148.05	4	4.03	0.43	2	-0.48	0.04	1
4368240	nnnnn	4598.31	68.41	3	4.48	0.14	4	-0.88	0.04	2
4474509	nnnnn	6436.46	113.44	8	3.68	0.14	6	-0.18	0.07	5
4586457	NnnnN	0	0	0
4617557	lnnnN	0	0	0
4632838	nnnnn	6171.83	67.72	8	3.86	0.15	6	-0.77	0.03	5
4705229	nnnnn	5233.11	148.70	3	4.54	0.19	2	-0.53	0.09	1
5018510	nnngn	4640.49	47.80	3	4.63	0.10	4	-1.16	0.10	2
5029857	nnnnn	4406.64	111.91	2	4.75	0.06	1	-0.98	0.07	1
5032510	nnnnn	5543.96	107.83	3	4.25	0.30	2	-0.95	0.06	1
5033294	nnnnn	4350.19	132.33	2	3.53	0.11	1	-0.26	0.06	1
5207400	nnnnn	5799.24	42.86	7	4.18	0.10	6	-0.14	0.05	4
5238672	nnnnn	5936.52	95.77	4	3.91	0.37	2	-0.62	0.04	1
5332371	nnnnn	5457.69	88.16	6	3.93	0.19	4	-0.50	0.05	4
5497729	nnnnn	6083.97	156.44	6	3.88	0.16	3	-1.22	0.03	2
5560498	Lnnnn	4062.49	2.97	2	3.69	0.73	2	-0.42	0.19	1
5781229	nnngn	4037.08	13.70	2	4.60	0.05	1	-1.40	0.07	1
5871760	LnnnR	0	0	0
5992697	nnBgn	4946.74	65.01	3	3.55	0.16	4	-1.03	0.15	3
6019175	nnnnn	4574.66	48.58	3	4.18	0.04	3	-0.35	0.07	1
4216500	nnnnn	6070.89	124.72	5	2.55	1.05	2	-1.24	0.04	1
4529997	NnnnN	0	0	0
4597945	DnnGn	4112.19	30.31	1	4.58	0.08	2	-1.07	0.20	1
4619428	nnnnN	0	0	0
4620222	nnnnn	4619.33	82.75	3	3.90	0.36	2	-0.20	0.08	1
4689437	nnnnn	5841.80	118.51	6	3.99	0.13	6	-0.62	0.03	3
4696226	nnnnn	5514.93	26.53	6	4.14	0.03	6	-0.17	0.06	5
4719667	nnnnn	5004.57	109.97	3	4.42	0.09	4	-0.18	0.10	1
4808454	nnnnn	5208.99	73.45	4	3.98	0.17	4	-0.40	0.11	1
5139465	VnBnX	0	0	0
5352697	nnnnn	5792.01	16.37	4	4.26	0.62	2	-0.48	0.04	1
5368567	nnnnn	4430.31	9.05	3	3.55	0.40	2	-0.23	0.08	1
5372323	nnBnn	5701.80	94.46	6	3.68	0.21	4	-0.39	0.04	4
5458795	nnnnn	6115.93	169.72	5	3.79	0.52	2	-0.66	0.05	1
5495114	nnnnn	5296.86	27.91	6	4.00	0.17	6	-0.44	0.01	2
5523946	Nnnnn	4953.71	328.37	3	4.47	0.28	2	-0.67	0.16	1
5563190	NnnnR	0	0	0
5954487	nnBnn	5512.14	111.65	5	4.45	0.17	4	-0.29	0.13	3
5972464	nnnnn	5806.40	25.58	8	4.15	0.13	6	-0.57	0.05	6
4204119	nnBnn	5189.26	36.77	4	3.71	0.09	5	-0.64	0.05	2
4379389	nnBnn	4930.43	76.46	4	3.62	0.16	5	-0.52	0.13	4
4481997	NnBnN	0	0	0
4627218	nnnnn	6045.35	41.98	8	4.18	0.09	6	-0.44	0.06	6
4741431	nnBnn	5521.88	238.47	3	3.52	1.36	2	-0.87	0.06	1
4813684	nnnnn	5917.30	202.12	6	3.78	0.17	4	-0.97	0.17	4

Table 7.5 (cont'd): SSPP Stellar Parameters for Hectospec Targets

UW ID ^a	flags	T_{eff} (K)	$\sigma(T_{\text{eff}})$ (K)	$N(T_{\text{eff}})^{\text{b}}$	$\log g$ (dex)	$\sigma(\log g)$ (dex)	$N(\log g)^{\text{b}}$	[Fe/H] (dex)	$\sigma([\text{Fe}/\text{H}])$ (dex)	$N([\text{Fe}/\text{H}])^{\text{b}}$
5080613	nnnnn	5944.59	47.31	8	3.80	0.09	6	-0.69	0.03	6
5167144	nnnnn	5278.14	95.65	4	4.42	0.07	4	-0.35	0.01	2
5208616	nnnnn	4348.77	58.25	3	4.36	0.51	2	-1.52	0.18	1
5269118	nnnnn	5727.75	78.71	4	3.82	0.38	2	-0.85	0.05	1
5300539	nnnGn	5191.21	115.36	3	4.08	0.46	2	-1.03	0.13	1
5377423	NnnnN	0	0	0
5466322	nnnnn	7636.24	62.51	4	4.17	0.24	3	-0.05	0.05	1
5487704	nnnnn	4202.81	169.07	2	2.90	0.13	1	-0.55	0.12	1
5724196	lCnnR	0	0	0
5777291	lCnnR	0	0	0
5808798	nnnnn	5478.09	191.92	3	4.21	0.66	2	-0.94	0.05	1
5810291	nnBgn	4695.97	133.19	3	4.05	0.26	2	-1.03	0.06	1
4156460	nnnnn	6395.80	80.21	4	3.03	0.63	3	-3.98	0.05	1
4260179	nnBnn	5543.37	61.59	6	4.17	0.13	6	-0.59	0.03	5
4276190	nnnnn	5804.12	36.02	4	4.34	0.31	2	-0.24	0.03	1
4379710	NnBnN	0	0	0
4506792	nnBnn	5292.13	69.81	3	4.49	0.31	2	-0.72	0.07	1
4575848	nnnnn	6045.35	57.39	7	3.99	0.16	4	-0.42	0.04	4
4694712	nnnnn	5952.02	91.13	8	4.20	0.14	6	-0.75	0.06	5
5028866	nnnnn	4891.32	83.82	3	4.53	0.10	4	-0.57	0.10	3
5087363	nnnGn	7344.17	355.41	4	2.80	0.39	2	-1.77	0.02	1
5155390	nnnnn	5756.42	45.53	7	4.18	0.08	6	-0.43	0.02	5
5549926	nnnnn	6141.43	141.70	5	3.74	0.25	2	-0.15	0.09	1
5769079	nnnnn	4797.50	157.71	3	4.01	0.10	2	-0.31	0.11	1
4269868	NCnnN	0	0	0
4278012	VnnnN	0	0	0
4399606	nnnnn	4299.89	108.91	3	3.79	0.19	4	-0.56	0.12	1
4461333	nnnnn	5065.28	98.42	4	4.54	0.14	5	-0.73	0.02	2
5057992	NnnnN	0	0	0
5061933	nnnnn	5028.98	335.60	3	3.93	0.02	2	-0.24	0.09	1
5155356	nnnnn	5366.98	104.87	6	3.77	0.11	6	-0.38	0.04	5
5346198	nnnnn	7304.72	27.94	8	2.58	0.20	6	-0.86	0.04	4
5358356	nnnnn	5460.02	44.31	7	4.37	0.08	6	-0.26	0.06	6
5442314	nnnnn	5459.48	36.28	6	4.37	0.12	6	-0.79	0.04	6
5711095	nnnnn	6319.17	54.54	8	2.63	0.21	6	-1.16	0.03	6
5764793	nnnnn	5301.59	156.86	4	3.86	0.08	5	-0.41	0.08	2
5855490	nnnnn	7882.62	54.61	4	4.61	0.27	3	-0.58	0.07	1
5935811	VnBnN	0	0	0
4172430	Dnnnn	4103.24	84.22	2	4.60	0.02	2	-0.81	0.20	1
4276507	nCnnR	0	0	0
4295584	nnnnn	4799.73	110.98	3	4.57	0.31	2	-0.82	0.07	1
4646974	nnngn	4844.51	34.56	3	2.47	0.09	4	-1.07	0.06	4
4680192	nnnnn	5891.22	45.76	7	4.06	0.16	6	-0.80	0.04	4
4839979	nnngn	4023.86	18.31	1	4.32	0.11	2	-1.56	0.09	1
5015818	LnnnR	0	0	0
5045619	nnnnn	6178.68	116.55	8	3.87	0.19	5	-0.43	0.02	2
5048856	nnngn	5175.82	67.94	6	2.35	0.17	6	-1.55	0.07	7
5092656	nnnnn	5078.02	86.16	4	3.49	0.07	5	-0.47	0.06	5
5127401	nnngn	5443.17	111.92	4	3.34	0.10	2	-1.40	0.13	1
5223413	nnnnX	0	0	0
5254149	nnBnn	5473.32	80.58	7	4.17	0.11	6	-0.45	0.05	5
5283135	nnnnn	5249.59	31.02	3	4.08	0.40	2	-0.89	0.06	1
5863558	NnnnR	0	0	0
6069934	nnnnn	5739.72	111.51	8	4.10	0.13	6	-0.39	0.04	6
4206445	nnnnn	4850.49	103.70	3	3.52	0.37	3	-0.58	0.09	2
4360398	nnnGn	7493.38	369.46	5	3.10	0.30	4	-1.94	0.08	1
4365373	nnnnR	0	0	0
4368723	VnBnN	0	0	0
4532728	nnnnn	6336.42	215.77	5	3.33	1.00	2	-1.28	0.09	1
4805491	nnnnR	0	0	0
4869732	NnBnN	0	0	0
5018719	nnnnn	6147.31	159.96	5	3.76	0.57	2	-0.43	0.08	1
5049055	nnnnn	6956.03	71.46	6	3.99	0.11	4	-0.47	0.09	1
5179595	Lnnn	4246.67	174.83	2	3.82	0.10	1	-0.61	0.08	1
5204284	nnBnn	4497.11	96.91	2	2.90	0.82	2	-0.64	0.13	1
5248480	nnnnn	4592.16	88.51	3	4.19	0.06	2	-0.17	0.09	1
5314483	nnnnn	6094.21	152.02	5	4.28	0.43	2	-0.58	0.05	1
5369333	LnnnR	0	0	0
5438430	nnngn	4560.91	158.69	3	4.37	0.51	2	-1.45	0.12	1
5628826	nnnnn	4605.94	100.37	3	3.97	0.19	3	-0.30	0.09	1
6027750	nnnnn	5488.49	402.83	3	4.24	0.33	4	-1.01	0.04	2
6058286	nnnnn	5033.34	127.55	4	4.20	0.14	5	-0.23	0.06	3
4206024	nnnnn	6208.83	104.52	5	2.84	0.13	2	-2.25	0.16	1
4297664	NnBn	5622.69	59.70	6	3.74	0.13	4	-0.35	0.07	5

Table 7.5 (cont'd): SSPP Stellar Parameters for Hectospec Targets

UW ID ^a	flags	T_{eff} (K)	$\sigma(T_{\text{eff}})$ (K)	$N(T_{\text{eff}})^{\text{b}}$	$\log g$ (dex)	$\sigma(\log g)$ (dex)	$N(\log g)^{\text{b}}$	[Fe/H] (dex)	$\sigma([\text{Fe}/\text{H}])$ (dex)	$N([\text{Fe}/\text{H}])^{\text{b}}$
4752334	NnnnN	0	0	0
5186700	nnnnn	6337.13	60.43	9	3.95	0.20	7	-1.34	0.01	2
5480537	nnnnn	5284.83	67.57	6	4.42	0.08	6	-0.33	0.03	5
5611985	NnnnN	0	0	0
5663707	nnnnn	5804.25	114.26	6	4.07	0.05	4	-0.07	0.12	2
5933250	nnnnn	6039.75	76.92	8	4.30	0.09	6	-0.51	0.06	5
4217301	nnnnn	4619.49	88.14	3	4.18	0.03	4	-0.51	0.23	2
5117011	nnnnn	5993.23	263.14	5	3.90	0.37	2	-0.71	0.05	1
5206900	lnnnR	0	0	0
5823168	nnnnn	4876.96	108.14	3	4.68	0.29	3	-0.96	0.09	1
4181591	nnnnn	5987.05	149.25	7	3.32	0.10	6	-0.88	0.10	5
4205907	lnnnX	0	0	0
4304904	nngn	5059.44	266.47	4	3.71	0.43	3	-1.61	0.14	2
4305476	nnnnn	5656.28	92.32	3	3.80	0.70	2	-0.27	0.09	1
4337652	nngn	5496.12	373.80	4	3.24	0.31	2	-1.46	0.14	1
4346910	nnnnn	5570.29	71.40	6	4.20	0.15	6	-0.15	0.07	4
4432290	nnnnn	5499.10	47.50	6	4.38	0.05	6	-0.56	0.04	7
4559000	lCnnR	0	0	0
4568788	nnBnn	5450.39	80.37	6	4.28	0.09	6	-0.63	0.06	6
4580865	nnnnn	4917.04	143.73	3	4.42	0.19	4	-0.60	0.12	3
4776172	lCnnR	0	0	0
4865480	nnnnn	5273.97	22.27	4	4.38	0.11	4	-0.41	0.11	1
5049077	nnnnn	6013.79	75.09	5	2.97	0.16	2	-0.95	0.11	1
5074533	nnnnn	5816.92	54.76	5	4.23	0.24	2	-0.73	0.03	1
5082868	nnnnn	4955.01	173.10	3	4.05	0.13	2	-0.06	0.12	1
5103474	nnnnn	6144.18	34.36	7	3.82	0.17	4	-1.31	0.03	3
5191854	nnnnn	5980.08	51.92	8	4.04	0.10	6	-0.46	0.02	6
5205492	nnnnn	5248.09	63.86	4	4.34	0.25	4	-0.70	0.14	4
5261443	nnnnn	6146.89	260.75	4	4.21	0.58	2	-0.69	0.05	1
5335441	nmmN	0	0	0
5661036	nnnnn	6689.41	70.41	5	3.42	0.81	3	-1.82	0.07	1
5696833	nnnnn	4874.53	58.22	3	4.13	0.08	4	-0.19	0.06	2
5703891	nnnnn	5072.36	155.19	3	3.60	0.36	2	-0.05	0.14	1
5813527	nnnnn	6157.25	76.43	8	2.62	0.49	5	-1.02	0.10	2
5815151	nnnnn	5987.00	57.66	7	4.05	0.13	4	-0.33	0.05	4
4189939	nnnnn	6777.05	64.35	8	2.78	0.19	6	-1.42	0.05	5
4247227	nCnnR	0	0	0
4479292	nnnnn	5039.34	126.49	3	4.15	0.23	2	-0.92	0.14	1
4530239	nnnnR	0	0	0
4620328	nnnnn	4853.88	134.61	3	4.27	0.18	4	-0.33	0.08	3
4809483	nnnnn	5681.22	148.25	6	3.84	0.13	6	-0.52	0.13	5
5317650	nnnnn	5577.33	82.30	6	4.01	0.19	6	-0.80	0.02	4
5356299	nnnnn	4986.10	65.38	3	3.46	0.11	4	-0.49	0.08	3
5401405	lnnnR	0	0	0
5408668	nnBnn	5479.36	61.48	3	4.03	0.60	2	-0.80	0.06	1
5434804	nnnnn	5507.38	99.56	5	3.37	0.34	4	-0.87	0.01	2
5468250	nnnnn	5028.06	153.63	3	4.29	0.31	2	-0.35	0.12	1
5528139	nnBnn	6460.04	261.74	5	4.07	0.81	2	-1.33	0.05	1
5681223	nnnnn	4864.91	84.35	3	4.16	0.43	3	-0.71	0.04	2
5987030	NnnnN	0	0	0
6039349	nnnnn	4196.91	117.91	2	3.83	0.25	1	-0.57	0.13	1
6063851	nnnnn	5976.37	206.44	4	3.46	0.37	2	-0.25	0.07	1
4188911	nCBnc	0	0	0
4224121	nnnnn	5442.24	121.58	6	3.89	0.10	4	-0.23	0.01	3
4422789	nnnnn	5498.62	52.09	6	3.57	0.03	6	-0.55	0.03	5
4438844	nnnnn	5733.35	53.96	4	3.79	0.03	2	-0.76	0.03	1
4519608	nnnnn	5642.90	64.42	7	3.82	0.05	6	-0.27	0.06	5
4553929	nmmN	0	0	0
4612360	lCnnR	0	0	0
4623100	nnnnn	4391.01	366.35	2	3.48	0.17	1	-0.88	0.10	1
4639580	NCnnR	0	0	0
5026523	nnnnn	4979.03	45.26	4	4.44	0.16	4	-0.93	0.01	2
5035746	nnBnn	5307.14	89.19	4	4.04	0.11	5	-0.29	0.09	4
5184098	NnnnN	0	0	0
5258151	nnnnn	5831.29	53.65	7	3.98	0.06	6	-0.28	0.02	5
5470212	nnnnn	5673.27	87.88	8	4.12	0.08	6	0.01	0.06	5
5593562	nnnnn	5307.27	119.88	3	4.53	0.30	2	-0.74	0.07	1
5636790	NnnnN	0	0	0
5808732	nnnnn	6111.75	124.93	5	3.50	0.17	2	-0.91	0.10	1
6028437	nnnnn	4710.32	57.19	3	3.35	0.02	3	-1.61	0.21	1
4175068	nnnnn	4505.06	36.07	3	3.98	0.08	4	-0.44	0.10	2
4244074	nnnnn	4520.62	68.51	3	4.23	0.12	4	-0.70	0.10	1
4277232	nnnnn	7524.26	58.73	5	4.26	0.68	4	-1.63	0.09	1
4328926	lCnnR	0	0	0

Table 7.5 (cont'd): SSPP Stellar Parameters for Hectospec Targets

UW ID ^a	flags	T_{eff} (K)	$\sigma(T_{\text{eff}})$ (K)	$N(T_{\text{eff}})^{\text{b}}$	$\log g$ (dex)	$\sigma(\log g)$ (dex)	$N(\log g)^{\text{b}}$	[Fe/H] (dex)	$\sigma([\text{Fe}/\text{H}])$ (dex)	$N([\text{Fe}/\text{H}])^{\text{b}}$
4459136	nnnnN	0	0	0
4492172	nnnnn	5091.23	300.24	3	4.46	0.42	2	-0.86	0.07	1
4533596	nnnnn	4688.27	136.28	3	4.16	0.07	2	-0.29	0.11	1
4712869	VnnnX	0	0	0
4731375	nnnnR	0	0	0
4826163	nnnnn	5730.07	108.89	6	4.37	0.14	4	-0.71	0.04	4
4828391	nnnnn	5665.36	35.15	7	3.67	0.07	6	-0.31	0.06	7
5181264	lCnnR	0	0	0
5225910	nnnnn	5326.39	80.70	4	4.19	0.12	5	-0.11	0.07	3
5331534	nnnnn	6038.45	28.18	7	3.86	0.07	6	0.07	0.07	5
5456949	nnnnn	5067.43	61.10	4	3.45	0.13	5	-0.76	0.05	5
5463335	nnnnn	5638.43	69.53	4	4.19	0.21	2	-0.70	0.02	1
5690145	nnnnn	5965.10	63.93	5	4.24	0.64	2	-0.86	0.09	1
5703924	nnnnn	4941.05	77.83	3	3.44	0.18	4	-0.03	0.08	3
5776753	NnnnN	0	0	0
5788233	nnnGn	4972.55	173.33	4	4.20	0.36	5	-1.46	0.06	4
4368844	nnBnn	6257.89	67.00	6	4.51	0.25	6	0.51	0.02	3
4394365	nCnnR	0	0	0
4519137	nnnnn	5509.09	59.57	6	4.08	0.04	6	-0.15	0.07	6
4580626	nnnnn	5422.23	49.10	6	4.23	0.05	6	-0.20	0.05	6
4639298	nnngn	4072.61	24.52	1	4.27	0.06	2	-1.32	0.17	1
4786094	nnnnc	0	0	0
4808809	nnnGn	6180.41	86.28	7	2.50	0.73	4	-1.44	0.15	4
4826093	nnnnn	5391.62	162.87	5	4.15	0.05	4	-0.45	0.04	2
5112690	nnnnn	5562.63	45.12	6	4.21	0.13	6	-0.15	0.04	6
5257780	nnBnn	5491.50	145.68	4	3.73	0.13	2	-0.50	0.06	1
5279235	nnnnn	5769.81	137.30	6	4.12	0.07	6	-0.71	0.10	5
5295038	lCnnR	0	0	0
5778213	nnnnn	5808.94	51.24	7	4.35	0.14	6	-0.67	0.05	6
5925519	nnngn	5389.29	42.16	6	2.58	0.12	6	-1.97	0.02	6
6037670	nnBnn	5060.52	131.76	4	4.14	0.19	5	-0.09	0.05	1
6073466	nnnnn	5167.77	270.73	3	3.62	0.17	4	-0.57	0.09	2
4187877	nnBnn	6601.74	313.90	6	4.39	0.36	4	0.04	0.01	2
4215294	nnnnn	5258.50	33.04	4	4.44	0.08	5	-0.56	0.06	5
4293655	nnnnn	4308.70	179.22	3	4.04	0.14	2	-0.32	0.11	1
4370120	NnnnN	0	0	0
4392595	nCnnR	0	0	0
4575745	nnnnn	5720.23	73.95	7	4.41	0.18	6	-0.53	0.04	7
5100654	nCnnn	5304.60	544.65	3	4.37	0.03	4	-0.81	0.07	2
5113033	nnnnn	5039.72	91.89	4	4.44	0.07	5	-0.65	0.10	5
5166231	nnnnn	5015.31	98.19	3	4.43	0.14	4	-0.71	0.15	3
5264709	NnnnN	0	0	0
5293198	nnnGn	6369.77	58.79	5	2.73	0.92	2	-1.13	0.03	1
5367588	nnnnn	7645.96	88.81	4	4.21	0.33	4	-0.60	0.00	2
5458607	lCnnR	0	0	0
5659897	nnnnn	4493.90	174.09	3	3.70	0.18	2	-0.27	0.15	1
5726697	nnnnn	5865.42	56.44	8	3.28	0.12	6	-0.91	0.05	4
5734139	nnngn	4142.88	88.28	3	4.87	0.02	4	-1.47	0.09	1
5960619	nnnnn	5316.55	95.70	6	3.50	0.17	6	-0.81	0.05	6
4164153	nnnnn	5399.71	26.96	4	4.35	0.15	5	-0.37	0.09	4
4227995	nnnnn	5621.95	82.51	6	4.10	0.05	6	-0.26	0.04	7
4249910	nnnnn	5684.52	72.16	7	3.82	0.07	6	-0.55	0.03	3
4367627	nnnnn	5193.75	104.01	3	4.19	0.35	2	-0.35	0.14	1
4511235	nnnGn	4036.67	28.75	1	4.29	0.19	2	-1.59	0.18	1
4577290	nnnnn	6297.81	25.62	8	3.77	0.03	6	-0.16	0.02	5
4593845	nnnnn	5378.13	36.57	6	3.84	0.11	6	-0.52	0.06	5
5125956	nnBnn	5382.27	61.94	5	4.30	0.49	3	-0.76	0.08	1
5196137	nnnGn	6800.75	198.09	5	3.56	0.06	2	-1.10	0.05	1
5225574	nnnnn	5678.03	216.05	4	3.99	0.45	5	-0.10	0.04	2
5228242	nnnnn	5877.21	33.33	7	4.19	0.07	6	0.01	0.05	5
5391945	nnnnn	4342.82	258.37	3	1.05	0.27	4	-1.38	0.02	4
5416746	lCnnR	0	0	0
5805286	nnnnR	0	0	0
5898015	nnnnn	5736.95	243.26	5	3.91	0.31	4	-0.88	0.12	3
6062831	nnnnn	6288.39	110.26	8	3.91	0.14	6	-0.58	0.03	7
4167016	nnnnn	4996.33	142.46	3	4.44	0.27	2	-0.38	0.08	1
4184757	nnnGn	4046.72	20.08	1	3.41	0.08	1	-1.84	0.07	1
4294806	nnnnn	5715.05	145.73	5	4.10	0.25	4	-0.57	0.10	4
4325520	Dnnnn	4461.78	132.27	3	3.47	0.20	4	0.13	0.06	2
4362982	nnnnn	4520.32	81.71	3	4.42	0.46	2	-1.39	0.07	1
4613612	nnnnn	5812.93	34.20	7	3.91	0.08	6	-0.42	0.03	5
4735932	nnBGn	5899.48	279.16	4	3.12	0.11	2	-1.16	0.06	1
4756551	Nnnnn	4501.30	82.60	3	3.30	0.77	2	-0.37	0.08	1
5216471	nnngn	4389.41	138.61	3	4.39	0.27	4	-1.03	0.09	1

Table 7.5 (cont'd): SSPP Stellar Parameters for Hectospec Targets

UW ID ^a	flags	T_{eff} (K)	$\sigma(T_{\text{eff}})$ (K)	$N(T_{\text{eff}})^{\text{b}}$ (dex)	$\log g$ (dex)	$\sigma(\log g)$ (dex)	$N(\log g)^{\text{b}}$ (dex)	[Fe/H] (dex)	$\sigma([\text{Fe}/\text{H}])$ (dex)	$N([\text{Fe}/\text{H}])^{\text{b}}$
5288224	lCnnR	0	0	0
5336878	nnnnn	5791.54	70.79	7	4.05	0.11	6	-0.16	0.04	6
5337533	lCnnR	0	0	0
6052646	nnnnn	5753.58	53.76	6	4.18	0.06	6	-0.47	0.05	5
6096965	nnnnn	5744.20	41.59	7	3.82	0.19	4	-0.64	0.03	3

^aSource ID in the UW VSC.

Acknowledgments

I am extremely grateful to Y. S. Lee who processed the Hectospec spectra with the SSPP, thereby enabling the majority of the analysis presented in this chapter. I thank N. Caldwell for helping me to properly configure the Hectospec observations, and who also assisted in the reduction of the Hectospec data. I thank J. Cabanela for making the `E-specroad` publicly available, and I thank `wise.io` for making their Random Forest algorithm available. Finally, conversations with G. Basri, J. Richards, and J. Bloom dramatically improved the contents of this chapter.

Observations reported here were obtained at the MMT Observatory, a joint facility of the University of Arizona and the Smithsonian Institution.

Appendix A

Publications

During my time as a graduate student at UC Berkeley I have contributed as an author to 28 refereed publications. For completeness a full bibliography is included below.

1. J. M. Silverman, P. E. Nugent, A. Gal-Yam, M. Sullivan, D. A. Howell, A. V. Filippenko, I. Arcavi, S. Ben-Ami, J. S. Bloom, S. B. Cenko, Y. Cao, R. Chornock, K. I. Clubb, A. L. Coil, R. J. Foley, M. L. Graham, C. V. Griffith, A. Horesh, M. M. Kasliwal, S. R. Kulkarni, D. C. Leonard, W. Li, T. Matheson, A. A. Miller, M. Modjaz, E. O. Ofek, Y.-C. Pan, D. A. Perley, D. Poznanski, R. M. Quimby, T. N. Steele, A. Sternberg, D. Xu, & O. Yaron (2013) “Type Ia Supernovae Strongly Interacting with Their Circumstellar Medium.” *ApJS*, 207, 3
2. S. B. Cenko, S. R. Kulkarni, A. Horesh, A. Corsi, D. B. Fox, J. Carpenter, D. A. Frail, P. E. Nugent, D. A. Perley, D. Gruber, A. Gal-Yam, P. J. Groot, G. Hallinan, E. O. Ofek, A. Rau, C. L. MacLeod, A. A. Miller, J. S. Bloom, A. V. Filippenko, M. M. Kasliwal, N. M. Law, A. N. Morgan, D. Polishook, D. Poznanski, R. M. Quimby, B. Sesar, K. J. Shen, J. M. Silverman, & A. Sternberg (2013) “Discovery of a Cosmological, Relativistic Outburst via its Rapidly Fading Optical Emission.” *ApJ*, 769, 130
3. L. A. Hillenbrand, A. A. Miller, K. R. Covey, J. M. Carpenter, S. B. Cenko, J. M. Silverman, P. S. Muirhead, W. J. Fischer, J. R. Crepp, J. S. Bloom, & A. V. Filippenko (2013) “Highly Variable Extinction and Accretion in the Jet-driving Class I-type Young Star PTF 10nvg (V2492 Cyg, IRAS 20496+4354).” *AJ*, 145, 59
4. J. W. Richards, D. L. Starr, A. A. Miller, J. S. Bloom, N. R. Butler, H. Brink, & A. Crellin-Quick (2012) “Construction of a Calibrated Probabilistic Classification Catalog: Application to 50k Variable Sources in the All-Sky Automated Survey.” *ApJS*, 203, 32
5. D. A. Perley, M. Modjaz, A. N. Morgan, S. B. Cenko, J. S. Bloom, N. R. Butler, A. V. Filippenko, & A. A. Miller (2012) “The Luminous Infrared Host Galaxy of Short-duration GRB 100206A.” *ApJ*, 758, 122

6. A. A. Miller, J. W. Richards, J. S. Bloom, S. B. Cenko, J. M. Silverman, D. L. Starr, & K. G. Stassun (2012) “Discovery of Bright Galactic R Coronae Borealis and DY Persei Variables: Rare Gems Mined from ACVS.” *ApJ*, 755, 98
7. S. B. Cenko, J. S. Bloom, S. R. Kulkarni, L. E. Strubbe, A. A. Miller, N. R. Butler, R. M. Quimby, A. Gal-Yam, E. O. Ofek, E. Quataert, L. Bildsten, D. Poznanski, D. A. Perley, A. N. Morgan, A. V. Filippenko, D. A. Frail, I. Arcavi, S. Ben-Ami, A. Cucchiara, C. D. Fassnacht, Y. Green, I. M. Hook, D. A. Howell, D. J. Lagattuta, N. M. Law, M. M. Kasliwal, P. E. Nugent, J. M. Silverman, M. Sullivan, S. P. Tendulkar, & O. Yaron (2012) “PTF10iaya: a short-lived, luminous flare from the nuclear region of a star-forming galaxy.” *MNRAS*, 420, 2684
8. J. W. Richards, D. L. Starr, H. Brink, A. A. Miller, J. S. Bloom, N. R. Butler, J. B. James, J. P. Long, & J. Rice (2012) “Active Learning to Overcome Sample Selection Bias: Application to Photometric Variable Star Classification.” *ApJ*, 744, 192
9. W. Li, J. S. Bloom, P. Podsiadlowski, A. A. Miller, S. B. Cenko, S. W. Jha, M. Sullivan, D. A. Howell, P. E. Nugent, N. R. Butler, E. O. Ofek, M. M. Kasliwal, J. W. Richards, A. Stockton, H.-Y. Shih, L. Bildsten, M. M. Shara, J. Bibby, A. V. Filippenko, M. Ganeshalingam, J. M. Silverman, S. R. Kulkarni, N. M. Law, D. Poznanski, R. M. Quimby, C. McCully, B. Patel, K. Maguire, & K. J. Shen (2011) “Exclusion of a luminous red giant as a companion star to the progenitor of supernova SN 2011fe.” *Nature*, 480, 348
10. N. Smith, W. Li, A. A. Miller, J. M. Silverman, A. V. Filippenko, J.-C. Cuillandre, M. C. Cooper, T. Matheson, & S. D. Van Dyk (2011) “A Massive Progenitor of the Luminous Type IIn Supernova 2010jl.” *ApJ*, 732, 63
11. A. A. Miller, L. A. Hillenbrand, K. R. Covey, D. Poznanski, J. M. Silverman, I. K. W. Kleiser, B. Rojas-Ayala, P. S. Muirhead, S. B. Cenko, J. S. Bloom, M. M. Kasliwal, A. V. Filippenko, N. M. Law, E. O. Ofek, R. G. Dekany, G. Rahmer, D. Hale, R. Smith, R. M. Quimby, P. Nugent, J. Jacobsen, J. Zolkower, V. Velur, R. Walters, J. Henning, K. Bui, D. McKenna, S. R. Kulkarni, C. R. Klein, M. Kandrashoff, & A. Morton (2011) “Evidence for an FU Orionis-like Outburst from a Classical T Tauri Star.” *ApJ*, 730, 80
12. E. Chatzopoulos, J. C. Wheeler, J. Vinko, R. Quimby, E. L. Robinson, A. A. Miller, R. J. Foley, D. A. Perley, F. Yuan, C. Akerlof, & J. S. Bloom (2011) “SN 2008am: A Super-luminous Type IIn Supernova.” *ApJ*, 729, 143
13. K. R. Covey, L. A. Hillenbrand, A. A. Miller, D. Poznanski, S. B. Cenko, J. M. Silverman, J. S. Bloom, M. M. Kasliwal, W. Fischer, J. Rayner, L. M. Rebull, N. R. Butler, A. V. Filippenko, N. M. Law, E. O. Ofek, M. Agüeros, R. G. Dekany, G. Rahmer, D. Hale, R. Smith, R. M. Quimby, P. Nugent, J. Jacobsen, J. Zolkower, V. Velur, R. Walters, J. Henning, K. Bui, D. McKenna, S. R. Kulkarni, & C. Klein (2011) “PTF10nvg: An Outbursting Class I Protostar in the Pelican/North American Nebula.” *AJ*, 141, 40

14. D. A. Perley, A. N. Morgan, A. Updike, F. Yuan, C. W. Akerlof, A. A. Miller, J. S. Bloom, S. B. Cenko, W. Li, A. V. Filippenko, J. X. Prochaska, D. A. Kann, N. R. Tanvir, A. J. Levan, N. R. Butler, P. Christian, D. H. Hartmann, P. Milne, E. S. Rykoff, W. Rujopakarn, J. C. Wheeler, & G. G. Williams (2011) “Monster in the Dark: The Ultraluminous GRB 080607 and Its Dusty Environment.” *AJ*, 141, 36
15. J. M. Silverman, M. Ganeshalingam, W. Li, A. V. Filippenko, A. A. Miller, & D. Poznanski (2011) “Fourteen months of observations of the possible super-Chandrasekhar mass Type Ia Supernova 2009dc.” *MNRAS*, 410, 585
16. S. B. Cenko, N. R. Butler, E. O. Ofek, D. A. Perley, A. N. Morgan, D. A. Frail, J. Gorosabel, J. S. Bloom, A. J. Castro-Tirado, J. Cepa, P. Chandra, A. de Ugarte Postigo, A. V. Filippenko, C. R. Klein, S. R. Kulkarni, A. A. Miller, P. E. Nugent, & D. L. Starr (2010) “Unveiling the Origin of Grb 090709A: Lack of Periodicity in a Reddened Cosmological Long-Duration Gamma-Ray Burst.” *AJ*, 140, 224
17. A. A. Miller, N. Smith, W. Li, J. S. Bloom, R. Chornock, A. V. Filippenko, & J. X. Prochaska (2010) “New Observations of the Very Luminous Supernova 2006gy: Evidence for Echoes.” *AJ*, 139, 2218
18. A. A. Miller, J. M. Silverman, N. R. Butler, J. S. Bloom, R. Chornock, A. V. Filippenko, M. Ganeshalingam, C. R. Klein, W. Li, P. E. Nugent, N. Smith, & T. N. Steele (2010) “SN 2008iy: an unusual Type IIn Supernova with an enduring 400-d rise time.” *MNRAS*, 404, 305
19. N. Elias-Rosa, S. D. Van Dyk, W. Li, A. A. Miller, J. M. Silverman, M. Ganeshalingam, A. F. Boden, M. M. Kasliwal, J. Vinkó, J.-C. Cuillandre, A. V. Filippenko, T. N. Steele, J. S. Bloom, C. V. Griffith, I. K. W. Kleiser, & R. J. Foley (2010) “The Massive Progenitor of the Type II-linear Supernova 2009kr.” *ApJ*, 714, L254
20. N. Smith, A. Miller, W. Li, A. V. Filippenko, J. M. Silverman, A. W. Howard, P. Nugent, G. W. Marcy, J. S. Bloom, A. M. Ghez, J. Lu, S. Yelda, R. A. Bernstein, & J. E. Colucci (2010) “Discovery of Precursor Luminous Blue Variable Outbursts in Two Recent Optical Transients: The Fitfully Variable Missing Links UGC 2773-OT and SN 2009ip.” *AJ*, 139, 1451
21. R. Margutti, F. Genet, J. Granot, R. Barniol Duran, C. Guidorzi, G. Chincarini, J. Mao, P. Schady, T. Sakamoto, A. A. Miller, G. Olofsson, J. S. Bloom, P. A. Evans, J. P. U. Fynbo, D. Malesani, A. Moretti, F. Pasotti, D. Starr, D. N. Burrows, S. D. Barthelmy, P. W. A. Roming, & N. Gehrels (2010) “GRB081028 and its late-time afterglow re-brightening.” *MNRAS*, 402, 46
22. A. Gal-Yam, P. Mazzali, E. O. Ofek, P. E. Nugent, S. R. Kulkarni, M. M. Kasliwal, R. M. Quimby, A. V. Filippenko, S. B. Cenko, R. Chornock, R. Waldman, D. Kasen, M. Sullivan, E. C. Beshore, A. J. Drake, R. C. Thomas, J. S. Bloom, D. Poznanski,

- A. A. Miller, R. J. Foley, J. M. Silverman, I. Arcavi, R. S. Ellis, & J. Deng (2009) "Supernova 2007bi as a pair-instability explosion." *Nature*, 462, 624
23. D. A. Perley, B. D. Metzger, J. Granot, N. R. Butler, T. Sakamoto, E. Ramirez-Ruiz, A. J. Levan, J. S. Bloom, A. A. Miller, A. Bunker, H.-W. Chen, A. V. Filippenko, N. Gehrels, K. Glazebrook, P. B. Hall, K. C. Hurley, D. Kocevski, W. Li, S. Lopez, J. Norris, A. L. Piro, D. Poznanski, J. X. Prochaska, E. Quataert, & N. Tanvir (2009) "GRB 080503: Implications of a Naked Short Gamma-Ray Burst Dominated by Extended Emission." *ApJ*, 696, 1871
 24. D. Poznanski, N. Butler, A. V. Filippenko, M. Ganeshalingam, W. Li, J. S. Bloom, R. Chornock, R. J. Foley, P. E. Nugent, J. M. Silverman, S. B. Cenko, E. L. Gates, D. C. Leonard, A. A. Miller, M. Modjaz, F. J. D. Serduke, N. Smith, B. J. Swift, & D. S. Wong (2009) "Improved Standardization of Type II-P Supernovae: Application to an Expanded Sample." *ApJ*, 694, 1067
 25. J. X. Prochaska, Y. Sheffer, D. A. Perley, J. S. Bloom, L. A. Lopez, M. Dessauges-Zavadsky, H.-W. Chen, A. V. Filippenko, M. Ganeshalingam, W. Li, A. A. Miller, & D. Starr (2009) "The First Positive Detection of Molecular Gas in a GRB Host Galaxy." *ApJ*, 691, L27
 26. J. S. Bloom, D. A. Perley, W. Li, N. R. Butler, A. A. Miller, D. Kocevski, D. A. Kann, R. J. Foley, H. Chen, A. V. Filippenko, D. L. Starr, B. Macomber, J. X. Prochaska, R. Chornock, D. Poznanski, S. Klose, M. F. Skrutskie, S. Lopez, P. Hall, K. Glazebrook, & C. H. Blake (2009) "Observations of the Naked-Eye GRB 080319B: Implications of Nature's Brightest Explosion." *ApJ*, 691, 723
 27. A. A. Miller, R. Chornock, D. A. Perley, M. Ganeshalingam, W. Li, N. R. Butler, J. S. Bloom, N. Smith, M. Modjaz, D. Poznanski, A. V. Filippenko, C. V. Griffith, J. H. Shiode, & J. M. Silverman (2009) "The Exceptionally Luminous Type II-Linear Supernova 2008es." *ApJ*, 690, 1303
 28. A. A. Miller, J. Irwin, S. Aigrain, S. Hodgkin, & L. Hebb (2008) "The Monitor project: the search for transits in the open cluster NGC 2362." *MNRAS*, 387, 349

Bibliography

- Abel, T., Bryan, G. L., & Norman, M. L. 2000, [ApJ, 540, 39](#)
- Abia, C., & Isern, J. 1997, [MNRAS, 289, L11](#)
- Adelman-McCarthy, J. K., Agüeros, M. A., Allam, S. S., et al. 2008, [ApJS, 175, 297](#)
- Agnoletto, I., Benetti, S., Cappellaro, E., et al. 2009, [ApJ, 691, 1348](#)
- Ahn, C. P., Alexandroff, R., Allende Prieto, C., et al. 2013, ArXiv e-prints, [arXiv:1307.7735 \[astro-ph.IM\]](#)
- Akerlof, C. W., Kehoe, R. L., McKay, T. A., et al. 2003, [PASP, 115, 132](#)
- Alard, C., & Lupton, R. H. 1998, [ApJ, 503, 325](#)
- Alcock, C., Allsman, R. A., Axelrod, T. S., et al. 1996, [ApJ, 461, 84](#)
- Alcock, C., Allsman, R. A., Alves, D. R., et al. 2001, [ApJ, 554, 298](#)
- Alksnis, A. 1994, Baltic Astronomy, 3, 410
- Alksnis, A., Balklavs, A., Dzervitis, U., et al. 2001, Baltic Astronomy, 10, 1
- Allende Prieto, C., Sivarani, T., Beers, T. C., et al. 2008, [AJ, 136, 2070](#)
- Arcavi, I., Gal-Yam, A., Cenko, S. B., et al. 2012, [ApJ, 756, L30](#)
- Aretxaga, I., Benetti, S., Terlevich, R. J., et al. 1999, [MNRAS, 309, 343](#)
- Arnett, W. D., Bahcall, J. N., Kirshner, R. P., & Woosley, S. E. 1989, [ARA&A, 27, 629](#)
- Aspin, C., & Reipurth, B. 2009, [AJ, 138, 1137](#)
- Aspin, C., Reipurth, B., Herczeg, G. J., & Capak, P. 2010, [ApJ, 719, L50](#)
- Astier, P., Guy, J., Regnault, N., et al. 2006, [A&A, 447, 31](#)
- Audard, M., Stringfellow, G. S., Güdel, M., et al. 2010, [A&A, 511, A63](#)
- Barbary, K., Dawson, K. S., Tokita, K., et al. 2009, [ApJ, 690, 1358](#)
- Barbon, R., Ciatti, F., & Rosino, L. 1979, [A&A, 72, 287](#)
—. 1982, [A&A, 116, 35](#)
- Barkat, Z., Rakavy, G., & Sack, N. 1967, [Physical Review Letters, 18, 379](#)
- Barnbaum, C., Stone, R. P. S., & Keenan, P. C. 1996, [ApJS, 105, 419](#)
- Barris, B. J., Tonry, J. L., Novicki, M. C., & Wood-Vasey, W. M. 2005, [AJ, 130, 2272](#)
- Basri, G., Walkowicz, L. M., Batalha, N., et al. 2010, [ApJ, 713, L155](#)
—. 2011, [AJ, 141, 20](#)
- Batalha, N. M., Rowe, J. F., Bryson, S. T., et al. 2013, [ApJS, 204, 24](#)
- Bauer, F. E., Dwarkadas, V. V., Brandt, W. N., et al. 2008, [ApJ, 688, 1210](#)
- Becker, A. C., Bochanski, J. J., Hawley, S. L., et al. 2011, [ApJ, 731, 17](#)
- Becker, A. C., Wittman, D. M., Boeshaar, P. C., et al. 2004, [ApJ, 611, 418](#)

- Benetti, S., Bouchet, P., & Schwarz, H. 1995, IAU Circ., 6170, 1
- Berta, Z. K., Irwin, J., Charbonneau, D., Burke, C. J., & Falco, E. E. 2012, *AJ*, 144, 145
- Bertin, E., & Arnouts, S. 1996, *A&AS*, 117, 393
- Bietenholz, M., & Bartel, N. 2008, The Astronomer's Telegram, 1657, 1
- Blake, C. H., Bloom, J. S., Latham, D. W., et al. 2008, *PASP*, 120, 860
- Blondin, S., & Tonry, J. L. 2007, *ApJ*, 666, 1024
- Bloom, J. S., & Richards, J. W. 2012, Data Mining and Machine Learning in Time-Domain Discovery and Classification, ed. M. J. Way, J. D. Scargle, K. M. Ali, & A. N. Srivastava, 89
- Bloom, J. S., Starr, D. L., Blake, C. H., Skrutskie, M. F., & Falco, E. E. 2006, in Astronomical Society of the Pacific Conference Series, Vol. 351, Astronomical Data Analysis Software and Systems XV, ed. C. Gabriel, C. Arviset, D. Ponz, & S. Enrique, 751
- Bloom, J. S., Perley, D. A., Li, W., et al. 2009, *ApJ*, 691, 723
- Bloom, J. S., Richards, J. W., Nugent, P. E., et al. 2012, *PASP*, 124, 1175
- Blumenthal, G. R., & Tucker, W. H. 1974, *ARA&A*, 12, 23
- Bond, J. R., Arnett, W. D., & Carr, B. J. 1984, *ApJ*, 280, 825
- Bonnell, I., & Bastien, P. 1992, *ApJ*, 401, L31
- Borucki, W. J., Koch, D., Basri, G., et al. 2010, *Science*, 327, 977
- Bramich, D. M., Vidrih, S., Wyrzykowski, L., et al. 2008, *MNRAS*, 386, 887
- Branch, D., Falk, S. W., Uomoto, A. K., et al. 1981, *ApJ*, 244, 780
- Branch, D., Jeffery, D. J., Blaylock, M., & Hatano, K. 2000, *PASP*, 112, 217
- Breiman, L. 2001, *Machine Learning*, 45, 5
- Brewer, J. M., Bloom, J. S., Kennedy, R., & Starr, D. L. 2009, in Astronomical Society of the Pacific Conference Series, Vol. 411, Astronomical Data Analysis Software and Systems XVIII, ed. D. A. Bohlender, D. Durand, & P. Dowler, 357
- Briceño, C., Vivas, A. K., Hernández, J., et al. 2004, *ApJ*, 606, L123
- Brink, H., Richards, J. W., Poznanski, D., et al. 2013, *MNRAS*, arXiv:1209.3775 [astro-ph.IM]
- Brown, T. M., Latham, D. W., Everett, M. E., & Esquerdo, G. A. 2011, *AJ*, 142, 112
- Burrows, D. N., Hill, J. E., Nousek, J. A., et al. 2005, *Space Science Reviews*, 120, 165
- Butler, N. R., & Bloom, J. S. 2011, *AJ*, 141, 93
- Butler, N. R., & Kocevski, D. 2007, *ApJ*, 668, 400
- Cappellaro, E., Patat, F., Mazzali, P. A., et al. 2001, *ApJ*, 549, L215
- Cardelli, J. A., Clayton, G. C., & Mathis, J. S. 1989, *ApJ*, 345, 245
- Catelan, M., Drake, A. J., Djorgovski, S. G., et al. 2009, Central Bureau Electronic Telegrams, 1780, 1
- Cenko, S. B., Fox, D. B., Moon, D., et al. 2006, *PASP*, 118, 1396
- Chalabaev, A., & Maillard, J. P. 1983, *A&A*, 127, 279
- Chevalier, R. A. 1986, *ApJ*, 308, 225
- Chornock, R., Miller, A. A., Bloom, J. S., & Perley, D. A. 2008a, The Astronomer's Telegram, 1644
- Chornock, R., et al. 2008b, Central Bureau Electronic Telegrams, 1462
- Chu, Y., Caulet, A., Montes, M. J., et al. 1999, *ApJ*, 512, L51

- Chugai, N. N. 1993, *ApJ*, **414**, L101
- Chugai, N. N., Blinnikov, S. I., Fassia, A., et al. 2002, *MNRAS*, **330**, 473
- Chugai, N. N., & Chevalier, R. A. 2006, *ApJ*, **641**, 1051
- Chugai, N. N., & Danziger, I. J. 1994, *MNRAS*, **268**, 173
- . 2003, *Astronomy Letters*, **29**, 649
- Chugai, N. N., Blinnikov, S. I., Cumming, R. J., et al. 2004, *MNRAS*, **352**, 1213
- Clarke, A. J., Oudmaijer, R. D., & Lumsden, S. L. 2005, *MNRAS*, **363**, 1111
- Clayton, G. C. 1996, *PASP*, **108**, 225
- . 2012, Journal of the American Association of Variable Star Observers (AAVSO), **40**, 539
- Clayton, G. C., Geballe, T. R., Herwig, F., Fryer, C., & Asplund, M. 2007, *ApJ*, **662**, 1220
- Clayton, G. C., Hammond, D., Lawless, J., et al. 2002, *PASP*, **114**, 846
- Clayton, G. C., Kerber, F., Pirzkal, N., et al. 2006, *ApJ*, **646**, L69
- Clayton, G. C., Kilkenny, D., Wils, P., & Welch, D. L. 2009, *PASP*, **121**, 461
- Clayton, G. C., Sugerman, B. E. K., Stanford, S. A., et al. 2011, *ApJ*, **743**, 44
- Clocchiatti, A., Wheeler, J. C., Kirshner, R. P., et al. 2008, *PASP*, **120**, 290
- Cohen, M., & Kuhi, L. V. 1979, *ApJS*, **41**, 743
- Cohen, M., Wheaton, W. A., & Megeath, S. T. 2003, *AJ*, **126**, 1090
- Connelley, M. S., & Greene, T. P. 2010, *AJ*, **140**, 1214
- Connelley, M. S., Reipurth, B., & Tokunaga, A. T. 2007, *AJ*, **133**, 1528
- Covey, K. R., Lada, C. J., Román-Zúñiga, C., et al. 2010, *ApJ*, **722**, 971
- Covey, K. R., Hillenbrand, L. A., Miller, A. A., et al. 2011, *AJ*, **141**, 40
- Croswell, K., Hartmann, L., & Avrett, E. H. 1987, *ApJ*, **312**, 227
- Cutri, R. M., Skrutskie, M. F., van Dyk, S., et al. 2003, 2MASS All Sky Catalog of point sources. (The IRSA 2MASS All Sky Point Source Catalog, NASA/IPAC Infrared Science Archive, <http://irsa.ipac.caltech.edu/applications/Gator>)
- Cutri, R. M., Wright, E. L., Conrow, T., et al. 2011, Explanatory Supplement to the WISE Preliminary Data Release Products, Tech. rep.
- Davenport, J. R. A., Becker, A. C., Kowalski, A. F., et al. 2012, *ApJ*, **748**, 58
- Davidson, K., Smith, N., Gull, T. R., Ishibashi, K., & Hillier, D. J. 2001, *AJ*, **121**, 1569
- Debosscher, J., Sarro, L. M., Aerts, C., et al. 2007, *A&A*, **475**, 1159
- Dobashi, K., Bernard, J., Yonekura, Y., & Fukui, Y. 1994, *ApJS*, **95**, 419
- Doggett, J. B., & Branch, D. 1985, *AJ*, **90**, 2303
- Dolphin, A. E. 2000, *PASP*, **112**, 1397
- Draine, B. T. 2003, *ARA&A*, **41**, 241
- Draine, B. T., & Li, A. 2001, *ApJ*, **551**, 807
- Drake, A. J., Mahabal, A., Djorgovski, S. G., et al. 2008, The Astronomer's Telegram, **1768**, 1
- Drake, A. J., Djorgovski, S. G., Mahabal, A., et al. 2009, *ApJ*, **696**, 870
- Drake, A. J., Djorgovski, S. G., Prieto, J. L., et al. 2010, *ApJ*, **718**, L127
- Dubath, P., Rimoldini, L., Süveges, M., et al. 2011, *MNRAS*, **414**, 2602
- Dwarkadas, V. V. 2005, *ApJ*, **630**, 892
- Dwek, E. 1983, *ApJ*, **274**, 175

- Eddington, A. S. 1918, MNRAS, 79, 2
—. 1919, MNRAS, 79, 177
- Edwards, S., Fischer, W., Hillenbrand, L., & Kwan, J. 2006, ApJ, 646, 319
- Egan, M. P., & Leung, C. M. 1991, ApJ, 383, 314
- Epcstein, N., de Batz, B., Copet, E., et al. 1994, Ap&SS, 217, 3
- Epcstein, N., Deul, E., Derriere, S., et al. 1999, A&A, 349, 236
- Eyer, L., & Mowlavi, N. 2008, Journal of Physics Conference Series, 118, 012010
- Fabian, A. C., & Terlevich, R. 1996, MNRAS, 280, L5
- Fabricant, D., Fata, R., Roll, J., et al. 2005, PASP, 117, 1411
- Fassia, A., Meikle, W. P. S., Chugai, N., et al. 2001, MNRAS, 325, 907
- Feast, M. W. 1997, MNRAS, 285, 339
- Fedele, D., van den Ancker, M. E., Petr-Gotzens, M. G., & Rafanelli, P. 2007, A&A, 472, 207
- Fesen, R. A., & Matonick, D. M. 1993, ApJ, 407, 110
- Filippenko, A. V. 1982, PASP, 94, 715
—. 1989, AJ, 97, 726
—. 1997, ARA&A, 35, 309
- Filippenko, A. V., & Halpern, J. P. 1984, ApJ, 285, 458
- Filippenko, A. V., Li, W. D., Treffers, R. R., & Modjaz, M. 2001, in Astronomical Society of the Pacific Conference Series, Vol. 246, IAU Colloq. 183: Small Telescope Astronomy on Global Scales, ed. B. Paczynski, W.-P. Chen, & C. Lemme, 121
- Findeisen, K., Hillenbrand, L., Ofek, E., et al. 2013, ApJ, 768, 93
- Foley, R. J., Smith, N., Ganeshalingam, M., et al. 2007, ApJ, 657, L105
- Fox, D. W., Lewin, W. H. G., Fabian, A., et al. 2000, MNRAS, 319, 1154
- Fox, O., Skrutskie, M. F., Chevalier, R. A., et al. 2009, ApJ, 691, 650
- Fransson, C., Lundqvist, P., & Chevalier, R. A. 1996, ApJ, 461, 993
- Fransson, C., Chevalier, R. A., Filippenko, A. V., et al. 2002, ApJ, 572, 350
- Frieman, J. A., Bassett, B., Becker, A., et al. 2008, AJ, 135, 338
- Fukugita, M., Ichikawa, T., Gunn, J. E., et al. 1996, AJ, 111, 1748
- Gal-Yam, A. 2012, Science, 337, 927
- Gal-Yam, A., & Leonard, D. C. 2009, Nature, 458, 865
- Gal-Yam, A., Leonard, D. C., Fox, D. B., et al. 2007, ApJ, 656, 372
- Gal-Yam, A., Mazzali, P., Ofek, E. O., et al. 2009, Nature, 462, 624
- Gehrels, N., Chincarini, G., Giommi, P., et al. 2004, ApJ, 611, 1005
- Gerardy, C. L., Fesen, R. A., Nomoto, K., et al. 2002, ApJ, 575, 1007
- Gezari, S., & Halpern, J. P. 2008, The Astronomer's Telegram, 1524
- Gezari, S., Grupe, D., Yuan, F., et al. 2008, The Astronomer's Telegram, 1578
- Gezari, S., Halpern, J. P., Grupe, D., et al. 2009, ApJ, 690, 1313
- González-Solares, E. A., Walton, N. A., Greimel, R., et al. 2008, MNRAS, 388, 89
- Grankin, K. N., Melnikov, S. Y., Bouvier, J., Herbst, W., & Shevchenko, V. S. 2007, A&A, 461, 183
- Grindlay, J., Tang, S., Simcoe, R., et al. 2009, in Astronomical Society of the Pacific Conference Series, Vol. 410, Preserving Astronomy's Photographic Legacy: Current State

- and the Future of North American Astronomical Plates, ed. W. Osborn & L. Robbins, 101
- Groot, P. J., Vreeswijk, P. M., Huber, M. E., et al. 2003, *MNRAS*, **339**, 427
- Guieu, S., Rebull, L. M., Stauffer, J. R., et al. 2009, *ApJ*, **697**, 787
- Guyon, I., & Elisseeff, A. 2003, *J. Mach. Learn. Res.*, **3**, 1157
- Hartmann, L., & Kenyon, S. J. 1996, *ARA&A*, **34**, 207
- Hastie, T., Tibshirani, R., & Friedman, J. 2009, *The Elements of Statistical Learning: Data Mining, Inference, and Prediction*, Second Edition, 2nd edn., Springer Series in Statistics (Springer)
- Heger, A., Fryer, C. L., Woosley, S. E., Langer, N., & Hartmann, D. H. 2003, *ApJ*, **591**, 288
- Herbig, G. H. 1977, *ApJ*, **217**, 693
- Herbig, G. H. 1989, in European Southern Observatory Conference and Workshop Proceedings, Vol. 33, European Southern Observatory Conference and Workshop Proceedings, ed. B. Reipurth, 233
- . 2007, *AJ*, **133**, 2679
- Herbig, G. H., & Bell, K. R. 1988, Third Catalog of Emission-Line Stars of the Orion Population (Santa Cruz, CA: Lick Obs.)
- Herbig, G. H., Petrov, P. P., & Duemmler, R. 2003, *ApJ*, **595**, 384
- Herbst, W., Herbst, D. K., Grossman, E. J., & Weinstein, D. 1994, *AJ*, **108**, 1906
- Herter, T. L., Henderson, C. P., Wilson, J. C., et al. 2008, in *Society of Photo-Optical Instrumentation Engineers (SPIE) Conference Series*, Vol. 7014, Society of Photo-Optical Instrumentation Engineers (SPIE) Conference Series
- Hertzsprung, E. 1913, *Astronomische Nachrichten*, **196**, 201
- Hewish, A., Bell, S. J., Pilkington, J. D. H., Scott, P. F., & Collins, R. A. 1968, *Nature*, **217**, 709
- Hoffleit, D. 1986, *Journal of the American Association of Variable Star Observers (AAVSO)*, **15**, 77
- Hogg, H. 1984, in *Astrophysics and Twentieth-Century Astronomy to 1950*, ed. O. Gingerich, 73
- Holtzman, J. A., Burrows, C. J., Casertano, S., et al. 1995a, *PASP*, **107**, 1065
- Holtzman, J. A., Hester, J. J., Casertano, S., et al. 1995b, *PASP*, **107**, 156
- Horne, K. 1986, *PASP*, **98**, 609
- Houck, J. C., Bregman, J. N., Chevalier, R. A., & Tomisaka, K. 1998, *ApJ*, **493**, 431
- Howard, A. W., Johnson, J. A., Marcy, G. W., et al. 2010, *ApJ*, **721**, 1467
- Hubble, E. 1929, *Proceedings of the National Academy of Science*, **15**, 168
- Hubble, E. P. 1925, *The Observatory*, **48**, 139
- Humphreys, R. M., & Davidson, K. 1979, *ApJ*, **232**, 409
- . 1994, *PASP*, **106**, 1025
- Iben, Jr., I., Tutukov, A. V., & Yungelson, L. R. 1996, *ApJ*, **456**, 750
- Immler, S., & Kuntz, K. D. 2005, *ApJ*, **632**, L99
- Immler, S., Pietsch, W., & Aschenbach, B. 1998, *A&A*, **331**, 601
- Immler, S., Brown, P. J., Milne, P., et al. 2007, *ApJ*, **664**, 435
- Ishihara, D., Onaka, T., Kataza, H., et al. 2010, *A&A*, **514**, A1

- Ivezić, Ž., Smith, J. A., Miknaitis, G., et al. 2007, *AJ*, **134**, 973
- Ivezić, Ž., Tyson, J. A., Acosta, E., et al. 2008a, ArXiv e-prints, [arXiv:0805.2366](https://arxiv.org/abs/0805.2366)
- Ivezić, Ž., Sesar, B., Jurić, M., et al. 2008b, *ApJ*, **684**, 287
- Jester, S., Schneider, D. P., Richards, G. T., et al. 2005, *AJ*, **130**, 873
- Johnson, J. A., Howard, A. W., Marcy, G. W., et al. 2010, *PASP*, **122**, 149
- Jones, D. O., Rodney, S. A., Riess, A. G., et al. 2013, *ApJ*, **768**, 166
- Joy, A. H. 1945, *ApJ*, **102**, 168
- Kalberla, P. M. W., Burton, W. B., Hartmann, D., et al. 2005, *A&A*, **440**, 775
- Kawabata, K. S., Tanaka, M., Maeda, K., et al. 2009, *ApJ*, **697**, 747
- Keenan, P. C., & Barnbaum, C. 1997, *PASP*, **109**, 969
- Kijbunchoo, N., Clayton, G. C., Vieux, T. C., et al. 2011, *PASP*, **123**, 1149
- Kilkenny, D., & Marang, F. 1989, *MNRAS*, **238**, 1P
- Klebesadel, R. W., Strong, I. B., & Olson, R. A. 1973, *ApJ*, **182**, L85
- Koekemoer, A. M., Fruchter, A. S., Hook, R. N., & Hack, W. 2003, in HST Calibration Workshop : Hubble after the Installation of the ACS and the NICMOS Cooling System, ed. S. Arribas, A. Koekemoer, & B. Whitmore, 337
- Kukarkin, B. V., Kholopov, P. N., Pskovsky, Y. P., et al. 1971, in General Catalogue of Variable Stars, 3rd ed. (1971), 0
- Kurucz, R. L. 1979, *ApJS*, **40**, 1
- . 1993, VizieR Online Data Catalog, 6039, 0
- Kwan, J., Edwards, S., & Fischer, W. 2007, *ApJ*, **657**, 897
- Kwok, S., Volk, K., & Bidelman, W. P. 1997, *ApJS*, **112**, 557
- Lada, C. J. 1987, in IAU Symposium, Vol. 115, Star Forming Regions, ed. M. Peimbert & J. Jugaku, 1
- Lada, C. J., & Wilking, B. A. 1984, *ApJ*, **287**, 610
- Lamers, H. J. G. L. M., Najarro, F., Kudritzki, R. P., et al. 1996, *A&A*, **315**, L229
- Langer, N. 1998, *A&A*, **329**, 551
- Langer, N., Hamann, W.-R., Lennon, M., et al. 1994, *A&A*, **290**, 819
- Law, N. M., Kulkarni, S. R., Dekany, R. G., et al. 2009, *PASP*, **121**, 1395
- Lawson, W. A., & Cottrell, P. L. 1990, *The Observatory*, **110**, 132
- Lawson, W. A., Cottrell, P. L., Kilmarin, P. M., & Gilmore, A. C. 1990, *MNRAS*, **247**, 91
- Leaman, J., Li, W., Chornock, R., & Filippenko, A. V. 2011, *MNRAS*, **412**, 1419
- Leavitt, H. S. 1908, *Annals of Harvard College Observatory*, **60**, 87
- Leavitt, H. S., & Pickering, E. C. 1912, *Harvard College Observatory Circular*, **173**, 1
- Lee, H., Skillman, E. D., Cannon, J. M., et al. 2006, *ApJ*, **647**, 970
- Lee, Y. S., Beers, T. C., Sivarani, T., et al. 2008a, *AJ*, **136**, 2022
- . 2008b, *AJ*, **136**, 2050
- Leonard, D. C., Filippenko, A. V., Barth, A. J., & Matheson, T. 2000, *ApJ*, **536**, 239
- Leonard, D. C., Filippenko, A. V., Gates, E. L., et al. 2002, *PASP*, **114**, 35
- Leoni, R., Larionov, V. M., Centrone, M., Giannini, T., & Lorenzetti, D. 2010, *The Astronomer's Telegram*, **2854**, 1
- Li, W., Chornock, R., Leaman, J., et al. 2011a, *MNRAS*, **412**, 1473

- Li, W., Filippenko, A. V., Chornock, R., & Jha, S. 2003, [ApJ](#), 586, L9
- Li, W., Filippenko, A. V., Van Dyk, S. D., et al. 2002, [PASP](#), 114, 403
- Li, W., Jha, S., Filippenko, A. V., et al. 2006, [PASP](#), 118, 37
- Li, W., Van Dyk, S. D., Filippenko, A. V., & Cuillandre, J. 2005, [PASP](#), 117, 121
- Li, W., Wang, X., Van Dyk, S. D., et al. 2007, [ApJ](#), 661, 1013
- Li, W., Leaman, J., Chornock, R., et al. 2011b, [MNRAS](#), 412, 1441
- Libert, Y., Gérard, E., Thum, C., et al. 2010, [A&A](#), 510, A14
- Lodato, G., & Clarke, C. J. 2004, [MNRAS](#), 353, 841
- Lomb, N. R. 1976, [Ap&SS](#), 39, 447
- Lorenzetti, D., Giannini, T., Larionov, V. M., et al. 2007, [ApJ](#), 665, 1182
- Luyten, W. J. 1932, Astronomische Nachrichten, 246, 437
- MacLeod, C. L., Ivezić, Ž., Kochanek, C. S., et al. 2010, [ApJ](#), 721, 1014
- MacLeod, C. L., Brooks, K., Ivezić, Ž., et al. 2011, [ApJ](#), 728, 26
- Maeder, A., & Meynet, G. 1994, [A&A](#), 287, 803
- Mahabal, A. . A., Drake, A. J., Djorgovski, S. G., et al. 2009, The Astronomer's Telegram, 2010, 1
- Marcy, G. W., Butler, R. P., Williams, E., et al. 1997, [ApJ](#), 481, 926
- Martin, D. C., Fanson, J., Schiminovich, D., et al. 2005, [ApJ](#), 619, L1
- Matheson, T., Filippenko, A. V., Ho, L. C., Barth, A. J., & Leonard, D. C. 2000, [AJ](#), 120, 1499
- Mathis, J. S., Rumpl, W., & Nordsieck, K. H. 1977, [ApJ](#), 217, 425
- Mauerhan, J. C., Smith, N., Filippenko, A. V., et al. 2013, [MNRAS](#), 430, 1801
- Mayor, M., & Queloz, D. 1995, [Nature](#), 378, 355
- McCray, R. 1993, [ARA&A](#), 31, 175
- Meynet, G., Maeder, A., Schaller, G., Schaerer, D., & Charbonnel, C. 1994, [A&AS](#), 103, 97
- Milisavljevic, D., Fesen, R. A., Leibundgut, B., & Kirshner, R. P. 2008, [ApJ](#), 684, 1170
- Mill, J. D., O'Neil, R. R., Price, S., et al. 1994, [Journal of Spacecraft and Rockets](#), 31, 900
- Miller, A. A., Irwin, J., Aigrain, S., Hodgkin, S., & Hebb, L. 2008a, [MNRAS](#), 387, 349
- Miller, A. A., Li, W., Nugent, P. E., et al. 2009a, The Astronomer's Telegram, 2183, 1
- Miller, A. A., Richards, J. W., Bloom, J. S., et al. 2012, [ApJ](#), 755, 98
- Miller, A. A., Smith, N., Li, W., et al. 2010a, [AJ](#), 139, 2218
- Miller, A. A., Bloom, J. S., Chornock, R., et al. 2008b, The Astronomer's Telegram, 1576
- Miller, A. A., Chornock, R., Perley, D. A., et al. 2009b, [ApJ](#), 690, 1303
- Miller, A. A., Silverman, J. M., Butler, N. R., et al. 2010b, [MNRAS](#), 404, 305
- Miller, J. S., & Stone, R. P. S. 1993, The Kast Double Spectrograph, Lick Observatory Technical Reports 66, University of California
- Modjaz, M. 2007, PhD thesis, Harvard University
- Modjaz, M., Li, W., Butler, N., et al. 2009, [ApJ](#), 702, 226
- Monet, D. G., Levine, S. E., Canzian, B., et al. 2003, [AJ](#), 125, 984
- Morales-Rueda, L., Groot, P. J., Augusteijn, T., et al. 2006, [MNRAS](#), 371, 1681
- Morgan, A. N., Long, J., Richards, J. W., et al. 2012, [ApJ](#), 746, 170
- Morse, J. A., Davidson, K., Bally, J., et al. 1998, [AJ](#), 116, 2443

- Munari, U., Milani, A., Valisa, P., & Semkov, E. 2010, The Astronomer's Telegram, 2808, 1
- Murakami, H., Baba, H., Barthel, P., et al. 2007, PASJ, 59, 369
- Nadyozhin, D. K. 1994, [ApJS, 92, 527](#)
- Najarro, F., Hillier, D. J., & Stahl, O. 1997, A&A, 326, 1117
- Nelemans, G., Yungelson, L. R., Portegies Zwart, S. F., & Verbunt, F. 2001, A&A, 365, 491
- Neugebauer, G., Habing, H. J., van Duinen, R., et al. 1984, ApJ, 278, L1
- Niemela, V. S., Ruiz, M. T., & Phillips, M. M. 1985, ApJ, 289, 52
- Nomoto, K., Tominaga, N., Tanaka, M., Maeda, K., & Umeda, H. 2007, in American Institute of Physics Conference Series, Vol. 937, Supernova 1987A: 20 Years After: Supernovae and Gamma-Ray Bursters, ed. S. Immler, K. Weiler, & R. McCray, 412
- Nugent, P. E. 2009, in Bulletin of the American Astronomical Society, Vol. 41, Bulletin of the American Astronomical Society, 419
- Ofek, E. O., Cameron, P. B., Kasliwal, M. M., et al. 2007, ApJ, 659, L13
- Oke, J. B., Cohen, J. G., Carr, M., et al. 1995, PASP, 107, 375
- Panagia, N., Vettolani, G., Boksenberg, A., et al. 1980, MNRAS, 192, 861
- Pandey, G., Lambert, D. L., & Rao, N. K. 2008, ApJ, 674, 1068
- Pastorello, A., Smartt, S. J., Mattila, S., et al. 2007, Nature, 447, 829
- Patat, F., Barbon, R., Cappellaro, E., & Turatto, M. 1993, A&AS, 98, 443
- Paxton, B., Bildsten, L., Dotter, A., et al. 2011, ApJS, 192, 3
- Percy, J. R. 1986, Journal of the American Association of Variable Star Observers (JAAVSO), 15, 126
- . 2007, Understanding Variable Stars (Cambridge: Cambridge University Press)
- Perley, D. A., Bloom, J. S., Klein, C. R., et al. 2010, MNRAS, 406, 2473
- Perley, D. A., Morgan, A. N., Updike, A., et al. 2011, AJ, 141, 36
- Perlmutter, S., Aldering, G., Goldhaber, G., et al. 1999, ApJ, 517, 565
- Perryman, M. A. C., Lindegren, L., Kovalevsky, J., et al. 1997, A&A, 323, L49
- Perryman, M. A. C., de Boer, K. S., Gilmore, G., et al. 2001, A&A, 369, 339
- Petrov, P. P., & Herbig, G. H. 2008, AJ, 136, 676
- Phillips, M. M. 1993, ApJ, 413, L105
- Pickles, A. J. 1998, PASP, 110, 863
- Pojmański, G. 1997, Acta Astron., 47, 467
- . 2000, Acta Astron., 50, 177
- Pojmański, G. 2001, in Astronomical Society of the Pacific Conference Series, Vol. 246, IAU Colloq. 183: Small Telescope Astronomy on Global Scales, ed. B. Paczynski, W.-P. Chen, & C. Lemme, 53
- . 2002, Acta Astron., 52, 397
- Poole, T. S., Breeveld, A. A., Page, M. J., et al. 2008, MNRAS, 383, 627
- Poznanski, D., Butler, N., Filippenko, A. V., et al. 2009, ApJ, 694, 1067
- Pozzo, M., Meikle, W. P. S., Fassia, A., et al. 2004, MNRAS, 352, 457
- Price, S. D., Smith, B. J., Kuchar, T. A., Mizuno, D. R., & Kraemer, K. E. 2010, ApJS, 190, 203
- Prieto, J. L., Garnavich, P. M., Phillips, M. M., et al. 2007, ArXiv e-prints, 706, [0706.4088](#)

- Quimby, R. 2006, in Bulletin of the American Astronomical Society, Vol. 38, Bulletin of the American Astronomical Society, 1216
- Quimby, R. M. 2008, in Astronomical Society of the Pacific Conference Series, Vol. 393, Astronomical Society of the Pacific Conference Series, ed. A. Frebel, J. R. Maund, J. Shen, & M. H. Siegel, 141
- Quimby, R. M., Aldering, G., Wheeler, J. C., et al. 2007a, *ApJ*, 668, L99
- Quimby, R. M., Wheeler, J. C., Höflich, P., et al. 2007b, *ApJ*, 666, 1093
- Quimby, R. M., Kulkarni, S. R., Kasliwal, M. M., et al. 2011, *Nature*, 474, 487
- Rakavy, G., & Shaviv, G. 1967, *ApJ*, 148, 803
- Rau, A., Ofek, E. O., Kulkarni, S. R., et al. 2008, *ApJ*, 682, 1205
- Rau, A., Kulkarni, S. R., Law, N. M., et al. 2009, *PASP*, 121, 1334
- Rayner, J. T., Cushing, M. C., & Vacca, W. D. 2009, *ApJS*, 185, 289
- Rebull, L. M., Guieu, S., Stauffer, J. R., et al. 2011, *ApJS*, 193, 25
- Reipurth, B., & Aspin, C. 2010, in Evolution of Cosmic Objects through their Physical Activity, ed. H. A. Harutyunian, A. M. Mickaelian, & Y. Terzian, 19
- Rest, A., Foley, R. J., Gezari, S., et al. 2011, *ApJ*, 729, 88
- Rettig, T. W., Brittain, S. D., Gibb, E. L., Simon, T., & Kulesa, C. 2005, *ApJ*, 626, 245
- Richards, J. W., Starr, D. L., Miller, A. A., et al. 2012a, *ApJS*, 203, 32
- Richards, J. W., Starr, D. L., Butler, N. R., et al. 2011, *ApJ*, 733, 10
- Richards, J. W., Starr, D. L., Brink, H., et al. 2012b, *ApJ*, 744, 192
- Richardson, D., Branch, D., Casebeer, D., et al. 2002, *AJ*, 123, 745
- Riess, A. G., Filippenko, A. V., Challis, P., et al. 1998, *AJ*, 116, 1009
- Riess, A. G., Filippenko, A. V., Li, W., et al. 1999, *AJ*, 118, 2675
- Roming, P. W. A., Kennedy, T. E., Mason, K. O., et al. 2005, *Space Science Reviews*, 120, 95
- Rupen, M. P., van Gorkom, J. H., Knapp, G. R., Gunn, J. E., & Schneider, D. P. 1987, *AJ*, 94, 61
- Russell, H. N. 1912a, *ApJ*, 35, 315
- . 1912b, *ApJ*, 36, 54
- Salamanca, I. 2000, Memorie della Societa Astronomica Italiana, 71, 317
- Salamanca, I., Terlevich, R. J., & Tenorio-Tagle, G. 2002, *MNRAS*, 330, 844
- Samus, N. N., Durlevich, O. V., & et al. 2008, VizieR Online Data Catalog, 1, 2025
- Sargent, W. L. W., & Filippenko, A. V. 1991, *AJ*, 102, 107
- Sato, S., Okita, K., Yamashita, T., et al. 1992, *ApJ*, 398, 273
- Savitzky, A., & Golay, M. J. E. 1964, Analytical Chemistry, 36, 1627
- Scannapieco, E., Madau, P., Woosley, S., Heger, A., & Ferrara, A. 2005, *ApJ*, 633, 1031
- Scargle, J. D. 1982, *ApJ*, 263, 835
- Schlegel, D. J., Finkbeiner, D. P., & Davis, M. 1998, *ApJ*, 500, 525
- Schlegel, E. M. 1990, *MNRAS*, 244, 269
- . 1996, *AJ*, 111, 1660
- Schlegel, E. M., & Petre, R. 2006, *ApJ*, 646, 378
- Schmidt, B. P., Kirshner, R. P., Leibundgut, B., et al. 1994, *ApJ*, 434, L19
- Schmidt, K. B., Rix, H.-W., Shields, J. C., et al. 2012, *ApJ*, 744, 147

- Semkov, E., & Peneva, S. 2010a, The Astronomer's Telegram, 2801, 1
 —. 2010b, The Astronomer's Telegram, 2819, 1
- Semkov, E. H., Peneva, S. P., Munari, U., Milani, A., & Valisa, P. 2010, *A&A*, 523, L3
- Sesar, B., Svilković, D., Ivezić, Ž., et al. 2006, *AJ*, 131, 2801
- Sesar, B., Ivezić, Ž., Lupton, R. H., et al. 2007, *AJ*, 134, 2236
- Sesar, B., Ivezić, Ž., Grammer, S. H., et al. 2010, *ApJ*, 708, 717
- Shapley, H. 1914, *ApJ*, 40, 448
- Silverman, J. M., Foley, R. J., Filippenko, A. V., et al. 2012, *MNRAS*, 425, 1789
- Skrutskie, M. F., Cutri, R. M., Stiening, R., et al. 2006, *AJ*, 131, 1163
- Smartt, S. J. 2009, *ARA&A*, 47, 63
- Smith, N. 2006, *ApJ*, 644, 1151
- Smith, N., & Brooks, K. J. 2007, *MNRAS*, 379, 1279
- Smith, N., Chornock, R., Li, W., et al. 2008a, *ApJ*, 686, 467
- Smith, N., Chornock, R., Silverman, J. M., Filippenko, A. V., & Foley, R. J. 2010a, *ApJ*, 709, 856
- Smith, N., Foley, R. J., & Filippenko, A. V. 2008b, *ApJ*, 680, 568
- Smith, N., Gehrz, R. D., & Goss, W. M. 2001, *AJ*, 122, 2700
- Smith, N., & Hartigan, P. 2006, *ApJ*, 638, 1045
- Smith, N., Hinkle, K. H., & Ryde, N. 2009a, *AJ*, 137, 3558
- Smith, N., & McCray, R. 2007, *ApJ*, 671, L17
- Smith, N., & Owocki, S. P. 2006, *ApJ*, 645, L45
- Smith, N., Vink, J. S., & de Koter, A. 2004, *ApJ*, 615, 475
- Smith, N., Li, W., Foley, R. J., et al. 2007, *ApJ*, 666, 1116
- Smith, N., Foley, R. J., Bloom, J. S., et al. 2008c, *ApJ*, 686, 485
- Smith, N., Silverman, J. M., Chornock, R., et al. 2009b, *ApJ*, 695, 1334
- Smith, N., Miller, A., Li, W., et al. 2010b, *AJ*, 139, 1451
- Soderberg, A. M., Gal-Yam, A., & Kulkarni, S. R. 2004, GRB Coordinates Network, 2586, 1
- Sollerman, J., Cumming, R. J., & Lundqvist, P. 1998, *ApJ*, 493, 933
- Soszyński, I., Udalski, A., Szymański, M. K., et al. 2009, *Acta Astron.*, 59, 335
 —. 2013, *Acta Astron.*, 63, 21
- Spitzer, L. 1978, Physical processes in the interstellar medium (New York: Wiley-Interscience)
- Stathakis, R. A., & Sadler, E. M. 1991, *MNRAS*, 250, 786
- Steinmetz, M., Zwitter, T., Siebert, A., et al. 2006, *AJ*, 132, 1645
- Stetson, P. B. 1987, *PASP*, 99, 191
 —. 1996, *PASP*, 108, 851
- Straizys, V., & Kuriliene, G. 1981, *Ap&SS*, 80, 353
- Subasavage, J. P., Bailyn, C. D., Smith, R. C., et al. 2010, in Society of Photo-Optical Instrumentation Engineers (SPIE) Conference Series, Vol. 7737, Society of Photo-Optical Instrumentation Engineers (SPIE) Conference Series
- Sugerman, B. E. K. 2005, *ApJ*, 632, L17
- Sugerman, B. E. K., & Crotts, A. P. S. 2002, *ApJ*, 581, L97
- Sugerman, B. E. K., Crotts, A. P. S., Kunkel, W. E., Heathcote, S. R., & Lawrence, S. S.

- 2005, *ApJ*, 627, 888
- Süveges, M., Sesar, B., Váradi, M., et al. 2012, *MNRAS*, 424, 2528
- Swope, H. H. 1928, Harvard College Observatory Bulletin, 857, 1
- Szeifert, T., Hubrig, S., Schöller, M., et al. 2010, *A&A*, 509, L7
- Tisserand, P. 2012, *A&A*, 539, A51
- Tisserand, P., Marquette, J. B., Beaulieu, J. P., et al. 2004, *A&A*, 424, 245
- Tisserand, P., Marquette, J. B., Wood, P. R., et al. 2008, *A&A*, 481, 673
- Tisserand, P., Wood, P. R., Marquette, J. B., et al. 2009, *A&A*, 501, 985
- Tisserand, P., Wyrzykowski, L., Wood, P. R., et al. 2011, *A&A*, 529, A118
- Tominaga, N., Tanaka, M., Nomoto, K., et al. 2005, *ApJ*, 633, L97
- Tonry, J., & Davis, M. 1979, *AJ*, 84, 1511
- Torres, G., Andersen, J., & Giménez, A. 2010, *A&A Rev.*, 18, 67
- Trundle, C., Pastorello, A., Benetti, S., et al. 2009, *A&A*, 504, 945
- Turatto, M., Cappellaro, E., Benetti, S., & Danziger, I. J. 1993, *MNRAS*, 265, 471
- Udalski, A., Szymanski, M., Kaluzny, J., Kubiak, M., & Mateo, M. 1992, *Acta Astron.*, 42, 253
- Uomoto, A., & Kirshner, R. P. 1986, *ApJ*, 308, 685
- Vacca, W. D., Cushing, M. C., & Rayner, J. T. 2003, *PASP*, 115, 389
- Van Dyk, S. D., Li, W., & Filippenko, A. V. 2006, *PASP*, 118, 351
- van Dyk, S. D., Weiler, K. W., Sramek, R. A., & Panagia, N. 1993, *ApJ*, 419, L69
- Voges, W., Aschenbach, B., Boller, T., et al. 1999, *A&A*, 349, 389
- Vogt, S. S., Allen, S. L., Bigelow, B. C., et al. 1994, in Society of Photo-Optical Instrumentation Engineers (SPIE) Conference Series, Vol. 2198, Society of Photo-Optical Instrumentation Engineers (SPIE) Conference Series, ed. D. L. Crawford & E. R. Craine, 362
- Vollmann, K., & Eversberg, T. 2006, *Astronomische Nachrichten*, 327, 862
- Wallerstein, G., & Knapp, G. R. 1998, *ARA&A*, 36, 369
- Wang, X., Li, W., Filippenko, A. V., et al. 2008, *ApJ*, 677, 1060
- Weiler, K. W., van der Hulst, J. M., Sramek, R. A., & Panagia, N. 1981, *ApJ*, 243, L151
- White, R. L. 1979, *ApJ*, 229, 954
- Williams, C. L., Panagia, N., Van Dyk, S. D., et al. 2002, *ApJ*, 581, 396
- Wizinowich, P. L., Le Mignant, D., Bouchez, A. H., et al. 2006, *PASP*, 118, 297
- Woosley, S. E., Blinnikov, S., & Heger, A. 2007, *Nature*, 450, 390
- Woosley, S. E., & Bloom, J. S. 2006, *ARA&A*, 44, 507
- Wright, E. L., Eisenhardt, P. R. M., Mainzer, A. K., et al. 2010, *AJ*, 140, 1868
- Young, K., Phillips, T. G., & Knapp, G. R. 1993, *ApJS*, 86, 517
- Yuan, F., Quimby, R., McKay, T., et al. 2008, The Astronomer's Telegram, 1515
- Zampieri, L., Mucciarelli, P., Pastorello, A., et al. 2005, *MNRAS*, 364, 1419
- Zaniewski, A., Clayton, G. C., Welch, D. L., et al. 2005, *AJ*, 130, 2293
- Začs, L., Mondal, S., Chen, W. P., et al. 2007, *A&A*, 472, 247
- Zechmeister, M., & Kürster, M. 2009, *A&A*, 496, 577